

MATARÉ

# DEFECT ELECTRONICS IN SEMICONDUCTORS

By HERBERT F. MATARÉ

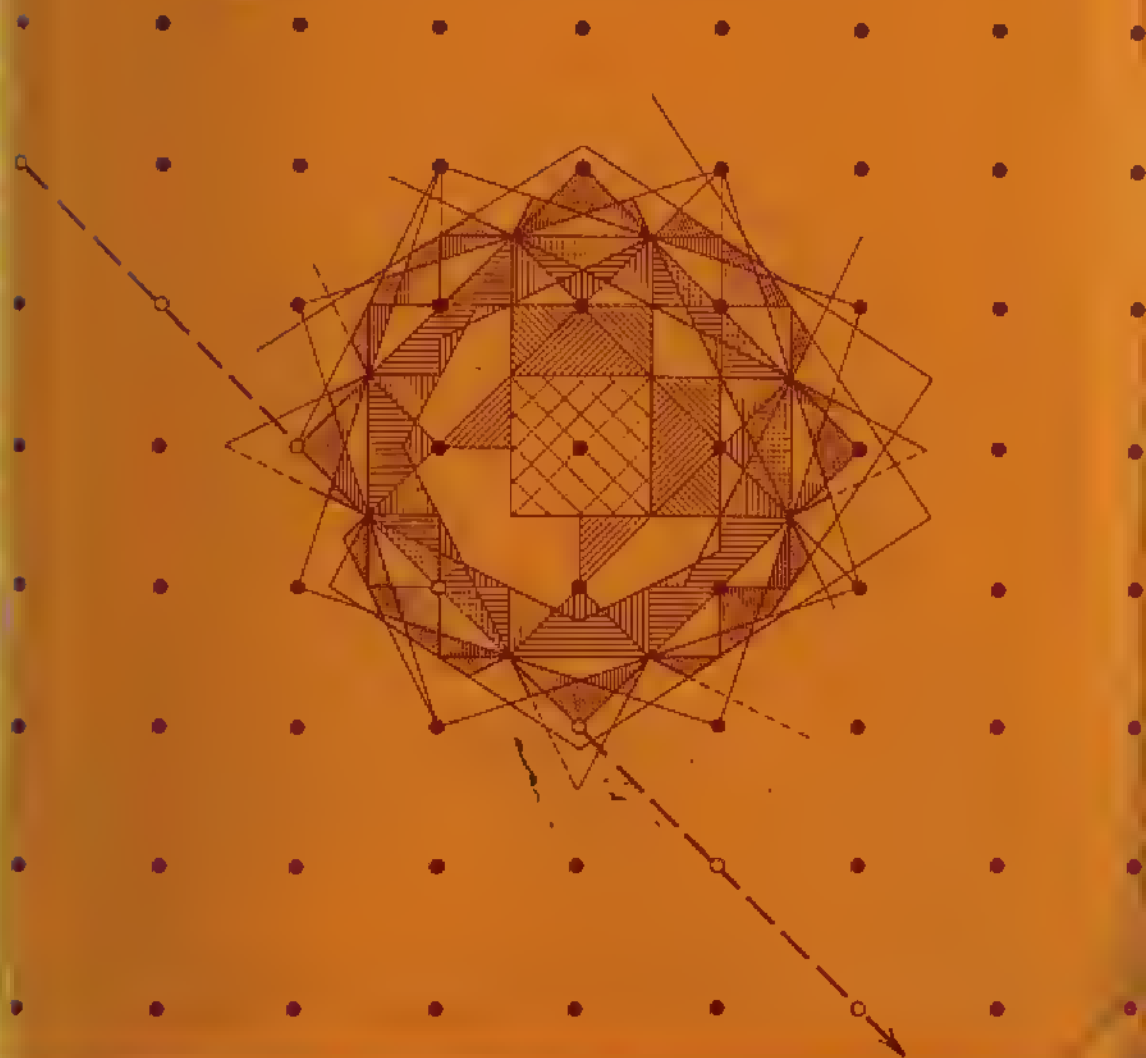
DEFECT  
ELECTRONICS IN  
SEMICONDUCTORS

548.  
842

MAT



WILEY-  
INTERSCIENCE



# **Defect Electronics in Semiconductors**

Διὰ τί, ἐὰν μὲν τις τὴν μέσην κινήσῃ ἡμῶν, ἀρμόσας τὰς  
ἄλλας χορδὰς καὶ χρῆται τῷ ὀργάνῳ, οὐ μόνον ὅταν κατὰ  
τὸν τῆς μέσης γένηται φθόγγον, λυπεῖ καὶ φαίνεται ἀνάρμοστον,  
ἀλλὰ καὶ κατὰ τὴν ἄλλην μελωδίαν.

Aristotle

*Harmony*, Problem XIX.20

Why is it that if anyone alters the tone in the middle string after the others have been tuned, and plays, everything sounds amiss, not merely when he comes to the middle tone, but throughout the entire melody?

# Defect Electronics in Semiconductors

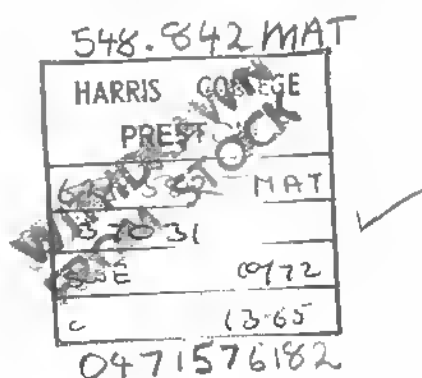
Herbert F. Mataré \*

*\* Science Advisor, International Solid State Electronics Consultants  
Consultant to Centralab-Semiconductors  
a division of Globe-Union, El Monte, California  
Visiting Professor, Physics Department,  
California State College, Fullerton*

**Wiley-Interscience**

a Division of John Wiley & Sons, Inc.  
New York · London · Sydney · Toronto





Copyright © 1971, by John Wiley & Sons, Inc.

All rights reserved. No part of this book may be reproduced by any means, nor transmitted, nor translated into a machine language without the written permission of the publisher.

Library of Congress Catalog Card Number: 79-138916

ISBN 0-471-57618-2

Printed in the United States of America

10 9 8 7 6 5 4 3 2 1

## Preface

This book deals with the electronic properties of defects mainly of the dislocation type. The transformation of electronics especially due to micro-miniaturization of solid-state devices would not have been achieved without significant progress in crystal growth. Dislocation-free monocrystals are a basic material today.

But as device design and monolithic technologies become more complex, a number of difficulties appear that have their origin in the very problem of crystalline perfection.

This is because process steps in device fabrication, e.g., diffusion, introduce defects such that originally defect-free monocrystals become imperfect and furthermore because semiconductor crystals in the form of thin films cannot be produced with sufficient perfection but are the necessary starting material in many technologies today. Although the reduction in size of individual devices allows for a better use of the good material between dislocations, there is a constant trend toward higher density of devices and yet higher-yield figures. Even for devices of an active area of only  $100 (\mu\text{m})^2$ , a crystal material of say  $10^6$  dislocations per  $\text{cm}^2$  puts an average of one dislocation on every junction surface.

In this state of affairs, it is important to know in detail what are the effects of defects, especially dislocations. As long as defect material is embedded into highly doped or metallized material, the field-free situation allows one to disregard the defects. Defects, however, contribute essentially to the behavior of devices, their performance characteristics, their life, and so on, when they appear within the zones of internal or applied electric fields.

It is therefore imperative to know the characteristics of defects in all field configurations and carrier-transport schemes and to understand their actual influence on device parameters. If a perfect state of the material cannot be achieved, at least the full knowledge of the influence of the defects can help

make pertinent predictions and derive useful design information from measured data. This is especially true for the case of radiation-induced damage in solid-state devices and for device production by ion implantation.

Most analyses in solid-state electronics and device physics start from idealized assumptions, such as a perfectly ordered crystal structure. The monocrystalline solid is already of high complexity without regard to defects because of the various forms of regular periodic lattices, their electronic band structure, and the impurity-carrier interactions.

When additional features, such as bipolar effects and geometrical zones like  $p$ - $n$  layers are discussed, the boundary conditions must be simplified in order to make solutions manageable. Therefore, the specific electronic effects of defects are generally treated as negligible. However, the field of electronics of defects, mainly dislocations, has gained such importance during the last years that refinements of the classical methods dealing with carrier transport in devices become desirable. Because the imperfect solid state in the form of thin films is the basis for devices being produced and because methods for device formation are applied that inherently cause defects and because defects are responsible for degradation, the full knowledge of all electronic effects of defects is imperative.

This text has been written to fill the gap between ideal and defect structure methods. Data and facts dealt with are scattered over a large body of literature in special areas covering the fields of chemical physics, metallurgy, physics, solid-state electronics, crystal growth, and device physics to infrared and quantum electronics. Based on material published over a period of more than ten years on our own work and covered in lectures that the author held in 1966 and 1967 as visiting professor at the engineering department of the University of California at Los Angeles, this book is intended to serve the researcher in the area of the defect solid state. It hopefully will simplify a search for basic facts and known results in the area of electronic effects of defects, mainly dislocations. It is also intended to be used as a textbook for graduate students in solid-state electronics and as a guide for the engineer in the semiconductor industry in the difficult task of evaluating the electronic material's parameters and their influence on device performance.

Starting with an introduction to the basic facts of carrier transport, but with an eye on the not-so-perfect or semiperiodic structure, the aspects of dislocations and their arrays are discussed. The intentional growth of dislocations and their behavior, as well as their possible use in devices, is also covered. It is actually the dislocation array or grain boundary that has revealed most of the striking properties of dislocations.

Although it is quite obvious that the electronic aspects of dislocations vary widely with the kind of semiconductor, e.g., III-V compounds versus the homopolar lattices of germanium and silicon, the prominent effects in

different materials are discussed under a general heading, because the basis of all these effects lies primarily in the lattice disturbance.

An important application of the knowledge about the electronic aspects of dislocations refers to the understanding of the behavior of thin films in devices and more generally the electronic behavior of amorphous materials. The case of the metal oxide semiconductor in the form of field effect devices has shown a number of astonishing effects, such as the mobility increase with gate field, which can be traced back to the surface states and the grained film structure as well as to the behavior of grain-boundary barriers under applied fields.

A general survey of all important measurement methods in order to assess crystal quality in the electronic sense concludes the treatise.

Choice and presentation of material has been influenced strongly by the questions and criticism during lecturing periods by the author both in industry and at universities. Fundamentals of charge carrier transport serve as an introduction in order to make the material presented independent to some extent as a textbook for lectures on crystal defects. In this form the text may be offered to graduate students with some background training in physics, solid-state fundamentals, or solid-state electronics. It is hoped that this, and the fact that such a treatise is timely, will help make this textbook a desired reference work for further research in this area and for introductory studies into the fascinating field of defect electronics, which is but one of the many new disciplines of solid-state electronics keeping this field a research area of high return.

The author wishes to express his gratitude to a number of colleagues for their assistance and advice.

In the early stages of the work on defined growth of dislocation arrays and their electronic properties, the author enjoyed the cooperation of Dr. G. Zielasek (Intermetall Corporation, Germany), Mr. A. McDonald, Drs. H. Kedesdy, J. Kohn, and R. Seidensticker (U.S. Army Electronics Laboratories, Fort Monmouth, New Jersey), Messrs. H. A. R. Wegener and H. Lawrence (Tung-Sol Electric Corporation, Bloomfield, New Jersey, and Bell Telephone Laboratories, New Jersey), Drs. P. H. Keck, B. Levinger, K. Arnold, G. Schwuttko, Messrs. O. Weinreich, and B. Reed (General Telephone & Electronics, Central Research Laboratories, Bayside, New York), and Dr. H. A. Schell (TEKADE Semiconductor Laboratory, Nuremberg, West Germany).

After 1960, in the course of low-temperature magnetoresistance and electro-optical studies on dislocation arrays, advice and assistance were given by Drs. D. C. Cronmeyer, J. Busse, and Mr. M. W. Beaubien (Bendix Research Laboratories, Southfield, Michigan) and by Drs. M. Macha and K. S. Cho (Advance Electronics Department, Missile & Space Systems Division, Douglas Aircraft Company, Santa Monica, California).

The author acknowledges gratefully the support and cooperation of Dr. B. Tougarinoff, Director of Research, Dr. R. Lescarts, Dr. Van Ouytsel, and a number of other specialists of Métallurgie Hoboken (Belgium) in the field of defects in crystal growth, a cooperation active for many years.

Thanks are also due to Dr. R. K. Mueller of Bendix for the submission of numerous preprints and reprints, to R. Maddox (Physics Department, California State College, Fullerton), to Dr. H. Lotsch (Autonetics), and Dr. S. Soclof (California State College, Los Angeles), for corrective criticism in reading the manuscript.

It is a pleasure to acknowledge the support of Mr. P. E. Corbiau, President and Administrateur Délégué of Métallurgie Hoboken, Belgium, Dr. R. Bowie, Vice President and Director of Research, General Telephone & Electronics, Inc., and Dr. W. Kock, Vice President and Corporate Director of Research of the Bendix Corporation.

Special thanks are extended to Dr. R. M. Ashby, Vice President of Technologies (Autonetics, A Division of North American Rockwell Corporation, Anaheim, California) for support and encouragement.

H. F. MATARÉ

*San Gabriel, California*

January 1, 1970

# Contents

<b>1</b>	<b>Introduction</b>	<b>1</b>
<b>2</b>	<b>Fundamentals of Charge Carrier Transport</b>	<b>5</b>
2-1	Wave Propagation in Periodic and Nearly Periodic Structures	5
2-2	Brillouin Zones, Bloch Wave Functions	12
2-3	Electrons in Periodic Fields [Band Theory]	25
2-4	Donors and Acceptors	29
2-5	Recombination	34
2-6	Photons, Phonons, and Electrons	38
2-7	Defect Electrons	43
2-8	The Effective Mass	47
2-9	Interband Transitions	53
2-10	Scattering	57
<b>3</b>	<b>Classification of Defects in Crystals</b>	<b>69</b>
<b>4</b>	<b>Dislocations as Imperfections of Linear and Planar Extent</b>	<b>83</b>
4-1	Edge Dislocations	85
4-2	Lineage and Low-Angle Boundaries	91
4-3	Screw Dislocations	94
4-4	Twinning	96
4-5	Dislocation Planes	101
<b>5</b>	<b>Continuum Theory of Dislocations</b>	<b>105</b>
<b>6</b>	<b>Radiation Damage and Dislocations</b>	<b>110</b>
		<b>ix</b>

<b>7</b>	<b>Main Mechanical Properties of Dislocation Planes</b>	<b>128</b>
7-1	Stress Field and Strain Energy	128
7-2	Grain-Boundary Energy and Stability	135
<b>8</b>	<b>Basic Electrical Properties of Dislocations in Semiconductors</b>	<b>145</b>
8-1	Electronic Properties of Twin Boundaries	149
8-2	Screw Dislocations	154
8-3	Edge Dislocations	157
8-4	Low-Angle Lineage and Grain Boundaries	162
8-5	Differences with Regard to the Host Lattice	167
<b>9</b>	<b>Anisotropy of Charge Carrier Transport</b>	<b>173</b>
9-1	The Edge Dislocation Pipe	173
9-2	Scattering by Dislocations [Statistical Distribution]	183
9-3	The Edge Dislocation and Resulting Space Charge	194
9-4	Electronic Occupation of Dislocation Centers	212
9-5	Dislocations and Nonradiative Recombination	222
9-6	Dislocations and Radiative Recombination	234
9-7	Electronic Noise and Dislocations	242
<b>10</b>	<b>The Electronic Properties of Dislocation Boundaries</b>	<b>252</b>
10-1	Lineage Boundaries	252
<b>11</b>	<b>Low-and Medium-Angle Grain Boundaries</b>	<b>261</b>
11-1	Sheet Conductance	261
11-2	Grain-boundary Barriers	282
11-3	Hall Effect Data	306
11-4	Magnetoresistance Effects	312
11-5	Transport Anisotropy	326
11-6	Field Effect	340
11-7	Photoelectric Effects	349
<b>12</b>	<b>Controlled Growth of Dislocations</b>	<b>365</b>
12-1	Plastic Deformation	365
12-2	Double-Seed Technique	367
12-3	Bicrystal Growth and Perfection	382
12-4	Grain-Boundary Diffusion and Impurity Distribution	393
<b>13</b>	<b>Device Applications</b>	<b>406</b>
13-1	Photoelectric (Micrometrical) Applications	406

	<b>Contents</b>	<b>xi</b>
13-2	Photoelectric Frequency Converters	414
13-3	The Dislocation Field-Effect Transistor	426
13-4	Stress-Strain Transducers	434
<b>14</b>	<b>Dislocations and the Electronic Properties of Semiconductor Devices</b>	<b>442</b>
14-1	Dislocations in Junction Devices in General	443
14-2	Dislocations and Semiconductor Laser Degradation	460
14-3	Dislocations in Bulk Devices	463
14-4	Dislocation Generation in Homoepitaxy and Heteroepitaxy	469
<b>15</b>	<b>Dislocations and Channel Conduction in Amorphous Semiconductors</b>	<b>509</b>
<b>16</b>	<b>Conclusions</b>	<b>536</b>
<b>Appendix</b>	<b>Measurements of Electronic Properties of Semiconductor Crystals and Films</b>	<b>539</b>
<b>Symbol Index</b>		<b>613</b>
<b>Author Index</b>		<b>621</b>
<b>Subject Index</b>		<b>627</b>





# Chapter 1 Introduction

Since the beginning of the intensified study of semiconductor crystals for the purpose of electronic-device applications, the understanding of dislocations in crystals has made great strides. The mechanical model of dislocations and its influence on the crystal lattice as a whole have been the basis also of the explanation of the marked changes in electronic-transport properties. This refers mainly to semiconductor crystals. In the case of metals, similar treatments have been pursued, but obviously the semiconductor, with its energy gap and need for explanations of detailed carrier-transport phenomena, is specifically useful in studying all phenomena involved.

While the mechanical theory of dislocations was progressing largely as a discipline of metallurgy, the electrical and electronic properties of dislocations were developed as a new field of solid-state electronics.

In dealing with the mechanical properties of dislocations, the question of the appropriate description arises. The continuum theory of dislocations as a macroscopic theory does not seem to allow for the necessary detailed knowledge, for it is not so much the question of the total change of the mechanical state of a crystalline solid with which we are concerned in solid-state electronics but the more localized state and its influence on electronic carrier transport. In addition, the continuum theory of crystal elasticity is based on the equilibrium conditions of a deformed body subjected to surface and volume forces. The relations between stress and strain tensors, however, are always assumed to be linear (Hooke's law). In this respect the theory is based on the reversible nature of small changes, but dislocations are permanent changes. The continuum theory can be usefully applied, however, once the total change of a crystal, due to built-in dislocations, is taken as a starting point and, again, small elastic changes are applied within Hooke's law in order to form a description of the body in terms of elasticity theory. Valuable information can be gathered this way, but the very desirable combination of plasticity theory

and residual stress for the calculation of state changes due to irreversible deformations is lacking. Such an elastoplasticity theory seems very desirable from the point of view of materials properties, but mainly for the determination of macroscopic mechanical changes. In such mechanical problems as workhardening and cold work, the sum of structural changes is the important magnitude. There is no principal difference between a monocrystal and a polycrystal as long as the orientation of the lattice is not important in itself.

The effects of point defects and disorder on crystal properties have found attention recently within the general activity in the field of *crystal dynamics*. Since the Mössbauer technique allowed one to study impurities as resonant nuclei directly either by the recoil-free fraction or the second-order Doppler shift, their dynamical properties became accessible. A. A. Maradudin\* has made important contributions and given excellent descriptions of this work.

The necessary impurity concentrations to study such effects lie, however, within ranges ( $10^{18} \text{ cm}^{-3}$  and higher) that are too high for our considerations concerning lasting defects like dislocations. Lattice dynamical methods are basically assessing the potential energy and the vibrations of the crystal as a whole and are thus a continuum-theoretical approach.

In the case of electronic properties of semiconductor crystals, a basic difference arises from the fact that microscopic layers of the crystal material are under consideration. In microminiaturization, thin-film physics and technology, in particular, layers in the range of 20 lattice constants are important. Polycrystals are out of the question if only because of the necessary reproducibility of electronic properties within defined crystal sections. Therefore, whenever we mention or use the continuum theory, we do so in order to make use of certain established rules for the calculation of mechanical results within the closer range of a stationary case of a formation of dislocations.

The primary task in dealing with the problems of the electronic properties of dislocations is then to deduce them from basic facts about their form and reaction on the lattice. Thus, a first task is the description of the generation of dislocations in a submacroscopic way, leaving room for a microscopic refinement.

In order to make the flow of information in this book coherent, Chapter 2 recapitulates some basic facts of carrier transport in solids, mainly semiconductors, and introduces the reader not so familiar with the subject to the main tools for dealing with electronic-transport problems. This is done, however, with an eye on defects and as a preparation for the use of these methods in special cases treated later. In order to give the reader a more detailed picture of the kinds of defects possible in crystals, we define, in Chapter 3, the different forms of defects and their interrelations.

\* See, for example, F. Seitz and D. Turnbull (eds.), "Solid State Physics," vol. 18, pp. 273ff.

In Chapter 4 the kinds of dislocations that can be singled out as linear or planar, constituting boundaries between crystal facets and having a special influence on carrier transport in crystals, are described in more detail.

The continuum theory and its advantage in dealing with some macroscopic consequences of microscopic displacements or arrays of displacements are outlined briefly in Chapter 5.

In Chapter 6 the dislocations from radiation damage are described briefly. The more detailed mechanical properties of dislocations are the subject of Chapter 7.

In Chapter 8 the electrical properties are derived from the preceding models. The more detailed electronic behavior of the main dislocations is the subject of Chapter 9. The outstanding planar dislocation in the form of lineage boundaries is discussed in Chapter 10. This is a dislocation structure subdividing a crystal into three distinct zones, two monocrystalline halves separated by the dislocation plane.

In Chapter 11 the more stable low- and medium-angle dislocation plane is introduced. Such a boundary can even be contacted by appropriate means and influences the carrier transport strongly. A detailed account is given of the influence of grain boundaries on conductivity, mobility, lifetime, and other important materials constants.

The controlled (not accidental) growth of dislocations and dislocation planes is described in Chapter 12.

As a consequence of the controlled growth of dislocation planes, a number of new device structures have been generated and are described in Chapter 13.

Finally in Chapter 14 the effect of dislocations on the electronic properties of devices is assessed. Special consideration is given to homoepitaxial and heteroepitaxial layers because of the increased importance of this field.

Chapter 15 finally describes the present situation in the field of disordered structures and correlates these facts with the features of dislocation arrays.

The approach chosen here emphasizes the free bond and the array of dangling bonds as the most important lattice disturbance.

There is no doubt that the resulting Cottrell atmosphere or the interaction between the dangling bonds and the impurity environment are complex problems, dependent on the kind of crystal dealt with. We have tried to assess this situation in the light of available facts. The new research field of amorphous structures is a very fruitful area of attack to the intricate problems of bond changes and phase changes.

The unusual degenerate channel conduction has features that seem to be related to the conduction in dislocation arrays.

The number of questions still unanswered is great in this field, and no attempt was made to decide if several switching effects exist or if they are all of the same kind. This field will develop in the near future, and it is hoped that

this book will help in the quest for a deeper understanding of the many influences of the disorder in periodic structures on carrier transport.

The main measurement methods to define electronic crystal properties are found in the appendix.

The areas of future research crystallizing out of the work reported so far are the following:

1. An assessment of the influence of diffusion on the grain-boundary properties by the growth of silicon and III-V compound bicrystals with very different doping ranges.
2. Measurement of diffusion profiles deeper within the bicrystal, where microcracking might play a minor role.
3. Study of the orientation dependence of the electronic properties of dangling-bond arrays.
4. Magnetoresistance of grain-boundary planes at low temperatures.
5. Noise of low-temperature field-effect devices based on bicrystals.
6. Photoelectric mixing at grain-boundary interfaces.
7. Recombination light emission and laser action from dislocation-plane junctions.
8. Measurements of the conductivity of amorphous semiconductor channels at low temperature (analogy to dangling-bond conduction?) (see Chapter 11).
9. Field effect at amorphous channels at low temperature.
10. Study of the band structure within a dislocation space-charge layer by cyclotron resonance in InSb bicrystals.

It goes without mentioning that beyond this there is a wealth of further lines of research related to thermoelectric and quantum-electronic effects worth pursuing.

## Chapter 2 Fundamentals of Charge Carrier Transport

### 2.1 WAVE PROPAGATION IN PERIODIC AND NEARLY PERIODIC STRUCTURES

A chain of particles of mass  $m$  coupled by elastic forces historically served as the first model of a periodic structure. If the  $x$  coordinate of the  $n$ th particle in equilibrium is given by

$$x_n = nd, \quad (2.1)$$

where  $d$  = particle distance,

a sine wave for  $y_n$  (vertical displacement of the  $n$ th particle) originates by a local displacement  $\Delta y_n$  of the  $n$ th particle:

$$\Delta y_n = A \cos 2\pi(vt - ax_n), \quad (2.2)$$

$$\Delta y_n = A \cos 2\pi(vt - and), \quad (2.3)$$

where  $v$  = frequency,

$a$  = wave number or  $1/\lambda$  ( $2\pi \cdot a$  is the wave vector  $\mathbf{k}$ ,  $\mathbf{k} \cdot \mathbf{d}$  is the wave phase angle.)

$A$  = constant (amplitude),

$t$  = time.

Here the wave number can be replaced by

$$a' = a \pm \frac{m}{d}, \quad (2.4)$$

where  $m$  = integer,

without any resulting change of the displacement form.

The frequency  $\nu$ , therefore, is, a periodic function of  $a$  with the periodicity  $1/d$ . The phase velocity  $v = \nu \cdot \lambda$  is the slope of the  $\nu(a)$  function, which, in turn, is given by

$$\nu(a) = B |\sin \pi a d|, \quad (2.5)$$

where  $B = \text{constant (amplitude)}$ .

To avoid ambiguity in wavelength and direction of motion, we define the region of positive phase velocity only, which restricts  $a$  to the interval

$$a = \pm \frac{1}{2d}$$

or, more precisely,

$$-\frac{1}{2d} \leq a \leq +\frac{1}{2d}. \quad (2.6)$$

The phase or propagation velocity of the wave is

$$v_p = \left| \frac{\nu(a)}{a} \right|, \quad (2.7)$$

and, with (2.5),

$$v_p = B \left| \frac{\sin \pi a d}{a} \right|. \quad (2.8)$$

Defining a velocity  $v_\infty$  for infinite wavelength  $\lambda = 1/a$ , that is,  $a = 0$ , we have

$$v_\infty = \pi d B \quad (2.9)$$

and thus the famous wave-velocity equation (Baden-Powell)<sup>1</sup>

$$v = v_\infty \frac{|\sin \pi d / \lambda|}{|\pi d / \lambda|} \quad (2.10)$$

for wave propagation in a cubic lattice structure represented by a monatomic linear chain of the simple kind shown in Figure 2.1. Frequency  $\nu$  and velocity  $v$  are both plotted versus the wave number  $a$ . With the restriction (2.6), the most important part of the dispersion curve  $\nu = f(a)$  or  $\nu = f(k)$ , with wave vector  $k = 2\pi a = 2\pi/\lambda$ , is situated between  $-1/2d$  and  $+1/2d$ , positive  $\nu(a)$  for  $a$  increasing, representing the first *Brillouin zone*<sup>1</sup>. Higher-order zones of lattice excitation are coherently shaded in Figure 2.1. These zones correspond to the same transversal-wave excitation and give similar dispersion curves  $\nu = f(a)$  with the same zero point. If the masses  $m$  and force constants  $\gamma$  are equal (see Figure 2.2), a displacement  $\Delta_n$  of the  $n$ th atom causes a force

$$F_n = \gamma(\Delta_{n+1} - \Delta_n) - \gamma(\Delta_n - \Delta_{n-1}). \quad (2.11)$$

This gives a motion equation (Newton's second law)

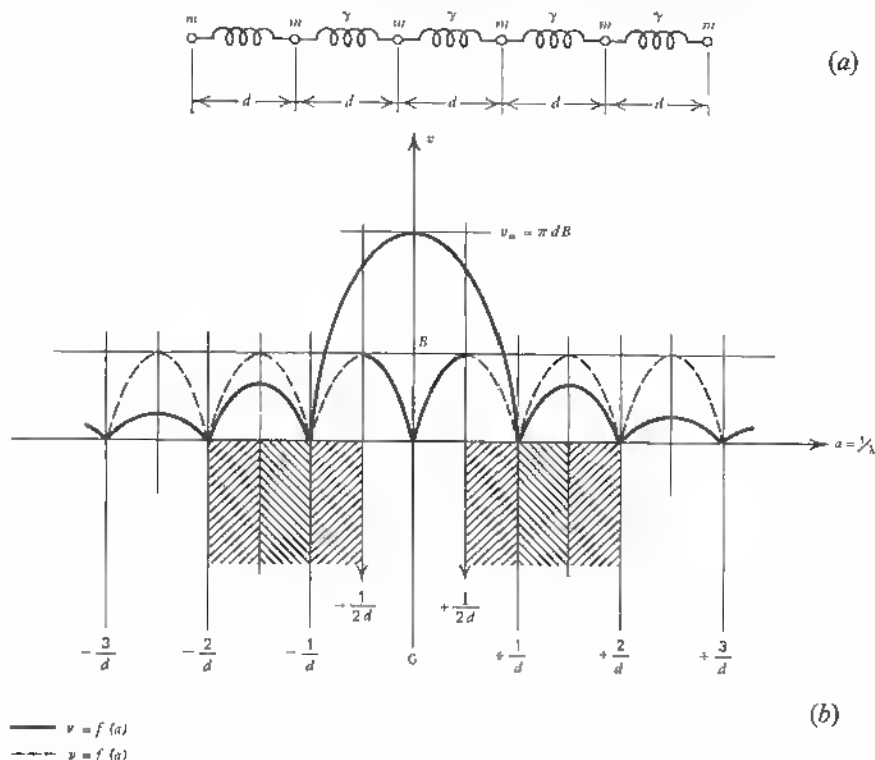


Fig. 2.1 (a) Mechanical equivalent of linear chain.

$\gamma$  = elastic force constant

$m$  = mass

$d$  = distance

(b) wave velocity and frequency as a function of wave number  $a$ .

$$m \frac{d^2 \Delta_n}{dt^2} = \gamma (\Delta_{n+1} + \Delta_{n-1} - 2\Delta_n) \quad (2.12)$$

for all atoms coupled by the force fields in the linear chain resulting in  $n$  equations for  $n$  atoms. These differential equations represent the possible lattice vibrational modes with angular frequency  $\omega = 2\pi f$ . The displacement  $\Delta_n$  can be represented by the complex form

$$\Delta_n(\omega, k) = A \exp[i(\omega t - knd)], \quad (2.13)$$

where  $A$  = amplitude of Fourier component,

$nd$  = equilibrium position of  $n$ th atom,

$k = 2\pi/\lambda$  = wave vector.



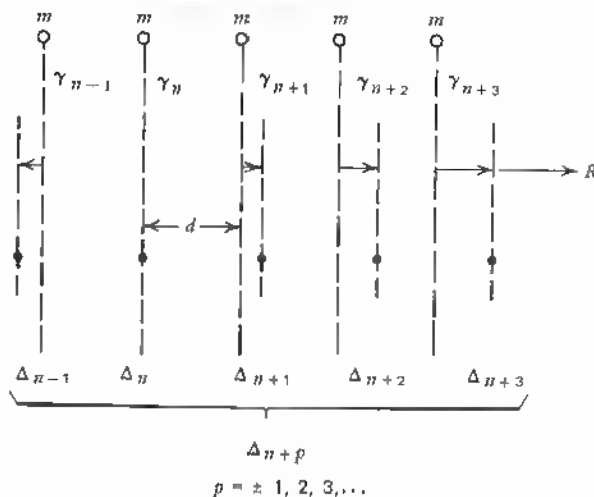


Fig. 2.2 Displacements in linear chain with equal masses  $m$ .

Equations like (2.13) are valid for all  $\Delta$ 's by appropriately changing from  $\Delta_n$  to  $\Delta_{n+1}$ , and so on. From (2.12) and (2.13), one gets

$$-\omega^2 m = \gamma [\exp(ikd) + \exp(-ikd) - 2], \quad (2.14)$$

or

$$\omega = \pm \left( \frac{4\gamma}{m} \right)^{1/2} \sin \frac{kd}{2}. \quad (2.15)$$

This is again the analytic  $\omega$  expression (2.5) derived previously in a heuristic way (see Figure 2.1). In the case of equal masses  $m$  and equal force constants  $\gamma$ , there is no reason for phase differences between the moving atoms of the chain. All particles are displaced by the same amount and in the same direction. If we consider physical crystal models, however, we generally have different masses or different forces or both e.g. Born's model for NaCl (see Figure 2.3). In this case, an important change takes place. The displacements of masses  $m_1$  and  $m_2$  can be out of phase. They generally move against each other in opposite directions (for neighboring atoms) and retain a stationary center of mass. Therefore, we have, for example, for different masses  $m_1$ ,  $m_2$  but equal forces

$$\begin{aligned} m_1 \frac{d^2 \Delta_{2n+1}}{dt^2} &= \gamma (\Delta_{2n+2} + \Delta_{2n} - 2\Delta_{2n+1}), \\ m_2 \frac{d^2 \Delta_{2n}}{dt^2} &= \gamma (\Delta_{2n+1} + \Delta_{2n-1} - 2\Delta_{2n}), \end{aligned} \quad (2.16)$$

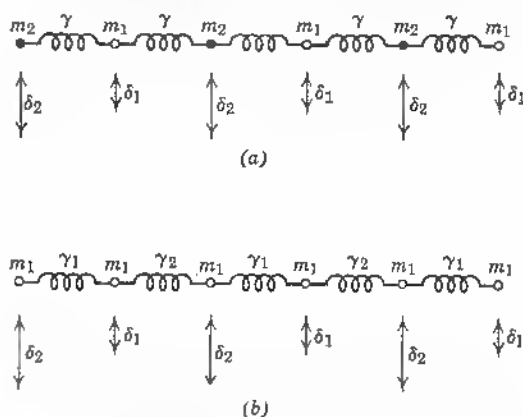


Fig. 2.3 (a) Linear chain models with two different masses  
(b) Linear chain model with two different forces

with the lattice displacements

$$\begin{aligned}\Delta_{2n} &= A \exp [i(\omega t + 2knd)], \\ \Delta_{2n+1} &= B \exp \{i[\omega t + k(2n+1)d]\}.\end{aligned}\quad (2.17)$$

Substituting (2.17) into (20.16) and solving for  $\omega$  yield the famous equation

$$\omega^2 = \gamma \left( \frac{1}{m_1} + \frac{1}{m_2} \right) \pm \gamma \left[ \left( \frac{1}{m_1} + \frac{1}{m_2} \right)^2 - \frac{4 \sin^2 kd}{m_1 m_2} \right]^{1/2} \quad (2.18)$$

typical of the two different vibrational modes shown in Figure 2.4. These modes are of great importance in real lattices and give the values for  $\omega$  at the limits. Since the lower function corresponds to in-phase movement of nearest neighbors (odd- and even-numbered atoms), it is called the *acoustical* branch, because the lower frequencies generated in this kind of excitation correspond to the acoustical frequency range for most crystals. The upper branch is called the *optical* branch, because these frequencies belong in the electromagnetic respectively infrared frequency range.

The frequency versus wave-number functions in Figure 2.4 can have different bands if more than two different particle masses or more than two force constants are involved, but the main difference between their frequency range remains the cophase or contraphase movement of nearest neighbors.

In looking at the periodic structure in the simple model, one can assess the effect of primitive lattice disturbances like vacancies or interstitials. Consider a less drastic form—a displacement of one atom by a heavier or lighter one,

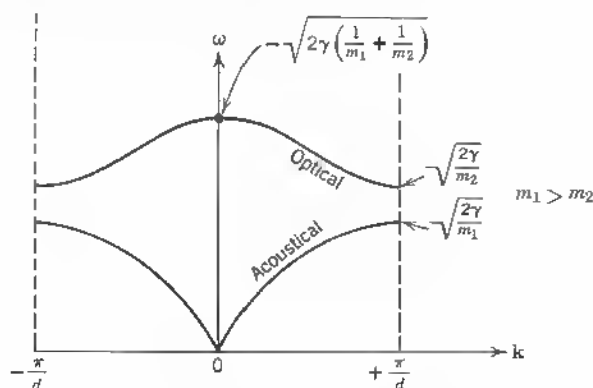
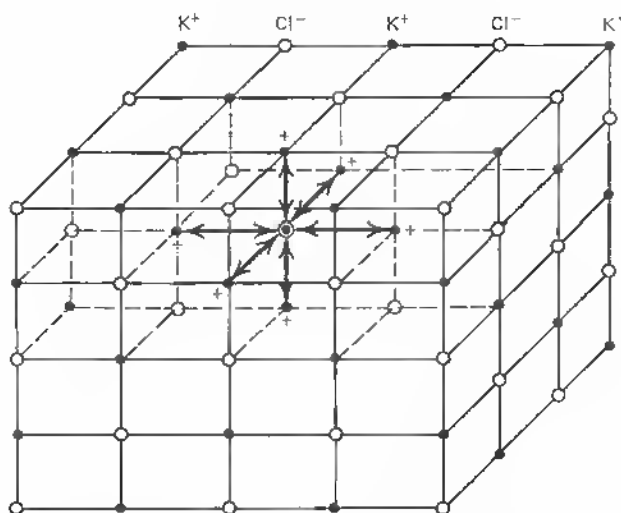


Fig. 2.4 Frequency versus wave vector.

Fig. 2.5 Replacement of  $\text{Cl}^-$ -ion by  $\text{H}^-$ -ion in  $\text{K}^+\text{Cl}^-$ -lattice and formation of a resonance center.

for example, or a displacement of an ion in an ionic lattice, such as  $\text{KCl}$  by hydrogen, for example (see Figure 2.5). In this case, the light ion ( $\text{H}^-$ ) within the positive  $\text{K}^+$  cloud has its own frequency of vibration with an optically active electric dipole moment.

On account of the very localized nature of this defect, the additional vibrational modes decrease rapidly with the distance from the defect (actually exponentially). In a simple mathematical case, a linear lattice of equal atomic

masses  $m$  contains one atom with a different mass  $m'$ . Assessing only nearest-neighbor interactions and putting the atom  $m' < m$  at the origin, the equations of motion, corresponding (2.12), can be written

$$m' \frac{d^2 \Delta_0}{dt^2} = \gamma(\Delta_1 + \Delta_{-1} - 2\Delta_0), \quad (2.19)$$

$$m \frac{d^2 \Delta_1}{dt^2} = \gamma(\Delta_2 + \Delta_0 - 2\Delta_1). \quad (2.20)$$

A solution of (2.19) and (2.20) has to be damped exponentially for increasing distance from  $v = 0$  (see Figure 2.1).

The dispersion relation or the  $\omega$  versus wave vector function is of the form (2.15), and since  $\sin^2(\alpha/2) = (1 - \cos \alpha)/2$ , the dispersion relation can also be written

$$\omega^2 = \frac{2\gamma}{m} (1 - \cos kd). \quad (2.21)$$

Hence the maximum frequency is

$$\omega_{\max} = \left( \frac{4\gamma}{m} \right)^{1/2}. \quad (2.22)$$

For higher frequencies,  $k$  cannot be real but has a form

$$k = k_r + ik_i.$$

By developing  $\cos(k_r + ik_i)nd$  and choosing  $k_r nd = n\pi$ , the imaginary part is eliminated and a solution to (2.19) and (2.20) can be found<sup>2</sup> that leads to the dispersion relation

$$\omega^2 = \omega_{\max}^2 \frac{m^2}{2mm' - m'^2}, \quad (2.23)$$

with  $\omega_{\max} = (4\gamma/m)^{1/2}$  as cutoff frequency of the unperturbed lattice. In this case  $m = m'$ . If  $m' \ll m$ , (2.23) reduces to

$$\omega = \omega_{\max} \left( \frac{m}{2m'} \right)^{1/2}. \quad (2.24)$$

We see that the localized phonon frequency at the  $H^-$ , or U center, where the lighter atom generates new modes, increases with increasing ratio  $m/m'$  or with decreasing  $m'$  at the defect point. In principle, a vacancy, therefore, can generate high local lattice modes. In the environment of heavy surrounding atoms the damping is considerable and leads to an early extinction within a few lattice constants.

If, however, a localized defect comprises several atom sites and especially if such a defect structure has some order on its own or represents, for example, a line defect (lineage) with a clear relation to the host lattice, such localized defect modes can substantially increase in amplitude. The lattice motions (see Figure 2.2) for such a lattice substructure lead to standing wave modes on account of the bounds on either side of a sublattice or periodic disturbance (see Figure 2.6). This is seen mathematically by representing the substructure

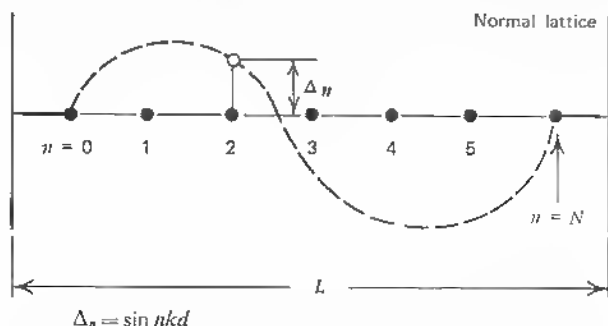


Fig. 2.6 Elastic line of  $n$  atoms or of  $n$  defect atoms within lattice structure.

again by, for example, a one-dimensional line of particles leading to a standing wave of the kind

$$\Delta_n = \Delta(0)e^{-i\omega t} \sin nkd. \quad (2.25)$$

On account of the limitation  $L$  of the size of the sublattice (fix points at either end),  $k$  is restricted to the values<sup>2</sup>

$$k = \frac{\pi}{L}; \frac{2\pi}{L}; \frac{3\pi}{L}; \dots; \frac{n\pi}{L}.$$

The solution (2.25) vanishes for  $n=0$  and  $n=N$  (fixed points) and yields, for points between, a number  $k = \pi/Nd$  independent values or modes.

The analogy between defect or sublattice excitation and bound lattice modes helps explain a number of effects connected with the infrared vibration spectra of imperfect crystals. "Imperfect" refers also to nonstoichiometric distribution of foreign atoms within the host atom and the influence of the resulting additional local modes on line spectra for the respective observed vibrational fine structures—in fluorescence measurements,<sup>3</sup> for example.

## 2.2 BRILLOUIN ZONES, BLOCH WAVE FUNCTIONS

A periodic lattice structure supports the transport of electron-wave packages as it supports elastic waves. The atomic center points form the potential

troughs. The electrostatic forces acting on the moving charges are described in the same mathematical form as the elastic forces.

As we noted in Section 2.1, the equations of motion or Newton's second law for the lattice particles leads to a solution in the form of a periodic function. In fact, Newton's equation for a lattice with only one kind of atom (see Figure 2.2) is, for example,

$$m \frac{d^2 \Delta_n}{dt^2} = \sum_p \lambda_p (\Delta_{n+p} - \Delta_n), \quad (2.26)$$

where  $p = 1, 2, 3, \dots$  indicates the lattice plane to which the force applies. In case of nearest-neighbor relations only,  $p = 1$ , (2.26) has the typical solution in form of a traveling wave:

$$\Delta_{n+p} = \Delta(0) e^{i[(n+p)kd - \omega t]}, \quad (2.27)$$

where  $d$  = spacing between planes,

$k$  = wave vector.

Introducing (2.27) into (2.26) leads to

$$-\omega^2 m \Delta(0) e^{i(nkd - \omega t)} = \Delta(0) \sum_p \lambda_p (e^{i(n+p)kd} - e^{inkd}) e^{-i\omega t}, \quad (2.28)$$

which, for  $n = 0$  leads to

$$\omega^2 m = - \sum_p \lambda_p (e^{ipkd} - 1). \quad (2.29)$$

Assuming a Bravais lattice (translational symmetry), one has

$$\lambda_p = \lambda_{-p},$$

and (2.29) can also be written

$$\omega^2 m = - \sum_{p>0} \lambda_p (e^{ipkd} + e^{-ipkd} - 2). \quad (2.30)$$

This equation leads again to the usual dispersion relation  $\omega^2 = (2\lambda/m) \times (1 - \cos kd)$  for  $p = 1$  [see (2.15)] since

$$2 \cos pkd = e^{ipkd} + e^{-ipkd}. \quad (2.31)$$

If a wave given in the form (2.27), either of the longitudinal or of the transversal kind, travels through a periodic structure, it is the lattice form or cell length  $d$  that defines the periodicity. In frequency versus wave-number space, however, the cell length is  $1/d$ . A *reciprocal* lattice, therefore, gives the periodicity of the *frequency* of the propagating waves. The reciprocal lattice gives important information on the conditions of wave propagation and reflection in periodic structures; it specifically satisfies the Bragg condition directly for the generation of reflected wave fronts, as will be shown. Defect structures

can also be transferred from the direct to the reciprocal lattice, and the consequent changes in the reflection of lattice waves can be found.

The methods are similar for one, two, or three dimensions. For simplicity, we consider only the two-dimensional case.

In Figure 2.7 the two-dimensional case is sketched for atoms of equal spacing and mass with an arbitrary intersection angle  $\theta$ . The two basic lattice

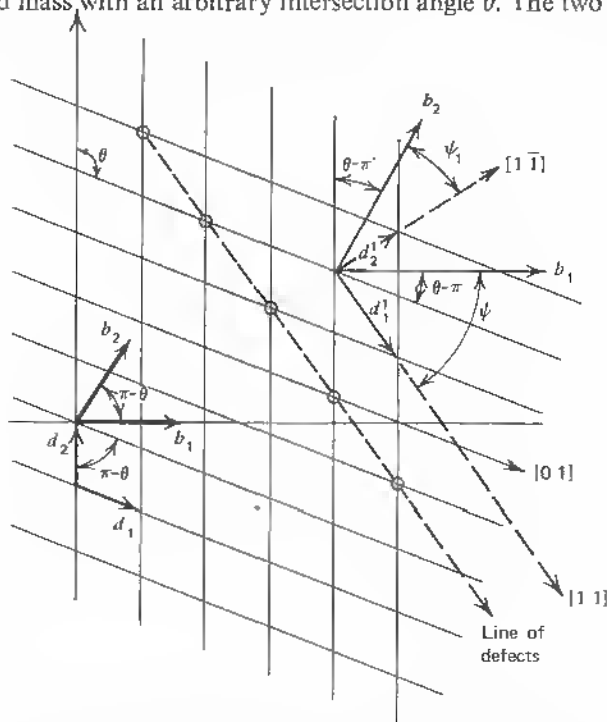


Fig. 2.7 Defect (vacancy) line in periodic lattice and Bragg-reflection conditions (see text).

vectors are  $d_1$  and  $d_2$  (direct lattice), and  $b_1$  and  $b_2$  represent the reciprocal lattice, which has to satisfy the conditions

$$(b_i \cdot d_k) = \delta_{ik} = \begin{cases} 1 & \text{for } i = k, \\ 0 & \text{for } i \neq k, \end{cases} \quad (2.32)$$

which also means that

$$\begin{aligned} b_1 &\perp d_2 \\ b_2 &\perp d_1 \end{aligned}$$

where  $\delta_{ik}$  = Kronecker's  $\delta$ .

The basic system or direct lattice can be represented by a matrix

$$D = \begin{pmatrix} d_{1x} & d_{1y} \\ d_{2x} & d_{2y} \end{pmatrix}, \quad (2.33)$$

and the reciprocal system by

$$B = \begin{pmatrix} b_{1x} & b_{2x} \\ b_{1y} & b_{2y} \end{pmatrix}. \quad (2.34)$$

Since  $B$  and  $D$  are connected by the product (2.32),  $\mathbf{d}_1$  and  $\mathbf{d}_2$  are row vectors and  $\mathbf{b}_1$  and  $\mathbf{b}_2$  column vectors. The reciprocal-lattice condition appears in the formation of the matrix product.

$$D \cdot B = \begin{pmatrix} d_{1x} & d_{1y} \\ d_{2x} & d_{2y} \end{pmatrix} \begin{pmatrix} b_{1x} & b_{2x} \\ b_{1y} & b_{2y} \end{pmatrix}, \quad (2.35)$$

$$D \cdot B = \begin{pmatrix} d_{1x}b_{1x} + d_{1y}b_{1y} & d_{1x}b_{2x} + d_{1y}b_{2y} \\ d_{2x}b_{1x} + d_{2y}b_{1y} & d_{2x}b_{2x} + d_{2y}b_{2y} \end{pmatrix}. \quad (2.36)$$

With the condition (2.32), this leads to

$$D \cdot B = \begin{pmatrix} 1 & 0 \\ 0 & 1 \end{pmatrix} = \delta, \quad (2.37)$$

or

$$B = D^{-1} \quad (\text{reciprocity}). \quad (2.38)$$

A consequence of this is the reciprocity also of the lattice-cell areas:

$$S_d \cdot S_r = 1. \quad (2.39)$$

This is immediately seen by forming

$$\begin{aligned} S_d &= \mathbf{d}_1 \times \mathbf{d}_2 = |\mathbf{d}_1| |\mathbf{d}_2| \sin \theta \\ S_r &= \mathbf{b}_1 \times \mathbf{b}_2 = |\mathbf{b}_1| |\mathbf{b}_2| \sin \theta \end{aligned} \quad (2.40)$$

(see Figure 2.7).  $\theta$  = angle of intercept of lattice rows.

Now, since, according to (2.32),

$$\begin{aligned} (\mathbf{b}_1 \cdot \mathbf{d}_1) &= 1 = |\mathbf{b}_1| |\mathbf{d}_1| \cos\left(\frac{\pi}{2} - \theta\right) \\ &= |\mathbf{b}_1| |\mathbf{d}_1| \sin \theta, \end{aligned} \quad (2.41)$$

and

$$\begin{aligned} (\mathbf{b}_2 \cdot \mathbf{d}_2) &= 1 = |\mathbf{b}_2| |\mathbf{d}_2| \cos\left(\frac{\pi}{2} - \theta\right) \\ &= |\mathbf{b}_2| |\mathbf{d}_2| \sin \theta, \end{aligned} \quad (2.42)$$

or

$$\begin{aligned} |\mathbf{b}_1| &= \frac{1}{|\mathbf{d}_1| \sin \theta}, \\ |\mathbf{b}_2| &= \frac{1}{|\mathbf{d}_2| \sin \theta}. \end{aligned} \quad (2.43)$$



The product  $S_d \cdot S_r$  is

$$S_d \cdot S_r = |\mathbf{d}_1| |\mathbf{d}_2| \sin \theta \frac{\sin \theta}{|\mathbf{d}_1| \sin \theta |\mathbf{d}_2| \sin \theta} = 1. \quad (2.44)$$

This condition is equivalent to stating that the distance  $d$  in the direct lattice that defines  $\lambda$  is equivalent to  $1/d$ , which, in turn, defines  $\nu$  in the reciprocal lattice.

In other words,

Direct lattice: Cell length  $d$ ;  $\lambda = f(d)$

Indirect lattice: Cell length  $1/d = a$ ;  $\nu = f(a)$

The propagation of waves through the two dimensional lattice structure is characterized by the wave functions

$$\psi = A e^{i(\omega t - 2\pi a_1 x - 2\pi a_2 y)} \quad (2.45)$$

or

$$\psi = A e^{i[\omega t - 2\pi(\mathbf{a} \cdot \mathbf{r})]} \quad (2.46)$$

as solutions of the wave equation

$$\nabla^2 \psi - \frac{1}{v^2} \ddot{\psi} = 0, \quad (2.47)$$

where  $v$  = phase velocity as  $f(d_1; d_2)$ .

If a reflected wave has the same wave numbers  $a_n$ , a Bragg reflection occurs. For the two-dimensional case,  $a_{n_1, n_2}$  is the wave number, and  $n_1$  and  $n_2$  define the atomic planes. Denoting  $a$  for which a Bragg reflection occurs  $a_0$ , the reflection condition is

$$|\mathbf{a}'_0| = |\mathbf{a}_0|, \quad (2.48)$$

where  $\mathbf{a}'_0$  stands for  $\mathbf{a}'_{n_1, n_2}$ . Introducing any new wave vector

$$\mathbf{a}'_0 = \mathbf{a}_0 - \mathbf{B} \quad (2.49)$$

and squaring yield

$$|\mathbf{a}'_0|^2 = |\mathbf{a}_0|^2 - 2(\mathbf{a}_0 \cdot \mathbf{B}) + |\mathbf{B}|^2. \quad (2.50)$$

Squaring  $\mathbf{a}_0 = \mathbf{a}'_0 + \mathbf{B}$  leads to

$$|\mathbf{a}_0|^2 = |\mathbf{a}'_0|^2 + 2(\mathbf{a}'_0 \cdot \mathbf{B}) + |\mathbf{B}|^2. \quad (2.51)$$

On account of condition (2.48), equations (2.50) and (2.51) must have the same value, which means that

$$|\mathbf{B}|^2 = 2(\mathbf{a}_0 \cdot \mathbf{B}) = -2(\mathbf{a}'_0 \cdot \mathbf{B}). \quad (2.52)$$

Therefore

$$|a_0| \cos(a_0, B) = -|a'_0| \cos(a'_0, B) = \frac{1}{2} |B|, \quad (2.52)$$

or

$$|a_0| \cos \varphi = \frac{1}{\lambda} \cos \varphi = \frac{B}{2} = \frac{1}{2\delta}. \quad (2.53)$$

Here we have introduced

$$B = \frac{1}{\delta}$$

where  $\delta$  = distance between successive rows of atoms.

This means that  $B$  defines the atom row responsible for the Bragg reflection. The condition (2.53)

$$\frac{1}{\lambda} \cos \varphi = \frac{1}{2\delta}$$

can be written in a general way:

$$m\lambda = 2\delta \cos \varphi, \quad (2.54)$$

which is the well-known Bragg reflection condition (see Figure 2.8). The construction of a reciprocal lattice (Brillouin zones), therefore, is a method to see quickly under which angles of incidence and for which wavelength a lattice gives a reflected beam.

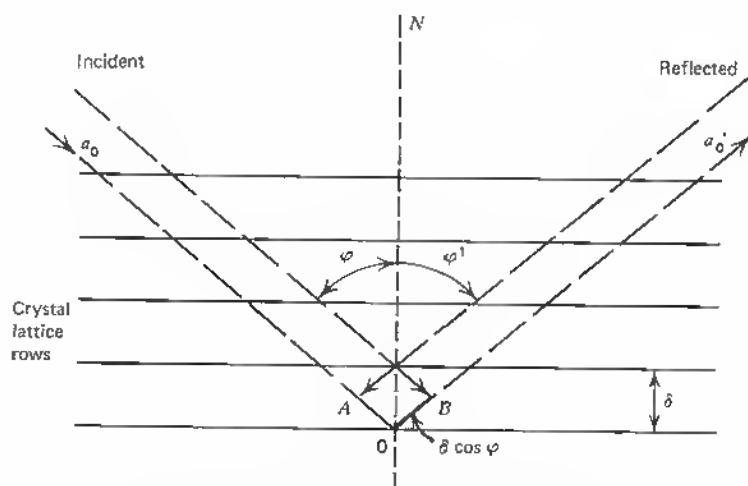


Fig. 2.8 Bragg-reflection condition:  $AOB = 2\delta \cos \varphi = n\lambda$ .

We can derive the same result or demonstrate the importance of the reciprocal lattice also starting with the Laue diffraction condition. Before doing so, we mention that in periodic structures the wave-function equations (2.45) and (2.46) can be considered to have an amplitude that is a function of the lattice periodicity or of the position and wave vectors:

$$A \cdot e^{-2\pi i(\mathbf{n} \cdot \mathbf{r})}$$

This is because the solution of the wave equation (2.47) has a time-dependent and space-dependent part:

$$\psi = \psi_0(x, y)e^{i\omega t}. \quad (2.55)$$

In solution (2.55) these parts are separable, and a time-independent wave equation for  $\psi_0$  follows:

$$\nabla^2 \psi_0 + \frac{\omega^2}{V^2} \psi_0 = 0. \quad (2.56)$$

$V$  = phase velocity (see Section 2.3).

The solution of (2.56) is generally expressed as

$$\psi = A(r)e^{2\pi i[(vt - (\mathbf{n} \cdot \mathbf{r}))]}, \quad (2.57)$$

which is the original form of Bloch's wave function (see Section 2.3).

In a one-dimensional case,  $r = nd$ , where  $n$  designates the point mass  $n$  at the coordinate  $r$ . Since  $a = 1/\lambda$ , the wave function  $\psi_n = A(r)e^{2\pi i(vt - and)}$  can also be written

$$\psi_n = A(r)e^{i(\omega t - knd)},$$

where

$$k = 2\pi a = \frac{2\pi}{\lambda},$$

$$v = v\lambda.$$

Thus

$$\begin{aligned} \psi_n &= A(r)e^{i(\omega t - 2\pi n v(d/v))} \\ &= A(r)e^{i\omega[1 - n(d/v)]}, \end{aligned} \quad (2.58)$$

which is the form of a running wave.

Another way of writing the Bloch wave is by introduction of the crystal momentum

$$\begin{aligned} P_{x, y, z} &= \pm \frac{\hbar}{\lambda} \\ &= \pm \frac{\hbar v}{v} \\ &= \pm \frac{E_p}{v} \end{aligned}$$

where  $E_p$  = energy of traveling wave. (Ref. 7).

Now

$$\psi_n(r) = A(r)e^{i(vt - knd)}$$

leads to the wave equation for one dimension, for example:

$$\begin{aligned}\psi_p(x, t) &= A_p(x) \exp \left( 2\pi i v \frac{x}{v} - iknd \right) \\ &= A_p(x) \exp \left[ \frac{2\pi i}{h} \left( p_x \cdot x - \frac{hkn d}{2\pi} \right) \right].\end{aligned}$$

Since

$$k = 2\pi/\lambda \quad \text{and} \quad kd = 2\pi \frac{x}{n} \frac{v}{v},$$

we have

$$nkd = 2\pi vt.$$

Therefore

$$\psi_p(x, t) = A_p(x) \exp \left[ \frac{2\pi i}{h} (p_x \cdot x - E_p \cdot t) \right]$$

(see, for example, Ref. 7).

In a three-dimensional case  $A(r)$  can be expressed by

$$A(r) = \sum A_{m_1 m_2 m_3} e^{2\pi i [m_1(b_1 \cdot r) + m_2(b_2 \cdot r) + m_3(b_3 \cdot r)]}. \quad (2.59)$$

Equations (2.57) and (2.59) combined in a Fourier sum yield

$$\psi = e^{i\omega t} \sum A_{m_1 m_2 m_3} \exp[-2\pi i(a'_{m_1 m_2 m_3} \cdot r)], \quad (2.60)$$

where

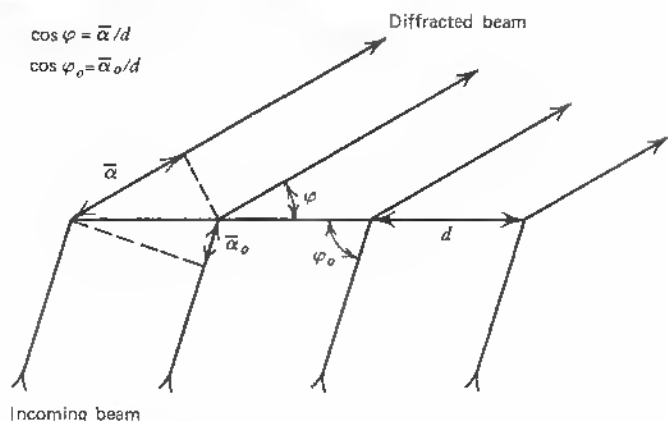
$$a'_{m_1 m_2 m_3} = a - m_1 b_1 - m_2 b_2 - m_3 b_3. \quad (2.61)$$

The last three terms in (2.61), which specify the lattice point in the reciprocal lattice, show the influence of lattice periodicity perturbations on the wave function. Lattice disturbances expressed by corresponding variations in the reciprocal lattice lead to nonharmonic terms in the amplitude function as the lattice-modulated part of the wave function  $\psi$ . In Figure 2.9 the Laue diffraction condition can be read

$$\mathbf{d}(\cos \varphi - \cos \varphi_0) = \mathbf{d}(\alpha - \alpha_0) = n \cdot \lambda \quad (n = 0; \pm 1; \pm 2; \dots), \quad (2.62)$$

where  $\alpha$  and  $\alpha_0$  = direction cosines,

$\mathbf{d}$  = lattice translation vector.



$$d (\cos \varphi - \cos \varphi_0) = d (\alpha - \alpha_0) = n \cdot \lambda$$

$$n = 0, \pm 1, \pm 2, \pm \dots$$

Fig. 2.9 Laue diffraction condition

In a three-dimensional lattice three simultaneous conditions have to be satisfied:

$$\begin{aligned} d(\alpha_{n_1} - \alpha) &= n_1 \lambda, \\ d(\beta_{n_2} - \beta) &= n_2 \lambda, \\ d(\gamma_{n_3} - \gamma) &= n_3 \lambda, \end{aligned} \quad (2.63)$$

with the additional condition for orthogonal axes

$$\alpha_{n_1}^2 + \beta_{n_2}^2 + \gamma_{n_3}^2 = 1. \quad (2.64)$$

Equation (2.63) can be rewritten

$$\begin{aligned} \frac{1}{2\pi} \left( \frac{2\pi}{\lambda} \alpha' - \frac{2\pi}{\lambda} \alpha \right) &= n_1 \frac{1}{d_1} + n_2 \cdot 0 + n_3 \cdot 0, \\ \frac{1}{2\pi} \left( \frac{2\pi}{\lambda} \beta' - \frac{2\pi}{\lambda} \beta \right) &= n_1 \cdot 0 + n_2 \frac{1}{d_2} + n_3 \cdot 0, \\ \frac{1}{2\pi} \left( \frac{2\pi}{\lambda} \gamma' - \frac{2\pi}{\lambda} \gamma \right) &= n_1 \cdot 0 + n_2 \cdot 0 + n_3 \frac{1}{d_3}. \end{aligned} \quad (2.65)$$

Here  $(2\pi/\lambda)\alpha$ ,  $(2\pi/\lambda)\beta$ ,  $(2\pi/\lambda)\gamma$ , and the like, are the rectangular projections of the wave vector  $\mathbf{k} = 2\pi\mathbf{a}$  ( $a = 1/\lambda =$  wave number) of the incoming wave on the three translation axes of the lattice. Introducing now the reciprocal lattice

vectors  $\mathbf{b}_1, \mathbf{b}_2, \mathbf{b}_3$ , which satisfy the conditions (2.32) for orthogonality:

$$(\mathbf{b}_i \cdot \mathbf{d}_k) = \delta_{ik}, \quad (2.32)$$

the Laue conditions read

$$\frac{1}{2\pi}(k' - k) = n_1 \mathbf{b}_1 + n_2 \mathbf{b}_2 + n_3 \mathbf{b}_3 = \mathbf{n} \quad \begin{aligned} (n_1 = 0, \pm 1, \pm 2, \dots), \\ (n_2 = 0, \pm 1, \pm 2, \dots), \\ (n_3 = 0, \pm 1, \pm 2, \dots). \end{aligned} \quad (2.66)$$

The general solution of this vector equation is

$$\frac{1}{2\pi} \mathbf{k}' = \frac{1}{2\pi} \mathbf{k} + \mathbf{n}, \quad (2.67)$$

but for the diffracted wave to have the same wavelength as the incoming wave, the additional condition

$$|\mathbf{k}'| = |\mathbf{k}|$$

must be satisfied. A geometrical construction satisfying these conditions is a vectorial addition of  $(1/2\pi)\mathbf{k}'$  and  $(1/2\pi)\mathbf{k}$  leading to  $\mathbf{n}$ , but such that  $\mathbf{n}$  is always the base of an isosceles triangle.<sup>4</sup>

This is accomplished by drawing the orthogonal plane through the end point of the vector

$$\pm \frac{1}{2} \mathbf{n} \quad (\text{see Fig. 2.10})$$

All plane waves  $e^{i\mathbf{k} \cdot \mathbf{r}}$  whose wave vectors are  $\mathbf{k}/2\pi$ , lying on these planes, form diffracted beams of order  $n_1 n_2 n_3$ . This leads to the construction of the Brillouin zones for two- and three-dimensional lattices, as indicated in Figure

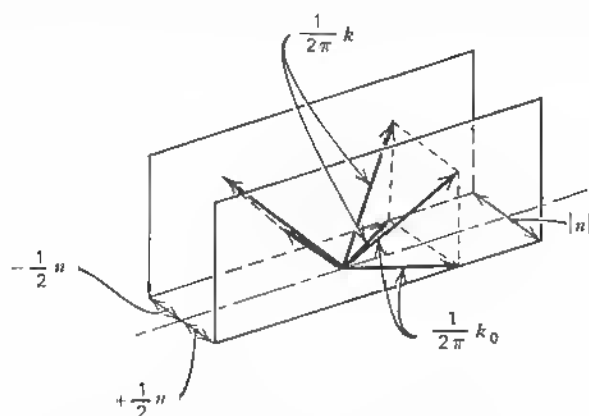


Fig. 2.10 Construction of Brillouin-Zones (see text).

2.11 for the square lattice. In this construction it is assumed that the [11] row of atoms is missing (vacancies). This leads to the elimination of those zones formed by the perpendicular bisectors of the lines joining the central lattice point to the missing atom sites.

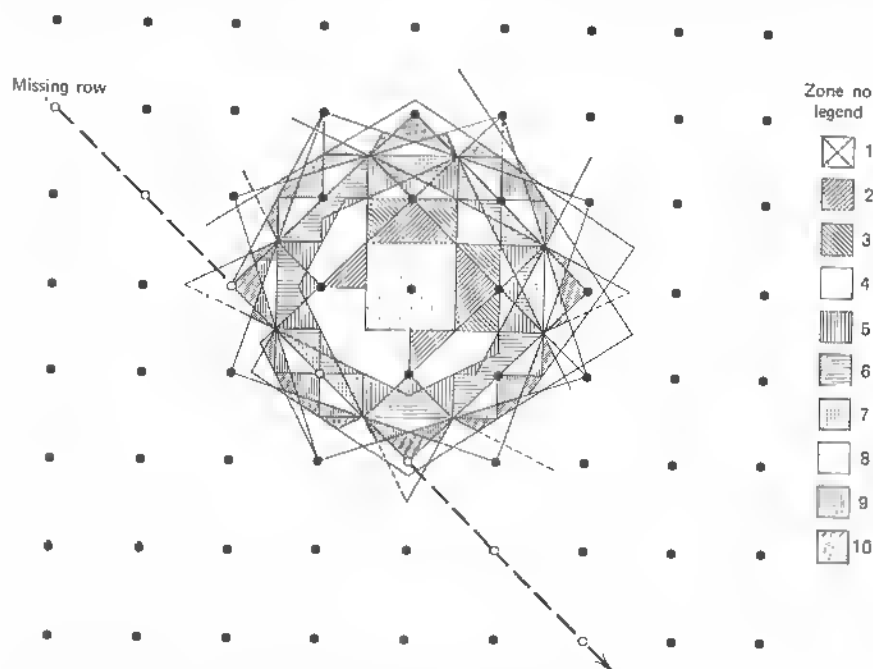


Fig. 2.11 Coalescing Brillouin zones in the neighborhood of a vacancy line in the [11]-direction.

The resulting deformation of the Brillouin zones of corresponding order shows the variations in Bragg reflections due to the defect line. Stronger changes occur in reality on account of the resulting lattice strain, which is not considered here. In the case of dislocations, even greater discrepancies can be expected on account of the charge separation at the site of a *dangling bond*.

In Figure 2.7a [11] line of defects is also drawn, and the question arises under which conditions such a *sublattice* structure or *regular disturbance* can cause Bragg reflections to occur. We have touched on the resonance character of such regular defects before. The vacancy line (it may also be a dislocation line formed, for example, by a regular array of edge or screw type's of dislocations) is geometrically defined by the direct lattice vector

$$\mathbf{d}'_1 = m_1 \mathbf{d}_1 - n_1 \mathbf{d}_2. \quad (2.68)$$

For  $m_1 = n_1 = 1$  the reciprocal lattice vector relation corresponds to the con-

dition  $(\mathbf{b}_i \cdot \mathbf{d}_k) = \delta_{ik}$ :

$$\begin{aligned}(\mathbf{b}_1 \cdot \mathbf{d}'_1) &= |\mathbf{b}_1| |\mathbf{d}_1 - \mathbf{d}_2| \cos \psi = 1, \\(\mathbf{b}_2 \cdot \mathbf{d}'_2) &= |\mathbf{b}_2| |\mathbf{d}_1 - \mathbf{d}_2| \cos \psi' = 1.\end{aligned}\quad (2.69)$$

For simplicity let us assume that  $|\mathbf{d}_1| = |\mathbf{d}_2|$ :

$$\begin{aligned}\cos \psi &= \cos\left(\frac{\theta}{2} - \frac{\pi}{2}\right) = \sin \frac{\theta}{2}, \\ \cos \psi' &= \cos\left(\frac{\pi}{2} - \frac{\theta}{2}\right) = \sin \frac{\theta}{2}.\end{aligned}\quad (2.70)$$

It follows that

$$\begin{aligned}(\mathbf{b}_1 \cdot \mathbf{d}'_1) &= (\mathbf{b}_2 \cdot \mathbf{d}'_2) = |\mathbf{b}_1| \overbrace{|\mathbf{d}_1 - \mathbf{d}_2|}^{|\mathbf{d}_1'|} \sin \frac{\theta}{2} \\ &= |\mathbf{b}_2| \overbrace{|\mathbf{d}_1 + \mathbf{d}_2|}^{|\mathbf{d}_2'|} \sin \frac{\theta}{2} = 1.\end{aligned}\quad (2.71)$$

Here

$$\begin{aligned}\mathbf{d}_1 - \mathbf{d}_2 &= \mathbf{d}'_1, \\ \mathbf{d}_1 + \mathbf{d}_2 &= \mathbf{d}'_2.\end{aligned}\quad (2.72)$$

Forming the lattice cell areas in the direct and reciprocal lattices,

$$S_d = (\mathbf{d}_1 - \mathbf{d}_2)(\mathbf{d}_1 + \mathbf{d}_2) \quad (2.73)$$

$$S_d = \mathbf{d}'_1 \cdot \mathbf{d}'_2$$

$$S_d = |\mathbf{d}'_1| |\mathbf{d}'_2| \sin \frac{\pi}{2}$$

and

$$S_r = |\mathbf{b}_1| |\mathbf{b}_2| \sin(\pi - \theta), \quad (2.74)$$

we find that their product  $S_d \cdot S_r$  is not 1, as in the normal case, but that

$$S_d \cdot S_r = |\mathbf{d}'_1| |\mathbf{d}'_2| |\mathbf{b}_1| |\mathbf{b}_2| \sin \theta. \quad (2.75)$$

Replacing from (2.71),

$$\begin{aligned}|\mathbf{b}_1| &= \frac{1}{|\mathbf{d}'_1| \sin(\theta/2)} \\ |\mathbf{b}_2| &= \frac{1}{|\mathbf{d}'_2| \sin(\theta/2)}\end{aligned}\quad (2.76)$$



yields

$$S_d S_r = |d'_1| |d'_2| \frac{\sin \theta}{|d'_1| |d'_2| \sin^2(\theta/2)}. \quad (2.77)$$

Equation (2.77) shows that the cell areas are no longer reciprocals independent of  $\theta$  but that

$$S_d \cdot S_r = 2 \frac{\sin \theta}{1 - \cos \theta}. \quad (2.78)$$

The condition for  $S_d \cdot S_r = 1$  is

$$2 \sin \theta + \cos \theta = 1, \quad (2.79)$$

or since (2.79) can be written

$$\sqrt{1 - \sin^2 \theta} = 1 - 2 \sin \theta, \quad (2.80)$$

squaring yields

$$1 - \sin^2 \theta = 1 - 4 \sin \theta + 4 \sin^2 \theta \quad (2.81)$$

or

$$5 \sin^2 \theta = 4 \sin \theta \quad (2.82)$$

and

$$\sin \theta = \frac{4}{5} = 0.8.$$

Thus

$$\theta = 53^\circ 8'. \quad (2.83)$$

For this angle between the direct lattice planes we should, therefore, have Bragg reflections because of the line of vacancies in the [11] direction. In other words, under special circumstances, a symmetrical arrangement of defects within the otherwise perfect structure can assume the role of a periodic substructure or of a linear (two- or three-dimensional) sublattice, which, in turn, can strongly influence the wave propagation. The collapsed Brillouin zones in the construction (see Figure 2.11) especially in the neighborhood of the line of vacancies show that missing atoms lead to coalescing zones. In other words, the reflection conditions are satisfied by a merger of the next lower and higher index Brillouin zones. Thus, there is a certain frequency "hole" in the wave-propagation spectrum of such a defect lattice. As we have seen, however, additional reflection conditions can arise when an ordered defect structure has specific relations to the host lattice. All these considerations are idealized and do not take account of the stress-strain conditions in real lattices, of the charge distribution, ionicity, and many other features of real lattice structures.

## 2.3 ELECTRONS IN PERIODIC FIELDS [BAND THEORY]

We may start our consideration with the wave equation for a three-dimensional continuum with periodic nonuniformities and time dependence:

$$\nabla^2 \psi - \frac{1}{V^2} \ddot{\psi} = 0, \quad (2.84)$$

where  $\nabla^2$  = Laplacian operator,

$V$  = phase velocity,

$\psi$  = wave function,

and assume that the time-dependent part of  $\psi$  is separable from the space-dependent part:

$$\psi' = \psi(x, y, z)e^{i\omega t} \quad (2.85)$$

This gives for  $\psi$  the differential equation

$$\nabla^2 \psi + \frac{\omega^2}{V^2} \psi = 0. \quad (2.86)$$

If we confine ourselves to waves in a periodic medium, we can assume that

$$\frac{1}{V^2} = F(\mathbf{r}). \quad (2.87)$$

For one dimension, (2.87) reduces to

$$\frac{\partial^2 \psi}{\partial x^2} + \omega^2 F(x) \psi = 0. \quad (2.88)$$

If  $F(x)$  with period  $d$  in  $x$ , for example, contains only one cosine term, we may write

$$F(x) = C_0 + 2C_1 \cos \frac{2\pi x}{d} \quad (2.89)$$

$$F(x) = C_0 + 2C_1 \cos \xi.$$

With

$$\xi = \frac{2\pi x}{d}, \quad (2.90)$$

(2.88) becomes, with  $\psi' = \psi(x)e^{i\omega t}$ , (2.85):

$$\frac{\partial^2 \psi}{\partial \xi^2} + (\eta + \gamma \cos \xi) \psi = 0, \quad (2.91)$$

where

$$\eta = \omega^2 \frac{d^2}{\pi^2} C_0 = 4v^2 d^2 C_0,$$

$$\gamma = 8v^2 d^2 C_1.$$

Equation (2.91) is Mathieu's equation.<sup>1</sup> Its solution is given by Floquet's theorem, which states that the solution consists of a superposition of two waves running in opposite direction (standing waves) with position-dependent amplitudes:

$$\psi(\xi) = A\psi(\xi)e^{ik\xi} + B\psi(\xi)e^{-ik\xi}. \quad (2.92)$$

Generally, (2.88) is the Schrödinger equation:

$$\frac{\partial^2 \psi(x)}{\partial x^2} + \frac{8\pi^2 m}{h^2} [E - V(x)]\psi(x) = 0. \quad (2.93)$$

$E$  = energy Eigenvalues

$U(x)$  = Lattice periodic potential energy

Because

$$\omega = 2\pi\nu = 2\pi \frac{v}{\lambda}$$

and, with the DeBroglie equation  $\lambda = h/p$ ,

$$\omega^2 \approx 4\pi^2 \frac{p^2}{h^2}$$

where  $p$  = impulse,

$h$  = Planck's constant.

The energy can be expressed as  $F(x) \frac{p^2}{2m} = [E - U(x)]$ , where  $m$  = electron mass. Then we get

$$\omega^2 \cdot F(x) = \omega^2 \frac{2m}{p^2} [E - U(x)] = \frac{8\pi^2 m}{h^2} [E - U(x)] \quad \text{see (2.86), (2.88).}$$

Another expression is  $F(x) = E_0[1 - \cos 2\pi x/d]$ , since the energy has a constant part  $E$  and a part  $U(x)$ , depending on the lattice periodicity. Equation (2.93) without the  $U(x)$  expression would describe the free-electron case.

Its solution for a wave function with fixed amplitude

$$\psi(x) = A \cdot e^{ikx}$$

where  $k$  = wave vector =  $2\pi/\lambda$ , leads to the energy expression

$$E = \frac{h^2}{2m} |k|^2 = \frac{h^2 v^2}{2m}.$$

With the DeBroglie relation or  $|k| = 2\pi(p/h)$  we get

$$\begin{aligned} E &= \frac{h^2}{4\pi^2} \frac{1}{2m} \frac{4\pi^2}{h^2} p^2 \\ &= \frac{1}{2} mv^2, \end{aligned}$$

or the classical expression for the energy of a free particle.

Referring to Floquet's theorem (2.92), the fact that the solution of the kind of wave equation (2.93) leads to wave functions with periodically modulated amplitude can be seen also from the periodicity and symmetry of the eigenfunctions. The fact that the potential function is periodic in space,

$$U(x) = U(x - nd) \quad (n = \pm 1; \pm 2; \pm 3; \dots) \quad (2.94)$$

where  $d$  = lattice spacing, leads to the eigenfunctions of the form

$$\psi(x - nd) = C^n \cdot \psi(x) = \psi(x) \quad (n = \pm 1; \pm 2; \pm 3; \dots). \quad (2.95)$$

The latter equality is due to the physical fact that incoming waves and reflected waves have to be equal or that no amplitude and frequency changes can occur during multiple repetition of the operation of parallel translation. This means that  $C^n = 1$  or that the  $n$  solutions of this equation are roots of unity:

$$C^n = e^{2\pi i l/n} \quad (l = 1, 2, \dots, n). \quad (2.96)$$

The wave function  $\psi$  must satisfy (2.95) and (2.96) for any value of  $x$ . This is possible for

$$\psi(x) = u_k(x) e^{2\pi i l x / nd}. \quad (2.97)$$

Therefore  $u_k(x)$  is periodic in  $x$  with a period  $d$ .

Since

$$k = \frac{2\pi}{nd},$$

we get

$$\psi(x) = u_k(x) e^{ikx}, \quad (2.98)$$

which is Bloch's wave function.

We may also express  $\psi(x)$  by a sum formula, starting with (2.95),

$$\psi(x) = \sum_{n=-\infty}^{+\infty} C^{-n} \psi(x - nd), \quad (2.99)$$

again  $C$  has the form

$$C = C_0 e^{2\pi i (n/G)} \quad (n = \pm 1; \pm 2; \dots), \quad (2.100)$$

$G$  = lattice cell number,

or

$$\psi(x) = C_0 \sum_{n=-\infty}^{+\infty} e^{2\pi i (n/G)} \psi(x - nd), \quad (2.101)$$

and with  $k = 2\pi/(d \cdot G)$

$$\psi(x) = C_0 \sum_{n=-\infty}^{+\infty} e^{iknd} \psi(x - nd). \quad (2.102)$$

If we write

$$\psi(x, k) = u(x, k)e^{ikx} \quad (2.103)$$

and express  $\psi(x, k)$  from (2.102), it follows that

$$u(x, k) = \psi(x, k)e^{-ikx} \quad (2.104)$$

$$\begin{aligned} &= C_0 \sum_{n=-\infty}^{+\infty} e^{iknd - ikx} \psi(x - nd) \\ &= C_0 \sum_{n=-\infty}^{+\infty} e^{-ik(x - nd)} \psi(x - nd). \end{aligned} \quad (2.105)$$

In other words,  $u(x, k)$  is the lattice-modulated amplitude of the wave function that is periodic in  $x$  and  $k$ . At this point we should conclude that any lattice irregularities would deprive the potential function

$$U(x) = U(x - nd)$$

of its periodicity and hence make unreal the existence of the Bloch kind of wave functions. In the modified Brillouin zone scheme (see Figure 2.11), we have seen that a change of minor extent like a line of vacancies causes zone coalescence but no disruption of the scheme for Bragg reflections. Similarly, a departure from periodicity in the form of a defect line or even defect plane would cause the amplitude function to be represented by

$$A'(\mathbf{r}) = A' + \varepsilon A''(\mathbf{r}) \quad (\varepsilon \ll 1).$$

One can show (see Brillouin or: (Ref. 1)) that this Ansatz for the periodic amplitude function in (2.86) leads to two distinct cases, depending on the relative values of the wave vectors of the undisturbed and disturbed waves. If these  $k$  values are far apart—( $\psi(x, k)$  is real only for  $k = 0$ )—the resulting wave function is only slightly perturbed, and we find again that certain energy values are forbidden, where

$$k = \pm \frac{\pi}{d}; \pm 2 \frac{\pi}{d}; \pm n \frac{\pi}{d}$$

with Bragg reflections occurring at these points:

$$\begin{aligned} \frac{k}{2\pi} &= \pm 1n \cdot \frac{1}{2d} \\ &= \pm 2n \cdot \frac{1}{2d} \\ &= \pm 3n \cdot \frac{1}{2d}, \text{ etc.} \end{aligned}$$

(see Brillouin zone construction).

This leads to the forbidden energy values  $e|V_1|$ ,  $e|V_2|$ , and so on, and thus to a split of atomic eigenvalues into allowed and forbidden bands. If the  $k'$  values of the disturbed portion of the wave function approaches  $k$  of the undisturbed part, the frequency has two possible values (see Figure 2.12).

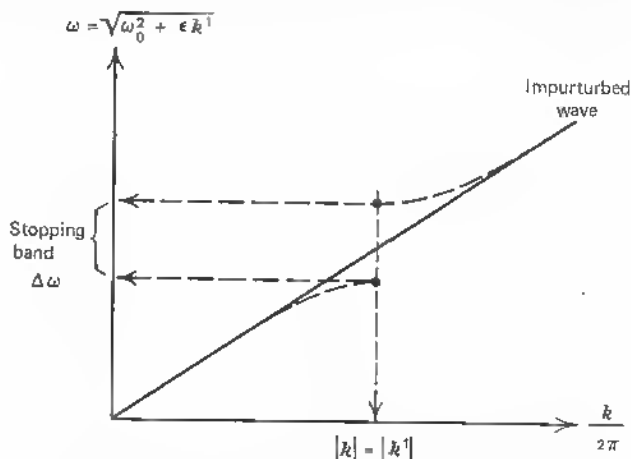


Fig. 2.12 Two solutions for the unperturbed wave equation and resultant split into passing and stopping bands.

Closer spacing of the atoms,  $d \rightarrow 0$ , also leads to the formation of broader bands<sup>4</sup> and, therefore, increased degeneracy. From Brillouin's perturbation treatment it appears that the zone scheme is still valid in periodic structures with limited defects and that the *basic discontinuities* still appear when the wave vector has its extremity on the perpendicular bisector of the vectors in the reciprocal lattice. Missing or dislocated atoms, however, change the relative extent of the individual zones. If strong disturbances occur, the perturbation treatment and, therefore, the zone construction break down. But, as mentioned before, the electronic effects of vacancies and dislocations (missing electronic charges or charge accumulation) have a much stronger effect on the local band structure than a purely perturbing influence on the wave functions. We discuss these effects mainly in Chapter 8.

## 2.4 DONORS AND ACCEPTORS

The usual description of the substitutional association of a donor atom with a host lattice is based on the position of its energy level near the conduction band and its occupational state at normal temperatures ( $\sim 300^\circ\text{K}$ )—antimony in germanium, for example. The same is true for acceptor impurities like indium in germanium, where one electron is missing to enter into the available

$s, p$  valence bonds of the germanium host lattice, and, therefore, a "free" hole is available.

The definition of a donor can, therefore, be given by the equation

$$D^* = D^+ + \ominus, \quad (2.106)$$

where  $D^*$  = neutral donor,

$D^+$  = positively charged donor residue

$\ominus$  = free electron.

The same equation in modified form describes an acceptor:

$$A^* = A^- + \oplus, \quad (2.107)$$

where  $A^*$  = neutral acceptor,

$A^-$  = negatively charged acceptor residue

$\oplus$  = free hole.

W. Schottky<sup>5</sup> has discussed in detail the discrepancy in this kind of terminology that leads to acceptor behavior of a donor after dissociation of the free electron or to donor behavior of an acceptor after the free hole has dissociated. The energy levels in the forbidden gap cannot be used for a good definition, since phosphor materials show donor levels near the valence band, and vice versa for acceptors. It is, therefore, the best choice to talk unambiguously about a "donor" if such an atom exists in both states, neutral  $D^*$  and positive  $D^+$ , and about an acceptor if such an atom exists in a neutral state  $A^*$  and in a negatively charged state  $A^-$ , the criterion being in both cases the character of the "recharging" mechanisms

$$D^* \rightarrow D^+,$$

$$A^* \rightarrow A^-.$$

Schottky proposes to discriminate between states near the conduction or valence bands by the prefix *trans* for higher states, *cis* for states below the Fermi level (see Figure 2.13). For the mid-band terms near the Fermi level we use Schottky's expression "medial" donor or "medial" acceptor, because such levels play a predominant role as Shockley's deathniums (lifeniums) and are connected to the appearance of dislocations and their influence on recombination mechanisms. Such mid-band levels may be located a few  $kT$  (0.025 eV) from the Fermi level and, therefore, can easily be converted from a donor to an acceptor. This property can play an important role in all radiative and nonradiative processes.

For nonradiative recombination such interband levels have been postulated<sup>6</sup> to explain the absorption of the total electron energy by successive absorption steps through these levels.

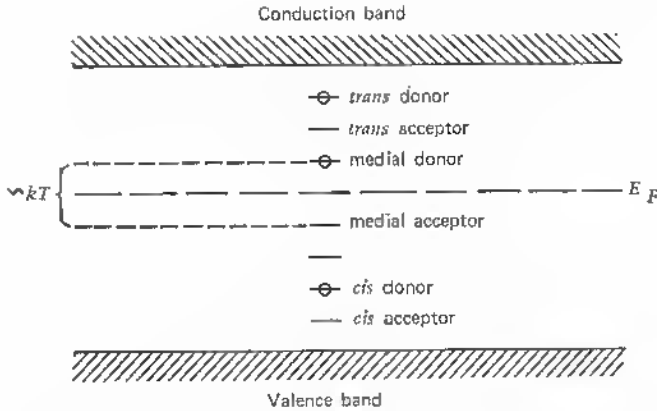


Fig. 2.13 Schottky- Terminology for interband energy levels.

For the recombination of holes and electrons from acceptors and donors—either directly, intrinsically, or via recombination centers, extrinsically—a rate equation can be derived:

$$N_r \left( \begin{array}{c} \text{per volume element} \\ \text{per time unit} \end{array} \right) = r \cdot n \cdot p, \quad (2.108)$$

where  $r$  = recombination coefficient,

$n$  = electron density,

$p$  = hole density.

Similarly a generation equation (pair production)

$$N_p = g = r \cdot n \cdot p \quad (2.109)$$

applies. In equilibrium  $N_r = N_p$ , and therefore

$$p \cdot n = \frac{g}{r} = n_i^2. \quad (2.110)$$

$n_i$  is defined for the intrinsic semiconductor as  $n_i = n = p$ . Equation (2.110) as the mass action law relates the donor-acceptor densities to the intrinsic density. In another way of expression it relates the effective state densities  $N_c$  and  $N_v$  in both the conduction and valence bands to the intrinsic density, since

$$n = N_c e^{(E_F - E_c)/kT} \quad (2.111)$$

and

$$p = N_v e^{(E_v - E_F)/kT}, \quad (2.112)$$

$E_c, E_v$  = conduction and valence band energies,

$E_F$  = Fermi level.



Equations (2.111) and (2.112) are valid only for the nondegenerate case of  $n$  and  $p \ll N_{c(v)}$ . Introducing them into (2.110) yields

$$n \cdot p = n_i^2 = N_c \cdot N_v \cdot e^{-(E_c - E_v)/kT} \quad (2.113)$$

or

$$n_i = \sqrt{N_c N_v} e^{-1/2(E_c - E_v)/kT} \quad (2.114)$$

$$n_i = 2.5 \cdot 10^{19} \text{ cm}^{-3} \left(\frac{m_n}{m}\right)^{3/4} \cdot \left(\frac{m_p}{m}\right)^{3/4} \cdot \left(\frac{T}{300^\circ\text{K}}\right) e^{-1/2(E_c - E_v)/kT}. \quad (2.115)$$

The intrinsic density thus depends on the effective mass of the carriers, the temperature, and the band gap  $E_c - E_v$ .

For germanium at 300°K this value is

$$n_i = 2.5 \cdot 10^{13} \text{ cm}^{-3}.$$

Since the number of atoms per cubic centimeter for germanium is

$$4.52 \cdot 10^{22},^7$$

this means that one has

$$\frac{4.52 \cdot 10^{22}}{2.5 \cdot 10^{13}} = 1.8 \cdot 10^9 \text{ germanium atoms per impurity atom.}$$

The purity of 1 part in  $10^9$  is astonishing from the point of view of action radius for impurities for lightly doped semiconductors. A defect or only a vacancy has similarly extended charge clouds. If we calculate the first Bohr radius multiplied by the dielectric constant of germanium:<sup>4</sup>

$$a_1 = \epsilon_{Ge} \cdot \frac{\hbar^2}{me^2} \quad (\epsilon = 16.1), \quad (2.116)$$

the result is

$$\begin{aligned} a_1 &= 16.1 \cdot 0.53 \cdot 10^{-8} \text{ cm} \\ &= 8.5 \cdot 10^{-8} \text{ cm.} \end{aligned}$$

Assuming that the charge cloud occupies a sphere with radius  $2a_1$ ,<sup>4</sup> the volume

$$\frac{4}{3} \pi (17 \cdot 10^{-8})^3$$

is occupied. With the lattice constant of germanium  $a = 5.61 \cdot 10^{-8} \text{ cm}$ , we can calculate the number of germanium lattice cells occupied:

$$\begin{aligned} \frac{4}{3} \pi \cdot \left(\frac{17}{5.62}\right)^3 &= \frac{4}{3} \pi \cdot 3.02^3 \\ &\simeq 114. \end{aligned}$$

Since each cell contains eight atoms, the total number of atoms within the charge cloud is over 900. It is evident that vacancies and dislocations with their free-bond charges have a similarly wide range of electrical field influence. Moving across the germanium lattice with intrinsic purity ( $n_i = 2.5 \cdot 10^{13} \text{ cm}^{-3}$ ), one can find that  $4.52 \cdot 10^{22} / 2.5 \cdot 10^{13} = 1.8 \cdot 10^9$  germanium atoms surround at an average one impurity atom. Or, on a linear basis, one can encounter

$$\sqrt[3]{1.8 \cdot 10^9} \simeq 1.2 \cdot 10^3$$

germanium atoms per impurity atom. The astonishingly wide reach of the influence of electronic charges within periodic structures is another expression for the loose binding of the fifth valence electron. But also in the case of vacancy- and dislocation-generated free charges, the fact remains that one free charge on 1000 lattice sites is sufficient to influence the resistivity and the mobility in the crystal. In other words, the main feature of the perfect lattice structure is the propagation freedom of an electron wave package over wide distance. Like the electron wave

$$\Psi(x, k) = Ae^{ikx}$$

in free space, the Bloch wave

$$\Psi(x, k) = u(x, k)e^{ikx}$$

cannot be associated with one lattice point, but is "smeared," or distributed, across a number of atoms because of the lattice periodic amplitude function  $u(x, k)$ . In the case of a free bond or *dangling bond*, the fourth valence electron represents initially a *transacceptor* near the conduction band (see Figure 2.14a). After accepting a free electron, this bond changes to a *cis-acceptor* below the middle of the gap but near  $E_F$  (Figure 2.14b). In the case of dangling bonds, it is thinkable that electrons are added as long as energy is gained to lower the energy level below the Fermi level. This explains the behavior of dislocations

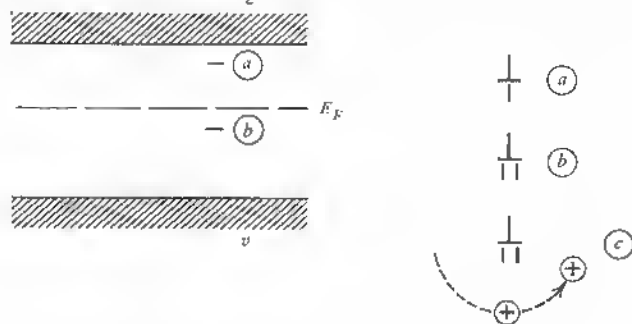


Fig. 2.14 Energy levels of dangling bond (a) unfilled (b) filled (c) compensated.

to act as "hole sinks" after they have been able to build a space charge cloud around themselves (see Figure 2.14c). After the covalent bond sharing in a tetragonal arrangement about the dislocated atom is disrupted, the  $s, p$  valence electrons are shared by hybrid orbital bonding with neighboring atoms in a higher energy state. This high-energy situation can be lowered by two atoms sharing a free electron, which brings each bond into a cis-acceptor state. By further electron association between bonds, a cis-donor state builds up when a compensating hole charge surrounds the atom. In this way a free bond creates a local small space charge cloud. It is, incidentally, this behavior which gives these mid-band levels their strong electronic influence on carrier transport (see Chapter 8). If the local density of holes around the dislocation has reached a value  $p_D \gg n_i$ , the material behaves  $p$  type, and the conductivity passes through the inversion point near to the dislocation.

The other important aspect to the mid-band level is the high recombination probability. If a barrier layer is combined with such a center, it also acts like a  $p$ - $n$  junction barrier separating electron-hole pairs.

The local barrier layer not only of coherent grain boundaries but also of individual dislocations has been elucidated recently by scanning electron microscopy and establishes a proof for a number of premises used in the refined transport theory of dislocations (see Chapter 8).

## 2.5 RECOMBINATION

If one wants to study the importance of a defect, especially a dislocation, for recombination processes, one has to remember, as mentioned, that the mid-band levels are especially active in this respect. This can be derived from the fact that holes and electrons require about equal energies to move halfway from the valence respectively the conduction band. In the treatment of the statistics of hole-electron recombination,<sup>8</sup> the energy level of the active trap  $E_t$  is generally assumed to be at some place above or below the Fermi level  $E_F$ . For  $E_F = E_t$ , the number of electrons in the conduction band is given by

$$n_1 = N_c \exp \frac{E_t - E_c}{kT}, \quad (2.117)$$

and the number of holes in the valence band is

$$p_1 = N_v \exp \frac{E_v - E_t}{kT}, \quad (2.118)$$

where  $E_v$  = energy of highest valence band level,

$E_c$  = energy of lowest conduction band level,

$N_c, N_v$  = effective densities in conduction and valence band for  $E_F \neq E_t$ .

If one defines the rate of capture for electrons  $U_{cn}$  in terms of  $n_1$ , one gets

$$U_{cn} = C_n f_{pt} n - C_n f_t n_1, \quad (2.119)$$

where  $n$  = number of electrons in conduction band,

$C_n$  = probability per unit time that electron in conduction band will be captured (in the case of empty traps),

$f_t$  = fraction of traps occupied by electrons,

$f_{pt}$  = fraction of traps occupied by holes.

Shockley and Read<sup>8</sup> have shown that the net rate of recombination  $U$  can be expressed as

$$U = \frac{C_n C_p (p \cdot n - p_1 n_1)}{C_n (n + n_1) + C_p (p + p_1)}. \quad (2.120)$$

$C_p$  is the expression corresponding to  $C_n$  that represents the probability, per unit time, that a hole will be captured if the traps are filled with electrons.

In equation (2.120), the product  $p_1 n_1$  is, according to (2.117) and (2.118),

$$p_1 n_1 = N_c N_v \exp \frac{E_v - E_c}{kT}. \quad (2.121)$$

This means that this product of the carrier densities (Fermi level at  $E_i$ ) is independent of the particular trap level and equal to  $n_i^2$ , where  $n_i$  is the intrinsic carrier concentration.

Since generally

$$p \cdot n = N_c N_v \exp \left( - \frac{E_c - E_v}{kT} \right) \quad (2.122)$$

is also equal to  $n_i^2$  in the intrinsic case, there is no net rate of recombination, according to (2.120) since  $p \cdot n = p_1 \cdot n_1$ .

In a medium temperature range the carrier-density difference is equal to the donor-acceptor difference:

$$n - p \simeq N_d - N_a, \quad (2.123)$$

and one can approximate

$$n \simeq N_d - N_a + \frac{n_i^2}{N_d - N_a}, \quad (2.124)$$

with

$$p \simeq \frac{n_i^2}{N_d - N_a}.$$

For strong  $n$ -type doping we have  $N_d \gg N_a$  and

$$\begin{aligned} n &\simeq N_d, \\ p &\simeq 0. \end{aligned}$$

In this case the net rate of recombination, according to (2.120), is

$$-U = \frac{C_n C_p n_i^2}{C_n(n + n_1) + C_p p_1}. \quad (2.125)$$

If it is assumed also that  $p_1$ , the trap-induced number of holes, is small, the net recombination rate is

$$-U = \frac{C_p n_i^2}{n + n_1}. \quad (2.126)$$

It follows that the capture of holes is predominant for electron-filled traps. This is in agreement with the measured behavior of dislocations with levels in the upper half of the forbidden gap. Shockley and Read relate the expression for  $U$  (2.120) to the case of  $p$ - $n$  junction biased in the reverse direction. In this case the space charge region  $U_{sp.ch.}$  may penetrate the  $n$ -type region, causing both  $n$  and  $p$  to be reduced below  $n_1$  and  $p_1$ , with the result

$$-U_{sp.ch.} = \frac{C_n C_p n_i^2}{C_n n_1 + C_p p_1} \quad (2.127)$$

The net recombination rate is now a space-charge-dominated process. In the case of dislocation-induced traps, the dangling bonds have the acceptor character first and fill up with electrons, leaving a number of holes in a space-charge configuration around the traps. An increase in carrier density in the sample—by carrier injection, for example—generally results in an additional number of holes to be bound to the space-charge region because of an increase of the quasi Fermi levels. Actually, a split in quasi Fermi levels occurs at the area of injection so that the electrochemical potential for electrons moves toward the conduction band, and the e.c.p. of holes toward the valence band.

In samples separated into two halves by a complete grain-boundary plane, for example, a sharp  $n$ - $p$ - $n$  double layer builds up with a carrier-dependent barrier height. If an external carrier flow is maintained through a potential drop, the situation becomes more complex, as discussed later.

The simplest recombination process is shown in Figure 2.15a. Either an intrinsic recombination takes place across the band gap or by way of a recombination center  $E_r$ . Electrons can also reach the recombination center from the valence band (see Figure 2.15b), process (4), or filled recombination centers can release electrons to both the valence and the conduction bands. In Figure 2.15b another process is drawn, showing how empty centers can accept an electron from the conduction band (1) or release a hole to the valence band (4) and how filled levels can release an electron to the conduction band (2) or accept a hole from the valence band (3). In addition to the fact that a

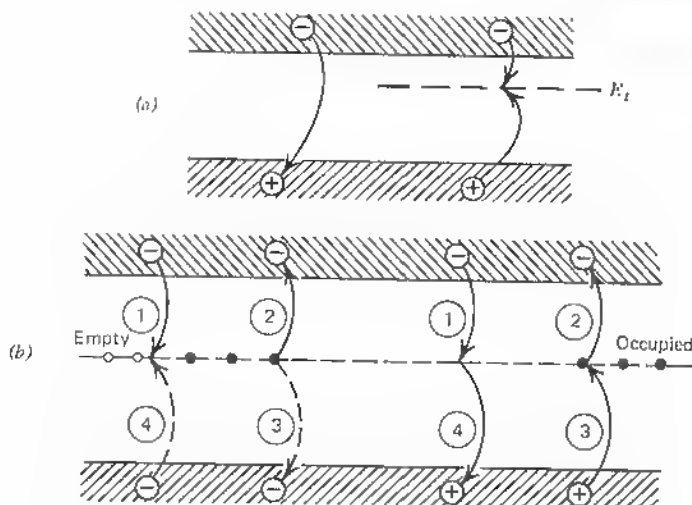


Fig. 2.15 (a) Hole-electron recombination (b) Different recombination processes via empty and filled centers in the forbidden gap

dislocation has an energy level in the forbidden gap, which may assume any of these functions, we have to consider a more detailed model distinct from ordinary impurity levels. When the lattice structure is disrupted and free bonds have formed and electrons have moved into shared positions, a strain field has been generated, and an area of higher energy is formed. Around an edge dislocation in particular the additional half plane causes a companion dilatation zone that is a lieu for anomalous lattice wave coupling and as such can supply phonon energies of varied amounts. At such points in the lattice structure, recombination, either radiative or nonradiative, is more likely to occur. The release of energy combined with a direct recombination process, as shown in Figure 2.15a, can be realized by the emission of the photon energy  $h\nu$ . This emission process of electromagnetic radiation, however, is subject to the quantum-mechanical selection rule that the wave vectors of electrons in their initial and final state must be conserved. Thus, direct transitions for equal wave vector  $k$  values are combined with the emission  $h\nu = E_D$  (see Figure 2.16). If, however, the transition process involves a satellite minimum— $k[100]$  in Figure 2.16, for example—of the conduction band, the energy  $E_i'$  is broken down into a portion I, entirely due to a wave vector adjustment  $k[000] \rightarrow k[100]$ , and a portion II, corresponding to the indirect gap  $E_I$ . Only this portion can be converted into radiative energy  $h\nu$ . The adjustment of  $k$ , which is necessary to effect this process, is facilitated in the field of a strong lattice disturbance like an edge dislocation. Here the phonon spectrum is broadened, and new vibrational modes can be generated, as described in Section 2.1 in the case of a small lattice disturbance.

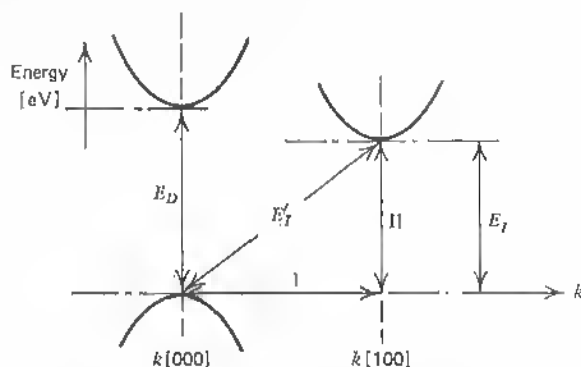


Fig. 2.16 Direct transition  $E_D$  from valence to conduction band valley and indirect transition:

$$E_I' = E_I + (k[000] \rightarrow k[100])$$

The cases of radiative and nonradiative recombination in the presence of dislocations are of great importance for the direct gap semiconductors of the III-V compound type<sup>9,10</sup> and are discussed in Sections 9.5 and 9.6 in more detail.

## 2.6 PHOTONS, PHONONS, AND ELECTRONS

The analogy between the quantum of energy in an elastic wave and the electromagnetic quantum accounts for a number of important interactions within the crystal continuum.

A phonon of wave vector  $\mathbf{k}$  has a momentum  $\hbar\mathbf{k}$ , as has the photon of the same wave vector. Their interaction occurs by way of the refractive index. If a phonon wave modulates the periodic structure and thereby changes the local state of strain, this is equivalent to a modulation of optical properties. The wave vector of the photons

$$k = \frac{n\omega}{c} \quad (k = \mathbf{k} \text{ from here on}),$$

where  $n$  = refractive index,

$c$  = light speed,

can be expressed as

$$k = \frac{n(k_{\text{phonon}}) \cdot \omega}{c}, \quad (2.128)$$

since  $n = f(k_{\text{phonon}})$ .

By conservation of wave vector, the condition

$$\hbar k_{\text{photon}} = \hbar k'_{\text{photon}} + \hbar K_{\text{phonon}} \quad (2.129)$$

has to be fulfilled (see Figure 2.17).<sup>2,11</sup>

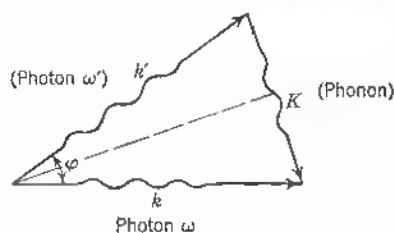


Fig. 2.17 Conservation of wave vector in photon-phonon interaction.

For the case of  $k = k'$  the triangle is isocceles and the phonon wave vector is

$$K = 2k \sin \frac{\phi}{2}^*$$

The similarity of phonons and photons is elucidated by a scheme that describes the historical parallelisms in their treatment. Since the scattering of light by thermal phonons (in equilibrium) is known as *Brillouin scattering*, lattice vibrations are a major cause of quantum interactions between electrons and phonons. In a corpuscular view, electrons interact with acoustical and optical phonons as they interact with other lattice imperfections like vacancies, interstitials, and dislocations. It is noteworthy that such defects as dispersion centers often allow for a more efficient coupling of lattice waves, electron wave packages, and photons. The wave-vector adjustment in multiple processes (2.129) can be facilitated when a defect level is available with the right components.<sup>9, 12</sup> In the case of elastic scattering of a photon by a crystal (Bragg diffraction), for example, the wave-vector conservation condition reads

$$k = k' + R, \quad (2.130)$$

where  $k$  = wave vector of incident photon,

$k'$  = wave vector of scattered photon,

$R$  = wave vector in reciprocal lattice.

If, however, the scattering is inelastic, a new phonon with wave vector  $K$  has to balance the difference:

$$k = k' + R + K. \quad (2.131)$$

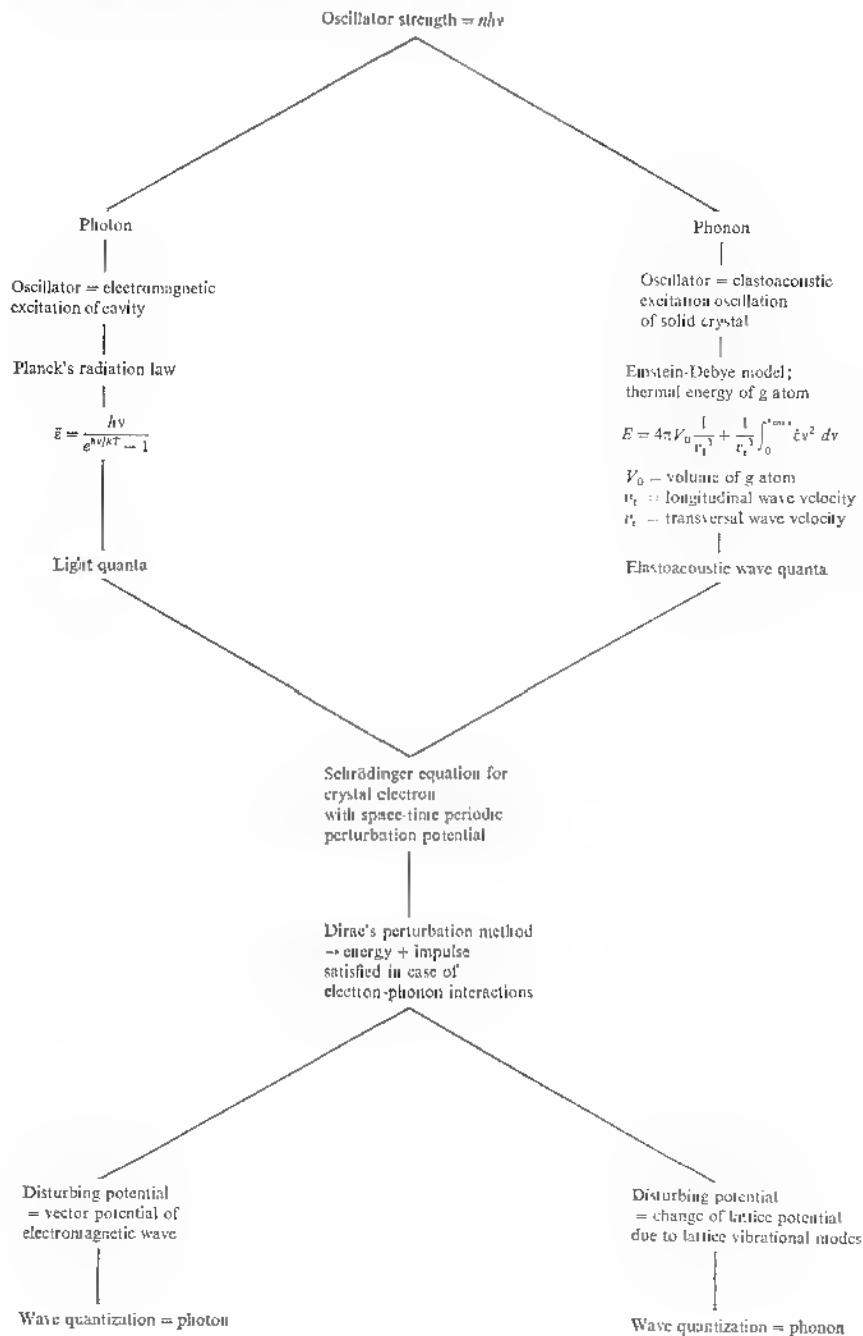
At a defect the new phonon may be absorbed easily if, for example,

$$k + K = k' + R, \quad (2.132)$$

and in this case the whole process may increase in probability.

\*  $K_n = \pm n 2\pi/\lambda$  is a pseudomomentum and defined only within an integral multiple of  $2\pi/\lambda$ . But in the presence of the periodic lattice, the additional momentum  $\hbar K_n$  can always be supplied.





### Comparison Scheme

The similarity of the methods in both cases shows that small lattice perturbations like defects can catalyze such multiple processes as photon-electron-phonon interactions, which are of importance in radiative recombination processes.

In our comparison (see also Reference 4) we have mentioned the crystal electron and its interaction with both photon and phonon perturbations. The distortions of the periodic potential field due to thermal vibrations (phonons) are directly imparted to the electrons.

### Electrons and Phonons

The Bloch wave function (2.58) can be considered periodic in crystal momentum  $P_x$  and energy  $E_x$ . If we define

$$P_x = \frac{\pm h}{\lambda} = \pm h \cdot \frac{v}{v}, \quad (2.133)$$

where  $v$  = local velocity of wave,  
and

$$E_x = hv \quad (2.134)$$

the normal Bloch wave takes the form

$$\psi_P(x, t) = A_P(x) e^{i[\omega t - \omega(nd/v)]} \quad (2.135)$$

$$= A_P(x) \exp 2\pi i \left( vt - v \frac{x}{v} \right) \quad (2.136)$$

$$= A_P(x) \exp \left( \frac{2\pi i}{h} \right) (E_x t - P_x x) \quad (2.137)$$

(see also eqn. (2.58)). With the introduction of the crystal momentum and the energy into the electronic wave function, we can assess the influence of local changes of the periodic potential field. The Bloch wave functions are then no longer exact solutions, and electrons starting with one value of momentum  $P_x$  make transitions to other states of momentum. Since the wave vector phase is  $k' = 2\pi(d/\lambda)$  ( $d$  = lattice constant) and also

$$hk' = 2\pi \frac{x}{n} \cdot \frac{v}{v} \cdot h, \quad (2.138)$$

or

$$hk' = 2\pi P_x \cdot d, \quad (2.139)$$

the momentum  $P_x$  is analogous to  $hk$ . As the wave vector satisfies the periodic boundary conditions, so does the momentum  $P_x$ . If the periodic structure is

distorted because of phonon waves, the lattice constant undergoes corresponding changes and the wave vector phase changes for equivalent amounts:  $\Delta k' = 2\pi(\Delta d/\lambda)$ . Therefore, a varying momentum

$$\Delta P = \hbar \Delta k \quad (2.140)$$

is to be introduced that is equivalent to the fact of varying the potential energy of the moving electron. These potential changes are generally referred to as *deformation potentials* when caused by changes of energy-band boundaries. A change in energy  $\delta E_x$  corresponds to

$$\delta E_x = \delta P_x \cdot v \quad (2.141)$$

[(2.133) and (2.134)] and since  $P_x = m_x v_x$ , we may write

$$\delta E_x = \frac{P_x \delta P_x}{m_x} \quad (2.142)$$

when all energies, momenta, and the mass are understood in the  $x$  direction for the lattice under consideration. A varying momentum

$$\begin{aligned} \delta P_x &= \hbar \delta k_x \\ \delta P_x &= \hbar \frac{\delta d_x}{d_x \lambda} \end{aligned} \quad (2.143)$$

is due to a lattice change  $\delta d_x$ . In (2.142) the energy change is therefore

$$\delta E_x = \left(\frac{\hbar}{\lambda}\right)^2 \frac{d_x}{m} \frac{\delta d_x}{d_x}, \quad (2.144)$$

a function of the relative dimensional change. In a three-dimensional crystal all three coordinates contribute to the actual energy change, and within the limits of Hooke's law we may write that the energy changes  $\delta E_c$ —in the conduction band, for example—are a linear superposition of all three dimensional changes. This leads to a volume change  $\delta V/V_0$  or to

$$\delta E_c = E_{in} \frac{\delta V}{V_0}. \quad (2.145)$$

This can be related to a pressure on the lattice with corresponding pressure ratio  $\delta p/p = -B(\delta V/V_0)$ , where  $B$  is the bulk modulus or reciprocal compressibility.  $E_{in}$  is the unchanged electron energy.

These relations are important for the assessment of defects in their influence on the band structure. Measurements of energy band changes with pressure as parameter have been made extensively, and the lattice strain around the major dislocations is known such that it is possible to derive the local electronic band changes. (We come back to this problem later.)

So far we have envisioned the most simplified case of changes in the electronic wave function by a lattice distortion (vibration) in a homopolar lattice. As phonon waves compress or dilate the lattice and change the local

electrostatic potential of the electron, scattering may occur. In this case the principle of the conservation of wave vector has to be valid as expressed in (2.131) or (2.132) for the photon-phonon interaction (or for phonon-phonon interactions). In reality the extension of the smeared-out electron cloud over thousands of lattice sites (see Section 2.4) does not move without deformation. The wave function extension creates a background gas, and the core moves relative to this gas, giving an ionic contribution to the overall charge cloud. The rigid and deformable ion cases have been treated by approximation methods<sup>1,2</sup>.

## 2.7 DEFECT ELECTRONS

The concept of the missing or defect-electron as a charge carrier is important in the context of defect structures, since a disrupted bond can have a negative as well as a positive core charge, as we have seen. Missing electrons or holes predominate carrier transport in cases of a space-charge buildup around dangling bonds in homopolar lattices and around the negative core charge—in germanium, for example.

In compound semiconductors the situation varies, depending on the geometrical arrangement of the *A* and *B* surfaces with respect to the slip vector.

Hall data show that the two kinds of carriers are present in samples even at thermal energies:  $kT \approx 2.5 \cdot 10^{-2}$  eV. (For positron liberation, energies would amount to  $E = mc^2 \approx 10^6$  eV.)

External fields as high as  $E = 10^5$  V cm<sup>-1</sup> still have a small influence at atomic distances of  $\sim 5 \cdot 10^{-8}$  cm. Atomic lattice fields would amount to  $5 \cdot 10^{-3}$  eV in this case, while the lattice potential variation along an electron path is of the order of 1 volt.

In an analogy between the free-moving electron and the crystal electron one can state the equality:

$$\text{External force} + \text{lattice forces} = m \frac{d\bar{v}}{dt} \quad (2.146)$$

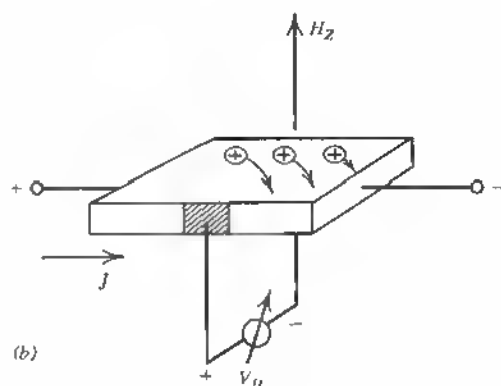
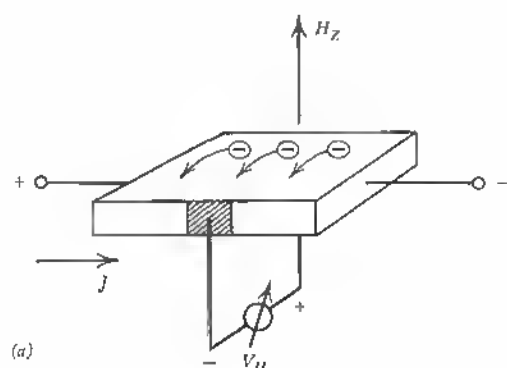
$$\text{External force} = m_{\text{eff}} \frac{d\bar{v}}{dt}, \quad (2.147)$$

where  $\bar{v}$  = mean electron velocity,

$m_{\text{eff}}$  = effective mass.

In (2.147) all influences of the lattice forces are lumped into the value of the effective mass. This is no longer a fixed value but a tensor in the three-dimensional case and can also assume negative values for quasi free carriers (see Section 2.8).

In the classical Hall measurement, the sign reversal clearly demonstrates the preponderance of positive charge carriers or holes (see Figure 2.18*a* and *b*), and the Hall angle is a direct measure of the respective mobilities see Fig. 2.18.



$$\text{Lorentz force } \frac{\pm e}{c} [\mathbf{v} \times \mathbf{H}]$$

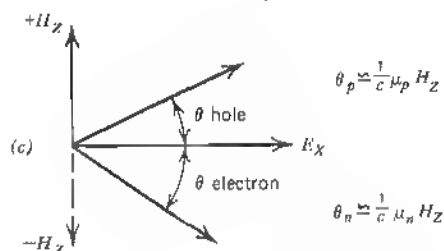


**Fig. 2.18** (a) Hall voltage in the case of electron conduction (b) Hall voltage in the case of hole conduction (c) Lorentz-force and Hall angles for hole and electron conduction

The probability that a state  $E_n$  is not occupied is  $1 - f(E_n)$ , with  $f(E_n)$  being the Fermi distribution function. Thus

$$1 - f(E_n) = \frac{1}{1 + \exp[-(E_n - E_F)/kT]} \quad (2.148)$$

$$= \frac{1}{\exp\{[(-E_n) - (-E_F)]/kT\} + 1}, \quad (2.149)$$

or if we designate  $-E_n = E_p$ , the energy of a hole, we have the equality

$$1 - f(E_n) = f(E_p). \quad (2.150)$$

The Fermi level is now above the hole energy level in a somewhat reversed situation in the bands.

With respect to the carrier mobility, this is not an equivalent situation, however. Since the defect electron represents a missing charge in the otherwise full valence band, its movement is more restricted than is the case with the excess electron in the conduction band. In a simple picture, the hole transfer across the lattice is generally represented as in the opposite direction of the electron such that one might be tempted to equate the mobilities of these carriers. Experience shows, however, that the higher the electron mobility, the lower generally the hole mobility (on a relative scale).

For InSb, for example, electron mobilities in the range of  $10^6$  cm/sec/V/cm have been measured, although the hole mobility is a few  $100$  cm<sup>2</sup>/V sec. In general, the hole-mobility-electron-mobility product is important for an assessment of the electronic features of a material with respect to device potential, the other important feature being the band gap and generally the band structure. In this respect germanium has prominent features and is surpassed only by the compound InSb, and approached by InAs, GaAs, GaSb (see Table 2.1).

Table 2.1

Crystal type	Band gap Eg, optical 300°K, eV	Melting point, °C	Mobility product $\mu_n \mu_p$ , cm <sup>4</sup> /(Vsec) <sup>2</sup>	$\mu_n \mu_p$ relative to germanium
AlSb	1.6	1065	$4.0 \times 10^4$	0.006
GaAs	1.46	1238	$4.0 \times 10^6$	0.55
Ge	0.66	940	$7.0 \times 10^6$	1
Si	1.12	1420	$6.5 \times 10^5$	0.1
GaSb	0.7	706	$2.8 \times 10^6$	0.4
InP	1.26	1058	$1.7 \times 10^5$	0.025
InAs	0.36	942	$5.5 \times 10^6$	0.8
InSb	0.18	530	$4.5 \times 10^7$	6.4

The fact that a moving hole in a similar doping situation encounters so much more scattering than an electron, stems from the fact that a displacement of a missing charge in the almost filled valence band undergoes a much stronger interaction with the lattice than a free excess charge in the almost empty conduction band.

This difference also accounts for the presence of different effective hole masses (light and heavy holes) and the possibility of negative masses within certain crystallographic directions (see Section 2.8).

Conforming to the original Heisenberg concept, there is transport equivalence between the cases:

Empty band: negative charges  
Almost full band: positive charges,

where the effective mass is of the same absolute value in both cases. Its sign changes, however, when the change in sign of the field force on the reverse charge is considered. This does not really mean that electron masses are negative but that a force applied in the direction of motion decelerates the charge carrier. This is spelled out in Section 2.8.

From resistivity and mobility plots versus  $1/T$ , the activation energy  $E_a$  in

$$\rho(\mu) = e^{-E_a/kT}$$

$$\ln \rho(\mu) = - \left( \frac{E_a}{k} \right) \cdot \left( \frac{1}{T} \right)$$

can be found. From the asymptotic values at high temperature (intrinsic case), the energy required to break an atomic bond can be found. The analysis of the activation energy at lower temperatures yields the energies required to remove an electron from its donor and a hole from its acceptor state. For silicon, representative values are:

energy to remove electron from donor = 0.054 eV,  
energy to remove hole from acceptor = 0.08 eV,  
energy to break Si bond = 1.11 eV.

In accordance with the stronger binding of holes to acceptor states, their mobility has to reflect this stronger force by lower  $\mu$  values than those found for electron mobilities. In this case the hole has a 1.5 tighter binding than the electron ( $\mu_n/\mu_p = 3$ ). In germanium this difference is smaller because of the smaller ratio  $\mu_n/\mu_p \approx 1.8$ . In  $A_{III}B_V$  compound semiconductors these differences can be extremely large. For InSb, for example, the ratio  $\mu_n/\mu_p$  is about  $10^2$  at 300°K, and consequently we find that holes must have a 50 times tighter binding than electrons in this case.

This situation may change drastically in the presence of defects that change the normal lattice structure. This is especially true for rows of dislocations (lineage, boundaries) in which defect conduction along such inhomogeneities can produce higher local hole mobility values (see Chapter 11).

## 2.8 THE EFFECTIVE MASS

Because the classical impulse of a wave package is proportional to the DeBroglie frequency (or wave vector), the *mass* of the moving charge carrier is a measure of the fine structure (second derivative of the energy versus wave-vector curve.)

This makes the *effective mass* an important piece of information and relates its values to the actual band structure of the crystal material under consideration.

In this sense the lattice configuration is expressed by effective-mass values. A free-electron wave package represents an impulse  $mv = p = h/\lambda$ , where  $\lambda$  is the DeBroglie wavelength. With the wave-vector representation

$$k = \frac{2\pi}{\lambda},$$

$$P = \hbar \cdot k,$$
(2.151)

the electron energy can be expressed as

$$E = \frac{1}{2} mv^2 = \frac{P^2}{2m},$$
(2.152)

and thus

$$E = \hbar^2 \frac{k^2}{2m}.$$
(2.153)

Differentiation with respect to  $k$  yields

$$\frac{\partial E}{\partial k} = \hbar^2 \frac{k}{m}; \quad \frac{\partial^2 E}{\partial k^2} = \frac{\hbar^2}{m}.$$
(2.154)

The particle mass can then be expressed by

$$m = m_{\text{eff}} = \frac{\hbar^2}{\partial^2 E / \partial k^2}.$$
(2.155)

Thus it is an aspect of the effective mass  $m_{\text{eff}}$  to change corresponding to the curvature of the energy versus wave-vector characteristics within the crystal,



or corresponding to the response of the Bloch wave functions to the particular lattice configuration. Equation (2.153) follows also directly from the Schrödinger equation

$$-\frac{\hbar^2}{2m} \nabla^2 \psi + E_{\text{pot}} \psi = i\hbar \frac{\partial \psi}{\partial t}. \quad (2.156)$$

$E_{\text{pot}}$  is the potential energy composed of external forces and the crystal field forces. In the most simple case of a free electron in a potential field  $U$  we can write  $E_{\text{pot}} = -eU$ . In this case the Schrödinger equation has the solution

$$\psi(r, t) = \psi(r, k) e^{-(i/\hbar) \cdot E \cdot t}, \quad (2.157)$$

and when no crystal-field-dependent amplitude function exists (plane waves), we can write

$$\psi(r, t) = A \cdot \exp \left[ i \left( k \cdot r - E \frac{t}{\hbar} \right) \right]. \quad (2.158)$$

Introducing this solution into (2.156) gives the result (2.153) if we interpret  $E(k) - E_{\text{pot}} = E(k) + eU$  as  $E$ , the total energy of the electron. Addition of an external force  $F$  changes  $E_{\text{pot}}$  to

$$E_{\text{pot}} = -eU - \mathbf{F}_e \cdot \mathbf{r}. \quad (2.159)$$

The external force is here defined by  $\mathbf{F}_e = -\text{grad}(-\mathbf{F} \cdot \mathbf{r})$  or the vector  $\mathbf{F}_e$  is the gradient of the scalar product of  $\mathbf{F}$  and local vector  $\mathbf{r}$  or the potential function  $(-\mathbf{F} \cdot \mathbf{r})$ . This leads to a Schrödinger equation

$$-\frac{\hbar^2}{2m} \nabla^2 \psi - (eU + \mathbf{F}_e \cdot \mathbf{r}) \psi = i\hbar \frac{\partial \psi}{\partial t}, \quad (2.160)$$

with the solution

$$\psi(r, t) = \psi[r, \mathbf{k}(t)] \exp \left\{ -\frac{i}{\hbar} \int_{\tau=0}^{\tau=t} E[\mathbf{k}(t)] d\tau \right\} \quad (2.161)$$

$$= A \exp \left\{ i \left[ \mathbf{k}(t) \cdot \mathbf{r} - \frac{1}{\hbar} \int_0^t E[\mathbf{k}(t)] d\tau \right] \right\} \quad (2.162)$$

and

$$E[\mathbf{k}(t)] = -eU + \frac{\hbar^2}{2m} |\mathbf{k}(t)|^2. \quad (2.163)$$

We see that the wave vector and  $E$  are again related by an equation of the kind of (2.153) and that

$$k = \frac{mv}{\hbar} = \frac{p}{\hbar}. \quad (2.164)$$

The force  $F_e$  is given by

$$\int F_e dt = m \int \frac{\partial v}{\partial t} dt \quad (2.165)$$

or

$$F_e \cdot t = m \cdot v. \quad (2.166)$$

Equations (2.166) and (2.164) indicate that an external force  $F_e$  applied, changes the wave vector from an initial value  $k(0)$  at time  $t = 0$  to a value

$$k(t) = k(0) + \frac{1}{\hbar} F_e \cdot t \quad (2.167)$$

or

$$k(t) = \frac{1}{\hbar} \cdot F_e. \quad (2.168)$$

In other words the time derivative of the wave vector is proportional to the external force  $F_e$ . Using again the DeBroglie relation (2.151), we see that

$$v = \frac{\hbar k}{m_0} \quad (2.169)$$

and the energy can be expressed as

$$E(k) = \frac{\hbar^2 k^2}{2m_0}. \quad (2.170)$$

Since

$$\frac{\partial E(k)}{\partial k} = \frac{\hbar^2 k}{m_0}, \quad (2.171)$$

we can establish the relation

$$v = \frac{1}{\hbar} \frac{\partial E(k)}{\partial k} = \frac{1}{\hbar} \nabla_k E(k). \quad (2.172)$$

This equation relates the local velocity of a wave package to the energy change in  $k$  space and is valid in all three dimensions. Equations (2.168) and (2.172) enable us to establish the general analogy  $F_e = m\dot{v}$  for  $F_e = \hbar \dot{k}$  (2.168) or to write the effective mass in its three-dimensional tensor form. From (2.172) we have

$$\begin{aligned} \dot{v}_x &= (\nabla_k v_x) \frac{\partial k}{\partial t} = \frac{\partial v_x}{\partial k_x} \frac{\partial k_x}{\partial t} + \frac{\partial v_x}{\partial k_y} \frac{\partial k_y}{\partial t} + \frac{\partial v_x}{\partial k_z} \frac{\partial k_z}{\partial t} \\ \dot{v}_y &= (\nabla_k v_y) \frac{\partial k}{\partial t} = \text{etc.} \\ \dot{v}_z &= (\nabla_k v_z) \frac{\partial k}{\partial t} = \text{etc.} \end{aligned} \quad (2.173)$$

From (2.172) we have

$$\frac{\partial v_x}{\partial k_x} = \frac{1}{\hbar} \frac{\partial^2 E}{\partial k_x^2} \quad (2.174)$$

and from (2.168)

$$\frac{\partial k_x}{\partial t} = \frac{F_e}{\hbar}. \quad (2.175)$$

Thus

$$\dot{v}_x = \frac{1}{\hbar^2} \left( \frac{\partial^2 E}{\partial k_x^2} F_{e_x} + \frac{\partial^2 E}{\partial k_x \partial k_y} F_{e_y} + \frac{\partial^2 E}{\partial k_x \partial k_z} F_{e_z} \right), \quad (2.176)$$

and so on for  $\dot{v}_y$  and  $\dot{v}_z$ .<sup>13</sup>

In defining the effective mass in real instead of  $k$  space, we use the analogy

$$F_e = \hbar k = mv = \text{crystal momentum},$$

which follows from (2.174) and (2.175), and write (2.176) as follows:

$$\left\| \frac{1}{m} \right\| = \frac{1}{\hbar^2} \begin{vmatrix} \frac{\partial^2 E}{\partial k_x^2} & \frac{\partial^2 E}{\partial k_x \partial k_y} & \frac{\partial^2 E}{\partial k_x \partial k_z} \\ \frac{\partial^2 E}{\partial k_y \partial k_x} & \frac{\partial^2 E}{\partial k_y^2} & \frac{\partial^2 E}{\partial k_y \partial k_z} \\ \frac{\partial^2 E}{\partial k_z \partial k_x} & \frac{\partial^2 E}{\partial k_z \partial k_y} & \frac{\partial^2 E}{\partial k_z^2} \end{vmatrix}. \quad (2.177)$$

For the free electron this reduces to

$$\left\| \frac{1}{m_0} \right\| = \begin{vmatrix} \frac{1}{m_0} & 0 & 0 \\ 0 & \frac{1}{m_0} & 0 \\ 0 & 0 & \frac{1}{m_0} \end{vmatrix}. \quad (2.178)$$

From (2.177) we can see how sensitive the effective mass is with respect to the energy surface. Any disturbance of the  $E(k)$  relation due to crystallographic defects changes  $m_{\text{eff}}$  and, therefore, the local carrier transport. If an entire band is filled—the valence band, for example—except for the eigenstate with wave vector  $\mathbf{k}$ , we have a hole with this  $\mathbf{k}$  vector. Heisenberg has shown that

this hole moves under the influence of a field as if it had the effective mass

$$\left\| \frac{1}{m} \right\|_{\text{hole}} = - \left\| \frac{1}{m} \right\|_{\text{electron}} \quad (2.179)$$

At the upper edge of the valence band, electrons usually have negative masses where the holes have positive effective masses. Or electrons have positive masses near the lower edge of the conduction band where holes have negative effective masses. (Holes behave in the half-empty conduction band like electrons in the full valence band). This can be shown by starting with the equality

$$\dot{v} = \left\| \frac{1}{m} \right\| (-eE) \quad (2.180)$$

of an electron subjected to the local field force  $-eE$ . Multiplying this by  $f(k)$ , the occupation density of the valence band in  $k$  space, and integrating over all electrons lead to

$$\iiint \frac{dv}{dt} f(k) d^3k = \left( \iiint f(k) \left\| \frac{1}{m} \right\| d^3k \right) (-eE). \quad (2.181)$$

Since for a full band  $f(k) = \text{const} = N = \text{number of electrons}$ , we get

$$N \frac{d\bar{v}}{dt} = \text{const} \left( \iiint \left\| \frac{1}{m} \right\| d^3k \right) (-eE) = 0, \quad (2.182)$$

since in a full band no acceleration occurs. At the surface of the reduced zone the slope of the energy change in a direction tangential to its surface is zero; that is, the integral (2.182) vanishes here. If, however, the band is full with one exception, one hole with wave number  $k = k'$ , then

$$N \frac{d\bar{v}}{dt} = - \left\| \frac{1}{m} \right\|_{k=k'} (-eE), \quad (2.183)$$

or the kinetic energy of holes is counted opposite that of electrons:

$$E_h(k) = -E_e(k) + \text{const.}$$

If in

$$\left\| \frac{1}{m} \right\| = \frac{1}{\hbar^2} \frac{\partial^2 E}{\partial k_{x,y,z}^2}$$

$\partial^2 E / \partial k^2$  is negative,  $m$  is negative.

The energy contours of heavy holes, for example, in germanium are partially concave (see, for example, Ref. 13), which means that the force field  $F(-eU)$  of a vector force in a certain crystallographic direction accelerates the electron or hole wave package in a different direction from the vector  $\hat{v}$ .

This means force  $F$  and vector  $\dot{v}$  do not coincide and  $\partial^2 E / \partial k_x^2$  at the upper band edge near the maximum of  $E(k)$  is negative, meaning that

$$m_{\text{eff}} = \frac{\hbar^2}{\partial^2 E / \partial k_x^2}$$

is negative. This situation is shown in Figure 2.19. Since

$$v = p/m = \hbar \frac{k}{m} = \frac{\partial E}{\partial k} \cdot \frac{1}{\hbar}$$

at the upper band edges,

$$\frac{\partial^2 E}{\partial k^2} < 0 \quad \text{or} \quad \frac{\partial \bar{v}}{\partial t} < 0,$$

which implies negative effective mass there. This means only, as we stated, that a force applied in the direction of motion decelerates the carrier. At the points  $\partial^2 E / \partial k^2 = 0$  the effective mass is

$$m_{\text{eff}} = \infty.$$

We see that within the allowed energy bands (see Figure 2.19) the electronic effective mass starts positive at the bottom, increases to the curvature change ( $m_{\text{eff}} \Rightarrow \infty$ ), and becomes negative at the upper edge of the bands. The reverse situation applies for the hole mass.

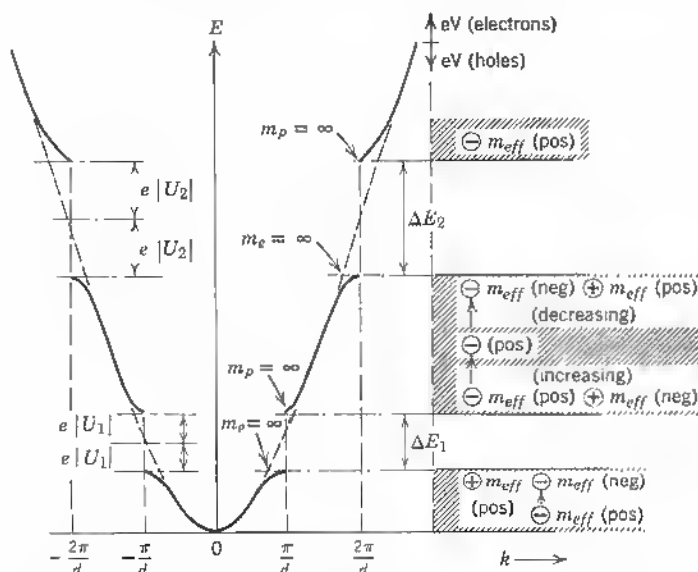


Fig. 2.19 Splitting of forbidden bands due to Bragg reflections (see Figure 2.12) and effective masses within the allowed bands.

In normal transport problems, therefore, only holes in the upper part of the lower band (valence band) and electrons in the lower part of the conduction band are considered.

## 2.9 INTERBAND TRANSITIONS

The addition of an external force  $F_e$  to the crystal field forces  $eU(\mathbf{r})$  gives the wave vector a time dependence, as we have expressed by (2.168). The corresponding time-dependent Schrödinger equation

$$-\frac{\hbar^2}{2m} \nabla^2 \psi(\mathbf{r}, t) - (eU(\mathbf{r}) + F_e \cdot \mathbf{r}) \psi(\mathbf{r}, t) = j\hbar \frac{\partial}{\partial t} \psi(\mathbf{r}, t) \quad (2.184)$$

can be solved by the Bloch wave function

$$\psi(\mathbf{r}, t) = \psi(\mathbf{r}, \mathbf{k}) \exp \left[ -\frac{j}{\hbar} \int_{\tau=0}^{\tau=t} E(k(\tau)) d\tau \right]. \quad (\text{W. V. Houston})^4 \quad (2.185)$$

This can be written in terms of the solution of the stationary Schrödinger equation

$$\psi(\mathbf{r}, \mathbf{k}(t)) = u(\mathbf{r}, \mathbf{k}(t)) e^{j\mathbf{k} \cdot \mathbf{r}} \quad (2.186)$$

or

$$\psi(\mathbf{r}, t) = u(\mathbf{r}, \mathbf{k}(t)) \exp \left[ j\mathbf{k}(t) \cdot \mathbf{r} - \frac{j}{\hbar} \int_{\tau=0}^{\tau=t} E(k(\tau)) d\tau \right] \quad (2.187)$$

This solution does not take into account that the force  $F_e$  can also induce transitions of electrons into higher energy bands. If the wave function is written as a sum of wave functions of the type (2.187), the exact solution is found. Each of these sums has a time-dependent amplitude coefficient and a probability for transitions of electrons into higher bands that can be given as the amplitude square of the corresponding order. The well-known approach by Zener<sup>4</sup> is based on the assumption of a quasi-stationary behavior of the wave functions within measurable distances in the lattice because an external field  $E_e$  in volts per centimeter represents a localized crystal potential of only  $10^{-8}$  V. External breakdown fields of  $10^6$  V/cm, for example, lead to internal crystal potentials of  $10^{-3}$  V. This is three orders of magnitude below the lattice potential, compare section 2.7. Along this line of argument the stationary Schrödinger equation

$$-\frac{\hbar^2}{2m} \psi''(x) - (eU(x) + F_e \cdot x) \psi(x) = E \psi(x) \quad (2.188)$$

can be contracted to

$$-\frac{\hbar^2}{2m} \psi''(x) - e \cdot U(x) \psi(x) = E_c \cdot \psi(x), \quad (2.189)$$

where  $E_c = E + F_e \cdot x_n$  is the local crystal field as a superposition of the electronic energy and the additional external field energy.

Since there are  $n$  steps of field influence along a distance  $x$  in the crystal, as assumed by our approximation, Zener's solution of the wave equation is simply

$$\psi(x) = u(x, k(x)) \exp \left[ i \int_{x=0}^x k(x) dx \right]; \quad (2.190)$$

in other words it is a solution like (2.98), but with the feature that the periodicity function in the Bloch wave is slowly varying with  $x$ . If the energy expression for the crystal electron increases to values beyond  $E + F_e x = E_c > E_{\text{band}}$ , where  $E_{\text{band}}$  are the allowed energy values in one band, the wave vector  $k$  becomes complex until the next higher allowed band can be penetrated. Introducing a specific function for the lattice potential, for example,

$$U(x) = 2A \cos 2\pi \frac{x}{d}, \quad (2.191)$$

where  $d$  = lattice constant,

$A$  = amplitude,

yields

$$k(x) = \frac{\pi}{d} \left[ 1 \pm i \frac{4md^2}{\hbar^2} \sqrt{A_1^2 - (F_e x)^2} \right]. \quad (2.192)$$

If  $k(x)$  within the crystal lattice changes from real to imaginary and back to real for the  $x$  values  $x_B$  and  $x_c$  (see Figure 2.20), or

$$\begin{aligned} k(x) &< k(x_B) \text{ real} \\ k(x) &> k(x_B) \text{ complex} \\ k(x) &> k(x_c) \text{ real,} \end{aligned}$$

we can define a probability of band penetration as in the tunnel effect

$$w = \frac{[|\psi(x_c)|]^2}{[|\psi(x_B)|]^2}. \quad (2.193)$$

With (2.190) we get

$$w = \left\{ \frac{|u[x_c, k(x_c)]|}{|u[x_B, k(x_B)]|} \exp \left( - \int_{x_B}^{x_c} \text{Im } k(x) dx \right) \right\}. \quad (2.194)$$

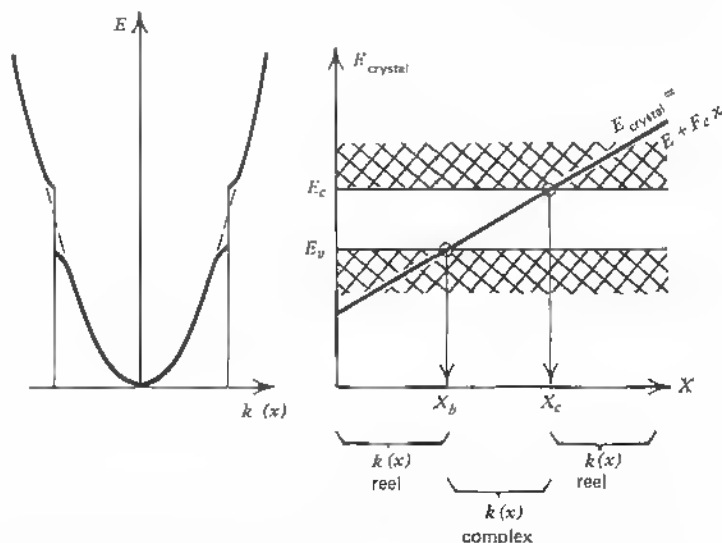


Fig. 2.20 Wave vector change from real to complex for electron transition through a forbidden band.

The part  $\text{Im } k(x) dx$  is the imaginary part of (2.192). In the Zener approximation the ratio of the lattice periodic amplitude functions is set equal to 1, and

$$w \simeq \exp \left[ -2 \int_{x_B}^{x_C} \text{Im } k(x) dx \right] \quad (2.195)$$

is evaluated with (2.192) leading to an expression for the probability of penetration:

$$w = \exp \left( -\frac{\pi^2 m d E_{cv}^2}{h^2 F_e} \right), \quad (2.196)$$

where  $E_{cv}$  = width of forbidden zone (upper edge of valence band to lower edge of conduction band),

$d$  = lattice constant,

$m$  = effective mass,

$F_e$  = external field,

$h$  = Planck's constant.

Equation (2.196) shows that relatively high fields  $|E| = (1/q)F_e$  are needed to give  $w$  a value so that the expectancy of band penetration becomes measurable for the usual band gaps  $E_{cv}$ .

If additional energy levels within the forbidden gap occur, field-aided localized tunneling may become possible.



W. Franz\* has evaluated (2.195) more thoroughly for the case of electrons in impurity levels and derives an expression

$$w = \exp \left[ - \frac{4}{3} \frac{\sqrt{2m_{\text{eff}}}}{\hbar \cdot q \cdot |E|} (E_{ic})^{3/2} \right], \quad (2.197)$$

where  $q$  = electronic charge,

$q|E| = F_e$ ,

$m_{\text{eff}}$  = effective mass,

$\hbar = \frac{h}{2\pi}$ ,

$E_{ic}$  = energy difference between impurity level and lower edge of conduction band.

As  $E_{ic}$  and  $m_{\text{eff}}$  become smaller and  $E$  higher, the probability of emission of electrons from interband levels to the conduction band increases. From this point of view it is obvious that an increase in the number of ionized centers with a certain spread in energy levels gives rise to field emission and breakdown phenomena at lower than critical field values ( $E_{cv}$ ). Dislocations introduce interband energy levels and, therefore, should lower the necessary field for interband transitions. From the work of Chynoweth and MacKay<sup>14</sup> it is known that an intimate correlation exists between junction breakdown phenomena and field emission. With decreasing junction width (increasing doping) Zener breakdown and avalanche multiplication (microplasmas) go over into field emission and soft breakdown. In the latter case the role of dislocations seems all important, and light-emission spots are clearly correlated to the etch-pit micrograms of the crystals. In the external field of the tilted bands a number of transitions are possible (see Figure 2.21). First, there are transitions from contacts or surface states into the conduction band (1); (2) represents a field ionization of a local energy level of an impurity, for example; here inter-level tunneling can also be involved from one lower level to a higher level. (3) would be a typical case for a dislocation-induced series of levels and subsequent field emission of electrons from the valence to the conduction band. Such areas are also preferred spots for the formation of microplasmas. (4) would be the ideal Zener breakdown and (5) the hole injection process from the valence band to the crystal anode.

If dislocations generate preferably mid-band energy levels, it is probable that they also are responsible for local field emission. Because of the space charge at the dislocation site and the high conductance in the axial direction of the space-charge cylinder, the dislocation pipe represents a strong local field inhomogeneity so that electrons reaching the conduction band through

\* *Ergebn. exact. Naturw.* Vol. 27; p. 16 (1953) and Ref. 4.

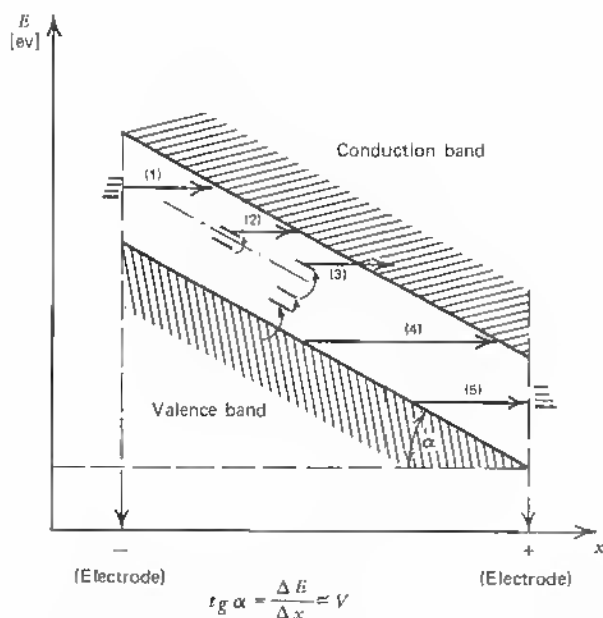


Fig. 2.21 Possible electron transitions from valence to conduction band (see text).

field transport easily recombine with lower-lying dislocation levels in a radiative process. The whole structure at a dislocation space-charge pipe is typical of preferred recombination due to the high barrier height at the pipe and the interband levels. In (2.197),  $w$  is large because  $F_e = q|E|$  is large and  $E_{ic}$  is small. A fact that has to be considered here also is the overlap of the electronic wave functions within a dislocation pipe where dangling bonds can be found at lattice spacings within the additional half atom plane (see Chapter 8).

## 2.10 SCATTERING

Impurities, defects, and phonons are the main scattering sources of moving charges in real crystals. Bloch waves in perfect periodic structures should move very freely when subjected to field forces or, for example, under the influence of incident photon energy. The group velocity expressed as

$$v = \frac{1}{\hbar} \text{grad}_k E(k) \quad (2.198)$$

shows that the dependence of the energy on  $k$  is the main factor (see Section 2.8).  $v \times m_{\text{eff}}$  gives the mean impulse of the Bloch wave. The thermal velocity

derived from the chemical potential  $\zeta$  (see footnote)\* shows, in fact, that for impurity densities near degenerate and small effective masses velocities in excess of  $10^{-2}$  to  $10^{-1} c$  are possible ( $c$  is light speed). Compare also Chapter 15. But collisions with defects randomize the velocity vector. Therefore, we

\* In terms of the effective state density in the conduction band

$$N_c = 2 \left( \frac{2\pi m_{\text{eff}} kT}{h^2} \right)^{3/2} = 2.5 \cdot 10^{-19} \left( \frac{m_{\text{eff}}}{m} \right)^{3/2} \left( \frac{T}{300^\circ\text{K}} \right)^{3/2} \text{ cm}^{-3}$$

$n$  is always large compared with  $N_c$ . For  $N \simeq n$  the temperature of the metal would have to be raised to

$$T \simeq 300^\circ\text{K} \left( \frac{4 \cdot 10^{22}}{2.5 \cdot 10^{19}} \right)^{2/3}.$$

For  $m_{\text{eff}} = m_0$ , it follows that:

$$T \simeq 300^\circ\text{K} \cdot (1.6 \cdot 10^3)^{2/3} \simeq 40,000^\circ\text{K},$$

that is, well beyond the melting point. In other words, the high density of electrons in the conduction band makes a metal "degenerate" in the sense of the Fermi distribution function. The energy difference between the Fermi level and the lower edge of the conduction band,  $\zeta = E_F - E_C$ , is given by

$$\zeta \simeq kT \left( \frac{3}{4} \right)^{2/3} \pi^{1/3} \left( \frac{n}{N_c} \right)^{2/3}.$$

Introducing here the expression for  $N_c$  yields

$$\zeta \simeq \frac{1}{2} \left( \frac{3}{8\pi} \right)^{2/3} \frac{h^2}{m_{\text{eff}}} n^{2/3},$$

showing that in the case of degeneracy the temperature dependence of the Fermi level difference  $E_F - E_C$  disappears. For electrons at the Fermi edge this temperature insensitivity is well known. It is especially visible for all transport processes within defect structures (grain boundaries) where strong degeneracy prevails (see Chapter 8).

The electron velocity can be assessed in this case from the equality

$$\begin{aligned} \zeta &= E_F - E_C = \frac{m_{\text{eff}}}{2} \cdot v_\theta^2, \\ v_\theta &= \left( \frac{3}{8\pi} \right)^{1/3} \cdot \frac{h}{m_{\text{eff}}} n^{1/3} \\ &\simeq 7.71 \cdot 10^7 \text{ cm} \cdot \text{sec}^{-1} \left( \frac{m}{m_{\text{eff}}} \right) \left( \frac{n}{10^{22} \text{ cm}^{-3}} \right)^{1/3}, \end{aligned}$$

or  $v_\theta$  is about  $10^8 \text{ cm sec}^{-1}$ .

One can also estimate  $v_\theta$  from the energy versus  $k$  relation at the band center, since

$$\frac{dE}{dk} = \hbar v_\theta$$

have to define a mean free time  $\bar{\tau}$  ( $\bar{\tau}$  is a probability parameter and as such a constant—see, for example, Ref. 7, pp. 191–195). Also, the mean free path is  $v_\theta \cdot \bar{\tau}$ , where  $v_\theta$  is the thermal velocity (of constant absolute value). In an electric field  $E$  the particle acceleration is

$$a = -\frac{eE}{m},$$

and we can define a drift velocity

$$v_d = \int_0^{\bar{\tau}} a \, dt = -\frac{e\bar{\tau}}{m} E. \quad (2.199)$$

The proportionality factor between  $v_d$  and  $E$  is the mobility

$$\mu = \frac{e}{m} \bar{\tau}. \quad (2.200)$$

The condition for  $\bar{\tau}$  being a constant (mean free time) is, however, that  $v_d \ll v_\theta$ . If this condition is not satisfied either by high local fields or operation at low temperature, Ohm's law is invalidated, and we enter the field of hot-carrier physics,<sup>15</sup> where  $|v_d| = \mu|E| \approx v_\theta$  and the critical field value is  $E_{\text{crit}} \approx v_\theta/\mu$ . Here we remain within the limit  $v_d \ll v_\theta$  and, therefore, write the current carried by  $n$  charges in a three-dimensional sample as

$$i = (-e \cdot n) v_d \quad (2.201)$$

$$= (-e \cdot n)(-\mu E) \quad (2.202)$$

$$i = e\mu n E, \quad (2.203)$$

where  $n$  = number of carriers.

With Ohm's law,  $i = \sigma \cdot E$ , the conductivity is then given by

$$\sigma[\text{ohm}^{-1} \text{cm}^{-1}] = 1.6 \cdot 10^{-19} \mu \left[ \frac{\text{cm}^2}{\text{V sec}} \right] \cdot n[\text{cm}^{-3}]. \quad (2.204)$$

(see Ref. 4), or use the crystal momentum equation

$$m_{\text{eff}} \cdot v_\theta = \hbar \cdot k,$$

where  $m_{\text{eff}} \approx 0.5 \cdot 10^{-28} \text{ g}$ ,

$$k = \frac{\pi}{2d} \approx \frac{1}{2} 10^8 \text{ cm}^{-1} \quad (\text{band center}),$$

$$v_\theta \approx \frac{10^{-27} \cdot \text{cm}^2 \text{ g sec}^{-1}}{9 \cdot 10^{-28} \text{ g}} \cdot \frac{1}{2} \cdot 10^8 \text{ cm}^{-1}$$

$$\sim 0.5 \cdot 10^8 \text{ cm sec}^{-1}.$$

In metals the number  $n$  of free electrons is about equal to the number of atoms:  $n \simeq 4 \cdot 10^{22} \text{ cm}^{-3}$ .

With a metallic conductivity of  $\sigma \simeq 4 \cdot 10^5 \text{ ohm}^{-1} \text{ cm}^{-1}$ , a mobility value  $\mu \simeq 60 \text{ cm}^2/\text{V sec}$  is found.

The mobility value for metals, found according to (2.204), is relatively low, compared with values measured in semiconductors. There are two reasons, evident from (2.200). First, the mean free time  $\bar{\tau}$  is between 10 and 100 times larger than in metals, and, in addition, the effective masses are at least  $(\frac{1}{10}) m_0$  and can be much smaller.

With  $\mu = 60 \text{ cm}^2/\text{V sec}$ , we find from (2.200) for metals

$$\bar{\tau} [\text{sec}] = \left( 300 \frac{m}{e} \right) \mu [\text{cm}^2/\text{V sec}],$$

$$\bar{\tau} \simeq 3.6 \cdot 10^{-14} \text{ sec.}$$

The mean free path is of the order of  $36 \text{ \AA}$ .

Generally

$$l = \bar{\tau} \cdot v_g \approx 10^7 \cdot 0.57 \cdot 10^{-15} [\text{cm}] = 0.57 \times \mu [\text{\AA}],$$

since

$$\tau = 5.7 \times 10^{-16} \mu [\text{sec}].$$

In semiconductors  $\mu$  can be an order of magnitude larger and consequently also  $\bar{\tau} \cdot v_g$ .

Aside from charged defects (foreign atoms) lattice vibrations (phonons) are the strongest disturbance for the electronic charge transport. For doping ranges below degenerate the impurity scattering is small in semiconductors at room temperature. In three-dimensional space the scattering leads to three current components for the electron. In momentum space a group  $n_i$  of electrons in a volume element  $dE d\Omega_i$  ( $d\Omega_i$  is the region of energy shell considered) produces a current density

$$\delta I = - \frac{e v_i}{V} \delta n_i, \quad (2.205)$$

where  $v_i$  = velocity component of group  $n_i$ ,

$V$  = crystal volume under consideration.

The fraction of carriers scattered into a new direction with velocity  $v_j$  during time  $dt$  changes the current increment to

$$d\delta I = dt \int_{\Omega(E)} \frac{-e(v_j - v_i)}{V} \delta n_i W_{ij} d\Omega_j, \quad (2.206)$$

where  $\Omega(E)$  = energy surface.

The  $W_{ij}$  is the transition probability from state  $i$  to  $j$  and a function of  $\theta$ , the angle between initial velocity  $v_i$  and final velocity  $v_j$ . In a set of spherical coordinates with  $\theta = 0$  parallel to  $v_i$ , the current change can be expressed by

$$d\delta I = -dt \delta I \int (1 - \cos \theta_j) W(\theta_j) d\Omega_j \quad (2.207)$$

$$= -dt \delta I W_0 \langle 1 - \cos \theta \rangle \quad (2.208)$$

(see, for example, Ref. 7). Here  $W(\theta_j)$  is the transition probability referring to the scattering angle, and

$$W_0 = \int W(\theta_j) d\Omega_j \quad (2.209)$$

is the average transition probability over the volume element in momentum space.  $\langle 1 - \cos \theta \rangle$  is introduced as the average scattering parameter for all collision processes:

$$\langle 1 - \cos \theta \rangle = \frac{1}{W_0} \int (1 - \cos \theta) W(\theta) d\Omega. \quad (2.210)$$

The current relaxation due to an arbitrary distribution of velocity vectors over the energy shell, using (2.208), can be written

$$d\delta I_i = -\delta I_i \frac{dt}{\tau_r}, \quad (2.211)$$

where  $\tau_r$  = relaxation time.

This equation, integrated over all current elements, leads to

$$d \sum_i \delta I_i = dI = - \left( \sum_i \delta I_i \right) \frac{dt}{\tau_r}, \quad (2.212)$$

$$\dot{I} = -\frac{I}{\tau_r}, \quad (2.213)$$

$$I = I_0 e^{-t/\tau_r}. \quad (2.214)$$

Comparing (2.208) and (2.211) shows that

$$\frac{1}{\tau_r} = W_0 \langle 1 - \cos \theta \rangle. \quad (2.215)$$

Since the probability of transition from one energy state to another is equal to the reciprocal mean free time  $\bar{\tau}$

$$W_0 = \frac{1}{\bar{\tau}}, \quad (2.216)$$

we get from (2.215) and (2.216) the relation

$$\bar{\tau} = \tau_r \langle 1 - \cos \theta \rangle. \quad (2.217)$$

For the case of thermal vibrations  $\langle \cos \theta \rangle = 0$ , (probability independent of  $\theta$ ),

$$\bar{\tau} = \tau_r.$$

For impurity scattering,  $\langle \cos \theta \rangle$  may approach unity for large  $\theta$  values; therefore,  $\tau_r \gg \bar{\tau}$ .

This can be seen from the application of the Conwell-Weisskopf scattering formula. For an electron, for example, the influence of a positively charged donor ion is equivalent to a negatively charged acceptor ion. Figure 2.22 shows the two equivalent cases of scattering for a fixed scattering angle  $\theta$  (equal ion charges, equal electron velocities). The value of the scattering parameter is

$$\langle 1 - \cos \theta \rangle = 2 \left( \frac{E_1}{2E} \right)^2 \ln \left[ 1 + \left( \frac{2E}{E_1} \right)^2 \right], \quad (2.218)$$

where  $E_1 = \text{electronic potential energy} = \frac{e^2}{\kappa(a_1/2)}$ ,

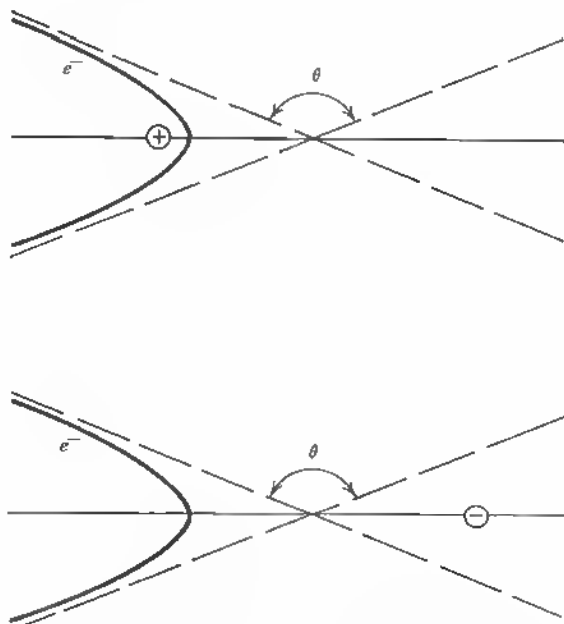


Fig. 2.22 Electron scattering at positive and negative ions.

$a_1$  = linear ion distance,

$\kappa = 16$  = dielectric constant (Ge),

$E = mv^2/2$  = electron kinetic energy,

$a_1$  depends on the doping range (see, for example, Ref. 7).

The scattering parameter  $\langle 1 - \cos \theta \rangle$  is actually an average with a maximum value at  $\theta = \pi$ :

Scattering angle $\theta$	Scattering parameter $\langle 1 - \cos \theta \rangle$
$\frac{\pi}{2}$	1
$\pi$	2
0	0

For an electron with energy  $E = kT$ , an estimate of the potential energy at a distance  $a_1/2$  from an impurity ion ( $a_1$  is the mean distance of ions in lattice) is as follows.

Assume that

$$N_d = 10^{15} \text{ cm}^{-3} \quad \text{or} \quad a_1 = \sqrt[3]{\frac{1}{N_d}}.$$

This gives

$$a_1 \simeq 10^{-5} \text{ cm} = 10^3 \text{ \AA}.$$

Now the potential energy is

$$E_1 = \frac{e^2}{\kappa(a_1/2)} = e \frac{4.8 \times 10^{-10}}{16(a_1/2) \cdot 10^{-8} \text{ \AA}} \text{ esu}$$

$$E_1 = \frac{10^{-2}}{3(a_1/2) \text{ \AA}} \cdot 300 \text{ eV}$$

or

$$E_1 = \frac{2}{a_1 \text{ \AA}} \text{ eV}.$$

A rough estimate of the potential energy of the electron if expressed in electron volts, in the case of germanium with the impurity density of  $10^{15} \text{ cm}^{-3}$  gives, therefore, twice the reciprocal mean ion distance in angstroms or  $E_1 \simeq 40/(a_1/2) \text{ kT}$  at  $300^\circ \text{K}$ . For  $a_1 = 1,000 \text{ \AA}$  we get  $E_1 \simeq 0.08 \text{ kT}$ . This shows that the interaction of an electron with an ion is only  $\frac{1}{12}$  of the thermal energy  $kT$  of the electron.

If we use Conwell-Weisskopf's formula (2.218) to assess the scattering parameter, we get

$$\begin{aligned} \langle 1 - \cos \theta \rangle &= 2 \left( \frac{0.08 kT}{2kT} \right)^2 \ln \left[ 1 + \left( \frac{2}{0.08} \right)^2 \right] \\ \langle 1 - \cos \theta \rangle &= 2(4 \cdot 10^{-2})^2 \ln[1 + 25^2] \\ &\simeq \frac{1}{50}, \end{aligned} \quad (2.219)$$



for  $E_1 = 0.08 \text{ kT}$ , and  $E = kT$ . This means that the interaction is  $\frac{1}{30}$  of the traveling distance  $a_1$ , or the mean free path is

$$\begin{aligned} 50a_1 &= 5 \cdot 10^{-4} \text{ cm} \\ &= 10^4 \text{ lattice constants,} \end{aligned}$$

showing that at  $300^\circ\text{K}$  impurity scattering is unimportant. With reference to the relation between relaxation time and mean free time, this means that

$$\tau_r = 50 \bar{\tau},$$

corresponding to (2.217). If the mobility is dominated by the relaxation time

$$\mu = \frac{e}{m} \tau_r = \frac{e}{m} (50\bar{\tau}), \quad (2.220)$$

we see that at low temperature ( $\tau_r \gg \bar{\tau}$ ) high mobility values occur. This is true, however, only for nondegeneracy or in a range of low-impurity scattering (for more detail see Ref. 7, p. 277). Dislocation sites are charged centers either because of a doping mismatch, when lattice dilation and compression react as sinks for specific ions, or because of the dangling bonds. In either case a strong core charge can be accompanied by a space charge. If more extended dislocation arrays are generated instead of point defects, dislocation space-charge pipes are formed and have as such a strong scattering influence on carriers that can be assessed in the same way as done for neutral impurities. In this case, one assumes that such a dislocation acts as an impenetrable cylinder rather than a strongly charged hole sink,\* and one can define a velocity change  $\Delta v$  of the carrier on impact. In the  $xy$  plane, the velocity change is  $\Delta v$  (see Figure 2.23)<sup>16</sup> for an electron coming in at a distance  $d$  from the axis of the dislocation cylinder with radius  $R$ , the scattering angle being  $\theta_1 = \pi - 2\phi$ ,

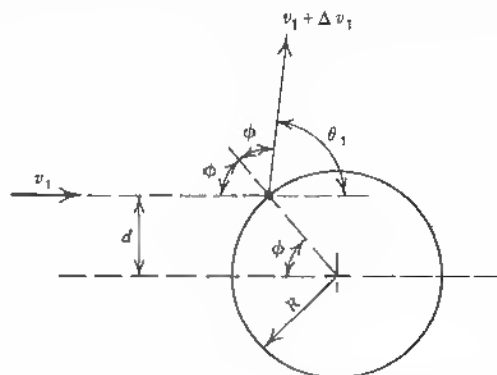


Fig. 2.23 Dislocation pipe scattering (see text).

\* See Chapter 9 and 11 for objections to this model.

where  $\cos \phi = \sin(\theta_1/2)$ . The average change in velocity  $\langle \Delta v \rangle$  is then

$$-v_1 \langle 1 - \cos \theta_1 \rangle, \quad (2.221)$$

and the mean free time of dislocation scattering is

$$\tau_1 = \frac{\tau_c}{\langle 1 - \cos \theta_1 \rangle}. \quad (2.222)$$

The time rate of change of velocity for electrons having incident velocity  $v$  is

$$\frac{dv}{dt} = \frac{\langle \Delta v \rangle}{\tau_c}, \quad (2.223)$$

where  $\tau_c$  = mean collision time (mean free time between collisions). Thus

$$\tau_c = \tau_1 \langle 1 - \cos \theta \rangle \quad (2.224)$$

is equivalent to (2.217),  $\tau_c$  standing for the mean free scattering time and  $\tau_1$  for the dislocation scattering (relaxation) time.

In addition to the role of the dislocations as scattering centers, their stress field enhances interaction of charge carriers with photons and phonons. Assume that a dilation area at the lower end of an edge dislocation is subjected to incoming photon energy  $h\nu$  (see Figure 2.24). The energy may be

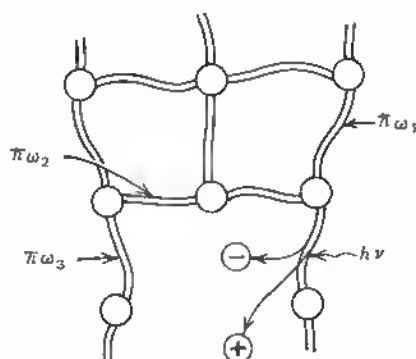


Fig. 2.24 Separation of electron-hole pair at dangling bond site.

sufficient to break a strained bond, liberating electron-hole pairs, separating at the dangling-bond site, with the electron joining the free bond and thereby lowering the energy level of the dangling bond, and the hole moving toward the space charge. Because the bonds are weakened at the mismatch area, we have different phonon energies around the compression-dilation zone:  $h\omega_1$ ,  $h\omega_2$ , and so on. For the carriers involved, energy balance and wave-vector

conservation have to be maintained:

$$E(k') = E(k) + \hbar\omega_{\text{lattice}}$$

and

$$k' = k + k_{\text{lattice}}.$$

These conditions can be fulfilled for a greater number of photon energies if the energy balance is satisfied by the correct vibrational energy  $\hbar\omega$  of the lattice. Because here a number of different phonon frequencies is available, a higher photon efficiency is obtained in the release of free carriers (see Chapter 9).

### PROBLEMS

- 2.1. Draw the known wave velocity versus wave number function (2.10) for varied lattice parameters  $d$  but constant wavelength  $\lambda$ . Show why the velocity maximum coincides more and more with the symmetry points  $d/\lambda = \frac{1}{2}, \frac{1}{3}, \frac{1}{4}, \dots, 1/n$  as  $n$  increases (compare with fringe visibility for a Fresnel slit source).
- 2.2. Describe the effect of a change in the ratio of lattice force  $\gamma$  and point mass  $m$ ,  $\gamma/m$ , for a fixed ratio  $m_1/m_2$  on the acoustical and optical phonon frequency versus wave vector function.
- 2.3. Calculate the angle  $\theta$  between the direct lattice vectors for which a line of vacancies in the [01] direction (two-dimensional plot) gives Bragg reflections (use Figure 2-7). (*Hint*:

$$\begin{aligned}\cos \psi &= -\cos \theta, \\ S_d &= |d'_1| |d'_2|, \\ S_r &= |b_1| |b_2| \sin (\pi - \theta) \quad (\psi' = 0), \\ (\mathbf{b}_1 \cdot \mathbf{d}'_1) &= |b_1| |d'_1| (-\cos \theta) = 1, \\ (\mathbf{b}_2 \cdot \mathbf{d}'_2) &= |b_2| |d'_2| = 1, \\ S_r \cdot S_d &= -\tan \theta, \\ \text{and } \theta &= 45^\circ.\end{aligned}$$

- 2.4. Discuss the equivalence of momentum and impulse for the free electron and the crystal electron:

$$\begin{aligned}m^* \cdot v &\doteq \pm \hbar k, \\ m^* \cdot \dot{v} &\doteq \pm \hbar \dot{k},\end{aligned}$$

- 2.5. Calculate the mean (linear) distance between impurity atoms in germanium of  $N_d = 10^{15} \text{ cm}^{-3}$  doping level (number of germanium atoms per  $\text{cm}^3 = 4.52 \cdot 10^{22}$ ).
- 2.6. If an impurity electron has a spherical charge cloud of radius

$$r_c = 7 \cdot 10^{-8} \text{ cm},$$

how many elementary germanium cubes are covered? How many germanium atoms? Calculate the same for diamond, silicon, and tin (gray):

Crystal	Lattice constant, Å	Number of atoms per cm <sup>3</sup>
Diamond	3.56	$17.7 \cdot 10^{22}$
Silicon	5.42	$5.0 \cdot 10^{22}$
Germanium	5.62	$4.52 \cdot 10^{22}$
Tin (gray)	6.46	$2.82 \cdot 10^{22}$

- 2.7. Show how Newton's Law  $F = m\dot{v}$  is modified as applied to the free-electron wave package with wave vector  $k(t)$ . (*Hint:* Start with the energy relations in  $k$  space:  $E(k) = -eV + (\hbar^2/2m)|k|^2$ , and differentiate twice with respect to  $k$ . Express  $m$ . Or start with energy expression  $E = \frac{1}{2}m_0v^2$ , and express  $v$  from DeBroglie's relation  $p = \hbar k = mv_0 = \hbar k$ .)
- 2.8. What is the density of antimony atoms (atomic weight = 121.76) in a germanium crystal (atomic weight = 72.6) if 100 g of germanium are molten together with  $3.22 \cdot 10^{-6}$  g of antimony (density of Ge = 5.46 g/cm<sup>3</sup>; 1 g atom = 72.6 g Ge =  $6 \times 10^{23}$  atoms)?
- 2.9. For a mobility  $\mu = 3,600$  cm<sup>2</sup>/V sec, what is the conductivity, resistivity, and sample resistance if its length  $l$  is 2 cm and its cross section  $q$  is 0.1 cm<sup>2</sup>?
- 2.10. Give the value of the Hall constant and the mobility for a semiconductor crystal sample of thickness  $d = 0.1$  cm, when direct current flowing along the sample axis of 100 mA produces a cross (Hall) voltage of  $\Delta U = 0.1$  volt in a vertical magnetic field  $H = 3$  kG and if the sample resistivity is 10 Ωcm.
- 2.11. What is the thermal velocity of a charge carrier with wave vector

$$k = \frac{\pi}{2a}$$

( $a = 5 \cdot 10^{-8}$  cm) and effective mass  $m^* = 0.1m_0 \simeq 10^{-28}$  g?

- 2.12. Show that  $\psi(r, t) = Ae^{i[kr - (E_t/\hbar)t]}$  as a plane wave is a solution of the time-dependent Schrödinger equation (sec p. 48).
- 2.13. What is the nearest neighbor distance for the impurity atoms of density  $N_A = 10^{18}$  cm<sup>-3</sup> in diamond (express in lattice constants).
- 2.14. In the case of electron-filled traps (strong  $n$ -type doping) and a negligible number of trap-induced holes,  $p_1$  in the valence band, calculate the net recombination rate for a crystal with  $10^{17}$  cm<sup>-3</sup> donor doping when the trap level  $E_t$  is 0.5 eV above the valence-band edge in germanium and the hole-capture probability per unit time is  $C_p = 10^{-5}$ .
- 2.15. Discuss the variation of the effective mass and its sign reversal along the wave-vector axis for a parabolic  $E(k)$  relation.
- 2.16. Calculate the mean free path in lattice constants of a thermal electron in silicon if the mobility is given as 300 cm/sec/V/cm and the doping range is  $10^{16}$  cm<sup>-3</sup>. Set  $m_{\text{eff}} \simeq 0.1m_0$ .

- 2.17. Indicate the value for the mean free time for electrons in Ge when the mobility  $\mu = 3.6 \cdot 10^3 \text{ cm}^2/\text{Vs}$  ( $m_{\text{eff}} \simeq 0.1 m_0$ .)
- 2.18. A photon of wavelength  $\lambda = 5 \cdot 10^{-3} \text{ cm}$  is transferred in the lattice into a photon of wavelength  $\lambda = 10^{-2} \text{ cm}$ , with the remainder of the energy appearing in phonon energy. Express its wavelength.
- 2.19. Calculate the potential energy in kT or eV of an electron at a distance of half the ion spacing from a singly ionized impurity atom for germanium of  $N_a = 10^{18} \text{ cm}^{-3}$  doping.
- 2.20. Calculate the Conwell-Weisskopf scattering parameter for the case of Prob. 2.19 for thermal electrons.

## REFERENCES

1. Brillouin, L.: "Wave Propagation in Periodic Structures," Dover, New York, 1965, p. 118.
2. Kittel, C.: Phonons in Perfect Lattices and in Lattices with Point Imperfections, in "Phonons," R. W. H. Stevenson (ed.), Plenum, New York, 1966, pp. 1-50.
3. Elliott, R. J.: Vibrations of Defects in Lattices, in "Phonons," R. W. H. Stevenson (ed.), Plenum, New York, 1966, pp. 377-402.
4. Spence, E.: "Electronic Semiconductors," translated by D. Jenny et al., McGraw-Hill, New York, 1958.
5. Schottky, W.: In "Semiconductor Problems" (Halbleiterprobleme), Vieweg, Braunschweig, 1945 (German), vol. I, p. 85ff.
6. Haug, A.: In "Semiconductor Problems" (Halbleiterprobleme), Vieweg, Braunschweig, 1954 (German), vol. I, p. 227ff.
7. Shockley, W.: "Electrons and Holes in Semiconductors," Van Nostrand, New York, 1953, p. 143ff.
8. Shockley, W.: and W. T. Read, Jr.: Statistics of the Recombination of Holes and Electrons, *Physical Review*, vol. 87, vol. 5, pp. 835-842, Sept. 1, 1952.
9. Brown, N.: Lattice Defects, in "Intermetallic Compounds," J. H. Westbrook (ed.), Wiley, New York, 1967.
10. Bakish, R.: Internal and External Interfaces, in "Intermetallic Compounds," J. H. Westbrook (ed.), Wiley, New York, 1967, pp. 283-300.
11. Beam, W. R.: "Electronics of Solids," McGraw-Hill, New York, 1965, p. 193ff.
12. Ziman, J. M.: "Electrons and Phonons," Clarendon Press, Oxford, 1960.
13. Kroemer, H.: Negative Effective Masses in Semiconductors, "Progress in Semiconductors," vol. 4, A. F. Gibson (ed.), Wiley, New York, 1960, pp. 3-34.
14. Chynoweth, A. G.: Internal Field Emission, in "Progress in Semiconductors," vol. 4, A. F. Gibson (ed.), Wiley, New York, 1960, pp. 97-123.
15. Conwell, E. M.: High Field Transport in Semiconductors, in "Solid State Physics," edited by Seitz-Turnbull-Ehrenreich, Academic, New York, 1967.
16. Read, W. T., Jr.: Theory of Dislocations in Semiconductors, *Philosophical Magazine*, vol. 45, pp. 775-796, August, 1954; vol. 45, pp. 1119-1178, November, 1954; vol. 46, pp. 111-131, February, 1955.

## Chapter 3 Classification of Defects in Crystals

This treatise is confined to the structural defects of linear and planar extent because of their strong electronic effects in bulk crystals. The point defects are mentioned for the sake of completeness and in reference to some later considerations in other paragraphs.

Seitz<sup>1</sup> has formulated a nomenclature for the different kinds of defects. He defines essentially six primary defects in crystals: (1) phonons (quanta of lattice vibrations), (2) electrons and defect electrons, (3) excitons, (4) lattice vacancies and interstitials, (5) foreign atoms in lattice or interstitial positions, and (6) dislocations.

The defects under (1) and (3) are not directly part of the lattice structure, because they have parameter-dependent densities (temperature, field, and the like). Under (4), the point defects are classified (they are the dominant defects under the influence of radiation). Under (5), all chemical defects (impurities) are classified. We emphasize the most outstanding and lasting defect, the dislocation. We shall see that point defects (vacancies, interstitials) are related to the dislocations inasmuch as they may represent elements of these linear and planar structures. Detailed descriptions of defects in general, mainly in metals, are available.<sup>2</sup> In this literature the point of view is predominantly mechanical. Electrical properties are rarely considered and only in connection with such bulk properties as specific resistivity or Hall constant.

The all-dominating mechanical aspect in the treatment of dislocations is due to the old effort to understand properties of metals or alloys with respect to work hardening, thermal behavior, deformation, plastic flow, pressure, recovery, and other mechanical parameters, to name only a few. This dominant aspect (see, for example, Ref. 3) of the mechanical problems is also due to the historical development. A defect and specifically the dislocation is viewed from a macroscopic point of view as an inhomogeneity of a perfect structure. Its foremost influence concerns the oldest use of materials, namely,

in mechanical structures, plastic flow and strength of materials taking the main part of the considerations.<sup>4</sup>

The basic ideas about the geometrical forms of dislocations and defects, in general, quantities such as the stress field around dislocations, the free energy of dislocations, forces between dislocations, have helped considerably in building a firm fundament for the evaluation and the understanding of their electronic properties in semiconductors. In a more recent monograph on imperfections in crystals, Van Bueren<sup>5</sup> gives a very exhaustive treatment of the problem. His list of defects is more complete than Seitz':

1. Zero-dimensional or point imperfections like vacancies, interstitials, colorcenters, vacancy pairs, clusters
2. One-dimensional or line imperfections, dislocations
3. Two-dimensional or surface imperfections like grain boundaries, twin boundaries, phase boundaries, stacking faults, surfaces
4. Three-dimensional or volume imperfections like voids, inclusions of a second phase impurity clusters and other volume defects.

It is obvious that a subdivision under item 1 can include, along these lines, foreign atoms (impurities), free electrons, holes, and excitons. Pick's<sup>6</sup> idea to subdivide along the lines of (a) chemical imperfections, (b) structural imperfections, (c) electronic imperfections is somewhat ambiguous in this context, since chemical and structural imperfections are accompanied by inherent electronic imperfections. The amount and kind of electrical disturbance is dependent on the basic lattice. A dangling bond in a homopolar lattice can have a donor or acceptor character, depending on the width of the forbidden gap (silicon: donor; germanium: acceptor). In the case of a heteropolar lattice, a dangling bond can be due to either element of the compound and have, correspondingly, a different core charge and energy level.

Van Bueren's treatise (the part on imperfections in nonmetallic crystals) is rather short insofar as electrical effects are concerned. In this respect, a treatise on electronic conduction in metals and semiconductors contains more than any work on imperfections.

There are many influences of atomic imperfections on carrier transport. In semiconductors this influence is due to lattice vibrations, foreign atoms in the form of substitutional and interstitial impurities, and vacancies (acting as centers of recombination and scattering). Charged centers are considered in the Conwell-Weisskopf scattering formula.<sup>7</sup> The scattering of the DeBroglie waves in a lattice subjected to thermal agitation (phonon scattering) was the starting point for Bloch's important contributions.<sup>8</sup> A short treatment of these basic facts can be found in Chapter 2 and in almost any textbook on electronic semiconductors (see, for example, Ref. 9). The classical treatment of carrier transport in the presence of imperfections takes into account neutral and charged centers as well as lattice vibrations. Excitons have been taken

into account recently,<sup>10</sup> mostly in connection with the work on phosphors. Cyclotron resonance and paramagnetic resonance have become extraordinary tools for the definition of defect structures.<sup>11,12</sup>

The anisotropy of an electron-spin resonance signal in connection with polarized optical absorption studies allows for the construction of models of defects.<sup>13</sup>

The penetration into and clarification of the lasting defects in the form of dislocations prompted a further study of their electrical effects. Read<sup>14</sup> contributed to a logical nomenclature and a consequent picture of the dislocations, while Amelinckx<sup>15</sup> contributed verification of the theoretical conclusions by elaborate microscopic and electron-microscopic studies. Finally, Read<sup>16</sup> established the first electronic theory of dislocations in semiconductors, which was a basis for further developments, as described by Bardsley in his treatise.<sup>17</sup>

Improvements concerning Read's model were made by Broudy<sup>18</sup> and are discussed later.

The dislocations in all these cases are basically linear arrangements of single-edge dislocations, and Read considers the space-charge pipe along a dislocation cylinder. In the latter part of this work we are mainly concerned with the two-dimensional (planar) case of an overlap of such dislocation pipes.

We shortly dealt with the problems of the imperfections 1 to 5 in Seitz' list, (Chapter 2) but since a line imperfection is built up of individual point defects (dangling bonds), Van Bueren's list is of more concern to us.

In order to assess the electrical effects of the main lattice defects, we start with vacancies and interstitials.

### Vacancies

A vacancy in the diamond lattice (see Figure 3.1) generally means that four

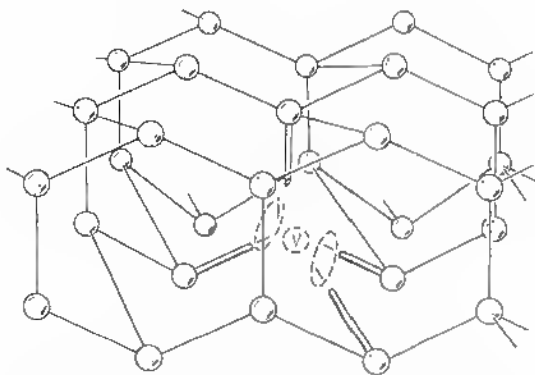


Fig. 3.1 Diamond lattice (schematic) and broken bonds around a vacancy.



valence bonds are broken. The free electrons may, however, combine in pairs to form low-energy configurations of hybridized bonds. This is somewhat different from the case of the dangling bonds of the additional half plane in an edge-dislocation arrangement in the diamond lattice (see Figure 3.2). Here the misfit between neighboring atoms prevents the sharing of electrons by covalent bonding in a tetragonal arrangement about the individual atom. Most of the atoms are still shared by hybrid orbital bonding with neighboring atoms in a higher-energy situation. Here this high-energy situation representing an unneutralized charge can be reduced by two atoms sharing one free electron. Because of electrostatic repulsion between bound electrons, the minimum-energy situation occurs when only a small fraction ( $10^{11}$  to  $10^{12}$   $\text{cm}^{-2}$ ) of the bonds is saturated.

The orbital electrons are neutralized in the body of the main lattice by free holes and ionized impurities. We analyze this case more closely in Chapter 4. Interstitials in the form of additional atoms of impurity elements may have many different positions within the diamond lattice, depending on their ionic radii. Their electrical effects depend on their valence. The interstitial host atom itself creates a situation of the same kind as the vacancy (see Figure 3.1). The four valence electrons in the case of germanium, for example, have to find suitable shared-bonding arrangements and create an energy level corresponding to the minimum-energy situation possible. In the case of the highly perfect monocrystals used presently in semiconductors, these interstitials are probably rare. Although vacancies may be created in a kind of

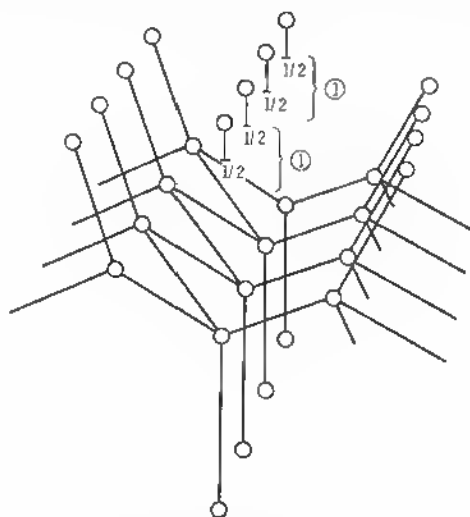


Fig. 3.2 Edge Dislocation in diamond lattice.

Schottky process (atoms migrating to the surface and leaving vacancies behind) the Frenkel defect is less likely to occur, since most of the doping elements of the third and fifth columns of the periodic chart are going into substitutional locations in the host lattice such that the replaced germanium atoms find themselves at the free surfaces.

Clustering of vacancies and impurity atoms is a frequent possibility in materials produced under strain because of high doping or temperature conditions that result in high temperature gradients within the material.

When crystals are damaged by radiation, formation of vacancies and interstitials is the result. We discuss this in Chapter 6. It is, however, to be mentioned in this context that in this specific case, Frenkel defects with an almost equal distribution of vacancies and interstitials are the probable consequence.

James and Lark-Horovitz<sup>19</sup> treated the interstitial as a donor center that might successively lose two or even three electrons before the ionization energy exceeds the forbidden gap. In the hydrogenic approximation, this energy is

$$E_i = Z_i^2 E_H \frac{m^*}{m_0 \kappa_{\text{eff}}^2}, \quad (3.1)$$

where

$E_i$  =  $i$ th ionization energy,

$Z_i$  = excess charge of core after removal of the  $i$ th electron,

$E_H$  = ionization energy for hydrogen atom (13.6 eV),

$m^*$  = effective mass of electron in conduction band,

$m_0$  = rest mass of electron,

$\kappa_{\text{eff}}$  = effective dielectric constant as experienced by  $i$ th electron.

It is not possible to calculate  $\kappa_{\text{eff}}$  for the different ionization stages, because the higher core charge reduces the orbit of the remaining electrons, so that they do not experience the full dielectric constant of the lattice.

The value  $\kappa_{\text{eff}} = 16$  is correct for the first ionization. For the next ones we can only obtain lower limits for the  $E_i$ 's. With  $m^* = 0.2m_0$ , one obtains

$$E_1 = 0.01 \text{ eV,}$$

$$E_2 \lesssim 0.04,$$

$$E_3 \lesssim 0.1 \text{ eV.}$$

On the other hand, a vacancy is considered an acceptor only, and it is concluded that two, perhaps three, electrons could be placed into its incomplete orbitals (see Figure 3.1) before the energy required would exceed the band gap. (In the case of copper as an impurity, for example, three successive acceptor levels have been observed in Ge and Si.) The schematic representation of the James-Lark-Horovitz model is then a series of states spread over the

forbidden gap (see Figure 3.3). The filled states of the interstitials lose electrons to the vacancy states if Frenkel defects are present. Therefore, the upper states of the interstitials  $E_1, E_2, E_3$  being empty, they can now accept electrons from the conduction band, and vacancies can accept holes from the valence band. This limited model does not provide information about the actual number or the positions of these states. It can help, however to understand why, for example,  $n$ -type Ge becomes  $p$ -type by damage introduction or why  $n$ - and  $p$ -types Si become intrinsic (the position of the Fermi level,  $\zeta^*$ , Fig. 3.3 being of great importance).

The role of vacancies and interstitials is manifold in crystal growth, annealing, and other treatments. Both can easily change place in the lattice, since they form the seat of a relatively weak elastic stress field. The neighboring atoms, for example, tend to relax around a vacancy. Accordingly, vacancies interact with each other and with other geometrical imperfections, particularly dislocations. Vacancies migrate to the dislocation, as do foreign atoms, the difference being that vacancies can absorb the free bond and impurities tend to be locked at the dilation zone just below a dislocation  $D$ , as in Figure 3.4. Here the case of the climb of the dislocation line perpendicular to the slip plane is shown.

Vacancies may also cluster and form pairs having distinct properties of their own. The mobility  $\mu_v$  of a vacancy at temperature  $T$  is proportional to

$$\mu_v \approx e^{-A/kT}, \quad (3.2)$$

where

$k$  = Boltzmann's constant,  
 $A$  = activation energy.

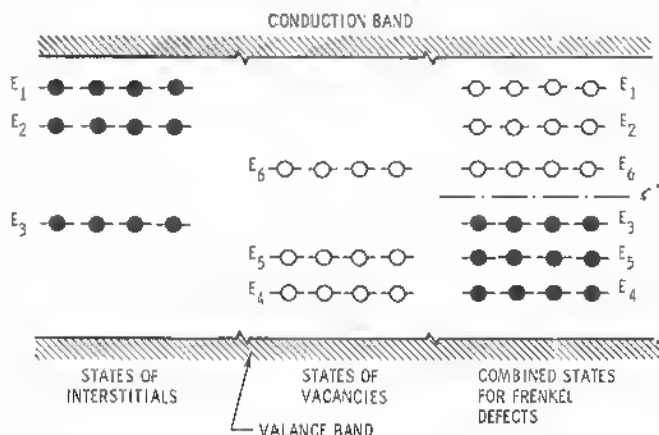


Fig. 3.3 Energy levels of defects in the forbidden gap of Germanium.

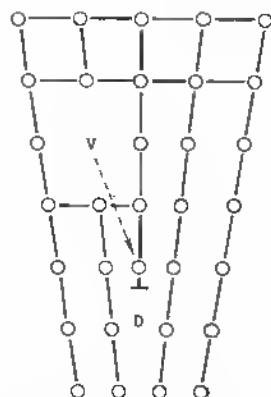


Fig. 3.4 Vacancy migration to a dislocation site.

If  $W$  is the activation energy for vacancy *formation*, the equilibrium concentration  $N_0$  for vacancies at the temperature  $T$  is proportional to

$$N_0 \approx e^{W/kT}, \quad (3.3)$$

since vacancies introduce a configurational entropy in a system. For copper, for example,  $W \simeq 1\text{eV}$ . For vacancy pairs,

$$\begin{aligned} A &\simeq 0.4\text{ eV}, \\ W &\simeq 1.6\text{ eV}. \end{aligned}$$

Closely associated with vacancies are their image defects, the interstitials. These are also mobile, have a stress field, cause climb of dislocations, and so on. Here, generally,

$$\begin{aligned} A &\simeq 0.1\text{ eV}, \\ W &\simeq 4\text{ eV}. \end{aligned}$$

Vacancies and interstitials obviously tend to annihilate each other if sufficiently close. The vacancy concentration increases exponentially with the temperature. Assume that there are  $N$  atoms and  $N'$  possible interstitial sites; then a number  $n$  of atoms that left their places can be accommodated in

$$\frac{N'!}{(N' - n)! n!}$$

ways in interstitial sites. The vacancies, in turn, can be arranged in

$$\frac{N!}{(N - n)! n!}$$

ways. This corresponds to an entropy increase:

$$\Delta S_n = k \left[ \log \frac{N!}{(N-n)! n!} + \log \frac{N'!}{(N'-n)! n!} \right], \quad (3.4)$$

where  $k$  = Boltzmann's constant.

From here one can show<sup>2</sup> that the number of vacancies  $n$  is a function of temperature:

$$n = \sqrt{NN'} \exp\left(-\frac{1}{2} \frac{W_F}{kT}\right), \quad (3.5)$$

where  $W_F$  = work required to bring an atom reversibly to a distant lattice point. This exponential increase in vacancy concentration with  $T$  is synonymous with an increasing number of vacancy interstitials or a disordering of the perfect lattice as vacancies diffuse into the bulk from the free surfaces. With further increasing temperature, the melting point is approached by an increasing number of vacancies and an increasing number of interstitials, and lattice vibrations reach the energy of the breaking point of the interatomic order. These general considerations can also be applied to dislocations, but for the latter, the activation energy is so high (1 eV per atom plane threaded by the dislocation line) that no dislocation could be created as a result of thermal-equilibrium requirements.

Conversely, a dislocation once formed is quite immune to thermal fluctuations, persisting indefinitely in metastable equilibrium unless annihilated by other dislocations, by condensation of point defects, or by exit at a free surface. In this respect dislocations are, in certain cases, even more stable than foreign atoms in substitutional lattice locations when their ionic radii generate stress fields.

We confine this general introduction about kinds of defects and do not introduce, at this point, stacking faults, jogs, partial dislocations, and the like, since their electrical effects are of minor importance. They are amply described in the general mechanical treatments<sup>2-5</sup> and others.

### Stoichiometric Defects

In the case of compound semiconductors like the important  $A_{100}B_V$  compounds, nonstoichiometry accounts for the predominant defects. In many ways the amount by which a compound is off stoichiometry is equal to a corresponding concentration of impurity atoms. This is seen from the fact that the alternate charge scheme in the polar lattice allows for an imbalance in positive as well as in negative lattice charges (see Figure 3.5). The fact that stoichiometry is disturbed (nonstoichiometry) is sufficient here to generate a strong influence on moving charges. Carrier transport in polar crystals, therefore, is more complex in many ways than in homopolar lattices. The

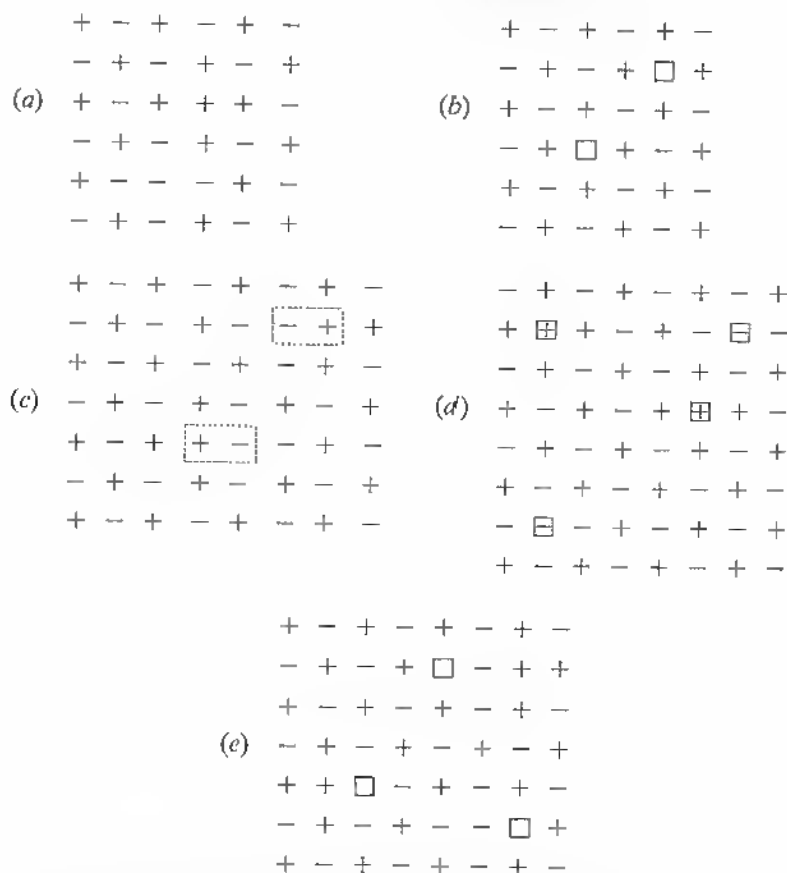


Fig. 3.5 Some examples of polar lattice defects (a) Substitutional (no excess charge) (b) Vacancy defect structure (excess positive) (c) Bound wrong pairs (d) Unbound wrong pairs (e) Vacancies with wrong pairs.

probability that one or the other nonstoichiometries, shown in Figure 3.5, occur during crystal growth of a compound semiconductor is very high. Even excellent monocrystals, free of dislocations, may have a considerable number of these low-energy defects in their stoichiometry. From the fact that the periodic lattice-charge structure is disturbed, we infer that there is a marked influence on resistivity and mobility even without a mechanical lattice defect. More important, all long-range process parameters, such as lifetime or the local transfer of a plasma wave, are likely to be seriously disrupted even without a detectable defect structure (dislocation etch pattern). Periodicity faults, stacking faults, slip boundaries, partials, twins, and the

like, play a more prominent role in polar lattices than in homopolar lattices.<sup>20</sup> This is one of the reasons for the difficulties to base reproducible and reliable device functions on III-V compound material parameters. After more than 15 years since the first announcement of the device potential of compound crystals, we are still unable to correlate doping type, concentration perfection, and the like, clearly with electronic parameters such as resistivity, mobility, lifetime, radiative recombination. This has lead to difficulties with crystal growth. Silicon is now known to be a major mobility poison in GaAs because of its ambipolar character (Si in Ga or As places).<sup>\*</sup> Its presence in quartz and the majority of containers used in crystal processing has complicated zone purification and other normal crystal-growth methods. Such problems have lead to the erroneous opinion that in GaAs, for example, device-grade material does not necessarily have to be free of defects.<sup>24</sup>

With stoichiometric defects, not visible to the eye under the microscope after etching, there is indeed room for the conclusion that even "perfect" crystals may have a low mobility or other undesirable parameters and that, therefore, "perfection" in the usual sense is unnecessary. This, however, is a

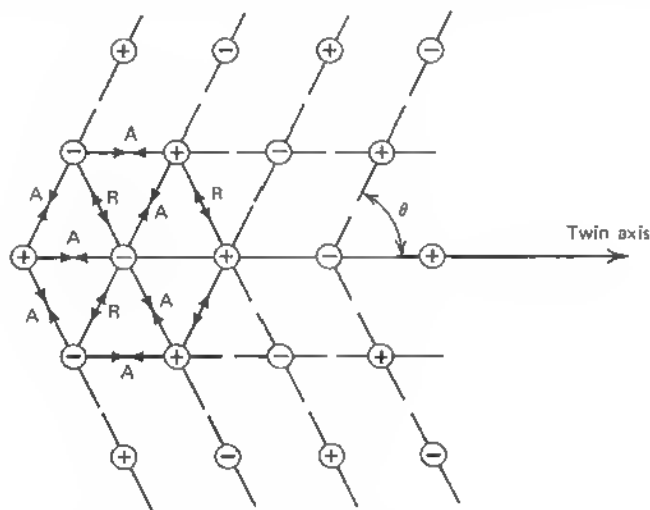


Fig. 3.6 Twin in hypothetical cubic lattice;  $R$  = repulsive force,  $A$  = attractive force,  $\theta \leq 45^\circ$ .

\*The problem of silicon as a dopant in GaAs has been studied thoroughly by Spitzer for some time. Optical absorption has revealed the spectral location of the main defects:

$$\begin{aligned} \text{Si}_{(\text{Ga})} & [384 \text{ cm}^{-1}]; \quad \text{Si}_{(\text{As})} [399 \text{ cm}^{-1}] \\ (\text{Si}_{(\text{Ga})} - \text{Si}_{(\text{As})}) & [367; 393; 464 \text{ cm}^{-1}] \end{aligned}$$

See references 21, 22, 23.

false conclusion. No crystalline defects are without importance for device parameters, but it may happen that slight stoichiometric defects, as shown in Figure 3.5, weigh more heavily in deteriorating certain electronic parameters than twin boundaries or other basic defects in which the polar nature of the lattice is not disturbed. But if, for example, the twinning angle reaches higher values (see Figure 3.6) by which new nearest-neighbor distances are established that cause electrostatically repulsive forces and lattice strain, changes of the local electronic band structure are effected.

In other ionic crystals we also have two kinds of vacancies. In cuprous oxide, for example, a Cu vacancy leaves a negative charge behind, since  $\text{Cu}^+$  is missing. For  $\text{Cu}_2\text{O}$ , for example,



$\text{Cu}_{\square}^+ = \text{Cu vacancy, negatively charged} = \text{acceptor},$

$\oplus = \text{defect electron},$

$\text{Cu}_{\square}^* = \text{neutral vacancy}.$

In a lattice of potassium chloride, for example, we have, similarly,



which is the usual *F* center in the classical sense.

Such vacancies can migrate as interstitials especially at higher temperatures. We see that the influence of defects in ionic crystals is more pronounced in that a strong charge imbalance is contributed directly from the lattice to the surrounding and the free carriers.

In homopolar structures broken bonds represent interband level with acceptor or donor character, depending on their location in the forbidden gap, while a broken heteropolar bond represents a priori a strong charge imbalance within the polar structure itself in addition to the energy level offered to moving charges. In the contravalent case, the valence electrons filling up incomplete shells of the ionic partner atoms are immediately establishing an extended space charge when the partner atom is missing, but in the case of the covalent bond or homopolar lattice, where exchange forces are lifted because of missing bonds, the energy levels generated are more of the kind of mid-band-recombination centers. Edge dislocations, however, represent localized centers of high electronic activity because of the dangling bond and its core charge or because of the states pulled out of the conduction band.\*

In compound semiconductors another important feature should be noticed when two-dimensional defects like grain boundaries (or also external surfaces)

\* As to the preferred interpretation of the origin of the localized levels, see Chap. 8. Also, V. Heine, Dangling Bonds and Dislocations in Semiconductors, *Phys. Rev.*, **146** (2): 568-570.



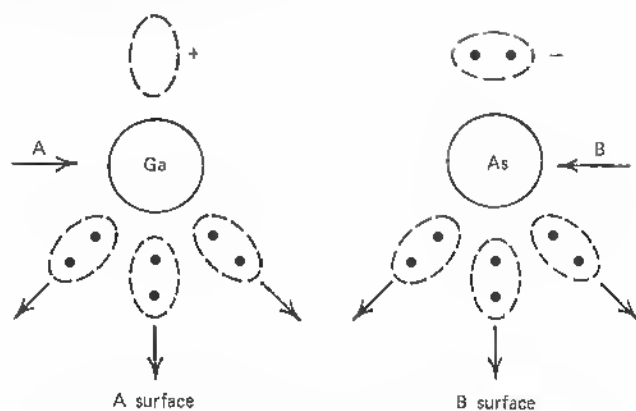


Fig. 3.7 Origin of different core charges for A and B dislocations in a GaAs lattice.

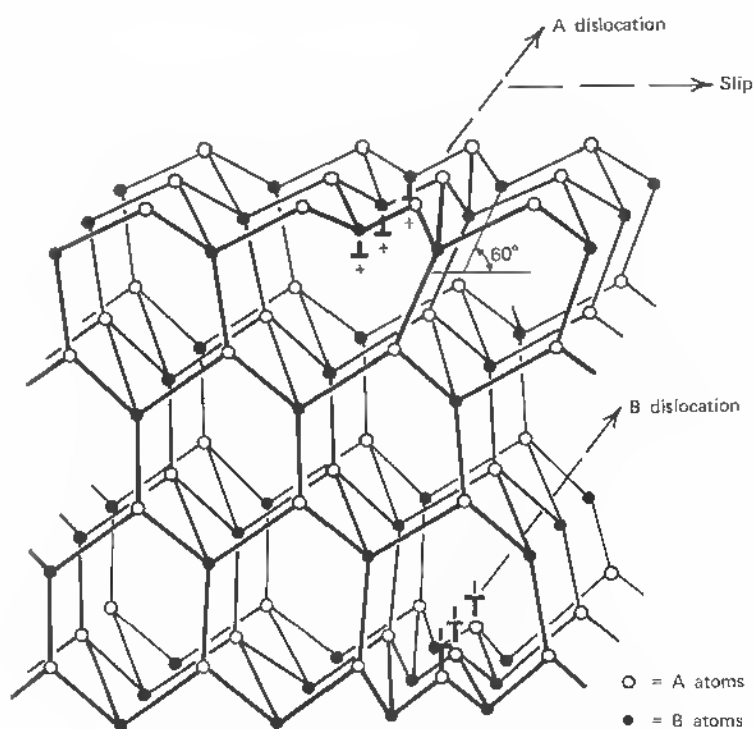


Fig. 3.8  $60^\circ$  dislocations in compound lattice of type A and B.

are created. Depending on the A or B atom termination at the dislocation site, these surfaces have different surface charges (see Figure 3.7).

This results in different core charges at the dislocation arrays. An atomic model for the A and B surfaces of GaAs, therefore, shows that the A surface is positively charged, the B surface negatively charged.<sup>25</sup> As Figure 3.8 describes, the 60° edge dislocation, leaving a row of dangling bonds of the A type, creates a positive core charge, and the intersection with the B-type row creates a negative core charge. In a real crystal the hexagonal symmetry, therefore, establishes alternating charges along a symmetric grain boundary ( $\theta = 90^\circ$ ). Such an extended dipole layer forms an electronic sublattice with very special conduction properties in the longitudinal direction because of wave-function overlap of the dangling bonds. The resulting degeneracy is an important feature to be discussed later in the text.

The grain boundary as a region of elastic strain also has special mechanical features. In general, this area of the crystal shows an increase in hardness. The degree of this, however, may depend on the predominance of one of the partners in the lattice. In general, however, the stoichiometric (50/50) case of exact atomic matching shows the most hardened grain boundary, because the correct lattice buildup forms the ideal line of polar interfaces in a maximum stability situation (compare Figures 21 and 22 in Ref. 22).

## PROBLEMS

- 3-1. Discuss the relations between the different kinds of defects as listed by Seitz and Van Bueren.
- 3-2. Draw a twin configuration for the hypothetical cubic lattice with gliding twin axis, and explain the probable effects on charge carriers.
- 3-3. Which would be the lowest-energy configuration of double vacancies in the ionic lattice (see Figure 3.5)?

## REFERENCES

1. Holloman, J. H., R. Maurer, and F. Seitz: "Imperfections in Nearly Perfect Crystals," W. Shockley (ed.), Wiley, New York, 1952.
2. Seeger, A.: Theory of Lattice Defects [German], "Encyclopedia of Physics," vol. VII, part I, Crystal Physics, pp. 381-676.
3. "Dislocations and Mechanical Properties of Crystals," Conference Record, Lake Placid Meeting, September 6-8, 1956, Wiley, New York, 1957.
4. Cottrell, A. H.: "Dislocation and Plastic Flow in Crystals," Clarendon Press, Oxford, 1951.
5. Van Bueren, H. G.: "Imperfections in Crystals," North-Holland Publishing Company, Amsterdam, 1961.

6. Pick, H.: *Naturwissenschaften*, vol. 41, p. 346, 1954.
7. Conwell, E., and V. F. Weisskopf: *Physical Review*, vol. 69, p. 258, 1946; *Physical Review*, vol. 77, p. 388, 1950.
8. Bloch, I.: *Z. Physik*, vol. 52, p. 555; 1928; vol. 57, p. 545, 1929.
9. Spenke, E.: "Electronic Semiconductors," McGraw-Hill, New York, 1958.
10. Nikitine, S.: Excitation Spectra in Semiconductors and Ionic Compounds-I and II, "Progress in Semiconductors," vol. 6, pp. 235-322.
11. Lax, B., and J. G. Mavroides: Cyclotron Resonance, "Solid State Physics," Academic, New York, 1960, vol. 11, pp. 261-400.
12. Ludwig, G. W., and H. H. Woodbury: Electron-spin Resonance in Semiconductors, "Solid State Physics," Academic, New York, 1962, vol. 13, pp. 223-304.
13. Watkins, G. D., J. W. Corbett, and R. M. Walker: *Journal of Applied Physics*, vol. 30, p. 1198, 1959.
14. Read, W. T., Jr.: "Dislocations in Crystals," McGraw-Hill, New York, 1953.
15. Amelinckx, S.; and W. Dekeyser: The Structure and Properties of Grain Boundaries, "Solid State Physics," Academic, New York, 1959, vol. 8, pp. 325-499.
16. Read, W. T., Jr.: Theory of Dislocations in Semiconductors, *Philosophical Magazine*, vol. 45, pp. 775-796, August, 1954; vol. 45, pp. 1119-1128, November, 1954; vol. 46, pp. 111-131, February, 1955.
17. Bardsley, W.: The Electrical Effects of Dislocations in Semiconductors, "Progress in Semiconductors," Wiley, New York, 1960, vol. 4, pp. 157-203.
18. Broudy, R. M.: The Electrical Properties of Dislocations in Semiconductors, *Advances in Physics*, vol. 12, no. 46, pp. 135-184, April, 1963.
19. James, H. M. and K. Lark-Horovitz: *Zeitschr. Phys. Chemie*, vol. 198, p. 107, 1951.
20. Brown, N.: Lattice Defects, in "Intermetallic Compounds," J. H. Westbrook (ed.), Wiley, New York, 1967.
21. W. G. Spitzer and W. Allred: "Site Transfer of Si in GaAs." *Applied Physics Letters*, vol. 12, No. 1, 1 January 1968, pp. 5-6.
22. W. G. Spitzer and W. Allred: "Local-Mode Absorption and Defects in compensated Silicon-doped Gallium-Arsenide." *Journal of Applied Physics*, vol. 39, no. 11, October 1968, pp. 4999-5009.
23. W. G. Spitzer and M. B. Panish: "Silicon doped Gallium Arsenide Grown from Gallium Solution. Silicon Site Distribution." *Journal of Applied Physics*, vol. 40, no. 10, September 1969, pp. 4200-4202.
24. Beam, W. R.: "Electronics of Solids," McGraw-Hill; New York, 1965, p. 193ff.
25. Bakish, R.: Internal and External Interfaces, in "Intermetallic Compounds," J. H. Westbrook (ed.), Wiley, New York, 1967, pp. 283-300.

## Chapter 4 Dislocations as Imperfections of Linear and Planar Extent

As we have mentioned, the dislocation deserves special consideration because of its outstanding stability as a defect structure and its marked electrical properties and influence on the electronic bulk properties of the host crystal. The elemental dislocation that has the most pronounced electrical effect is the edge dislocation. As we see from Figure 4.1, for the case of the hypothetical cubic lattice, the additional half plane at the dislocation generates two distinct features governing its electronic behavior.

1. A lattice deformation or a stress field resulting in a compression zone C just above the dangling bond and a dilatation zone D below the free bond.
2. The introduction of a free or dangling bond with its direct electrical property of forming an energy level in the forbidden gap.

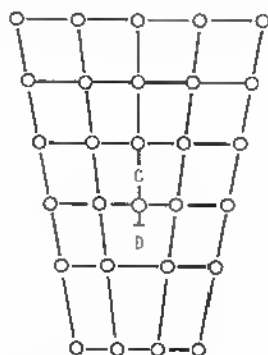


Fig. 4.1 Compression and dilatation regions at edge dislocation site.

At this point it is useful to develop more detail of the energy situation at the site of a dislocation. This is important for the question of artificial growth of defined dislocations and in order to understand the electrical properties. A most valuable parameter to define the state of slip that generates a dislocation or has been generated by a dislocation is the Burgers vector  $b$ . It specifies the direction and distance by which atoms in one plane have moved with respect to atoms in another plane. Or Burgers vector is defined as a closure failure arising in a cycle in perfect material surrounding the dislocation. If we assume a linear relationship between stress and strain tensor (Hooke's law), the work done on a cut that relieves the strain or is given by the surface forces  $T_x, T_y, T_z$  with their relative displacement  $u, v, w$ , is

$$E = \frac{1}{2} \sum \text{forces} \times \text{displacements},$$

$$E = \frac{1}{2} \int_S (T_x u + T_y v + T_z w) ds, \quad (4.1)$$

or  $E$  is the strain energy of material enclosed within  $S$ . In other words, an external force  $T$  (components  $T_x, T_y, T_z$ ) per unit area over the surface  $S$  on the body causes single-valued elastic displacements  $u, v, w$ . Reciprocally the surface force  $T$  can be produced by the dislocations. In the case of plane deformation, only the stress components  $\sigma_{xx}, \sigma_{yy}, \sigma_{xy}$  have to be considered,  $\sigma_{xx}$  and  $\sigma_{yy}$  are the normal stresses along the  $x$  and  $y$  axes, respectively, and  $\sigma_{xy}(\sigma_{yz})$  is the stress acting in the direction of the  $y$  axis on planes perpendicular to the  $x$  axis and vice versa (see Figure 4.2).

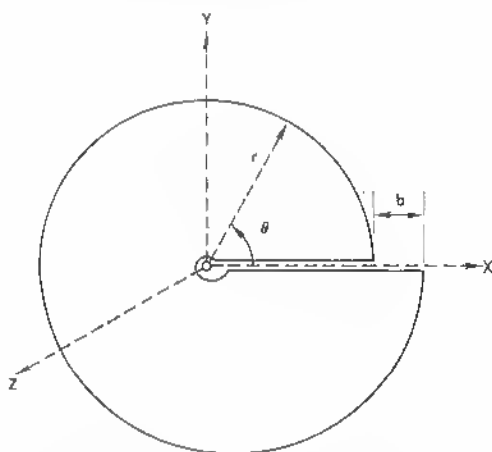


Fig. 4.2 Burgers cycle and closure failure  $b$  in coordinate system around edge dislocation.

The third stress  $\sigma_{zz}$  can be expressed by the others:  $\sigma_{zz} = \nu(\sigma_{xx} + \sigma_{yy})$  with  $\nu$  = Poisson's ratio, and  $\sigma_{yz}$  ( $=\sigma_{zy}$ ) and  $\sigma_{zx}$  ( $=\sigma_{xz}$ ) are zero. Generally, we use polar coordinates  $r, \theta, z$  (Figure 4.2) defined by

$$x = r \cos \theta, \quad z = r \sin \theta, \quad z = z. \quad (4.2)$$

Then the stresses are  $\sigma_{rr}, \sigma_{\theta\theta}$ , normal to radial and circumferential directions, and the shear stress  $\sigma_{r\theta}$  ( $=\sigma_{\theta r}$ ) and again  $\sigma_{zz} = \nu(\sigma_{rr} + \sigma_{\theta\theta})$ . Using (4.1), the shear stress on the slip plane of an edge dislocation (slip vector  $\perp$  to slip plane) is given by  $\sigma_{xy}$ . With the corresponding Burgers' vector  $b$ , the energy of the edge dislocation is

$$E_{\perp} = \frac{b}{2} \int_s \sigma_{xy} ds, \quad (4.3)$$

where  $s$  = surface considered.

Equation (4.3) is an important expression of the density of strain energy and can be modified so that one can calculate the energy per dislocation in terms of surface forces in the following way. Assume a cylindrical cut surrounding a dislocation pipe with radius  $r$ , large compared with the pipe radius  $r_0$  ( $\approx 10^{-7}$  cm) so that the remaining stress field is negligible;  $r = 1$  cm, for example; (the stress is decreasing as  $1/r$ .) Then one may write for the energy of the edge dislocation

$$E_{\perp} = \frac{b}{2} \int_{r_0}^{r_1} \sigma_r dr. \quad (4.4)$$

The radial stress function can be expressed in terms of the shear modulus, lattice constant, and Poisson's ratio, using the classical Volterra derivation as stress function (see Chapter 3, Refs. 2 and 4):

$$\sigma_r = \frac{\mu b}{2\pi r} (1 - \nu), \quad (4.5)$$

where  $\mu$  = shear modulus ( $\approx 10^{12}$  dyn/cm<sup>2</sup> for germanium),

$\nu$  = Poisson's ratio ( $\approx 0.4$  for germanium)

(see Chapter 7).

#### 4.1 EDGE DISLOCATIONS

We define, with Read, three regions around a dislocation of the edge type. The region closest to the dislocation site defines the energy  $E_1$  of atomic misfit within a circle  $r_e$  about the dislocation. Here the distortion is so severe that atoms are not properly surrounded by their neighbors and Hooke's law

fails.  $E_{II}$  is one part of the energy of elastic deformation extending over distances comparable with the spacing between dislocations.

The radius for  $E_{II}$  is chosen to be a fraction of the slip vector  $b$  (in this simple case, equal to the Burgers vector):

$$r = K \frac{b}{\theta} = KD, \quad (4.6)$$

where  $K = \text{constant} < 1$ ,

$$D = \text{dislocation spacing} = \frac{b}{2 \sin(\theta/2)} \approx \frac{b}{\theta}, \quad (4.7)$$

$\theta = \text{angle of tilt between generating monocystal sides, here considered to be small as the approximation shows (see Figure 4.3).}$

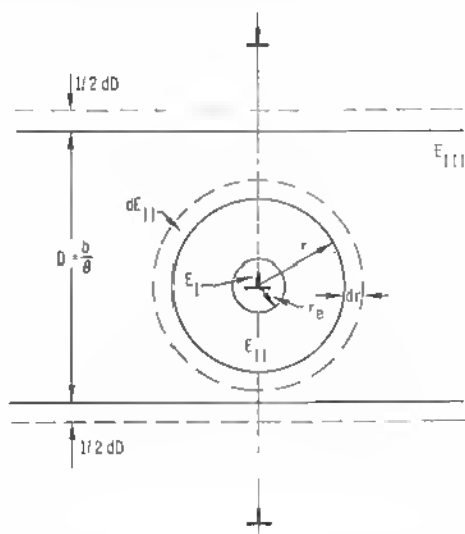


Fig. 4.3 Energy distribution around dislocations before and after the spacing has changed for the amount  $dD$ .

The Burgers vector  $b$  is here perpendicular to the slip plane, defining the edge dislocation ( $b \parallel \text{slip plane}$  is the case of the screw dislocation to be discussed later).

Thus, the energy  $E_{II}$  represents the elastic distortion caused by the dislocation included. The radius  $r$  has to satisfy the conditions  $r \gg b$ ,  $r < D$ , so that within the region defined by  $r$ , the stress is entirely due to the included dislocation.

$E_{\text{II}}$  is the remainder of the energy. This contribution is mostly due to a superposition of the stress fields of other dislocations (see Figure 4.4). The total energy is

$$E_{\perp} = E_I + E_{\text{II}} + E_{\text{III}}. \quad (4.8)$$

We need the stress distribution around a dislocation (screw or edge type) in an isotropic crystal in order to proceed from here. This can be accomplished by the linear elasticity theory as applied to the crystal with exception of the small cylinder of radius  $r = r_e$  along the  $z$  axis (see Figures 4.2 and 4.3). Stress and strain are thus considered monotonous, analytic functions or continuously differentiable (see Chapter 3, Ref 14). In this case, the stress components are independent variables and must satisfy the equation of equilibrium in the  $z$  direction :

$$\frac{\partial}{\partial r} r \sigma_{rz} = - \frac{\partial}{\partial \theta} \sigma_{\theta z}, \quad (4.9a)$$

$$\frac{\partial}{\partial r} r \sigma_{\theta z} = \frac{\partial}{\partial \theta} \sigma_{rz}. \quad (4.9b)$$

Equation (4.9b) is the compatibility equation (Timoshenko<sup>1</sup>). Elimination of  $\sigma_{\theta z}$  by differentiation of (4.9b) by  $\partial/\partial\theta$  and inserting into (4.9a) yields

$$\frac{\partial}{\partial r} r \frac{\partial}{\partial r} r \sigma_{rz} + \frac{\partial^2 \sigma_{rz}}{\partial \theta^2} = 0. \quad (4.10)$$

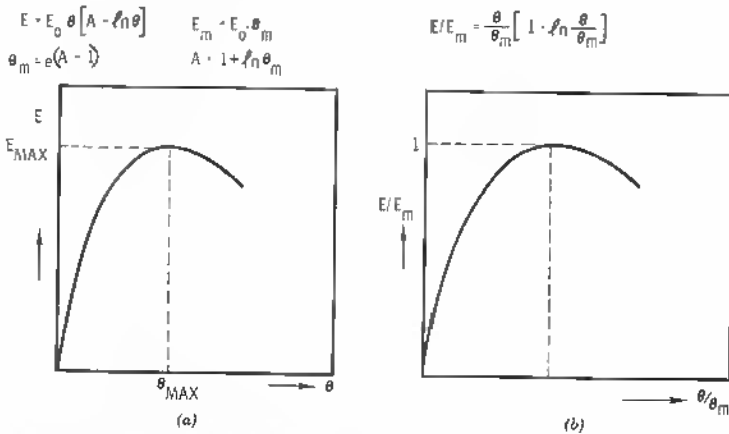


Fig. 4.4 Grain-boundary energy versus angle of misfit  $\theta$  and normalized angle of misfit.



A similar equation applies to  $\sigma_{r\theta}$ .

The stress is a continuous function along radius  $r$  across the lattice. The distribution of stress on a circle  $r = \text{constant}$ , therefore, is a Fourier series with amplitude functions  $R(r)$ :

$$\sigma_{rz} = R_0(r) + R_1(r) \cos \theta + R_2(r) \cos 2\theta + \cdots + R_n(r) \cos n\theta \cdots S_n(r) \sin n\theta. \quad (4.11)$$

A similar equation results for  $\sigma_{\theta z}$ . Since

$$\sigma_{rz(r \rightarrow \infty)} = 0,$$

only negative powers of  $r$  are allowed. Thus

$$\sigma_{rz} = \frac{A_0}{r} + \sum_{n=1}^{\infty} \left( \frac{A_n \cos n\theta + B_n \sin n\theta}{r^{n+1}} \right). \quad (4.12)$$

Inserting (4.12) into (4.9) and integrating gives

$$\sigma_{r\theta} = \frac{C_0}{r} + \sum_{n=1}^{\infty} \left( \frac{-B_n \cos n\theta + A_n \sin n\theta}{r^{n+1}} \right). \quad (4.13)$$

Taking  $\theta = 0$  as the slip plane (screw), the shearing stress on the slip plane in the slip direction is

$$\sigma = \sigma_{r\theta}(r, \theta). \quad (4.14)$$

This gives, from (4.13),

$$\sigma = \sigma_0 \frac{b}{r} + \sigma_1 \frac{b^2}{r^2} \cdots \sigma_n \frac{b^{n+1}}{r^{n+1}}, \quad (4.15)$$

with

$$\sigma_0 = \frac{C_0}{b}, \quad (4.16)$$

$$\sigma_n = -\frac{B_n}{b^{n+1}}. \quad (4.17)$$

In (4.16) the stress component  $\sigma_0$  times the lattice translation vector  $b$ —in this simple case, Burgers vector—is a constant  $C_0$ . In general, we consider only cases with an angular deviation  $\theta$  small. This means that we need to know the stress only where  $r/b$  is large enough to neglect the higher-order terms:

$$\sigma \cong \sigma_0 \frac{b}{r}. \quad (4.18)$$

Coming back to Figure 4.3, we now derive the change in energy of the dislocation due to a step in radial direction and integrate. If  $\theta$  decreases by  $d\theta$ ,  $D$  increases by  $dD$ . With (4.6) and (4.7), this yields

$$\frac{dD}{D} = -\frac{d\theta}{\theta} = \frac{dr}{r}. \quad (4.19)$$

The total change in energy is—see (4.8):

$$dE_{\perp} = dE_I + dE_{II} + dE_{III}.$$

$E_{\perp}$  is the localized energy of atomic misfit at the core and does not change upon a step  $dr$ , since it is independent of the other dislocations; hence  $dE_I = 0$ .

$E_{II}$  changes with step  $dr$  and equals the energy in the ring bounded by  $r = kD$  and  $r + dr = k(D + dD)$ . Finally,  $E_{III}$  does not change, since with the increase in  $D$ , the area for  $E_{III}$  changes for  $D^2$  and the energy density varies as  $b^2/D^2$ . Therefore

$$dE_{\perp} = dE_{II}$$

and with (4.8) or (4.9)

$$dE_{\perp} = \frac{1}{2}\sigma b \, dr, \quad (4.20)$$

or with (4.18)

$$dE_{\perp} = \frac{1}{2}\sigma_0 b^2 \frac{dr}{r}, \quad (4.21)$$

or with (4.19)

$$= -\frac{1}{2}b^2\sigma_0 \frac{d\theta}{\theta}, \quad (4.22)$$

which, if integrated, gives readily

$$E_{\perp} = \frac{b^2\sigma_0}{2} (A - \ln \theta) \quad (4.23)$$

as the energy of an edge dislocation.  $\theta$  can be considered the angle of misfit between two grains and defines the density of dislocations. In perfect grain boundaries this is the most important parameter. Since the grain-boundary energy  $E$  per unit area is  $E_{\perp} \times$  density of dislocations

$$E = \frac{E_{\perp}}{D} = \frac{E_{\perp}\theta}{b}, \quad (4.24)$$

we get with (4.23)

$$E = E_0 \theta (A - \ln \theta), \quad (4.25)$$

with  $E_0 = b\sigma_0/2$ .

Equation (4.25) is the well-known Read-Shockley energy expression for a grain boundary. There are a few particular features to be remembered when one deals with dislocation energies. The equation consists of two parts:

$$(1) \quad E_0 \theta A, \quad (4.26)$$

which is increasing with  $\theta$  and represents a constant energy per dislocation for a fixed angle  $\theta$ . This energy amount includes the unknown energy of atomic misfit per unit area:

$$(2) \quad -E_0 \theta \ln \theta = E_0 \theta \ln \left( \frac{1}{\theta} \right). \quad (4.27)$$

This energy is the variable term in the elastic energy. As  $\theta$  decreases, this term decreases.  $\theta$  approaches 0 faster than  $\ln(1/\theta) \rightarrow \infty$ .

These two balancing functions result in a maximum curve, rising steeply at small angles  $\theta$  and reaching a maximum at  $\theta = 25^\circ$  for most materials (see Figure 4.4). Part 1 of (4.25) is not dependent on the number of dislocations and their mutual stress fields, and part 2 of (4.25) becomes infinite for  $\theta \rightarrow \infty$ . The elastic energy of one dislocation becomes infinite, as  $\theta \rightarrow 0$ , since it is given by

$$bE_0 \ln \frac{1}{\theta}, \quad (4.28)$$

where  $\theta = b/D = b$  for one dislocation. (density  $1/D = 1$ ).

As  $\theta$  increases in a grain boundary, the elastic energy per dislocation decreases, because the stress fields of the individual dislocations overlap and cancel. This is an important feature that lends stability to such dislocation planes and is discussed in more detail later in connection with the growth conditions.

In summary, we have to note the two cases.

1. Elastic energy of a dislocation:

$$\begin{aligned} E_{\perp} &= -E_0 b \ln \theta \\ &= E_0 b \ln \left( \frac{1}{\theta} \right), \end{aligned}$$

$$E_{\perp(\theta \rightarrow 0)} \rightarrow \infty,$$

$$E_{\perp(\theta \rightarrow \infty)} \rightarrow 0.$$

2. Elastic energy per unit area of a grain boundary:

$$E'_\perp = -E_0 \theta \ln \theta$$

$$= \theta E_0 \ln \left( \frac{1}{\theta} \right),$$

$$E'_{\perp(\theta \rightarrow 0)} \rightarrow 0,$$

$$E'_{\perp(\theta \rightarrow \infty)} \rightarrow \infty.$$

## 4.2 LINEAGE AND LOW-ANGLE BOUNDARIES

The definition of defects of the lineage type coincides in time with the development of crystal-growth methods for industrial production of monocrystals. The step-up from a crystal grown by a point seeding of accidental nature in a temperature-gradient growth (Bridgman method) to the controlled Czochralski growth, using an oriented seed crystal, was decisive. The expression *lineage* had been used in a more undefined way before, as also the expressions *twins* and *grain boundaries* were used with a very loose definition. It must be clarified that second-phase structures and zones of totally different orientation are no longer intermingled as in polycrystals of the old days of semiconductor research, but that we are able today to grow any material in a rather controlled manner and that the kinds of defects can be defined and recognized clearly. Therefore, we want to define as lineage the occurrence of low-angle grain boundaries with little or no coherency of growth due to very small overlap of dilation and compression zones. This missing self-stabilizing energy is the cause of the random orientation of such lineage lines in a crystal. These lines of defects may follow straight lines for some limited distance, but in general, they follow curved pathways, appear in groups, and disappear at some spot without recognizable reason, either absorbed by a vacancy cluster or other dislocations. The famous etch picture of Vogel, Pfann, Corey, and Thomas of Bell Telephone Laboratories in 1953 (see Chapter 3, Ref. 16) of a low-angle grain boundary ( $\theta < \text{one minute of an arc}$ ) shows clearly the features of lineage as no stable straight line, but of a somewhat curved and irregular path. This is due to the practically nonexistent stabilizing energy. The dislocation distance being  $D = b/2\sin\theta/2$  is equal to many lattice constants (see Figure 4.5). Expressed in lattice constants, we list for a normal lattice constant  $a = 5 \text{ \AA}$  the following distances for the tilt angles:

$\theta^\circ$	4	6	10	15	20	25	30	
$D$	12	9.6	5	3.8	2.7	2.5	1.9	in lattice constants in $\text{\AA}$
	60	48	25	19	13.6	12.5	9.5	

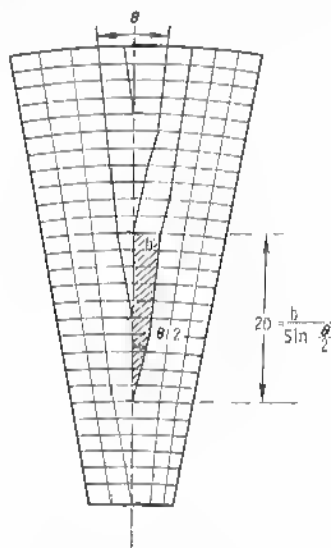


Fig. 4.5 Model of symmetric grain boundary.

If we pursue this toward smaller angles, the distance  $D$  becomes so large that it can be measured in microns on a crystal. It is astonishing that in such a case any coherency of growth exists, as in the case mentioned above, for example. This is mainly because the condition for such a boundary is the slight orientation misfit between two crystal halves that in turn maintain the boundary in its form as long as it stores the free energy arising from the atomic misfit.

As a matter of definition it seems appropriate to use the expressions *lineage* and *low-angle grain boundary* within certain regions for the angle of misfit between the two grains. In this book we use the expression *lineage* only for misfit angles clearly below  $1^\circ$ . Boundaries originating from grains with  $\theta > 1^\circ$  are classified, in general, as low-angle or medium-angle grain boundaries.

In a finer subdivision we use the range

$$1^\circ < \theta < 25^\circ$$

for medium-angle grain boundaries, the range

$$0.1^\circ < \theta < 5^\circ$$

for low-angle grain boundaries and the range

$$0 < \theta < 1^\circ$$

for lineage. There is a certain overlap in the low-angle range, since there is no clear-cut discrimination between both (see Figure 4.6).

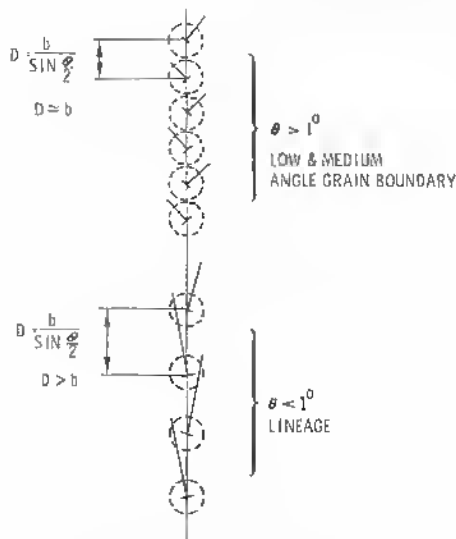


Fig. 4.6 Grain boundaries of low and medium tilt angle.

### The range of large-angle boundaries

$$25^\circ < \theta < 90^\circ$$

is rare and is less important, as we shall see, since this structure is subject to microcracking and other basic changes of the crystal, including strong influences of impurity segregation and impurity diffusion.

Low-angle boundaries ( $\theta \leq$  a few degrees) have been studied with an eye on their grid structures and potential in devices. Shockley and others have made proposals in this direction, and R. Mueller<sup>2,3</sup> has devised elaborate seeding and growth methods for their study. It was revealed, however, that the increased difficulties of their growth were not justified by their properties. In general, a few degrees guarantee electronic overlap, since 20 lattice constants, for example, can easily be bridged electrically from one dangling bond to the next if the impurity density is of the same order or less than the dangling-bond density. For example, consider nearly degenerate germanium (impurity density  $N(x) = 10^{19} \text{ cm}^{-3}$  corresponding to  $4.6 \times 10^{12} \text{ cm}^{-2}$  or  $2.2 \times 10^6 \text{ cm}^{-1}$ ). With  $5 \times 10^{-8} \text{ cm}$  interatomic distance or  $0.2 \times 10^8 \text{ atoms/cm}$ , this means that the impurity atoms are about 10 lattice constants apart. In general, the doping range is a factor of 10 to 100 less, which means a factor of 3 to 10 wider distance between impurity atoms. In this case the dislocations with 20

lattice constants distance are close compared with the impurity states with 30 to 100 and more lattice constants distance. Therefore, electronically these low-angle boundaries are still coherent structures.

### 4.3 SCREW DISLOCATIONS

It is known that this kind of dislocation is basic in many processes, especially in the growth of crystals in general. As we mentioned, the only difference in the generation of these dislocations compared with the edge dislocation is the fact that the slip vector or Burgers vector (in the simple cubic case) is parallel to the dislocation. This, however, has an important consequence in view of their electric properties in the crystal. The fact that the screw step leads to a smoothing of the deformation in the lattice along a spiral path is fundamental, and no dangling bonds are formed. Energetically, the situation looks quite similar to the edge dislocation, since the lattice strain energy is

$$E_s = \frac{1}{2} \int_{r_0}^{r_1} \sigma_{\theta z} b \, dr \quad (4.29)$$

$$\simeq \frac{\mu b^2}{4\pi} \left( \log \frac{r_1}{r_0} \right), \quad (4.30)$$

where  $\mu$  = shear modulus

(see chapter 7). For the edge dislocation in comparison, one has

$$E_{\perp} = \frac{1}{2} \int_{r_0}^{r_1} \sigma_{\theta z} b \, dr$$

$$E_{\perp} = \frac{\mu b^2}{4\pi(1-\nu)} \left( \log \frac{r_1}{r_0} \right), \quad (4.31)$$

where  $\nu$  = Poisson's ratio (0.4 for germanium, e.g.),

$r_0$  = dislocation core radius.

We see that the edge dislocation has a somewhat higher strain energy. This is due to the way in which the displaced atoms have adjusted to the lattice deformation. A spiral ramp (Figure 4.7) is a crystallographically natural mechanism and is considered a low-energy way to build up new crystal material in crystal-growth processes.

A Burgers cycle around the screw dislocation results in a similar closure failure, as in the case of edge dislocations (circles I to II in Figure 4.8; note that the Burgers vector I to II lies in the slip plane). The electronic disturbance in the lattice, however, is very minor for the screw dislocation. In

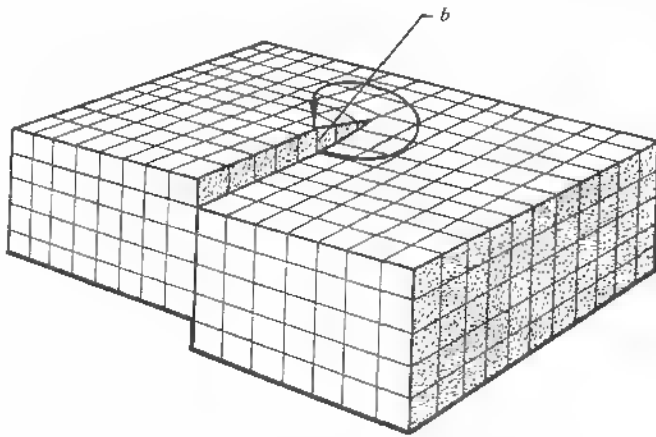


Fig. 4.7 Spiral ramp of a screw dislocation.

fact, any grain boundary formed by screw dislocations yields only slightly stronger electronic effects than a twin.

There is a strong relation between twinning and screw dislocations, which we show later.

The screw dislocation has no additional half plane, and so there is no non-conservative motion and the dislocation is free to move on any cylindrical

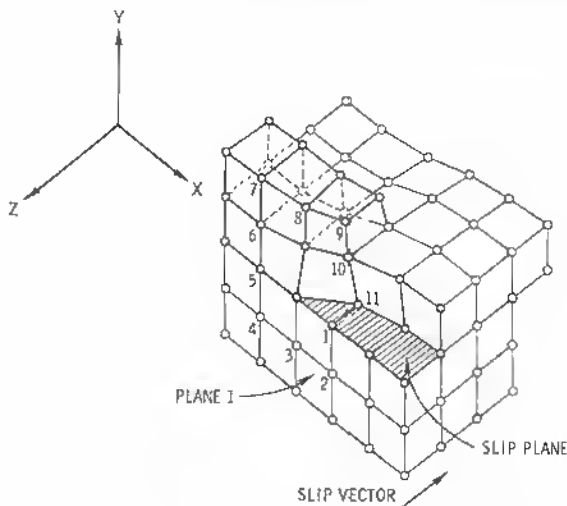


Fig. 4.8 Model of a screw dislocation with Burgers cycle.



surface having the slip direction for its axis. This is the reason for the importance of this dislocation for crystal-growth processes. In crystal growth from the vapor phase, Frank's theory predicted that atoms reaching the crystal surface near a partially grown spiral ramp of a screw dislocation can join three nearest neighbors more easily than only one on a perfect surface. The surface mobility of impinging atoms is so high, generally, that they can diffuse to such positions before reevaporation occurs. This process is of primary importance for the growth of perfect thin films by vapor deposition.

Assume the step in Figure 4.7 has not grown fully to the outside, since the spiral growth is faster in the center (less atoms per circle), there are many positions with three next nearest neighbors available. In the case of crystal growth from the melt, this mechanism certainly plays a similar role at the liquid-solid interface. Its form has not been proved so clearly and is not photographically recorded, as in the case of vapor growth. Spiral ramps have been found though in germanium crystals and silicon crystals grown from the melt, which proves that the high mobility of atoms in the liquid phase at the solid seed-crystal interface allows their direction and association into such screw ramps.

We have touched on these problems here only to enhance the understanding of the relationship between the screw dislocation and twin on one hand and edge dislocations on the other hand.

It is important to connect with each dislocation the idea of a frozen-in energy amount. In crystal growth, parameters such as seed-crystal pulling speeds and temperature gradients across the liquid and in the growth direction (vertically) define the probability of the occurrence of these defects. The highest amount of energy is stored by edge dislocations or grain boundaries, as planar defects, and a lesser energy is necessary to form screw defects. Still less energy is required to form twins.

In crystal growth any misfit among the growth rate, the energy of crystallization, and the cooling mechanism is expressed by a corresponding amount of energy stored in the appropriate kind of dislocation. We do not mention in this context the many other kinds of dislocations like partials or multiples or stacking faults, since their distribution is generally statistical within the lattice and their electrical effects can be described as less important than those of edge dislocations.

#### 4.4 TWINNING

The next-nearest-neighbor violations lead to twin configurations. In face-centered cubic lattices any wrong sequence such as



is a twin.

The energy of a twin is relatively low, since only a slight change in the diagonal atomic distances occurs. As an average, a twin boundary has  $\frac{1}{10}$  to  $\frac{1}{100}$  the energy of a grain boundary. Twins may, however, have a more complicated pattern than the ideal diagonal displacement. Figure 4.9 gives a description of this process in a body-centered cubic crystal. In the unit cube shown in the upper part of the picture, the twinning plane (211) is indicated. It stands perpendicular to the lower part of the picture and intersecting it along the dot-dashed horizontal line. The shear force of atoms below is indicated by arrows. Movements of an atomic layer which produce a twin are similar to those which produce slip. The strain energy stored can be judged roughly by the change in interatomic bond distance (distortion). This energy is obviously small, and, therefore, small changes in the electronic band structure are to be expected. In fact, in cases of undisturbed twins, no electrical effects of significance have been observed, not even in lifetime measurements of minority charge carriers. This most structure-sensitive electronic magnitude is almost independent of twins in the path of the carriers if no doping gradient occurs.

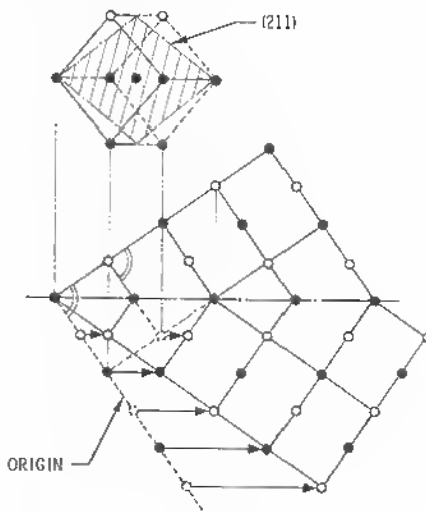


Fig. 4.9 Movements of atoms in the production of a twin.

This is because the twin is the natural way to absorb surplus energy during growth or in other thermal processes like quenching. The diagonal displacement along a twin axis generates a zone of higher energy but without broken bonds. Therefore, we have to be very specific in our expressions. Grain boundaries are strictly connected to the broken-bond picture. In case of

screw dislocations, we do not use the expression but speak about screw-dislocation planes. The latter, incidentally, show much similarity to a geometrical twin with respect to the electronic properties. If a pure tilt boundary has a twist error, a screw geometry may diminish the number of broken bonds and, therefore, diminish the strong electrical effects of the grain boundary on carrier transport (see Chapter 10). Twins may have numerous configurations and may form higher-energy contact zones than the normal diagonal displacement in Figure 4.9.

The twin axis may be gliding, or other defects may occur within the twin to make it a higher-energy area or zone within the crystal. It was found that also higher-order twinning is common in the diamond lattice if nonequilibrium energy situations are generated during crystal growth.

Kohn has studied the effects of higher-order twins, mainly in silicon, that show a strong tendency for twinning in the  $[111]$  crystallographic direction. Because of the possibilities of higher-order twinning relations and the tendency inherent in this crystal material to "repair" broken bonds by establishing either screw or twin relations, silicon is to be considered a less "noble" lattice than germanium. In other words, broken bonds are easier to freeze into the germanium lattice than into the silicon lattice.

Multiple twinning, observed in silicon crystals grown by the Czochralski method, were the origin of the work done by Kohn<sup>4,5</sup> who discovered and, explained a whole set of first- and second-order twins in silicon. Very unusual, regular twin patterns have been observed in silicon crystals pulled from the melt. Cyclic twinning can be generated from a set of nonparallel twinning operations. For example, an initial twinning generates a twin, I, on  $[111]$  of the host crystal. A second twinning operation generates a twin, II, on  $[\bar{1}\bar{1}\bar{1}]$  of the same host crystal. The relationship between the host and each of twins I and II is that of simple or first-order twinning; that between individuals I and II is of higher order.

Deviation from normal bonding in silicon begin with tertiary coordination. Primary and secondary coordinations remain unaffected by the twinning operation; therefore, only a slight energy difference exists between normal and twinned configurations. This accounts for the high frequency of twinning in such material. Kohn proposed and verified the following twin boundaries:

$$\left. \begin{array}{l} [015]-[111] \\ [112]-[112] \\ [001]-[221] \\ [110]-[114] \end{array} \right\} \text{ first order}$$

$$\left. \begin{array}{l} [221]-[221] \\ [115]-[111] \\ [114]-[114] \end{array} \right\} \text{ second order}$$

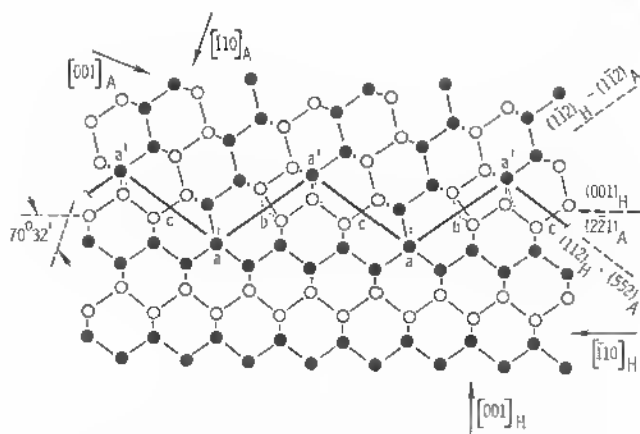


Fig. 4.10  $[001]$ - $[221]$  lateral twin boundary after Kohn [4.5].

Figure 4.10 shows a  $[001]$ - $[221]$  lateral-twin-boundary configuration. Full points are in the plane of the drawing; open points are  $(\sqrt{2}/4)a_0$  from the plane of the drawing. The arrows indicate the crystallographic directions of the host crystal H and the twinned crystals A.

Figure 4.11 shows a second-order twin joint. Twin crystals are A and B. In essence, such "repaired" lattice structures along twin lines show interatomic bonding deformations rather than dangling bonds or broken bonds. As we have mentioned, this is the lower-energy configuration, and this tendency of crystal material makes it difficult to grow grain boundaries with a maximum of broken bonds (for electronic purposes).

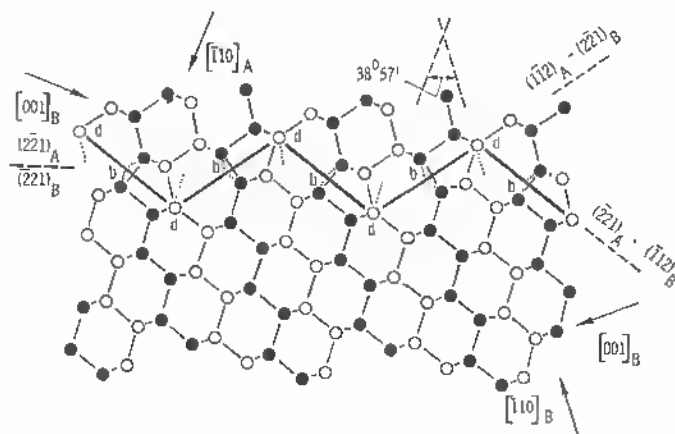


Fig. 4.11  $(\bar{2}21)$ - $(\bar{2}21)$  second-order twin joint after Kohn [4.5].

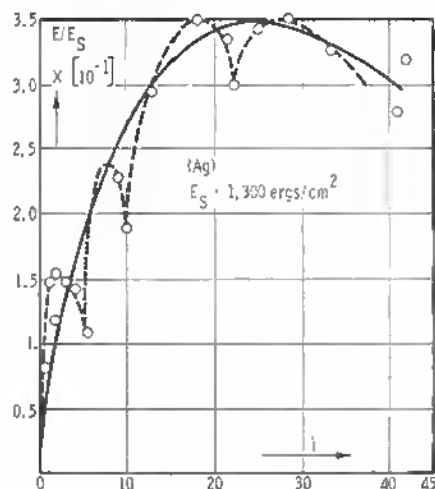


Fig. 4.12 Energy versus tilt angle for grain-boundary and measured values for silver bicrystals (see text).

In the Shockley-Read energy curve plotted over the tilt angle  $\theta$ , energy cusps have been observed whenever the boundary approaches a twin configuration (see Figure 4.12, which shows measured values of  $E_L$  of Greenough and King—Chapter 3, Ref. 14, Figure 13.3—for silver.)  $E_s$  is surface energy. Energy cusps are clearly visible at certain tilt orientations  $i$ . Also the grain boundary orientation  $\phi$  should be of influence in this respect.

Second-order twins accumulate a sensible amount of lattice energy in the form of bond deformation (see Figure 4.11), and it was found that such twins are measurable electronically as photoelectrically active regions (hole-electron separation across  $\Delta p/\Delta x$  isocycles).

Also, such lattice deformations can be the cause of inhomogeneities of the impurity distribution, the segregation constant for impurities being altered by a stress field within the twinned region. This again can cause  $p$ - $n$  changes in compensated material, which, in turn, have a strong influence on carrier flow resembling those of a grain boundary under voltage applied. It is generally unlikely that the twin forms an  $n$ - $p$ - $n$  (or  $p$ - $n$ - $p$ ) junction like a grain boundary. Under voltage applied, however, one of the junctions is biased in the forward direction and disappears electrically, showing a similar result as the twin joins with  $p$ - $n$  behavior. A clear test, as described later in detail, is the photovoltaic test of a crystal boundary with no external voltage applied and the sign reversal of the photovoltage at the grain boundary that does not occur at a perfect twin boundary.

## 4.5 DISLOCATION PLANES

To extend the theory of the edge dislocation (see Section 4.1) to include the edge-dislocation plane, we start with the energy expression (4.3) for the edge dislocation. The shear stress  $S$  on the slip plane (slip vector  $\perp$  to slip plane) can be expressed by the sum of the individual stress components  $\sigma_{xy}(x, y)$  in the  $xy$  plane:

$$S = \sum_{n=-\infty}^{n=+\infty} \sigma_{xy}(x, nD), \quad (4.32)$$

where  $n$  = number of individual dislocations,  
 $D$  = dislocation spacing

(see Figures 4.5 and 4.13). As we have shown in Section 4.1, the energy  $E_{\perp}$  per

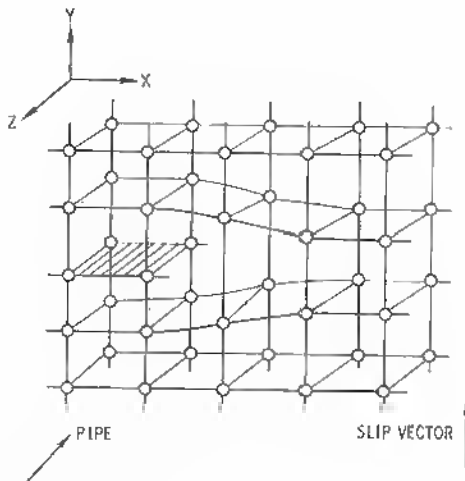


Fig. 4.13 Edge dislocation in hypothetical cubic lattice.

dislocation is  $b/2$  times the shear stress integrated over the slip plane:

$$E_{\perp}(D) = \frac{b}{2} \int_0^{\lambda} \sum_n \sigma_{xy}(x, nD) dx, \quad (4.33)$$

where  $\lambda$  = crystal dimension considered,  
 $\lambda \rightarrow \infty$  for infinitely large crystal.

The strain energy consists of three parts, assuming the surface of the body to be free from external forces:

1. The self-energy of the first dislocation. Using (4.32) and (4.33) and integrating, the energy of the dislocation can be expressed by

$$E_{\perp} = \frac{b}{2} \int_{r_0}^{r_1} \sigma_r dr,$$

$$E_{\perp} = \frac{\mu b^2}{4\pi(1-\nu)} \log\left(\frac{r_1}{r_0}\right) \quad \text{dyn.} \quad (4.34)$$

2. The self-energy of the second dislocation.

3. The mutual-interaction energy.

If one uses the classical Volterra derivation for the local shear-stress (see Chapter 3, Refs. 4 and 14),

$$\sigma_{xy} = \frac{\mu b}{2\pi(1-\nu)} \frac{x(x^2 - y^2)}{(x^2 + y^2)^2}, \quad (4.35)$$

The energy per dislocation can be written

$$E_{\perp} = \frac{\mu b^2}{4\pi(1-\nu)} \int_{r_0}^{\infty} \sum_{n=-\infty}^{+\infty} \frac{x(x^2 - y^2)}{(x^2 + y^2)^2} dx. \quad (4.36)$$

The sum can be evaluated by Fourier series transformation (see Chapter 3, Ref. 4) and the whole expression leads to the well-known formula for the energy per unit area of the grain boundary:

$$E_{\perp} = \frac{\mu b}{4\pi(1-\nu)} \theta(A - \log \theta) \quad \text{ergs/cm}^2, \quad (4.37)$$

where

$$E_0 = \frac{\mu b}{4\pi(1-\nu)} \quad \text{compare (4.23) and (4.25)}$$

and  $A = 1 + \log(b/2\pi r_0) = \text{constant}$ ,

$\theta = b/D = \text{lattice translation vector/dislocation spacing} - (\text{tilt angle})$

Expression (4.37) was first derived in a rigorous way by Read and Shockley.<sup>6</sup> Comparisons with experimental data have shown that it is valid to high angles of misfit (see, for example, Figure 4.12) even beyond the range of the validity of the assumptions (see Chapter 3, Ref. 14).

The salient features of the theoretical curve are a rapid rise of  $E_{\perp}$  with  $\theta$ , at small values of  $\theta$ , and a relatively broad, flat maximum (at  $25^\circ$  for most crystals of the diamond type structure).

In general, the experimental values are scattered around the theoretical curve, but in certain cases the energy cusps discussed in Section 4.4 are clearly measured for certain distinct angles of misfit (see Figure 4.12).

It is important to note, however, that Mott's picture of a grain boundary as a "glassy" layer (unordered structure) has become unlikely as progress is made in understanding the grain boundary. It is believed now, and there is ample evidence for this, especially in the electronic area, that low- and medium-angle grain boundaries ( $1^\circ < \theta < 25^\circ$ ) in most cases of bulk crystal growth represent ordered structures and can as such be represented by a dislocation model. In the area of optical observation either by light, x-ray, or electron microscopy, the grain-boundary model based on the tilt or twist process gained ground also because of observations by Amelinckx et al. (see Chapter 3, Ref. 15). Amelinckx used the general description of a grain boundary expressed by Frank's formula:

$$\sum_i b_i = \omega \times r, \quad (4.38)$$

where  $\sum_i b_i$  = sum of Burgers vectors in dislocation lines cut by  $r$ ,

$r$  = arbitrary vector lying in contact plane,

$\omega$  = rotational vector. (see Chapter 5)

The resulting dislocation models for boundaries and intersecting sets of dislocations were essentially found in NaCl crystals. Even in cases of junctions of several tilt boundaries, the corresponding dislocations were discovered in actual crystals. It must be concluded that the low-angle boundaries and, to a certain extent, the medium-angle grain boundaries are ordered structures obeying the laws of the mathematical dislocation models described.

In measurements designed to check the grain-boundary energy expression Wagner and Chalmers<sup>7</sup> confirmed the Read-Shockley energy formula for germanium in the range of tilt angles  $10^\circ < \theta < 15^\circ$ . For higher angles of misfit the grain-boundary energy begins to be independent of  $\theta$ . It has to be assumed that the model may be applied successfully up to  $25^\circ$ , since the energy maximum is flat and since microcracking and dissolution of structure occurs apparently only at higher than  $25^\circ$  angles of misfit.<sup>8,9</sup>

The grain-boundary behavior with respect to diffusion, which is discussed later, lends support to the model described. Much depends, however, on the growth conditions and detailed orientation of the grain boundary. Asymmetrical boundaries  $\phi \neq 90^\circ$  ( $\phi$  = angle between grain-boundary plane and the perpendicular to the symmetry plane of the two grains) and mixed tilt-twist boundaries may have a more complex and disturbed structure.

## PROBLEMS

4-1. The edge dislocation in Figure 4.1 is symmetrical about a plane of atoms on the compression side of the slip plane (the slip plane runs horizontally across the drawing through the dislocation). If we draw a dislocation having the same



- direction and slip vector but symmetrical about a plane of atoms on the tension (dilation) side (lower part), what changes?
- 4-2. What is the equivalent replacement of a row of vacancies in terms of edge dislocations?
  - 4-3. In considering a Burgers cycle stress integration around a dislocation  $a$  in Figure 4.2, discuss why the integration ( $r, \theta$ ) must avoid cutting through the center of the dislocation.
  - 4-4. Find the influence of the difference in radii for the integration cycle  $r_1$  and the size of the bad region  $r_0$  on the edge-dislocation energy.
  - 4-5. In surrounding an edge dislocation with a tubular surface separating the good from the bad material, show that the net total force exerted by the good material on the bad material vanishes.
  - 4-6. Consider two parallel grain boundaries similar to the one given in Figure 4.5. Show that the two boundaries can reduce their energy by combining to form a single boundary with  $\theta = \theta_1 + \theta_2$ . (Hint: Develop  $E_1 + E_2$ , and compare with  $E = E_0 (\theta_1 + \theta_2) [A - \ln (\theta_1 + \theta_2)]$ . Make  $\theta_1 = \theta_2$  for a fast test.)
  - 4-7. Discuss the influence of the change in dislocation spacing on the grain-boundary energy (see Figure 4.5). Decide, with the aid of the grain-boundary energy  $E$  per unit area, which grain boundary has the lower energy—the one with many dislocations of small Burgers vector or the one with few dislocations with larger Burgers vector ( $\theta$  is the same in both cases).
  - 4-8. Draw a twinning dislocation or a sidewise step in an otherwise coherent twin boundary. Show why such defects have a higher energy than pure twins.

## REFERENCES

1. Timoshenko, S.: *Theory of Elasticity*, McGraw-Hill, New York, 1951.
2. Mueller, R.: Current Flow across Grain Boundaries in N-type Germanium, II, *J. Appl. Phys.*, vol. 32, no. 4, pp. 640–645, April, 1961.
3. Mueller, R., and R. L. Jacobson: Growth Twins in Indium-Antimonide, *J. of Appl. Phys.*, vol. 33, no. 3, 550–551, March, 1961.
4. Kohn, J. A.: Twinning in Diamond Type Structures: High Order Twinning in Silicon, *The American Mineralogist*, vol. 41, pp. 778–784, 1956.
5. Kohn, J. A.: Twinning in Diamond Type Structures: A Proposed Boundary Structure Model, *The American Mineralogist*, vol. 43, pp. 263–283, 1958.
6. Read, W. T., and W. Shockley: *Physical Review*, vol. 78, p. 275, 1950.
7. Wagner, R. S., and B. Chalmers: *Journal of Applied Physics*, vol. 31, pp. 581–587, 1960.
8. Van der Merwe, J. H., *Proceedings of Physics Society*, vol. 63, pp. 616–637, 1950.
9. Bullough, R., and H. F. Mataré: Discussion on Materials—I, Record on International Convention on Transistors, *Proceedings Inst. Electr. Engineers*, vol. 106, part B, supplement no. 15, p. 329, May, 1959.

## Chapter 5 Continuum Theory of Dislocations

The description of a dislocation in the macroscopic language of the continuum theory does not allow for a detailed description on a microscopic scale. Here we have the overall crystal state in mind as it is affected by dislocations within the material.

For one dislocation line the Burgers vector  $b$  is representative; for several dislocation lines, the respective Burgers vectors can be added together to describe their influence on the crystal:  $\sum_i b_i = \mathbf{r} \times \boldsymbol{\omega}$ , where  $\mathbf{r}$  = arbitrary vector in the plane of the boundary and  $\boldsymbol{\omega}$  = rotational vector (see Figure 5.1).

Proof: Assume an arbitrarily oriented area element  $dS$  represented by a vector  $\mathbf{r}$  lying in the contact plane. The total closure failure or the sum of the Burgers vectors is then given by the vector product of  $\mathbf{r}$  and the relative rotation  $\boldsymbol{\omega} = \mathbf{u}\theta$  about the axis  $\mathbf{u}$  ( $\mathbf{u}$  is parallel to the dislocation lines). The boundary

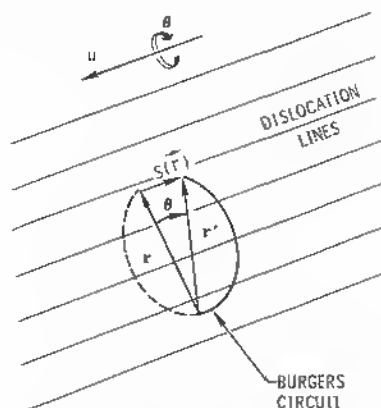


Fig. 5.1 Burgers cycle in dislocation arrays.  $\mathbf{S}(\mathbf{r})$  = closure failure.  $\mathbf{r}'$  originates from  $\mathbf{r}'$  by rotation  $\mathbf{u}\theta$ .

is a tilt or a twist boundary dependent on the fact that  $\mathbf{u}$  has components only within or at right angles to the boundary. In mixed cases,  $\mathbf{u}$  has components in both orthogonal planes.<sup>1, 2</sup>

In the case of a symmetric boundary between two crystalline halves, the misorientation is  $\theta/2$  to either boundary side. The sum of the Burgers vectors at either side can be expressed by

$$\frac{1}{2} \sum_i b_i = (\mathbf{r} \times \mathbf{u}) \cdot \sin \frac{\theta}{2} \quad (5.1)$$

(see Figure 5.2). If  $\theta$  is small, this can be written

$$\sum_i b_i = (\mathbf{r} \times \mathbf{u}) \theta \quad (5.2)$$

or:

$$\sum_i b_i = \boldsymbol{\omega} \times \mathbf{r}, \quad (5.3)$$

which is Frank's generalized formula for small  $\theta$ . For the case that the vector

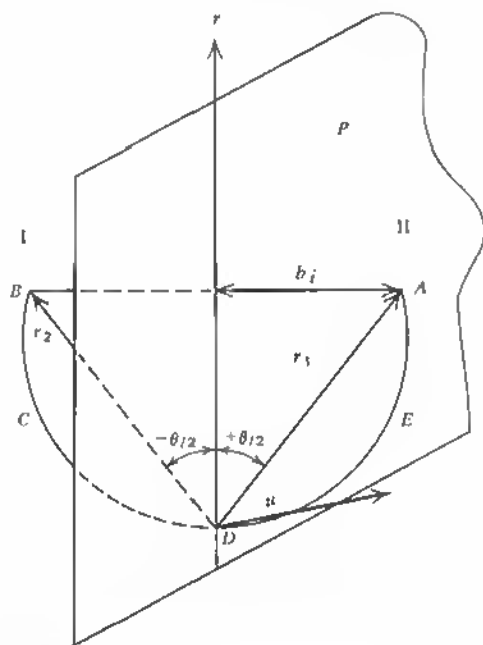


Fig. 5.2 Boundary plane  $B$  between two grains I and II. Grains are rotated around  $\mathbf{u}$  by  $\theta$ .  $AEDCB$  is Burgers circle with closure failure  $2b_1$ .

$\mathbf{u}$  is taken perpendicular to the Burgers cycle surface, (5.1) can be written

$$\frac{1}{2} \sum_i b_i = |\mathbf{r}| \cdot |\mathbf{u}| \underbrace{\sin(\mathbf{r}\mathbf{u})}_1 \cdot \sin \frac{\theta}{2} \quad (5.4)$$

and for small  $\theta$

$$\sum_i b_i = |\mathbf{r}| |\mathbf{u}| \cdot \theta,$$

corresponding to (5.1) for  $\mathbf{u} \perp \mathbf{r}$ .

The Frank formula may also be derived from Nye's generalized equation for the total Burgers vector of all dislocations that pierce through an arbitrarily orientated area element:

$$\sum_i b_i = d\mathbf{S} \times \alpha. \quad (5.5)$$

The second-rank tensor  $\alpha$  defined in this form conveys an average knowledge about the dislocation distribution at  $\mathbf{r}$ .

The diagonal components of this *tensor of the dislocation density* belong to dislocations that have a Burgers vector and line direction that are parallel and represent screw dislocations, and the off-diagonal components of  $\alpha$  correspond to edge dislocations.

The displacements characterized by the Burgers vector are the cause of stress fields within the crystal altering the energy state as a whole (frozen-in energy in crystal growth). Volume forces can be represented by surface forces (tensions). In the case of anisotropic crystals, they are defined by symmetric tensors  $\sigma_{ik}$  such that

$$\sum_k \sigma_{ik} df_k$$

is the  $i$ th component of the force to be applied to a surface element  $df$  of an internal cut within the crystal in order to maintain equilibrium. The relations between stress tensors  $\sigma_{ik}$  and strain tensors  $\varepsilon_{mn}$  are linear as long as the validity of Hooke's law is assumed:

$$\sigma_{ik} = \sum_{mn} C_{ik, mn} \varepsilon_{mn}, \quad (5.6)$$

where  $C_{ik, mn}$  = tensor of fourth degree (elastic constant tensor).

Since tensors  $\sigma_{ik}$  and  $\varepsilon_{mn}$  are symmetric, the elastic energy is

$$E = \frac{1}{2} \sum_{ik} \sigma_{ik} \varepsilon_{ik}$$

and with (5.6)

$$E = \frac{1}{2} \sum_{ik, mn} \varepsilon_{ik} C_{ik, mn} \varepsilon_{mn}. \quad (5.7)$$

The total strain energy of a piece of material is given by the integral of (5.7) over the volume  $V$  of the material in question:

$$E_t = \frac{1}{2} \int_V \sum_{ik} \sigma_{ik} \varepsilon_{ik} dV. \quad (5.8)$$

If the material is assumed to be isotropic, the elastic constant tensor  $C_{ik, mn}$  reduces to two independent constants, and Hooke's law (5.6) reduces to

$$\sigma_{ik} = \lambda \varepsilon_{mn} \delta_{ik} + 2\mu \varepsilon_{ik}, \quad (5.9)$$

where  $\lambda$  = Lamé's constant,

$$\lambda = 2\mu\nu/(1 - 2\nu),$$

$\mu$  = elastic constant,

$\nu$  = Poisson's constant,

$\delta_{ik}$  = Kronecker's delta, that is,

$$\delta_{ik(i \neq k)} = 0, \quad \delta_{ik(i=k)} = 1.$$

As described earlier, the stress arising from a dislocation within perfect material is equivalent to  $\frac{1}{2}$  times forces  $\times$  displacement. Based on this concept (4.1), the energy of typical dislocations, such as the screw dislocation (4.29) and the edge dislocation (4.31), were derived. In a more general way, any state of internal stress can be derived on the basis of Frank's formula (5.4) or Nye's formula (5.5). Kröner<sup>4</sup> uses the form

$$b_n = \int_S \alpha_{ij} dS_i \quad (5.11)$$

where  $b_n$  = total Burgers vector of all dislocations crossing the arbitrary surface  $S$  in a material,

$\alpha_{ij}$  = density of dislocations with Burgers vector in  $x_j$  direction crossing plane perpendicular to  $x_i$  direction (asymmetric dislocation tensor).

Based on the analogy between magnetostatics and dislocation theory, interaction energies can be expressed in elegant form. In this way, a generalized treatment is possible in which, for example, strain  $\varepsilon_{ij}$  is coordinated to the magnetic intensity  $H_i$ , the stress  $\sigma_{ij}$  to the magnetic induction  $B_i$ , Burgers vector  $b_i$  to the current  $i$ , and the like. In this way the energy expression

$$E = \frac{1}{2} \int_V \sigma_{ij} \varepsilon_{ij} dV \quad (5.12)$$

is equivalent to

$$E = \frac{1}{2} \int_V B_i H_i dV. \quad (5.13)$$

The mutual interaction energy can thus be derived in magnetostatics as a counterpart to the dislocation energy and reinterpreted for the mechanical

case. For the straight edge dislocation, the energy expression derived in this way is

$$E' = L \frac{\mu b^2}{4\pi} \frac{m}{m-1} \left( \ln \frac{2L}{r_0} - 1 \right) \quad (5.14)$$

(see equation (17.5) in Ref. 5).

Since  $L$  is the dislocation length and  $m$  is the reciprocal of Poisson's constant  $1/\nu$ , this can be written as an energy-per-unit length:

$$E = \frac{\mu b^2}{4\pi} \left( \ln \frac{2L}{r_0} - 1 \right) \frac{1}{1-\nu}. \quad (5.15)$$

This is identical to (4.31) when  $r_1$  is a large path compared with  $r_0$ , since  $L \gg r_0$ .  $r_0$  is the dislocation core radius  $\approx 10\text{\AA}$ .

The methods developed in the continuum-theoretical treatment of dislocations are of great importance for all calculations of mechanical forces arising in defect structures. Forces on foreign atoms due to dislocations and other problems can be dealt with in a more detailed way, since the mechanism of a deduction of general formulas for the stress-strain relations has been developed.

In the case of the electronic behavior of dislocations, which we are dealing with here, the problem of the mathematical formulation of the energy due to defects is not predominant, however. Such a formulation does not directly help understand the phenomenon of the carrier transport in and around dislocations. The main reason is that the energy situation at a macroscopic scale (Burgers cycle in perfect material,  $r_1 \gg r_0$ !) is not sensitive to detailed (microscopic) features, such as local compression and dilation, band changes, carrier redistribution, carrier depletion, and all other transport mechanisms.

One can use the knowledge gained by the continuum theory, however, in all cases when configurational problems are of minor importance and where the resulting stress field is the main quantity desired.

## REFERENCES

1. Read, W. T., Jr., "Dislocations in Crystals," McGraw-Hill, New York, 1953, pp. 181ff.
2. Amelinckx, and W. Dekeyser, The Structure and Properties of Grain Boundaries, in "Solid State Physics," F. Seitz and D. Turnbull (ed.), Academic, New York, 1959, vol. 8, pp. 325ff.
3. Seeger, A., Theorie der Gitterfehl-Stellen, in "Encyclopedia of Physics," S. Flügge (ed.), vol. VII, part 1, Springer-Verlag, 1955.
4. Kroener, E., Continuum Theorie der Versetzungen und Eigenspannungen, *Ergebn. Angew. Math.*, vol. 5, 1958.
5. DeWit, R., The Continuum Theory of Stationary Dislocations, "Solid State Physics," Academic, New York, 1960, vol. 10, p. 249.

## Chapter 6 Radiation Damage and Dislocations

In general, defects caused by radiation are of the point defect type. A nuclear particle incident on a crystal readily loses some of its energy to the lattice with its interatomic forces where it is dissipated in vibrational modes. If energetic particles are able to knock out atoms from their sites in the lattice, this remains a rather localized defect, since disrupted bonds are left behind by the free atom that has moved into an interstitial position (Frenkel defect) or to the crystal surface or an intercrystalline boundary (Schottky defect). Disrupted bonds take up a large amount of the energy available. The energy needed to break up lattice bonds is many times larger than that needed to displace atoms within the lattice after they are set free and have moved into interstitial positions. In ionic crystals, for example, typical values of activation energy for motion,  $E_+$ (eV), and the energy of formation of a vacancy pair,  $E_f$ (eV), are

Crystal	$E_+$ , eV	$E_f$ , eV
NaCl	0.86	2.02
LiF	0.65	2.68
LiBr	0.31	1.80
AgCl	0.39	1.40

In the case of materials like Ge, Si, or diamond, these values are much higher. Binding energies of  $E_d = 3$  to 10 eV are normal. A factor of 2 for the process of a lattice disruption (Frenkel defect formation) must be assumed so that values above 20 eV for  $E_d$  are possible.

For electrons the necessary minimum amount of energy  $E_{min}$  to impart  $E_d$  is calculated according to

$$E_d = \frac{2E_{min}m}{M} \left( \frac{E_{min}}{mc^2} + 2 \right), \quad (6.1)$$

where  $c$  = light velocity,  
 $m$  = electron mass,  
 $M$  = mass of the atom under impact.

Measurements of the threshold value obtained in resistivity measurements by E. Klontz and K. Lark-Horovitz<sup>1</sup> resulted in a value  $E_{\min} = 0.63$  MeV. Electrons impart damage for relatively high energies only, since their mass is very small. A particle of energy  $E$  and mass  $m$  colliding with an atom of mass  $M$  imparts the energy amount

$$\Delta E = E \frac{4M^*^2}{m + M} \sin^2 \frac{\delta}{2}, \quad (6.2)$$

where  $M^* = \frac{mM}{m + M}$  is "reduced" mass,

$\delta$  = angular deviation of injected particle with respect to center of gravity.

$M^*$  is very nearly equal to  $m$  for  $M \gg m$ .  $M^*$  being introduced quadratically, the small value squared has to be compensated by the energy amount  $E$ .

In the case of heavy particles  $m \gg M$ , the transferred energy amount  $\Delta E$  is

$$\Delta E = E \frac{4M}{m} \sin^2 \frac{\delta}{2} \quad (6.3a)$$

instead of

$$\Delta E = E \frac{4M}{M} \sin^2 \frac{\delta}{2} \quad (6.3b)$$

for  $m \ll M$ .

The maximum energy  $\Delta E_{\max}$  transferrable to a particle of mass  $M$  by an incident particle of mass  $m$  and energy  $E$  is

$$\Delta E_{\max} = 4E \frac{M/m}{(M/m + 1)^2}. \quad (6.4)$$

Similar laws apply to cases in which heavy particles interact with the lattice and are slowed down by ionization rather than atomic impact. Also uncharged particles such as neutrons cause interactions with the shell electrons of the lattice, thereby changing the electronic equilibrium and causing ionization. Application of (6.4) to this case, where  $m = m_e$  is the electron mass and  $M$  is the mass of incident heavy particle ( $M \gg m_e$ ), leads to

$$\Delta E_{\max} \cong 4E \frac{m_e}{M} \quad (6.5)$$



(see Ref. 2). Although the primary effect of radiation is a disturbance of charge distribution, the next step is either a direct or indirect point defect or a Frenkel pair. Finally, a Brinkman displacement spike marks the path of an energetic particle.<sup>3,4</sup> Such a zone that has undergone strong local heating is an area of uncontrolled crystalline regrowth and, therefore, is marked by dislocations (see Ref. 5, p. 438), which cannot be annealed out so easily as point defects.

In metals the usual parameter considered in electronic measurements is the resistivity of a bar of the material. Although correlation between resistivity change and kind of defect is a problem, the overlapping bands simplify the situation compared to semiconductors. In the latter case, the forbidden gap is the medium of many complicated configurations of energy-level schemes and carrier-transport problems (see Ref. 1, Figure 3.3).

This situation has been demonstrated by the first general measurements of the change of the conductivity type of semiconductors by a bombardment by, for example, 10 MeV deuterons and fast neutrons from a nuclear reactor. Table 6.1 shows this tendency of some of the more known elemental and compound semi-conductors.

Table 6.1

Crystal type	Final conductivity type
Ge	<i>p</i> -type
Si	Intrinsic
InSb	<div style="display: inline-block; vertical-align: middle;"> <i>n</i>-type for room temperature irradiation <i>p</i>-type for radiation below 200°K </div>
GaSb	<i>p</i> -type
AlSb	<i>n</i> -type
InAs	<i>n</i> -type
CdTe	<i>n</i> -type

The difficulty in predicting changes due to irradiation in semiconductors is caused by several unknowns:

1. There is no simple model for the energy levels of lattice defects.
2. The kind of interactions between defects and imperfections (impurity atoms and dislocations) already present before irradiation and the radiation-induced defects. This may alter the energy-level structure of the defects both during and after bombardment.
3. The relaxation of electronic effects (trapped minority carriers) after low-temperature radiation that obscure relaxation processes involving defects.

In metals the low-temperature investigation of defect production and annealing cannot easily be interpreted, since conforming with 1 and 2 above, a detailed knowledge of the original defect and impurity configuration would be necessary. Also the defect-impurity interactions are mostly unknown. A point defect of the Frenkel type generally displays amphoteric action, depending on the position of the Fermi level and its change due to irradiation. The Fermi level generally lies between the lowest empty and highest filled state (see Figure 3.3 and James Lark-Horovitz' model) after bombardment. Therefore, if  $\zeta^*$  (Fermi level for the material in which the defect-state levels are preponderant over the states of impurities originally present) lies in the upper half of the gap, the end result is an *n*-type specimen with a limiting electron concentration:

$$n^* = N_c \exp \left[ - \frac{(E_c - \zeta^*)}{kT} \right] \quad (6.6)$$

and for  $\zeta^*$  in the lower half of the gap, a *p*-type specimen with

$$p^* = N_v \exp \left[ - \frac{(\zeta^* - E_v)}{kT} \right] \quad (6.7)$$

results.

$E_c$  and  $E_v$  are the positions of the conduction and valence band edges. The state densities are as usual

$$\begin{aligned} N_c &= \frac{2(2\pi m_e kT)^{3/2}}{h^3} \\ N_v &= \frac{2(2\pi m_h kT)^{3/2}}{h^3} \end{aligned} \quad (6.8)$$

where  $m_e, m_h$  = electron and hole masses,  
 $h$  = Planck's constant.

In the case of germanium and silicon, initially dislocation-free crystals can be made available for radiation experiments, but even their other defects present, such as vacancies, impurity clusters, can complicate the final result.

Generally, the overall resistance of materials to irradiation is of importance in order to assess the materials properties under radiation environment. The *threshold energy*  $E_d$  is defined as the limiting energy to be imparted to a crystal atom in order to effect a transfer into an interstitial position. A sudden rise in the conductivity versus, for example, the irradiated electron energy in million electron volts is identified with this minimum energy amount. This threshold energy is different from the displacement energy needed to displace atoms further from a dislocated state.

There is a natural difference in this respect between different crystal types because of atomic mass and bonding strength differences.

Tabel 6.2

Energy of electrons, MeV	$E_{\max}$ (Ge), eV	$E_{\max}$ (Si), eV
0.01	0.3	0.8
0.1	3.2	8.2
0.3	12	30.7
0.5	23	59
1.0	59	152
2.0	177	455
3.0	354	920

In the case of incident electrons of small mass  $m$ , (6.3b) shows that the transferred energy amount to the lattice atom  $M$  decreases with increasing mass  $M$ .

Assuming a center-of gravity injection ( $\sin^2(\delta/2) = 1$ ), the maximum imparted energy of incoming electrons can be calculated. There is already a marked difference between silicon and germanium due to the difference in atomic mass:

$$M_{\text{Si}} \cong 5 \times 10^4 m \quad M_{\text{Ge}} \cong 1.3 \times 10^5 m,$$

where  $m$  = electron mass.

Calculated imparted energy amounts for different electron energies give the values for  $E_{\max}$  shown in Table 6.2. The calculation is based on the impact model (see Figure 6.1). If the kinetic energy of the atom after the collision is

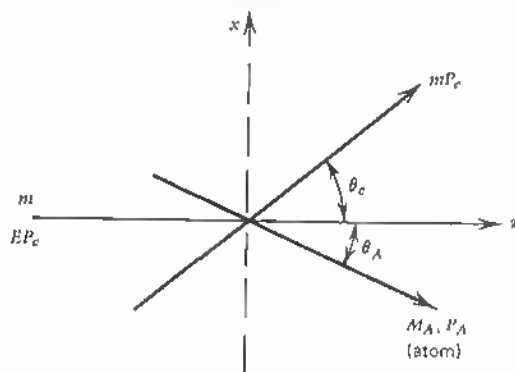


Fig. 6.1 Impact model for fast electrons:  $E$  — energy;  $m$  = electron mass;  $P_e$  = electron impulse;  $M_A$  = atom mass;  $P_A$  = atom impulse.

$E_A = P_A^2/2M_A$  ( $P_A$  = momentum) and  $mc^2 = 0.511$  MeV =  $\varepsilon$  is the rest energy of the electron, one gets for the imparted energy

$$E_A = \varepsilon \frac{2m}{M_A} \left[ \left( \frac{E}{\varepsilon} \right)^2 + 2 \frac{E}{\varepsilon} \right] \cos^2 \theta_A - E_{A_{\max}} \cos^2 \theta_A, \quad (6.9)$$

with  $\theta_A = 0$  and  $\theta_e = \pi$ , the maximum imparted energy can be calculated<sup>5</sup>. J. H. Cahn<sup>6</sup> has calculated the number of displacements in silicon and germanium crystals as a function of electron energy in million electron volts with the parameter

$$E_d = E_{A_{\max}} \cos^2 \theta_{A_{\max}}$$

in (6.9). For  $E_d = 15$  and 30 eV he finds higher displacement numbers for silicon, which is in agreement with the mass difference (see Figure 6.2).

For very thin samples, however, this situation reverses. This discrepancy is due to the superposition of integral limits in the expression for the number of displacements and might not have a real value.

The considerations thus far have not included the resistance of the lattice due to bond strength and especially the case of mixed homopolar and heteropolar cases (III-V compounds).

R. Bäuerlein<sup>7</sup> has detailed the differences between materials as far as threshold energy and displacement energy are concerned. He summarizes his results as given in Table 6.3.

In germanium the energy threshold is about a factor of 2 higher than for silicon. For the semiconducting III-V and II-VI compounds, the threshold energies are higher for all compound components (except for S in CdS) than for silicon but somewhat less than in germanium. It has to be kept in mind that the bonding strength of the partially ionic bond in III-V compounds is higher than in the pure homopolar bond.<sup>8</sup> This makes these compounds interesting from the point of view of radiation hardening. Energetically higher situations in crystals are of general interest in such cases. When the energy of dislocation arrays is high compared with the normal crystal structure, it is interesting to consider planar defect structures from a radiation point of view. Not much work is available in this area, since measurements of the specific properties of dislocations have started recently and not many crystal types have been grown into dislocation arrays.

When electronic measurements are carried through, it has to be considered that a barrier layer formed by a dislocation plane extends far into the bulk crystal material and, therefore, is subject to changes that take place in the unstrained normal crystal.

Neutron irradiation tests have been carried through with germanium bicrystals.<sup>9</sup> Although an integrated neutron dose, in nvt, of  $10^{15}$  and above is fatal to all device characteristics measured, there are differences. Bulk materials

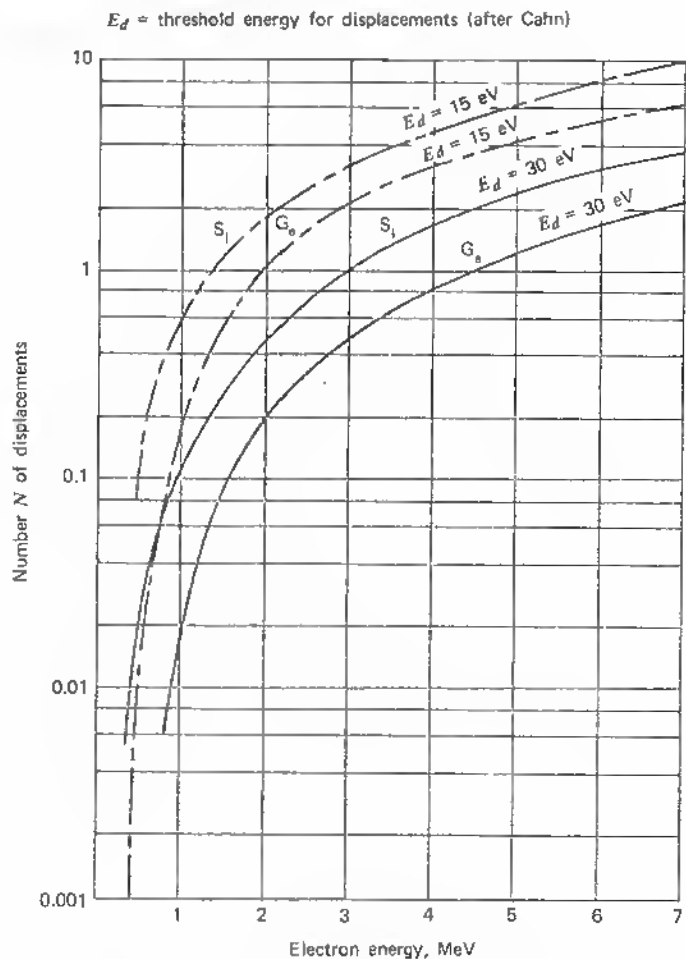


Fig. 6.2 Calculated number of displacements in silicon and germanium versus electron energy in MeV.

with doping levels in the 1 to 10 ohm-cm range for germanium show an increase in zero bias resistance for the  $n$ - $p$ - $n$  structure at an integrated flux rate of  $10^{14}$  and above. The resistance falls off definitely at radiation levels  $> 10^{15}$  nvt (neutrons/cm<sup>2</sup>). (A change in conduction type from  $n$ -type to  $p$ -type of the bulk germanium causes an increase in base resistance.)

The conversion of the bulk material from  $n$ - to  $p$ -type by radiation damage changes the I-V characteristics of the  $n$ - $p$ - $n$  structure of the grain boundary to a straight line. This occurs for all doping ranges ( $4.7 \times 10^{13}$  to  $2.2 \times 10^{16}$

Table 6.3 Threshold and Displacement Energies

Materia	Si	Ge	GaAs		InP		InAs		InSb		ZnSe		CdS	
			Ga	As	In	P	In	As	In	Sb	Zn	Se	Cd	S
Displaced atom	Si	Ge												
Energy threshold, keV	173	355	228	273	270	110	277	236	247	286	238	325	290	115
Displacement energy, eV	15.8	14.5	8.8	10.1	6.6	8.8	6.7	8.5	5.8	6.8	9.9	11.9	7.3	8.7
Self-diffusion energy, eV		2.98	5.60	10.2	3.85	5.65			1.82	1.94				

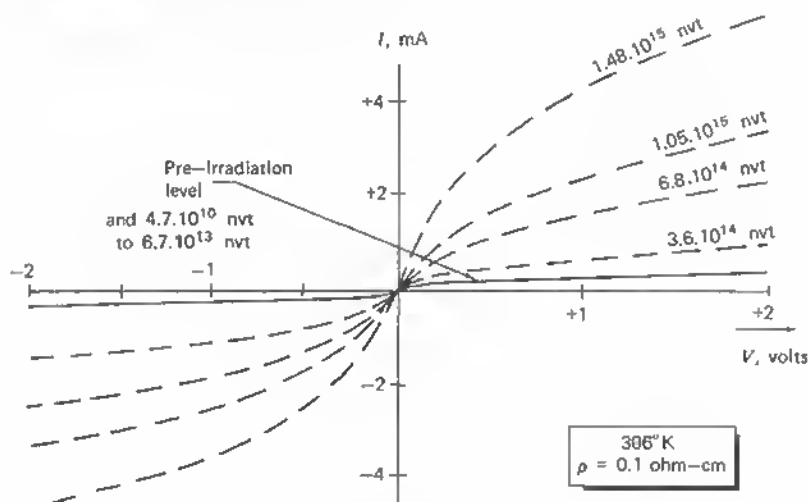


Fig. 6.3  $I$ - $V$  characteristics of grain boundary photocells as a function of integrated neutron flux.

$\text{cm}^{-3}$ ) at a mean value of carrier removal rate of 1.3 carriers/cm-neutron. The carrier removal rate of 1.3 is considerably lower than values found for bulk material.

Figure 6.3 shows the bicrystal  $I$ - $V$  characteristics for various irradiation levels and Figure 6.4 shows the zero bias resistance with increasing integrated

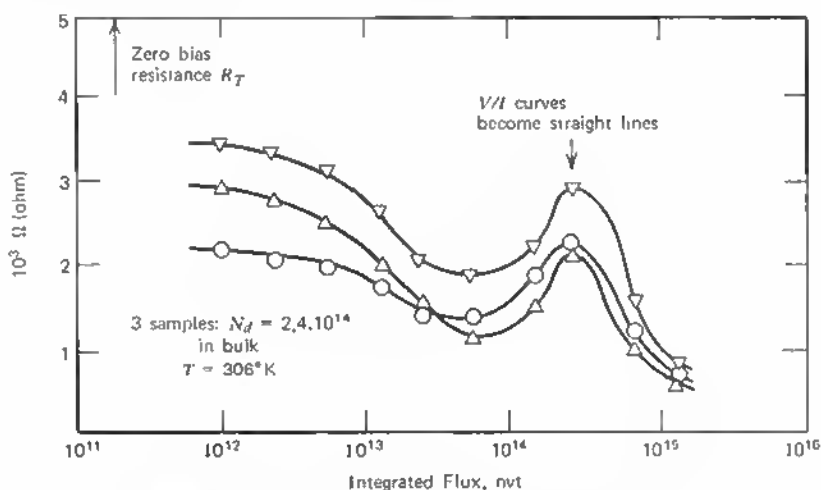


Fig. 6.4 Zero bias resistance of grain boundary photocells versus neutron flux, nvt.

neutron dose. The peak at  $3 \times 10^{14}$  nvt has been explained by Taulbee and Nunn as due to a conversion of the bulk sample from  $n$  to  $p$ . In comparing these changes with the changes in normal diffused or alloyed  $p$ - $n$  structures, destructive irradiation levels are similar. A germanium diode increases in leakage current for a factor of 3 at a dose rate of  $10^{13}$  to  $10^{14}$  neutrons/cm<sup>2</sup>. A germanium transistor input resistance (open collector or short-circuit collector) shows a similar degradation.

Even materials like gallium arsenide do not essentially improve classical  $p$ - $n$  junction device resistance to radiation for normal configurations. There is, however, a marked improvement with regard to radiation resistance if the material's properties are combined with the device's geometry and properties. A grain boundary itself is definitely hard material, and a device using the degenerate conduction mechanism of the boundary should be relatively hard. Such a device is the grain-boundary field effect transistor described in the literature.<sup>10, 11</sup> (see Chapter 13, Section 3)

In considering the grain-boundary structure in detail (see Figure 6.5), the overlapping dilation and compression regions  $D$ ,  $C$  form a *hardened* structure

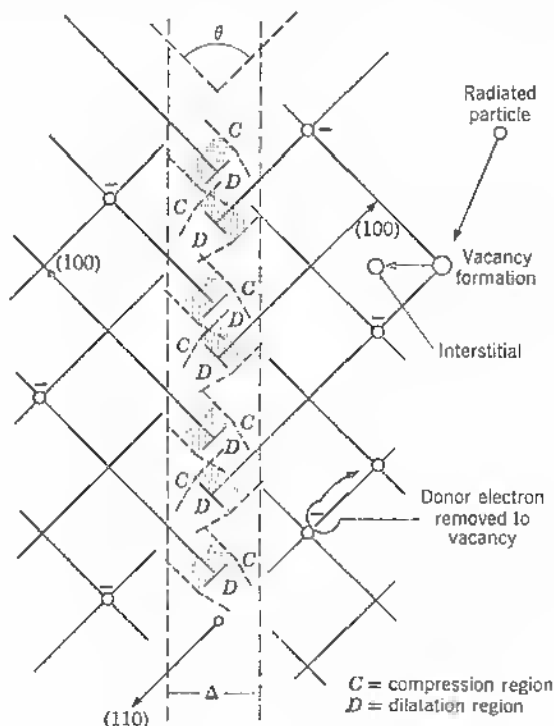


Fig. 6.5 Grain boundary structure as hard material.



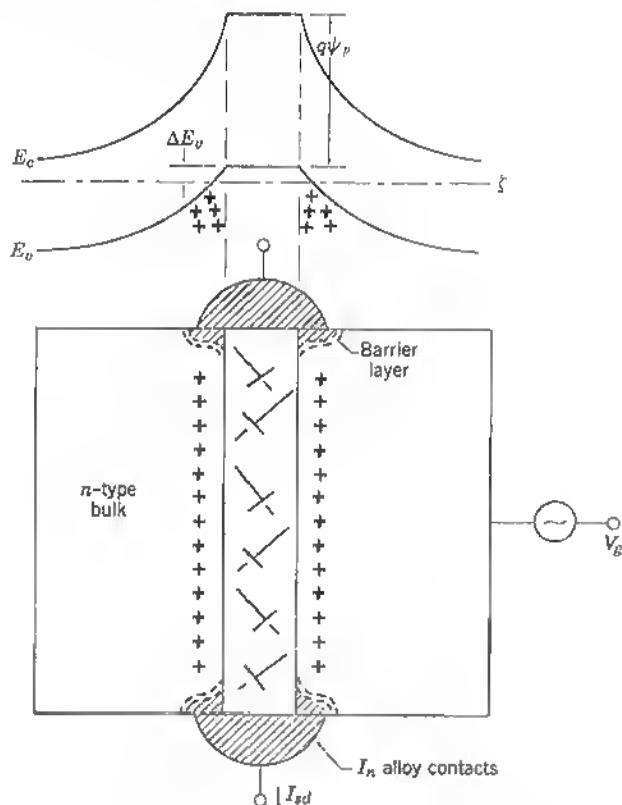


Fig. 6.6 Grain boundary field effect transistor and band scheme

because of an increase in local energy. Current flow along the inner  $p^+$ -type layer or sheet, where holes have accumulated, is totally degenerate, since the valence band overlaps the Fermi level. In the adjacent lattice there exists, therefore, a narrow conduction region of a hard character.

If the doping of the bulk crystal is low compared with the dangling-bond density (approximately  $10^{18} \text{ cm}^{-3}$ ), the barrier layer adjacent to either side of the grain-boundary sheet widens. For highly pure bulk lattices, the current is carried by an increasing portion of undisturbed material and, therefore, normal irradiation changes occur. If, however, the doping in the bulk lattice does approach  $10^{18} \text{ cm}^{-3}$ , this conduction sheet is close to the grain-boundary layer and shows a relatively high hardness.

Current flow in field-effect devices is different from that studied by Taulbee and Nunn, who measured only the barrier-layer resistances (zero bias and saturation) as well as photovoltages and all magnitudes of voltage versus current flow across the barrier layer. In a field-effect device, however, the

essential aspect is that the source-drain current  $I_{sd}$  (see Figure 6.6) flows along the sheet of  $p^+$ -type material, with current flow into the bulk material being blocked by the alloy zone recrystallized barrier layers—indium dots in the case of  $n$ -type germanium, for example. The bulk-crystal contact serves as input to the field or gate voltage  $V_g$  only and is essentially not current-conducting.

In this mode the barrier layer is not directly part of the current-flow structure but acts as a flow-control electrode. This function, however, is dependent on the barrier layer, which is subject to changes by irradiation. These changes are small for small barrier-layer width. Hence, the interest in highly doped bulk material, as in the case of tunnel devices.

In looking into the possible energy levels introduced by radiation defects into silicon and germanium crystals, a multitude of configurations appears possible, depending on the association of defects and chemical impurities. Measurements of ultraviolet absorption, spin resonance, photoconductivity, Hall voltages, and recombination velocity yield levels in all parts of the forbidden gap.

A scheme of the energy levels found in germanium with different radiation types is shown in Figure 6.7. The scheme for silicon in Figure 6.8 is plotted for

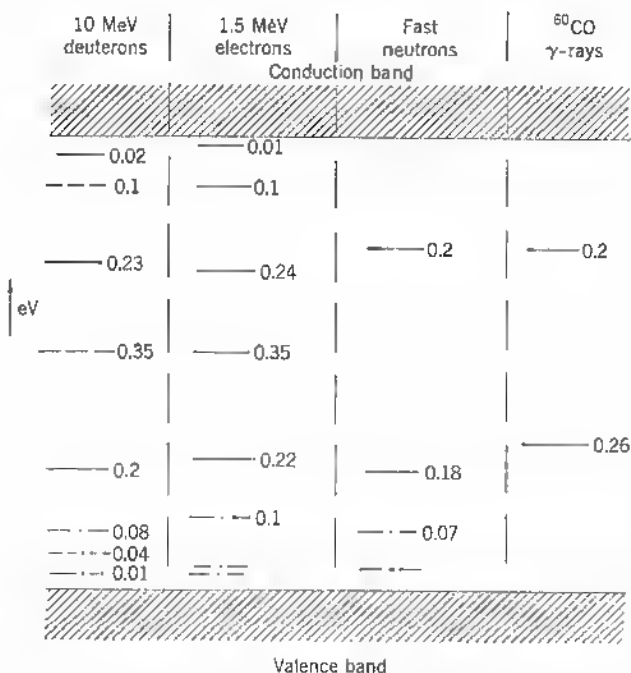


Fig. 6.7 Defect energy levels in germanium produced by different particles.

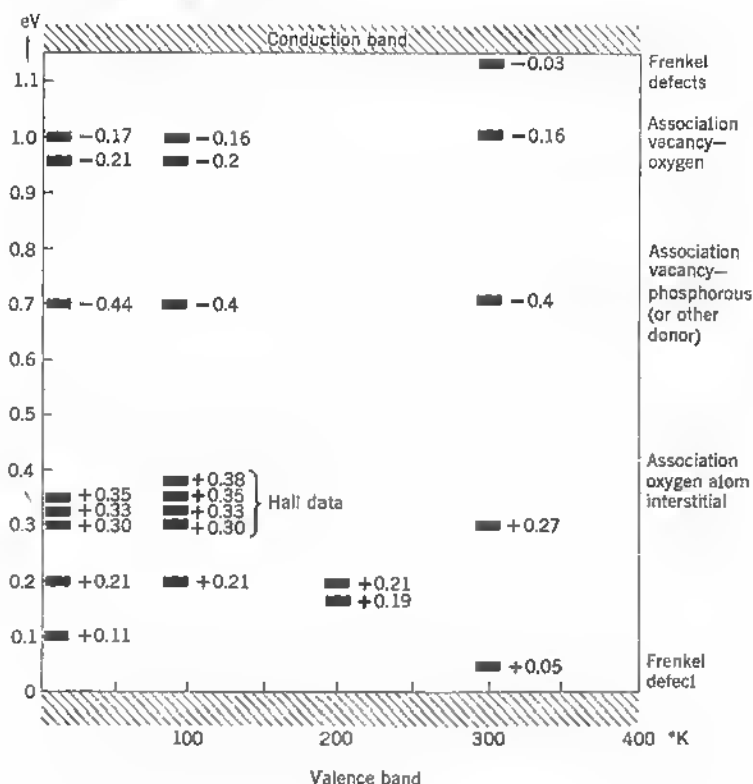


Fig. 6.8 Defect level scheme for silicon.

equal radiation (electrons) but at different temperatures. Some of the possible defect associations are indicated.

An important factor for the evaluation of irradiated monocrystals is the change in photoconductivity. It is well known that irradiated crystals show an extension of their frequency response as well as additional energy levels.

In Figure 6.9 we see, for example, the photoresponse of a germanium monocrystal, *n*-type, before and after irradiation with an integral dose of  $2.2 \times 10^{15}$  electrons  $\text{cm}^{-2}$  (1 MeV; temperature is 100°K).

Such displacement of response curves toward longer optical wavelengths (lower eV numbers) is well known. Irradiation-induced defects and mechanically induced defects give similar electronic effects.<sup>12</sup>

Grown-in dislocation arrays also induce photosensitivity extensions in both the long- and short-wavelength regions.<sup>13, 14</sup> Plastically bent monocrystals show photoconductance curves of a similar nature with a cutoff at 0.45 eV.<sup>15</sup>

Photoconductivity has become a major tool for the measurement of the

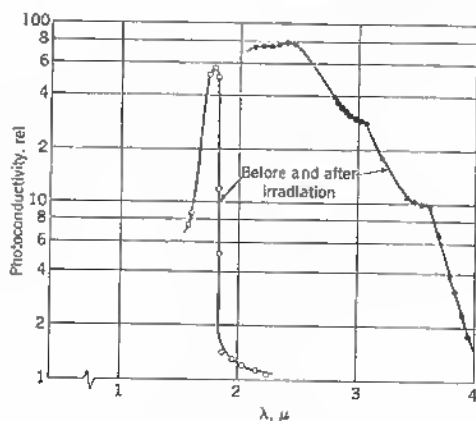


Fig. 6.9 Photoconductivity before and after irradiation.

energy-level scheme in irradiated semiconductor crystals. A wealth of data on material subjected to different radiation types is available. The type of energy levels is dependent on many factors: (a) the initial state of doping, compensation, dislocation density, and the like; (b) the temperature range during irradiation; (c) the annealing and its influence on the final level scheme—defect “ripening” stage, donor annealing stage, and the like.

In general, the result of fast electron and fast neutron irradiation seems to be similar. An energy-level scheme measured in the first case is shown in Figure 6.10.<sup>15</sup>

The Fermi level is at  $\zeta = E_v + 0.27$  eV in this case. Figure 6.11 gives the result for germanium irradiated with fast neutrons (77°K).<sup>16</sup> It is obvious that a rather complicated and often unpredictable behavior results if interactions of impurities and dislocations are taken into account.

Another method of studying the energy-level scheme is by way of recombination radiation. Here also the introduction either of dislocations or of radiation defects is responsible for a frequency shift.

The field of radiation effects in semiconductors has found great attention in the past because of its obvious importance.

Displacement effects in particles, because of neutron injection (lasting defects) have been studied in connection with military projects on electronic materials and devices subjected to nuclear radiation. All fission products as neutrons, protons, electrons, and gamma rays, can have lasting effects, depending on their energy, the important area being the energy range between 0.1 and 10 MeV for neutrons.

The transient effects are also important for electronic devices. Most of the damaging particle injection has its greatest impact at the time of incidence,

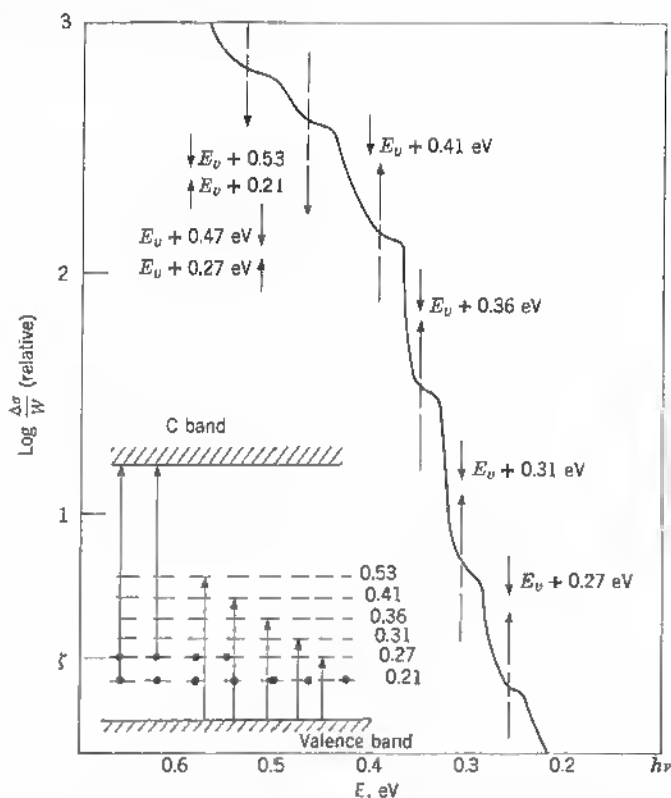


Fig. 6.10 Photoconductivity spectrum and electron transition diagram for germanium irradiated by fast electrons.

since even under room-temperature conditions a gradual annealing of defects sets in. This is enhanced by thermal heating, a method proposed and used for certain Silicon-devices for equipment subject to radiation. Severe irradiation, especially by x-rays, causes a high density of electrically charged particles at the surface of the devices which may shunt electronic functions for a short time. In this case external shielding is the only protection. Most of the intensive work on radiation effects has been performed in the area of radiation-induced materials and device changes. The forms and influence of point defects, especially, have been investigated. Vacancies, interstitials, vacancy-interstitial pairs, and impurity-vacancy-configurations have been invoked to explain the multiplicity of effects measured. As emphasized in recent gatherings of specialists in this field, the questions of impurity and defect interactions, particularly between originally present defects and those introduced by nuclear

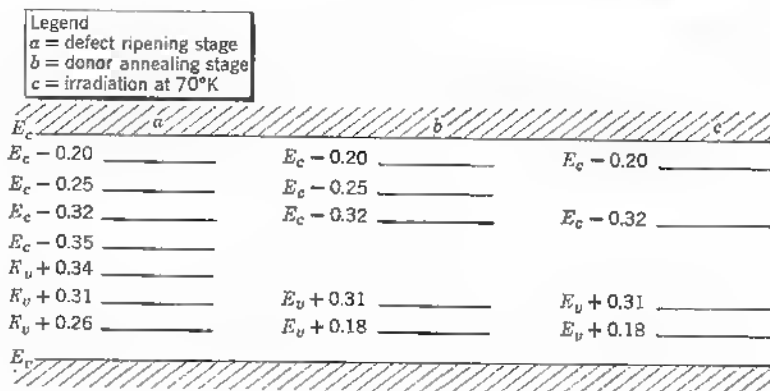


Fig. 6.11 Photoconductivity-energy level spectrum in germanium irradiated by fast neutrons.

irradiation, have not been answered sufficiently. Recovery and diffusion as interrelated processes are not fully understood and the localized state as criterion for the presence of defects can be interpreted in many ways, to mention only divacancies.<sup>17</sup>

The same state of affairs is true for ion implantation. As is well known, the defects imparted by energetic ions in channeling processes have to be removed by heat treatment. Or, since the ion-doped front ( $p$ - $n$  interface) is being moved further into the crystal by diffusion, the damaged area is left behind within the doped layer and a clean junction is built-up. Damage associated with ion implantation has been clearly demonstrated.<sup>18</sup> The amount of work published in this area can be judged from recent conference proceedings.<sup>19</sup> But much more information can be found if the many classified reports on government projects are made accessible. There are numerous reports available on different semiconductor materials and devices with as yet uncorrelated results. The space agencies added more contracts in the area of defects due to gamma-rays, neutron, proton, and electron-impact in radiation environment. Especially the Van Allen Belts (electron and proton damage) were considered here.

The tremendous amount of material available in the device area concerning radiation damage, has been reviewed to some extent to make studies manageable and results somewhat predictable,<sup>20</sup> but clear correlation between cause and effect is still missing. There are unrelated groups looking into the engineering-type of effects in devices and on the other hand there are physicists studying the radiation effects in solids in a more general sense. The material available on crystals and devices in radiation environment presents, as we have mentioned, an unmanageable amount of information due to the fact that in crystals a multiplicity of vacancy-defect-impurity associations are

possible for which unifying interpretations are lacking, a state of affairs which makes it difficult to correlate often seemingly similar experiments. In the case of Silicon, for example, any changes due to heat treatment before and after irradiation have to be analyzed with respect to the formation of thermal donors and acceptors and vacancy-impurity cluster formation and therefore no conclusions can be drawn without a test-sample undergoing the same treatment as the irradiated sample. But for Silicon and Germanium, a number of facts have been worked out which form a basis for prediction in relatively well defined cases.

In the context of this treatise, we emphasize the lasting defect with a major electronic influence namely the dislocation and have to limit our discussion of point defects. Energetic particles and ion beams will generate point defects along their pathway through the crystals, but also dislocations at the end of their trajectory where their energy is transferred to the crystal in form of a melting-spot or-spike.<sup>3</sup> This is then the area of greatest impact on the electronic properties of the material and for an understanding of the electrical behavior of such a defect zone we have again to understand the electronic features of dislocations.

## PROBLEMS

- 6-1. How is the expression for the sum of the Burgers vectors (5-1) altered for the nonsymmetric case if the tilt axis  $u$  is perpendicular to the dislocation.
- 6-2. What is the amount of energy in  $\text{erg cm}^{-1}$  for an edge dislocation in germanium of length 1 cm, assuming a core radius of  $r_0 = 10^{-7}$  cm (5-15).
- 6-3. Calculate the energy liberated at the end of the trajectory of energetic nitrogen atoms of 2 MeV energy into the silicon lattice (6-4). Is local melting of the crystal probable? (Compare G. H. Schwuttke et al. in F. L. Vook (ed.), "Radiation Effects in Semiconductors," Plenum Press, New York, 1968, p. 406ff.)
- 6-4. Assuming equal masses for both constituents in GaAs ( $\approx 70$ ), calculate the maximum imparted energy in the GaAs lattice by 2 MeV nitrogen atoms respectively the number of displaced atoms (see threshold energies in Table 6-3, and compare the result with Figure 6-2).

## REFERENCES

1. Klontz, E. F., and K. Lark-Horovitz: *Physical Review*, vol. 82, p. 763, 1951; *Physical Review*, vol. 86, p. 643, 1952.
2. Holmes, D. K.: Terms and Concepts in Radiation Damage Theory, *Radiation Damage in Solids*, Proceedings of the International School of Physics, "Enrico Fermi," XVIII Course, D. S. Billington (ed.), Academic, New York, 1962.
3. Brinkman, J. A.: On the Nature of Radiation Damage in Metals, *Jr. of Applied Physics*, vol. 25, p. 961, 1953.

4. Chadderton, L. T.: "Radiation Damage in Crystals," Methuen, London; Wiley, New York, 1965.
5. Vavilov, V. S.: Strahlungsdefekte in Halbleitern, *Physica Status Solidi*, vol. 11, p. 447, 1965.
6. Cahn, J. H.: Irradiation Damage in Germanium and Silicon due to Electrons and Gamma Rays, *Jr. of Applied Physics*, vol. 30, no. 8, pp. 1310-1316, August, 1959.
7. Bäuerlein, R.: Displacement Thresholds in Semiconductors, *Radiation Damage in Solids*, Proceedings of the International School of Physics, "Enrico Fermi," XVIII Course, D. S. Billington (ed.), Academic, New York, 1962. See also *Zschr. f. Phys.* vol. 176, pp. 498-509, 1963.
8. Welker, H.: Semiconducting Compounds, *Z. f. Naturforschung*, vol. 7a, p. 744, 1952.
9. Taulbee, C. D., and D. E. Nunn: A Neutron Irradiation Test of Germanium Bicrystals, *III/PTGNS Special Technical Conference on Nuclear Radiation Effects*, Seattle, Washington, July, 1964, Proceedings RLDP-64-23.
10. Weinreich, O., H. F. Mataré, and B. Reed: The Grain Boundary Amplifier, *Proceedings of the Physical Society*, vol. 73, pp. 696-972, June, 1959.
11. Mataré, H. F.: Low Temperature Field Effect Transistor Using Dislocation Planes, *Direct Current*, vol. 6, no. 5, pp. 2-8, August, 1961.
12. Newman, R.: *Physical Review*, vol. 105, no. 6, p. 1715, Mar. 15, 1957.
13. Mataré, H. F., D. C. Cronmeyer, and M. W. Beaubien: Germanium Bicrystal Photoresponse, *Solid State Electronics*, vol. 7, pp. 583-588, 1964.
14. Mataré, H. F., and K. S. Cho: Field Dependence of Photoresponse in Germanium Bicrystals, *Jr. of Applied Physics*, vol. 36, no. 11, pp. 3427-3431, November, 1965.
15. Golacki, Z., et al.: Extrinsic Photoconductivity in Plastically Bent Germanium, *Physica Status Solidi*, vol. 11, p. K35, 1965.  
Gerasimov, A. B., et al.: Impurity Photoconductivity in Germanium Irradiated by Fast Electrons, *Soviet Physics Solid State*, vol. 6, p. 3, September, 1964.
16. Novikov, S. R., et al.: Photoconductivity of Germanium Irradiated by Fast Neutrons at 77°K, *Soviet Physics Solid State*, vol. 6, p. 5, November, 1964.
17. Callaway, J., and A. J. Hughes: Localized States Associated with the Divacancy in Silicon, in "Radiation Effects in Semiconductors," F. L. Vook (ed.), Plenum, New York, 1968, p. 27.
18. Schwuttke, G. H., K. Brack, and E. E. Gardner: High Energy Nitrogen Doping of Single Crystal Silicon, in "Radiation Effects in Semiconductors," F. L. Vook (ed.), Plenum, New York, 1968, p. 406.
19. "Radiation Effects in Semiconductors," F. L. Vook (ed.), Plenum, New York, 1968.
20. Larin, F.: "Radiation Effects in Semiconductor Devices," New York, 1968.



## Chapter 7 Main Mechanical Properties of Dislocation Planes

### 7.1 STRESS FIELD AND STRAIN ENERGY

The Burgers vector of a dislocation is defined by not only the degree of imperfection present but also by the particular lattice type.

A dislocation can be *perfect* or *imperfect*. It is perfect if the Burgers vector produces identity translations and imperfect if the Burgers vector describes a new configuration. The Burgers vector also gives a measure of the energy of a dislocation. In a cubic lattice, for example, a Burgers vector representing the  $[100]$  lattice translation vector is the lowest energy displacement. Obviously, composite vectorial displacements or dissociations are possible:

$$\begin{aligned}a[110] &\rightarrow a[100] + a[010], \\a[111] &\rightarrow a[100] + a[010] + a[001].\end{aligned}$$

In these (see Figure 7.1) no lowering of the energy results. There are dissociations accompanied by a lowering of the displacement energy:

$$\begin{aligned}a[110] + a[1\bar{1}0] &\rightarrow a[100] + a[100] \\&\rightarrow 2a[100].\end{aligned}$$

In considering the difference between the edge and the screw dislocation in more detail, we see that an edge dislocation is defined by a slip vector  $\mathbf{s}$  perpendicular to the Burgers vector and in a screw dislocation, Burgers and slip vectors are parallel (see Figure 7.2). There is deformation and stress in both cases. However, the screw dislocation does not show the compressional and dilational lattice arrangement that forms around the extra half plane in an edge dislocation. In evaluating the shear stress in both cases, we have to define a coordinate system with the center point at the center of a Burgers

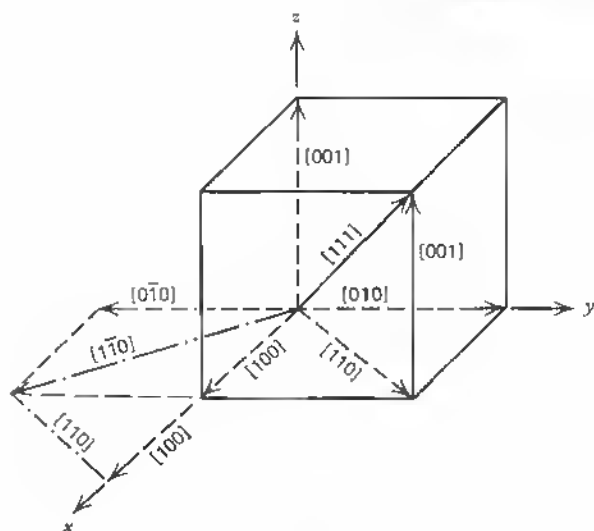


Fig. 7.1 Vectorial dissociation in cubic lattice.

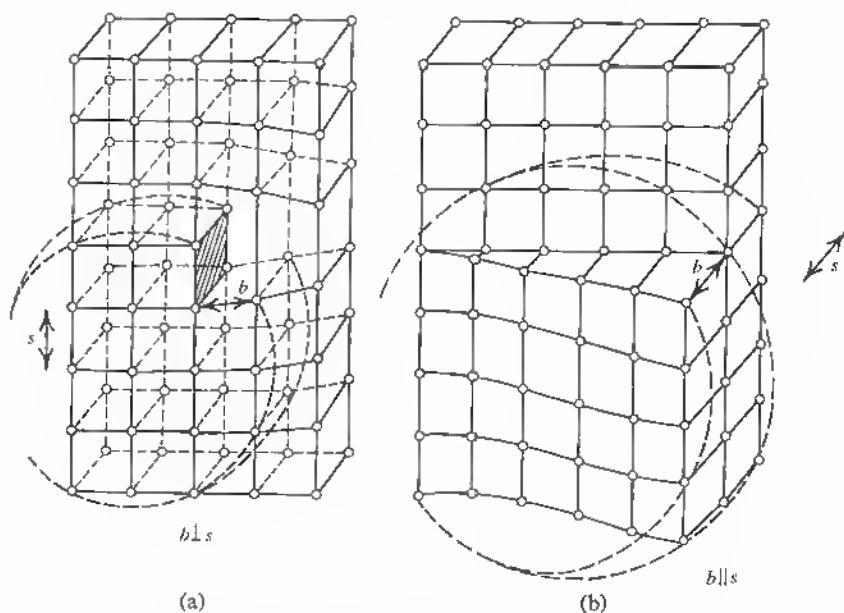


Fig. 7.2 Difference between edge and screw dislocations.  
 (a) Burgers vector  $\perp$  slip vector.  
 (b) Burgers vector  $\parallel$  slip vector.

circle. Figure 7.3 shows the two typical cases: Burgers vector perpendicular to the slip vector (edge dislocation) and parallel to the slip vector (screw dislocation). Here a sheet (ring) of material is cast out around the dislocation so that the displacement vector is a function of the displacements in the coordinate system. In elasticity theory the shear stress  $\sigma_{xy}$  acts in the  $y$  direction on planes perpendicular to the  $x$  axis and  $\sigma_{yx}$  acts in the direction of the  $x$  axis on planes perpendicular to the  $y$  axis. In plane-deformation theory  $\sigma_{xy} = \sigma_{yx}$ . If Hooke's law is assumed (small deformations or linear relation between stress and strain tensor), the normal stresses along  $x$  and  $y$  are  $\sigma_{xx}$  and  $\sigma_{yy}$ , and  $\sigma_{yz} = \sigma_{zy} = 0$ .  $\sigma_{xx}$  and  $\sigma_{yy}$  can be positive (dilation or

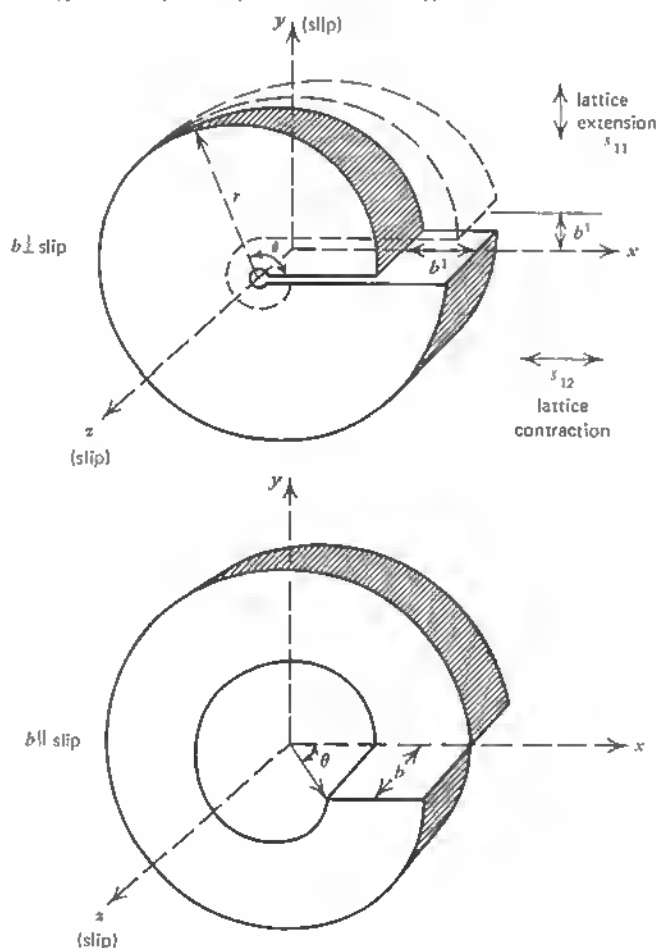


Fig. 7.3 Coordinate systems for edge and screw dislocation.

tension) or negative (compression). The strain tensor in general form has six components:

$$\begin{aligned} S_1 &= s_{11}\sigma_{xx} + s_{12}\sigma_{yy} + s_{13}\sigma_{zz} + s_{14}\sigma_{xy} + s_{15}\sigma_{yz} + s_{16}\sigma_{zx}, \\ S_2 &= s_{21}\sigma_{xx} + s_{22}\sigma_{yy} + s_{23}\sigma_{zz} + s_{24}\sigma_{xy} + s_{25}\sigma_{yz} + s_{26}\sigma_{zx}, \\ S_3 &= \text{etc.}, \end{aligned} \quad (7.1)$$

where the  $s_{ij}$  terms form the elastance tensor.<sup>2</sup>

In the case of plane-deformation theory (see Chapter 4) we stated that only the first three members of (7.1) are considered. The stress in one direction— $\sigma_{zz}$ , for example—is then related to the orthogonal stresses ( $\sigma_{yy}$ ,  $\sigma_{xx}$ ) by Poisson's ratio  $\nu$ .

For a cut along the slip plane,  $\theta = 0$ , a Burgers cycle determines the total strain:

$$2\pi r\sigma_r(s_{11} + s_{12}) = b\mu s_{11}, \quad (7.2)$$

where the elastance coefficients  $s_{11}$  and  $s_{12}$  represent the relative elongation and contraction of the lattice in two perpendicular directions and  $\mu$  is the shear modulus. It follows that

$$\sigma_r = \frac{b}{2\pi r} \mu \frac{s_{11}}{s_{11} + s_{12}}. \quad (7.3)$$

In this case the ratio  $-s_{12}/s_{11}$  represents Poisson's ratio  $\nu$ , which is 0.25 for most materials and 0.4 for germanium in particular<sup>3</sup>. Thus, the radial stress is

$$\sigma_r = \frac{b}{2\pi r} \left( \frac{\mu}{1 - \nu} \right) = \frac{D_e}{r} \quad (7.4)$$

for the edge dislocation.

Because of the parallelism of Burgers vector and slip vector, the basic stress function for the screw dislocation is

$$\sigma_z = \frac{b}{2\pi r} \mu = \frac{D_s}{r}. \quad (7.5)$$

We see that the basic stress  $D_e$  for the edge dislocation is  $1/(1 - \nu)$  times larger than for the screw dislocation and depends largely on the material. Since in semiconductors  $\nu$  is larger than for metals, there is a greater energy difference between edge and screw dislocations in semiconductor crystals. In polar coordinates  $r$ ,  $\theta$ ,  $z$ , defined by

$$x = r \cos \theta, \quad y = r \sin \theta, \quad z = z, \quad (7.6)$$

the stresses to be determined for the edge dislocation are

$$\sigma_{rr} = \sigma_{\theta\theta} = -D_e \frac{\sin \theta}{r}, \quad (7.7)$$

$$\sigma_{r\theta} = \sigma_{\theta r} = D_e \frac{\cos \theta}{r},$$

where  $\sigma_{rr} = \sigma_{\theta\theta}$  = normal stresses along radial and circumferential directions,  
 $\sigma_{r\theta} = \sigma_{\theta r}$  = shear stress.

Using now the expression for the strain energy

$$E = \frac{1}{2} \sum \text{forces} \times \text{displacement}, \quad (7.8)$$

we can derive the strain energy expression for both kinds of dislocations:

1. Edge dislocation:

$$E_e = \frac{1}{2} \int_{r_0}^{r_1} \sigma_{r\theta} b \, dr \quad (7.9)$$

$$E_e = \frac{1}{2} \int_{r_0}^{r_1} \frac{D_e b}{r} \, dr$$

( $\cos \theta = 1$  for a cut along the slip plane)

$$E_e = \frac{\mu b^2}{4\pi(1-\nu)} \log\left(\frac{r_1}{r_0}\right). \quad (7.10)$$

2. Screw dislocation:

$$E_s = \frac{1}{2} \int_{r_0}^{r_1} \sigma_z b \, dr = \frac{\mu b^2}{4\pi} \log\left(\frac{r_1}{r_0}\right). \quad (7.11)$$

Evaluation of these energy expressions has to be carried out with care, since  $E_s$  would lead to extremely high values for  $r_1 \gg r_0$ . In a realistic case, we may take the values

$$r_1 = 1 \text{ cm},$$

$$r_0 = 10 \text{ \AA} = 10^{-7} \text{ cm}.$$

$r_0$  defines the inner core of the disturbed region. With  $\mu = 10^{12}$  dyne  $\text{cm}^{-2}$  and  $b = 5 \cdot 10^{-8}$  cm and  $\nu = 0.4$  (Ge), the strain energy is

$$E_e = \frac{10^{12} \cdot 5^2 \cdot 10^{-16}}{4\pi(1-0.4)} \log(10^7) \\ \simeq 5 \cdot 10^{-3} \text{ erg cm}^{-1}.$$

Considering now the superposition of these dislocations in a grain-boundary plane, as we did in Section 4.1, we must now form the sum of the individual stress components. In the  $xy$  plane this is

$$S = \sum_{n=-\infty}^{+\infty} \sigma_{xy}(x, nD), \quad (7.12)$$

where  $n$  stands for the number of dislocations and  $D$  is their spacing. For a symmetric grain boundary ( $\phi = 90^\circ$ ), we have

$$2D = \frac{b}{\sin \theta/2} \quad (7.13)$$

(see Figure 7.4).

The grain-boundary energy follows from the integration of (7.11) over the crystal volume  $\lambda$  under consideration of (7.8):

$$E_{\perp}(D) = \frac{b}{2} \int_0^{\lambda} S \, dx \quad (7.14)$$

$$= \frac{b}{2} \int_0^{\lambda} \sum_n \sigma_{xy}(x, nD) \, dx \quad (7.15)$$

where  $n$  = number of dislocations.

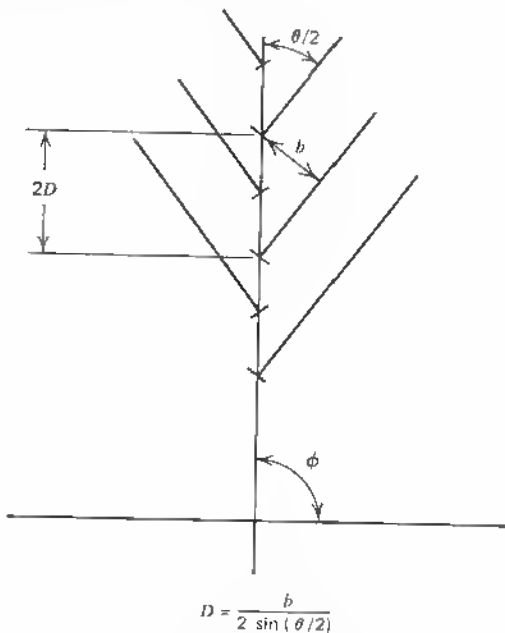


Fig. 7.4 Distance between dangling bonds in grain boundary.

Or in the cylindrical case for polar coordinates

$$E_{\perp}(D) = \frac{b}{2} \int_{r_0}^r \sum_n \sigma_{r\theta}(r, nD) dr. \quad (7.16)$$

$E_{\perp}(D)$  times the density of dislocations is the grain-boundary energy per unit area:

$$E = \frac{E_{\perp}}{D} \simeq E_{\perp} \frac{\theta}{b}. \quad (7.17)$$

Thus

$$E = \frac{\theta}{2} \int_{r_0}^r \sum_n \sigma_{r\theta}(r, nD) dr. \quad (7.18)$$

Using (7.5) for the edge dislocation, we get

$$E = \frac{\theta}{2} \frac{b}{2\pi} \mu \frac{1}{(1-\nu)} \int_{r_0}^r \frac{dr}{r}. \quad (7.19)$$

Since  $dr/r = -d\theta/\theta$ , we have again

$$E = \frac{\mu b}{4\pi(1-\nu)} \theta [A - \log \theta]. \quad (7.20)$$

Generally a zero energy amount

$$E_0 = \frac{b\sigma_0}{2} = \frac{\mu b}{4\pi(1-\nu)} \quad (7.21)$$

is introduced here.

This form is equivalent to (7.10), since it is expressed as per-unit area. Assuming overlap of the compression regions in boundaries with a tilt angle  $\theta > 5^\circ$  (medium-angle tilt boundary), the resulting unit compression or pressure ratio is

$$\frac{\delta P}{P} \simeq \frac{\nu}{b} \frac{\text{relative surface energy } [E'_{\perp} \text{ in dyn/cm}]}{\mu [\text{dyn/cm}^2]}, \quad (7.22)$$

where  $b$  = Burgers vector,

$\mu$  = shear modulus,

$\nu$  = Poisson's constant.

Since the relative surface energy corresponds to the grain-boundary energy,  $E_{\perp}$ , calculated from (7.10) divided by the width of the grain boundary, gives for a width  $W$  of 100 Å

$$\begin{aligned} E'_{\perp} &= E_{\perp} \cdot 100 \cdot 10^{-8} \\ &= 5 \cdot 10^3 \text{ dyn/cm}, \end{aligned} \quad (7.23)$$

and therefore

$$\frac{\delta P}{P} = \nu \frac{5 \cdot 10^3 [\text{erg/cm}^2] \cdot (\frac{1}{3} \cdot 10^8) [\text{cm}^{-1}]}{1.3 \cdot 10^{12} [\text{dyn/cm}^2]} \\ \simeq 3 \cdot 10^{-2}.$$

With the known pressure-band gap coefficient for germanium of  $\Delta E_g [\text{eV}] = -5(dP/P)$ , corresponding to a gap widening, we get

$$\Delta E_g = 0.15 \text{ eV},$$

a relatively strong change of the forbidden gap. We see that the influence of the dislocation on the electronic performance of the crystal is not only due to the free bond and other direct electrical changes in the neighborhood of the defect but also to such influences as lattice strain and thus local band changes. In addition, the changes in lattice spacing  $\partial d_{x,y,z}$  introduce deformation potentials, as discussed in Section 2.6, due to the variation of the crystal momentum

$$\Delta P = \hbar \Delta k.$$

With the momentum expression for the moving electron, in one coordinate direction,

$$P_x = m_x \cdot v_x \quad (7.24)$$

the energy change is

$$\partial E_x = P_x \frac{\delta P_x}{m_x} \quad (7.25)$$

$$\partial E_x = \left(\frac{\hbar}{\lambda}\right)^2 \frac{d_x}{m_{\text{eff}}} \frac{\delta d_x}{d_x}. \quad (7.26)$$

See Chapter 2 (2.144).

The full range of the influence of the dislocation on the electronic carrier transport is discussed in Chapter 8.

## 7.2 GRAIN BOUNDARY ENERGY AND STABILITY

A linear dislocation, such as a line of edge, or screw dislocations due to tilt or twist between adjacent crystal facets shows a coherency even for a very minute misfit. It is well known that for pure tilt boundaries the dislocation spacing, as discussed earlier (see Figure 7.4), can be measured at the surface of suitably etched crystals and corresponds to the values given by

$$D = \frac{b}{2 \sin(\theta/2)}$$



down into the range of arc seconds for  $\theta$ . This means that even for such large distances  $D$  as a few microns, forces of lateral dilational-compressional overlap cause the structure to be coherent. It is well known, however, that very low misfit angles of twist or tilt do not give a line structure in general but tend to deviate in the face of other crystallographic disturbances. It is a fact that larger-angle dislocations are more stable and that, at the intersection of two dislocation lines, the dislocation with the larger misfit continues its path but the lower-angle dislocation is stopped or deviated. Very low-angle disturbances of the *lineage* type are also unstable with respect to climb and can be absorbed in the stress field of a large-angle boundary by this process. Typical cases are shown in Figures 7.5 and 7.6 for germanium. In Figure 7.5 a lineage boundary ( $\theta \approx 33$  arc sec) is absorbed by a medium-angle grain boundary artificially grown with a double seed ( $\theta = 20^\circ$ ).<sup>5</sup> The latter boundary runs across the picture from left to right in a straight line dividing the bicrystal into the two halves according to the original two seeds of  $[100]$  orientation. Small-angle lineage boundaries generally pile up in the immediate neighborhood of such a large-angle grain boundary where the stress field is high (see Figure 7.6). That the growth of rather perfect bicrystals is possible follows from the particular force field around a dislocation.

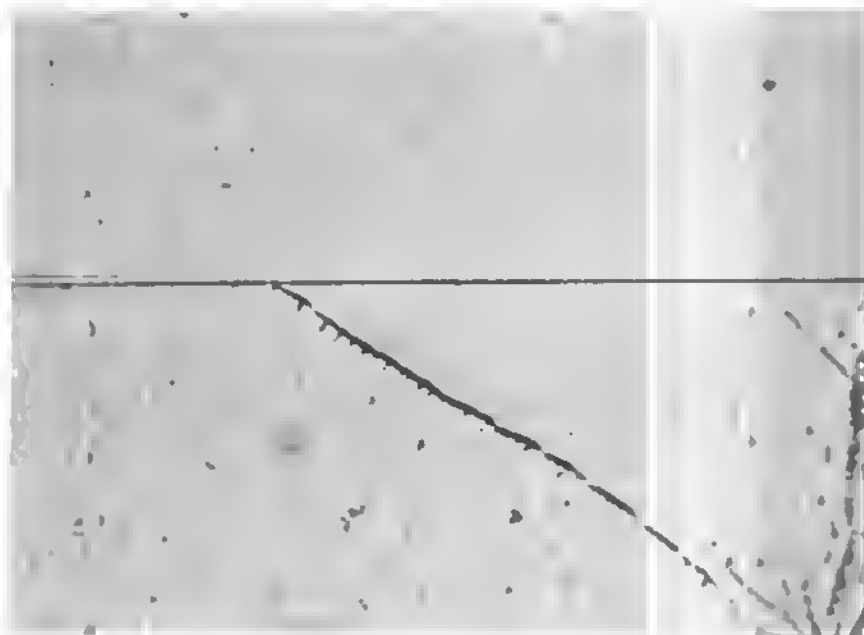


Fig. 7.5 Low angle grain boundary (lineage) of  $\theta = 33$  arc seconds terminating on  $[100] - \theta_1 - \{100\}$  grain boundary (horizontal). ( $\theta_1 = 20^\circ$ )



Fig. 7.6 Bicrystal (germanium) and lineage boundaries discontinued in high energy field of 20°-tilt grain boundary. Individual tilts are

No.	$\theta_1$ (arc sec.)	No.	$\theta_1$ (arc sec.)	No.	$\theta_1$ (arc sec.)	No.	$\theta_1$ (arc sec.)
1	42	4	48	7	63	10	67
2	47	5	87	8	80	11	68
3	48	6	136	9	75	12	117

To evaluate the forces between individual dislocations and the interaction between fixed dislocations (grain boundaries) and mobile dislocations, one needs the interaction energy  $E_i$  or the work performed in creating the second dislocation in the stress field of the first one.  $E_i$  can be derived by integrating over the shear stress times the displacement vector  $b$  in the slip plane  $S$  of the second dislocation within the stress field of the first dislocation:

$$E_i = \int_S \sigma_{xy} b \cdot dS. \quad (7.27)$$

Since the component of the force along the slip plane is of primary interest, we have to evaluate

$$F_x = - \frac{\partial E_i}{\partial x} = b \cdot \sigma_{xy}. \quad (7.28)$$

The component of the force, perpendicular to the slip plane, is

$$F_y = b \cdot \sigma_{xx}. \quad (7.29)$$

A. H. Cottrell<sup>1</sup> and S. Amelinckx and W. Dekeyser<sup>4</sup> have analyzed these forces, starting with the classical expressions for the stress field of a single edge dislocation oriented along the  $z$  axis. In this case

$$\begin{aligned} F_x &= b\sigma_{xy} = \frac{b\sigma_r x(x^2 - y^2)}{x^2 + y^2}, \\ F_y &= b\sigma_{xx} = \frac{b(-\sigma_r)y(3x^2 + y^2)}{x^2 + y^2}. \end{aligned} \quad (7.30)$$

In polar coordinates one has

$$\begin{aligned} F_r &= \sigma_r \cdot b \cdot \frac{1}{r}, \\ F_\theta &= \sigma_r \cdot b \cdot \frac{\sin 2\theta}{r}. \end{aligned} \quad (7.31)$$

The force field in cartesian coordinates (7.30) can be plotted as a function of  $x/y_0$ , for example, with  $y_0$  the coordinate for the slip plane of the mobile dislocation (see Figure 7.7). From (7.30) it is seen immediately that two dislocations of opposite sign attract each other along the slip planes when  $x > y$  and repel each other when  $x < y$ . At  $x = y$  there is a stable equilibrium. Conversely, two dislocations of the same sign have a mirror attraction-repulsion curve (see Figure 7.7a). In three dimensions this gives a cone of attraction for two dislocations of the same sign (shown in cross section in Figure 7.7b). If a wall of dislocations has been built up to a length  $L$ , one can

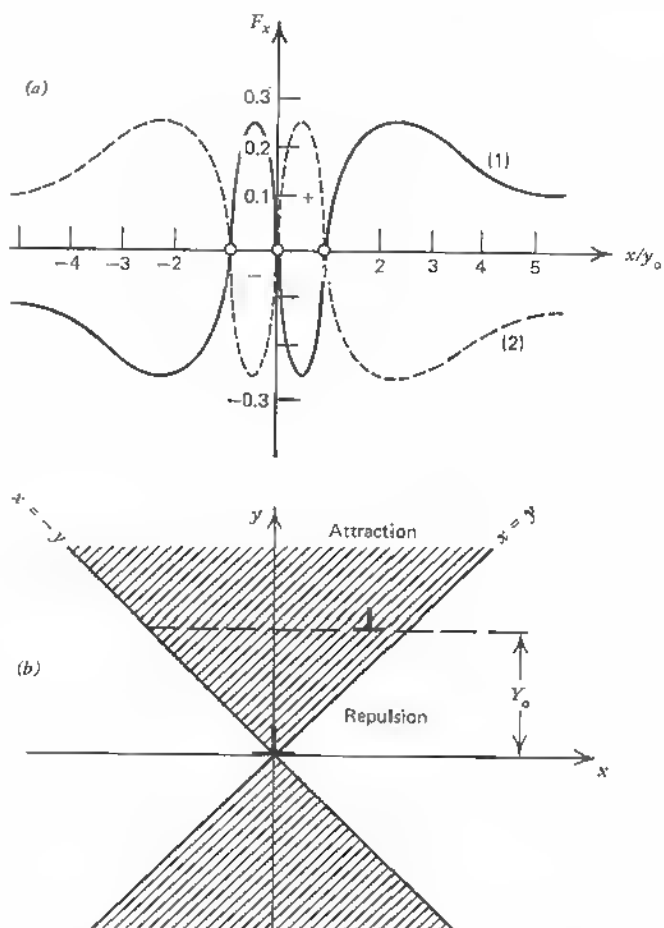


Fig. 7.7 (a) Force  $F_x$  in slip direction exerted by fixed dislocation at origin on mobile dislocation in slip plane  $y = y_0$ : (1) same sign; (2) opposite sign. (b) Two dislocations of the same sign in parallel glide planes. The mobile dislocation in plane  $y = Y_0$  is attracted by the fixed one at the origin. (After Amelinckx and Dekeyser).

evaluate the force  $F_x$  exerted by the array on an edge dislocation in a slip plane  $y = y_0$ , for example, by summing up over all forces (7.28) or (7.30). Since the individual shear stress is

$$\sigma_{xy} = \frac{\sigma_r x(x^2 - y^2)}{(x^2 + y^2)^2}, \quad (7.32)$$

we get

$$\sum_n \sigma_{xy} = \frac{\sigma_r}{D} \sum_n \frac{x[x^2 - (ny)^2]}{[x^2 + (ny)^2]^2}, \quad (7.33)$$

which can be replaced by an integration over the wall length from  $-L$  to  $+L$  (see Figure 7.8).

$$\sum_n \sigma_{xy} = \frac{\sigma_r}{D} \int_{-L}^{+L} \frac{x[x^2 - (y + \eta)^2]}{[x^2 + (y + \eta)^2]^2} d\eta \quad (7.34)$$

$$= \frac{\sigma_r}{D} \cdot \frac{2Lx(x^2 - y^2 + L^2)}{[x^2 + (y + L)^2][x^2 + (y - L)^2]}, \quad (7.35)$$

where  $D = \frac{b}{2 \sin \theta/2}$  (dislocation distance),

$$\sigma_r = \text{basic stress} = \frac{b}{2\pi r} \frac{\mu}{1 - \nu},$$

$b$  = Burgers vector.

Function (7.35) shows that the numerator defines the sign (denominator positive for  $y > L$ ) and that a hyperbolic separation exists between the attraction and repulsion regions with  $x = \pm y$  as asymptotes (denominator). It is, clear, therefore, that single dislocations are attracted toward the grain-boundary top whenever they fall into the crosshatched region in Figure 7.8 and are repulsed in the remainder of the room between hyperboloids of rotation. The growth of bicrystals of defined orientational misfit would not be possible if this ordering force for the growth of dislocation walls were too small to withstand the crystallographic ordering forces during buildup of the bicrystal at the solid-liquid interface. For the same reasons it is also impossible to anneal out dislocation arrays of misfit angles  $\theta$  greater than a few minutes of arc. If a grain-boundary plane approaches a free surface, an incomplete wall of dislocations forms and the lattice dilation can reach enormous values giving rise to microcracks. At this point the ordered array structure is broken up, and very high diffusion constants and abnormally high impurity penetration mark these areas (see Figure 7.9 and Chapter 12 Section 4).

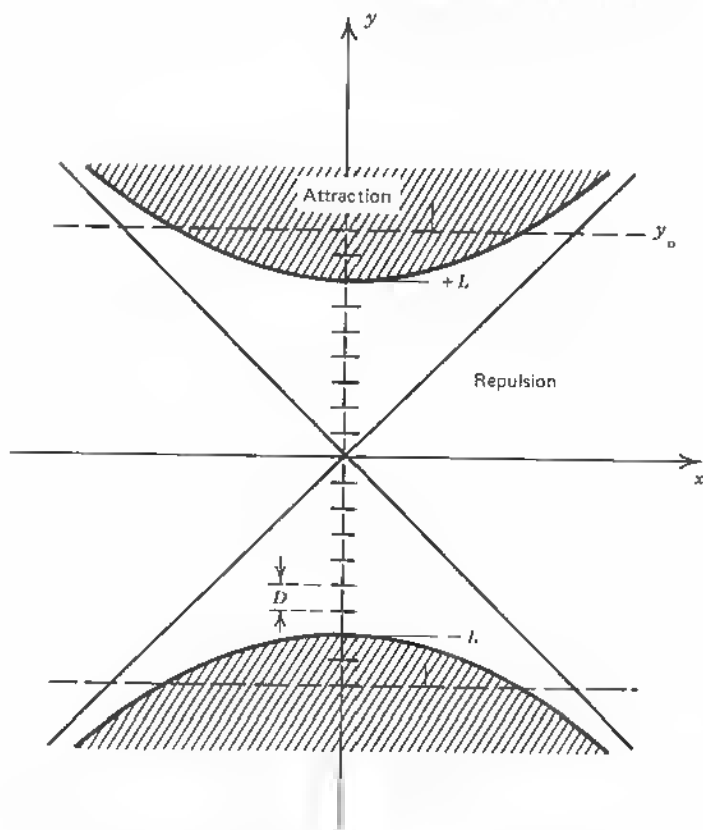


Fig. 7.8 A finite wall of edge dislocations of the same sign. Similar dislocations in parallel glide planes intersecting the hyperboloid are attracted in the crossed-hatched regions.

It is important to consider in this context the interaction of a wall of edge dislocations and a solute atom. As shown in Ref. 4, the force acting in the  $x$  direction on the impurity atom in the field of a dislocation (see Figure 7.8) is given as

$$F_x = F_0 \sin \frac{2\pi y}{D} \exp \frac{-2\pi x}{D}, \quad (7.36)$$

with

$$F_0 = \frac{4}{3} \frac{\pi^2 r^2 \mu b (1 + \nu) \Delta r}{D^2 (1 - \nu)},$$

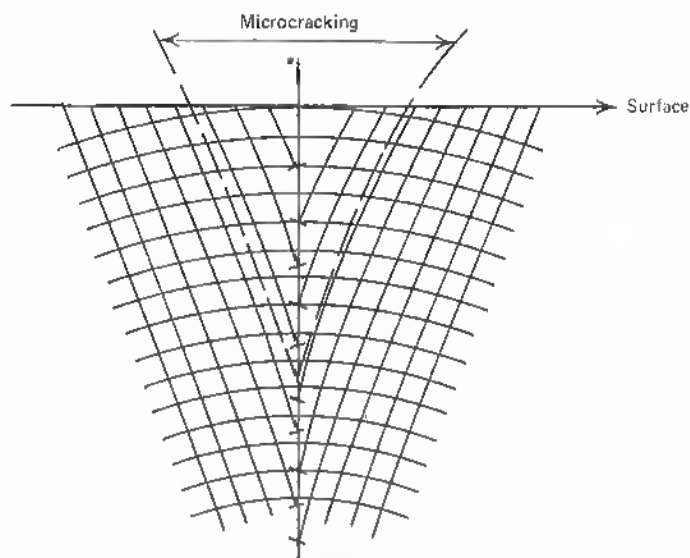


Fig. 7.9 Lattice widening (microcracking) near free surface due to grainboundary stress field.

where  $D$  = dislocation spacing ( $D \ll x$  is assumed),  
 $\Delta r$  = difference in radius between impurity and solvent atom,  
 $r$  = radius of solvent atom,  
 $\mu$  = shear modulus,  
 $b$  = Burgers vector,  
 $\nu$  = Poisson's ratio.

Equation (7.36) shows that this force falls off exponentially in the  $x$  direction when  $x \gg D$ . A similar equation applies to the  $y$  direction:

$$F_y = -F_0 \cos \frac{2\pi y}{D} \exp \frac{-2\pi x}{D}. \quad (7.37)$$

This shows that the magnitude of the force is to a first approximation independent of  $y$  (exponential term is predominant). The angle between the wall direction and the force direction is

$$\phi = \frac{2\pi y}{D}. \quad (7.38)$$

From this, the direction of motion of atoms near the boundary can be established. These flow lines move in and out of the dilation and compression regions, depending on the ratio  $\Delta r/r$ . If  $\Delta r/r > 0$  (radius of impurity atom larger than the one of the solvent atom), there is a net flow toward the

boundary in the dilation plane but a reverse flow in the compression plane. For wider spacing  $D$  of the dislocations (misfit angles  $\theta$  less than a few minutes of arc), the net flow toward the boundary in the dilation planes may be predominant. For medium-angle boundaries, however, the overlap of these zones is so complete that the flow pattern becomes a wavy line near the boundary, as shown in Figure 7.10. This is the case where either  $x$  is larger (flow lines distant from boundary) or  $D$  is small. Since in medium-angle grain boundaries  $D$  is of the order of a lattice constant of  $5 \cdot 10^{-8}$  cm, the case  $x/D \gg 1$  is predominant already at very small distances from the dislocation line or plane—say, at distances of the order of  $1/100 \mu$ .

It follows that during the growth of bicrystals with double seeds—from a doped melt, for example—a dopant enrichment in the boundary does not amount to measurable quantities as distinguished from surface diffusion. The specific problems with respect to diffusion of impurities and its dependence on the angle of misfit, is discussed in Chapter 12.

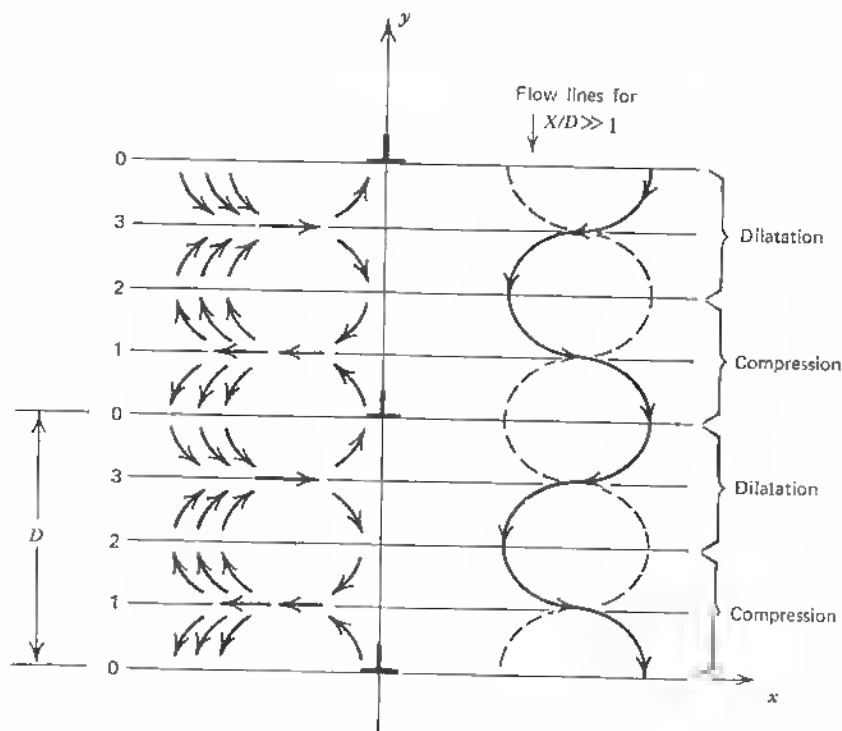


Fig. 7.10 Flow lines of solute atoms toward wall of edge dislocations. Oversized atoms with diffusion toward dislocation ( $\perp$ ) in dilatation region.



Details of the stress field around groups of dislocations (pile-ups of edge and screw dislocations) have been calculated by T. E. Mitchell<sup>6</sup> and show that these stress field patterns, although different in form, are basically of similar extent within the crystal.

### PROBLEMS

- 7-1. Determine the composite vectorial displacements in the cubic lattice case that are equivalent to

$$\begin{aligned} &2a[111]? \\ &a[010] + a[100]? \\ &a[001] + a[100] + a[\bar{1}\bar{1}0]? \end{aligned}$$

- 7-2. Discuss the main difference between an edge and a screw dislocation in terms of lattice strain. Show the consequence of the difference in slip vector with respect to the Burgers vector (see Figure 7.2).
- 7-3. Evaluate the difference in strain energy between the edge dislocation and the screw dislocation of a Burgers vector  $b$  of  $4.10^{-8}$  cm, elasticity modulus  $\mu = 5 \times 10^{-12}$  dyne/cm<sup>2</sup>, and Poisson's constant  $\nu = 0.35$ .
- 7-4. Explain the influence of microcracking at the surface interface of a dislocation plane with respect to the stress field of the grain boundary.
- 7-5. Analyze the form of the resultant shear stress of a dislocation wall (7.35) for the cases (a)  $L \ll X$ ;  $L \ll Y$ ;  $Y < X$ , (b)  $X = Y \gg L$ , (c)  $X \gg Y \gg L$ .
- 7-6. Discuss the impurity atmosphere around a dislocation wall for small and large dislocation spacing  $D$ . How does the dependence of  $\gamma$  (the plane direction) vary with  $X/D$  see (7.36) and (7.37)?

### REFERENCES

1. Cottrell, A. H.: "Dislocations and Plastic Flow in Crystals," Clarendon Press, Oxford, 1953.
2. Timoshenko, S., and J. N. Goodier: "Theory of Elasticity," McGraw-Hill, 1951.
3. Beam, W. R.: "Electronics of Solids," McGraw-Hill, New York, 1965, pp. 553ff.
4. Amelinckx, S., and W. Dekeyser: The Structure and Properties of Grain Boundaries, in "Solid State Physics," F. Seitz and D. Turnbull, (eds.), Academic, New York, 1959, p. 362.
5. Mataré, H. F., and H. A. R. Wegener: Oriented Growth and Definition of Medium Angle Semiconductor Bicrystals, *Zsch. f. Physik*, vol. 148, pp. 631-645, 1957.
6. Mitchell, T. E.: The Stress Fields around Groups of Dislocations in Face Centered Cubic Metals, *Phil. Mag.* Vol. 10, p. 301, 1964.

## Chapter 8 Basic Electrical Properties of Dislocations in Semiconductors

In treatments of the effect of lattice imperfections on the flow of electrons or heat (phonons), scattering deserves foremost attention. In the purely mechanical theory of Rayleigh scattering, one can describe a number of effects simply on account of the scattering of the phonon wave of wave vector  $k$ , for example, at a sphere of radius  $r$ . Within this sphere the relative change in density is assumed to be  $\delta D/D$ , and the relative change of the modulus of rigidity  $\delta G/G$ . The scattering cross section for a wave with wave vector  $k$  is then

$$Q(k) = \left(\frac{2}{3}r\right)^2 (kr)^4 \pi \left[ \left(\frac{\delta G}{G}\right)^2 + \frac{1}{3} \left(\frac{\delta D}{D}\right)^2 \right] \quad (8.1)$$

(see Ref. 1). Neutral scattering can be evaluated in more detail by taking into account the three possible modes of the polarization of phonons. Difficulties arise, because, for local changes, especially in three dimensions, the modulus of rigidity and its anisotropy have to be known. Obviously, more important are the electronic effects of imperfections. As we saw in Section 2.6, the deformation-potential description can account for the change in the electronic energy due to a lattice distortion  $\delta d_x$ . The resulting change in energy in one dimension is

$$\begin{aligned} \delta E_x &= \left(\frac{h}{\lambda}\right)^2 \frac{\delta d_x}{m_{\text{eff}}} \\ &= E_{\text{in}} \frac{\delta d_x}{d_x}, \end{aligned} \quad (8.2)$$

where  $E_{\text{in}}$ —constant for small changes—see (2.144).

In Chapter 7 we assessed the energy of the edge dislocation in terms of lattice strain and consequent band change. Values of  $\frac{1}{10}$  eV are typical for the edge dislocation line. The value for the screw dislocation line is lower,  $(1 - \nu)$  times, or about 60 percent of the value for the edge dislocation line. Polar scattering, as treated by Brooks-Herring and Conwell-Weisskopf (see Section 2.10), is a classical case of moving-charge deflection at charged centers. The restricting assumptions (only charge carriers are considered that pass the scattering center at a distance smaller than half of the average impurity spacing) are not strongly influencing the scattering cross section or the calculated mobility. This method is applied to randomized charged centers and not to a dislocation line or plane.

The effect of point imperfections, such as impurities, vacancies, and interstitials, on the electronic properties are mainly based on the resultant charge effects or the redistribution of the conduction electrons and not on lattice strain effects. This is well known from the study of imperfections in metals (see Ref. 2 and literature cited). The application of the Bloch wave function scattering process to screw and edge dislocations with a subsequent expression of the electron charge density variation (oscillation) shows that the charge redistribution accounts for 80 percent of the electric field gradient around dislocations in metals like copper<sup>2</sup>. In such treatments the dislocation is considered neutral but introducing a perturbing potential due to a displacement in the positive-ion background lattice. This causes a redistribution of the free-electron population, and the resulting potential can be considered self-consistent (Hartree). A first-order perturbation theory is carried out that precludes the formation of bound states on the dislocations. The self-consistent field potential is then given by an expression

$$V(\mathbf{r}) = V_0(\mathbf{r}) + V_F(\mathbf{r}) + \sum_n U_n(\mathbf{r}), \quad (8.3)$$

where  $V_0(\mathbf{r})$  = unperturbed periodic lattice potential,

$V_F(\mathbf{r})$  = free-electron contribution,

$U_n(\mathbf{r})$  = perturbing potential

(see Ref. 3). Because of the periodic form of the stress field around an edge dislocation

$$\left. \begin{matrix} \sigma_{rr} \\ \sigma_{r\theta} \end{matrix} \right\} = \frac{D_e}{r} \begin{Bmatrix} \sin \theta \\ \cos \theta \end{Bmatrix} f(\phi), \quad (8.4)$$

where  $f(\phi) = 1$  for the symmetric case  $\phi = 90^\circ$ ,  $D_e = (b/2\pi) \cdot [\mu/(1 - \nu)]$ ; for the screw dislocation  $D_e$  is replaced by  $D_s = (b/2\pi) \cdot \mu$  (Section 7.1),

the perturbation potential and thus the electric field gradient plotted versus the distance  $r$  in angstroms is oscillatory in character (see Ref. 2, Figure 2),

The model used for the Bloch wave scattering at a screw dislocation for example, is shown in Figure 8.1. The screw dislocation is considered a line defect, and the component of the incident wave vector parallel to the Burgers vector  $b$  is conserved in magnitude and direction. The asymptotic form of a wave function representing scattering from such a defect can be shown to be

$$\varphi_{ki}(\mathbf{r}) = \varphi_{ki}(\mathbf{r}) + \frac{f(\mathbf{k}_i, \mathbf{k}_s)}{r^{1/2}} \varphi_{ks}(\mathbf{r}), \quad (8.5)$$

where

$$|\mathbf{k}_i| = |\mathbf{k}_s|, \quad (8.6)$$

and  $f(\mathbf{k}_i, \mathbf{k}_s)$  = scattering amplitude,

$\mathbf{k}_i$  = incident wave vector,

$\mathbf{k}_s$  = scattered wave vector.

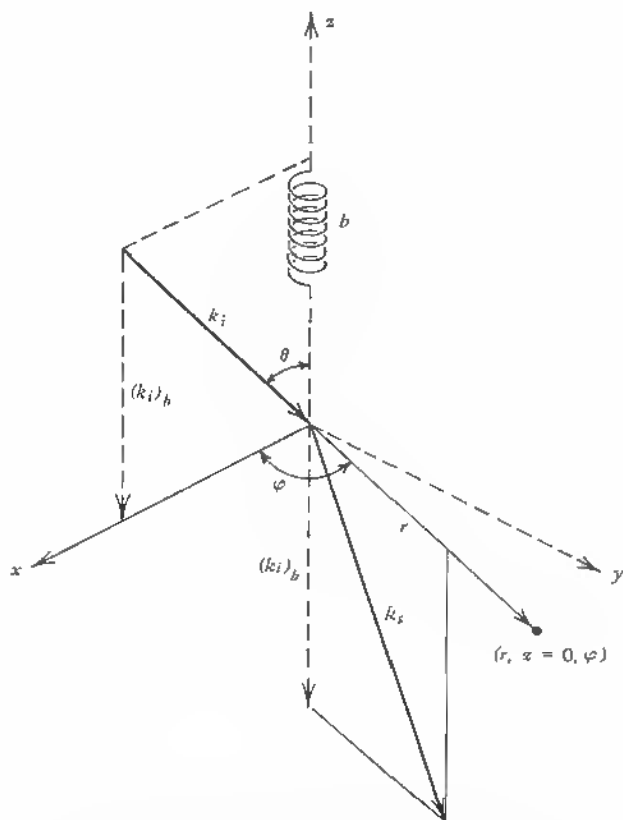


Fig. 8.1 Incident and scattered wave vectors  $k_i$  and  $k_s$  at screw dislocation (line defect).  $(k_i)_b$  is  $\parallel$  to Burgers vector  $b$  is conserved in magnitude and direction.

The result of the perturbation calculation in plane wave scattering is a charge accumulation a few angstroms from the dislocation obviously due to the very localized character of the line imperfection considered. In a number of publications<sup>1</sup>, the influence of dislocations on the electronic wave functions has been considered in this way, but, as Ziman notes, the correct way seems to set up the problem in terms of the local strains produced by the dislocations. Since there is, in principle, no difference between a strain field of a phonon and the static dislocation field, the method of the deformation potentials seems appropriate. Scattering cross-section values calculated, however, have been much too small to account for the experimental findings of the electric field gradients produced even in metals. The perturbation methods are certainly insufficient because of the assumptions of slowly varying strains and the exclusion of those electrons passing close to the core of the dislocation. An important part of the missing detail, however, lies in the assumption of the shielding of the dislocation charge by the conduction electrons even in metals.

In insulators and semiconductors the localized charge is obviously not shielded, and a redistribution of charges in the form of space-charge domains results, with great influence on charge carrier transport.

## 8.1 ELECTRONIC PROPERTIES OF TWIN BOUNDARIES

As described in Section 4.4, an ideal twin configuration does not produce free bonds but only diagonal atomic displacements with relatively little strain. A pure twin boundary, therefore, has only some scattering power and does not greatly influence carrier flow. The main effect of perfect twin boundaries in semiconductors is secondary, by way of the stress field and the impurity distribution. Because of the local lattice-orientation variation, segregation constants during the growth process of the crystal are altered. The different lattice orientations at the solid-liquid interface produce slightly varied impurity distribution and, therefore, a change in dopant and impurity concentrations at the twin interface. These effects are generally of minor importance if pure twin relations prevail. If a crystal contains many twins, however, it must be assumed that stacking faults are present, ending in partial dislocations (Burgers vector smaller than a full lattice spacing). Also, gliding twin axes in many cases can form dangling bonds or free lattice valences that attract conduction electrons and form space-charge domains. Therefore the effect of such disturbances is much too large to be treated by perturbation methods. The electronic-transport properties in the case of such *macroscopic* disturbances are then based on diffusion and space-charge equations taking these large-area disturbances into account (see Chapter 9 and 11). As distinguished from the extension of a few lattice constants of point defects or defect clusters or in the case of the inner core of grain boundaries (width of

disturbed layer around 20 lattice constants or 100 Å), the extension of space-charge domains embraces thousands of lattice sites.

A large class of important twin boundaries is the *lateral* or *noncoherent* twin, in which the twin plane and the boundary plane are not identical. Figure 8.2 shows a typical case of noncoherent twins. The plane of the figure [101] is normal to the dislocation. The twinning dislocations are sidewise steps in the otherwise coherent twin interface. This kind of noncoherent twin generally appears in groups, as shown in the figure, and the cyclic change in lattice strain can be observed optically in birefringence experiments. If the crystal—silicon, for example—with such cyclic twin layers is brought between two polarizer crystals in the infrared spectral region in which the crystal displays transparency (near  $1\mu$  wavelength) and an infrared converter tube is used at the end to photograph the influence of the crystal on the polarization plane of the incident beam, one finds bright lines alternating with dark bands in the crystal that, on external pressure, change from bright to dark, and so on (see Figure 8.3).

The very complicated *higher-order twinning configurations*, especially in silicon, have been discussed by J. A. Kohn<sup>4,5</sup> (see also Section 4.4). He showed that lateral twin boundaries have a tendency to orient themselves along rows of lattice sites in the coincidence-site superlattice for first-order twinning. There are changes in nearest-neighbor situations at points  $a'$  in

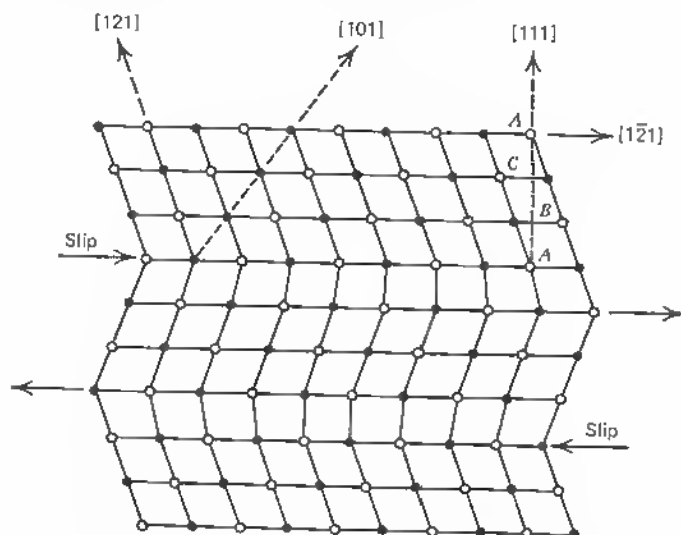


Fig. 8.2 Noncoherent twins (gliding twin axis) in FCC-cubic Plane of figure [101]. Twin boundary  $\neq$  twin plane. Open circles are atoms in plane of drawing.

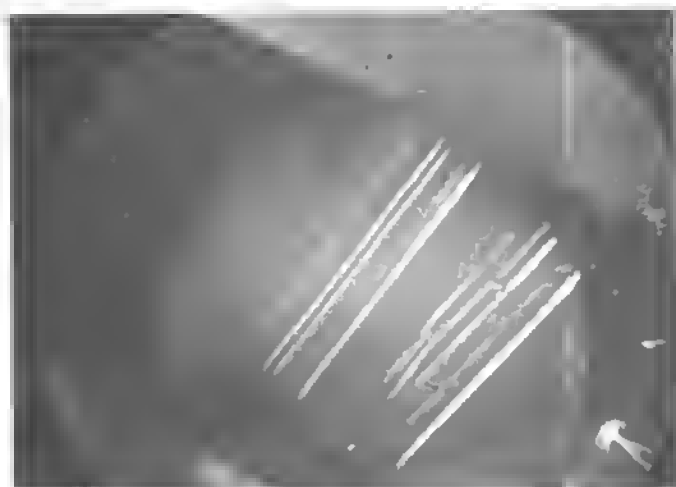


Fig. 8.3 Silicon wafer with cyclic twins in the beam of polarized L.R.

Figure 4.10, and at points *b* two bonds have combined into one. In the  $[\bar{2}21]$ - $[\bar{2}\bar{2}1]$  second-order twin join (see Figure 4.11), bonds at position *d* have been rotated, and so on. All these changes produce strain, and it is generally the twin that takes care of the surplus energy on freezing if no stronger discontinuities (boundaries) are generated.

Lateral twin boundaries, therefore, are areas by which structure-sensitive parameters like mobility and lifetime are affected. Large-size space charges due to junctions are less affected by twins and it is well known that monocrystals with a considerable number of twin boundaries can still be considered electrically "good" material. This means that a certain reproducibility, for example, in the performance of diode arrays can be maintained. In chemical vapor deposition of silicon on sapphire, for example, (see Figure 8.4), multiple twins occur but generally allow for a reproducible production of diodes. Also metal oxide semiconductor field-effect structures can be made from such material with moderate yield. A reliable and reproducible device production with a guarantee of favorable yield, however, should not use such material from the outset. The reason for this lies in the effects of defects on device structures (junctions) under bias condition and the possible local heating associated with the stress field in the crystal causing irreversible changes. In general, it is not easy to correctly separate real twin boundaries and grain boundaries. Often a grain boundary starts to grow, and the end result may be an ideal twin. Here the local resistivity and the photovoltage across the structure reveal a cusp or a slight maximum at the twin due to an impurity gradient (see Figure 8.5). This situation is most common in silicon for the

[111]-growth direction. As shown in Figure 4.12, certain misfit angles between the individual crystallites lead to low-energy cusps. This tendency rules out a clear separation between grain boundaries and twin boundaries in many cases.<sup>6</sup> No grain-boundary energy, small photoelectrical response, and no appreciable space charge are mostly the signs of twin configurations rather than a proof that segregation of impurities (oxygen) is responsible for certain electronic effects of grain boundaries.<sup>6</sup> If free bonds are formed, their electronic effects are so multifold that, with or without foreign impurities in the lattice, strong effects are seen. These are discussed in Chapter 9 through 11.

As we saw in Figure 8.2, a step in an otherwise coherent twin boundary is

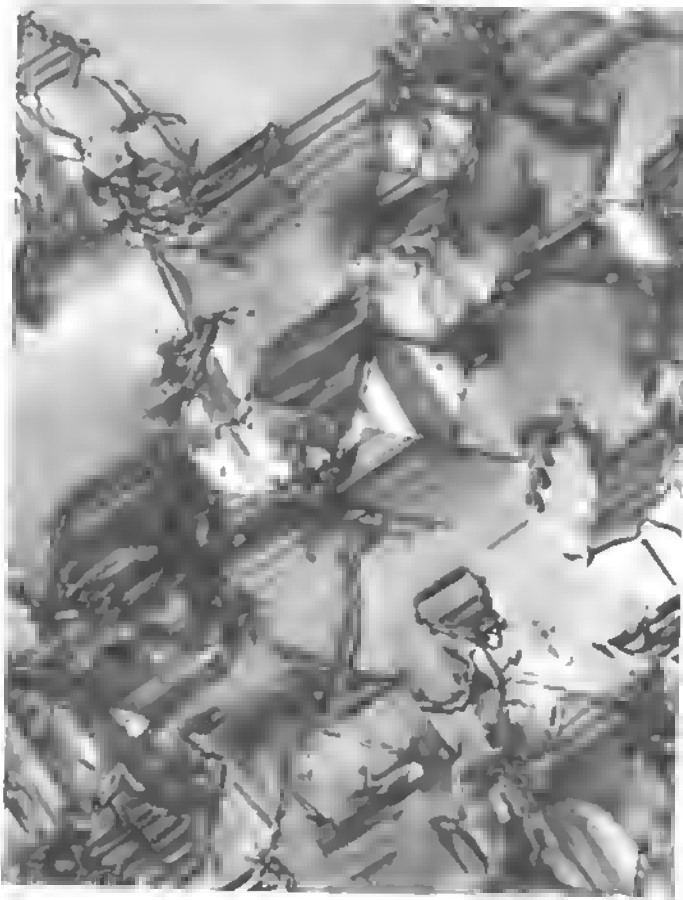


Fig. 8.4 |——| Twins and stacking faults in silicon on sapphire.  
1  $\mu$



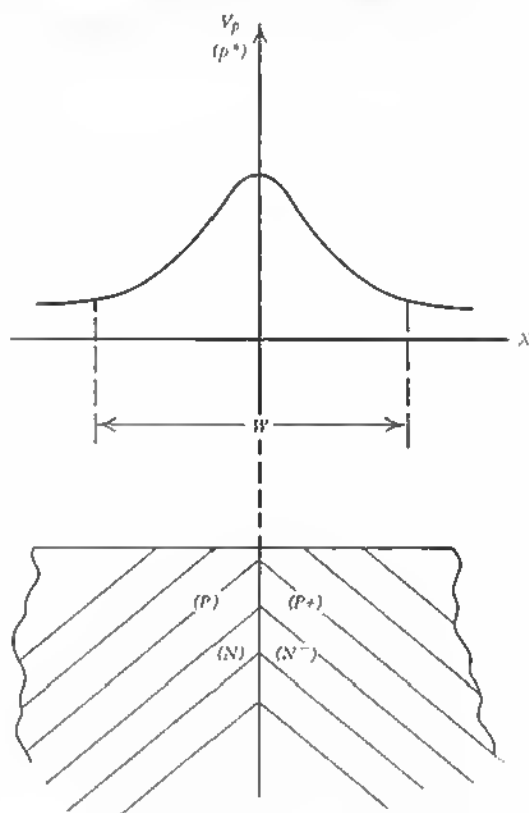


Fig. 8.5 Photovoltage and resistivity change across ideal twin boundary.

similar to a partial dislocation (Shockley partial). A stacking fault that ends inside of the crystal on a partial can be viewed as a one-layer twin. Considering the face-centered cubic lattice (FCC), a perfect structure is defined by an atomic-layer sequence

$$A C B A C B A C B \cdots$$

A partial, as shown in Figure 8.6a, results in a center-sequence shift

$$A C B \downarrow C B A C B \cdots$$

Elimination of ribbon A results in an imperfection, with a Burgers vector less than  $a$  (lattice constant), or a partial, as shown in Figure 8.6b, results in a lateral sequence

$$A C B A \downarrow B A C B \cdots$$

and a cyclic reversal of the stacking order is a pure twin



Considering the Bloch wave in the neighborhood of a fault, one may proceed as in the application of the *orthogonalized-plane-wave* method (OPW) or *augmented-plane-wave* method (APW), in which linear combinations of Bloch sums approximate the effect of the ion cores and are superimposed on the plane wave with  $\exp(i\mathbf{k} \cdot \mathbf{r})$ :

$$\psi_{\mathbf{k}} = \exp(i\mathbf{k}\mathbf{r}) \left\{ 1 + \sum_{\mathbf{g} \neq 0} A_{\mathbf{g}} e^{i\mathbf{g}\mathbf{r}} \right\}. \quad (8.7)$$

Assuming that the stacking fault does not begin nor end in the atomic centers, but in the interstitial region, the fault can be considered the transition region

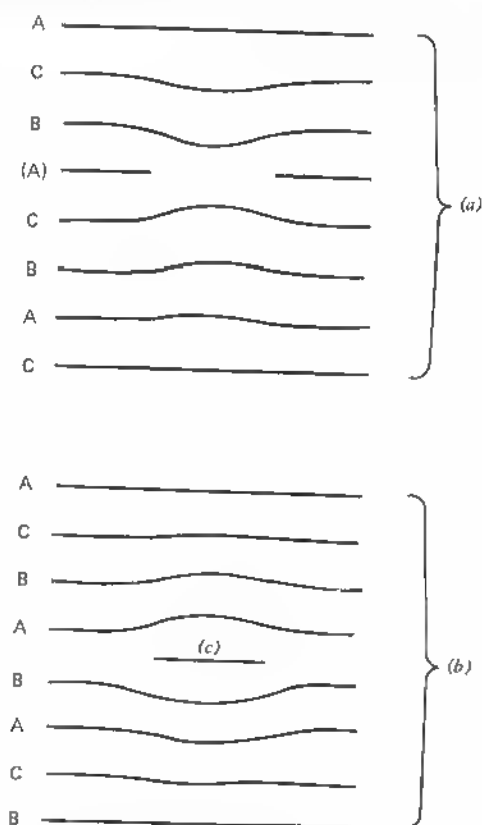


Fig. 8.6 Partial dislocations:  
 (a)  $A C B \downarrow C B A C B \dots$   
 (b)  $A C B A \downarrow B A C B \dots$

where incoming and reflected Bloch waves meet. On the other side of the fault one has

$$\psi'_k = \exp[ik(\mathbf{R} + \mathbf{r})] \left\{ 1 + \sum_{g \neq 0} A_g e^{ig(\mathbf{R} + \mathbf{r})} \right\}. \quad (8.8)$$

The reflection coefficient is a sum of terms like

$$|A_g|^2 \sin^2 (\frac{1}{2} \mathbf{g} \cdot \mathbf{R})$$

(see Ref. 1). Although these effects are relatively small (reflection coefficients of a few percent), the major effects in semiconductors are generated by way of the lattice strain and the change in band gap directly affecting the mobility. When twins, and especially multiple twins, are found in material like thin films of silicon on sapphire (see Figure 8.4) or on other substrates, it is clear that the difference in expansion coefficient has caused lattice slip during cooling. In this way the material relieves the stress, but the originating twins are often of the high-energy type with partials and second-order lateral joins and thus represent localized strained regions causing strong scattering and, in the case of disrupted bonds, space charge. Figure 8.4 shows a typical electron transmission microscopy picture of a silicon-on-sapphire crystal.<sup>7</sup>

In summary, we may say that it is established that ideal twins do not cause measurable changes in the case of simple crystal domains (diode junctions) in devices or in unipolar structures, but their appearance can easily be coupled with major defects and disrupted bonds. In this case, strong effects may be expected, as shown in Sections 8.3 to 8.6.

## 8.2 SCREW DISLOCATIONS

As we saw in Section 4.3, the screw dislocation is similar to a twin inasmuch as no disrupted bonds are formed. The spiral ramp generated during outgrowth of a screw dislocation is, in effect, considered the lowest-energy-growth step. F. C. Frank points out that in this case there is no need for a fresh two-dimensional nucleation, since the "spiral staircase" offers molecular terraces on which low-energy growth can continue (see Figure 4.7 and 4.8). Growth spirals are usually observed in most crystal-growth processes. In a screw dislocation the strain is mostly pure shear; hence the atoms may be represented by undisturbed cubes slipped over one another. The total strain, however, is greater than in the case of a twinlike lateral displacement. Two twisted seed crystals with a lattice translation vector as a slip vector form a screw boundary (see Figure 8.7). Since the energy of the screw dislocation is only  $(1 - \nu)$  times smaller than that of the edge dislocation ( $\nu$  is Poisson's

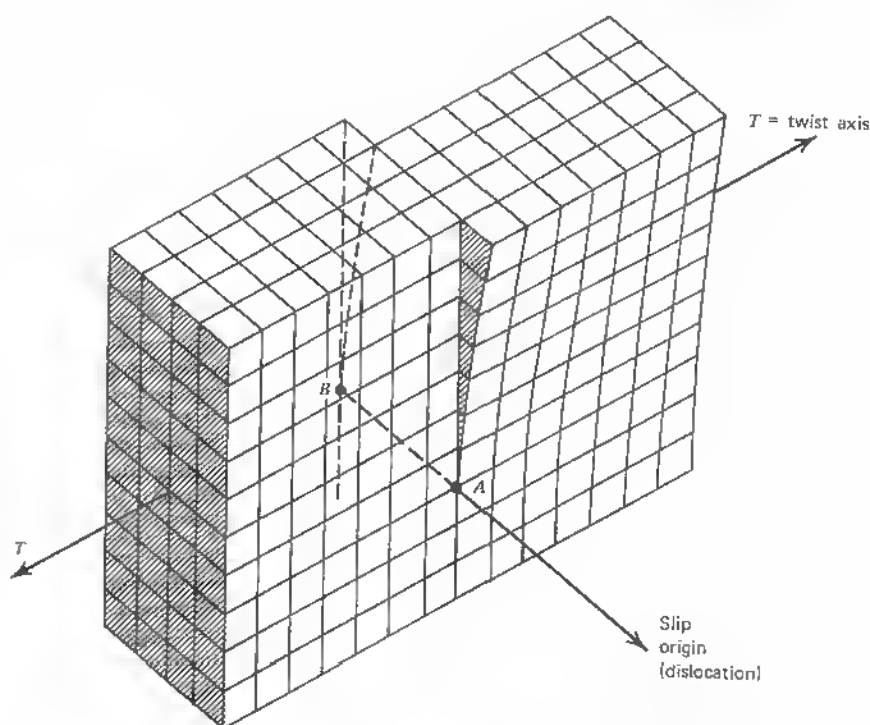


Fig. 8.7 Two twisted crystals with slip vector = lattice translation vector.

ratio), the lattice disturbance due to strain and resultant band change is similar. An ideal screw dislocation, however, does not show, the special aspect of the disrupted bond with its acceptor (donor) level and the consequent buildup of a space charge.

Figure 8.8a shows the model of the ideal screw dislocation and its electronic band picture. Figure 8.8b shows for comparison the disturbed screw or *bent dislocation*, which does not lie in a single plane parallel to the slip vector. In this case the boundary of the slipped area is an edge dislocation.

Here the band structure has to accommodate the interband levels and the strong space charge around the slipped area, as in the case of edge-dislocation arrays. Experiments with bicrystals grown by the double-seed method show that screw dislocations generated by twisted seeds generally show an electric behavior similar to edge dislocation boundaries. This is because, in most cases, slippage is not confined to a single atomic plane. Since slip occurs preferentially on densely packed crystallographic planes, the growth of a screw

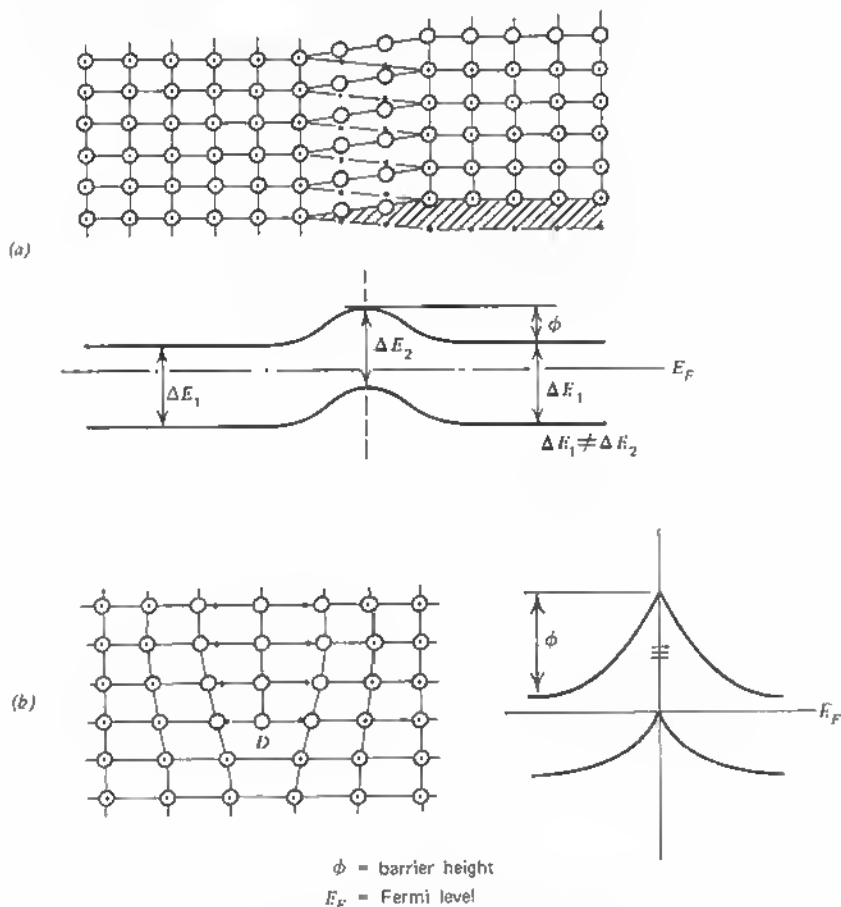


Fig. 8.8 (a) Model of ideal screw dislocation and band scheme. (b) Disturbed screw dislocation (not in single plane  $\parallel$  slip vector).

dislocation from twisted seeds, for example, is subjected to forces that tend to divert the slip plane into lower-energy positions, thereby creating edge dislocations. As a consequence it is rarely possible to study screw dislocations in their pure form as is possible with twins. From the point of view of their electronic behavior, therefore, we have to view the model of a screw dislocation as shown in Figure 8.8b.

The general electronic features derived for the edge dislocation are therefore applicable to the screw dislocation whenever a pronounced space charge is measured by photoelectric injection, point probing, electron injection, or other means. In the absence of space-charge effects in the form of  $n$ - $p$ - $n$  or  $p$ - $n$ - $p$  layers, the situation resembles that of the twin boundary (see Section 8.1).

### 8.3 EDGE DISLOCATION

As we saw in Sections 4.1 and 4.5, there is considerable lattice disturbance due to edge dislocations:

1. The local stress field around such a dislocation
2. The disrupted or dangling bond with its specific charge and energy level
3. The space-charge domain that forms immediately in semiconductors and surrounds the dislocation line in the form of a space-charge pipe

In an elastically isotropic crystal the edge dislocation introduces a strong discontinuity into the local stress pattern, changing from pure compression to pure dilation along the additional half plane (see Figure 8.9). This has the effect of changing the forbidden gap of the semiconductor because of the

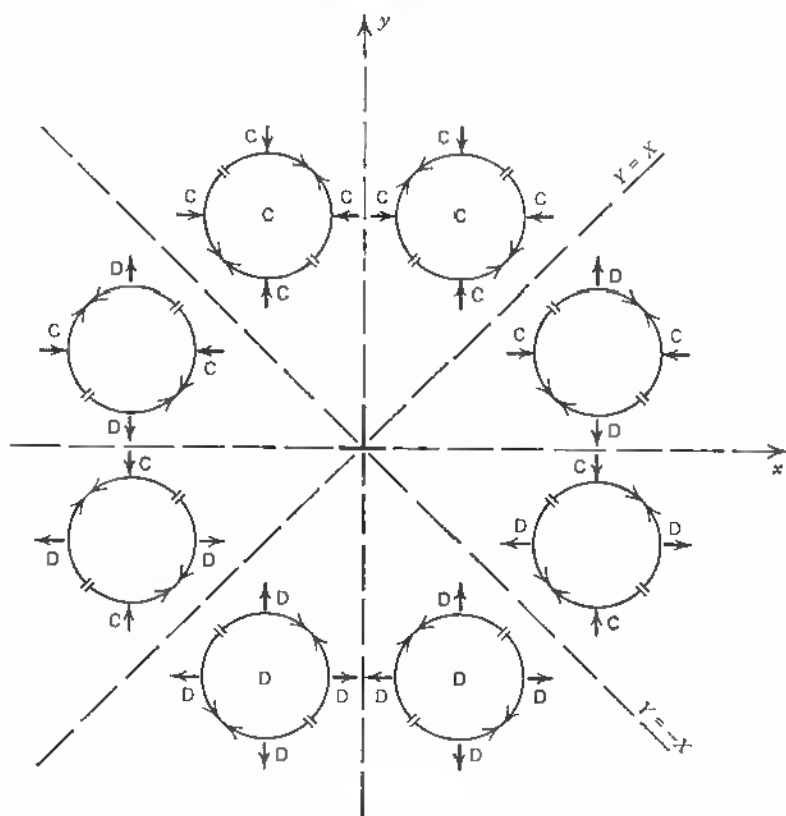


Fig. 8.9 Local stress-vector field around edge dislocation as seen e.g. by an impurity atom.

C = Compression  
D = Dilation

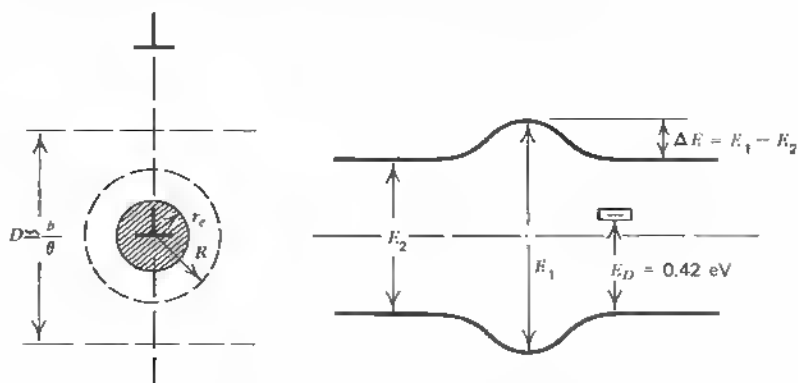


Fig. 8.10 Electronic energy level of edge dislocation and band scheme.

resulting local compression increment in the deformation potential relation (band widening for germanium), as we have seen. Another influence is due to the free or dangling bond and the resulting energy level within the forbidden gap, mostly an acceptor (see Figures 8.10 and 8.11). As a result, the electronic band structure at the site of a dislocation of the edge type is rather complicated. If the distance between the individual sites is larger than the lattice constant, alternating bandgap widening and narrowing occur. This can be viewed as in Figure 8.12, where the original gap  $E$  would change for the

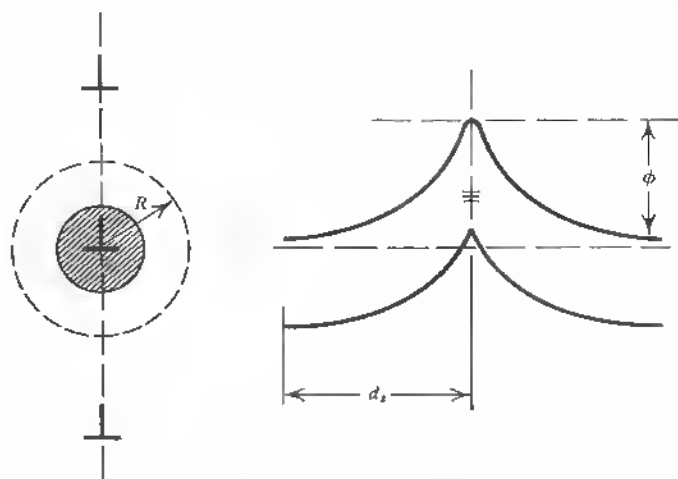


Fig. 8.11 Dislocation barrier layer and resulting space charge.

amount  $\Delta E$  because of isolated compression alone. Closely superimposed dilation would reduce this amount to  $\Delta E'_1$  at the dilation site or to approximately  $\Delta E'_1/2$  for the overall structure. Since  $\Delta E'_1 \simeq \Delta E/2$ , the resulting effective bandgap is

$$E_{\text{eff}} \simeq E = \frac{2 \Delta E'_1}{2}$$

or

$$E_{\text{eff}} \simeq E + \Delta E'_1 \simeq E + \frac{\Delta E}{2}$$

(see Figure 8.12). This overall increase in gap at the lieu of closely spaced edge dislocations has been shown to exist in grain boundaries because of the behavior in electronic injection experiments and optical response measurements, as will be discussed later.

The influence of the resulting pressure field on the band structure of the material is rather complex if one considers the complete band structure in the Brillouin zone along

$$k[111] \rightarrow k=0 \rightarrow k[100].$$

The changes due to pressure are felt mostly in the optical application of semiconductors, since in the case of a grain boundary, for example, the material under stress is prevalent in a thin layer only (a few 100 Å) and forms the core

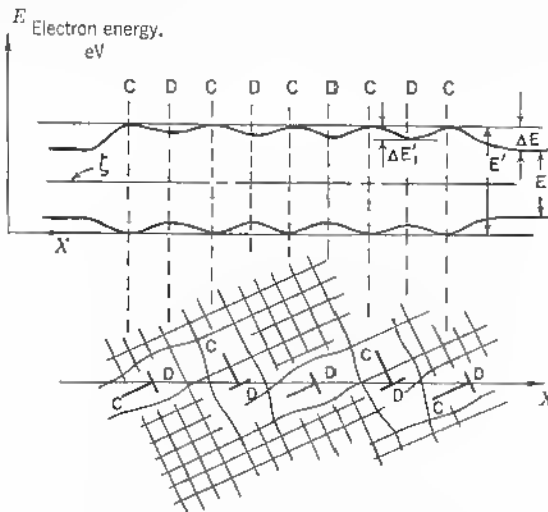


Fig. 8.12 Model of grain-boundary band with compressional and dilational influence on gap.



of a  $p$ -type zone, although the adjacent material is  $n$ -type. In this way the space charge layer, which is optically activated, covers both band structure zones and makes new transitions possible. We discuss this under "Photoelectric Properties" in Chapter 11.7.

When we consider the edge dislocation in more detail, we conclude that the dangling electron, as part of the four valence electrons—in germanium, for example—is unlikely to jump into the conduction band and thus form a donor. If the energy level of the single dangling electron above the valence band is  $E_1$  (see Figure 8.13), the energy required for transfer into the conduction band is  $E_c - E_1$ . In most cases, however, the dangling electron attracts a free electron and lowers its energy to a value  $E_2$  from the valence band and is located below the Fermi level  $F_F$ . Its energy can be lowered again by addition of yet another free electron, but in this case it would represent rather a *cis* donor (see Section 2.4; Figure 2.13 and 3.8; as well as Chapter 2, Ref. 5, and in the present chapter, Ref. 9).

This result is likely in materials with a higher bandgap and has been found in silicon. From here on, the term *empty site* is applicable only to the dislocation site with a single dangling electron (active acceptor), and a *full site* means that this free electron has accepted another electron in order to lower its energy.

Dislocations must be viewed as linearly repetitive steps as distinguished from point defects. The density of such line defects is expressed as a flux density or the number cutting a unit crystal area normal to their direction. If  $c$  is the spacing between dangling bonds, the volume site density is  $N_s = N/c$ . Not all available sites are filled with conduction electrons yielding the energy level  $E_2$ . (see Figure 8.13). A filling factor

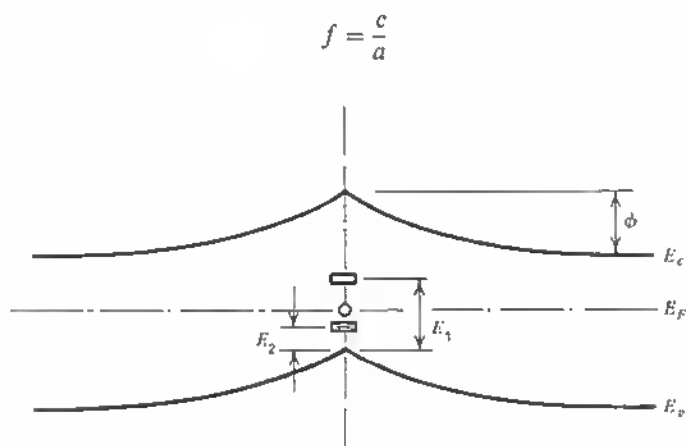


Fig. 8.13 Empty and filled dangling bond level.

can be defined in which  $a$  is the spacing between filled sites or occupied sites and  $1/a$  is the density of added electrons.

For the fraction of sites that are full, a Fermi distribution function can be given<sup>10</sup>:

$$f = 1 + \exp\left(\frac{E_2 - E_F}{kT}\right)^{-1}. \quad (8.9)$$

The spacing  $c$  can vary with the direction of slip. The angle  $\alpha$  between the dislocation and its Burgers vector defines  $c$ , since

$$c \approx \frac{1}{\sin \alpha}.$$

For  $\alpha = 0^\circ$  there are no dangling bonds,  $c = \infty$  (screw dislocation), and for  $\alpha = 90^\circ$  the spacing is minimal. For the  $60^\circ$  dislocation (see, Figure 3.2)  $c = d$  ( $d$  = lattice spacing; from here on  $d = b$  = Burgers' vector), and, therefore,

$$c \sin \alpha = b \sin 60^\circ. \quad (8.10)$$

For the  $90^\circ$  dislocation (pure edge) the spacing is therefore

$$c = 0.866b$$

or slightly below the interatomic spacing. It is generally not very relevant to quote volume densities of dislocations when they appear in the form of lincage or grain boundaries, since their character is linear or planar. The latter is true for larger crystal areas twisted or tilted with respect to each other. Surface densities of dislocations in this case are of the order of  $10^{12} \text{ cm}^{-2}$ . This corresponds to a volume density of  $10^{18} \text{ cm}^{-3}$ . If we assume, for example, a dislocation density equal to an impurity density of  $10^{15} \text{ cm}^{-3}$ , we arrive at very small values for the angle between slip vector and dislocation line—from (8.10):

$$\alpha \approx \frac{b}{c} \sin 60^\circ,$$

and with  $b \approx 5 \text{ \AA}$  and  $c = \sqrt[3]{1/10^{15}} = 10^{-5} \text{ cm}$ ,  $\alpha$  is of the order of  $10^{-3}$  radians. In this case the dislocation is almost entirely screw. More often two crystal regions are tilted with respect to each other but under a very small tilt angle  $\theta$ . In this case the dislocation distance  $D$  is

$$D = \frac{b}{2 \sin(\theta/2)}$$

(see Figure 4.5), and we arrive at tilt angles of a few seconds of arc for dislocation distances in the  $\mu$  range. Since the spread of the space-charge region

around the dislocations is of the order of several  $\mu$ —depending on doping, it can be extended upward to 100  $\mu$  for lightly doped crystals—these dislocation pipes are still overlapping and thus form coherent  $p$ -type layers with high pipe conductivity (see Chapter 9).

Under applied lateral fields the dislocation pipe accepts more free electrons, and the density evaluated on account of a Fermi distribution law (8.9) is no longer valid in a range where coulombic repulsive forces compete with overlapping wave functions leading to a smeared-out line charge.

This was first established in probe measurements by Hogarth et al.<sup>11</sup> who measured the extension of localized space charge layers around individual dislocations and found values in the range of 10 to 100  $\mu$  in good agreement with later measurements (see Chapters 8.4 and 9.3).

#### 8.4 LOW-ANGLE LINEAGE AND GRAIN BOUNDARIES

The definition of these forms, based mostly on edge dislocations, is by way of dislocation distance  $D$ , as in Section 4.2 and Figure 4.6. Isolated dislocation lines are rare, since in most cases crystal areas of three-dimensional extent are involved in generating a superposition of line charges in a two-dimensional, planar form. If the tilt angle  $\theta$  is very small and consequently  $D$  very large, the lateral overlap of compression and dilation is also small, and a small stabilizing force results, with attendant line deviation. In lineage the form of the lines deviates in all directions, because small obstacles like point defects can cause a deviation in the original straight-line pattern.

In medium- and high-angle boundaries, the energy is so high, as we have seen, that the tendency of a straight line and planar growth is very pronounced, even repulsing growing low-angle lineage (see Section 7.2). As  $D$  decreases, or  $\theta$  increases, different regions can be envisioned (see Figure 8.14). As  $D$  is reduced in proportion to a single-line space-charge radius  $R$ , the individual space-charge pipes overlap and finally form a two-dimensional boundary within the crystal. The increase in screening distance over and above the isolated space-charge radius  $R$  is limited. As the bonds move closer together, the acceptor levels in the forbidden gap rise up toward the Fermi level. Finally, the valence band peaks over the Fermi level, and a degenerate  $p$ -type conductivity path forms. Further increase in  $\theta$  (decrease in  $D$ ) then leads to highly concentrated defect layers of increased lateral dimension where microcracking results in material of polycrystalline nature.

If we assume an original net donor density  $N_d - N_a$  in the material, the negatively charged line of acceptors repels conduction electrons and forms an average positive charge per unit volume:

$$e(N_d - N_a). \quad (8.10)$$

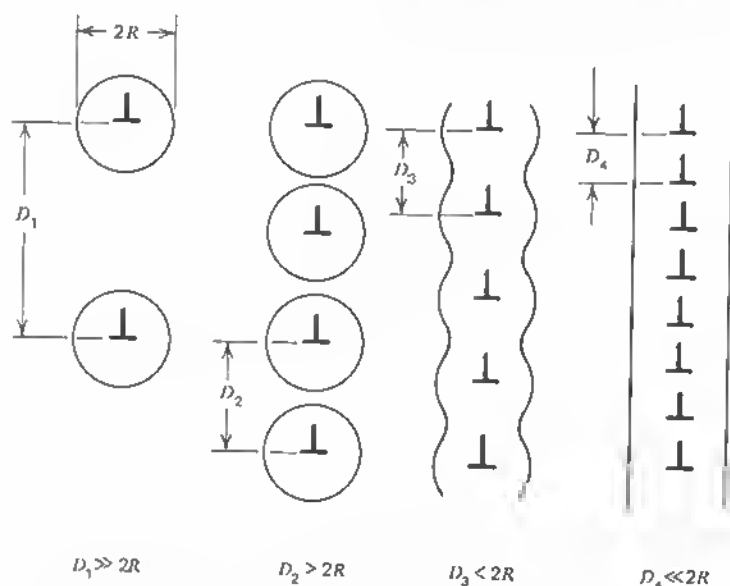


Fig. 8.14 Space charge cylinder overlap for decreasing dislocation spacing.

A cylinder of radius  $R$  around the dislocation can be drawn so that

$$e\pi R^2(N_d - N_a) = \frac{ef}{c} = \frac{e}{a}, \quad (8.11)$$

or the positive charge in the cylinder equals the negative line-charge density on the dislocation. This leads to a space charge radius

$$R = [a\pi(N_d - N_a)]^{-1/2} \quad (8.12)$$

or

$$= \left[ \frac{f}{c} \frac{1}{\pi(N_d - N_a)} \right]^{1/2} \quad (8.13)$$

in terms of filling factor  $f$ , dangling-bond number  $c$ , and state density in the space-charge region. Within the space-charge region, the impurities seem to be ionized at all temperatures, although bulk impurities freeze out as  $T$  is lowered. The impurity gradient at the space-charge pipe or layer decreases as the temperature is increased. The net charge density in the semiconductor is actually

$$\rho = e(N_d - N_a + p - n), \quad (8.14)$$

where  $p$  and  $n$  are the free hole and electron charges. Here we generally neglect this contribution of free carriers to the space charge. At higher temperatures the space-charge gradient is lowered until it finally is smeared out over a wider distance and disappears. In normal temperature ranges and for nondegenerate doping we neglect the free-carrier contribution. The introduction of the Fermi distribution function into (8.12) or (8.13) leads to the expression

$$R = \left( \frac{\{1 + \exp[(E_2 - E_F)/kT]\}^{-1}}{c\pi(N_d - N_a)} \right)^{1/2}. \quad (8.15)$$

Typical values for  $n$ -type germanium of an impurity range  $N_d - N_a = 10^{15} \text{ cm}^{-3}$  and  $f \approx 0.5$  (dislocation level below Fermi level) give, with  $c = 5 \times 10^{-8} \text{ cm}$ ,

$$\begin{aligned} R &\approx 10^{-4} \text{ to } 10^{-3} \text{ cm}, \\ R &\approx 1 \text{ to } 10 \mu. \end{aligned}$$

W. T. Read has already argued that the value of  $f$  is different from that derived by Fermi statistics, because the occupation law for a line of closely spaced acceptor centers is not governed by Fermi statistics. We shall see later that in fact such a line charge can accept a higher number of additional charges under bias and that in this situation another charge-distribution law has to be invoked. If we assess the total increase in free energy of the line charge, the decisive part is the electrostatic energy per added electron  $E_s(f)$ , since the total increase is

$$F(f) = E_s(f) + E_2 - E_F. \quad (8.16)$$

$E_s(f)$  represents the work done per electron to form the space charge, starting with electrically neutral material:

$$E_s = E_e + E_c + E_{ee} + E_{ec}. \quad (8.17)$$

$E_e$  is the energy of interaction per electron, or

$$E_e = \frac{1}{2} e \phi_{e0},$$

where

$$\phi_{e0} = \frac{2e}{ka} \sum_{n=1}^{N/2} \frac{1}{n} = \text{potential at one electron due to all other } (n) \text{ electrons,} \quad (8.18)$$

where  $k$  = dielectric constant.

$E_c$  is the energy of the positive space charge alone:

$$E_c = \frac{a}{2} \int_0^R \rho \phi_c(r) 2\pi r dr. \quad (8.19)$$

Here the space-charge potential can be found from an integration of Poisson's equation as

$$\phi_c(r) = \frac{\pi\rho}{k}(R_0^2 - r^2), \quad (8.20)$$

where  $\rho = \text{charge density} = e(N_d - N_a)$ .

$E_{ce}$  and  $E_{ec}$  are interaction energies of electrons and positive space charge and can be assumed equal:

$$E_{ce} = E_{ec} = \int_r \int_z \frac{1}{2} \rho \phi_c(r, z) dr dz. \quad (8.21)$$

W. T. Read<sup>10</sup> has evaluated the expression for  $E_s$ , by developing (8.18) (8.19) and (8.21) the result being

$$E_s = \frac{e^2}{ka} \left( \ln \frac{R}{a} - 0.866 \right). \quad (8.22)$$

If we use the relations (8.12) and the interaction energy

$$E_0 = \frac{e^2}{kc} \quad (8.23)$$

and define a distribution function  $f_c$  for the case in which  $f = f_c$  when  $R = a$ :

$$f_c = c[\pi(N_d - N_a)]^{1/3}, \quad (8.24)$$

we arrive, with (8.13), at

$$\frac{f}{f_c} = \pi^{2/3} \cdot R^2 (N_d - N_a)^{2/3} \quad (8.25)$$

and

$$\frac{3}{2} \ln \frac{f}{f_c} = \ln \pi R^3 (N_d - N_a), \quad (8.26)$$

which is, with  $R/a = \pi R^3 (N_d - N_a)$  from (8.13),

$$\frac{3}{2} \ln \frac{f}{f_c} = \ln \frac{R}{a} \quad (8.27)$$

or

$$E_s = fE_0 \left( \frac{3}{2} \ln \frac{f}{f_c} - 0.866 \right). \quad (8.28)$$

Equation (8.28) expresses the work done per added electron in forming the space-charge distribution starting from neutral material. In order to find the potential at one electron due to all other electrons in the line charge and the

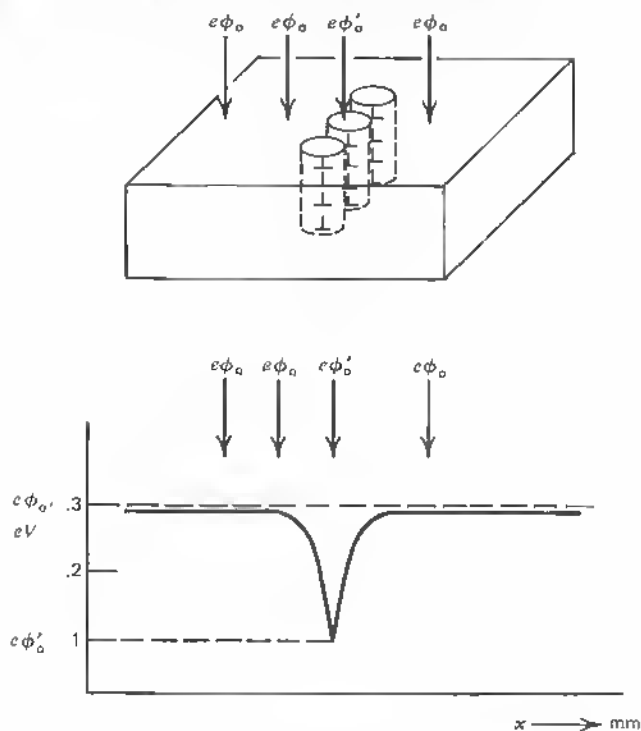


Fig. 8.15 Lowering of surface contact potential at the site of dislocations.

positive space charge, we calculate

$$\phi_0 = \phi_{e0} + \phi_r, \quad (8.29)$$

where  $\phi_{e0}$  = potential due to other electrons,

$\phi_r$  = potential due to space charge.

Combining the solutions to (8.18)

$$\phi_{e0} = -\frac{2e}{ka} \left( \ln \frac{N}{2} + 0.577 \right), \quad (8.30)$$

where 0.577 = Euler's constant,

and to (8.20), leads to a potential function

$$\phi_0 = -\frac{e}{kc} f \left( 3 \ln \frac{f}{f_c} - 1.232 \right) \quad (8.31)$$

given by Read.

This equation accounts for the increase in potential at the site of a dislocation and should give, quantitatively, the increase in potential, for example, on a semiconductor surface at the lieu of a lineage boundary or grain boundary. With (8.23) one can write

$$|e\phi_0| = E_0 f \left( 3 \ln \frac{f}{f_c} - 1.232 \right) \quad (8.32)$$

for the barrier in electron volts. Surface-contact-potential measurements show, however, that the supposed increase of the work function at the dislocation site is reversed into a trough or decrease in work function.<sup>12</sup> In fact, the line charge is a region of higher conductivity, and the contact potential is lowered from the surface down into the bulk when the dislocation is oriented perpendicular and not parallel to the free surface (see Chapter 9).<sup>9,13</sup> This situation is schematically shown in Figure 8.15. At the location of the dislocations the contact potential  $e\phi_0$  is lowered considerably to a value  $e\phi'_0$ .<sup>12</sup>

## 8.5 DIFFERENCES WITH REGARD TO THE HOST LATTICE

In ionic crystals the fundamental properties of dislocations, as they have been elaborated so far, remain the same. The mechanical aspects are very similar in nature with slight changes due to acting coulombic forces whenever lattice deformations become important, for example, in the case of a [010] edge dislocation (see Figure 8.16). The mechanical strain at the end of the additional half plane ending here with a positive charge leads to a balance between the coulomb repulsive forces of the positive charges and the dialational lattice forces. The area of the edge dislocation attracts free electrons in this case, therefore, acting as an acceptor. In the opposite case, where the additional half plane ends with a negative charge, holes are attracted to the core of the dislocation, and donor character results. Similar situations arise in the [011] dislocation and have been discussed before.<sup>14</sup>

In III-V compounds, like InSb and GaAs, all [111] planes are arranged in pairs: GaAs...GaAs...GaAs, and so on. For energetic reasons, the dislocations form preferentially in the gap between the pairs. X-ray data and surface etching have shown that these lattices are differently charged in the [111] and  $\bar{[111]}$  directions, for example. In each double layer the gallium (indium) atoms precede the arsenic (antimony) atoms in one direction but succeed them in the other (see Figure 8.17).<sup>15</sup>

X-ray diffraction close to the absorption edge reveals clearly the reciprocal behavior of the two crystallographic planes, as White and Roth have shown (see Chapter 3).<sup>15</sup>

Hornstra<sup>16,17</sup> has shown that in the diamond lattice all dislocations can be



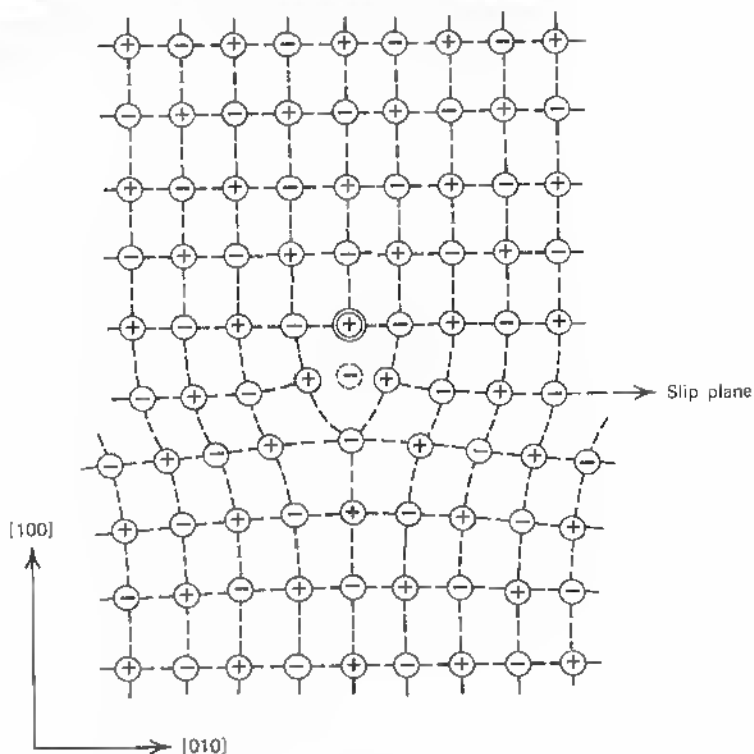


Fig. 8.16 Sodium-chloride type polar lattice with edge dislocation. Burgers vector  $\frac{1}{2}a[010]$ .

derived from three basic dislocations extending in the  $\langle 110 \rangle$  direction, with a  $[110]$  Burgers vector. These are the  $[110]$  edge, the  $[110]$  screw, and the  $[110]$ - $60^\circ$  dislocation.

The  $60^\circ$  dislocation has a  $(111)$  glide plane. In zinc-blende structures the  $[111]$  direction is polar, as we have seen (Figure 8.17, for example), and no allowed symmetry operations can transform a  $[111]$  into a  $[\bar{1}\bar{1}\bar{1}]$  direction. The  $(111)$  plane, therefore, is a two-sided polar plane in heteropolar crystals of the zinc-blende type, and dislocations are of either type  $\alpha$  or  $\beta$  depending on whether the glide plane is  $A(111)$  or  $B(111)$ . In  $\text{InSb}$ , for example, all atoms on the  $A(111)$  plane are  $\text{In}$  atoms, and all broken bonds of the  $\alpha$  dislocations are on  $\text{In}$  atoms and all broken bonds of the  $\beta$  dislocations are on  $\text{Sb}$  atoms. The  $[110]$  edge dislocations in the zinc-blende lattice have alternating kinds of dangling bonds because of symmetry and, therefore, do not show the typical polar character. Their line charges are diminished by the

alternating charge sign at the free bonds, and the number of added electrons corresponds only to the lower-energy level resulting from the remaining charge imbalance in the dislocation array. These aspects have been studied in bicrystals grown from InSb double seeds by R. K. Mueller et al.,<sup>18</sup> with the conclusion that the  $\alpha$  dislocation attracts electrons in  $n$ -type material and forms a negative core and positive space charge. This dislocation in  $p$ -type material attracts positive charges and again forms a barrier, but with donor-core character. The  $\beta$  dislocations, however, show donor character independently of the  $n$ - or  $p$ -type environment at least within the normal doping ranges used. These results can be understood to some extent by the model advanced by Gatos, et al.<sup>19</sup> according to which the B surfaces show a higher reactivity on account of their impaired electrons. The A surface atoms are distorted from their original tetrahedral symmetry with only three of the  $s-p$  orbitals occupied. In the growth process a B atom is added to an A atom and acquires the  $sp^3$  tetrahedral configuration. This is more difficult for the addition of an A atom to a B atom and leads to a distortion (see Figure 8.18). Gatos et al. have shown that this model explains also the fact that crystals of higher perfection can be grown using the B surface of the seed crystal in Czochralski crystal growth. The probability of twinning is markedly increased if a crystal is grown from an A[111] seed, where three families of  $\{111\}$  planes exist for which the twinning conditions can be easily satisfied.<sup>20</sup>

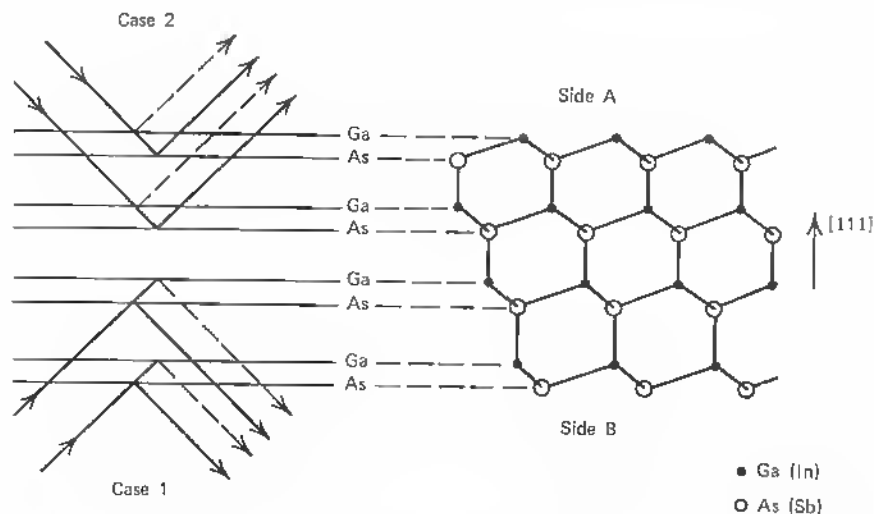


Fig. 8.17 Correlation of x-ray [111] and  $\{111\}$  diffraction and layer structure of III-V compound crystal.

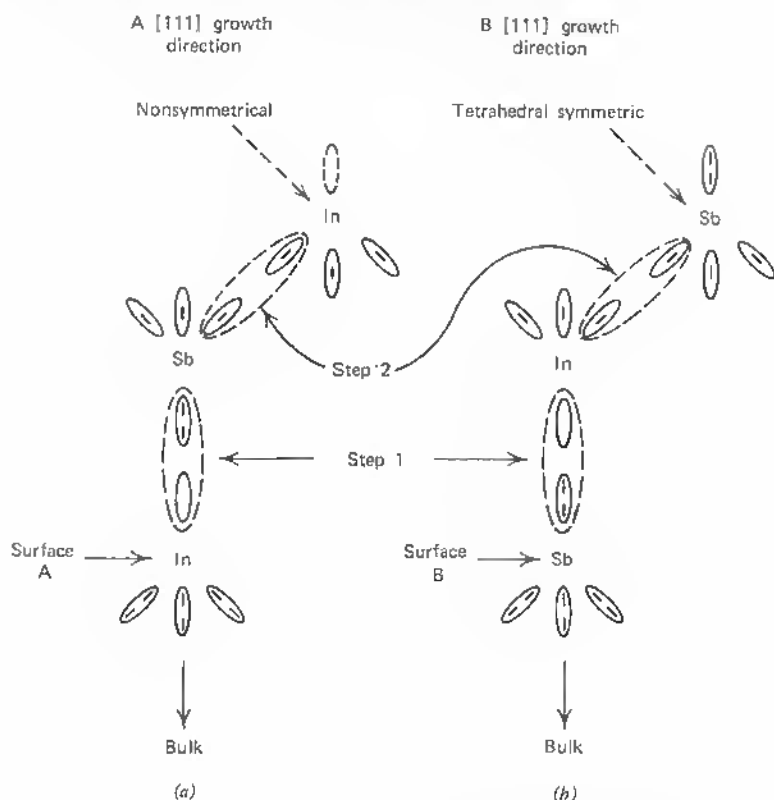


Fig. 8.18 Growth process in InSb for A and B surface.

## PROBLEMS

- 8-1. In what sense is the bent screw dislocation different from the edge dislocation?
- 8-2. What is the influence on the electronic barrier height at the dislocation site of a stress-field-induced band-gap widening (see Figure 8.10 and 8.11)?
- 8-3. Calculate the tilt angle between two crystal regions for a dislocation spacing of  $2 \mu$  when the Burgers vector is equal to  $5 \times 10^{-8}$  cm.
- 8-4. Calculate the space-charge cylinder radius  $R$  for a bulk impurity density of  $(N_d - N_a) = 10^{17} \text{ cm}^{-3}$  and a dislocation spacing of  $5 \times 10^{-8}$  cm (filling factor  $f \approx 0.05$ ).
- 8-5. Discuss the effect of temperature on the space-charge pipe radius (8.15).
- 8-6. Integrate Poisson's equation

$$\frac{\partial^2 \phi}{\partial r^2} = -\frac{2\pi\rho}{\epsilon}$$

for the integral limits  $r \rightarrow R_0$  ( $R_0$  = space-charge radius  $\geq r$ ). Integrate for the case when  $r \geq R_0$  (see Section 9.5).

- 8-7. Draw a schematic of the edge dislocation in the NaCl lattice as sectioned by a [100] plane when the slip plane is [011] and Burgers vector  $\frac{1}{2}a[0\bar{1}1]$ .
- 8-8. Discuss the difference in crystal growth on A and B surfaces of III-V-compound crystals and their dangling-bond behavior.

## REFERENCES

1. Ziman, J. M.: "Electrons and Phonons," Clarendon Press, Oxford, 1960.
2. Ogurtani, T. O., and R. A. Huggins: Theory of Electric Field Gradient due to Conduction Electron Charge Density Redistribution around Screw Dislocations in Metals, *Physica Status Solidi*, Vol. 24, p. 301, 1967.
3. Brown, R. A.: Electron Distribution about an Edge Dislocation in a Metal, *Phys. Rev.*, Vol. 141, no. 2, pp. 568-572, January, 1966.
4. Kohn, J. A.: Twinning in Diamond-type Structures: High-order Twinning in Silicon, *Am. Mineralogist*, vol. 41, pp. 778-784, 1956.
5. Kohn, J. A.: Twinning in Diamond-type Structures: A Proposed Boundary-structure Model, *Am. Mineralogist*, vol. 43, pp. 263-284, March-April, 1958.
6. Queisser, H. J.: Failure Mechanisms in Silicon Semiconductors, *Quarterly Status Report 3*, Rome Air Development Center Contract AF30(602)-2556.
7. Nolder, R. L., D. J. Klein, and D. H. Forbes: Twinning in Silicon Epitaxially Deposited on Sapphire, *J. Appl. Phys.*, 36, no. 11, pp. 3444-3450, November, 1965.
8. Frank, F. C.: The Influence of Dislocations on Crystal Growth, in *Crystal Growth, Proceedings of the Faraday Society*, no. 5, 1949, London, Apr. 12-14, 1949, Butterworth Scientific Publications, 1959.
9. Mataré, H. F.: Grain Boundary Structure and Charge Carrier Transport in Semiconductor Crystals, *Z. f. Naturforschung*, Vol. 10a, no. 8, pp. 640-652, 1955.
10. Read, W. T., Jr.: Theory of Dislocations in Semiconductors, *Philosophical Magazine*, vol. 45, pp. 775-796, August 1954; vol. 45, pp. 1119-1128, November, 1954; vol. 46, pp. 111-131, February, 1955.
11. Hogarth, C. A., and A. C. Baynham: Electrical Methods for Determining the Positions of Dislocation Regions in Germanium, *Proceed. Phys. Soc.*, (Britain), 71, pp. 647-653, 1958.
12. Lagowski, J.: Local Changes of the Work Function of Germanium and Silicon Due to Dislocations, *Physica Status Solidi*, vol. 5, p. 555, 1964.
13. Figielski, T.: Theory of Carrier Recombination at Dislocations in Germanium, *Physica Status Solidi*, vol. 6, p. 429, 1964.
14. Nabarro, F. R. N.: "Theory of Crystal Dislocations," Clarendon Press, Oxford, 1967, pp. 596ff.
15. White, T. G., and W. C. Roth: Polarity of Gallium Arsenide Single Crystals, *J. App. Phys.*, vol. 30, no. 6, pp. 946-947, June, 1959.
16. Hornstra, J.: Dislocations in the Diamond Lattice, *J. Phys. Chem. Solids*, 5, vol. 5, pp. 129-141, 1958.

17. Hornstra, J.: Models of Grain Boundaries in the Diamond Lattice, *Physica*, vol. 25, pp. 409-422, June, 1959; vol. 26, pp. 198-208, 1960.
18. Mueller, R. K., and R. L. Jacobson: Alpha and Beta Grain Boundaries in Indium Antimonide, *J. Appl. Phys.*, vol. 33, no. 7, pp. 2341-2345, July, 1962.
19. Gatos, H. C., P. L. Moody, and M. C. Lavine: Growth of InSb Crystals in the [111] Polar Direction, *J. Appl. Phys.*, vol. 31, no. 1, pp. 212-213, January, 1960; see also P. L. Moody et al., *J. Appl. Phys.*, vol. 31, no. 9, pp. 1696-1697, September, 1960; H. C. Gatos et al., *J. Appl. Phys.*, vol. 32, no. 6, pp. 1174-1175, June, 1961.
20. Mueller, R. K. and R. L. Jacobson: Growth Twins in Indium Antimonide, *J. Appl. Phys.*, vol. 33, no. 3, pp. 550-551, March, 1961.

## Chapter 9 Anisotropy of Charge Carrier Transport

### 9.1 THE EDGE DISLOCATION PIPE

Before entering into a more detailed discussion of the effects of dislocations on carrier-transport phenomena (conductivity, lifetime, magnetoresistance, Hall mobility, and the like), we have to assess the real character of the dislocation pipe when subjected to carrier flow. Measurements of the effects of dislocations in plastically deformed crystals cannot easily be interpreted as to the full extent of the dislocation-pipe properties. Even if orientated mono-crystals are being bent about a defined axis and the pipe direction has a preferred orientation, the measurements are concerned with statistically arranged dislocation pipes of small dimension (pipe radius in the micron range). In this case the pipes are mainly scattering centers for carriers because of their impenetrable and extended space charge. Their longitudinal high conductance, which is an important part of their properties, is not measured within the dominating bulk conduction at room temperature. From the initial model advanced by W. Shockley, it was derived that on formation of edge dislocations with their additional electron or dangling bond, a specimen should become more conducting (see Chapter 8, Ref. 10). In early experiments on plastically deformed crystals<sup>1</sup> it was found, however, that the effect on *n*-type samples is a decrease in electron density and a decrease in electron mobility. In *p*-type samples the effects, if any, were very small or negligible. These results are now understandable because of the formation of space-charge regions around the dislocation pipes that essentially eliminate the pipes from carrier-transport phenomena, as long as they are laterally separated. The models advanced for the current flow on account of the picture of *voids* in the material are applicable, however, only when the transversal conductance of the pipes can be disregarded. Such models are the basis for a number of

works, for example, on recombination or changes in lifetime.<sup>2a</sup> The results show that a relatively low dislocation density of the order of  $10^9$  to  $10^{10} \text{ cm}^{-2}$  has drastic effects on the lifetime of minority carriers, since the capture radius of the dislocations is as large as  $3.4 \times 10^{-8} \text{ cm}$  at room temperature. The lifetime in *n*-type germanium is a function.

$$\tau = 2.5N_d^{-1} \text{ sec}$$

of the dislocation density  $N_d$  in  $\text{cm}^{-2}$ , and in *p*-type germanium we have

$$\tau = 0.7 \times N_d^{-1} \text{ sec}$$

within the range  $N_d = 10^3$  to  $10^8 \text{ cm}^{-2}$ . Lifetime of minorities in silicon is somewhat less dependent on  $N_d$  and obeys a law of the form  $\tau = 15 \times N_d^{-1} \text{ sec}$ .<sup>2b</sup>

As we consider the model of these pipes, it is obvious that the extension of the space charge varies with the doping range of the bulk material and with the kind of crystal. In germanium the acceptor dislocation is clearly established. Even in *p*-type crystals we have found  $p^+$  behavior of the dislocation and thus a formation of a space charge. In silicon, however, the Cottrell atmosphere at the dislocation or the effect of the stress field on the impurity environment can be of much greater variety. Heat treatment with the attendant Si—O bond variations in silicon can have strong effects. Also the impurity distribution around the dislocation can be drastically rearranged by heat treatment. In aluminum or phosphorous-doped silicon crystals, for example, a first annealing at  $1200^\circ\text{C}$  generates *n*-type dislocations, and further heat treatment at  $1275$  to  $1375^\circ\text{C}$  forms *p*-type dislocations or an *n-p-n* structure as in germanium.<sup>3</sup>

For plastically deformed samples bent around a major axis, for example,  $\{110\}$ , the etch pits on the  $[111]$  face lie in rows along the traces of the two active slip planes,  $(\bar{1}11)$  and  $(1\bar{1}1)$ . We deal with the different forms that can be produced later. Our basic assumption at this point is that the pipes are arranged in a statistical manner and are separated. In fact, the normal density of the order of  $10^6$  to  $10^7 \text{ cm}^{-2}$  or  $10^{-2} \mu^{-2}$  rules out any lateral overlap of the space charges that would be significant, as in the case in lineage and grain-boundary planes. In this case the two major effects are the following:

1. The mean free path depends on the direction of the current flow.
2. The mobility is direction-dependent, smaller perpendicular to the pipes and larger along the pipe direction.

In the case of parallel flow, the dislocations are ineffective in scattering the component of momentum parallel to their length direction. In the early measurements on samples after plastic deformation, resistivity and mobility changes were observed in the direction perpendicular to the pipes,<sup>4</sup> and W. T.

Read makes a distinction between parallel and perpendicular current flow. This difference was later confirmed experimentally by Logan et al.<sup>5</sup> Values of recombination velocities of  $2 \times 10^3$  cm/sec reported on low-angle boundaries are relative, since obviously the dislocation spacing or the tilt angle of the grains are decisive (for a general survey of this field compare Refs. 6 and 7).

F. L. Vogel et al.<sup>8</sup> show the effect of a lineage boundary with wide spacing on lifetime values. A plot of the potential variation  $(1 - V/V_0)$  ( $V$  = actual collector potential,  $V_0$  = potential without lineage boundary) over the distance of the light injection point from the boundary ( $x_b - x_l$ ) reveals clearly an exponential voltage drop and, within the bounds of the diffusion equation, a recombination velocity  $v$  on the order of the value found on clean surfaces.

With increased tilt angle, lateral overlap of these dislocations, and formation of a dislocation plane, the results of such measurements are more pronounced and complex<sup>9, 10</sup> and are discussed later. Here we want to emphasize that the model (see Figure 9.1) can be used successfully for isolated, statistically distributed dislocations and can account for a number of aspects like those given according to W. T. Read's theory.

The anisotropic effects due to the properties of parallel dislocation pipes have been summarized by Bardsley.<sup>4</sup> Experimental work, mainly the measurements of carrier diffusion length by the traveling light spot method, show that the hole diffusion constants parallel to the pipes are greater by factors than diffusion lengths perpendicular to the dislocation arrays. Typical values for mobility and carrier diffusion constants are the following:

Filament cut $\parallel$ dislocations		Filament cut $\perp$ dislocations
$\mu$	$\mu_{\parallel} = 1,850 \pm 100 \text{ cm}^2 \text{ V}^{-1} \text{ sec}^{-1}$	$\mu_{\perp} = 1,950 \pm 100 \text{ cm}^2 \text{ V}^{-1} \text{ sec}^{-1}$
$D$	$D_{\parallel} = 400 \pm 100 \text{ cm}^2 \text{ sec}^{-1}$	$D_{\perp} = 80 \pm 30 \text{ cm}^2 \text{ sec}^{-1}$

Although the mobility in  $n$ -type Ge samples is less affected:  $\mu_{\parallel} \simeq \mu_{\perp} \simeq \mu_n$  ( $\mu_n$  = mobility in control crystal for lower field values,  $E < 100 \text{ V cm}^{-1}$ ), the minority carrier diffusion constant is strongly affected:

$$D_{\parallel} > D_{\perp} \simeq D_n$$

for minorities in  $n$ -type samples, that is, holes. For higher fields ( $> 100 \text{ V cm}^{-1}$ ) one finds  $\mu_{\perp} < \mu_{\parallel} \simeq \mu_n$ , which means that also the mobility is affected if carriers are drifting at higher speeds.

It is not astonishing that in  $p$ -type Ge samples  $D$  is isotropic and normal-valued and that only  $\tau_{\parallel} > \tau_{\perp}$  (lifetime difference due to diminished space charge around dislocation core compared to the  $n$ -type case).

In both,  $n$ -type and  $p$ -type Ge samples, the conductivity did not show



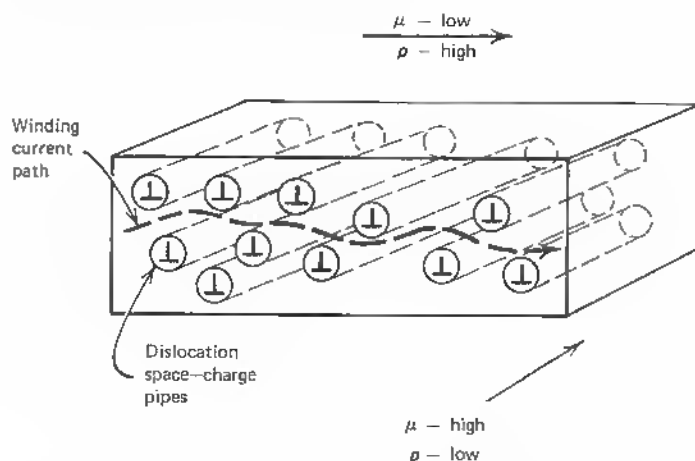


Fig. 9.1 Current flow in crystal with dislocations along one major axis.

anisotropy for lower dislocation counts:  $N_D < 10^6 \text{ cm}^{-2}$ . Measurements of Logan, Pearson, et al.<sup>5</sup> carried through for  $N_D = 5 \cdot 10^7 \text{ cm}^{-2}$  showed the distinctly strong conduction anisotropy also seen in the case of overlapping dislocation pipes, especially for grain-boundary planes, as shown in Chapter 11.

As we apply the space-charge-pipe model to the dislocation arrays, some authors<sup>4</sup> have compared the pipe with a conduction-line analog to a coaxial transmission line where an injected hole becomes a majority carrier (within the positive space charge adjacent to the dangling-bond line) and travels down the line. This represents a conduction mechanism independent of the bulk mobility value, since no capture within the line is possible. In a lumped impedance form, a model, as shown in Figure 9.2, is possible when  $R$  is the resistance per unit length of the inner  $p$ -type conductor of radius  $r_0$ . Between the radii  $r_0$  and  $r_1$  lies the space charge or the relatively carrier-depleted region of the  $p$ - $n$ -junction with barrier capacitance  $C$  and conductance  $G$  per unit length. The characteristic impedance of such a line is

$$Z = (G + i\omega C)^{-1}, \quad (9.1)$$

where  $\omega$  = frequency.

A signal  $S$  is transferred as

$$S = S_0 \exp \left[ -l \left( \frac{R}{Z} \right)^{1/2} \right], \quad (9.2)$$

along the line (where  $l$  = length).

The signal attenuation per unit length is

$$\frac{d(\ln S)}{dl} = \left(\frac{RC}{2}\right)^{1/2} \left[ \left(1 + \frac{\omega^2 C^2}{G^2}\right)^{1/2} + 1 \right]^{1/2}, \quad (9.3)$$

and the phase shift is

$$\frac{d\theta}{dl} = \left(\frac{RG}{2}\right)^{1/2} \left[ \left(1 + \frac{\omega^2 C^2}{G^2}\right)^{1/2} - 1 \right]^{1/2}. \quad (9.4)$$

Traveling light spot techniques have been used to measure  $D$  and  $\tau$  with simultaneous measurement of phase and amplitude (modulation frequency 4 kc/s).<sup>4</sup> If only the hole current is considered (electron conduction is minimized in space-charge pipes in  $n$ -type germanium), the number of holes  $P$  per unit dislocation length can be assessed on account of the charge neutrality condition:

$$P = \frac{f}{a} - \pi r_1^2 (N_d - N_a), \quad (9.5)$$

where  $f$  = fractional occupation of dangling bonds,  
 $a$  = separation of occupied sites,  
 $N_d - N_a$  = excess charge density in space charge.

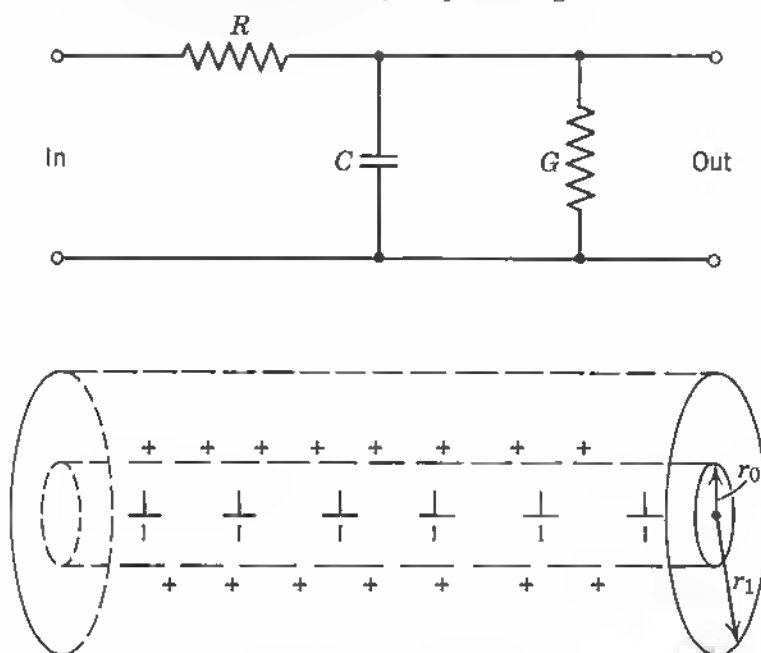


Fig. 9.2 Model of dislocation transmission line.

Since

$$\pi r_1^2(N_d - N_a) = \frac{f}{c},$$

where  $c$  = spacing between dangling bonds,  
we can write

$$P = f\left(\frac{1}{a} - \frac{1}{c}\right), \quad (9.6)$$

and the reciprocal value of  $P \cdot \mu_{pd}$ , where  $\mu_{pd}$  is the hole mobility in the pipe, gives the resistance  $R$ :

$$R = \left[ f\left(\frac{1}{a} - \frac{1}{c}\right) \mu_{pd} \right]^{-1}. \quad (9.7)$$

Now the traveling light spot measurements allow one to measure  $D$  and  $\tau$  by way of signal amplitude  $S$  and phase-shift  $\theta$  measurements of the light spot modulation frequency  $\omega$ :

$$\frac{d[\ln(rS/r_0)]}{dr} = (2D\tau)^{1/2}[(1 + \omega^2\tau^2)^{1/2} + 1]^{1/2}, \quad (9.8)$$

$$\frac{d\theta}{dr} = (2D\tau)^{-1/2}[(1 + \omega^2\tau^2)^{1/2} - 1]^{1/2}. \quad (9.9)$$

Comparing these equations with the network-model equations (9.3) and (9.4), one concludes that

$$\begin{aligned} D_d &= (RC)^{-1}, \\ t_d &= CG^{-1}, \end{aligned} \quad (9.10)$$

where  $D_d$  = effective diffusion constant within pipe,  
 $t_d$  = release time from entrance to exit.

These interesting results allow one to account for the diffusion-length increases measured along the pipe direction.

If one assumes that entrance of holes into the cylinder biases the  $p$ - $n$  junction in the forward direction (lowering of the barrier height), holes leave and electrons enter the  $p$  region. If  $t_r$  = average time of hole in cylinder before recombination and  $t_e$  = average time of hole in cylinder before escape from cylinder, we must have

$$t_e = CG_p^{-1} \quad \text{and} \quad t_r = CG_n^{-1} \quad (9.11)$$

$G_p, G_n$  = conductances for holes and electrons respectively. For the total

drift time one has the relation:

$$\frac{1}{t_d} = \frac{1}{t_r} + \frac{1}{t_e}. \quad (9.12)$$

The fraction of time spent in the cylinder is

$$\eta = \frac{t_d}{t_c + t_d}, \quad (9.13)$$

with

$$t_c = \left[ 2 \left( \frac{2}{3} \right)^{1/2} r_1 \cdot v_T \cdot N_D \right]^{-1}, \quad (9.14)$$

where  $N_D$  = dislocation density,  
 $v_T$  = hole thermal velocity.

The minority carrier lifetime is then

$$\tau = \frac{t_r}{\eta} = \frac{t_r(t_c + t_d)}{t_d}. \quad (9.15)$$

In drift-mobility measurements the time  $t_e$ , defined earlier, is the analog to the trapping time. If the drift field is normal to the dislocation pipes, trapping does not take place, and so the drift velocity is

$$v_d < \frac{r_1}{t_e}. \quad (9.16)$$

If the field increases to a value

$$E_c = \frac{v_d}{\mu_p}, \quad (9.17)$$

trapping occurs and lowers the mobility, and so the effective drift velocity is

$$v_{\text{eff}} = \frac{r_1}{t_e} \eta' + v_d(1 - \eta'), \quad (9.18)$$

where

$$\eta' = \frac{t_c}{t_c + t_e},$$

$v_d$  = normal drift velocity.

If the drift field is applied parallel to the pipes, the effective mobility is

$$\mu_{\text{eff}} = \mu_{pd} \cdot \eta' + \mu_p(1 - \eta'). \quad (9.19)$$

The measurements suggest that  $\eta' \simeq 0.5$  or  $t_c \simeq t_e$ . Thus the effective mobility (9.19) is then

$$\mu_{\text{eff}} = 0.5(\mu_{pd} + \mu_p) \quad (9.20)$$

or the average of pipe and normal drift mobility. These measurements have been made for a dislocation density of

$$N_D = 10^6 \text{ cm}^{-2},$$

leading to the following values:

$$r_1 = 0.8 \times 10^{-4} \text{ cm},$$

$$t_c = t_e = 5 \times 10^{-10} \text{ sec},$$

with  $\eta' \simeq 0.5$  and  $\mu_{\parallel} \simeq \mu_p$ .

The diffusion constant in the pipes  $D_d$  (9.10), as calculated for 20 ohm cm germanium, gives

$$D_d = \frac{1}{RC} = \frac{1}{RG_p t_e} = 200 \text{ cm}^2 \text{ sec}^{-1}.*$$

Actual values used are

$$N_d - N_a = 10^{14} \text{ cm}^{-3}, \quad p_n = 3 \cdot 10^{12} \text{ cm}^{-3},$$

$$E_F - E_V = 0.42 \text{ eV}, \quad L_0 = 2 \cdot 10^{-2} \text{ cm (diffusion length)}.$$

For the condition that  $L_0 \gg r_1$ ,  $G_p$  could be evaluated and  $D_d$  calculated. The dislocation energy level for  $f = 0.1$  and  $c = 4 \text{ \AA}$  was found to be  $E_D - 0.4 \text{ eV}$  below the conduction band:

$$R = 1.2 \times 10^{10} \text{ ohm cm}^{-1} \text{ and } \mu_{pd} \simeq \mu_p.$$

According to this the injected holes spend about half of their lifetime in the inversion cylinders. There the observed value of the diffusion constant lies between the value of  $D_d$  given above and the normal value of  $47 \text{ cm}^2 \text{ sec}^{-1}$ , i.e.  $D_{\text{eff}} \simeq 100 \text{ cm}^2 \text{ sec}^{-1}$ , which is the observed value.

These measurements confirm later studies of the anisotropy of carrier transport in dislocation planes. Since bent and grown dislocated crystals show the same behavior, it is suggested that impurity atmospheres play a minor role in these experiments.

It is already concluded by these authors<sup>4</sup> that the binding energy of the dislocations is a function of the local electric field caused by the space charge. In fact, as we derive in Chapter 11, the space charge widens for increasing orthogonal pipe field, thus establishing increased barrier action for holes, attracting them into the space charge and keeping them within the confines of the dislocation array for higher drift velocities.

Electronic noise measurements on such samples made of silicon crystals

\* Note that  $R$  in ohm/cm  $G$  in mho/cm.

have also shown that the dislocations can act as arrays of acceptors. These act as traps for electrons below room temperature and as recombination centers above room temperature. The energy level of the sites  $E_1$  is  $0.60 \pm 0.03$  eV from the top of the valence band, and the fractional occupation  $f$  (filling factor) is about 0.05 at room temperature.

The potential barrier height  $\phi$  at room temperature is here 0.2 eV for silicon ( $n$ -type of 200 ohm cm).<sup>11</sup>

To complete the picture of the edge dislocation pipe, it has to be pointed out that the array within the pipe is built up of closely spaced dangling bonds or states "pulled out of conduction band."

V. Heine<sup>12</sup> argues that such states arise mainly because of the extra space represented by the dislocation core and should therefore be equally present in the case of screw dislocations without disrupted bonds.

It is difficult at least to clearly establish the fact if a screw-dislocation boundary is really devoid of dangling bonds. As we saw in Section 8.2, the disturbed screw or bent dislocation that does not lie in a single plane parallel to the slip vector can form dangling bonds. Therefore measurements on screw dislocations have to be analyzed carefully with respect to the presence of such bent dislocations. Measurements on edge dislocations and twins have clearly shown the importance of the dangling bond, and it is not unreasonable to associate the dangling electron with an acceptor state before filling and with a donor state after filling. The negative excess charge in the last case is responsible for this level to act as a hole trap.

The model is, however, more complex because of the dependence of the filling factor  $f$  on the voltage applied to the lateral space charge (see later in the text). The increase in  $f$  means a stronger overlap of the individual electronic wave functions within the array and an increased array conductivity. The array behaves like a degenerate piece of semiconductor, the degeneracy being a function of the lateral field across the space-charge domain. A dislocation pipe situated, for example, between a  $p$ - $n$  junction and a contact area acts in two ways (see Figure 9.3a):

1. It carries excess current with increased field between the  $p$ -type layer and the contact.
2. The amount of current is dependent on the lateral field across the space charge, increasing for increased lateral field.

This situation can be the main cause of difficulty in junction devices, for example, in a case where the dislocation runs across a  $p$ - $n$  junction space-charge layer (see Figure 9.3a). It can draw a higher current than the surrounding high-resistivity inversion layer and strongly increase the leakage current. In power devices and junction lasers, for example, such spots are the areas of microplasma formation and burnout. (Compare Chapter 14 Sections 14.1 and 14.2.)

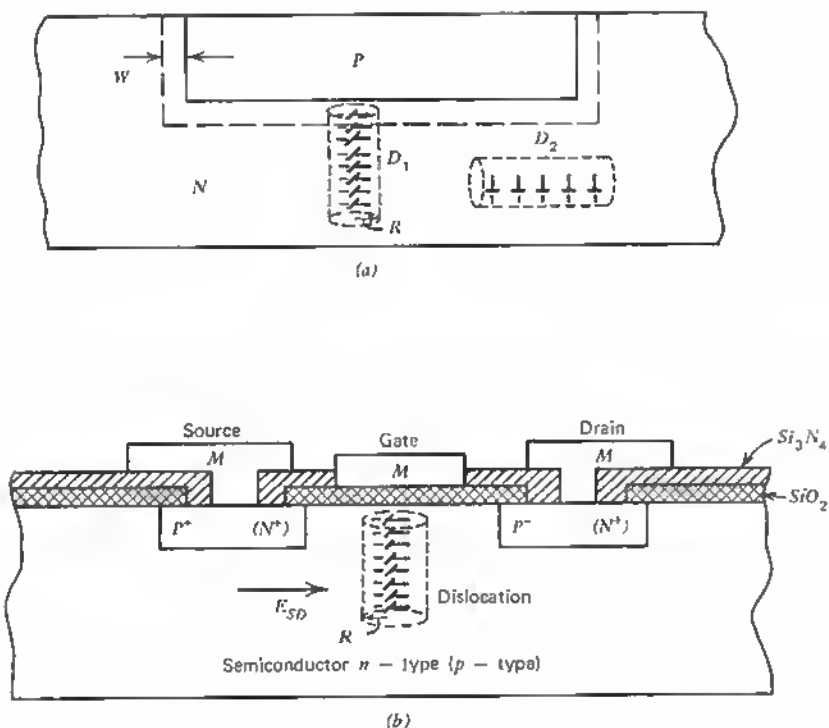


Fig. 9.3 (a) Dislocation  $D_1$ , as shunt in  $p$ - $n$ -junction, shunt emitter-base in planar transistor, or shunt in emitter or collector junction space charge in lateral transistor;  $D_2$  inactive. (b) Dislocation a shunt in  $N$ -channel surface barrier MOS-transistor.

The configuration in Figure 9.3a applies in the case of diode structures and transistors. In the case of a field-effect transistor the additional field  $E$  across the space charge has a widening effect on the pipe, and thus the pipe draws more current through the space charge. In planar transistors pipes could reach the lower collector contact which is not possible in lateral transistor structures. The latter are therefore the logic device forms when numerous dislocations are present, as in all heteroepitaxial material. Figure 9.3b shows the case of a metal oxide semiconductor  $FET$  with an  $N$  channel depletion layer at the gate. There the dislocations in the vertical position are most disadvantageous. In thin-film transistors with surface barriers of the  $P$  channel type, the effects are less pronounced, but in all cases the performance suffers and reproducibility and yield are downgraded. We deal with these questions in some detail in Chapter 14.

## 9.2 SCATTERING BY DISLOCATIONS [STATISTICAL DISTRIBUTION]

If we assume spacially separated dislocations, as presented in Section 8.4, the main effects on carrier flow are due to the impenetrable space-charge pipes and their activity as traps and recombination centers. The treatment by W. T. Read starts with the assumption that electron scattering at the edges of the space-charge tubes is predominantly specular. Broudy<sup>13</sup> made it a specific point to assume "diffuse" scattering, introducing a "diffuse scattering factor  $\theta$ ."

As Read indicates, specular scattering would be applicable in all cases where the spacing  $a = c/f$ , of occupied states within the space-charge cylinder is small compared with the radius  $R$  of the space-charge cylinder, which is the usual case. Read takes the example of  $N_d - N_a = 10^{15} \text{ cm}^{-3}$  (1.7 ohm cm,  $n$ -type germanium). With  $f \approx 0.1$  for  $0 < T < 150^\circ\text{K}$  (dislocation acceptor level at 0.225 eV below the conduction band),  $R$  lies at a value of

$$R = 2830 \text{ \AA},$$

which is large compared with  $a = c/f = 4 \text{ \AA}/0.1 = 40 \text{ \AA}$ . The spacing between excess chemical donors is here

$$\sqrt[3]{\frac{1}{N_d - N_a}} = 10^{-5} \text{ cm} \\ \approx 0.1 \mu = 1000 \text{ \AA}.$$

For higher doping ranges  $f$  increases linearly, since  $f = \pi R^2 c (N_d - N_a)$  and  $a$  decreases for fixed  $c$  (number of available states):

$$R \gg (N_d - N_a)^{-1/3}.$$

Therefore, Broudy's conditions

$$R \gg (N_d - N_a)^{-1/3} \gg a \quad (9.21)$$

should be maintained for normal doping ranges.

The treatment of the space-charge cylinders as holes or voids in isotropic conductors starts with the assumption that a fraction  $\varepsilon$  of the volume is occupied by the space-charge cylinders:

$$\varepsilon = R^2 \cdot N_s, \quad (9.22)$$

where  $N_s$  = number of dislocations per  $\text{cm}^2$ . We define an actual average electron concentration:

$$\langle n \rangle = n(1 - \varepsilon), \quad (9.23)$$



or

$$\varepsilon = 1 - \frac{\langle n \rangle}{n}. \quad (9.24)$$

The electron depletion  $\delta n$  per centimeter of dislocation is

$$\delta n = \pi R^2 (N_d - N_a) = \frac{f}{c} = \frac{1}{a} \quad (9.25)$$

see (8.11). The total relative electron depletion  $\varepsilon$  due to the existence of  $N_s$  dislocations is then

$$\varepsilon = \frac{\delta n \cdot N_s}{N_d - N_a} = N_s \pi R^2 = \frac{N_s \cdot f}{C(N_d - N_a)}, \quad (9.26)$$

where  $N_s \cdot f/c = N_s/a$  = number of dislocation acceptors per  $\text{cm}^2$ .

In this form  $\varepsilon$  is a measure of  $f$ , the filling factor of the dislocations, if their number and the general impurity concentration are known.

As the electrons  $\langle n \rangle$  taking part in the conduction process wind through the space-charge cylinders, their mobility is reduced and therefore also the conductivity.

Assuming that a field is applied in the  $x$  direction, the average field  $\langle E_x \rangle$  is different from the local field  $E_x$  and also from the average field  $\langle E_x \rangle_n$  which is active just over the normal material. Introducing a weighting factor (distortion factor)

$$g(\varepsilon) = \frac{\langle E_x \rangle_n}{\langle E_x \rangle}, \quad (9.27)$$

$g(\varepsilon)$  defines the relative contribution of the field in the neutral  $n$ -type material to the average field. We can express the sample current

$$\langle I_x \rangle = e\mu \langle n \rangle \langle E_x \rangle_n \quad (9.28)$$

as

$$\langle I_x \rangle = e\mu \langle n \rangle \langle E_x \rangle g(\varepsilon) \quad (9.29)$$

or with (9.23)

$$\langle I_x \rangle = e\mu n (1 - \varepsilon) \langle E_x \rangle_n. \quad (9.30)$$

Now  $\langle I_x \rangle / \langle E_x \rangle_n$  defines the effective conductivity

$$\sigma_{\text{eff}} = e\mu n (1 - \varepsilon), \quad (9.31)$$

and the conductivity in  $n$ -type material only amounts to

$$\sigma = \frac{\langle I_x \rangle_n}{\langle E_x \rangle_n} = e\mu n. \quad (9.32)$$

The actually measured conductivity  $\sigma^*$  is therefore

$$\sigma^* = \frac{\langle I_x \rangle}{\langle E_x \rangle} = \sigma_{eff} \frac{\langle E_x \rangle_n}{\langle E_x \rangle} \quad (9.33)$$

or

$$\begin{aligned} \sigma^* &= e\mu n(1 - \varepsilon)g(\varepsilon) \\ &= \sigma(1 - \varepsilon)g(\varepsilon) \quad (\text{as } \varepsilon \rightarrow 0, g(\varepsilon) \rightarrow 1 \text{ and } \sigma^* \rightarrow \sigma). \end{aligned} \quad (9.34)$$

The relation between measured and local conductivity is

$$\begin{aligned} \frac{\sigma^*}{\sigma} &= \frac{\langle n \rangle}{n} \frac{\langle E_x \rangle_n}{\langle E_x \rangle} \\ &= \frac{\langle n \rangle}{n} \cdot g(\varepsilon) \end{aligned} \quad (9.35)$$

or with the current equations

$$\begin{aligned} \langle I_x \rangle &= e\mu \langle n \rangle E_x \\ \langle I_x \rangle_n &= e\mu n E_x \\ \frac{\sigma^*}{\sigma} &= \frac{\langle I_x \rangle}{\langle E_x \rangle} \frac{\langle E_x \rangle_n}{\langle I_x \rangle_n} \end{aligned} \quad (9.36)$$

In the simple-void model an increase in the number of cylinders would increase  $\varepsilon$  or decrease  $g(\varepsilon)$ . Finally, for complete overlap, when all space-charge cylinders touch each other,  $g(\varepsilon) = 0$ . For small values of  $\varepsilon$  ( $\varepsilon < 0.7$ ),  $g(\varepsilon)$  can be represented by  $(1 + \varepsilon)^{-1}$ . Broudy<sup>13</sup> discusses the three main cases of orientation of the pipes with respect to electric and magnetic field vectors, based on Read's model.

We have plotted these cases in Figures 9.4 and 9.5.

Figure 9.4 shows the sample orientation with regard to the pipe orientations. The pipes can have three different basic orientations in the sample, *A*, *B* and *C*. If the electric field vector  $E_e$  (current vector  $I$ ), the magnetic field vector  $H$ , and the Hall field vector  $E_H$  are fixed as a coordinate system, case *A* represents the usual configuration in which the current flow is orthogonal to the pipe direction and the magnetic field in the pipe direction. In case *B*, the magnetic field is orthogonal to the pipe, and the current runs along the length of the pipes; and in case *C* one has a case like *A* with respect to current flow but with the magnetic field orthogonal to the pipe direction. Although Read considers only cases *A* and *C* in detail, Broudy discusses all three.

Logan, Pearson, and Kleinman<sup>5</sup> remarked that Read's treatment neglected the dislocation effect by the pipes, dealing only with the scattering. Obviously

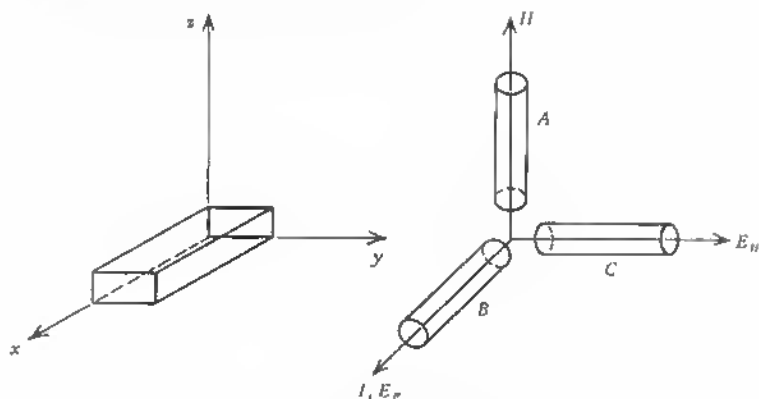


Fig. 9.4 Basic orientations of dislocation pipes with respect to:  $I$ ,  $E$ ,  $H$ . ( $E_H$  = Hall field).

the introduction of space-charge pipes increases the average electric field, which is equivalent to a decrease in mobility. Also, the inhomogeneity in electron distribution would have to be considered.

These effects operate on the electron distribution in momentum or  $k$  space. Logan et al. obtain the mobility reduction due to distortion and scattering by multiplying the separate reduction factors.

Another improvement of their treatment is concerned with the ratio of Hall to drift mobility.

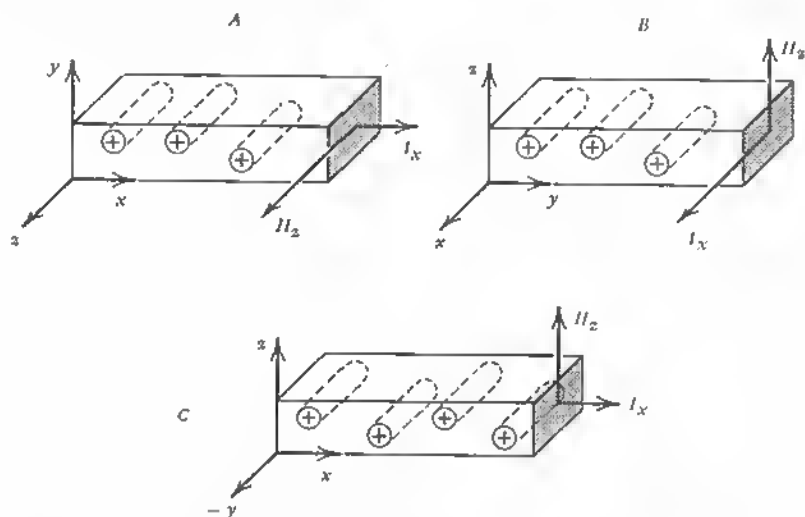


Fig. 9.5 Corresponding three cases for current flow and magnetic field direction in relation to pipe direction.

Changing over from the spherical conduction-band valley to four ellipsoidal energy surfaces, this value changes from

$$\frac{\mu_H}{\mu_d} = \frac{3\pi}{8} \quad (9.37)$$

to

$$\frac{\mu_H}{\mu_d} = 1. \quad (9.38)$$

In the trivial cases

$$(a) \quad \mathbf{H} = 0 \quad \mathbf{I} \parallel D,$$

$$(b) \quad \mathbf{H} = 0 \quad \mathbf{I} \perp D,$$

the effective mobility  $\mu(\varepsilon)$  is given as

$$(a) \quad \mu(\varepsilon) = \mu, \quad (9.39)$$

$$(b) \quad \mu(\varepsilon) = \mu g(\varepsilon) F(X). \quad (9.40)$$

In case *a*, the pipes are disregarded altogether. For low-mobility bulk material and high dislocation density, this could be a fallacy because of the relatively high mobility within the space-charge pipes.

In case *b* the distortion factor  $g(\varepsilon)$  and the scattering factor  $F(X)$  are multiplied in the result.  $F(X)$  has been derived by Logan et al. and is given by

$$F(X) = \frac{3}{2} \int_0^{\pi/2} \frac{\sin^3 \phi}{1 + X \sin \phi} d\phi, \quad (9.41)$$

where  $X = \text{ratio } l/l_D$ ,

$l = \text{mean free path, bulk,}$

$l_D = \text{mean free path due to dislocation scattering}$

$$l_D = \frac{3}{8} \left( \frac{\pi}{N\varepsilon} \right)^{1/2}, \quad (9.42)$$

$N = \text{dislocation density,}$

$F(X)$  has the bounds 0 and 1 (see Figure 9.6),

$F(X)$  is 0.5 for  $X = 1$  and approaches 1 for decreasing  $X$  and 0 for increasing  $X$ ,

$\phi = \text{scattering angle (see Figure 2.23),}$

For  $\mathbf{H} \neq 0$  we always assume  $\mathbf{H} \perp \mathbf{I}$ .

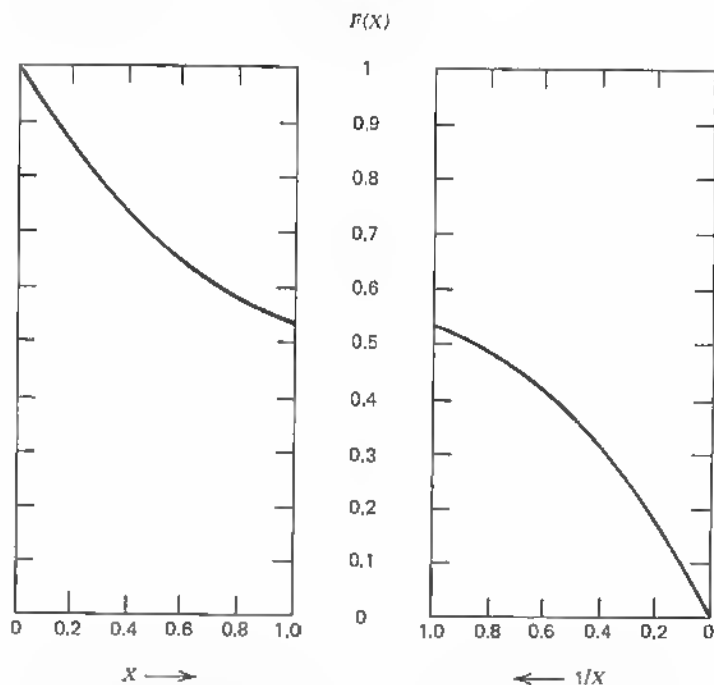


Fig. 9.6 Scattering factor:  $F(X) = 3/2 \int_0^{\pi/2} \sin^3 \phi / (1 + X \sin \phi) d\phi$ ,  $X = l/l_D$ ,  $l$  = mean free path in bulk,  $l_D$  = mean free path in dislocated area.

### Magnetic Field Parallel to the Dislocations

CASE A. The Hall field is normal to the dislocations and assumed to be of small magnitude (no current flow in  $z$  direction):

$$\mathbf{I} = e\mu n\mathbf{E} - \frac{\mu_H}{c} \mathbf{I} \times \mathbf{H}, \quad (9.43)$$

where  $\mu_H$  = Hall mobility,  
 $c = 3 \cdot 10^{10}$  cm/sec.

The  $y$  component of the field  $E$  in (9.43) gives

$$\langle I_x \rangle \frac{\mu_H \cdot H_z}{c} = e\mu \langle nE_y \rangle \quad (I_y \equiv 0). \quad (9.44)$$

With

$$\begin{aligned} \frac{\langle nE_y \rangle}{\langle E_y \rangle} &= \frac{\langle nE_x \rangle}{\langle E_x \rangle} \\ &= \langle n \rangle g(\varepsilon) \end{aligned} \quad (9.45)$$

from symmetry, we can write

$$\langle I_x \rangle \frac{\mu_H H_z}{c} = e\mu \langle n \rangle \langle E_y \rangle g(\varepsilon). \quad (9.46)$$

The Hall angle is

$$\begin{aligned} \theta &= \frac{\langle E_y \rangle}{\langle E_x \rangle} \\ \theta &= \mu_H \cdot \frac{H_z}{c}, \end{aligned} \quad (9.47)$$

or unchanged by the dislocations.

In this treatment we have assumed, like Read, that there is no current flow parallel to the dislocations, which is correct as long as their alignment is precise.

### Magnetic Field Perpendicular to the Dislocations

CASE B. In this case, Broudy assumes that the electrons in the dislocation acceptors make a negligible contribution to the conductivity in the  $x$  direction. This is by no means the case. As we describe later, a dislocation pipe acts like a line charge or a filament of degenerate material with high conductivity. The higher their number, the greater their contribution to the carrier flow in the longitudinal direction ( $x$  in case B). The Hall voltage develops in the  $y$  direction perpendicular to the pipes. Broudy finds that the Hall constants with and without dislocations should relate to each other as

$$\frac{R}{R_0} = \frac{1}{(1 - \varepsilon)} = \frac{n}{\langle n \rangle}. \quad (9.48)$$

This model cannot describe the facts due to another aspect. If the dislocation space charge (pipe) is subjected to a lateral field (here the Hall field  $E_y$ ), the space charge widens like any  $p$ - $n$  junction under bias and the pipe increases in conductivity.

CASE C. This case is discussed in detail by Read and leads to the result that the Hall angle is

$$\theta = \frac{\mu_H \cdot H_z}{c} g(\varepsilon) \quad (9.49)$$

or that the dislocations reduce the Hall angle, since  $g(\varepsilon) < 1$  (the scattering factor  $F(X)$  is assumed equal to 1).

Here again the Hall field  $E_y$  would induce a current along the pipes, and because of the much stronger field  $E_x$ , perpendicular to the pipes in this case, the space charge would widen considerably and the pipe conduction cannot be discarded. (This refers also to the treatment by Logan et al.<sup>5</sup>)

Broudy notes for this case that neither

$$\text{grad } E \quad \text{nor} \quad \text{curl } I$$

would disappear, but  $\nabla \times E$  as well as  $\nabla I$  are zero. Current components in the  $y$  direction definitely change all assumptions. It is also known that the mobility within the pipes is relatively high (see Chapter 11). In Figure 9.7 we have tabulated the values of interest for the three main cases  $A$ ,  $B$ , and  $C$  (Read, Broudy, Logan, et al.). The index 0 refers to the value without dislocations.

The dislocation pipe scattering or its influence on the mean free path was discussed in Section 2.10. The ratio of mean collision time  $\tau_c$  to the mean free time  $\tau_1$  is equal to the scattering parameter:

$$\frac{\tau_c}{\tau_1} = \langle 1 - \cos \theta_1 \rangle.$$

Read pursues this analysis in order to find an expression for the ratio of Hall mobility for combined thermal and dislocation scattering to Hall mobility for thermal scattering alone. His assumptions that:

1. The fields  $E$  and  $H$  are constant throughout the material
2. The velocity distribution of the electrons incident on the pipes is the same as the average distribution over the material

are reasonable but are limited to the case of large dislocation pipe spacing. Although Read assumes that  $\Delta v = \Delta v_1$  (specular reflection), Broudy suggests a space-charge cylinder with a smooth region  $l$ .  $l$  is added to the space-charge cylinder  $R$  and is assumed to be of the order of  $\frac{1}{6}R \simeq 1\text{MFP}$  (mean free path). In this way measured data of magnetoresistance are fitted to theoretical values on account of the simple scattering model.

There is no doubt that these models can be used to predict resistance and Hall data correctly for the case of wide dislocation spacing (low density), exact alignment in one crystallographic direction and simple geometry as in case  $A$ .

Logan, Pearson, and Kleinman have shown that bent samples with the dislocations running in the  $\{112\}$  direction, for example (see Figure 9.8), display remarkable anisotropy. Current flow parallel to the dislocation pipe

Case	Magnetic field direction	Current direction	Hall angle $\theta$	Hall constant $R$	Conduct. rel. $\sigma/\sigma_0$	Hall angle rel. $\theta/\theta_0$	Hall constant rel. $R/R_0$
A	$H \parallel D$	$I \perp D$	$\mu_H \cdot \frac{H}{c}$	$\frac{\mu_H}{\mu_D} \cdot \frac{1}{ecn}$	$\frac{1-\varepsilon}{1+\varepsilon}$	1	1
B	$H \perp D$	$I \parallel D$	$\mu_H \cdot \frac{H}{c}$	$\frac{\mu_H}{\mu_D} \frac{1}{ec\langle n \rangle}$	$1-\varepsilon$	1	$\frac{n}{\langle n \rangle} = (1-\varepsilon)^{-1}$
C	$H \perp D$	$I \perp D$	$\frac{\mu_H \cdot H}{c} g(\varepsilon)F(X)$	$\frac{\mu_H}{\mu_D} \frac{1}{ec\langle n \rangle}$	$\frac{1-\varepsilon}{1+\varepsilon}$	$g(\varepsilon)F(X)$	$\frac{n}{\langle n \rangle} = (1-\varepsilon)^{-1}$

Fig. 9.7 Table of major electronic transport constants depending on direction of magnetic field  $H$  and current  $I$  with respect to dislocation pipe axis  $D$ .



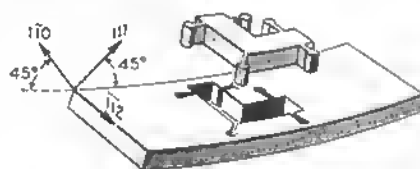


Fig. 9.8 Samples as cut from wafer uniformly bent about  $(112)$  axis. (After Logan, Pearson and Kleinman [9.5].)

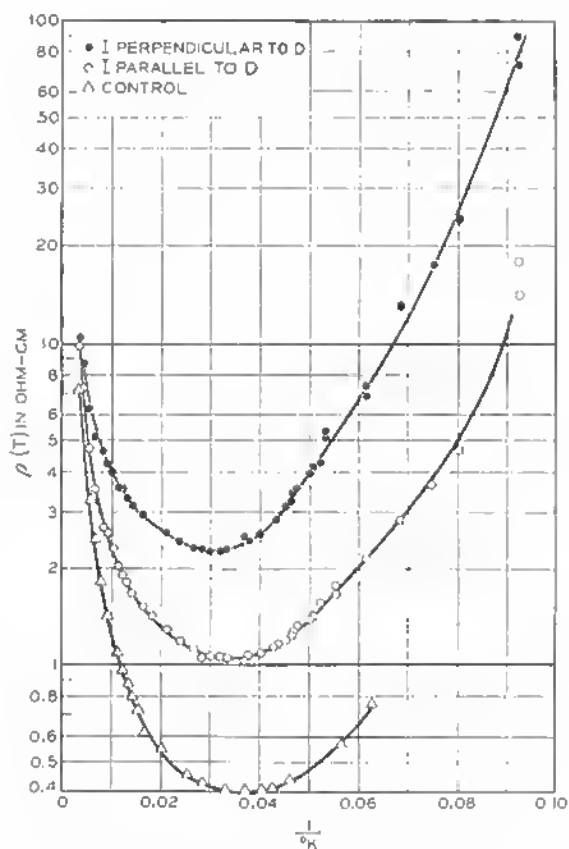


Fig. 9.9 Measured resistivity as function of  $1/T$ . (After Logan, Pearson and Kleinman [9.5].)

axis  $D$  shows a much less increased resistivity than current flow perpendicular to the pipes ( $I \perp D$ )—see Figure 9.9. The carrier mobility for the case of  $I \perp D$  shows a decrease roughly given by (9.40) and no mobility change in the case of  $I \parallel D$  (see Figure 9.10). The change of  $\varepsilon$  (9.23) has been plotted by these authors and shows relatively low values for 300°K (see Figure 9.11).

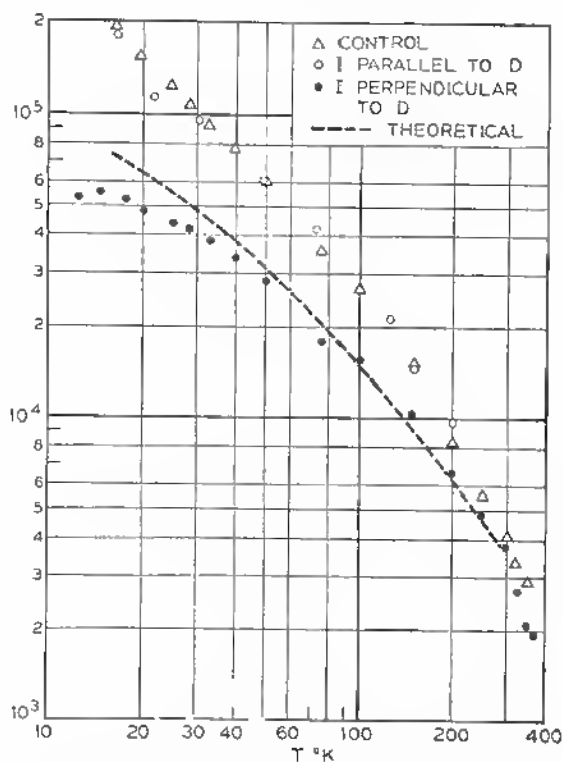


Fig. 9.10 Mobility as function of  $T$ . Theoretical curve calculated from (9.40). (After Logan, Pearson and Kleinman [9.5].).

In all cases, however, where lineage occurs or dislocations are clustered and where random orientation predominates, the very strong space-charge effects and the strong pipe conduction have to be considered in order to understand the effects of dislocations on carrier-transport phenomena. These data are discussed later in connection with the properties of grain-boundary planes, accessible to measurements (see Chapter 11).

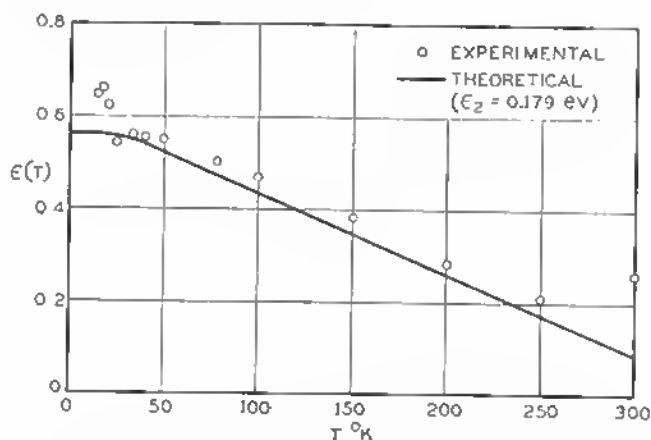


Fig. 9.11 The function  $\epsilon$  defined by (9.23) showing experimental points and theoretical fit for  $E_D = 0.179$  eV. (After Logan, Pearson and Kleinman [9.5].)

### 9.3 THE EDGE DISLOCATION AND RESULTING SPACE CHARGE

The question of the actual width of the space charge and its importance for carrier transport is of primary concern in solving problems of device performance, reproducibility, and yield.

Especially in modern high-density microcircuitry the chances to meet a dislocation have to be minimized. A dislocation density of  $10^5 \text{ cm}^{-2}$  means, for example, that junctions of the size of  $1000 \mu^2$  meet with one dislocation on the average. In power devices of large dimensions the action of several dislocations vertically arranged to the junction space-charge layer can produce gradual or catastrophic changes especially under applied fields. Within junction space-charge layers the field is high and generally of the order of  $10^5$  to  $10^6 \text{ V/cm}$ .

Therefore, it is our concern to assess the real importance of mainly the edge dislocation space charge for crystal performance.

Early measurements on dislocations by point-to-point probing are not conclusive because of the point extension beyond the dislocation range or the surface potential problems, discussed in Chapter 8.

The contact or light spot probing of grain-boundary layers is discussed in Chapter 10. Here we describe the results of electron-beam scanning of individual dislocations on crystal surfaces.

Extensive studies have been made of the surface and subsurface of semiconductor crystals and of devices by the use of the scanning electron microscope (SEM). The electron-beam probing, however, has been extended beyond

the typical SEM mode. R. F. W. Pease<sup>14</sup> recently described the three main signal derivations from a sample under SEM study:

1. Secondary electron emission
2. Recombination radiation
3. Induced current across the sample surface or subsurface

Actually methods 2 and 3 are not SEM in the strict sense. In the cases reported here, an electron microprobe was used with a scanning attachment.

Each of the methods, 1 to 3 has specific applications, depending on the kind of materials and configurations under study. For the detection of inhomogeneities in semiconductors (crystals, devices, microcircuits), method 3 has shown great promise and versatility. In this case we call the method SEB (scanning electron beam). Because here the sample current is monitored, the method reveals regions of varied conductivity like metallizations, barrier layers, semiconductor surfaces, and a beam-induced electron-hole pair generation changes the current in proportion to the number of carriers excited. This again is a function of the crystal surface and subsurface condition, with local high-field regions being more effective carrier-generation areas. Numerous oscillograms have been made in the past on semiconductor devices and microcircuits using all three methods.<sup>15, 16</sup> Although defect metallizations, junction misalignments, and breakdown areas are easily located, individual dislocations have been seen only where the dislocation is located directly within or near the space charge of a diffused junction.<sup>17</sup>

In what follows we describe the imaging of individual dislocations with their space charge by the simultaneous application of a high local surface field and electron beam excitation with scanning.

The general setup is shown in Figure 9.12. The semiconductor crystal or film under study is covered by two metal electrodes (evaporated aluminum or other metal layer) separated by a small distance (millimeter range) to apply a sizable field across the surface to be scanned ( $E \approx 10^3$  V/cm). In this way the localized space-charge regions around dislocations and defects are biased to produce visible carrier density differences at both barrier sides. Here no diffusion is applied to produce a high field. The barrier present is due to the dislocation space charge and is widened and made visible in the SEB. A diffused junction would not allow one to assess clearly localized barriers under varied field conditions in a surface scanning mode. The electron beam generates electron-hole pairs separated at the dislocation junction or defect junction. One has to keep in mind that surface damage also, like scratches, causes dangling bonds and that these also build up a surrounding space charge, as we shall show. The instrument used in this case was the Applied Research Laboratories (ARL) electron microprobe x-ray analyzer (EMX), which contains the basic microprobe, beam-scan console, analog recorder, and digital recording system with additional peripheral device operation or sample biasing

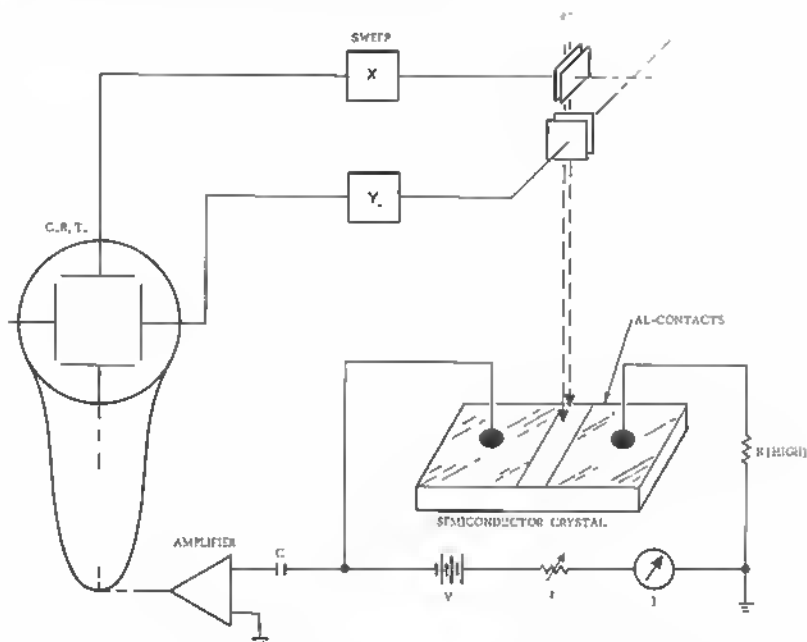


Fig. 9.12 Sample arrangement in scanning electron microscope set (schematic).

equipment. Beam voltages are of the order of 10 to 30 kV, with beam currents in the order of  $10^{-7}$  amp.

In order to calibrate this method it is desirable to start with samples with well-known defect structures. To this end, first germanium bicrystals, artificially grown from tilted perfect double seeds are used. Tilt angle is  $\theta = 10^\circ$ , individual seed orientation is  $[100]$  in order to avoid twinning. Twist angle and rotational misfit (screw components) are kept below  $1^\circ$  each.<sup>18</sup> Dopant is antimony (Sb), and the bulk resistivity is 0.1 ohm cm. Dislocation density in the bulk is  $N_D < 6 \times 10^3 \text{ cm}^{-2}$ .\*

These bicrystals are grown for photoelectronic devices and are small enough (1 by 1 by 0.5 mm) to be contacted at the ends for operation as  $n$ - $p$ - $n$  devices with an extremely thin  $p$ -type center layer.<sup>18, 19</sup> This causes a double barrier in the center of the crystal in the unbiased state. If the electron beam moves across the grain-boundary barrier (in a horizontal mode without scanning) the double barrier appears clearly (see Figure 9.13). The small replicas of the

\* Such bicrystals are produced by Metallurgie Hoboken, Belgium, and have been kindly supplied for such studies.

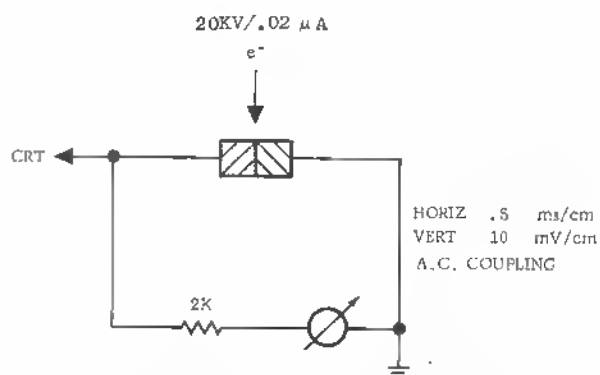
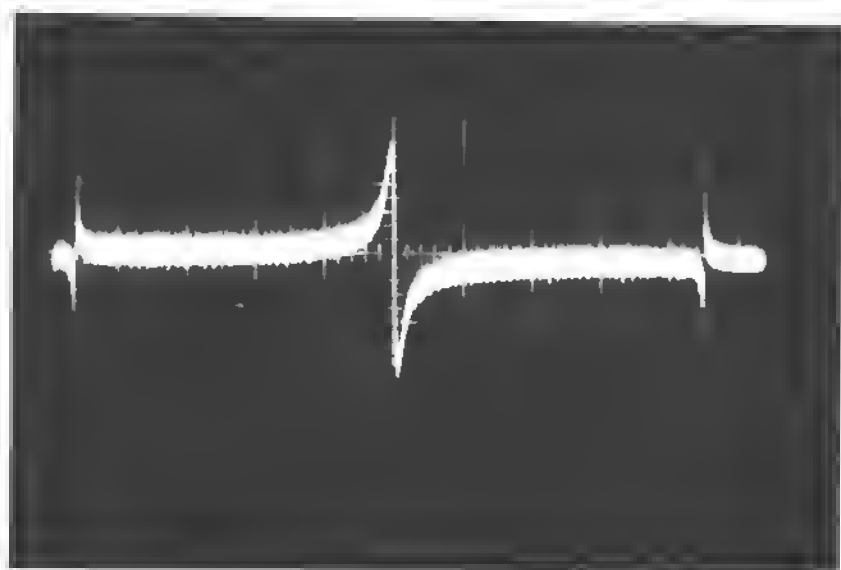


Fig. 9.13 X-scanning of germanium bicrystal without bias ( $n$ - $p$ - $n$  structure).

central barrier at both sides of the oscillograms are due to the retrace signals and can be disregarded.

When bias is applied, one of the  $n-p-n$  barriers is forward-biased and thus does not produce a voltage drop. In this case only one peak can appear (see Figure 9.14).

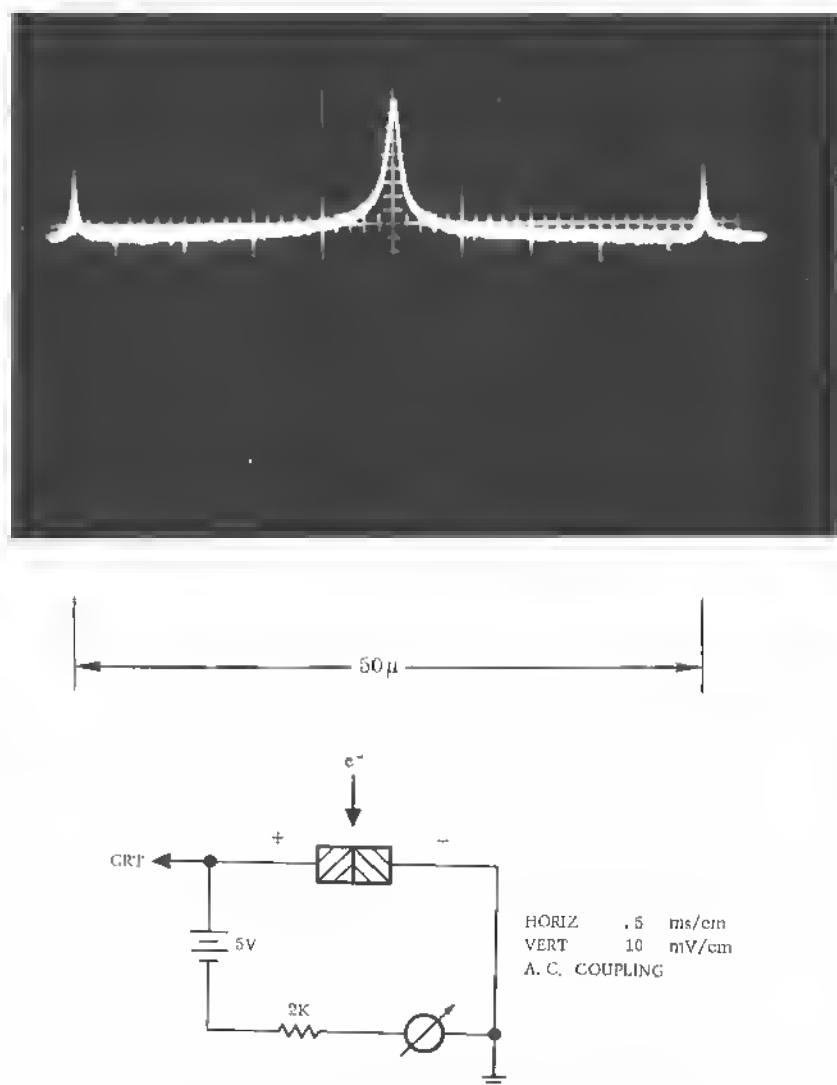


Fig. 9.14 X-scanning of germanium bicrystal with bias (showing left barrier layer).

In the scanning mode the whole grain-boundary barrier appears (see Figure 9.15). Here no bias is applied, and the dislocation plane appears as a bright line in the center, its width is about  $2\ \mu$  and corresponds to the barrier-layer width at both sides of the central grain boundary, which is about  $100\ \text{\AA}$  wide.

With bias applied in one direction, a darker line appears at the right of the bright line (see Figure 9.16), and in a reversed bias mode the dark line appears at the left of the central grain boundary (see Figure 9.17). The change in the direction of the depletion region (light side) is clearly visible in the oscillogram taken while the bias polarity is switched back and forth, as shown in Figure 9.18.

In such samples where a grain boundary divides the entire cross section, the outer bias voltage is not even necessary for visibility. Working with a smaller resistor, as in Figure 9.15 and using dc coupling instead of ac coupling would also produce a strong barrier picture. This behavior can be expected on account of the buildup of a symmetric grain boundary, as illustrated schematically in Figure 9.19.<sup>18, 19</sup> While the innermost disturbed region (energy  $\Delta E$ , in Figure 9.19) is only about  $100\ \text{\AA}$  wide,<sup>19, 20</sup> the space charge can have wide extension up into the range of many microns.

Individual edge dislocations are not so easy to subject to a biasing field especially when they run vertically to the surface. With appropriate bias and surface conditions, however, similar SEB pictures can be obtained also on these circular space-charge domains.

Germanium and silicon monocrystals of low dislocation count can be prepared so that a group of dislocations may be subject to a surface field. The voltage to be applied across evaporated contacts is somewhat dependent on the resistivity of the material.

For 2 ohm cm germanium and 10 ohm cm silicon, for example, and an electrode spacing of 1.5 mm, a typical voltage value of 65 volts proved to be sufficient (or a field of  $\approx 400\ \text{V/cm}$ ) and revealed clearly the circular space charge around the dislocation sites.

In Figure 9.20 a germanium sample is scanned, showing triangular etch pits in  $[111]$  orientation, usually seen in microtwinning regions. As seen from their light and dark regions, they are associated with space charge and disrupted bonds. The silicon sample (see Figure 9.21) is marked by similarly extended ( $20\ \mu$ ) space-charge domains around the edge dislocation  $[111]$ .

Smaller dislocation spots are visible, only a few microns in diameter. The diameter of the space-charge pipe also depends on the amount of misfit and the direction of the dislocation line with respect to the surface, the inclined position resulting in extended spots and the  $90^\circ$  position in minimum spot size approaching the theoretical space-charge pipe extension.

In Figure 9.21 surface damage in the form of scratches is also seen. We discuss this later.



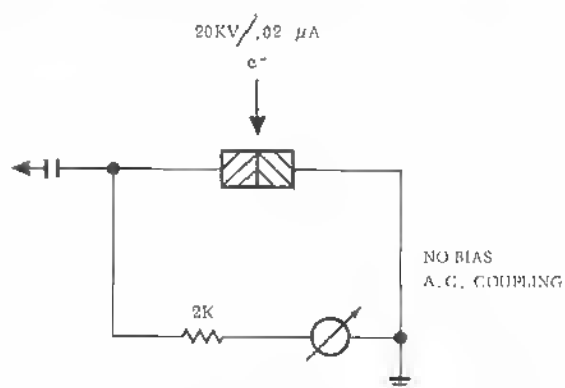
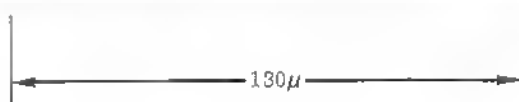
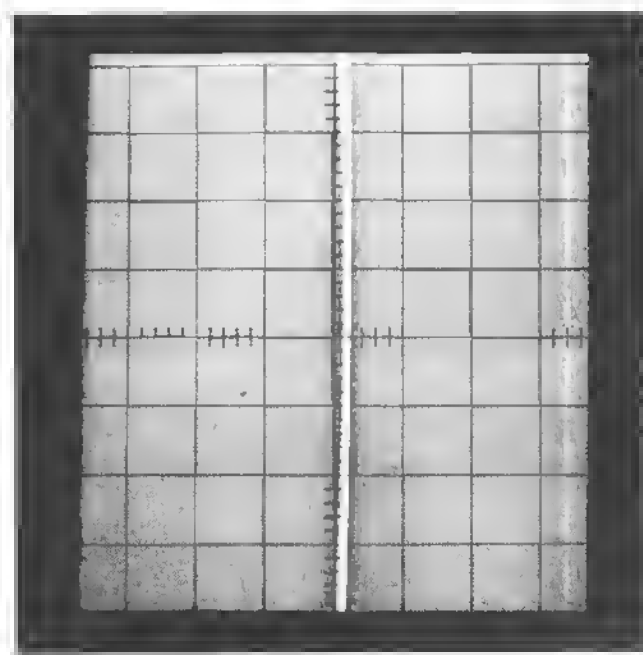


Fig. 9.15 X-Y scanning of bicrystal without bias ( $n-p-n$  structure).

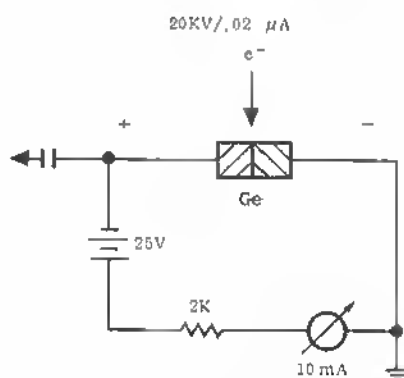
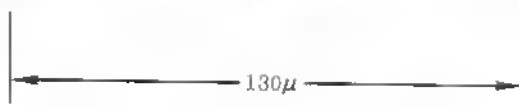
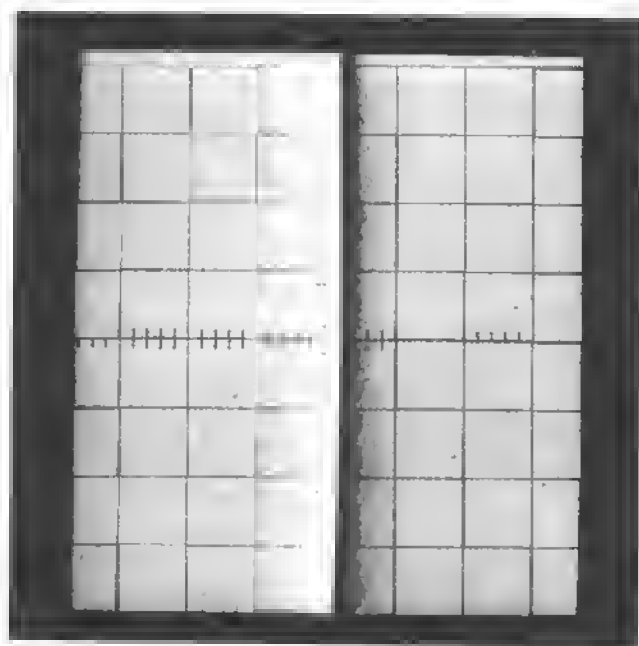


Fig. 9.16 X-Y scanning of bicrystal with bias (showing barrier layer at left).

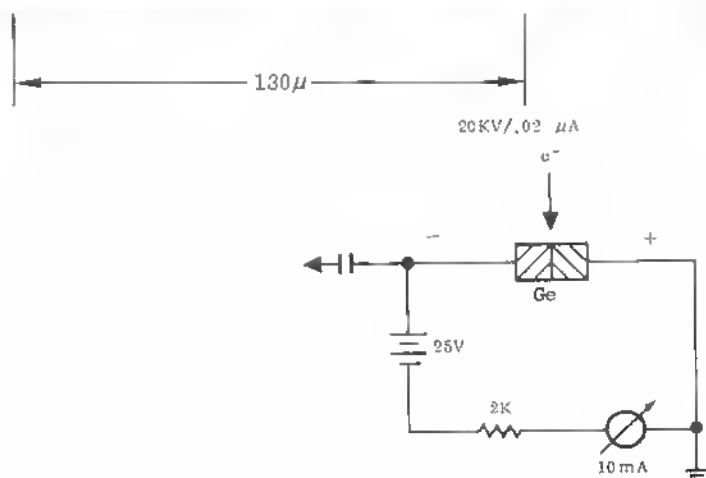
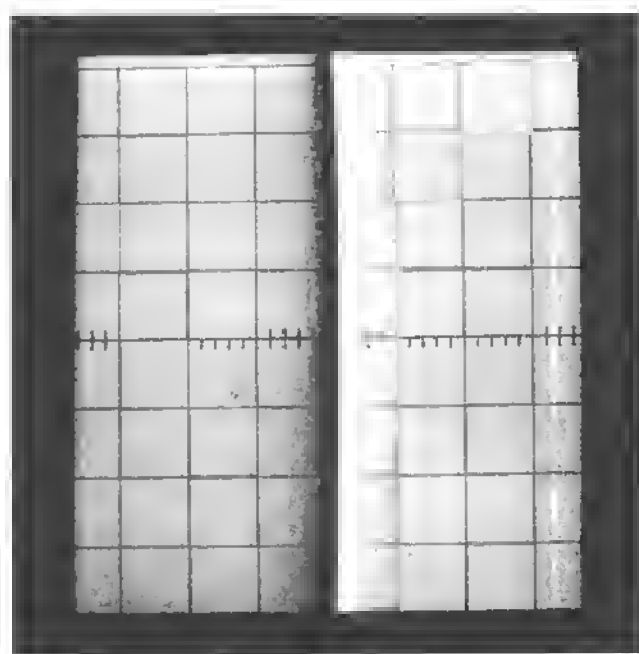


Fig. 9.17 X-Y scanning of bicrystal with reversed bias (showing barrier layer at right).

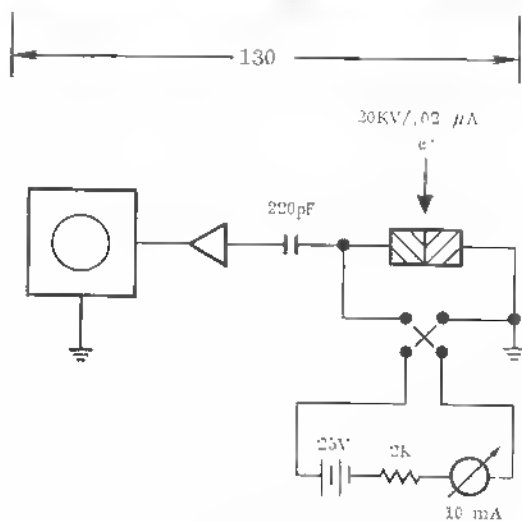
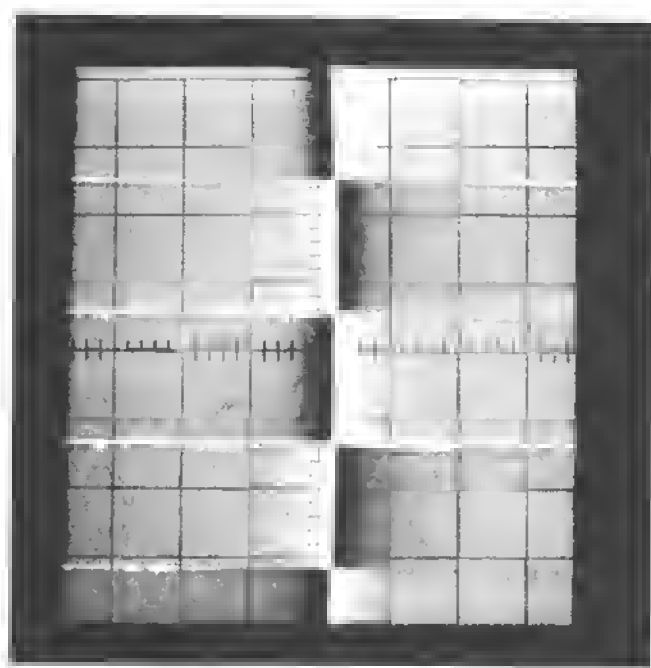


Fig. 9.18 Germanium bicrystal sample under X-Y scanning with cyclic bias reversal.

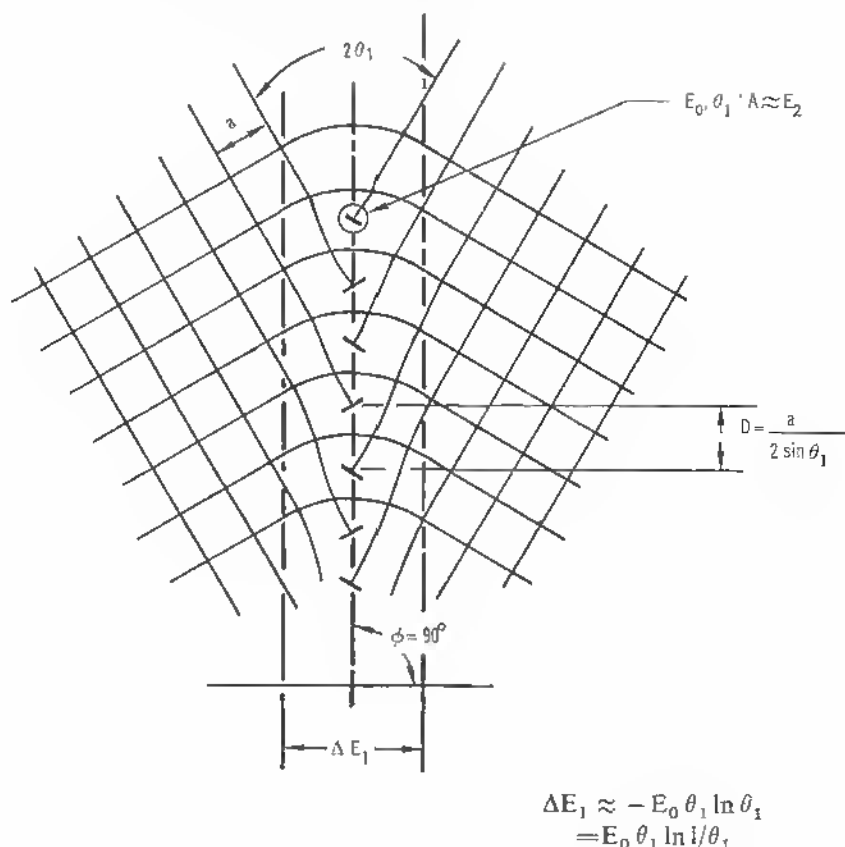


Fig. 9.19 Model of symmetric grain boundary in hypothetical cubic lattice.

Considering the model of an edge dislocation in a homopolar lattice, we are led to the conclusion that the additional half plane of free- or dangling bonds forms a space charge. The negative core charge in germanium, and in most cases also in silicon, is produced by attraction of free electrons to the dangling bonds in a hybridized bonding. This gives rise to a localized space charge. In an extended lattice structure the lattice points within the additional half plane form a line charge around which a space-charge cylinder is established. The properties of these space-charge cylinders have been described first by W. T. Read,<sup>21</sup> and their electronic behavior has been the subject of further work.<sup>19, 22, 23, 24</sup> According to Read's model, the edge dislocation forms a

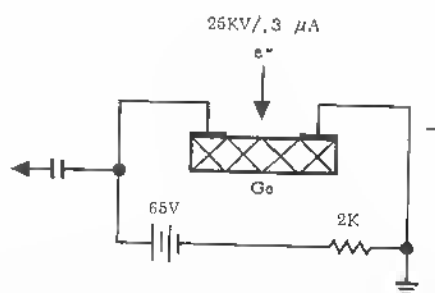
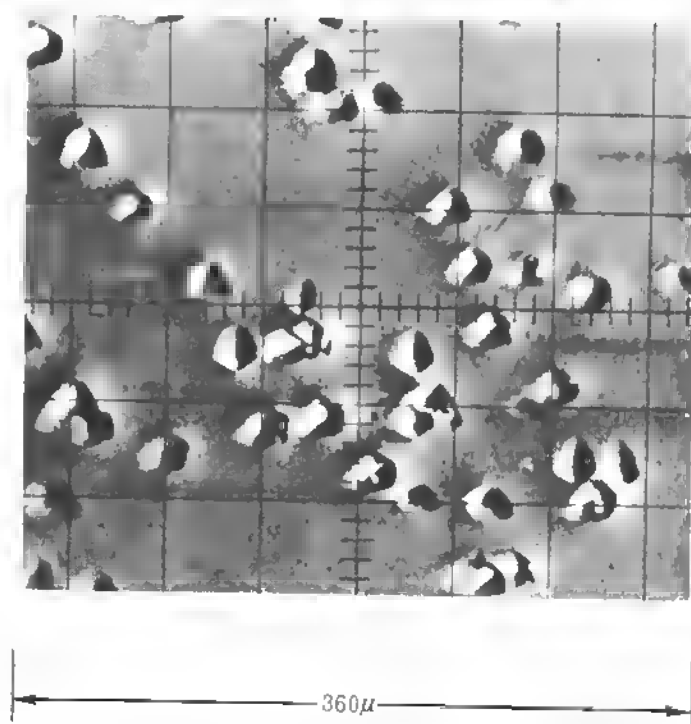


Fig. 9.20 SEB picture of germanium monocrystal ( $2\Omega\text{ cm}$ , Sb-doped) with triangular dislocations (microtwins) under lateral bias condition.

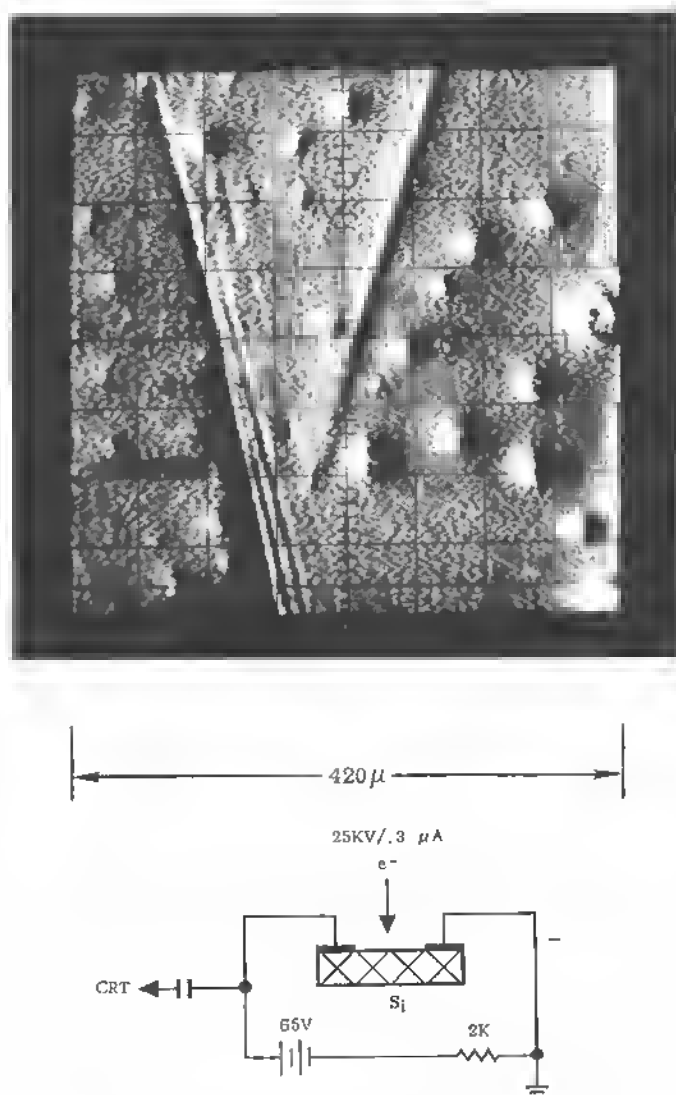


Fig. 9.21 SEB picture of silicon monocrystal ( $10\ \Omega\ \text{cm}$ ) with edge dislocations at surface under lateral bias condition.

space-charge pipe, as shown in Figure 9.22. Actually, the space-charge pipe comprises hundreds of lattice points but is reduced here for obvious reasons. The application of a field of the sign indicated biases one side of the  $n$ - $p$ - $n$

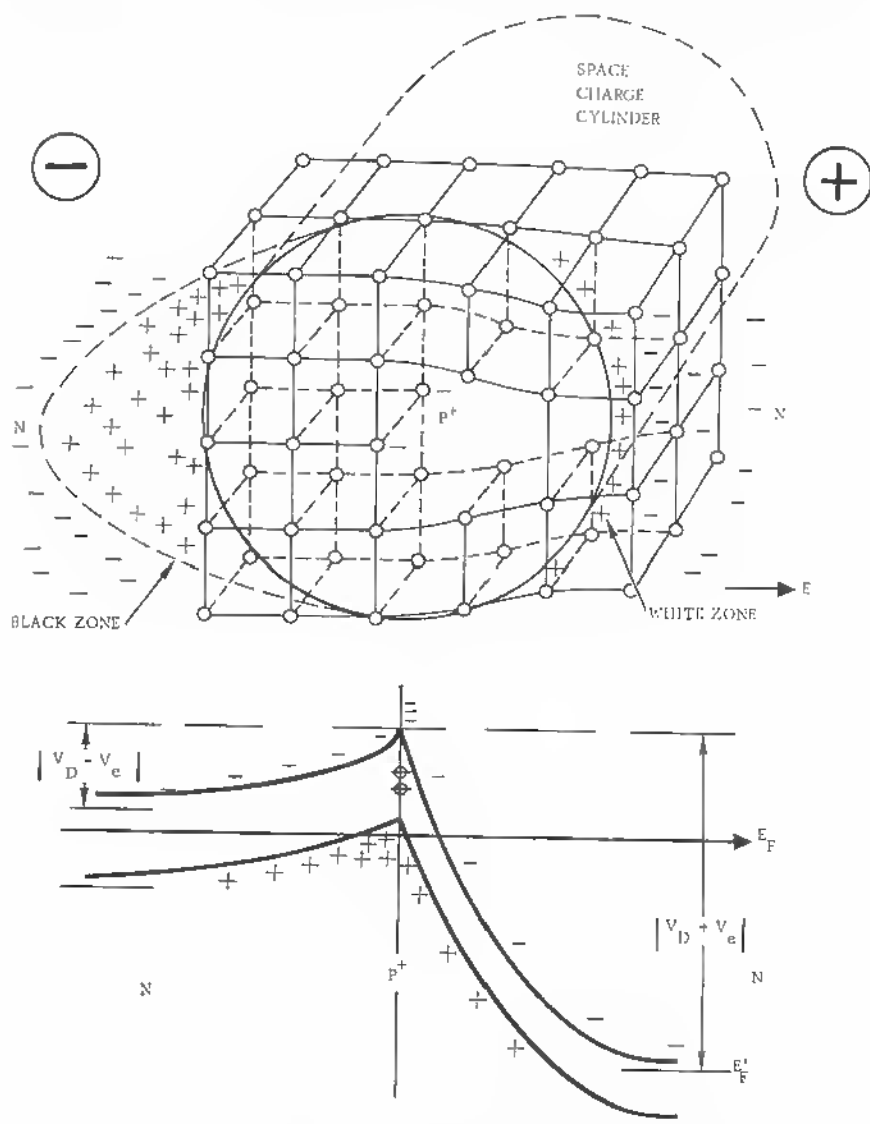


Fig. 9.22 Model of edge dislocation space charge pipe in hypothetical cubic case and band structure.



structure in the forward direction, limiting the space charge, depressing the barrier, and decreasing the number of carriers generated by electron impact. At the other side, however, ( $\oplus$  in Figure 9.22), the high carrier generation-recombination rate enhances the sample current drawn and results in a brightening of the oscilloscopic picture. If  $c$  is the spacing between dangling bonds and  $a$  the spacing between added electrons, their distribution function is

$$f = \frac{c}{a}, \quad (9.50)$$

for which a Fermi distribution can be assumed in a first approximation:

$$f_0 = \left( 1 + \exp \frac{E_D - E_F}{kT} \right)^{-1}, \quad (9.51)$$

where  $E_D$  = dislocation level,

$E_F$  = Fermi level.

(This assumption<sup>21</sup> is not valid for closely spaced arrays, as in grain boundaries, since there charge density is limited by coulomb interaction.) If each dislocation carries a charge  $e$ , the average positive charge on the space-charge cylinder is

$$\frac{e}{a} = e(N_d - N_a - n + p)\pi R^2 = e \cdot \frac{f_0}{c}, \quad (9.52)$$

where  $R$  = radius of coulomb cylinder,

$e$  = electron charge,

$N_d - N_a$  = donor minus acceptor concentration.

Neglecting the free carrier densities  $n$  and  $p$ , the space charge cylinder has the radius

$$R = \left[ \frac{f_0}{\pi c(N_d - N_a)} \right]^{1/2}, \quad (9.53)$$

where  $f_0$  is in the range of  $\frac{1}{10}$  at 300°K, which gives, for a net carrier density of  $10^{15} \text{ cm}^{-3}$ , a space-charge radius in the micron range. The barrier height can be found from the potential of the line charge. If a distance  $r_k$  is defined so that  $R > r_k > a$ , the potential due to  $n$  electrons in dangling bonds can be derived. For  $r < r_k$  and  $n > n_k$ , where  $n_k$  is a sufficiently large number of line electrons, and assuming  $n_k \gg r_k/a$ , one obtains<sup>25</sup>

$$\varphi_e(r) = -\frac{2e}{\kappa a} \left[ \sum_{n=1}^{n_k} \frac{1}{\sqrt{n^2 + (r/a)^2}} + \ln \frac{N}{2n_k} \right], \quad (9.54)$$

where  $\kappa$  = dielectric constant,

$N$  = total number of electrons in dislocation levels.

The potential due to the positive space charge is<sup>21</sup>

$$\varphi(r) = + \frac{e}{\kappa a} \left[ 1 + 2 \ln \frac{N \cdot a}{R} - \left( \frac{r}{R} \right)^2 \right]. \quad (9.55)$$

The total potential being  $\varphi(r) = \varphi_e(r) + \varphi_c(r)$ , we have, in the limit for  $r_k \rightarrow R$ ,  $n_k \rightarrow N/2$ ,

$$\varphi(r) = - \frac{e}{\kappa a} \left[ 2 \sum_{n=1}^{N/2} \frac{1}{\sqrt{n^2 + (r/a)^2}} + 2 \ln \frac{R}{Na} + \left( \frac{r}{R} \right)^2 - 1 \right]. \quad (9.56)$$

From (9.56) the potential barrier  $\phi = \varphi(0)$  can be found, and the barrier height in electron volts can be calculated. Numerical evaluations<sup>25, 26</sup> show that  $\phi$  lies in the range of a fraction of an electron volt in most unbiased cases or that the barrier should withstand only a small blocking voltage. In this model the influence of the external field on the space charge is not taken into account.<sup>27</sup> Considering the contact between the degenerate core of the dislocation pipe and the bulk semiconductor, a Schottky barrier layer width of

$$W_b = \left[ \frac{\varepsilon(V_D + V_e)}{2\pi e(N_d - N_a)} \right]^{1/2}, \quad (9.57)$$

where  $\varepsilon$  = dielectric constant = 16 (germanium),  
 $V_D$  = diffusion voltage,

results. With  $V_e$  = external voltage ( $V_e \approx 10 \text{ V} \gg V_D$ ), this could give higher space-charge width values of the order of

$$W_b \approx 10^2 \text{ to } 10^3 \mu.$$

A correct model, however, must consider the voltage dependence, of the actual number of carriers in boundary states, which influences considerably the distribution function  $f_0$ . Since the ratio of the actual charge density to the equilibrium density in boundary states is given by

$$\frac{q}{q_0} = \frac{1}{2} \left[ 1 + \left( 1 + \frac{eV_e}{\phi} \right)^{1/2} \right] = \frac{f}{f_0}, \quad (9.58)$$

where  $f_0$  = Fermi distribution function at equilibrium,

$\phi$  = barrier height,  $eV^{19, 22}$

we have an actual distribution:

$$f = \frac{1}{2} \left[ 1 + \exp \frac{E_D - E_F}{kT} \right]^{-1} \left[ 1 + \left( 1 + \frac{eV_e}{\phi} \right)^{1/2} \right] \quad (9.59)$$

and consequently a space-charge extension:

$$R = \left( \frac{1 + (1 + eV_e/\phi)^{1/2}}{2\pi e(N_d - N_a) \{1 + \exp[(E_D - E_F)/kT]\}} \right)^{1/2} \quad (9.60)$$

With higher external voltage values  $V_e$  and a barrier height of a fraction of an electron volt, the  $R$  values can also be considerably in excess of  $1\mu$ . Direct measurements of the barrier-layer width of grain-boundary junctions confirm the larger values. Local changes in work function of germanium and silicon due to dislocations have been measured by J. Lagowski<sup>26</sup> that show a space-charge extension of a fraction of a millimeter.<sup>22</sup>

More precise are double-probe potential measurements of the higher conductance parallel to the grain boundary that give values of  $W_b \simeq 60\mu$ ,<sup>27</sup> a value in agreement with the space-charge width in Figures 9.20 and 9.21.

The inner core of the space-charge pipe is a highly conducting path within the crystal due to wave function overlap in dangling bonds.<sup>22-24</sup> This explains the inconsistency in Lagowski's work<sup>26</sup> and why he did not measure an increase in work function at a dislocation site, but rather a reduction in the surface potential.

A scratch on the semiconductor surface shows as a similar lattice disturbance under lateral fields (see Figure 9.21). The extension of the barrier is in accordance with the calculated space-charge extension.

A reverse bias situation appears on the scratches in Figure 9.21. In the disturbed-lattice model of the semiconductor surface, the scratch position is important for the direction of unsaturated scratch-disrupted bonds and results in different lateral charges (see model in Figure 9.23).<sup>28</sup>

In compound crystals like GaAs, the polarity of the lattice complicates this situation, but the essential features of an edge dislocation remain the same. There are different possible core charges, depending on whether an  $\alpha$  or a  $\beta$  surface is being cut by the slip vector and depending on the doping (see Section 8.5). The edge dislocation pipe with the space-charge cylinder also forms, and highly conducting sheets are present at both sides of the boundary.<sup>24</sup> H. C. Casey, Jr.,<sup>29</sup> has argued that, in his recombination radiation experiments, the white regions surrounding the black dislocation spots (3 to  $6\mu$  size) are so wide (10 to  $50\mu$  size) and bright that this must be caused by "more than just the line associated with the extra half plane of atoms." The total spot sizes of the dislocations shown in Figures 9.20 and 9.21 are of the size of the dark spots in Casey's recombination pictures, and the current signal used in our case tends to localize the effect within the direct space-charge area. In Casey's case, however, the very wide, bright regions surrounding the dislocations are coincident with etch-pit free regions around the dislocations at the preferentially etched surface. It seems, therefore, that these areas are either strained or contain precipitates (tellurium atoms) of the dopant that introduce energy levels suitable to radiative recombination. Although in Casey's experiments, the bright areas are due to a high radiative recombination efficiency  $\eta_q$ , in our experiments the bright spots are those with a low radiative recombination efficiency  $\eta_q$ . Since  $\eta_r = 1 - \eta_q$ , we find for the nonradiative

(100) CRYSTAL SURFACE  
BOND STRUCTURE, DISTORTED:

$$\frac{2a_y}{y} = \frac{a_x}{x}$$

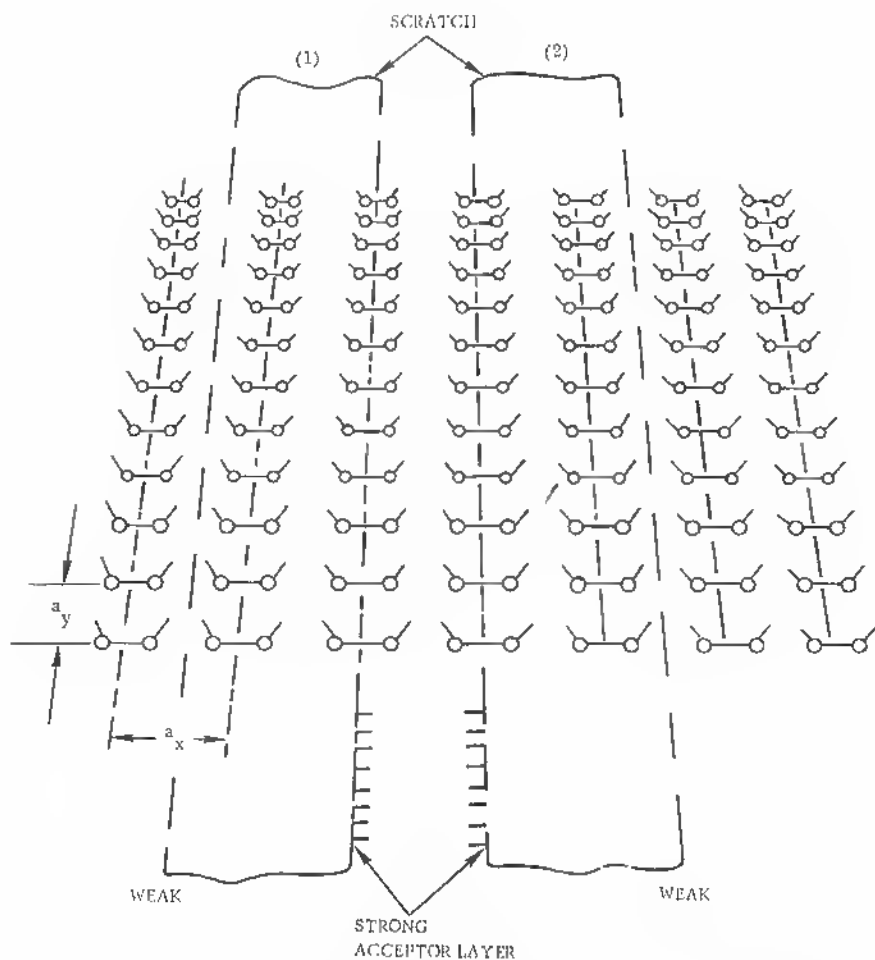


Fig. 9.23 Distorted surface bond structure of [100] surface,  $2a_y = a_x$ . (After Schlier and Farnsworth [28].)

recombination efficiency

$$\eta_r = 1 - \frac{C}{n_i^2} \tau_{nr} n_0 \int_0^\infty \alpha(h\nu) \exp\left(-\frac{h\nu}{kT}\right) d(h\nu), \quad (9.61)$$

where  $C = \text{constant}$

$n_i^2 = \text{electron-hole density product at equilibrium}$

$\tau_{nr} = \text{nonradiative lifetime}$

$\alpha(h\nu) = \text{absorption coefficient at } h\nu$

In this case (SEB) we expect  $\eta_q \ll 1$  for a high current signal, or the reverse, of Casey's experiments.

#### 9.4 ELECTRONIC OCCUPATION OF DISLOCATION CENTERS

The line of dangling bonds in the otherwise perfect crystal periodicity can be treated as isolated disturbance for charge carriers in the conduction-band continuum.

The point charges of the dangling bonds,  $q_i$ , are arranged at distances  $r_{ij}$  in the lattice.  $r_{ij}$  is given by the filling factor  $c$ , which is the ratio of filled to available free bonds. At room temperature it may amount to  $\frac{1}{10}$ . The total electrostatic energy of a row of charged lattice points is

$$E_i = \frac{1}{2} \sum_i \psi_i q_i, \quad (9.62)$$

$\psi_i$  is the potential function given by

$$\psi_i = \sum_{j(\neq i)} \frac{q_j}{kr_{ij}}; \quad (9.63)$$

thus we get

$$E_i = \frac{1}{2} \sum_i q_i \sum_{j(\neq i)} \frac{q_j}{kr_{ij}}, \quad (9.64)$$

where  $k = \text{material constant}$ .

This line charge in the otherwise perfect crystal structure is of the order of 100 Å wide. The electronic width of the space-charge cylinder may, however, be 100 times wider. Assume that a function  $f$  of all available dangling bonds has been filled with a second electron and has formed double dangling bonds:

$$f = \frac{c}{a}, \quad (9.65)$$

where  $c$  = spacing between dangling-bond levels,

$a$  = spacing between filled levels;

for example,  $a = 10c$  at  $300^\circ\text{K}$  and  $f = \frac{1}{10}$ .

Defining the electrostatic energy per added electron

$$E_s = E(f)$$

and assuming a uniform space charge of density

$$\rho = e(N_d - N_a),$$

Read has derived an expression for  $E_s$ :

$$E_s = \frac{e^2}{ka} \left( \ln \frac{R}{a} - 0.866 \right) \quad (9.66)$$

see (8.22) and (8.28).

$e^2/kc$  is the interaction energy  $E_0$  of electrons within the line charge—see (9.64)—( $k$  = dielectric constant; germanium:  $k = 16$ ) and can be written

$$E_0 = \frac{e^2}{kaf} \quad (9.67)$$

Here:

$$f = c\pi R^2(N_d - N_a) \quad \text{See (8.11).} \quad (9.68)$$

We define:

$$f_c = c\pi^{1/3}(N_d - N_a)^{1/3}, \quad (9.69)$$

the distribution function  $f$ , where  $R = a$ , or when the filled levels are as far apart as the width of the space-charge radius.

We have then:

$$\left( \frac{f}{f_c} \right)^{3/2} = \pi R^3(N_d - N_a)$$

or:

$$\left( \frac{f}{f_c} \right)^{3/2} = \frac{R}{a}$$

and with (9.66)

$$E_s = fE_0 \left( \frac{3}{2} \ln \frac{f}{f_c} - 0.866 \right). \quad (9.70)$$

According to the Fermi distribution the free energy per site is

$$f[E_D - E_F + E_s(f)], \quad (9.71)$$

where  $E_D$  = dislocation acceptor level measured upward from valence band edge.

Minimizing (9.71) with respect to  $f$  would mean

$$E^*(f) = E_F - E_D = \frac{d}{df} f E_s(f). \quad (9.72)$$

In the range where (9.66) is valid,  $E_s$  is approximately linear in  $f$ . Therefore, the electrostatic energy  $fE_s$  per site varies as  $f^2$ , and  $E^*$  has the same form as  $E_s$ . This leads to

$$E^*(f) = \frac{e^2}{ka} f \left( 3 \ln \frac{f}{f_c} - 0.232 \right), \quad (9.73)$$

a form also given by Read.

Logan, Pearson, and Kleinman<sup>5</sup> have plotted the fraction  $\varepsilon$  occupied by the space-charge cylinders as a function of temperature as given by (9.30) and find that for a dislocation level of  $E_D = 0.179$  eV the measured curve (see Figure 9.11), can be fitted very well. Accordingly, they conclude,  $\varepsilon$  is in the range of 0.1 to 0.2 at room temperature.

It has to be considered here that the uncertainty with respect to the dislocation level is real.

There is no doubt that thinly distributed dislocations form lower-lying levels than more densely packed dislocation pipes. On merger of the individual space-charge pipes, other energy levels arise, particularly one which is located farther away from the valence band, as we shall see later.

Logan, Pearson, and Kleinman also point out the difficulties in counting the dislocations from etch-pit patterns and in assessing the value for  $X = l/l_D$ , where  $l$  is the mean free path without dislocation,  $l_D$  the mean free path with dislocations.

Using the relaxation time  $\tau$  according to deformation-potential theory,

$$\tau = \frac{l_D}{v(E)},$$

where  $v(E)$  = energy shell velocity  $= (2E/m^*)^{1/2}$ ,

$E$  = electron energy,

$m^* = (m_1 m_2 m_3)^{1/3}$  = density of state mass,

there is a question of the correct effective mass values due to band deformation by the stress fields of the dislocations.

In general, we assume a dislocation level of 0.2 eV for a dislocation density in the range of  $5 \cdot 10^7 \text{ cm}^{-2} \approx 3.5 \cdot 10^{11} \text{ cm}^{-3}$ .

So far we have applied Fermi statistics for the function  $f$ . As Read noted already, a closely spaced line of acceptors, however, cannot be governed by

Fermi statistics. Read has compared the different methods of deriving  $f(T)$  (see Figure 9.24). The different curves for  $f(T)$  relate to Fermi statistics ( $F$ ), Boltzmann statistics ( $B$ ), harmonic oscillator approach (H.O.), and the minimum energy (M.E.) for  $E^* = E_F - E_D$ .

There are several regions for  $f = c/a$  because of varied spacing  $a$  between filled levels. In form of the interaction energy (9.64) or the electrostatic interaction

$$fE_0$$

we can define several regions, depending on the ratio of interaction energy between neighboring electrons in dangling-bond sites and the thermal energy:

- (1)  $fE_0 \ll kT$ ,
- (2)  $fE_0 < kT$ ,
- (3)  $fE_0 \approx kT$ ,
- (4)  $fE_0 > kT$ .

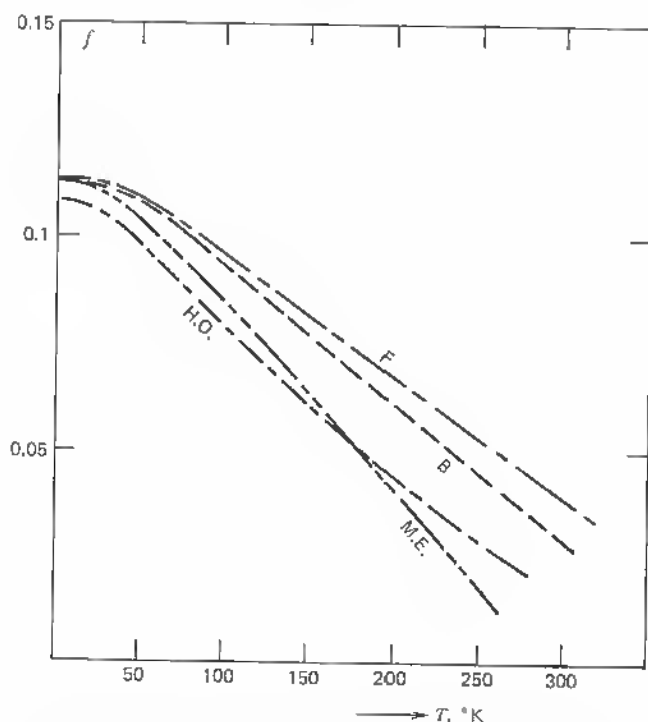


Fig. 9.24 Dislocation occupation factor (filling or distribution function)  $f(T)$  for different statistics:  $F$  = Fermi;  $B$  = Boltzmann; H.O. = harmonic oscillator; M.E. = minimum energy.



In case 1, the spacing between filled sites is large (or the temperature high) or the dilution of electrons in line bonds is high. This case can be treated by nondegenerate Maxwellian statistics. A minimum-energy treatment may be applied such that  $f$  can be approximated by

$$f \simeq \int k \ln \left( \frac{N_d - N_a}{N_a} \right) dT. \quad (9.74)$$

Read has shown that this treatment can best account for the case of low temperature. For case 2, Fermi statistics are applicable, since here  $f$  is already large enough so that the  $W$  ways of arranging  $N$  electrons over the sites have approximately the same energy.

Other solutions lying between the Fermi and ME (minimum energy) solution are the Boltzmann approximation and the harmonic oscillator approximation.<sup>21</sup> The results show that the filling factor  $f$  should at best be around  $10^{-2}$  at room temperature for reasonable values of the added free energy. In reality, much larger values are measured. Although in a normal Fermi distribution

$$f = \frac{1}{1 + \exp(-\Delta E/kT)}, \quad (9.75)$$

where  $\Delta E = E_F - E_D \simeq 0.3$  eV (for germanium),

one would get a limiting value of  $f = \frac{1}{2}$ ; measurements of  $f$  in the case of grain boundaries with lateral bias applied give higher values.

Cases 3 and 4 above therefore apply to low temperature but also to high dislocation density and high bond occupancy. If in the case of close spacing lateral overlap occurs, the degree of degeneracy apparently can be increased by space-charge widening (lateral bias). In the extreme case of increased occupancy to the point  $a=c$ , or total wave function overlap, there is a transition from discrete energy levels to an energy band with  $f$  being the average number of energy quanta per electron available. In such a case we could conceivably suppose that a Planck distribution in electron states applies and that

$$f = \frac{1}{\exp(\Delta E/kT) - 1} \approx \frac{1}{1 + (\Delta E/kT) - 1} \approx kT/\Delta E \quad (9.76)$$

for  $\Delta E$  small. Assuming a Fermi function for the filling factor gives

$$f = \frac{1}{1 + \exp[(E_2 - E_F)/kT]}, \quad (9.77)$$

where  $E_2$  = dislocation level,  
 $E_F$  = Fermi level.

The space-charge cylinder around the dislocation array depends on  $1/a$  the inverse spacing between filled levels. Therefore, one defines

$$\pi R^2(N_d - N_a) = \frac{1}{a} \quad (9.78)$$

with decreasing spacing between filled bonds

$$R^2 = \frac{1}{\pi a(N_d - N_a)} \quad (9.79)$$

increases. Replacing  $a = c/f$  and introducing (9.77) into (9.79) yield the radius  $R$  of the space-charge cylinder:

$$R = [\pi c(N_d - N_a)\{1 + \exp[(E_2 - E_F)/kT]\}^{1/2}]^{-1/2}. \quad (9.80)$$

Typical values for  $n$ -type germanium ( $N_d - N_a \approx 10^{15} \text{ cm}^{-3}$ ) and  $f = \frac{1}{16}$  at  $300^\circ\text{K}$  lie between  $10^{-4}$  and  $10^{-3} \text{ cm}$ .

The radius of this space-charge cylinder is large compared with  $a$ , the mean spacing between filled levels, and even compared with the mean spacing between excess donors in the bulk for ordinary doping ranges:

$$(N_d - N_a)^{-1/3} \approx (10^{15})^{-1/3} = 10^{-5} \text{ cm}.$$

In degenerate material ( $>10^{19} \text{ cm}^{-3}$ ), the impurity atoms would be 10 lattice constants apart ( $10^{19} \text{ cm}^{-3}$  corresponds to  $2.2 \times 10^6 \text{ cm}^{-1}$ ; with  $a = 5 \times 10^{-8} \text{ cm}$  interatomic spacing there would be 10 lattice constants between impurity atoms). This density would compete with the density of filled levels in the grain boundary and eliminate its electronic features, because:

1. Bulk conduction competes with conduction along dangling-bond levels.
2. No measurable space charge and thus barrier layer can be formed, since degenerate material decreases the effective space-charge width to tunnel-type barrier widths.

Another aspect is connected with the space-charge formation. This is the increase in  $f$  by an applied external voltage. If  $q_0$  is the equilibrium number of charges in boundary states, and  $q$  the number of charges under bias  $V_e$ ,

$$\frac{q}{q_0} = \frac{1}{2} \left[ 1 + \left( 1 + \frac{eV_e}{\phi} \right)^{1/2} \right], \quad (9.81)$$

where  $\phi$  = barrier height,  
 $e$  = electron charge,  
 $V_e$  = external voltage.

(for derivation see Section 11.2). This changes the space-charge cylinder radius to a value

$$R = \left\{ \frac{1/2[1 + (1 + eV_e/\phi)^{1/2}]}{e\pi(N_d - N_a)} \right\}^{1/2}. \quad (9.82)$$

Considering now the whole grain-boundary plane as superposition of space-charge cylinders in a planar envelope, one can define a filling factor  $f'$  perpendicularly to the pipes with a spacing

$$D = \frac{b}{2 \sin(\theta/2)}, \quad (9.83)$$

where  $b$  = Burgers vector

(see Section 4.2), between free bonds. Thus, the spacing between filled levels is

$$a' = \frac{D}{f'}. \quad (9.84)$$

The area state density in the grain-boundary plane is therefore

$$N_D = \frac{f \cdot f'}{D \cdot c} \quad \text{cm}^{-2}. \quad (9.85)$$

For  $\theta > 1^\circ$ , the distance  $D$  approaches  $b$ , the Burgers vector, which is equal to a lattice translation vector for simple cubic cases and therefore nearly equal to  $c$ . Under applied external voltage  $V_e$ , both  $f$  and  $f'$  depend on  $V_e$ , as indicated by (9.81). Therefore, the area state density is given by

$$N_D = \frac{f \cdot f'}{b^2} = \frac{1/4[1 + (1 + eV_e/\phi)^{1/2}]^2}{b^2}. \quad (9.86)$$

$f$  and  $f'$  being equal for medium-tilt angles,

$$N_D \simeq \frac{f^2}{b^2} \quad \text{cm}^{-2}.$$

With  $f \simeq 0.1$  and  $b \simeq 5 \cdot 10^{-8}$  cm, we calculate

$$N_D \simeq 4 \times 10^{12} \text{ cm}^{-2},$$

or, on a volume basis,

$$N_D^* \simeq 8 \times 10^{18} \text{ cm}^{-3}.$$

This is a near degenerate density and explains the high conductivity and the degenerate behavior of these grain boundary planes (or pipes):

$$f = \frac{q}{q_0} = \frac{1}{2} \left[ 1 + \left( 1 + \frac{eV_e}{\phi} \right)^{1/2} \right]. \quad (9.87)$$

According to (9.87), the filling factor can reach values in excess of 1, and the state density  $N_D^*$  is for  $f = 1$

$$N_D^* = 8 \times 10^{21} \text{ cm}^{-3}.$$

This explains why even in degenerate bulk crystal material with an impurity density of  $10^{19} \text{ cm}^{-3}$ , grain boundaries still constitute high-conductivity paths and form a space charge. There are then roughly 10 dislocation charges per impurity charge spacing even in degenerate material.

We may infer from the knowledge of the behavior of degenerate semiconductors that a strong temperature independence of resistivity and mobility occurs. The flatness of the  $\rho$  and  $\mu_H$  curves versus  $T$  has been observed earlier by E. M. Conwell<sup>30</sup> for degenerate germanium and silicon crystals and noted as the disappearance of the distinction between impurity levels and conduction-band levels. Total wave function overlap is the criterion for this kind of conduction phenomenon.

The resulting questions concerning the space charge, the barrier height, the magneto-resistance, sheet conduction and mobility, and the like, are treated in Chapter II.

#### APPENDIX A9.4 ELECTRONIC TRANSPORT ACROSS DISLOCATION COULOMB CYLINDERS

In carrier-transport problems across such a line charge, the free carriers originate in the space-charge region in the perfect crystal and penetrate the dislocation line in a form that can be derived from a solution of the Schrödinger equation for an allowed energy band deformed by a perturbing potential, namely, the grain-boundary potential  $V(x, y, z)$ . Using Slater's procedure,<sup>41</sup> the wave equation

$$\nabla^2 \psi - \frac{\hbar^2}{2m} [V_p(x, y, z) + V(x, y, z)] \psi = -E\psi, \quad (9.88)$$

where  $V_p(x, y, z)$  = periodic potential,

$E$  = total energy,

$\hbar$  = Dirac's constant  $= \frac{h}{2\pi}$ ,

can be solved for the one-dimensional case by a wave function

$$\psi(x) = \sum_k \phi(x_k) a(x - x_k), \quad (9.89)$$

where  $a(x - x_k)$  are the *Wannier functions*<sup>27</sup> defined by

$$a(x - x_k) = \sum_p \exp\left(\frac{ipx_k}{\hbar}\right) \cdot \psi_0(p, x). \quad (9.90)$$

Thus the solution of (9.88) as a function of the effective momentum  $p$  and space coordinates  $x$

$$\psi(p, x) = \sum_k \phi(x_k) \sum_p \psi_0(p, x) \exp\left(\frac{ipx_k}{\hbar}\right) \quad (9.91)$$

represents a superposition of Bloch functions with

$$\phi(x_k)$$

as coefficients for amplitude and phase of the wave functions in the neighborhood of the  $k$ -th atom that have to satisfy the condition

$$E_{0p} \phi(x) + V(x) \phi(x) = E \phi(x), \quad (9.92)$$

with the operator

$$E_{0p} = E_0 \left( -i\hbar \frac{\partial}{\partial x} \right), \quad (9.93)$$

which replaces  $E_0(p)$  in the unperturbed case.

WBK solutions of (9.92) are possible<sup>2, 23</sup> if one defines  $E_0(p)$  as a periodic function of  $p$  of the form

$$E_0(p) = E_0(-p) = \sum_n b_n \cos \frac{pna}{\hbar} = \sum_n c_n p^n, \quad (9.94)$$

where  $b_n$  respectively  $c_n$  are constants that depend on the specific form of the periodic potential  $V_p(x)$ .  $a$  is the lattice constant.

With (9.93) and (9.94) equation (9.92) can be written

$$\sum_n c_n \left( \frac{-i\hbar a}{dx} \right)^n \phi(x) + V(x) \phi(x) = E \cdot \phi(x). \quad (9.95)$$

This infinite-order operator equation can be solved if one defines a periodic perturbing potential function  $P(E - V)$  depending on  $V$ , the perturbing potential, in the form

$$E - V = \sum_n c_n P^n. \quad (9.96)$$

If a function  $P$  satisfies (9.96), so does  $\pm [P + (2m\pi\hbar/a)]$ ,  $m = 0, \pm 1, \pm 2$ , etc. And since the perturbing potential  $V$  depends on  $x$ ,  $P$  is also a multiple-valued function of  $x$ .

$$E - V(x) = \sum_n c_n P^n(x). \quad (9.97)$$

The solution of (9.95) can then be written

$$\phi(x) = C \left( \frac{dV}{dp} \right)^{-1/2} \exp \left[ \frac{i}{\hbar} \int P(x) dx \right]. \quad (9.98)$$

$C$  = integration constant.

In the case of a distorted band, for example, by a line of broken bonds as here, the general function satisfying (9.97) can be written

$$P(x) = \pm p(x) + \frac{2m\pi\hbar}{a} \quad (m = 0, \pm 1, \dots). \quad (9.99)$$

This gives the solution corresponding to (9.98):

$$\phi(x) = C \left( \frac{dV}{dp} \right)^{-1/2} \exp \left[ \pm \frac{i}{\hbar} \int p(x) dx \right] e^{2\pi m x i / a}. \quad (9.100)$$

Now we have

$$dV/dp = -d(E - V)/dp \quad (9.101)$$

and in the perturbed crystal the right side of (9.101) represents the local velocity value of the Bloch wave

$$d(E - V)/dp = v(x). \quad (9.102)$$

This leads to a modified equation (9.100):

$$\phi(x) = \frac{C}{[v(x)]^{1/2}} \exp \left[ \pm \frac{i}{\hbar} \int p(x) dx + \frac{2\pi m x i}{a} \right] \quad (9.103)$$

as solution of (9.92). Both are equations of infinite order. Considering only solutions at certain lattice points of interest, one may write (9.103) also simply as a linear combination of two functions:

$$\phi(x) = \frac{C}{[v(x)]^{1/2}} \exp \left[ \pm \frac{i}{\hbar} \int p(x) dx \right]. \quad (9.104)$$

With the modified local velocity of the wave package according to (9.102) and (9.64):

$$v(x_0) = \frac{d}{dp} \left[ E - \frac{1}{2} \sum_i q_i \sum_{j \neq i} \frac{q_j}{k r_{ij}} \right] \quad (9.105)$$

at the dislocation array we get the solution

$$\phi(x) = \frac{C \exp \left( \pm \frac{i}{\hbar} \int p(x) dx \right)}{\left\{ \frac{d}{dp} \left[ E - \frac{1}{2} \sum_i q_i \sum_{j \neq i} \frac{q_j}{k r_{ij}} \right] \right\}^{1/2}}. \quad (9.106)$$

One sees immediately that without a perturbing potential or  $V(x) = 0$ ,  $p(x) = \text{constant}$ ,  $v(x) = \text{constant}$ , (9.104) leads to

$$\phi(x_k) = c_1 e^{ipx_k/\hbar} + c_2 e^{-ipx_k/\hbar}, \quad (9.107)$$

a linear combination of two independent Bloch waves.

With the perturbing potential, the local velocity of the wave package depends strongly on the form of the disturbance. For some specific examples, the grain-boundary electrostatic energy  $E = \frac{1}{2} \sum \Psi_i q_i$  can be evaluated, as we have seen, and solutions of (9.106) can be considered.

In a general time-dependent Bloch wave, functions can be modified to include the perturbing potential energy:

$$E = \frac{1}{2} \sum \psi_i q_i, \quad (9.62)$$

the result being

$$\psi_{p_x}(x, t) = u_{p_x}(x) \exp \left[ \frac{2\pi i}{h} (E - E_{p_x} t) \right] = u_{p_x}(x) \exp \left[ \frac{2\pi i}{h} \left( \frac{1}{2} \sum \psi_i q_i - E_{p_x} t \right) \right], \quad (9.108)$$

where  $u_{p_x}(x)$  = lattice periodic amplitude function. (Compare Chapter 2, page 19.)

## REFERENCES

- A1. Slater, J. C.: "Electrons in Perturbed Periodic Lattices," *Phys. Rev.*, **76**(11): 1592-1601, December 1 (1949).
- A2. James, H. M.: "Electronic States in Perturbed Periodic Systems," *Phys. Rev.*, **76**(11): 1611-1628, December 1 (1949).
- A3. Feuer, P.: "Electronic States in Perturbed Periodic Lattices," *Phys. Rev.*, **99**(4): 1092-1097, August 15 (1955).

## 9.5 DISLOCATIONS AND NONRADIATIVE RECOMBINATION

This section is confined to the case of statistically distributed and sufficiently separated dislocations. This means that the spacing between individual dislocation pipes is larger than the pipe radius.

$$d_D > R$$

(see Figure 8.14). The case of dislocation clusters, lineage, and low-angle boundaries is treated in Chapters 10 and 11. We start our considerations with the barrier layer around the dislocations, which is at the root of all problems of recombination and trapping.

S. R. Morrison<sup>31</sup> has shown that discrepancies with the Shockley-Read theory of recombination for the case of the slow decay of injected carriers can be explained on account of the space-charge model. In this case there is no need to postulate unknown deep-lying traps.

If we start with the basic concept, as outlined in Figure 9.25, we can express the barrier potential  $\phi_b$  by integration of Poisson's equation:

$$\frac{d^2\phi_b}{dr^2} = -\frac{2\pi\rho}{\epsilon}, \quad (9.109)$$

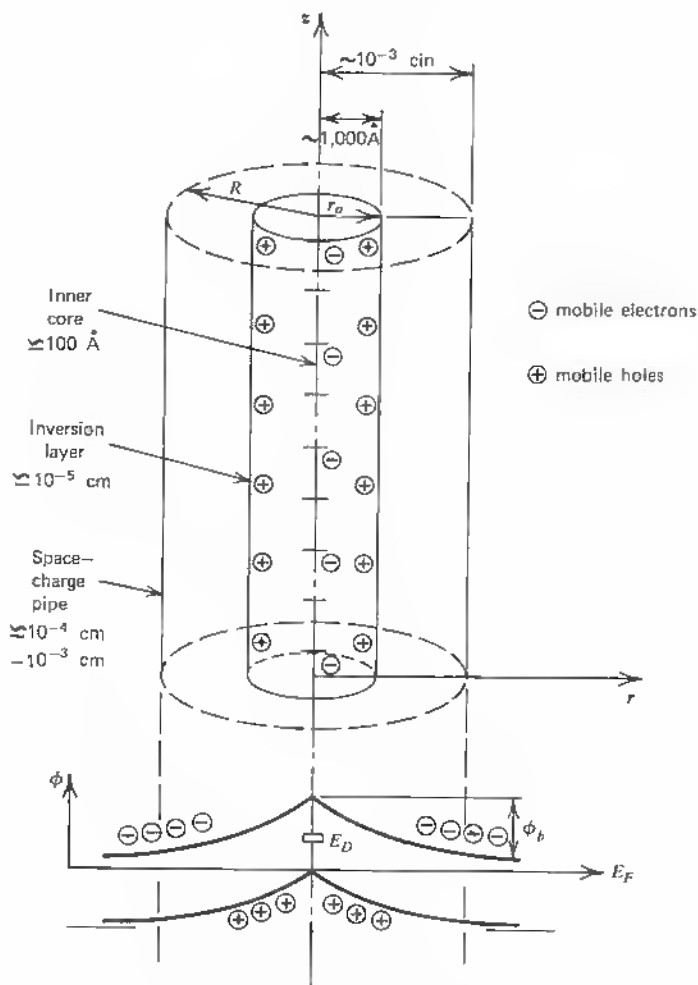


**Fig. 9.25** Dislocation space charge pipe model.



where  $\rho$  = radial charge density due to dislocation array:  $\pi R^2 \cdot \rho = e/a$ ,  
 $\epsilon$  = dielectric constant;  $R$  = dislocation space charge radius.

For  $r \leq R$

$$\phi_b(r) = \frac{\pi \rho}{\epsilon} (R^2 - r^2), \quad (9.110)$$

where  $R_0$  = integration constant determined by continuity of  $\phi_b(r)$  at  $r = R$ .

For  $r \geq R$

$$\phi_b(r) = \frac{\pi \rho R^2}{\epsilon} \int_{-Na/2}^{+Na/2} \frac{dz}{\sqrt{r^2 + z^2}} \quad (9.111)$$

(see Figure 9.25),

$$\phi_b(r) = 2 \frac{\pi \rho R^2}{\epsilon} \ln \left\{ \frac{z}{r} + \left[ 1 + \left( \frac{z}{r} \right)^2 \right]^{1/2} \right\}_0^z. \quad (9.112)$$

$z$  along the pipe axis is measured in charge number  $N$  times the linear spacing  $a$ :

$$\phi_b(r) = \frac{2\pi \rho R^2}{\epsilon} \ln \frac{Na}{r}. \quad (9.113)$$

Considering the dislocation array as a line charge and evaluating the barrier potential at some small distance  $\lambda$  from the array, one may express the barrier height  $\phi$  also from

$$d\phi = \frac{dV}{dr} = \frac{\rho}{2\pi\epsilon r}$$

as

$$V = - \frac{\rho}{2\pi\epsilon r} \ln \frac{R}{\lambda}, \quad (9.114)$$

as did S. R. Morrison.<sup>31</sup> Here  $\rho = eN_E$  and  $N_E$  is the number of trapped electrons per unit dislocation length:

$$N_E = \pi N_D R^2 = N \cdot \frac{f}{c} = N \frac{1}{a}. \quad (9.115)$$

Electrons with sufficient energy can penetrate the space-charge cylinder and remain trapped. The capture rate  $R_c$  times a lifetime constant  $\tau_n$  can be approximated by the sum of the quantum states with energy in excess of a value  $\alpha V_0$ :

$$R_c \tau_n \simeq n \sum_{\xi=\alpha V_0}^{\infty} \exp \xi, \quad (9.116)$$

where  $\alpha = e/kT$ ,

$V_0$  = equilibrium value of potential.

Equation (9.116) can be replaced by the integral with the limits  $\alpha V_0 \rightarrow \alpha V$ :

$$R_e \tau_n \simeq n \int_{\alpha V_0}^{\alpha V} e^{\xi} d\xi \quad (9.117)$$

$$\simeq n \exp \frac{eV}{kT} - n_0 \exp \frac{eV_0}{kT}. \quad (9.118)$$

Introducing the expression for the barrier height  $\phi = \frac{V}{r}$  (9.114), one has

$$R_e \tau_n \simeq n \exp \frac{e}{kT} \left( -\frac{\rho}{2\pi\epsilon} \ln \frac{R}{\lambda} \right) - n_0 \exp \frac{e}{kT} \left( -\frac{\rho_0}{2\pi\epsilon} \ln \frac{R}{\lambda} \right). \quad (9.119)$$

Since  $\rho = eN_E$ ,

$$R_e \tau_n n \exp(-yN_E) = n_0 \exp(-yN_{E0}) \quad (9.120)$$

with

$$y = \frac{e^2}{2\pi\epsilon kT} \ln \frac{R}{\lambda}. \quad (9.121)$$

Morrison relates the distance  $\lambda$  to the electric wavelength ( $y$  is of the order of  $10^{-7}/kT$  [cm], when  $kT$  is in electron volts)  $n_0$  the equilibrium number of electrons as well as the actual number  $n$  are also fractions of  $N_E$ , but since  $yN_E > 1$  (for  $T < 300^\circ\text{K}$ ), the exponential factors vary more rapidly, and (9.120) can be assumed correct.

For the hole capture a similar expression is derived:

$$R_h \tau_p \simeq p - p_0 \exp[y(N_{E0} - N_E)]. \quad (9.122)$$

where  $p$  = hole density,

$p_0$  = equilibrium hole density.

Here the assumption is that no holes are trapped in the dislocation level (not valid at low temperatures) and that the capture cross section is independent of the dislocation level, which varies with the barrier changes. With these assumptions one may relate  $\tau_n$  and  $\tau_p$  to the Shockley-Read<sup>12</sup> lifetimes  $\tau_{n0}$  and  $\tau_{p0}$  in  $n$ -type material, or  $\tau_{n0} = \tau_n$ ,  $\tau_{p0} = f \cdot \tau_p$ .

From (9.120) and (9.122) we can derive

$$\exp(-yN_E) = \frac{p + n_0(-yN_{E0})}{n + p_0 \exp(yN_{E0})}, \quad (9.123)$$

assuming that in steady state  $R_e = R_h$  and that  $\tau_n \simeq \tau_p$ . Using (9.123) to calculate  $R_e$  or  $R_h$  from (9.119) and (9.120) leads to

$$R_e = R_h = \left( \frac{\Delta p}{\tau} \right) \frac{n_0}{n + p_0 \exp(yN_{E_0})} \\ = \frac{n_0}{\tau} [\exp(-yN_{E_0})][\exp(y\Delta N_E) - 1] \quad \text{for } n_0 \gg p, \quad (9.123)$$

where  $\Delta p = p - p_0$ ,

$\Delta N_E \equiv N_{E_0} - N_E$ , which is positive for injection in  $n$ -type material:

$$n \simeq n_0 \text{ is valid for } \tau_p \simeq \tau_n$$

As  $\Delta p'$  holes are injected, they distribute over the available dislocation levels and the valence band:

$$\Delta p' = \Delta p + N_D \Delta N_E, \quad (9.124)$$

where  $N_D$  = dislocation density  $\text{cm}^{-2}$ .

An excess conductivity  $\Delta\sigma = e\mu\Delta p$  is due to  $\Delta p'$  electrons going to the conduction band to neutralize  $\Delta p$  holes going into the valence band:

$$\frac{\Delta\sigma}{e\mu} = 2\Delta p + N_D \Delta N_E. \quad (9.125)$$

Combining (9.125) with (9.123) gives

$$\frac{\tau}{e\mu} \frac{d\Delta\sigma}{dt} = n_0 \exp(-yN_{E_0}) \left( \exp \frac{y\Delta\sigma}{e\mu N_D} - 1 \right), \quad (9.126)$$

where  $N_D \Delta N_E \gg \Delta p$  is assumed.

Equation (9.126) shows that the decay is not simply exponential in this case. If, however,  $N_D \Delta N_E \ll \Delta p$ , the simple exponential decay (Shockley-Read) follows. Morrison concludes from an evaluation of the temperature at which the slow decay should go over into a fast decay that his model accounts for dislocation recombination. In fact, above 200°K. the slow decay leads over into the normal (exponential) decay, in agreement with measurements by Fan et al. (see Section 11.2).

Another interesting fact is that measurement results of photoconductance versus illumination level can be interpreted with this model, leading to a correct value of the barrier height: 0.3 eV (experimental 0.27 eV). Also, the absence of the slow decay in  $p$ -type material follows from the barrier model, since no space-charge layer of significance can form in predominantly  $p$ -type material (case of germanium).

Refinements of this theory are mainly concerned with the temporary trapping of holes at low temperatures or the peculiar hole conduction within the space-charge pipe. Figielski<sup>32</sup> has applied Read's potential expression

$$\phi_0 = -\frac{e}{\epsilon} \frac{f}{c} \left( 3 \ln \frac{f}{f_c} - 1.232 \right), \quad (9.127)$$

where  $f$  = filling factor,

$$f_c = \sqrt[3]{\pi(N_d - N_a)}$$

(see Section 8.4), which is valid at the lieu of one electron because of all other electrons and the positive space charge, using a model of electron capture, neglecting tunneling through the barrier and eventual stress-field and Cottrell atmosphere contributions. Expressions for the net rate of electron capture  $R_e$  and hole capture  $R_h$  are then

$$R_e = \frac{N_d}{a} [c_e n_b (1 - f) - c'_e N_e \cdot f], \quad (9.128)$$

$$R_h = \frac{N_d}{a} [c_h p_b f - c'_h N_v (1 - f)], \quad (9.129)$$

where  $N_d$  = donor density in bulk,  
 $a$  = spacing between occupied dislocation sites,  
 $c_e$  = probability per unit time that electron will be captured by available site,  
 $c'_e$  = probability that electron will be emitted from site into conduction band,  
 $c_h, c'_h$  = same for holes,  
 $f$  = distribution function,  
 $n_b, p_b$  = electron, hole concentrations at the dislocations (within space charge),  
 $N_e, N_v$  = conduction, valence band densities.

The electron and hole concentrations at the dislocation are

$$\begin{aligned} n_b &= n \exp\left(-\frac{e\phi}{kT}\right), \\ p_b &= p \exp\left(\frac{e\phi}{kT}\right), \end{aligned} \quad (9.130)$$

as expressed by the barrier potential  $\phi$ .

In thermodynamical equilibrium  $R_e = R_h$ , and therefore one has, from (9.128) and (9.129), for the emission coefficients

$$\begin{aligned} c'_e &= \frac{c_e n_{b0}(1-f)}{N_c \cdot f_0}, \\ c'_h &= \frac{c_h p_{b0} f_0}{N_v(1-f_0)}. \end{aligned} \quad (9.131)$$

Since  $f_0 < 1$ , one gets, with (9.131) introduced into (9.128) and (9.129),

$$\begin{aligned} R_e &= \frac{c_e N_d}{a} \left[ \frac{n_b(1-f) - n_{b0}f}{f_0} \right], \\ R_h &= \frac{c_h N_d}{a} [p_b f - p_{n0}(1-f)f_0]. \end{aligned} \quad (9.132)$$

These rate equations for dislocation capture are then modified by introducing  $\Delta n = n_0 - n$ ,  $\Delta p = p_0 - p$ ,  $\Delta f = f_0 - f$ ,  $\Delta \phi = \phi_0 - \phi = \eta \phi_0$ ;  $\beta = e/kT$   $\eta = \frac{\Delta f}{f_0}$  is called the trapping level.

Therefore (9.132) takes the form

$$\begin{aligned} R_e &= \frac{c_e n_0 N_d}{a} \exp[-\beta \phi_0(1-\eta)] [1 - (1-\eta)\exp(-\beta \phi_0 \eta)], \\ R_h &= \frac{c_h p_0 f_0 N_d}{a} \exp[\beta \phi_0(1-\eta)] \left[ \left(1 + \frac{\Delta p}{p_0}\right)(1-\eta) - \exp(\beta \phi_0 \eta) \right]. \end{aligned} \quad (9.133)$$

At steady state  $R_e = R_h = G$  (rate of electron-hole-pair generation per unit volume), (9.133) can be solved to yield an expression for  $\Delta p$ :

$$\Delta p = \frac{c_e n_0}{c_h f_0(1-\eta)} \exp[-2\beta \phi_0(1-\eta)] [1 - (1-\eta)\exp(-\beta \phi_0 \eta)]. \quad (9.134)$$

From (9.134) and the expression for  $R_e$  (9.133) one can derive a relation

$$\Delta p = G \cdot \tau_h, \quad (9.135)$$

where  $\tau_h$  can be defined as a stationary lifetime of holes:

$$\tau_h = \frac{a \exp[-\beta \phi_0(1-\eta)]}{c_h f_0 N_d(1-\eta)}. \quad (9.136)$$

Equations (9.133) and (9.135) are the basic equations for the steady state.

They can be written

$$G = \frac{c_e n_0 N_d}{a} \exp[-\beta \phi_0(1-\eta)][1 - (1-\eta) \exp(-\beta \phi_0 \eta)] \quad (9.137)$$

$$\tau_h = \frac{a \exp[-\beta \phi_0(1-\eta)]}{c_h f_0 N_d(1-\eta)}. \quad (9.138)$$

From (9.137)  $\eta$  can be obtained as a function of the generation rate  $G$  at different temperatures. ( $\phi_0(T)$  is assumed to be known.) Thus  $\eta = f(T)_{G=\text{const}}$  is obtained. Subsequently making use of the  $\eta(T)$  relation, one can find the temperature dependence of the hole lifetime  $\tau_h$  from (9.138).

If a crystal is subject to homogenous illumination, the conductivity change  $\Delta\sigma$  can be written

$$\Delta\sigma = e \left[ \Delta p(\mu_e + \mu_h) + \Delta f \frac{N_d}{a} \mu_e \right]. \quad (9.139)$$

The first term on the right describes the usual photoconductivity of electron-hole pairs, and the second term describes the contribution of those electrons which compensate for the excess charge of holes trapped at dislocations. With the relations  $\mu_e/\mu_h \simeq 2$ , equation (9.135), and  $\eta = \Delta f/f_0$ , one obtains

$$\Delta\sigma = e\mu_e \left[ 1.5G\tau_h + f_0 \frac{N_d}{a} \eta \right]. \quad (9.140)$$

Introducing the dimensionless values

$$G^* = \frac{Ga}{c_e n_0 N_d} \quad \text{and} \quad \tau_h^* = \frac{\tau_h \cdot c_h N_d}{a}$$

leads to an expression for the relative conductivity change:

$$\frac{\Delta\sigma}{\sigma} = \frac{1.5G^*\tau_h^*c_e}{c_h f_0} + f_0 \frac{N_d}{an_0} \cdot \eta, \quad (9.141)$$

which allows one to compare measured values of  $\Delta\sigma$  for different intensities with calculated values of  $\eta(G^*)$  and  $\eta(\tau_h^*)$ .

Good agreement with experiments is obtained for the  $\eta = f(G^*)$  function when the calculated relation for 125°K is compared with a monopolar electron photocurrent in plastically deformed germanium as a function of light intensity.

Figielski points out that, in the case of inhomogeneous generation, the assumption of a mean carrier diffusion length is a problem, since carrier diffusion occurs preferably along dislocation lines. A hole is transmitted

easily along the inner pipe, accounting for more and more of the carrier transport as the temperature is lowered (see Chapter 11).

Another problem is the behavior of the coefficients  $c'_e$  and  $c_e$  as well as  $c'_h$  and  $c_h$ , which define the sticking and emission probabilities, respectively, for electrons and holes.

Figielski assumes temperature independence of these probabilities. In comparing the measured values in photoconductivity measurements with equations derived for the barrier-dependent capture rate:

$$c_e \simeq c_h \simeq 4 \times 10^{-8} \text{ sec}^{-1} \text{ cm}^3,$$

Wertheim and Pearson<sup>33</sup> find that for their lifetime law

$$\tau \simeq N_D^{-1}$$

and dislocation densities around  $N_D \simeq 10^7 \text{ cm}^{-2}$  the capture time is  $\sim 7 \times 10^{-8} \text{ sec}$  and the capture radius is  $3.4 \times 10^{-8} \text{ cm}$  (or capture circle  $3.3 \times 10^{-15} \text{ cm}^2$ ) at room temperature.

For this dislocation density the capture rate of  $c_e \simeq 4 \times 10^8 \text{ sec}^{-1} \text{ cm}^3$  corresponds to  $400 \text{ sec}^{-1}$  per dislocation. Figielski points out that a dislocation represents electronically a giant center extending over a number of interatomic distances and that such a system depends very much on its charge state. The number of electrons per unit length of dislocation may continuously change from zero to a value of the order of  $10^6$ , depending on the space-charge field (barrier height and its quasi Fermi levels). Therefore the capture rates of electrons and holes depend on the electrostatic potential at the barrier height of the dislocation line. The behavior of such defects as recombination centers (high temperature) and trap centers (low temperature) are intimately connected.<sup>36</sup>

A theory for giant traps developed by M. Lax<sup>34</sup> introduces the concept of excited capture or large capture radii due to excited states and gradual energy transfer in a *cascade* of one-phonon transitions. In this way the improbable higher or multiphonon transitions can be avoided. Lax was able to account for the enormous capture cross sections in the range of  $10^{-15} \text{ cm}^2$  to  $10^{-12} \text{ cm}^2$ , which were found experimentally for different impurities. The largest values found for *p*-type impurity centers like In and Ni in germanium (77°K) can conceivably be associated with lattice defects, a mechanism not to be excluded in all doping processes where diffusion or doping-induced defects are easily generated. Figielski<sup>35, 32</sup> also assumes an excited state for the dislocation in order to explain the giant trap and recombination properties in analogy to the Lax model.

The latter starts from the assumption that the cross section can be represented by

$$\sigma(E_0) = \int 2\pi b \, db P_c(E_0, b), \quad (9.142)$$

where  $b$  = impact parameter (cross-section radius),  
 $P_e(E_0, b)$  = probability that electron with impact parameter  $b$  and energy  $E_0$ , somewhere along its orbit, has effective capturing collision.

Equation (9.142) is assumed to be at sufficiently large distance from the Bohr radius (classical treatment). Here we have to add that the Bohr radius for a dislocation is certainly larger than for an impurity atom. As described briefly in Section 2.4, Ref. 4 the nuclear charge number  $Z$  in the vacuum problem has to be replaced by  $Z_{\text{eff}} \approx 1/\epsilon$  for a coulomb field of the positively charged atom-core in a crystal environment. The weakening of the coulomb field widens the first Bohr radius to a value

$$a_0 = \frac{1}{Z_{\text{eff}}} \frac{\hbar^2}{m^* e^2} = \epsilon \frac{\hbar^2}{m^* e^2}. \quad (9.143)$$

For  $\epsilon = 16$  (germanium)

$$a_0 \approx 8.5 \cdot 10^{-8} \text{ cm.}$$

In the Schrödinger equation for the hydrogen atom, the  $1s$  eigenfunction is of the form

$$\psi_a(1) = \frac{1}{\sqrt{\pi}} \left( \frac{1}{a_0} \right)^{3/2} e^{-r/a_0}. \quad (9.144)$$

This charge-cloud extension is confined to  $\frac{3}{4}$  of its extent within a sphere of radius

$$2a_0 = 17 \cdot 10^{-8} \text{ cm.}$$

Now the elementary cube of germanium, for example, has a side length of  $5.62 \cdot 10^{-8}$  cm and contains eight atoms, and so the charge cloud embraces

$$4 \frac{\pi}{3} \left( \frac{17 \cdot 10^{-8}}{5.62 \cdot 10^{-8}} \right)^3 = 925 \text{ atoms.}$$

Because the dislocation has a stress field, the  $\epsilon$  value is even higher than assumed. In addition, the effective-mass value changes in the neighborhood of the dislocation. Under pressure the  $\Gamma'_{25}$  valence-band peak shifts in a negative energy direction (see Chapter 11), increasing contributions from the low mass split-off valence band. In summary, the value of 1,000 atoms covered by the charge cloud of a defect is very conservative for dislocations.

M. Lax' treatment does not take into account a space charge as it is given in the dislocation case and cannot account for the fact that a dislocation has a large cross section for hole capture but is repulsive for electrons. Here Figielski<sup>35</sup> develops an interesting model for the "excited state of a dislocation." Assuming overlap of the electronic wave functions in broken bonds



within an array or within a boundary (for small  $D$  values), one is led also to assume strong coulombic interaction among all electrons within an array. Figielski starts from the assumption of collective motion allowing for electrostatic wave propagation along a dislocation line and uses a formula derived by W. T. Read<sup>21</sup> for the energy of nonuniformity within a line charge:

$$eE(x) = \frac{4.8 \cdot E_0}{c^2} f^3 \cdot x \left[ 1 + 1.72 \left( \frac{x^2}{a} \right)^2 + \dots \right], \quad (9.145)$$

where  $E_0 = e^2/\epsilon c =$  interaction energy of electrons in neighboring sites. Since  $f = c/a$ , this may be written

$$eE(x) = \alpha x \left[ 1 + 1.72 \left( \frac{x}{a} \right)^2 + \dots \right], \quad (9.146)$$

where  $\alpha = (4.8 \cdot e^2)/\epsilon a^3$ .

Considering now a deviation  $\delta x$  from the equilibrium position of the charges in the  $a = c/f$  occupied sites, one can write for the force

$$F = -\alpha \delta x \left[ 1 + 1.72 \left( \frac{\delta x}{a_0} \right)^2 + \dots \right], \quad (9.147)$$

where  $a_0 =$  equilibrium spacing  $= c/f_0$ .

For a linear system the maximum frequency of oscillation is then

$$\omega_{\max} = 2 \left( \frac{\alpha}{m^*} \right)^{1/2}, \quad (9.148)$$

which yields for  $m^* \simeq m_e$  (free electron mass), for example,

$$\hbar \omega_{\max} = 0.078 \text{ eV}$$

for a dislocation with  $a = 4 \text{ \AA}$  at 200°K. Even if  $m^* \gg m$  the energy  $\hbar \omega_{\max}$  exceeds  $kT$  at that temperature. Therefore an electron falling from the conduction-band level into a vibrational dislocation level can lose all its energy in a single act, and one does not have to take recourse to M. Lax' cascading process. If the electron is treated as an independent harmonic oscillator with the energy spectrum

$$E = \hbar \omega_0 (n + \frac{1}{2}) \quad (n = 0, 1, 2, \dots), \quad (9.149)$$

where  $\omega_0 = (\alpha/m^*)^{1/2}$ ,

one can estimate the probability of the capture process at the dislocations. For the capture probability  $c_e$  Figielski finds the expression

$$c_e = \frac{\omega_0 f_0 V}{\pi} \exp \left( \frac{e \phi_0 + E_F - E_D}{kT} \right), \quad (9.150)$$

where  $V$  = volume in momentum space ( $E, E + dE$ ),

$\phi_0$  = barrier height,

$E_F$  = Fermi level,

$E_D$  = dislocation level.

This can be written

$$c_e = \frac{\omega_0 f_0 V}{\pi} \exp\left(-\frac{\zeta f_0}{kT}\right), \quad (9.151)$$

where  $\omega_0 f_0$  varies for no more than a factor of 3 in the temperature range of 100 to 300°K.

Although  $\zeta f_0 = e^2 f_0 / \epsilon a$ , the energy of the coulomb interaction of neighboring electrons on the dislocation line is of the order of  $kT$ , on the whole,  $c_e$  changes only slightly with temperature, in confirmation of the earlier assumption.

The question of the eventual contribution of barrier tunneling has been treated also by Figielski,<sup>25</sup> with the result that the dislocation barrier is almost unpenetrable for electrons down to 180°K. We described his approach to the barrier potential earlier (Section 9.3). According to (9.56) the barrier potential can be calculated. The result for  $N_D - N_A = 10^{15} \text{ cm}^{-3}$ ,  $a = c/f = 28.5 \text{ \AA}$  (or  $f = 0.14$  for a distance  $c = 4 \text{ \AA}$  of broken bonds), and  $E_D = 0.4 \text{ eV}$  below the conduction band is plotted in Figure 9.26.

According to the estimation by Figielski the contribution of the tunnel current to the capture process is small, where the potential barrier is lower than the energy  $W$ , defined so that the thermal flux due to all electrons with energies in excess of  $W$  is equal to the tunnel flux through the barrier.

Down to 180°K (crossover point) no appreciable influences of the tunnel

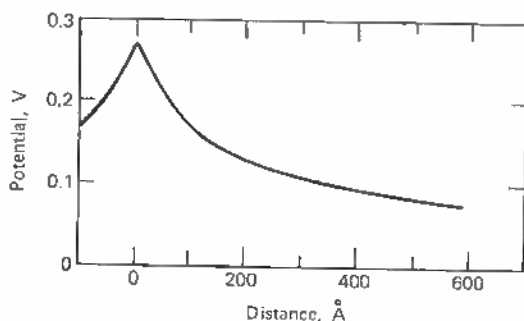


Fig. 9.26 Electrostatic potential as function of distance from dislocation line.

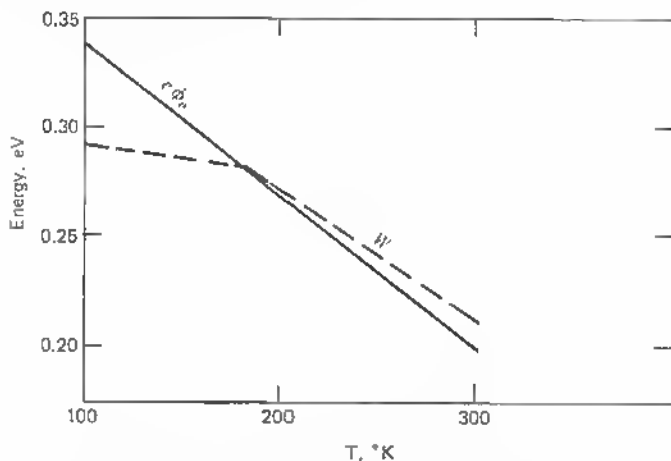


Fig. 9.27 Barrier potential height  $e\phi_0$  —; energy for which thermal flux of electrons equals tunnel flux through barrier —. ( $W$ )

current can be seen. Where  $e\phi_0 > W$  (lower temperature), however, the contribution of the tunnel current to the capture process is felt (see Figure 9.27).

## 9.6 DISLOCATIONS AND RADIATIVE RECOMBINATION

So far we have not assumed that the electron energy on capture can be released also by way of photon energy. This process, however, is very probable specifically in the case of dislocations. There are several reasons for this.

In a general way, the dislocation supplies the center for the isolated state in which electrons can be kept in an excited state. Such states, somewhat separated from the rest of the lattice structure, can bind electrons in a similar way to excited states in gases or similar to ionized impurities like copper in ionic crystals like ZnS.<sup>37</sup> The fact that the coupling to the lattice by way of phonons is decreased makes these centers efficient for radiative recombination. It may be that such a recombination takes place in two steps with a non-radiative component for the transition from the valence band to the center or the conduction band to the center (see Figure 9.28).

In distinction to homopolar semiconductors, like germanium, the III-V compounds like GaAs show a preponderance of radiative recombination because of the increased rate of direct recombination ( $\Delta k = 0$ ) and the corresponding low lifetime of minority carriers.

It is well known for example that in ZnS, the recombination light intensity is highest in areas of dislocations or dislocation arrays.<sup>37</sup> At mid-band levels,

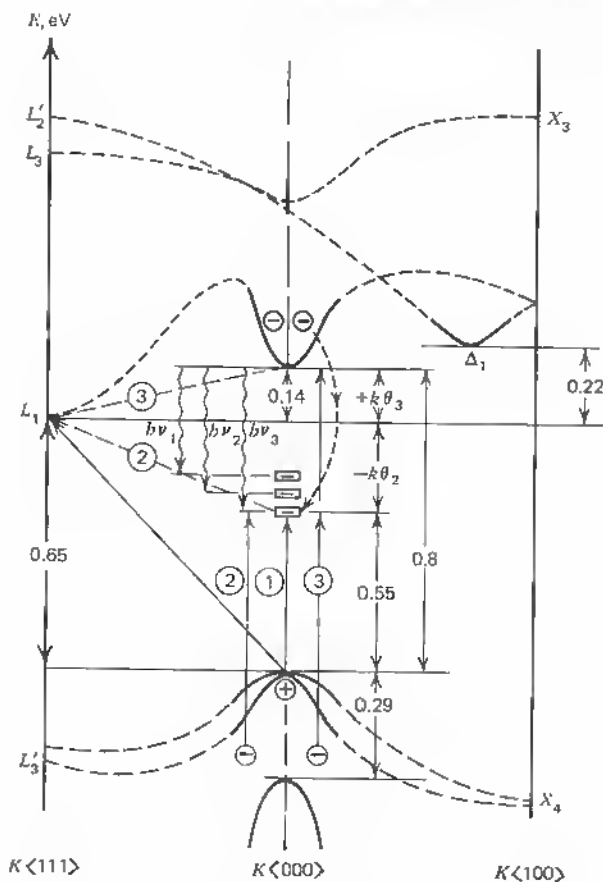


Fig. 9.28 Energy band of germanium. Direct ① and indirect ② ③ transitions.

the dislocations are ideally suited for hole-electron recombination with equal participation of carriers from valence and conduction band. Injection of carriers into the neighborhood of such traps or recombination centers leads to enhanced recombination either of pairs of carriers from both bands or from such midband levels as would serve as the intermediate steps in a cascade process of a transition from the conduction to the valence band. Another reason for enhanced radiative processes due to dislocations is the space-charge pipe around dislocations. Here, as in a  $p$ - $n$  junction, high local fields accelerate electrons until they gather enough momentum to excite other electrons into the conduction band. Finally, recombination takes place under release of surplus energy in form of radiative energy  $h\nu$ .

The lateral wave-function overlap of the dislocation levels within the arrays and the unusually strong longitudinal conduction for holes contribute to carrier transport parallel to the dislocations, and a transverse electric field increases the number of bound electrons and enhances the space charge (see Chapter 11), and finally increases carrier recombination within the space charge while carrying more current along the pipes.

In Figure 9.28 the possible processes within the band structure in  $k$  space have been plotted for germanium. The hole transition ① from the [000] peak of the valence band permits an electron transfer from the conduction band into the dislocation level or levels with radiative output  $h\nu$  corresponding to the level used because of the possible wave-function screening or excitation in this level. This *direct* transition, therefore, has become more probable than the indirect transition of a valence band electron ② to the dislocation level and simultaneous release of a phonon  $k \cdot \theta_1$ , or the phonon-assisted process ③.

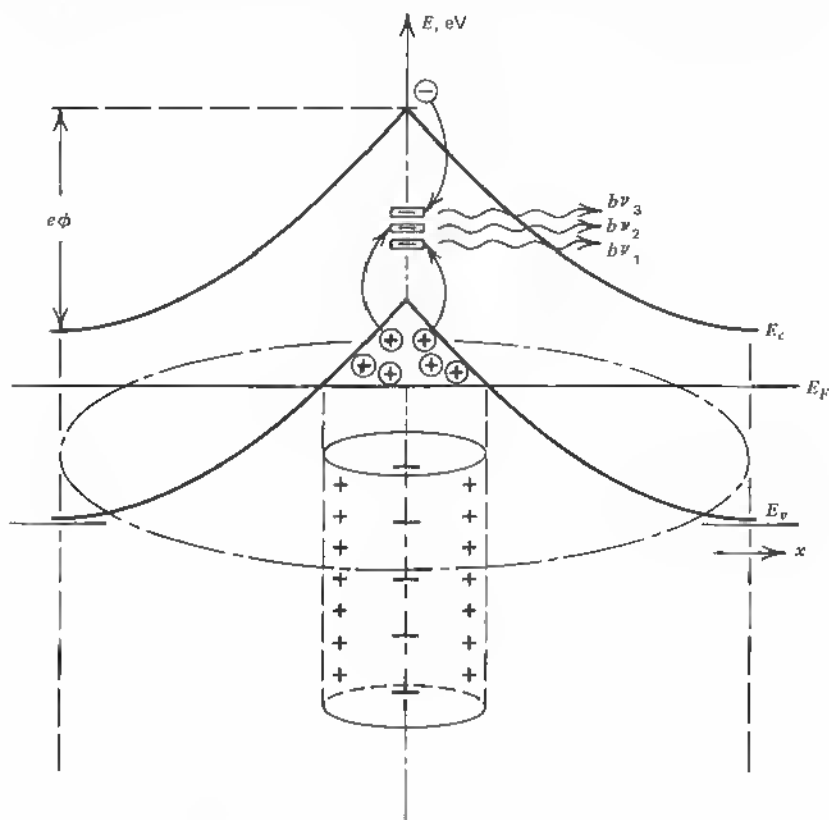


Fig. 9.29 Energy band around space charge cylinder and radiative recombinations.

Therefore, the recombination light also in material like silicon and germanium emanates preferentially at dislocation sites or grain boundaries.<sup>36</sup> Here, as in *p-n* junctions, the high-field region at the space charge is furnishing the necessary carrier momentum for transitions and also the interband states (in most grown or diffused *p-n* junctions, the interface is also covered with a layer of dislocations).<sup>38</sup>

The situation around the dislocation space-charge cylinder is therefore best described by the scheme in Figure 9.29. Holes from the degenerate part of the valence-band peak move into dislocation levels, thereby forcing conduction electrons to move also into the space-charge layer under release of radiative energy  $h\nu$  corresponding to the difference in energy between conduction band and interband level.

The levels in the gap or their frequencies  $\nu_n$  emitted are not fixed and depend on the bulk material properties, the dopant, and the doping level. As the Fermi level moves up, the filling of the levels closer to the conduction band increases, and they begin to play an important role in the recombination process.<sup>39</sup>

Measured values for germanium are, for example,

Doping level, $\text{cm}^{-3}$	Peak wavelength, $\mu$	
$5 \times 10^{13}$	2.42	
$2 \times 10^{14}$	2.4	
$5 \times 10^{14}$	2.35	Satellite peaks
$3.4 \times 10^{15}$	2.12	2.24
		2.37
$9 \times 10^{15}$	2.1	2.25
		2.36

It is interesting for the explanation of semiconductor laser-threshold lowering and degradation studies that the light intensity emitted by the dislocated areas or the dislocation band is relatively high for low-injection current values and that the fundamental band exceeds the dislocation band in intensity only for very high current density values (see Figure 9.30).

It is also seen that the efficiency of light conversion is much higher in the dislocation band. Only above 100 mA in this case the fundamental band exceeds the dislocation band in light intensity. From this point of view, a dislocation plane junction should be a much more efficient light converter than a normal bulk junction.

These findings were confirmed by Ivanov<sup>40</sup> and also by the fact that with increasing injection current the frequency of radiation moves toward higher values.

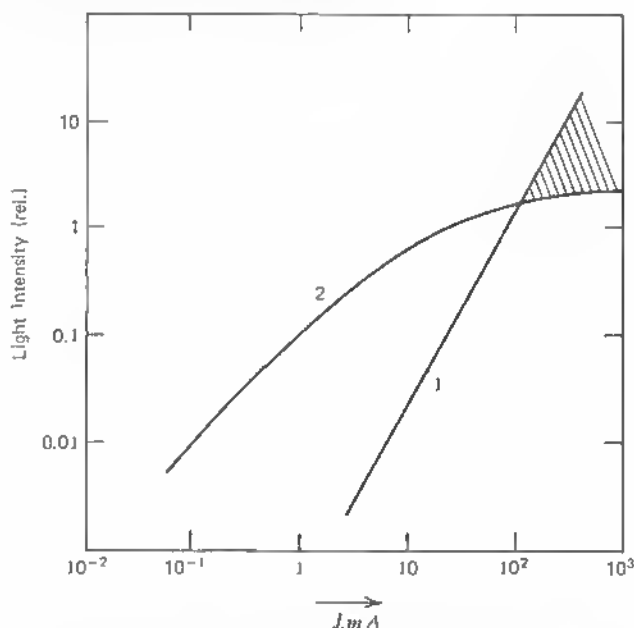


Fig. 9.30 Dependence of recomb. light intensity on injection current for *N*-type Ge sample ( $n = 5 \times 10^{13} \text{ cm}^{-3}$ ): ① fundamental, ② dislocation band. (After Gippins and Vavilov [9.38].)

Interesting work has been done on gallium arsenide where  $\alpha$  and  $\beta$  type dislocations and their influence on the recombination radiation have been studied<sup>41</sup>.

Samples of Czochralski-grown GaAs crystals were plastically deformed and *p-n* junctions introduced by diffusion along different crystallographic directions, [001] and [110], thereby arranging the dislocations either perpendicular or parallel to the junctions.

Prominent aspects of these light emitters were that  $\alpha$  and  $\beta$  dislocations have opposite effects on the power characteristics with regard to their position in the junction plane ( $\perp$  or  $\parallel$  to junction plane).

In summary,  $\alpha_{\perp}$  dislocations resulted in higher light output and  $\alpha_{\parallel}$  dislocations in low output;  $\beta_{\perp}$  dislocations gave a low conversion efficiency and  $\beta_{\parallel}$  dislocations a high conversion efficiency. It seems, however, that the radiative conversion efficiency is highest for the  $\alpha_{\perp}$  dislocations. The difference in effect stems from the different core charges for  $\alpha$  and  $\beta$  dislocations. The negative core charge of the  $\alpha$  dislocation apparently builds up an efficient space-charge cylinder in *n*-type material within the junction depletion region which enhances carrier recombination. The orientation dependence is an effect due to the different space charge and its position in the junction field.

To summarize the role of interband levels in radiative processes, we have plotted several processes in Figure 9.31. The possibilities here are:

1. *Lattice absorption of quanta resulting in conduction electrons and holes in the filled band.* Migrating holes capture electrons from ground states of centers, thus emptying these and rendering them available for the capture of conduction electrons and subsequent emission as the electrons make transitions to the center ground state. (Holes may also move to trapped electron sites and, by recombining with these electrons with nonradiative loss of excess energy, remove the possibility of these electrons' reaching emission centers by thermal or other activation into the conduction band).

2. *Absorption of quanta in emission centers.* Centers are emptied of electrons, but no free holes are created unless the temperature is high enough to raise filled-band electrons into the empty centers. In this case, the holes created may migrate to traps and remove the trapped electrons, process as in 1.

3. *Absorption of quanta by filled-band electrons which are raised into traps.* This creates mobile holes which can empty traps, as in process 1. Radiative recombination.

4. *Absorption of quanta in centers raising electrons to excited states.* No mobile electrons or holes are created. Radiative recombination.

These processes, among others, explain the occurrence of electroluminescence.<sup>42</sup>

From this general scheme, it becomes evident that midband levels, as in the case of dislocations, can be active as radiative recombination centers. The importance of the medial donor and acceptor states, stressed in Chapter

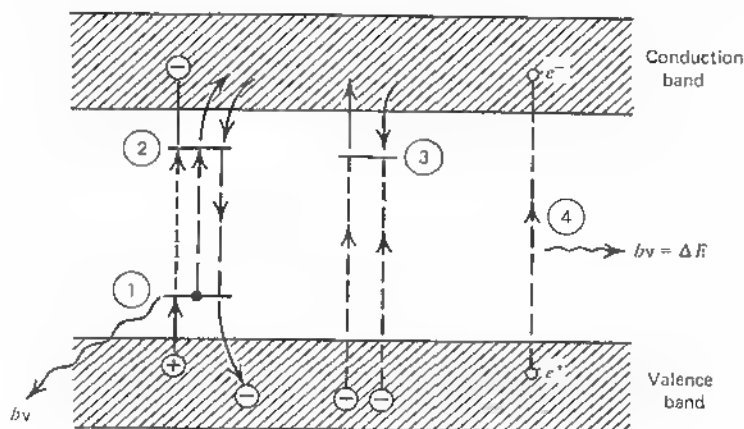


Fig. 9.31 Four cases of radiative recombination.



2, is evident here, and the sequence of events can be assumed as in Figure 9.32 (1) Impurity centers near the valence band, which are filled, are emptied by free holes. (2) These holes can be due to an excited state—for example, radiation excited—or due to field acceleration in dislocation pipes. Empty traps near the conduction band can serve as intermediate steps to the conduction band (3), and the subsequent filling of dislocation midband levels. Both transitions from the filled traps and dislocation levels are radiative transitions. (4).

In a band-to-band excitation, as in a semiconductor laser, the energy for a number of electron transitions into trap or dislocation levels is supplied, and strong induced emission occurs if the relaxation-time relations for these processes are such that, for example,  $\tau_2 > \tau_3$ , a condition for laser action.

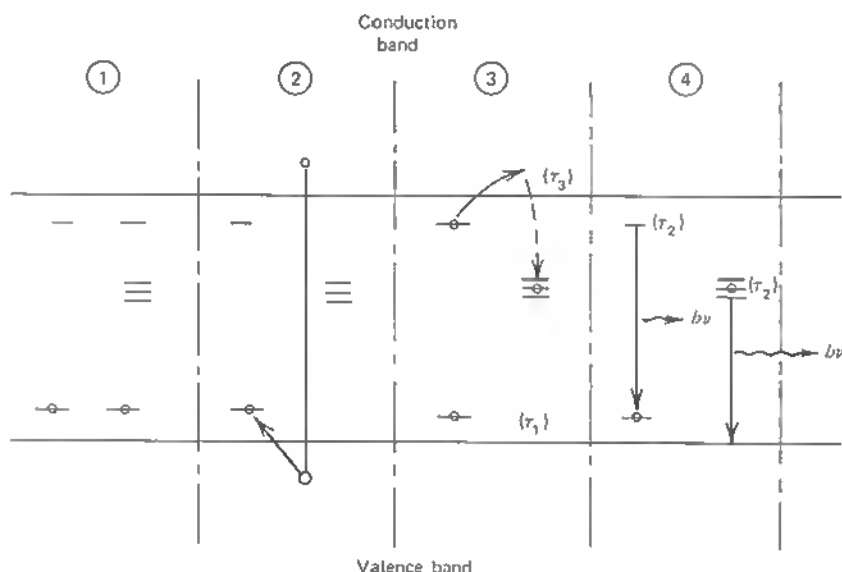


Fig. 9.32 Four steps in radiative recombination.

Many properties of electroluminescent materials are understandable if one assumes the strong cooperative action of the dislocation midband levels. In electroluminescent powders, the high conversion efficiency has probably to do with the innumerable number of intergrain boundaries and their enhancement of the radiative recombination process.

The picture of the grain boundary as developed later in the text will explain a number of aspects of intergrain structures in electro-luminescence.

Other phenomena, like *triboluminescence*, show as well that energy released

from dislocations can give rise to light emission. This effect, appearing when quartz is shattered or broken or when crystals are scratched, can be explained as follows: The dislocation boundaries formed during casting are the loci of stored electric energy. Their energy levels generally are filled with conduction electrons in the process. On release of the stress field and band rearrangement, these electrons migrate into lower-lying traps or fall back into the valence band under radiative energy release  $h\nu$ .

It is generally a question of how the relatively high fields of  $10^7 \text{ V cm}^{-1}$  are generated that are needed in electroluminescence to activate directly the emission centers in the crystal.

With the assumption of the dislocation space-charge layers, it is easy to explain localized fields of this magnitude when the usual low voltages (typical  $10^2$  volts) are applied to the material electrodes, since barrier layers around dislocations are of the order of  $10^{-5} \text{ cm}$ .

In most cases of radiative electron-hole recombination, the simple mode of band-to-band transitions under consideration of the respective state densities and the application of the principle of detailed balance (see Section 2.12) are not valid.<sup>43</sup> This is especially the case for higher electron densities at localized regions respectively for near-degenerate semiconductors. Here the simple consideration of two-particle coulomb interactions is not necessarily correct, since screening reduces interaction. Deeper band-tail states, as they exist in GaAs, usually used in recombination light-emitting diodes and lasers, cannot be considered to be in thermal quasi equilibrium.

Especially at lower temperatures, the density of occupied states per unit energy can increase continuously into the band, so that the total thermal equilibrium carrier concentration becomes indeterminate.

Southgate<sup>43</sup> discusses the numerous efforts which have been made to describe tailing in the density of states and at the absorption edge.

Measured absorption and emission spectra in, for example, *n*-type GaAs have a tail involving states separated by less than the average band gap. A comparison of the spectra shows that the lowest energy states—about 5% of the radiative recombination at 77°K results from these—are not in thermal equilibrium with the rest of the band. In emission from the bulk of a material, it is often these states which give rise to the majority of the externally observed radiation.

If tail states are represented by small regional variations of the band gap, measured values of photoluminescence could be accounted for.

Especially in degenerate material, gap shrinkage must be occurring. Considering the radiative rate constant  $B$  in

$$\frac{dn}{dt} = -Bnp,$$

a maximum correction for this effect gives a  $B$  that decreases with increasing degeneracy.

These facts and the observed small temperature dependence of the absorption tail slope point to a possible role of dislocations in band tailing.

## 9.7 ELECTRONIC NOISE AND DISLOCATIONS

Because of the importance of the electronic noise in semiconductor devices we add a short summary of the known facts as they relate to the contribution of the dislocation to the electronic noise in crystals.

It is now well established that recombination centers like dislocation levels have a strong effect on the electronic noise due to the generation-recombination noise (g-r noise).

Many different experimental results have been reported in the literature, seeming contradictory in some cases. This was due again to the neglect of the orientation of the dislocations with respect to the direction of carrier flow. If (majority) carriers are moving orthogonal to the space-charge cylinders, the scattering is maximized, as is the generation-recombination noise. Carriers are partially kept at the dislocation core after penetrating the space charge and are again released after a number of subsequent charge penetrations.

This is generally expressed by the influence of dislocations on the mean free time  $\tau_n$  of electrons. The current pulse generated by a free-moving charge carrier during its free time  $\tau_n$  is

$$\int_{t_0}^{t_0+\tau_n} I dt = \frac{q}{l} \mu_n E \tau_n, \quad (9.152)$$

where  $q$  = electron charge,

$l$  = length of semiconductor crystal,

$\mu_n$  = electron mobility,

$E$  = electric field strength =  $\frac{V}{l}$ .

Thus the current pulse is proportional to the local field in the semiconductor crystal and the mean free time of the carriers. Dislocations, as scattering—and recombination centers, shorten  $\tau_n$ , but, at the same time, they add additional current pulses. Although the noise current  $\bar{i}^2$  is linearly dependent on  $\tau_n$ , it is quadratically dependent on the charge  $\times$  velocity product, or

$$\bar{i}^2 \simeq (q\mu_n E)^2; \quad (9.153)$$

thus the more the number of individual charge movements increases, the higher the noise current  $\bar{i}^2$ , which is given by the sum of all Fourier com-

ponents from  $f$  to  $f + \Delta f$ :

$$\overline{i^2} = \frac{1}{l} q^2 \mu_n^2 E^2 \cdot n_0 \cdot \tau_n \cdot C \int_f^{f+\Delta f} \frac{\sin^2(\omega \tau_n/2)}{(\omega \tau_n/2)^2} df, \quad (9.154)$$

where  $C$  = crystal cross section,

$$n_0 = \text{mean electron density} = Z \frac{\tau_n}{C \cdot l},$$

$Z$  = number of supposed current pulses

(see, for example, summary article by D. Sautter,<sup>44</sup> where literature survey is also given).

The effect of interband levels of either the donor or acceptor type on the noise current has been considered in the past, and so have the corresponding expressions for the mean free time and the mean square noise current. In the case of trap levels a Shockley-Read model is applied, and transitions from the conduction band to the traps (and reverse) as well as transitions from the valence band to the traps (and reverse) define the carrier density fluctuations. With two different relaxation times  $\tau_1$  and  $\tau_2$ , a mean square noise current of the form

$$\overline{i^2} = \frac{4q^2 E^2}{l^2} \left[ g_1 \frac{\tau_1}{1 + (\omega \tau_1)^2} + g_2 \frac{\tau_2}{1 + (\omega \tau_2)^2} \right] \Delta f \quad (9.155)$$

is obtained.

Here  $g_1$  and  $g_2$  are functions of the noise amplitudes in the equations for the carrier density fluctuations.<sup>42</sup>

Generally, the frequency dependence of the noise current is of the form

$$F(f) = \frac{\tau_0}{1 + (\omega \tau_0)^2}. \quad (9.156)$$

For  $\omega \tau \gg 1$ , the behavior is  $F(f) \simeq 1/\omega^2$ , and for  $\omega \tau \ll 1$ ,  $F(f) = \text{constant}$ . Here at low frequencies the  $1/f$  noise has to be added, which, in turn, can be derived from a model with an even distribution of mean free times between the values  $\tau_1$  and  $\tau_2$ :

$$\overline{i^2} \simeq \int_{\tau_1}^{\tau_2} g(\tau) \frac{\tau}{1 + (\omega \tau)^2} d\tau \quad (9.157)$$

compare (9.155)—with  $g(\tau)$  as distribution function.

Recently Yu, Jordan, and Longini<sup>45</sup> have made an extensive study of the noise behavior in the presence of dislocations (see also the literature cited in this paper). Parallel arrays of edge dislocations have been introduced into  $n$ -type silicon by plastic deformation in vacuo (950°C for silicon). The direction of the dislocation arrays was controlled optically (etch pits), and

conductivity measurements in a direction orthogonal to the pipes confirmed the reduced carrier concentration, according to Read's model, by a factor  $(1 - \epsilon)$ .

Here  $\epsilon$  is the fraction of space occupied by space charges:

$$\epsilon = \pi R^2 \cdot d_{\perp},$$

where  $R$  = space-charge-cylinder radius,

$d_{\perp}$  = average dislocation density

(see Section 9.2). Control samples were also measured in order to eliminate the influence of heat treatment during plastic deformation.

It turns out that the drift mobility for current flow parallel to the dislocations is the same as in the control or heated samples, and the drift mobility for the perpendicular case is reduced by a factor  $(1 + \epsilon)^{-1}$ , as expected (see Section 9.2).

The results of the noise measurements on dislocated samples show clearly that the  $1/f$  noise is overshadowed at higher frequencies by the  $g$ - $r$  noise. However, the frequency range can vary, and control samples sometimes also show  $g$ - $r$  noise at frequencies as low as  $10^2$  to  $10^3$  cps.

These authors developed a method to resolve graphically the total excess noise into the two components of  $1/f$  noise and  $g$ - $r$  noise of dislocated samples (see Figure 9.33).

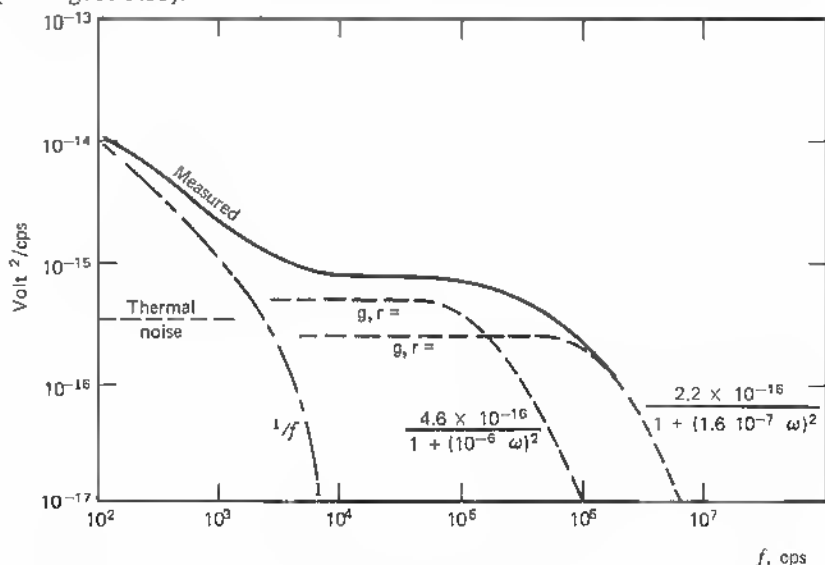


Fig. 9.33 Resolving total excess noise into  $1/f$  noise and  $g$ - $r$  noise spectra ( $106^{\circ}\text{C}$ ) [9.43].

In many cases of such resolutions more than 2 g-r noise components are needed to arrive at the measured curves. This is due to the presence of several recombination levels.

To analyze their results Yu, Jordan, and Longini used Van Vliet's admittance functions<sup>46</sup> in the generalized Nyquist theorem. This theorem states that the spectral densities of the fluctuating parameters are  $4kT/\omega^2$  times the real part of the admittance functions that relate forces and fluxes in a perturbed system.

Starting with the assumption that the noise is due to fluctuations in  $\varepsilon$  one can write for the mean square value of the current fluctuations

$$\langle (\Delta I_m)^2 \rangle = \left\langle \frac{I_m^2}{F^2(\varepsilon)} \right\rangle \langle (\Delta F)^2 \rangle. \quad (9.158)$$

Here  $\langle \rangle$  denotes the ensemble average over all different  $\Delta I$  and  $\Delta F$ .  $F(\varepsilon) = (1 - \varepsilon)/(1 + \varepsilon)$  is the current factor due to dislocations (orthogonal case):

$$\begin{aligned} I_m &= I_0 F(\varepsilon) \\ &= I_0(1 - \varepsilon)g(\varepsilon) \end{aligned} \quad (9.159)$$

(see Section 9.2). A more physical interpretation of this assumption is based on the fact that dislocations distributed at random within a current path cause reflections of carriers as well as recombination and trapping (below room temperature). Since the effective  $\varepsilon$  for one carrier is changed when a space-charge pipe incorporates another charge carrier, the fluctuation in  $\varepsilon$  is a statistical coupling of several functional ensembles. This can explain why in some instances the noise current is proportional to a high power of the sample current. Generally

$$\overline{i^2} \simeq CI_s^2,$$

where  $I_s$  = sample current,

but noise currents as high as

$$\overline{i^2} \simeq CI_s^4$$

have been found.<sup>44</sup>

The explanation for the higher current power law can be found in noise-interaction mechanisms where one ensemble is impressing random variations on another.<sup>47</sup>

The exchange of carriers from the conduction band (1) with a dislocation level (3) in the gap, for example, can be calculated if one assumes a Boltzmann distribution in energy for the conduction electrons. The transition

probabilities are then

$$P_{13} = k_{13} n \exp(-\beta\phi) \left( \frac{d_{\perp}}{a - n_{\perp}} \right) \quad (9.160)$$

$$P_{31} = k_{31} N_c n_{\perp},$$

where  $k_{13}$ ,  $k_{31}$  = transition coefficients,

$n$  = electron concentration at any instant

$n_{\perp} = (d_{\perp}/a)f_{\perp}$  = total number of captured electrons in all dislocations  $d_{\perp} \text{ cm}^{-3}$ ,

$a$  = distance of filled states along dislocations,

$f_{\perp}$  = fractional occupancy (approx. Fermi distribution),

$N_c$  = effective state density  $\gg n$ ,

$\beta\phi = e\phi/kT$  = barrier height.

With the introduction of expressions for the barrier height of the space-charge cylinders (see Sections 8.4 and 9.3, for example,) one can derive from here the *spectral density* of the current fluctuations<sup>44</sup> as function of  $\varepsilon$ , barrier height, and relaxation time  $\tau$  of the regression of a fluctuation  $\Delta n_{\perp}$  toward equilibrium  $n_{\perp 0}$ :

$$\tau^{-1} = \left( \frac{dP_{31}}{dn_{\perp}} \right)_{n_{\perp} \Rightarrow n_{\perp 0}} - \left( \frac{dP_{13}}{dn_{\perp}} \right)_{n_{\perp} \Rightarrow n_{\perp 0}}. \quad (9.161)$$

The expression for the spectral density in the orthogonal current flow case is then

$$S_{I\perp}(\omega) = \left[ \frac{4I_m}{(1 - \varepsilon)^2} \right]^2 \left( \frac{\varepsilon}{\partial n_0 \beta \phi_0} \right) \frac{\tau}{1 + (\omega\tau)^2}, \quad (9.162)$$

where  $\theta$  = sample volume.

The corresponding voltage noise spectrum is simply

$$S_{v\perp}(\omega) = S_{I\perp}(\omega) \cdot R_{\perp}^2, \quad (9.163)$$

where  $R_{\perp}$  = resistance of sample for current flow orthogonal to dislocations.

The time constants for transition processes from the conduction band to the dislocation levels have the form

$$\tau_n = f_{\perp 0} \exp \frac{(\beta\phi_0)}{k_{13} n_0 \beta \phi_0}, \quad (9.164)$$

( $n_0 = n + n_{\perp}$ ), and for transitions from the dislocation level to the valence band (2)

$$\tau_p = \exp \frac{(-\beta\phi_0)}{k_{32} n_{\perp 0}}. \quad (9.165)$$

The *shape* of the noise spectrum is the same for current flow parallel and perpendicular to the dislocations, but the noise is four times as large for current flow perpendicular to the dislocations. Yu, Jordan, and Longini did not produce measurements at low temperature in order to check the derived trapping case but based their comparisons on the higher temperature recombination case. The difference lies in the calculation of  $\langle(\Delta\epsilon)^2\rangle$  or the average fluctuation of the occupancy. In the recombination case

$$\epsilon = \frac{n_{\perp}}{n_0} = \frac{(d_{\perp}/a)f_{\perp}}{n_0}, \quad (9.166)$$

and

$$\epsilon = \frac{(n_d - n_a) + p - n}{n_0}, \quad (9.167)$$

and thus the fluctuation average is

$$\langle(\Delta\epsilon)^2\rangle = \left(\frac{1}{n_0}\right)^2 \{ \langle(\Delta p)^2\rangle + \langle(\Delta n)^2\rangle - \langle 2(\Delta p)(\Delta n) \rangle \}. \quad (9.168)$$

From here the spectral density of  $\langle(\Delta\epsilon)^2\rangle$  can be found, and, using Van Vliet's method,<sup>45, 46</sup> the spectral densities for the various transitions  $P_{23}$ ,  $P_{32}$ ,  $P_{13}$ ,  $P_{31}$  can be derived.

Yu, Jordan, and Longini compared theory and measurements by way of the temperature dependence of the noise amplitudes and the time constants. The agreement is fair, but the calculated noise amplitudes in a higher temperature range ( $T > 300^\circ\text{K}$ ) are too high compared with experimental results. The authors propose the explanation that additional holes can exist in the space charge that are not accounted for in the theory.

But, in general the g-r noise can be explained in terms of fluctuation in  $\epsilon$ , which, in turn, is caused by fluctuation in the number of captured electrons in the dislocation sites. The generation and recombination of the captured electrons are treated in a similar way to that of ordinary trapping and recombination centers (Shockley-Read) except that the concentrations of free carriers available for interaction are different from the usual bulk case by a Boltzmann factor because of the potential barrier at the dislocation.

It is assumed here that in the trapping case, captured electrons communicate with only one band (conduction band) and, in the recombination case, captured electrons can communicate with both the conduction and the valence band. It is observed that to about  $170^\circ\text{C}$  only the recombination case can explain the temperature behavior of the time constants and near room temperature the trapping case gives the best fit. The  $1/f$  part of the noise in dislocated samples is accounted for by Morrison's explanation<sup>48</sup> in which he



considered the fact that for an array of levels, the trapped charge causes the existence of a potential barrier to further trapping of like charges and that a fluctuation in the trapped charge produces proportional fluctuations in the barrier height.

## PROBLEMS

- 9-1. Assume that the bulk conductance at the dislocation pipes is dominated by the hole conductance  $G_p$ , and calculate  $G \simeq G_p$ , using a diffusion constant  $D_p = 200 \text{ cm}^2 \text{ sec}^{-1}$  and an average escape time  $t_e = 5 \cdot 10^{-10} \text{ sec}$ , as well as a pipe resistance per unit length of

$$R = 10^{10} \Omega/\text{cm}.$$

Calculate also the pipe capacity  $C$  per unit length (note:  $t_e \simeq t_c = t_r$ )

$$t_d = \frac{t_r \cdot t_e}{t_r + t_e} \simeq \frac{t_e}{2}.$$

Using  $C = D_d^{-1} \cdot R^{-1}$  as a pipe space-charge capacity, calculate  $C$ , and draw the representative scheme in Figure 9.2 with values.

- 9-2. Discuss the effect of a dislocation pipe on carrier flow in a bipolar transistor structure, if the pipe is (a) arranged vertically across the collector space charge, (b) arranged parallel within the collector space charge.
- 9-3. Discuss the limitations of the different scattering models for the carrier mobilities  $\mu = e\sigma \cdot R$  on account of the changes in Hall constant  $R$  and conductivity  $\sigma$  due to dislocations ( $c = \text{constant} = 3 \cdot 10^{10} \text{ cm/sec}$ ).
- 9-4. Calculate the mobility loss due to dislocation scattering in case C, Fig. 9.7, when the ratio of the mean free paths in the bulk with and without dislocations is  $x = l_D/l = 0.2$ .
- 9-5. Measure the space-charge extension in the different scanning-electron-beam photographs, and calculate the width using (9.53), (9.57), and (9.60). Discuss limitations of different models.
- 9-6. Calculate the interaction energy  $E_0$  of electrons in a line charge in germanium using (9.64) and assuming an occupation factor  $f$  for a temperature range of 100 to 150°K (see Fig. 9.24). Use different statistics.
- 9-7. What is the area state density in a grain boundary (planar case) for germanium at 150°K (9.76)?
- 9-8. Plot the change in filling factor  $f$  with the external voltage  $V_e$  at the space charge according to (9.77), assuming a constant barrier height  $\phi$ .
- 9-9. Calculate the maximum frequency of oscillation (9.102) for a dislocation line charge with a distance  $a$  between filled states of  $5 \times 10^{-7} \text{ cm}$  for germanium ( $\epsilon = 16$  and  $m^* = 0.1 m$ ). Indicate the optical phonon wavelength and wave number. Which experimental setup would be used to measure this oscillation by spectroscopy (optical absorption)?

- 9-10. Discuss the different possibilities for radiative recombination due to interband levels (Section 9.6).
- 9-11. Explain the typical frequency dependence of the generation-recombination noise.

## REFERENCES

1. Pearson, G. L., W. T. Read, and F. J. Morin: Dislocations in Plastically Deformed Germanium, *Phys. Rev.*, vol. 93, no. 4, pp. 666-667, Feb. 15, 1954.
- 2a. Werthein, G. K., and G. L. Pearson: Recombination in Plastically Deformed Germanium, *Phys. Rev.*, vol. 107, no. 3, pp. 694-698, Aug. 1, 1957.
- 2b. Lemke, H.: Zur Abhängigkeit der Lebensdauer von der Versetzungsdichte bei tiegelfreien Silizium-Einkristallen. *Physica Status Solidi* vol. 12, p. 125, 1965.
3. Newman, R. C., J. Wakefield, and J. B. Willis: The Formation of *p-n-p* Structures around Dislocations in Silicon, *Solid State Electronics*, vol. 8, pp. 180-182, 1965.
4. Bardsley, W.: The Electrical Effects of Dislocations in Semiconductors, "Progress in Semiconductors," Wiley, New York, 1960, vol. 4, pp. 157-203.
5. Logan, R. A., G. L. Pearson, and D. A. Kleinman: Anisotropic Mobilities in Plastically Deformed Germanium, *Journal Applied Physics*, vol. 30, p. 885, 1959.
6. Rhodes, R. G.: "Imperfections and Active Centers in Semiconductors," Pergamon Press, New York, 1964.
7. Billig, E., and P. J. Holmes: Defects in Diamond-type Semiconductor Crystals, in "Advances in Electronics and Electron Physics," L. Marton (ed.), Academic, New York, vol. X, pp. 71-105, 1958.
8. Vogel, F. L., W. T. Read, and L. C. Lovell: Recombination of Holes and Electrons at Lincage Boundaries in Germanium, *Phys. Rev.*, vol. 94, no. 6, pp. 1791-1792, June. 15, 1954.
9. Mataré, H. F., H. Kedesdy, A. MacDonald, and A. Petersen: Study of Electrical Characteristics of Grain Boundaries, *Phys. Rev.*, vol. 98, p. 1179, 1955.
10. Mataré, H. F., and B. Reed: Anomaly of Carrier Lifetime in Germanium Bicrystals, *Zschr. f. Naturf.*, vol. 11a, no. 10, pp. 876-878, 1956.
11. Yu, K. K., A. G. Jordan, and R. C. Longini: Relations between Electrical Noise and Dislocations in Silicon, *Journal Applied Physics* vol. 38, no. 2, pp. 572-583, February, 1967.
12. Heine, V.: Dangling Bonds of Dislocations in Semiconductors, *Phys. Rev.*, vol. 146, no. 2, pp. 568-570, Jun. 10, 1966.
13. Broudy, R. M.: The Electrical Properties of Dislocations in Semiconductors, *Advances in Physics*, vol. 12, no. 46, pp. 135-184, April, 1963.
14. Pease, R. F. W.: The Screening Microscope, *IEEE Spectrum*, pp. 96-102, October, 1967.
15. Thornton, P. R., K. A. Hughes, Htin Kyaw, C. Millward, and D. V. Sulway: Failure Analysis of Microcircuitry by Scanning Electron Microscopy, "Microelectronics and Reliability," Pergamon, New York, 1967, vol. 6, pp. 1-16.

16. Nealey, C. C., C. W. Laakso, and P. J. Hagon: Planar Silicon Device Analyses with the Electron Probe Microanalyzer, Microprobe Symposium, E. C. S., Washington, D.C., October, 12, 1964.
17. Czaja, W., and J. R. Patel: Observations of Individual Dislocations and Oxygen Precipitates in Silicon with a Scanning Electron Beam Method, *Journal of Applied Physics*, vol. 36, pp. 1476-1482, 1965.
18. Mataré, H. F., and H. A. R. Wegener: Oriented Growth and Definition of Medium Angle Semiconductor Bicrystals, *Zschr. f. Phys.*, vol. 631, 1967.
19. Mataré, H. F.: Dislocation Planes in Semiconductors, *Journal of Applied Physics*, *Phys.* vol. 30, pp. 581-589, Apr. 4, 1959.
20. Hamakawa, Y., et al.: Galvanomagnetic Effects in Boundary Layer of Germanium Bicrystals, *Procced. Int. Conf. Crystal Lattice Defects*, 1962, *Journal Soc. Japan*, vol. 18, suppl. II, pp. 166-171, 1963.
21. Read, W. T.: Theory of Dislocations in Semiconductors, *Phil. Mag.*, vol. 45, p. 775, 1954; vol. 45, p. 1119, 1954; vol. 46, p. 111, 1955.
22. Mataré, H. F.: "Anisotropy of Carrier Transport in Semiconductor Bicrystals," *Proceedings of the International Conference on Solid State Physics in Electronics and Telecommunications*, Academic, New York, 1959, pp. 73-96.
23. Mueller, R. K., and R. L. Jacobson: Alpha and Beta Grain Boundaries in Indium Antimonide, *Journal of Applied Physics*, vol. 33, no. 7, pp. 2341-2345, July, 1962.
24. Mueller, R. K., and R. N. Maffit: Grain Boundary Conductance in InSb, *Journal of Applied Physics*, vol. 35, no. 3, pp. 734-735, March, 1964.
25. Figielski, T.: Dislocations as Traps for Holes in Germanium, *Physica Status Solidi*, vol. 9, pp. 555-566, 1965.
26. Lagowski, J.: Local Changes in Work Function of Germanium and Silicon Due to Dislocations, *Physica Status Solidi*, vol. 5, p. 555, 1964.
27. Mataré, H. F.: Electrical Behavior of Bicrystal Interfaces, *Zschr. f. Phys.* vol. 145, pp. 206-234, 1956.
28. Schlier, R. E. and H. E. Farnsworth: "Semiconductor Surface Physics," R. H. Kingston (ed.), University of Pennsylvania Press, Philadelphia, 1957, p. 3.
29. Casey, H. C., Jr.: Investigation of Inhomogeneities in GaAs by Electron Beam Excitation, *Journal of the Electrochemical Society*, vol. 114, no. 2, pp. 153-158.
30. Conwell, E. M.: Impurity Band Conduction in Germanium and Silicon, *Phys. Rev.*, vol. 103, no. 1, pp. 51-61, Jul. 1, 1956.
31. Morrison, S. R.: Recombination of Electrons and Holes at Dislocations, *Phys. Rev.*, vol. 104, no. 3, pp. 619-623, Nov. 1, 1956.
32. Figielski, T.: Theory of Carrier Recombination at Dislocations in Germanium, *Phys. Stat. Solidi*, vol. 6, pp. 429-440, 1964.
33. Wertheim, G. K., and G. L. Pearson: Recombination in Plastically Deformed Germanium. *Phys. Rev.*, vol. 107, no. 3, pp. 694-698, Aug. 1, 1957.
34. Lax, M.: Cascade Capture of Electrons in Solids, *Phys. Rev.*, vol. 119, no. 5, pp. 1502-1523, Sept. 1, 1960.
35. Figielski, T.: Mechanism of Electron Capture by a Dislocation, *Physica Stat. Solidi*, vol. 10, pp. 75-78, 1965.

36. Chynoweth, A. F., and K. G. McKay: Photon Emission from Avalanche Breakdown in Silicon, *Phys. Rev.*, vol. 102, p. 369, 1956.
37. Bowen, E. J., and G. F. J. Garlick: Luminescence, *International Science and Technology*, pp. 18-29, August, 1966.
38. Gunn, J. B.: High Electric Field Effects in Semiconductors, "Progress in Semiconductors," Wiley, New York, 1957, vol. 2, pp. 213-247.
39. Gippins, A. A., and V. S. Vavilov: Radiation Recombination at Dislocations in Germanium, *Soviet Physics—Solid State*, vol. 4, no. 9, pp. 1777-1782, March, 1963.
40. Ivanov, V. L.: Radiation Recombination at Edge Dislocations in Germanium, *Soviet Physics—Solid State*, vol. 7, no. 3, pp. 629-632, September, 1965.
41. Osvenskii, V. B., G. P. Proshko, and M. G. Mil'vidskii: Effect of Dislocations on the Structure of Diffused  $p$ - $n$ -Junctions in Gallium Arsenide and on Recombination Radiation Parameters, *Soviet Physics—Semiconductors*, vol. 1, no. 6, pp. 755-760, December, 1967.
42. Garlick, G. F. J.: The Electrical Properties of Phosphors, in "Progress in Semiconductors," Gibson, Burgess, Aigrain (eds.), Wiley, New York, 1956, vol. 1, pp. 101-133.
43. Southgate, P. D.: Radiation Recombination and Equilibrium between Near-band-edge Tail States in  $n$ -Type GaAs, *J. Appl. Phys.*, vol. 40, no. 13, pp. 5333-5342, December, 1969.
44. Sautter, D.: Noise in Semiconductors, in "Progress in Semiconductors," Gibson, Kröger, Burgess (eds.), Wiley, vol. 4, 1960, pp. 127-133.
45. Yu, K. K., A. G. Jordan, and R. L. Longini: Relations between Electrical Noise and Dislocations in Silicon, *J. Appl. Phys.*, vol. 38, no. 2, pp. 572-583, February, 1967.
46. Van Vliet, K. M.: Irreversible Thermodynamics and Carrier Density Fluctuations in Semiconductors, *Phys. Rev.*, vol. 110, no. 1, pp. 50-61, Apr. 1, 1958.
47. Mataré, H. F.: Interaction between Barrier Layers in Transistors, *Z. f. Physik.*, vol. 131, no. 82, 1951.
48. Morrison, S. R.: Generation of  $1/f$ -Noise by Levels in a Linear or Planar Array, *Phys. Rev.*, vol. 99, no. 6, 1904, 1955; vol. 104, no. 619, 1956.

## Chapter 10 The Electronic Properties of Dislocation Boundaries

### 10.1 LINEAGE BOUNDARIES

The definition of lineage boundaries, as advanced in Section 4.2, incorporates the fact that some coherency energy between the edge dislocation arrays remains. We have seen that partially overlapping dilation and compression regions stabilize such structures. Even for distances in the micron range, where the tilt angle  $\theta$  is below the minute of an arc range, some coherency (see also Section 7.2) is visible, but the lineage direction is easily changed in case of external forces, temperature variations, strain in the crystal, and the like.

Because of this sensitivity of the lineage, small-angle misfit boundaries present themselves as curved structures in electron-transmission micrographs of thin-film semiconductors like silicon. If layers of a few 1,000 Å are grown, for example, by chemical vapor deposition (using  $\text{SiH}_4$  or  $\text{SiCl}_4$ ) on  $\text{Al}_2\text{O}_3$  (sapphire), the nuclei misalignment, the lattice mismatch, and the mismatch of thermal expansion coefficients all cause a high dislocation density (see Chapter 14, Sect. 4), and transmission photomicrographs reveal a tremendous structural disturbance. Figure 10.1 shows two micrographs, one with 44,000, the other with 70,000 magnification, of a silicon-on-sapphire layer grown by chemical vapor deposition near the  $\text{Al}_2\text{O}_3$  interface.

In the film taken with higher magnification the line structure is clearly dissolved, and some orientation of the line pattern becomes visible.

Now considering a fine structure, as shown in Figure 4.6, the question of the electrical properties of this structure arises. McKelvey and Longini<sup>1</sup> have treated this problem by applying kinetic theory to the minority carrier flow across a lineage boundary. Relations for the recombination velocity or the transmission coefficient  $T$  (= probability that a carrier does not recombine in an encounter with the array) are then derived on the basis of boundary

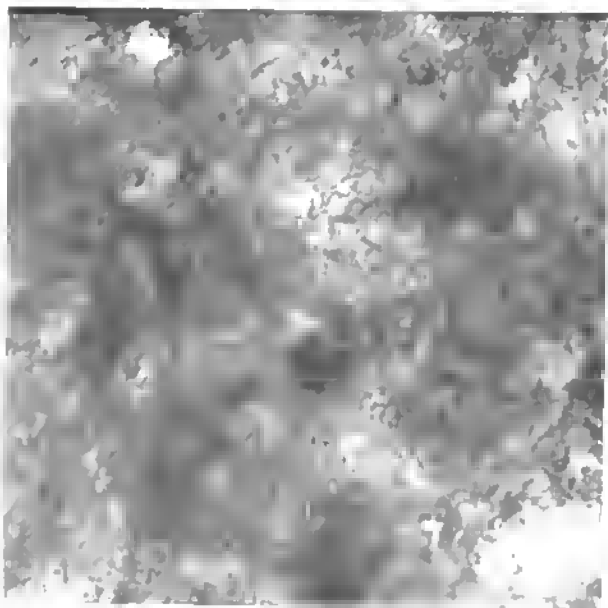


**Fig. 10.1a** Silicon on sapphire-electron transmission photo-  
micrograph 44000 $\times$ , or 1 cm  $\simeq 2.10^3$  Å.



**Fig. 10.1b** Silicon on sapphire-electron transmission photo-  
micrograph 70000 $\times$ , or 1 cm  $\simeq 10^3$  Å.

conditions for the continuity equation for injected carriers by way of the method of *multiple reflections*. Schematically the situation is such that incoming charge carriers (in this case, minority carriers) are transmitted (transmission coefficient  $T$ ) or reflected (reflection coefficient  $R$ ) (see Figure 10.2).

The bulk reflection coefficient  $B$  expresses the probability that a carrier starting out from the lineage plane does not recombine as a result of processes unrelated to the dislocation array before returning to the lineage plane.

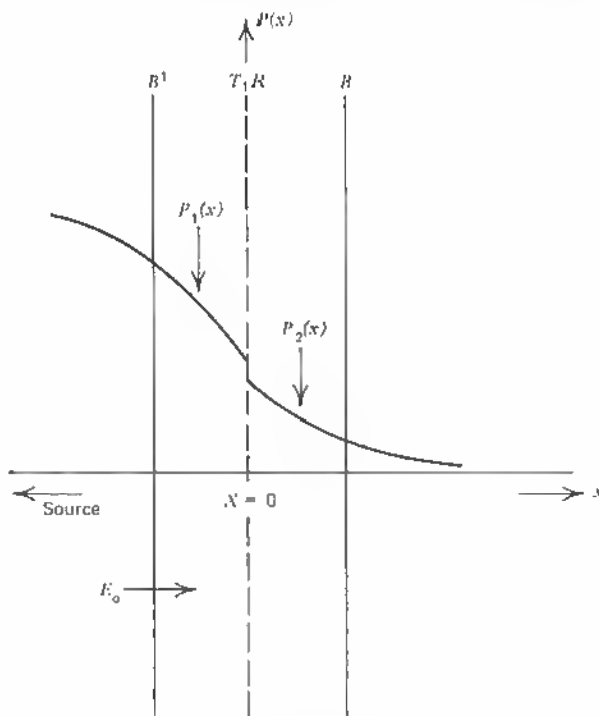


Fig. 10.2 Schematic of injected carrier concentrations at a lineage boundary at  $x = 0$ ; driving field  $E_0$ ; bulk reflection boundaries  $B$  and  $B'$ .

In more detail, the model assumes a diameter  $g$  of the cylindrical recombination area around an edge dislocation (see Figure 10.3). For a given angle of incidence  $\theta$ , carriers initially in the shaded regions recombine.

For  $|\theta| > |\theta_0|$ , where  $\cos \theta_0 = g/h$ , there is no transmission of carriers

through the boundary. In this simple model the transmission coefficient  $T$  can be expressed in terms of  $g$  and  $h$ :

$$T = \frac{2}{\pi} \cos^{-1} \left( \frac{g}{h} \right) - \frac{2g}{\pi h} \ln \left\{ \frac{h}{g} \left[ 1 + \left( 1 + \frac{g^2}{h^2} \right)^{1/2} \right] \right\}, \quad (10.1)$$

In other words,  $T$  is only a function of the relations between the assumed recombination cross section  $g$  and the dislocation distance  $h$ .

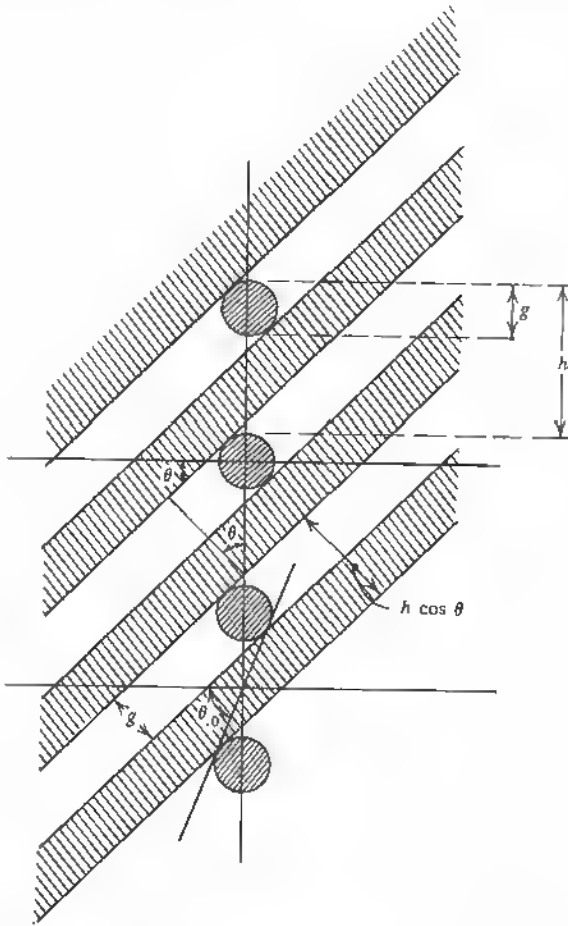


Fig. 10.3 Transmission and absorption of carriers obliquely incident on array of cylindrical recombination centers. (After McKelvey and Longini [10.1].)



The boundary conditions on the continuity equation that describes the concentration  $p(x)$  of injected minority carriers as a function of position  $x$  are then

$$-D \frac{\partial p_1(0)}{\partial x} = s_1 p_1(0), \quad (10.2)$$

$$-D \frac{\partial p_2(0)}{\partial x} = s_2 p_2(0), \quad (10.3)$$

$$\frac{p_2(0)}{p_1(0)} = \eta, \quad (10.4)$$

$$\lim_{x \rightarrow \infty} p_2(x) = 0, \quad (10.5)$$

where

$$s_1 = \frac{1}{2} V_T \left[ 1 - \frac{v_+}{v_-} \left( R + \frac{T^2 B}{1 - RB} \right) \right] / \left[ 1 + \frac{v_+}{v_-} \left( R + \frac{T^2 B}{1 - RB} \right) \right], \quad (10.6)$$

$$s_2 = \frac{1}{2} V_T \left( 1 - \frac{v_+}{v_-} B \right) / \left( 1 + \frac{v_+}{v_-} B \right), \quad (10.7)$$

$$\eta = \left( \frac{T}{1 - RB} \right) \left( 1 + \frac{v_+}{v_-} B \right) / \left[ 1 + \frac{v_+}{v_-} \left( R + \frac{T^2 B}{1 - RB} \right) \right]. \quad (10.8)$$

$V_T$  is the mean thermal velocity and  $v \pm = \frac{1}{2} V_T \pm \frac{1}{2} \mu E_0$ .  $E_0$  = applied field. In all practical cases  $\eta = 1$ . If the recombination velocity  $s_2$  is obtained by measuring bulk properties away from any lineage plane, the bulk reflection coefficient  $B$  can be found on account of (10.7).

McKelvey<sup>2</sup> uses a two-point-probe measurement set to find the recombination velocities  $s_1$  and  $s_2$  in (10.6) and (10.7). If the points are separated by undisturbed bulk material,  $s_2$  is measured, and  $s_1$  may be measured by arranging the sample so that the lineage plane falls between the two measuring point probes. Minorities are injected at one point by light. The two points are arranged at 0.15 mm distance for measurements of  $s$ , and the carrier diffusion length  $L$  is measured with large probe spacings (1 to 2 mm).

Starting from the continuity equation for a long sample of uniform cross section (one-dimensional carrier-flow conditions) and arrangement of the lineage boundary perpendicular to the carrier flow (steady-state condition),

$$\frac{\partial^2 p}{\partial x^2} - \frac{\mu E_0}{D} \frac{\partial p}{\partial x} - \frac{p}{L^2} = \frac{\partial p}{\partial t} = 0, \quad (10.9)$$

where  $D$  = diffusion constant for minority carriers,

$p$  = minority carrier density

$L$  = diffusion length in bulk,

$\mu$  = mobility

we arrive at the solution

$$p(x) = C_1 \exp \frac{\gamma_+ x}{L} + C_2 \exp \frac{\gamma_- x}{L}, \quad (10.10)$$

where

$$\begin{aligned} \gamma_{\pm} &= \gamma \pm (\gamma^2 + 1)^{1/2}, \\ \gamma &= \frac{\mu E_0 L}{2D}. \end{aligned} \quad (10.11)$$

In the trivial case of no boundary,  $R = 0$ ,  $T = 1$ , and thus  $s_1 = s_2$ ,  $\eta = 1$ . In this case the concentration of injected carriers is of the form

$$p(x) = p_0 \exp \frac{\gamma_- x}{L}. \quad (10.12)$$

With two probes at points  $x_1$  and  $x_2$  outside of the lineage region one can now measure a ratio

$$K = \frac{p(x_1)}{p(x_2)} = \exp \frac{\gamma_-(x_1 - x_2)}{L}, \quad (10.13)$$

where  $x_1 - x_2 = d$  = distance between probes:

$$\ln K = \frac{d}{L} [(\gamma^2 + 1)^{1/2} - \gamma]. \quad (10.14)$$

Substituting now  $\gamma$  from (10.11) into (10.14) and solving for  $L$  and noting that  $\mu/D = e_0/kT$ , we have the expression for the diffusion length

$$L = d \left[ \ln K \left( \ln K + \frac{e_0 E_0 d}{kT} \right) \right]^{-1/2}, \quad (10.15)$$

which relates  $K$  (10.13)  $\gamma$ ,  $T$ ,  $B$  (10.8) and  $s_2$  (10.7).

In the case where the lineage boundary is now placed between the collector probes and a sweep field and light injection are applied,  $T$  and  $R$  are arbitrary, and, according to (10.4), the solution of (10.9) is discontinuous for  $x = 0$  (boundary location); that is, two carrier density functions are to be considered  $p_1(x)$  and  $p_2(x)$  in the form of (10.9). Because of (10.5) the coefficient of  $\exp(\gamma_+ x/L)$  in the expression for  $p_2(x)$  must vanish, therefore:

$$\begin{aligned}
 p_1(x) &= C_1 \exp \frac{\gamma_+ x}{L} + C_2 \exp \frac{\gamma_- x}{L}, \\
 p_2(x) &= C_3 \exp \frac{\gamma_- x}{L}.
 \end{aligned}
 \tag{10.16}$$

Conforming to the boundary conditions (10.2) to (10.4), only the ratios of the coefficients  $C_1$ ,  $C_2$ ,  $C_3$  can be found. Physically this stems from the fact that the injection source strength is arbitrary (light-injection ratio, collector potential and position):

$$\begin{aligned}
 \frac{C_1}{C_3} &= -\frac{1}{\eta} \left( \frac{s_1 L/D + \gamma_-}{\gamma_+ - \gamma_-} \right), \\
 \frac{C_2}{C_3} &= \frac{1}{\eta} \left( \frac{s_1 L/D + \gamma_+}{\gamma_+ - \gamma_-} \right).
 \end{aligned}
 \tag{10.17}$$

Substituting these coefficients into the first equation (10.16), one has

$$p_1(x) = \frac{C_3}{\eta(\gamma_+ - \gamma_-)} \left[ \left( \gamma_+ + \frac{s_1 L}{D} \right) \exp \left( \frac{\gamma_- x}{L} \right) - \left( \gamma_- + \frac{s_1 L}{D} \right) \exp \left( \frac{\gamma_+ x}{L} \right) \right].
 \tag{10.18}$$

By substituting the second equation (10.16) into (10.3), one obtains a relation between  $L$  and  $s_2$ :

$$s_2 = -\frac{D\gamma_-}{L}.
 \tag{10.19}$$

Experimentally the quantity  $K \equiv p_1(-a)/p_2(+a)$  is significant, since the boundary is located in the center between the collector probes, which are  $2a$  distant. One finds  $K$  by using (10.18) and (10.16):

$$\begin{aligned}
 K \equiv \frac{p_1(-a)}{p_2(a)} &= \frac{1}{\eta(\gamma_+ - \gamma_-)} \left[ \left( \gamma_+ + \frac{s_1 L}{D} \right) \exp(-2\alpha_0 \gamma_-) \right. \\
 &\quad \left. - \left( \gamma_- + \frac{s_1 L}{D} \right) \exp(-2\alpha_0 \gamma_+) \right],
 \end{aligned}
 \tag{10.20}$$

where

$$\alpha_0 = a/L.
 \tag{10.21}$$

Here the carrier density ratio is expressed in terms of the recombination velocity  $s_1$ , the diffusion length  $L$ , diffusion constant  $D$ ,  $\gamma_-$  and  $\gamma_+$  respectively, and the expressions (10.11) that contain the carrier mobility  $\mu$ .

In most experimental cases the thermal velocities are equal:

$$\frac{v_+}{v_-} \simeq 1$$

when  $R \ll 1$ . Also  $B$  and  $T$  are practically unity. Then  $\eta$ , in (10.8), is also near unity and in (10.20)  $K$  is governed by  $s_1$ . Actually, only  $1 - R \gg 1 - B$  needs to be assumed when  $\eta \simeq 1$ .

Solving (10.20) for  $s_1 L/D$  yields

$$\frac{s_1 L}{D} = \frac{\gamma_+ [K - \exp(-2\alpha_0 \gamma_-)] - \gamma_- [K - \exp(-2\alpha_0 \gamma)]}{\exp(-2\alpha_0 \gamma_-) - \exp(-2\alpha_0 \gamma)}. \quad (10.22)$$

Under the conditions outlined, one can approximate

$$T^{*2} \equiv \frac{R}{B} + \frac{T^2}{1 - RB} \simeq (R + T)^2 \quad (10.23)$$

or also

$$1 - T^{*2} \simeq 1 - (T + R), \quad (10.24)$$

where the functional error in the approximation (10.24) is only  $1 - B + R$ .

Using (10.24) in (10.6) for  $s_1$ ,  $v_+$   $B/v_-$  being eliminated by using (10.7) for  $s_2$ , leads to a solution for  $(T + R)$ :

$$(T + R)^2 = T^{*2} = \left[ \frac{1 - (2s_1/V_T)}{1 + (2s_1/V_T)} \right] \left[ \frac{1 + (2s_2/V_T)}{1 - (2s_2/V_T)} \right]. \quad (10.25)$$

Conservation of particle flux requires that

$$A + R + T = 1.$$

Here  $A$  is the absorption coefficient or recombination probability of the lineage plane with respect to a single minority carrier, and

$$A = 1 - (R + T) \simeq 1 - T^*. \quad (10.26)$$

Returning now to the derivation of the expression for  $R + T$  or  $1 - A$  in terms of  $g$ , the diameter of the cylindrical recombination regions of the individual dislocation arrays, and  $h$ , the average dislocation spacing (10.1), we have:

$$1 - A = \frac{2}{\pi} \left[ \cos^{-1} \left( \frac{g}{h} \right) - \frac{g}{h} \sec h^{-1} \left( \frac{g}{h} \right) \right], \quad (10.1)$$

for the recombination cross section of a single dislocation belonging to the lineage boundary.

With the above set of elaborate equations, McKelvey was able to measure  $s_1 - s_2$  (cm/sec), the absorption coefficient  $A$ , and the individual recombination region  $g$ . Resistivity  $\rho$  (ohm cm), mobility  $\mu$  (cm<sup>2</sup>/volt sec), diffusion length  $L$  (cm), and distance  $d$  (cm) between the probes as well as  $h$ , the distance between the dislocations, were measured by usual methods. The ranges measured are

$$\begin{aligned}
\rho & (7.7 \text{ to } 8.4 \text{ ohm cm}), \\
\mu & (1780 \text{ to } 3310 \text{ cm}^2/\text{V sec}), \\
L & (0.0259 \text{ to } 0.0475 \text{ cm}), \\
d & (0.01615 \text{ to } 0.02584 \text{ cm}), \\
s_1 \sim s_2 & (2463 \text{ to } 11496 \text{ cm/sec}), \\
A & (2.323 \cdot 10^{-4} \text{ to } 8.36 \cdot 10^{-4}), \\
h & (1.24 \text{ to } 3.28 \mu), \\
g & (0.71 \text{ to } 2.87 \text{ \AA}).
\end{aligned}$$

A plot of  $A$  the absorption coefficient of carriers versus the driving field  $E_0$  in volts per centimeter reveals systematic deviations of up to 30%.

These results show that the arbitrary probe spacing and the assumption of a field-independent recombination region  $g$  are not appropriate and that the considerable scatter observed points to a principle neglect in the model used.

Although the general way of attack on the problem of small-angle lineage boundaries with wide-array spacing  $h$  (several microns) is correct, later measurements of the extended space charge originating at edge dislocations specifically in  $n$ -type material show that the  $g$  values should be much larger (see Section 9.3) and that, in effect, the collector probes in these experiments were probably spaced close to or within those space-charge regions.

If, in this case, the driving field  $E_0$  is changed from a fraction of a volt to several volts, a strong change in the measured values of  $s_2$  (10.19) and  $s_1$  (10.22) is to be expected, and therefore  $A$  from (10.25) respectively (10.26) is not correct.

Although the  $h$  values are measured microscopically, we see that  $d$  is in the range of  $100h$  or  $d/2 \simeq 50h \simeq 50\mu$ , which is close to the expected space-charge extension of the dislocations. Obviously  $g$  must be different for holes and electrons, depending on the core charge of the dislocations. McKelvey also observed that the cross section is larger on a sample that showed a smaller distance  $h$  between the individual dislocations.

A higher dislocation density certainly gives rise to some overlap of the individual space-charge pipes, and the boundary starts to react as a closed line of charges with  $T \simeq 0$  (see Chapter 11).

## REFERENCES

1. McKelvey, J. P., and R. L. Longini: Recombination of Injected Carriers at Dislocation Edges in Semiconductors, *Phys. Rev.*, vol. 99, no. 4, pp. 1227-1232, Aug. 15, 1955.
2. McKelvey, J. P.: Experimental Determination of Injected Carrier Recombination Rates at Dislocations in Semiconductors, *Phys. Rev.*, vol. 106, no. 5, pp. 910-917, Jun. 1, 1957.

## Chapter 11 Low- and Medium-Angle Grain Boundaries

### 11.1 SHEET CONDUCTANCE

The dislocation array with closer spacing of the individual pipes is formed when two seed crystals are tilted with respect to each other for an angle  $\theta$  in excess of a few minutes of arc. As we have defined before (see Section 4.2), the low- and medium-angle grain boundaries fall into the tilt-angle ranges

$$\begin{array}{ll} 0.10 < \theta < 5.0^\circ & \text{(low),} \\ 1.0 < \theta < 25^\circ & \text{(medium).} \end{array}$$

In these cases, overlap of the individual space-charge pipes can be assumed, and the whole structure resembles a sheet of complex properties. The inner core is a sequence of partially filled levels with negative core charge in germanium, a hole accumulation layer on either side, and an extended space charge from there on into the bulk crystal sides. As we saw in Section 9.3, the space charge of individual dislocations can extend over many microns. Therefore, even low-angle boundaries (lineage) in many cases represent coherent electronic structures, depending on the bias situation or local field strength and on the bulk doping. The often described  $60^\circ$  dislocation in the diamond lattice, that is, a dislocation running at  $60^\circ$  to its slip vector, shows rows of dangling bonds at a distance

$$D = 0.866 \cdot b \cdot \cos \sec \alpha,$$

where  $\alpha = 60^\circ$ ,

$b$  = interatomic spacing (approximately equal Burgers vector)

(see Figure 11.1). The dislocation plane dissects the crystal essentially into three parts, as we have seen: a central part that has new properties on account

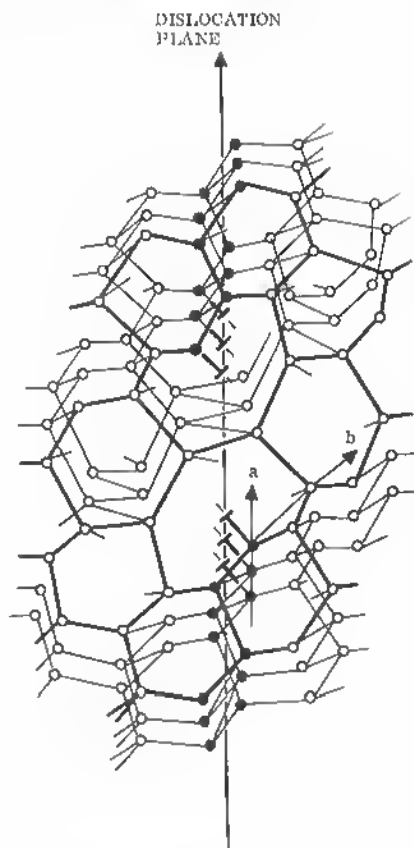


Fig. 11.1 Model of  $60^\circ$  dislocation plane in diamond lattice:  $a$  - axis;  $b$  = Burgers vector; black atom sites denote extra half plane; heavy lines = atoms above projection plane.

of the high density of dangling-bond states with their specific core charge and adjacent space charge and the two normal sides of the bulk crystal. Such a form can be considered an *internal surface* because of the similarities of internal and external broken bonds. However, a difference arises because of the missing surface states at a free surface and the attendant chemical reactions with the ambient. In a sense the internal surface in the form of a two-dimensional grain boundary can be equaled to a clean surface in ultrahigh vacuum or a cleaved surface. Such analogy was clearly established by work done on *mated surfaces*.<sup>1</sup> Germanium monocrystals split parallel to  $[111]$  planes

within a high-vacuum chamber ( $10^{-9}$  torr) and brought into contact immediately thereafter show clearly the effects of grown bicrystals. In  $n$ -type germanium, a  $p$ -type interface appears with the properties of a grown grain boundary with edge dislocations: photovoltage reversal for a light beam crossing the boundary, disappearance of the  $p$ -type region after annealing, nonappearance in  $p$ -type bulk doping. The latter effect is due to the non-availability of free electrons to associate with the broken bonds and the missing space charge. The mated clean surfaces, therefore, are comparable with the grown-in tilt boundaries, because they can be produced with high precision by the double-seed Czochralski growth, to be described later. A microscope picture of a bicrystal [100] surface is shown in Figure 11.2.

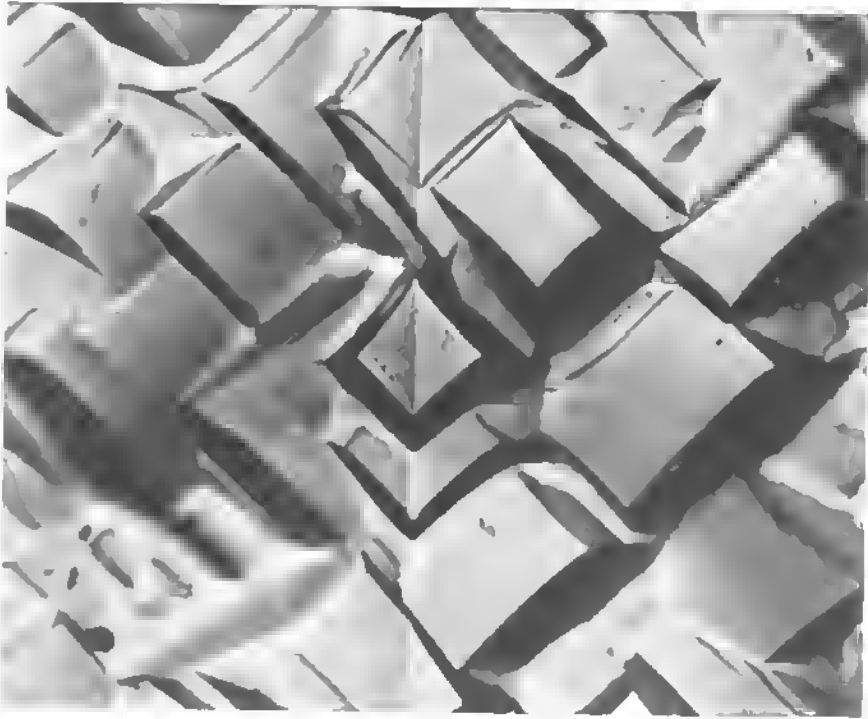


Fig. 11.2 Crystallographic etch of bicrystal surface, germanium 3250 X.

Such inner surface structures constitute boundaries for electronic transport that have been dealt with from a general point of view for any conducting medium. In metals with overlapping bands, consideration of a reflecting boundary (for example, at  $45^\circ$  with the lattice translation vector  $\mathbf{d}$ ) leads to wave functions of a form<sup>2</sup>



$$\psi_k = f(\mathbf{d} \cdot \mathbf{r})(e^{i\mathbf{k}\cdot\mathbf{r}} + e^{-i(\mathbf{k}\cdot\mathbf{r} + \phi)}) + A(\mathbf{d} \cdot \mathbf{r})e^{-n\cdot\mathbf{r}}, \quad (11.1)$$

where  $\phi$  = phase angle,

$$\mathbf{k} = \text{wave vector} = \frac{2\pi}{\lambda}$$

(see also Section 2.2). The last term in (11.1) is a nonpropagating state that decays in the  $n$  direction normal to the boundary. This state represents the surface effect and depends on the type of boundary and its orientation, while the first term is a superposition of incoming and reflected Bloch waves.

In solving the Schrödinger equation subject to the appropriate boundary conditions, one finds that multiple Bragg reflections can occur (specular reflection at the surface boundary assumed) and that the boundary introduces evanescent parts to the wave function. These again introduce into the electron states a spread in momentum in the direction normal to the boundary. They also increase the charge density contributed by a state in the vicinity of the surface. They further change the electron wave function at the surface, affecting chemical reactions that may occur at the surface.

Especially in the optical range where the usual theory does not allow transitions unless the  $k$ 's differ by  $\mathbf{d}$ , such boundaries introduce new kinds of optical absorptions.

It has also been found that charge oscillations can exist near a crystal boundary.

In summary, surface effects penetrate many interatomic spacings into the bulk, form evanescent parts to the wave function, distort the electron distribution, and can create charge oscillations near the boundary.

In semiconductors, surface states form localized wave functions with energy levels within the forbidden zone. These wave functions are exponentially damped going into the crystal and also toward the outside because of the image forces (Tamm levels). Although a number of models have been advanced to explain this particular case, it seems that the main property to consider is the wave function overlap of the closely spaced surface bonds and the resultant space charge that extends eventually thousands of lattice constants deep into the bulk crystal. P. Handler and W. M. Portnoy<sup>3</sup> have made careful measurements of the surface conductivity under various conditions. From their results, it appears that a clean surface (sputtered with argon at 600°C in ultrahigh vacuum) has a nearly temperature-independent conductivity in the range of 100 to 300  $\mu$  mhos/ $\square^*$  and has  $p$ -type character. Handler and coworkers conclude that the surface states are perturbed out of the conduction band to form a surface-state band that overlaps with the curved-up valence band. The holes in the upper valence band move in a potential well formed by the Fermi level valence band crossover and the surface boundary. The well is assumed to be 50 to 100 Å wide (see Figure 11.3).

\* Compare Fig. 11.13.

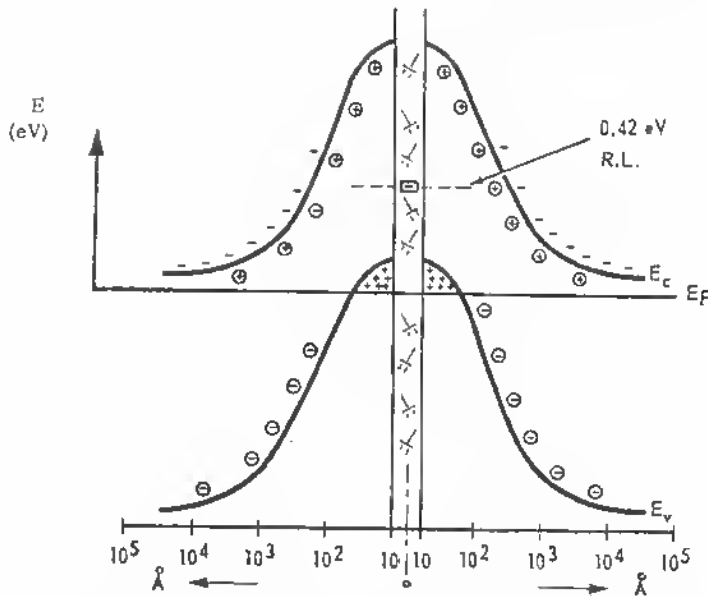


Fig. 11.3 Electronic band structure of grain boundary after Handler.<sup>3</sup>

These assumptions are, as Handler and coworkers point out, in agreement with models advanced by Shockley and Read and measurements on grain boundaries by Tweet<sup>4</sup> and Mataré and coworkers.<sup>5</sup> Tweet produced germanium bicrystals of a rather imperfect form. His measurements of the grain-boundary conductance and mobility were facilitated by the use of gold doping. In this way, the bulk conductivity was minimized in order to bring out the predominant conduction features of the high-conductivity boundaries. As Tweet found, the grain boundaries of very small misfit angle of less than  $1^\circ$  are less conductive than larger-angle boundaries, which is in agreement with our picture of partially overlapping dangling bonds for larger misfit. The Hall mobilities measured by point probes against a base-plate contact are relatively high. With the resistivity probes at a distance  $s$  and the Hall probes at a distance  $w$  the mobilities were calculated on account of

$$\mu = \frac{10^8}{H} \frac{V_H}{V_s} \cdot \frac{s}{w} \quad \text{cm}^2/\text{V sec}, \quad (11.2)$$

where  $H$  = magnetic field strength, gauss,

$V_H$  = Hall voltage,

$V_s$  = sample voltage.

One finds values between  $10^3$  and  $10^4$   $\text{cm}^2/\text{V sec}$  with peak values at  $150^\circ\text{K}$ . The samples cut along the  $[110]$  axis (actual tilt axis) show the real tilt boundary mobility, which remains rather constant from 150 down to  $50^\circ\text{K}$  and below; the samples cut along  $[100]$  in the lower (deviating) part of the boundary show a lower and stronger decreasing mobility. This is to be expected, since a kink in the grain boundary indicates a lower energy configuration or a twinlike arrangement with a lesser number of dangling bonds. Tweet confirmed this by growing pure twin boundaries which did not reveal any preferred conduction (see Section 8.1). Early work on controlled grown grain boundaries has shown that, in fact, the conduction along the grain-boundary space-charge sheet is degenerate.

Clear indications of a preferred conduction along the path of a grain-boundary plane were found in early measurements on rather perfectly grown bicrystal samples even at room temperature.<sup>6</sup> Figure 11.4a shows the case of a bicrystal seed arrangement with tilt angle  $\theta_1$ , grain-boundary orientation  $\phi = 90^\circ$  and rotational ( $\theta_2$ ), and twist misfit ( $\theta_3$ ), which are kept at minimum. Two point-probe measurements across the bicrystal sample (see Figure 11.4b) result in a typical potential maximum at the grain boundary, here expressed in resistivity  $\rho$  (see Figure 11.5).

A double point probing, so that the probes move across the bicrystal, as shown in Figure 11.4c, results in a potential minimum or decrease in resultant

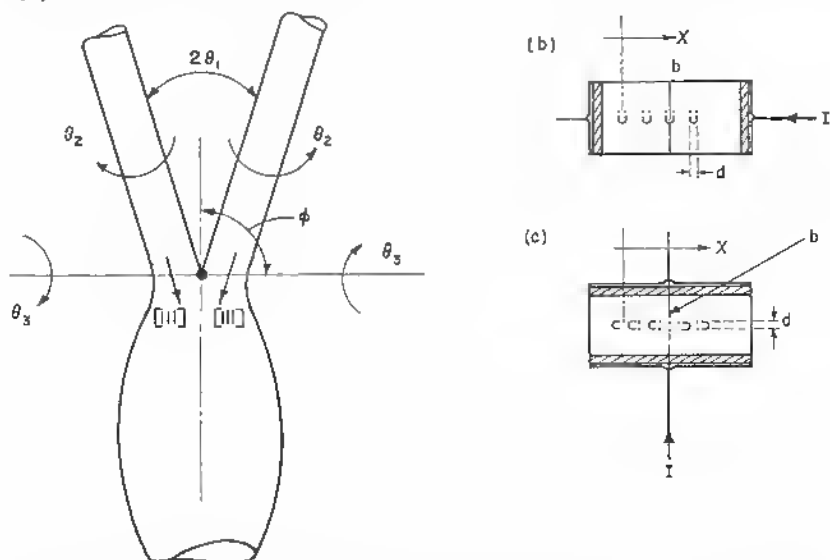


Fig. 11.4 (a) Bicrystal seed arrangement ( $\theta_1$  tilt angle,  $\theta_2$  rotational misfit,  $\theta_3$  twist angle), (b) Double-probe potential measurements across grain boundary. Probe distance  $d$ , (c) Double probe potential measurements with probes in a plane parallel to grain boundary plane.

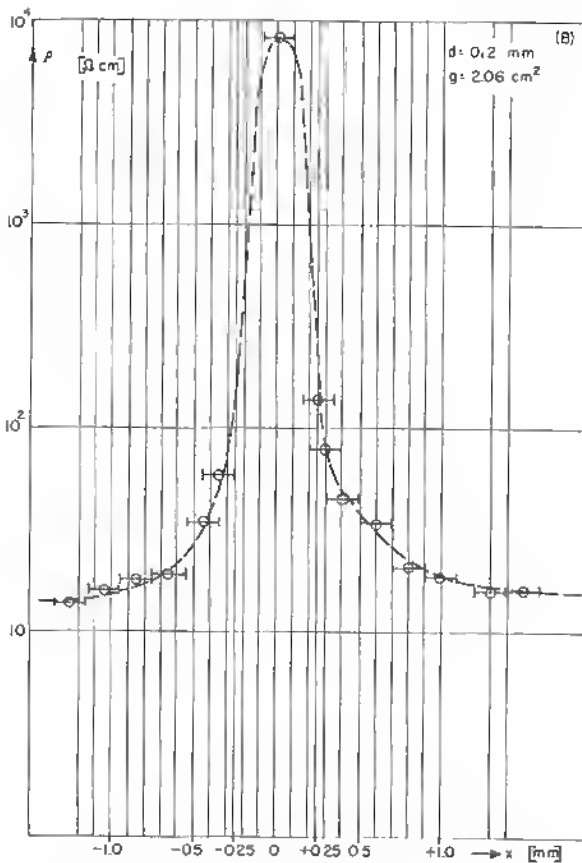


Fig. 11.5 Result of potential probing conforming to Figure 11.4(b). Ordinate in ohm cm.

resistivity when both probes are sitting within the space-charge region of the central grain boundary (see Figure 11.6).

We discuss later, in Chapter 12, why it is unlikely that these findings are explainable by a Cottrell atmosphere at the grain boundary (see also Section 9.2).

Further measurements by potential probing and light injection<sup>7</sup> established the fact that lifetime of injected carriers in  $n$ -type crystals with a grain boundary becomes extremely large when transport within the narrow boundary region is effected (see Figure 11.7). This is actually an indication of a  $p$ -type channel through which holes can move freely when subjected to the negative collector field. Increased diffusion length of holes parallel to dislocations had been found already by Bell et al.<sup>8</sup> for germanium in photoconductance

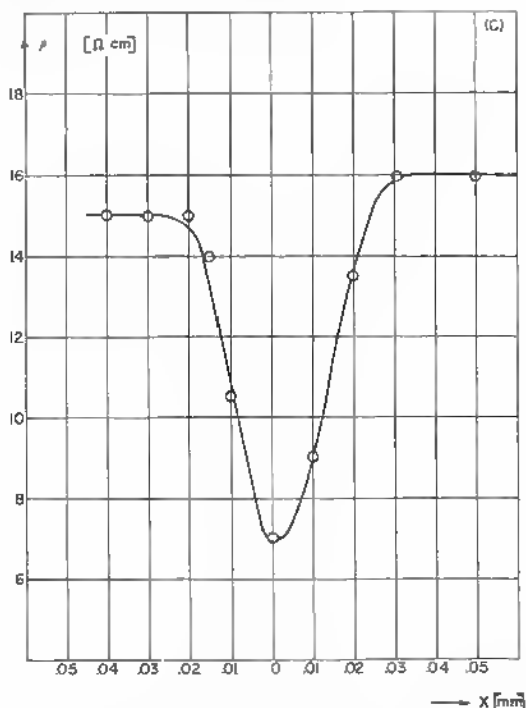


Fig. 11.6 Result of potential plot according to Figure 11.4(c).

measurements. Further measurements on controlled grown bicrystals<sup>9</sup> by a refined probing method confirmed the early measurements and showed clearly the decrease in resistance along the grains.<sup>10</sup>

Measurements on precisely grown bicrystal samples with indium-alloy contacts to the grain-boundary layer were made subsequently. Such contacts applied to *n*-type bulk crystals establish a blocking contact to the bulk and an ohmic contact to the boundary. Results of measurements at decreasing temperature reveal clearly the strong degeneracy of a plane in which the dislocation line charges are regularly arranged and form laterally overlapping space-charge pipes.

A comparison of the resistivity of equally shaped samples with equal contact areas, but *p*-type (indium) in the case of the grain boundary, *n*-type (antimony) in the case of the bulk crystal, shows the strong difference (see Figure 11.8). The absolute value of  $\rho$  is without importance here (calculated for a 100 Å grain boundary width), the temperature variation is the most important feature. Although the bulk crystal shows the usual strong

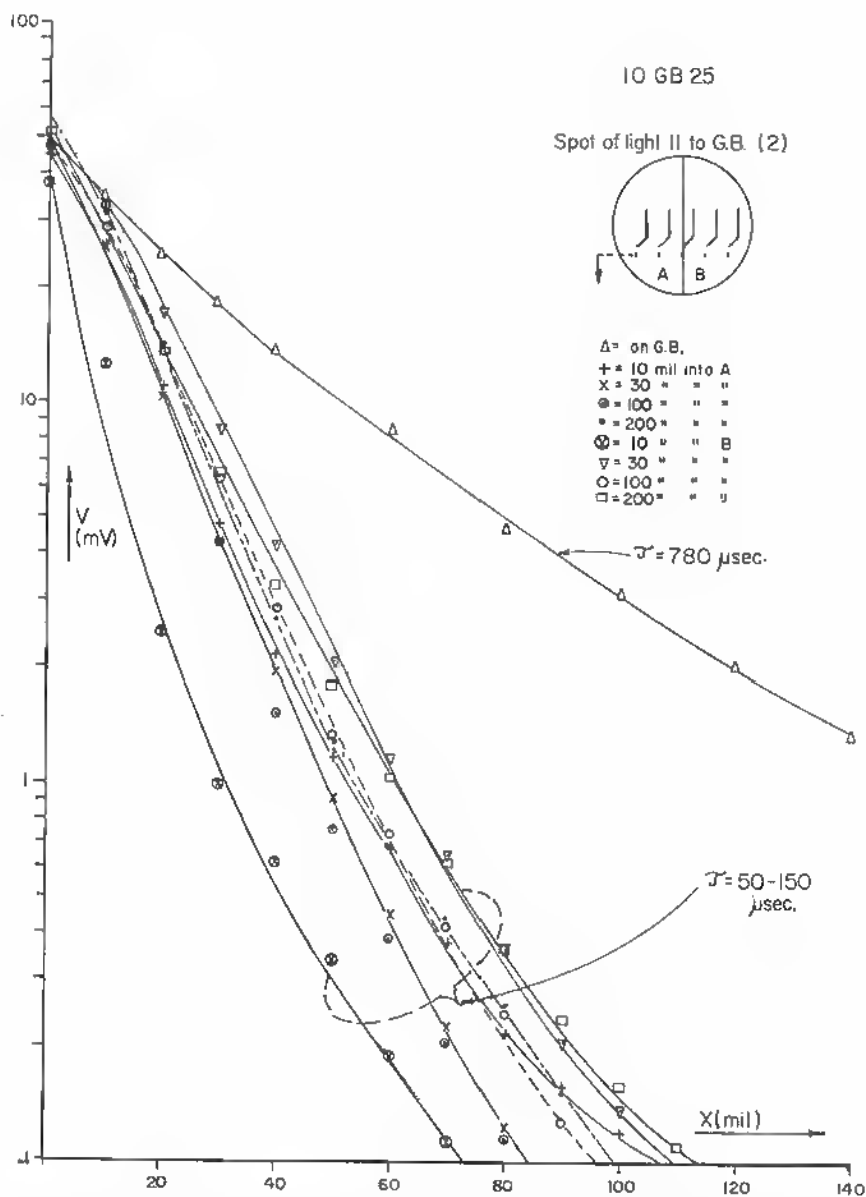


Fig. 11.7 Light injection-point and collector-point moving across bicrystal. Plot of resultant decay curve at each location and apparent lifetime with excessive value when light injection and collector-point are located on grain boundary.

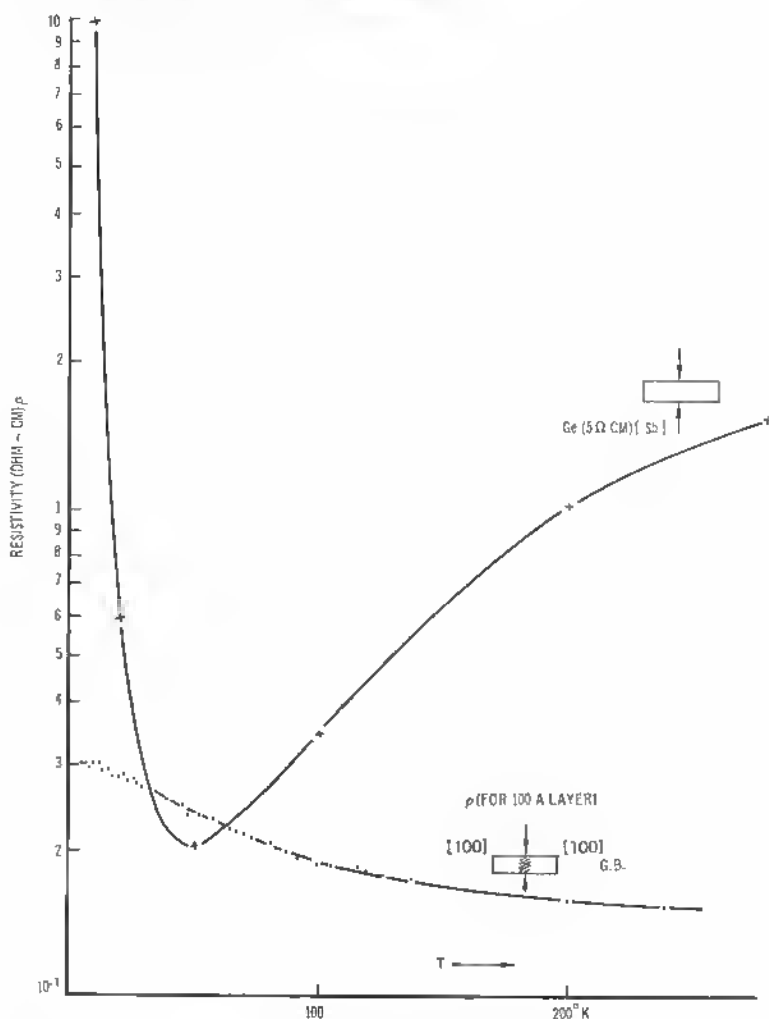


Fig. 11.8 Plot of reduced resistivity as a function of temperature in  $^{\circ}\text{K}$  showing extreme degeneracy for bicrystal case.

changes for high and low temperatures, the bicrystal is almost insensitive to these changes from room temperature down to liquid helium temperature<sup>10, 5</sup>.

As a further test of the validity of the model of the overlapping space charge of the dangling bonds, with respect to the conduction mechanism based on overlapping wave functions, many bicrystal samples with different bulk doping were prepared and their grain-boundary conduction tested at low temperature. The results at 4.2  $^{\circ}\text{K}$  show no correlation of the  $\rho^*$  values (in

ohms per square) with the impurity range or type. From  $N = 10^{13}$  (intrinsic) to  $N = 10^{16} \text{ cm}^{-3}$  and from  $p$ -type doping (Ga) to  $n$ -type doping (Sb) and also with copper (Cu) and gold (Au) doping, the resistivity remains in a range between 3 and  $11 \times 10^3$  ohms per square.<sup>11,12</sup>

Samples with the geometry shown in Figure 11.9 were used. When the thickness  $t$  of the conducting channel is not known, use is made of reduced resistivity  $\rho^* = \rho/t$ . To elucidate the effect of the grain-boundary conductance, Weinreich et al.<sup>13</sup> measured the current across bicrystals where the bulk crystal had different thickness. Figure 11.10 gives the results. These bicrystals were grown in the [100] direction with tilt around [001] of  $10^\circ$  to  $30^\circ$ . They were  $p$ -type (1.1 ohm cm) and thus forming  $p$ - $p^+$ - $p$  layers. At both ends they were indium-plated for contacts. The low temperature measurements were extended from  $300^\circ$  to  $2.5^\circ\text{K}$ . To ensure that in this temperature range no disturbing impurity band conduction or other interference occurred, three samples were prepared and measured simultaneously in one temperature run. All three had the same length and height. Two were samples 0.03 and 0.003 in. wide, with grain boundaries and the third was a bulk sample (no bicrystal) of 0.03 in. width. In the current plot versus  $1/T$ , it is shown that the bulk sample of the same type and doping as the bicrystals ( $p$ -type, 1.1 ohm cm) carries a 50 times smaller current below  $10^\circ\text{K}$  or represents a 50 times higher resistivity. It can also be seen that this is the case even when the cross

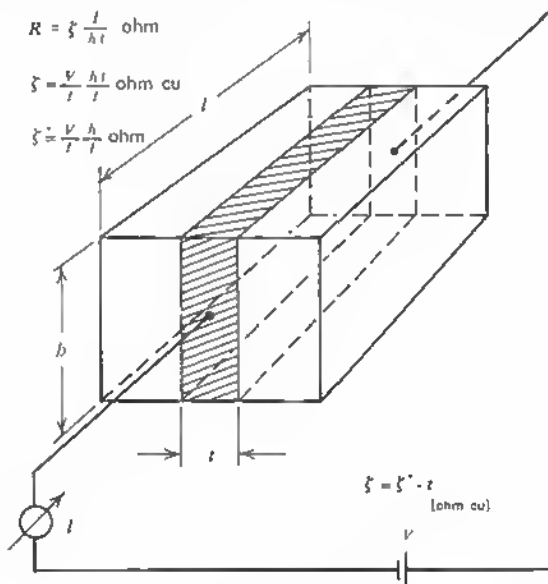


Fig. 11.9 Sample geometry and representation of reduced resistivity.



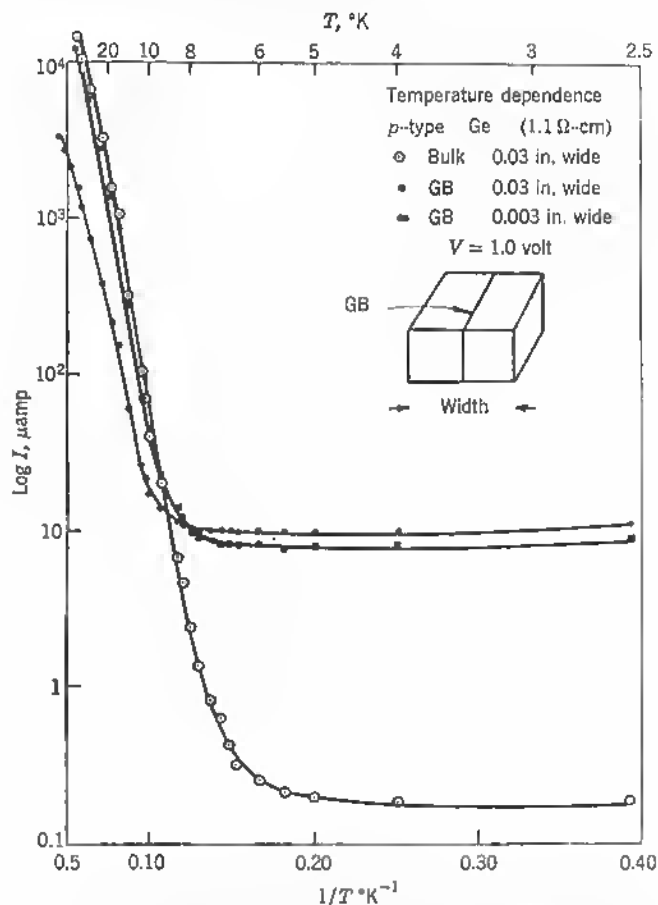


Fig. 11.10 Temperature dependence of the conductivity of 1.1 Ω cm *P*-type germanium and of the grain boundary region (sheet conductance).

section of the bulk is 10 times larger. In the bicrystal case, the width of the sample is, in fact, of little importance, since all current below 10°K is carried by the space-charge pipes along the dislocation sheet. The striking difference in resistance between bicrystals and monocrystals of the same crystal material and with the same contact shows that no difference in contact resistance is at the root of this constant and high conductivity of the dislocation arrays. In *n*-type crystals, the measurements have to be carried out with In alloy material, forming in this case a blocking layer with respect to the bulk. One side of the sample always being biased negatively, one side of these junctions

is always in the reverse mode so that current through the bulk is essentially nil (see Figure 11.11—current for 2.7 ohm cm sample). In high-resistivity crystals, the junction leakage current is increasingly competing with the dislocation sheet conductance from 30° upward.

For comparison, the temperature dependence of the conductance (or the current) for a 5 ohm cm  $n$ -type bulk crystal (Ge) is drawn.

A further remarkable property of the conduction in overlapping wave functions of dangling bonds is that it is entirely ohmic except for the leakage current and before the avalanche current contribution sets in. Figure 11.12 shows an example. The grain-boundary conductance is ohmic over 6 decades.

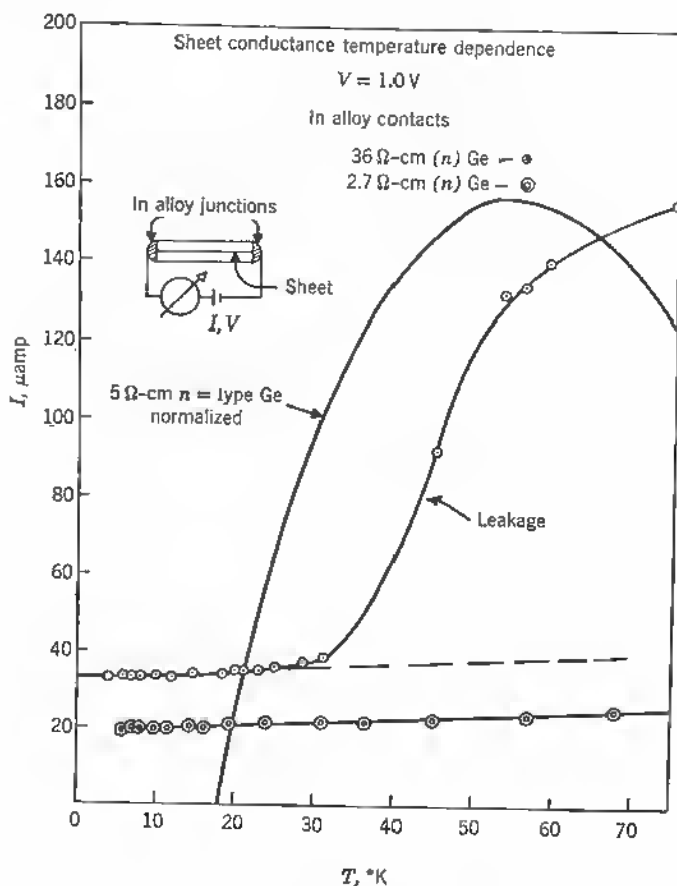


Fig. 11.11 Temperature dependence of sheet conductance.

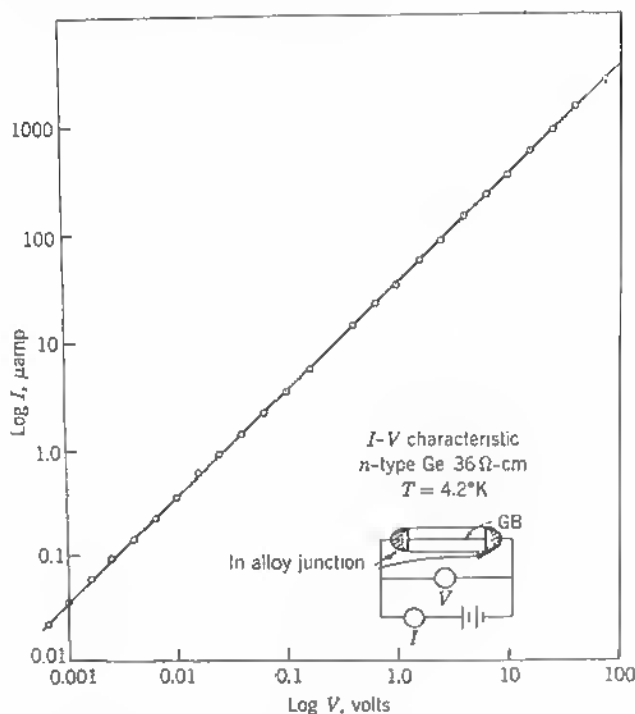


Fig. 11.12 *I-V* characteristic of the sheet conductance.

Finally, Figure 11.13 gives the list of differently doped bicrystal samples of the shape shown in Figure 11.14, and their grain-boundary resistivity  $\rho^*$  in ohms per square, as described earlier.<sup>11, 12</sup> We see that at 4.2°K for a doping change of three orders of magnitude and for varied doping agents (*n* and *p*), the sheet resistivity changed between 3.6 and 11.2 kΩ/□. Considering that the contact formation is not always ideal, especially on high-resistivity bulk and that leakage-current contributions at the much wider bulk-crystal halves cannot be excluded (compare the contact area to the bulk,  $2.9 \cdot 10^{-4}$  cm<sup>2</sup>, with the contact area to the grain-boundary barrier, at most  $1.7 \cdot 10^{-6}$  cm<sup>2</sup>), the independence of the grain-boundary conductance on sample doping and resistivity is striking.

Such conduction goes beyond the normal impurity conduction in degenerate semiconductors. The physical reasons for this extraordinary behavior are found in the difference between a normal impurity as acceptor and a broken bond. The dangling bonds are able to pick up electrons in a lower energy state until the energy lost by adding an electron is compensated for by the energy

Sample no.	$\rho$ bulk, $T = 300^\circ \text{K}$ , ohm-cm	Type	Impurity $N$ , atoms/cc	Type	$\rho^*$ ohms per square, $T = 4.2^\circ \text{K}$
7	1.3	$n$	$1.4 \times 10^{15}$	Sb	7,800
42	1.6	$n$	$1.1 \times 10^{15}$	Sb	5,100
6	2.7	$n$	$7 \times 10^{14}$	Sb	7,500
17	4	$n$	$4.5 \times 10^{14}$	Sb	3,600
3	5	$n$	$4 \times 10^{14}$	Sb	3,600
35	27		Intrinsic		3,600
64	30		Intrinsic		5,600
29	36		Intrinsic		4,100
31	4	$p$	$2 \times 10^{14}$	Ga	11,200
9	1.75	$p$	$3 \times 10^{14}$	Ga	8,200
11	1.1	$p$	$8 \times 10^{14}$	Ga	10,200
12	1.1	$p$	$8 \times 10^{14}$	Ga	11,200
27			$10^{15}$	Cu	2,900
15			$10^{16}$	Cu	3,700
(Tweet)			$10^{16}$	Au	8,000

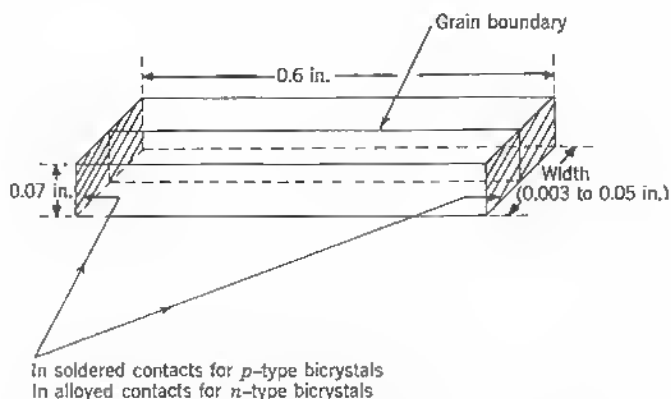
Fig. 11.13 Dependence of grain boundary sheet resistivity  $\rho^*$  on doping of crystal.

Fig. 11.14 Dimensions of grain boundary samples for conductivity measurements.

increase due to electron repulsion. As we have seen (Chapter 9), the electron density in boundary states is also dependent on the external potential at the dislocation space-charge layer, which increases the number of compensating free holes also. The space-charge cylinder radius

$$R = \left[ \frac{f}{D\pi(N_d - N_a)} \right]^{1/2},$$

being dependent on the bond distance  $D = a/2 \sin \theta$  ( $a$  = lattice constant,  $\theta = 2 \times$  tilt angle), is of the order of  $10^4 \text{ \AA}$  at room temperature or  $2 \cdot 10^3$  lattice constants. This is roughly four times the mean spacing between excess donors for  $N_d - N_a \approx 10^{15} \text{ cm}^{-3}$  in the bulk, since the spacing of electrons in dangling-bond levels is  $S = D/f \approx 40 \text{ \AA}$ ,  $S \ll R$ , or the space-charge cylinders are overlapping.

Thus the electronic width of the grain-boundary plane is of the order of magnitude of the inversion layers at both sides of the dislocation array.

With a filling factor of  $f \approx 1/10$  and an assumed width of the disturbed layer of  $10^2$  to  $10^3 \text{ \AA}$ , the state density for angles of misfit  $\theta > 10^\circ$  is  $N_a \approx 8 \cdot 10^{14}$  to  $10^{16} \text{ cm}^{-3}$ . With these levels strongly localized, the Fermi level falls into the top of the valence band.

The strong filling for values of the bias voltage below  $kT/e$  is visible when the detailed characteristics under bias is measured (see Figure 11.15), where a current rise to  $25 \mu\text{A}$  on both sides is measured before the saturation value is reached.

The rather astonishing conduction with this high degree of degeneracy has been tested subsequently in III-V compound bicrystals also.

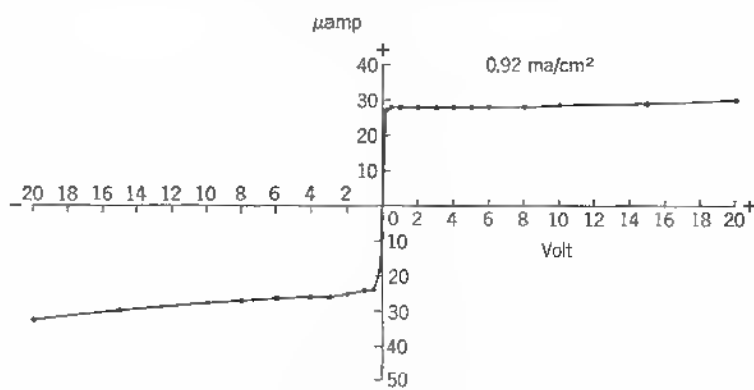


Fig. 11.15  $I$ - $V$  characteristic across grain boundary barrier at room temperature.

R. K. Mueller and coworkers have found that indium antimonide bicrystals produce a clear degeneracy over a wide temperature range. Already from a temperature of  $100^\circ\text{K}$  downward, the resistance or conductance is a constant down to liquid helium temperature. The values published by Mueller and Maffitt<sup>14</sup> are shown in Figure 11.16. Here the complete lack of temperature dependence of the conductance is striking. It can be assumed that the conductance value of  $10^{-2}$  ohms per square in this case is also maintained at higher temperature beyond  $100^\circ\text{K}$ . The increased conductivity here stems from the fact that the alloy zone to the boundary begins to draw leakage current at higher temperatures, adding bulk material to the conductive path. Figure 11.16 shows the case of  $\beta$  dislocations parallel to the grain-boundary plane. As the authors have shown, there is only a very small difference between the conductances of  $\beta_{\parallel}$  and  $\beta_{\perp}$  planes and also the  $\alpha$  dislocation plane. All are equally degenerate. It is significant that the Hall mobilities measured in the channel at, for example,  $78^\circ\text{K}$  are as high as  $1.3 \times 10^4 \text{ cm}^2/\text{V sec}$  for an  $\alpha$  bicrystal and  $2.3 \times 10^4 \text{ cm}^2/\text{V sec}$  for a  $\beta$  bicrystal. These high interfacial mobilities suggest the use of  $\text{InSb}$  grain boundaries in magnetic fields. Such extremely narrow  $H$  field probes are desirable in many cases where localized magnetic field changes have to be monitored. The observed electron density in the conducting sheet is  $n = 2.5 \times 10^{12} \text{ cm}^{-2}$  or nearly two orders of magnitude higher than the net number of positive surface charges  $N^+ = N_d - n(\text{cm}^{-2})$ , where  $N_d$  = number of ionized donors per unit boundary area.

The reason for the increase in electron density in grain-boundary sheets

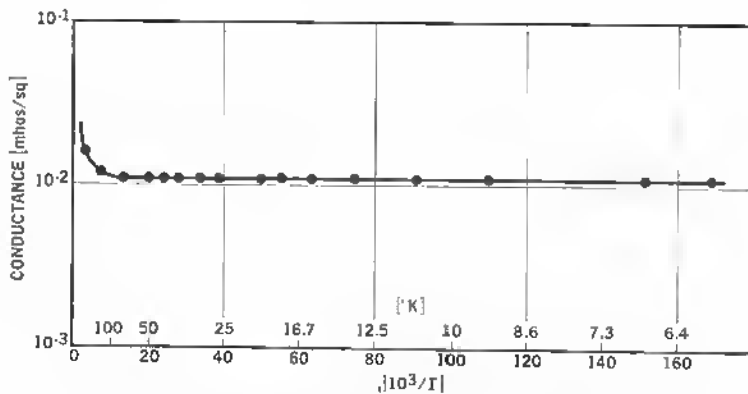


Fig. 11.16 Conductance in [mhos/square] of grain-boundary layer in Indium-Antimonide. (R. K. Mueller and K. N. Maffitt,<sup>14</sup>)

beyond the number of available surface states is discussed in Section 11.2.

In considering the unusual and complete degeneracy of the conducting space-charge sheet of a grain boundary, two reasons can be given for the extraordinary conductivity. First, the spacing between dangling-bond sites is only of the order of a lattice constant. Even for low filling factors  $f = c/a \approx 10^{-2}$ , a sufficient wave-function overlap is guaranteed. This becomes clear from a comparison with the mean density of impurity atoms in the bulk. In degenerate germanium, for example, a density of  $10^{19} \text{ cm}^{-3}$  corresponds to a linear density of  $2.2 \times 10^6 \text{ cm}^{-1}$  or a sheet density of  $4.6 \times 10^{12} \text{ cm}^{-2}$ , which is clearly comparable with the sheet density of electrons in dangling-bond states, as measured. With  $5 \times 10^{-8} \text{ cm}$  interatomic spacing in bulk material or  $0.2 \times 10^8 \text{ atoms/cm}$ , a distance of 10 lattice constants is responsible for degeneracy. Since the filling factor for the grain boundary increases with decreasing temperature, degeneracy is also increasing. In silicon a higher density at degeneracy has to be assumed:  $N_D = 10^{19} \text{ to } 10^{20} \text{ cm}^{-3}$ , so that here grain-boundary conduction would be prominent for doping ranges below this value. The second cause of the high conductance of the sheet is related to the discussed special transmission-line behavior of the grain-boundary pipes (see Section 9.1). Since carriers confined to the inner pipe by a space charge undergo little scattering, their mobility within the sheet is relatively high.

In comparing the temperature independence of conduction with the electronic conduction of metals within the same temperature range, it is striking that metals like copper, silver, and zinc show some degeneracy only at the lower temperature ranges (below  $10^\circ\text{K}$ ) and generally display a change of three orders of magnitude between 5 and  $50^\circ\text{K}$  (see Figure 11.17, with resistivity plotted in nano-ohm cm).

Considerable experimental evidence for the high conduction in grain boundaries was furthermore collected by numerous authors working with grown bicrystals in germanium and silicon.

Landwehr and Handler<sup>15</sup> and R. K. Mueller<sup>16</sup> show the degeneracy over a wide temperature range with only slight conductivity variations in the higher temperature range (contact potential and bulk contribution).

Hamakawa and Yamaguchi<sup>17</sup> studied the transport mechanism along grain boundaries and found increased hole density with decreased dangling-bond spacing.<sup>18,19</sup>

In a further publication, Landwehr tries to analyze the particular form of the conductivity versus temperature curve.<sup>20</sup> Based on the number of defect electrons in surface states at  $4.2^\circ\text{K}$  of  $5 \times 10^{12} \text{ cm}^{-2}$  as revealed by Hall measurements, an application of the Thomas-Fermi method to the channel at either boundary side leads to an evaluation of the carrier density change with distance from the grain boundary.

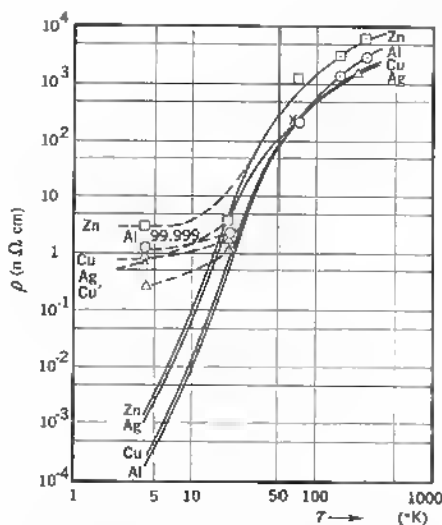


Fig. 11.17 Ideal resistivity of silver, copper, aluminium, and zinc, according to the Bloch-Grüneisen formula and resistance measurement of commercially purest silver, aluminium, copper, zinc, and zone-refined copper samples. (Cu)

Assuming that the defect-electron density  $p(x)$  within the space-charge region is governed by Poisson's equation:

$$\frac{d^2\varphi}{dx^2} = -\frac{4\pi e}{\epsilon} p(x), \quad (11.3)$$

where  $\varphi$  = electrostatic potential,

$e$  = electron charge,

$\epsilon$  = dielectric constant,

and that  $p(x)$  and the potential energy  $e(\varphi_{\max} - \varphi)$  are related as

$$e(\varphi_{\max} - \varphi) = \frac{h^2}{2m^*} \left( \frac{3}{8\pi} \right)^{2/3} [p(x)]^{2/3}, \quad (11.4)$$

$h$  = Planck's constant,

$e\varphi_{\max}$  = maximum energy of defect electron = Fermi energy  $E_F$  at  $T = 0$ ,

$m^*$  = effective mass,

one finds, by combining (11.3) and (11.4), that

$$p \frac{d^2 p}{dx^2} - \frac{1}{3} \left( \frac{dp}{dx} \right)^2 - Cp^{7/3} = 0, \quad (11.5)$$



with a constant

$$C = \left(\frac{8\pi}{3}\right)^{2/3} \frac{12e^2\pi m^*}{\epsilon h^2}. \quad (11.6)$$

Landwehr's result of the integration of (11.5) with the boundary conditions:

$$\begin{aligned} \left(\frac{d\phi}{dx}\right)_{x \rightarrow \infty} &= 0, \\ \epsilon \operatorname{div} \left(\frac{d\phi}{dx}\right)_{x=0} &= -4\pi e p_F, \end{aligned} \quad (11.7)$$

gives a defect-electron density  $p(x)$ :

$$p = \left(\frac{C}{30}\right)^{3/5} \left(\frac{5}{2} p_F\right)^{6/5} \left[ \left(\frac{C}{30}\right)^{3/5} \left(\frac{5}{2} p_F\right)^{1/5} x + 1 \right]^{-6}, \quad (11.8)$$

where  $p_F$  is the surface-charge density of the defect electrons ( $5 \times 10^{12} \text{ cm}^{-2}$ ). Corresponding to (11.8), the net density  $p$  decreases from a high value of  $10^{19} \text{ cm}^{-3}$  at the boundary to  $10^{17} \text{ cm}^{-3}$  at  $100 \text{ \AA}$  from the grain boundary already. A zone of  $140 \text{ \AA}$  width thus contains 90 percent of all defect electrons. In a  $2 \text{ ohm cm}$  crystal, this concentration lies two orders of magnitude above the donor concentration in the bulk, which therefore can be neglected.

The strong potential change near the boundary at  $x = 0$  makes it doubtful, however, if the Thomas-Fermi method can be applied. Landwehr points out that for the center hole density of  $3.4 \times 10^{18} \text{ cm}^{-3}$  at the grain boundary, a mobility value of  $400 \text{ cm}^2/\text{V sec}$  as measured in bulk germanium corresponds well to the measured mobility values of holes in grain-boundary barriers ( $\sim 300 \text{ cm}^2/\text{V sec}$ ).

Landwehr found that resistivity and Hall constant show an increase from  $20^\circ\text{K}$  upward, with a soft maximum at  $\sim 100^\circ\text{K}$ , and assumes that this is due to the contribution of defect electrons of higher mobility (no diffuse scattering at the boundary) farther out from the boundary. It has also to be considered that the indium alloy junctions diminish their blocking action with respect to the bulk material as the temperature increases, thus drawing an increased number of bulk carriers into the conduction process.

## REFERENCES

1. Haneman, D., W. D. Roots, and J. T. P. Grant: Atomic Mating of Germanium Surfaces, *J. Appl. Phys.*, Vol. 38, no. 5, pp. 2203-2212, April, 1967.
2. Stern, E. A.: Electron States near Boundaries, *Phys. Rev.*, Vol. 162, no. 3, pp. 565-574, Oct. 15, 1967.

3. Handler, P., and W. M. Portnoy: Electronic Surface States and the Cleaned Germanium Surface, *Phys. Rev.*, Vol. 116, no. 3, pp. 516-526, Nov. 1, 1959.
4. Tweet, A. G.: Properties of Grain Boundaries in Gold Doped Germanium, *Phys. Rev.* vol. 99, no. 4, pp. 1182-1189, Aug. 15, 1955.
5. Mataré, H. F.: Dislocation Planes in Semiconductors, *J. Appl. Phys.*, vol. 30, no. 4, pp. 581-589, April, 1959.
6. Mataré, H. F.: Grain Boundary Structure and Carrier Transport in Semiconductor Crystals, *Z. f. Naturforschung*, vol. 10a, no. 8, pp. 640-652, 1955.
7. Mataré, H. F., and B. Reed: Anomaly of Carrier Lifetime in Germanium Bicrystals, *Z. f. Naturforschung*, vol. 11a, no. 10, pp. 876-878, 1956.
8. Bell, R. L., and C. A. Hogarth: Anisotropic Diffusion Lengths in Germanium and Silicon Crystals Containing Parallel Arrays of Edge Dislocations, *Journal of Electronics and Control* 3, 445-470, 1957.
9. Mataré, H. F., and H. A. R. Wegener: Oriented Growth and Definition of Medium Angle Semiconductor Bicrystals, *Z. f. Physik*, Vol. 148, pp. 631-645 1957.
10. { Mataré, H. F.: Electrical Behavior of Bicrystal Interfaces, *Zschr. f. Physik*, vol. 145, pp. 206-234, 1956.  
Mataré, H. F.: Dislocation Planes in Semiconductors, *Scientia Electrica*, vol. 4, no. 4, pp. 1-16, 1958.
11. Reed, B., O. A. Weinreich, and H. F. Mataré: Conductivity of Grain Boundaries in Grown Germanium Bicrystals, *Phys. Rev.*, vol. 113, no. 2, pp. 454-456, Jan. 15, 1959.
12. Mataré, H. F., B. Reed, and O. A. Weinreich: Conductivity in Grown Germanium Bicrystals, *Z. f. Naturforschung*, Vol. 14a, no. 3, pp. 281-284, 1959.
13. Weinreich, O. A., H. F. Mataré, and B. Reed: Electrical and Photoelectrical Properties of Grain Boundary Layers, "Solid State Physics in Electronics and Telecommunications," Academic, New York, 1960, vol. 1, part 1, pp. 97-108.
14. Mueller, R. K., and K. N. Maffitt: Grain Boundary Conductance in InSb, *J. Appl. Phys.*, vol. 35, no. 3, pp. 734-735, March, 1964.
15. Landwehr, G., and P. Handler: Galvanomagnetic Properties of Grain Boundaries in Germanium Bicrystals from 1.25 to 240°K, *J. Phys. Chem. Solids*, vol. 23, pp. 891-906, 1962.
16. Mueller, R. K.: Capture Diameter of Dislocations in Low Angle Grain Boundaries in Germanium, *J. Phys. Chem. Solids*, Vol. 8, pp. 157-161, 1959.
17. Hamakawa, Y., and J. Yamaguchi: Electrical Conduction in Germanium Grain Boundary Plane, *Jap. Journal of Applied Physics* Vol. 1, no. 8, pp. 334-342, December, 1962.
18. Hamakawa, Y., and J. Yamaguchi: Galvanomagnetic Effects in Boundary Layer of Germanium Bicrystals, *Proceed. Internat. Conf. on Crystal Lattice Defects*, 1962, *J. Phys. Soc. Japan*, vol. 18, suppl. II, pp. 166-170, 1963.
19. Hamakawa, Y., T. Nishino, and J. Yamaguchi: Carrier Mobility and Dislocation Scattering in the Boundary Layer of Germanium Bicrystals, *Japan J. Appl. Phys.*, vol. 2, pp. 371-273, 1963.
20. Landwehr, G.: Interpretation of the Electrical Conductivity of Grain Boundaries in Germanium Bicrystals, *Phys. Stat. Sol.*, vol. 3, pp. 440-446, 1963.

## 11.2 GRAIN-BOUNDARY BARRIERS

The interesting fact of the blocking behavior of dislocations and especially grain boundaries when current flows across these structures was known for a long time before systematic work on these structures started. In crystal growth and testing, it was known since the early days of germanium diode production, which started systematically during the war years 1943 and 1944, that boundary layers in polycrystals had no useful properties for point-contact diodes and that such boundaries in front of base-contact areas lead to high spreading-resistance values.

Several authors noticed grain-boundary barriers in the subsequent years of activity in the germanium crystal field, but it was not until 1952 that grain-boundary barriers were clearly described by Fan and coworkers at Purdue.<sup>1</sup> Further interesting facts concerning their use as transistor injection layers or base layers<sup>2</sup> focused attention on the particular structural zone that at the same time could be used to study the electronic aspects of dislocations in a more direct way than is feasible when individual dislocations are statistically embedded in bulk material and are not accessible to contacts. First systematic studies on grain-boundary barriers<sup>3,4</sup> showed remarkable aspects of the blocking layer, which were independent of the doping of the bulk. Initial experiments with bicrystals produced under controlled seed conditions in Czochralski equipment<sup>5</sup> provided strong evidence of the role of the dangling bonds in this structure. In some cases, *p*-type contacts to the grain boundary operated as efficient minority carrier injection zones. In a compilation of the facts concerning grain-boundary action, a preponderance of diffusion of impurities had to be ruled out as a reason for the degenerate behavior and also for the barrier layer built up<sup>6</sup>. There is, however, a question with respect to the buildup of Cottrell atmospheres in the case of wide dislocation spacing or grain boundaries of the lineage type. H. Queisser and W. Shockley concluded from measurements on silicon bicrystals that oxygen plays an important role in the electronic behavior of grain boundaries<sup>7</sup>. The known photoresponse with photovoltage reversal did not appear in bicrystals with low oxygen content (floating-zone-grown). Also, this response, typical for grown bicrystals starting with high-resistivity silicon material grown in an oxygen atmosphere (boat-grown) disappeared after heat treatment. It has to be added here that the photoresponse or the existence of a double barrier hinges on the existence of a space charge. As germanium grain-boundary barriers disappear when the bulk material is converted into strong *p*-type, so silicon boundaries with a positive core charge do not form an appreciable space charge when the bulk material is converted by the formation of electrically active thermal donor centers. As has been shown<sup>8</sup> in the past, SiO and SiO<sub>2</sub> complexes begin to form by heat treatment at temperatures as low as a few hundred degrees. But

all these experimental results are not conclusive so long as the kind of boundary is not clearly defined as a grain boundary of the dangling bond type. Twin joins of first, second, and higher order (see Section 4.4) are discontinuities in a "repaired" lattice with fewer, widely spaced dangling bonds. Their number does not correspond to  $1/D = [2 \sin(\theta/2)]/b$  ( $b$  = Burgers vector,  $\theta$  = tilt angle), and therefore their behavior is comparable with the case of lineage boundaries with no appreciable wave function overlap (formation of a Cottrell atmosphere around the individual dangling bonds). The bicrystals grown in silicon, therefore, are mostly of the twin type, with wide spacing between broken bonds, and behave like low-angle lineage boundaries. This was also confirmed in measurements on hundreds of silicon grain boundaries as they occur in polycrystals. The author found that in 1 case in 20 a silicon grain boundary in the same crystal block displayed photovoltage reversal and a high blocking layer. Queisser<sup>7</sup> reports that there is no detectable diffusion enhancement in these boundaries as evidenced by diffusion experiments on bicrystals. The conclusion is that there are apparently few dislocations in these boundaries. This corresponds to the statement above that "repaired" lattice joints display only a few widely spaced broken bonds and behave generally like twin boundaries, which do not represent major lattice disturbances.

Experimental evidence for a strong barrier formation at grain boundaries grown under controlled conditions is convincing. For the wide range of impurity doping indicated in Section 11.1 (see Refs. 11 and 12 there) for which no systematic change in longitudinal conductivity occurs, transversal barrier measurements indicate a high barrier potential. In Figure 11.18 the voltage reading at a probe moving over the bicrystal perpendicular to the grain boundary shows a sharp peak for the integrated resistivity measured against one side contact. A similar increase in voltage, measured between two migrating probes, is seen when the two probes are connected to a voltmeter (see Figure 11.19). The quantitative increase of the integrated resistivity or the voltage depends on the bias applied (see later in the present chapter). The bicrystals with optimum barrier reproducibility are grown in the form indicated in Figure 11.20. Tilt axis is  $[001]$ , seed orientations are  $[100]$ , and grain boundary orientation is  $\phi = 90^\circ$  (symmetric case). The idealized structure of the symmetric grain boundary is shown in Figure 11.21. As described in Section 4.2, the innermost zone of atomic misfit is very small (below 100 Å). In this zone, the total energy due to atomic misfit and strain is given by the sum

$$E = E_0 \theta \ln \frac{1}{\theta} + E_0 \theta \cdot A, \quad (11.9)$$

where, as we have seen, the first term is a measure of the elastic energy

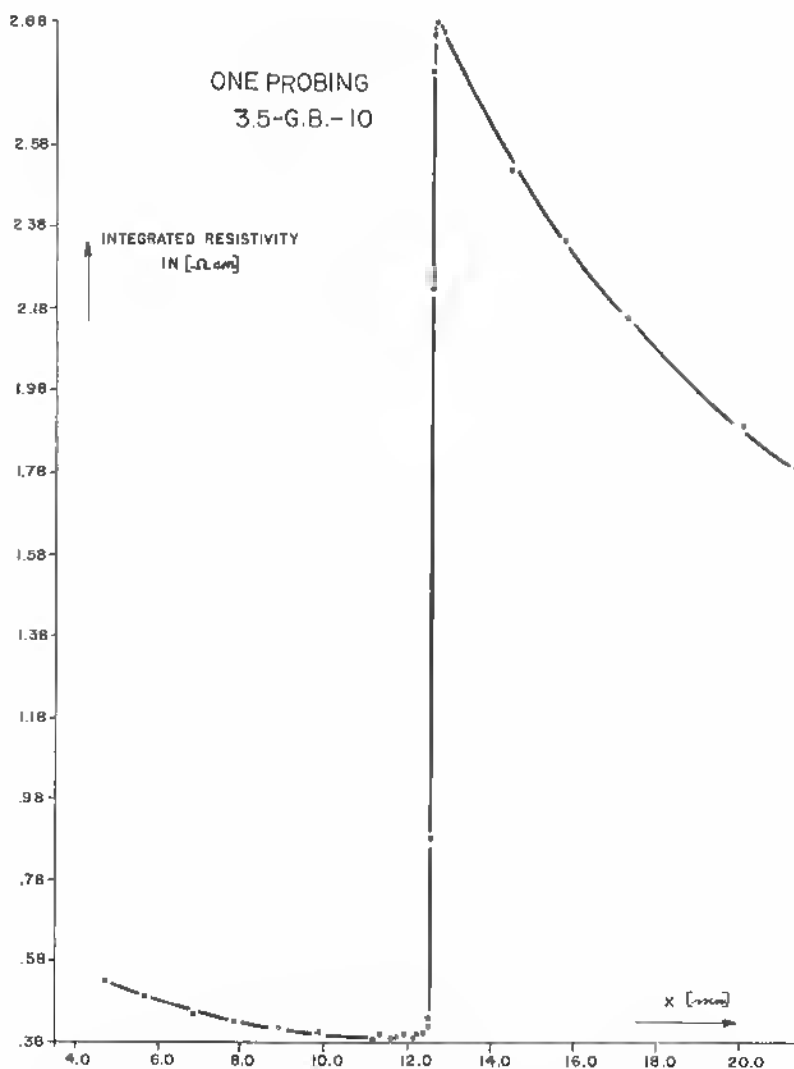


Fig. 11.18 Plot of integrated resistivity measured between a point contact and a base contact across a grain boundary in Germanium. [See Mataré, 9.22.]

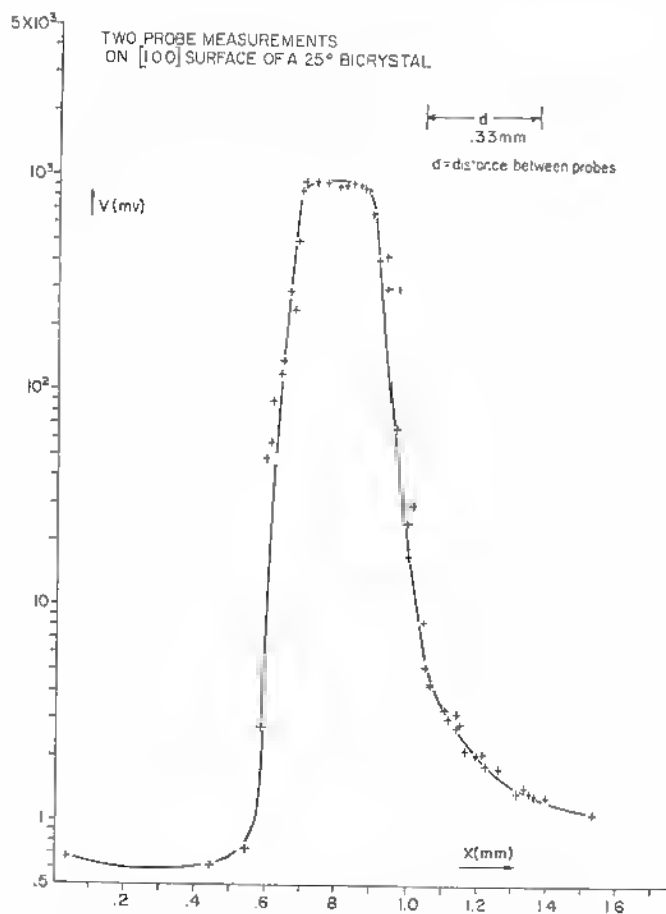


Fig. 11.19 Double probe-potential plot across a grain boundary in a Germanium bicrystal. [See Matarè, 9.22.]

stored and the second term represents the constant energy per dislocation:

$$E_0 = \frac{b\sigma_0}{2},$$

where  $b$  = Burgers vector,  
 $\sigma_0$  = shearing stress.

$A$  is a constant and can be expressed in terms of the energy

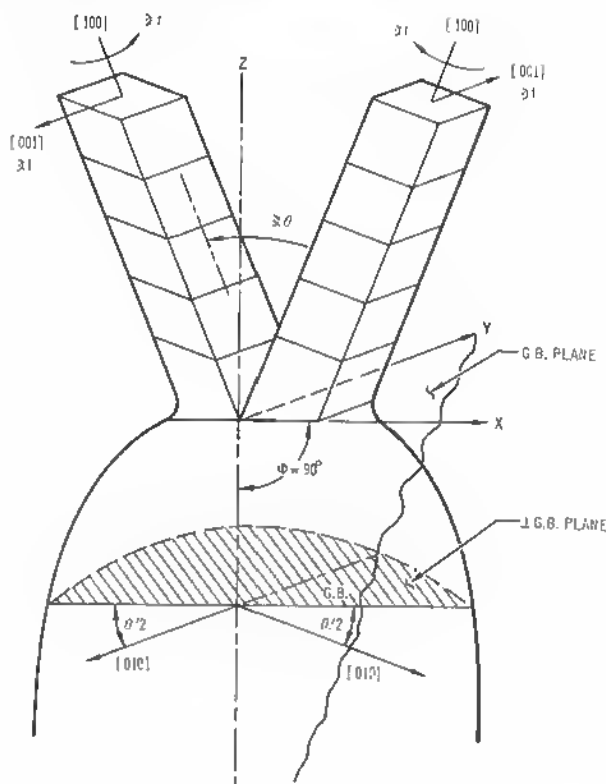


Fig. 11.20 Bicrystal seed orientation.

amounts  $E_i$  near the dislocation misfit area and  $E_{11}$  at a distance  $d < D$ :

$$A = \frac{2}{b^2 \sigma_0} (E_i + E_{11}) + 1 + \ln \frac{b}{2\pi r_e}, \quad (11.10)$$

where  $r_e$  = core radius

(see Section 4.1). The question arises if and how much the grain-boundary-barrier height may be related to the stored energy. In Figure 11.22, a few symmetric grain-boundary-barrier values (relative resistance change across barrier) are plotted with the tilt angle as abscissa. Plotting the Read-Shockley energy curve in the same scale does not leave the impression of a functional relationship. At least it can be concluded that the barrier layer built up is sensitive with respect to the tilt angle,  $25^\circ$  being the optimum.

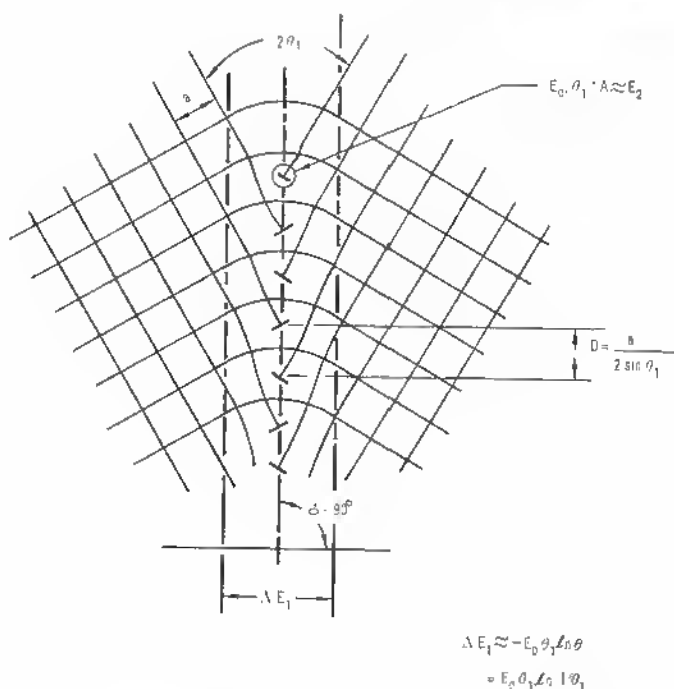


Fig. 11.21 Model of grain boundary interface with energy relations (see text).

We now have to answer the questions concerning the nature of the barrier. In a simple schematic one would plot a band scheme  $E(x)$ , as shown in Figure 11.23. Fixed donor ions are indicated by  $\ominus$ , fixed acceptors by  $\oplus$ . Free holes,  $+$ , accumulate in the valence-band peak at the center near the Fermi level and are responsible for the longitudinal conduction in the grain boundary. Electrons from the conduction band move into the interband levels in the free-bound region at the center. The space charge extends from  $x_{T_p}$ , the edge of the disturbed layer to  $x_{T_n}$ . Application of an external voltage  $V_e$  causes a depression to the quasi Fermi level  $E'_F$ . This situation of two diodes mounted back-to-back is apparent from the current and voltage characteristics as measured on bicrystal samples with two ohmic contacts on the ends. Figure 11.24 shows the usual characteristics for a germanium bicrystal as specified before. There are three basic regions. In region *A* of the characteristics, a strong current increase within a small voltage range points to the filling of boundary states by free carriers. A saturation region *B* follows, which has the blocking character of the usual reverse portion of  $I$  and  $V$  characteristics. Finally, in region *C*, the avalanche breakdown occurs.



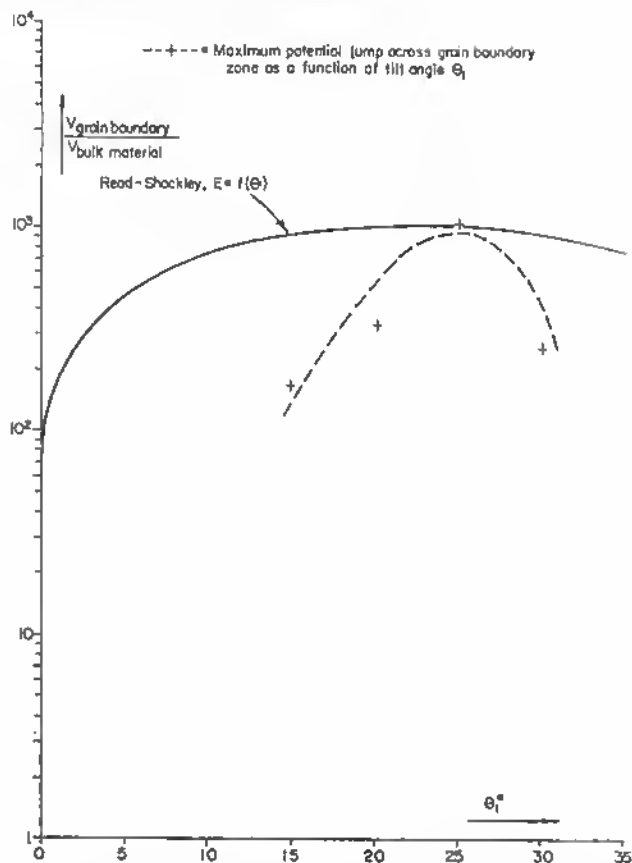


Fig. 11.22 Read-Shockley energy versus tilt angle  $\theta$  and barrier height of some grain boundaries of different tilt angle in Germanium.

As a first step in the understanding of the barrier with voltage-dependent filling factor for the free bonds, we establish a general relation between the external voltage  $V_e$  and the barrier height given by the voltage  $V_D$  (see Figure 11.23). In the case of the application of  $V_e$ , the left side of the barrier has a drop of  $V_1 = V_D + V_e$ . In the general scheme,  $V_D$  is replaced by  $V_2$ , corresponding to side 2. Sides 1 and 2 may also be inverted. The charge distribution within the grain boundary must satisfy Poisson's law:

$$\operatorname{div} \mathbf{E} = -\frac{4\pi s}{\kappa}, \quad (11.11)$$

where  $\mathbf{E}$  = electric field vector,  
 $\rho = en$  = charge density,  
 $\kappa$  = dielectric constant.

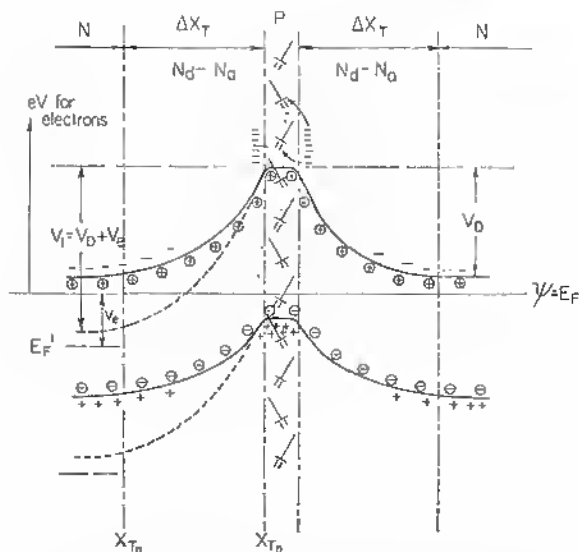
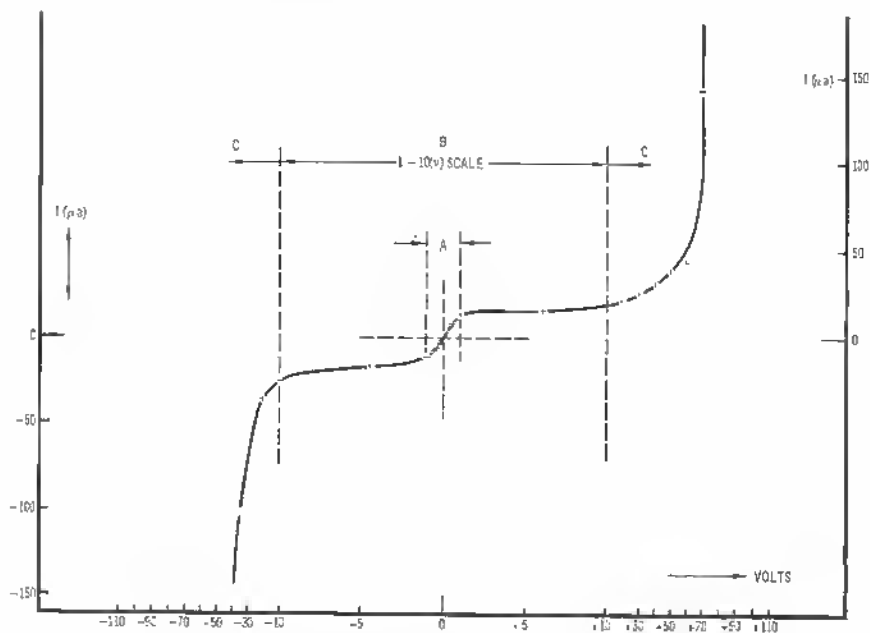


Fig. 11.23 Energy band model in real space at grain boundary.

Fig. 11.24  $I$ - $V$  characteristics of bicrystal (see text).

We can represent the energy integral of these distributed charges in a volume  $v$  as

$$\varepsilon = \int_v \mathbf{E} \mathbf{D} \, dv = \kappa \int_v E^2 \, dx \, dy \, dz, \quad (11.12)$$

where  $\mathbf{D} = \kappa \mathbf{E}$ .

Since  $E \, dx = V$  and  $dy \, dz = ds$ , (11.12) can be represented by a surface integral:

$$\varepsilon = \oint_s E V \, ds. \quad (11.13)$$

Application of Gauss' theorem leads to the equality

$$\oint_s E V \, ds = \int_v \nabla(\mathbf{E} V) \, dv \quad (11.14)$$

$$= \int_v \mathbf{E} \, \text{grad} \, V \, dv + \int_v \text{div} \, \mathbf{E} \, dv. \quad (11.15)$$

Expanding the surface  $s \rightarrow \infty$  is equivalent to

$$\oint_{\infty} E V \, ds \rightarrow 0. \quad (11.16)$$

In (11.15) this leads to the equality

$$\int_v \mathbf{E} \, \text{grad} \, V \, dv = - \int_v V \, \text{div} \, \mathbf{E} \, dv \quad (11.17)$$

or to

$$\int_v E^2 \, dv = \int_v V \left( \frac{4\pi\rho}{\kappa} \right) \, dv. \quad (11.18)$$

Now the volume integral at the left includes the surface charges:

$$\int_v E^2 \, dv = \frac{1}{2} \int_v V \rho \, dv + \frac{1}{2} \oint_s V \sigma \, d\sigma. \quad (11.19)$$

The second part of (11.19) can be considered zero in the context of the derivation (11.16), and thus

$$\frac{1}{2} \int_v E^2 \, dv = \int_v V \cdot \frac{4\pi\rho}{\kappa} \, dv. \quad (11.20)$$

This leads to the known expression for the voltage

$$V = \frac{\kappa E^2}{8\pi en}. \quad (11.21)$$

Equation (11.21) can also be found by expressing  $V$  from Poisson's equation. For one dimension

$$\frac{d^2 V}{dx^2} = - \frac{4\pi\rho}{\kappa}, \quad (11.22)$$

$$V = -2\pi \frac{x^2 \rho}{\kappa}. \quad (11.23)$$

Here the field is

$$E = \frac{dV}{dx} = - \int_0^l \frac{4\pi\rho}{\kappa} dx, \quad (11.24)$$

or

$$E = - \frac{4\pi\rho l}{\kappa}, \quad (11.25)$$

$$E^2 = \frac{16\pi^2\rho^2 l^2}{\kappa^2}. \quad (11.26)$$

$E$  is the maximum field strength at the barrier layer, and  $l$  is the depth of the space-charge zone in the  $x$  direction. At the limit  $x = l$  ( $x_{T_n}$  in Figure 11.23), the voltage corresponds to  $V = -2\pi\rho/\kappa l^2$  and by comparison with (11.26),

$$|V| = \frac{\kappa E^2}{8\pi\rho} = \frac{\kappa E^2}{8\pi en} \quad (11.27)$$

see (11.21).

If two different fields prevail at both boundary sides, one has

$$V_e = V_1 - V_D = \frac{\kappa}{8\pi en} (E_1^2 - E_2^2), \quad (11.28)$$

and for different carrier densities  $n_1$  and  $n_2$  at either side

$$V_e = V_1 - V_D = \frac{\kappa}{8\pi e} \left( \frac{E_1^2}{n_1} - \frac{E_2^2}{n_2} \right). \quad (11.29)$$

Following the argument of Fan and coworkers,<sup>1</sup> one can establish a relation between the number of charges within the barrier layer  $\Delta x$  and the fields at either side in order to find the actual number of charges in grain-boundary surface states.

In moving from field  $E_1$  to field  $E_2$  across the grain-boundary barrier, one has for the line integral

$$\int_{E_1}^{E_2} \frac{dE}{dx} dx = \frac{1}{\kappa} \int_{x_1}^{x_2} 4\pi\rho \cdot dx, \quad (11.30)$$

or

$$E_2 - E_1 = \frac{4\pi}{\kappa} \underbrace{\rho(x_1 - x_2)}_l. \quad (11.31)$$

In (11.31) the charge density  $\rho l$  corresponds to the actual number of charges in dangling-bond states,  $q$ . If we express  $E_1^2$  from (11.31) and introduce this into

(11.28), we get an expression linking  $E_1$  and  $E_2$  with  $q$ , the number of grain-boundary (g.b.) states:

$$E_1^2 = E_2^2 - \frac{8\pi q}{\kappa} E_2 + \left(\frac{4\pi q}{\kappa}\right)^2, \quad (11.32)$$

which, introduced into (11.28), yields

$$V_e = \frac{\kappa}{8\pi en} \left[ \left(\frac{4\pi q}{\kappa}\right)^2 - \frac{8\pi q}{\kappa} E_2 \right], \quad (11.33)$$

where  $n$  refers to the bulk crystal doping and  $q$  refers to the actual charge density in g.b. states. A similar result for  $E_1$  yields two equations expressing the two fields as a function of  $q$ , the external voltage  $V_e$  and their relation to the bulk doping  $n$ :

$$\begin{aligned} E_2 &= \frac{2\pi q}{\kappa} - \frac{en}{q} V_e, \\ E_1 &= -\frac{2\pi q}{\kappa} - \frac{en}{q} V_e. \end{aligned} \quad (11.34)$$

In equilibrium one has

$$V_{10} = -V_{20} = \frac{\phi}{e}. \quad (11.35)$$

This means that in terms of the barrier height  $\phi$  in electron volts

$$\phi_1 = \phi_2 = \phi_0.$$

Since according to (11.31)

$$E_2 - E_1 = \frac{4\pi q}{\kappa}, \quad (11.36)$$

we have for the equilibrium case

$$E_1 = E_{10}, \quad E_2 = E_{20}; \quad (11.37)$$

and

$$E_{10} = -E_{20} = -\frac{2\pi q_0}{\kappa}, \quad (11.38)$$

where  $q_0$  = equilibrium number of filled g.b. states.

Introducing now  $E_{20}$  instead of  $E_2$  into (11.34) leads to

$$\frac{2\pi q_0}{\kappa} = \frac{2\pi q}{\kappa} - \frac{en}{q} V_e. \quad (11.39)$$

This can be written in terms of the ratio  $q/q_0$  of actually occupied states to their number at thermal equilibrium:

$$\frac{q}{q_0} = \frac{1}{2} \left[ 1 + \left( 1 + \frac{eV_e}{\phi} \right)^{1/2} \right], \quad (11.40)$$

where  $\phi = \pi q_0^2 / 2\kappa n$  barrier height in equilibrium.

This ratio of actual to equilibrium charge density in g.b. states as a function of  $V_e$  can be used to assess the g.b. voltage dependence and will be referred to in the future quite frequently.

As a matter of fact, it is this dependence which gives the grain-boundary double barrier its remarkable properties of a barrier height increase with voltage (see Figure 11.25). As  $V_e$  is increased to  $V'_e$ , the quasi Fermi level at side 2 of the barrier is moved from  $\zeta_1$  to  $\zeta'_1$  and at the same time the barrier height increases from  $eV_1$  to  $eV'_1$ .

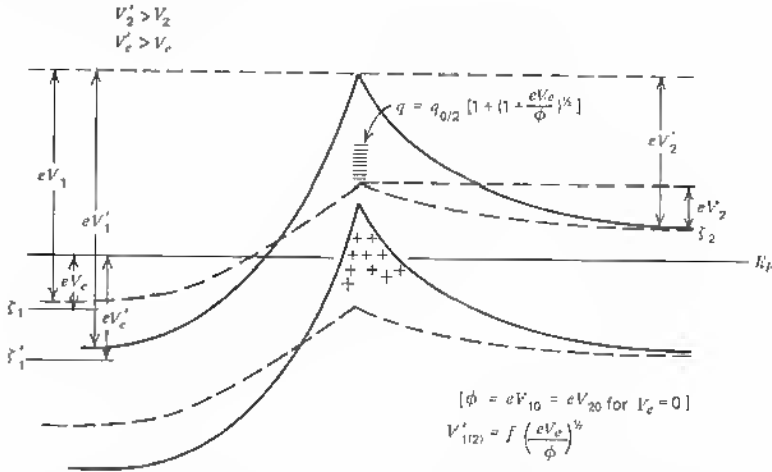


Fig. 11.25 Voltage dependence of grain boundary barrier height. Shown is increase in  $V_e$  ( $\rightarrow V'_e$ ) and resultant increase of  $V_1 \rightarrow V'_1$  respectively  $V_2 \rightarrow V'_2$ . Barrier height  $\phi = eV_{10} = eV_{20}$  for  $V_e = 0$ . Since  $q = q_0/2 \left[ 1 + \left( 1 + \frac{eV_e}{\phi} \right)^{1/2} \right]$ ,  $V'_1$  and  $V'_2$  are  $f\left(\frac{eV_e}{\phi}\right)^{1/2}$ .

Expressions for the voltages at both sides follow from (11.21) with (11.34):

$$V_1 = \frac{\kappa}{8\pi en} \left( \frac{2\pi q}{\kappa} + \frac{enV_e}{q} \right)^2, \quad (11.41)$$

$$V_2 = \frac{\kappa}{8\pi en} \left( \frac{2\pi q}{\kappa} - \frac{enV_e}{q} \right)^2. \quad (11.42)$$

These voltages reduce to zero for the critical  $V_e$  value

$$V_{crit} = \pm \frac{2\pi}{\kappa en} q^2. \quad (11.43)$$

Fan and coworkers pointed out already that a constant number of charges in g.b. states would lead to very small critical voltage values.

For  $q = q_0$ , (11.32) is valid, and thus

$$E_{10}^2 = \frac{4\pi^2 q_0^2}{\kappa^2},$$

consequently

$$V_{crit} = E_{10}^2 \frac{\kappa}{2\pi en}. \quad (11.44)$$

On the other hand

$$E_{10}^2 = E_{20}^2 = \frac{8\pi en V_{10}}{\kappa}$$

see (11.27). Therefore

$$V_{crit} = 4V_{10} = 4 \frac{\phi}{e} = 2 \frac{\pi q_0^2}{\kappa en} \quad (11.45)$$

compare (11.40). With the value of  $\phi$  in the range below 1 eV, the critical voltage values would be very low. In reality blocking voltages well above normal junction saturation values have been measured. This gives increased importance to (11.40).

Introducing this expression for  $q/q_0$  into (11.41) and (11.42) leads to expressions for the two potentials in terms of  $V_e$  and  $\phi$ :

$$V_1 = \frac{\kappa}{8\pi en} \left\{ \frac{\pi q_0}{\kappa} \left[ 1 + \left( 1 + \frac{eV_e}{\phi} \right)^{1/2} \right] + \frac{2enV_e}{q_0} \left[ 1 + \left( 1 + \frac{eV_e}{\phi} \right)^{1/2} \right]^{-1} \right\}^2, \quad (11.46)$$

$$V_2 = \frac{\kappa}{8\pi en} \left\{ \frac{\pi q_0}{\kappa} \left[ 1 + \left( 1 + \frac{eV_e}{\phi} \right)^{1/2} \right] - \frac{2enV_e}{q_0} \left[ 1 + \left( 1 + \frac{eV_e}{\phi} \right)^{1/2} \right]^{-1} \right\}^2 \quad (11.47)$$

see (11.14). Concentrated in one, these equations can be written

$$V_{1(2)} = \frac{\pi q_0^2}{8en\kappa} \cdot a \pm \frac{1}{2} V_e + \frac{en\kappa}{2\pi q_0^2} \cdot \frac{V_e^2}{a}, \quad (11.48)$$

(minus sign for  $V_2$ ),

where  $q_0$  = equilibrium charge density in g.b. states,

$n$  = bulk carrier density,

$\kappa$  = dielectric constant,

and with

$$a = 2 \left[ 1 + \left( 1 + \frac{eV_e}{\phi} \right)^{1/2} \right] + \frac{eV_e}{\phi} \quad (11.49)$$

the function (11.48) for the voltages at either barrier side can be developed into a series for

$$\alpha = \frac{eV_e}{\phi}.$$

With the functional relations

$$\begin{aligned} x^2 &= 1 + \alpha \\ (x + 1)^2 &= a = 1 + \alpha + 2\sqrt{1 + \alpha} + 1 \end{aligned}$$

and the abbreviation

$$C = \frac{\pi q_0^2}{en\kappa} \quad (11.50)$$

(11.48) becomes

$$V_{1(2)} = \frac{C}{8} (x + 1)^2 + \frac{1}{2C} \frac{\phi^2}{e^2} (x - 1)^2 \pm \frac{1}{2} \frac{\phi}{e} (x^2 - 1) \quad (11.51)$$

or,

$$V_{1(2)} = \frac{C}{8} [2 + \alpha + 2(1 + \alpha)^{1/2}] + \frac{1}{2C} \left( \frac{\phi}{e} \right)^2 [2 + \alpha - 2(1 + \alpha)^{1/2}] \pm \frac{V_e}{2}. \quad (11.52)$$

This function is now to be considered for different  $\alpha$  values.

If  $\alpha < 1$  (or  $eV_e < \phi$ ), we can develop

$$(1 + \alpha)^{1/2} = 1 + \frac{1}{2}\alpha - \frac{1}{8}\alpha^2 + \frac{1}{16}\alpha^3 \dots$$

and obtain

$$V_{1(2)} \simeq \frac{C}{8} \left[ 4 + 2\alpha - \frac{\alpha^2}{4} \right] + \frac{1}{2C} \left( \frac{\phi}{e} \right)^2 \left[ 4 + \frac{\alpha^2}{4} \right] \pm \frac{V_e}{2}. \quad (11.53)$$

We have developed to the  $\alpha^2$  term only. This means that  $V_{1(2)}$  is quadratically increasing with  $V_e$  for  $eV_e < \phi$  or within the diffusion voltage range of the g.b. barrier, a fact apparent from the characteristics, as we have seen (see Figure 11.24).

For increased  $\alpha$ , for example,  $\alpha > 1$  or  $\alpha \gg 1$ , we get from (11.52)

$$V_{1(2)} \simeq \frac{C}{8} \alpha + \frac{1}{2C} \left( \frac{\phi}{e} \right)^2 \alpha \pm \frac{V_e}{2} = \alpha \left[ \frac{C}{8} + \frac{1}{2C} \left( \frac{\phi}{e} \right)^2 \right] \pm \frac{V_e}{2}, \quad (11.54)$$

which is linear in  $V_e$  only.



In other words, if the external voltage surpasses  $\phi/e$ , the barrier height is only linearly dependent on  $V_e$ , as in ordinary  $p$ - $n$  structures.

So far, we have considered voltage-field and barrier-height relations with respect to g.b. charge densities. Now we wish to know more about the actual current-voltage relationships and the number of electrons and holes in boundary states at the barrier top. Here we start with the model of a Schottky double barrier. The current density  $j$  on either side of the g.b. barrier has a field and a diffusion part:

$$j = e\mu nE(x) + \mu kT \frac{dn(x)}{dx}, \quad (11.55)$$

where  $\mu$  = electron mobility,

$E(x)$  = local field strength,

$n$  = carrier density,  $\text{cm}^{-3}$ ,

$e$  = electron charge,

$k$  = Boltzmann constant,

$n(x)$  = local carrier density.

From here the blocking current density is found by integration under appropriate boundary conditions and corresponds to the usual rectifier expression

$$i = i_f \left[ 1 - \exp\left(-\frac{eV_1}{kT}\right) \right]. \quad (11.56)$$

$V_1$  is the voltage measured from the barrier top to the end of the space charge (see Figure 11.25), and  $i_f$  is the field current. In the situation of a g.b. layer where a carrier density gradient from the top  $n_{et}$  to the bulk  $n_{e0}$  is established, the current is given by

$$i = e\mu E \left[ n_{et} - n_{e0} \exp\left(-\frac{eV_1}{kT}\right) \right]. \quad (11.57)$$

Equating (11.56) and (11.57) results in a field current:

$$i_f = e\mu_e E \frac{[n_{et} - n_{e0} \exp(\mp V_1/kT)]}{1 - \exp(\mp V_1/kT)}. \quad (11.58)$$

Here the minus sign refers to electrons, the plus sign to holes.

With the condition  $eV_1 \gg kT$ , we may simplify (11.58) to read

$$i_f = e\mu_e E \left[ n_{et} - n_{e0} \exp\left(-\frac{eV_1}{kT}\right) \right] \quad (11.59)$$

In a balanced condition the field currents  $i_{f1}$  and  $i_{f2}$  from either barrier side have to be equal.

This means that

$$e\mu_e E_1 \left[ n_{e_t} - n_{e_0} \exp\left(-\frac{eV_1}{kT}\right) \right] = e\mu_e E_2 \left[ n_{e_t} - n_{e_0} \exp\left(-\frac{eV_2}{kT}\right) \right], \quad (11.60)$$

or

$$n_{e_t}(E_1 - E_2) = n_{e_0} \left[ E_1 \exp\left(-\frac{eV_1}{kT}\right) - E_2 \exp\left(-\frac{eV_e}{kT}\right) \right]. \quad (11.61)$$

If we eliminate  $n_{e_t}$  from (11.59) and (11.61), we have

$$i_e = -e\mu_e \frac{E_1 E_2}{E_1 - E_2} n_{e_0} \exp\left(-\frac{eV_2}{kT}\right) \cdot \left[ 1 - \exp\left(-\frac{eV_e}{kT}\right) \right]. \quad (11.62)$$

Here  $V_e = V_1 - V_2$ .

Correspondingly the hole current  $i_h$  is given by

$$i_h = e\mu_h E_1 E_2 \frac{n_{h_2} \exp(-eV_1/kT) - n_{h_1} \exp(-eV_2/kT)}{E_1 \exp(-eV_1/kT) - E_2 \exp(-eV_2/kT)}. \quad (11.63)$$

Since  $n_h \ll n_e$  this field current is small.

If we are interested in the derivation of the dependence of  $n_{e_t}$ , the electronic state density at the barrier top, from the applied external voltage  $V_e$ , we start with (11.61), but under the conditions  $V_1 > V_2$ ,  $V_e \gg kT/e$ .

This leads immediately to

$$n_{e_t}(E_1 - E_2) \simeq -n_{e_0} E_2 \exp\left(-\frac{eV_2}{kT}\right). \quad (11.64)$$

If we assume that  $E_1 - E_2 = -q$  number of negative charges in g.b. niveaus and set  $q = q_0 = \text{constant}$  for a first-order estimate, we can find  $\partial n_{e_t} / \partial V_e$ .

The hole concentration is

$$n_{h_t} \simeq 2n_{h_0} \exp \frac{eV_2}{kT}. \quad (11.65)$$

With the relation

$$|E_2| \approx V_2^{1/2}$$

(11.64) reads

$$n_{e_t} \simeq -n_{e_0} \frac{V_2^{1/2}}{-q} \exp\left(-\frac{eV_2}{kT}\right), \quad (11.66)$$

and differentiation with respect to  $V_e$  results in

$$\frac{\partial n_{e_t}}{\partial V_e} \simeq V_2^{1/2} \frac{n_{e_0}}{q} \frac{e}{kT} \left( \frac{kT}{2eV_2} - 1 \right) \exp\left(-\frac{eV_2}{kT}\right) \frac{\partial V_2}{\partial V_e}. \quad (11.67)$$

For the hole density we have from (11.65)

$$\frac{\partial n_{h_e}}{\partial V_e} \simeq 2n_{h_0} \frac{e}{kT} \exp\left(\frac{eV_2}{kT}\right) \frac{\partial V_2}{\partial V_e}, \quad (11.68)$$

since

$$V_e = V_1 - V_2, \\ \partial V_e = -\partial V_2.$$

For  $V_2 \gg kT/e$  (11.67) is positive, which means that  $n_{e_e}$  increases with  $V_e$ . The sign of (11.68) indicates that the hole density  $n_{h_e}$  decreases with  $V_e$ .

At this point we should consider, however, that  $q \neq \text{constant}$  and should introduce

$$q(V_e)$$

according to (11.40).

Starting again with (11.66), we find

$$n_{e_e} \simeq \frac{n_{e_0}}{q} \frac{2V_2^{1/2}}{[1 + (1 + eV_e/\phi)^{1/2}]} \exp\left(-\frac{eV_2}{kT}\right). \quad (11.69)$$

Differentiation yields

$$\frac{\partial n_{e_e}}{\partial V_e} = \frac{\partial}{\partial V_e} \left\{ \left[ 1 + \left( 1 + \frac{eV_e}{\phi} \right)^{1/2} \right]^{-1} \frac{2V_2^{1/2}}{q_0} n_{e_0} \exp\left(-\frac{eV_2}{kT}\right) \right\}, \quad (11.70)$$

or

$$\frac{\partial n_{e_e}}{\partial V_e} = \frac{n_{e_0}}{q_0} V_2^{1/2} \frac{2e}{kT[1 + (1 + eV_e/\phi)^{1/2}]} \left\{ \left( \frac{kT}{2eV_2} - 1 \right) \frac{\partial V_2}{\partial V_e} - \frac{kT/\phi}{2(1 + eV_e/\phi)^{1/2}[1 + (1 + eV_e/\phi)^{1/2}]} \right\} \cdot \exp\left(-\frac{eV_2}{kT}\right). \quad (11.71)$$

This is a positive function of  $V_e$ , since the second term in the large brackets is small compared with the first.

In a rigorous treatment one should, however, start from the more general relations

$$V_1 > V_2, \quad V_1 \gg \frac{kT}{e}, \quad V_2 \gg \frac{kT}{e},$$

and thus consider the filling of the free bond states. This means that the condition  $eV_e \gg \phi$  is no longer maintained.

Starting again with (11.58) for  $i_f = i_e = f(V_1)$ ,

$$i_e = e\mu_e E \frac{[n_{e_e} - n_{e_0} \exp(-eV_1/kT)]}{[1 - \exp(-eV_1/kT)]}, \quad (11.72)$$

and assuming

$$eV_1 \gg kT, \quad eV_2 \gg kT,$$

the equilibrium case is

$$i_e(V_1) = i_e(V_2), \quad (11.73)$$

or

$$n_{e_i}(E_1 - E_2) = n_{e_0} \left[ E_1 \exp\left(-\frac{eV_1}{kT}\right) - E_2 \exp\left(-\frac{eV_2}{kT}\right) \right]. \quad (11.74)$$

See (11.61).

Here the dependence of  $n_{e_i}$  on  $V_e = V_1 - V_2$  is the question. Therefore, we have again to form the differential:

$$\begin{aligned} \frac{\partial n_{e_i}}{\partial V_e} = \frac{n_{e_0}}{q} \frac{e}{kT} \left[ V_2^{1/2} \left( \frac{kT}{2eV_2} - 1 \right) \frac{\partial V_2}{\partial V_e} \exp\left(-\frac{eV_2}{kT}\right) \right. \\ \left. - V_1^{1/2} \left( \frac{kT}{2eV_1} - 1 \right) \frac{\partial V_1}{\partial V_e} \exp\left(-\frac{eV_1}{kT}\right) \right]. \end{aligned} \quad (11.75)$$

This is a positive function of  $V_e$ , indicating that there will be increase in g.b. charges with bias.

Introducing now again

$$q = \frac{q_0 [1 + (1 + eV_e/\phi)^{1/2}]}{2} \quad (11.40)$$

instead of  $q = \text{constant}$  into (11.74) leads to

$$n_{e_i}(q) = n_{e_0} \frac{2}{q_0 [1 + (1 + eV_e/\phi)^{1/2}]} \left[ V_2^{1/2} \exp\left(-\frac{eV_2}{kT}\right) - V_1^{1/2} \exp\left(-\frac{eV_1}{kT}\right) \right]. \quad (11.76)$$

Differentiation leads to

$$\begin{aligned} \frac{\partial n_{e_i}}{\partial V_e} = \frac{2n_{e_0}}{q} \frac{1}{1 + (1 + eV_e/\phi)^{1/2}} \left\{ V_2^{1/2} \left( \frac{1}{2V_2} - \frac{e}{kT} \right) \frac{\partial V_2}{\partial V_e} \right. \\ \cdot \exp\left(-\frac{eV_2}{kT}\right) - V_1^{1/2} \left( \frac{1}{2V_1} - \frac{e}{kT} \right) \frac{\partial V_1}{\partial V_e} \exp\left(-\frac{eV_1}{kT}\right) \\ \left. + \frac{1}{1 + (1 + eV_e/\phi)^{1/2}} \frac{e/\phi}{2(1 + eV_e/\phi)^{1/2}} \right. \\ \left. \times \left[ V_1^{1/2} \exp\left(-\frac{eV_1}{kT}\right) - V_2^{1/2} \exp\left(-\frac{eV_2}{kT}\right) \right] \right\}, \end{aligned} \quad (11.77)$$

where  $V_2 = V_D$  = voltage on one barrier side,

$V_1$  = voltage on other barrier side,

$V_e$  = external (bias) voltage =  $V_1 + V_2$ ,

$\phi$  = barrier height, eV.

We see from (11.77) that  $n_e$  increases rapidly with  $V_e$  for small values of  $V_e$  in accordance with the earlier derivations and with the measured  $(I/V)$  characteristics.

Finally we have to consider the influence of the variable grain-boundary state density, as expressed by (11.40) on the Fermi distribution function. The normal distribution function

$$f_0 = \left(1 + \exp \frac{E_D - E_F}{kT}\right)^{-1},$$

where  $E_D$  = dislocation energy level,

$E_F$  = Fermi level,

is then altered into

$$f = f_0 \frac{q}{q_0} = f_0 \frac{1 + (1 + eV_e/\phi)^{1/2}}{2}, \quad (11.78)$$

or

$$f = \frac{1}{2} \left(1 + \exp \frac{E_D - E_F}{kT}\right)^{-1} \left[1 + \left(1 + \frac{eV_e}{\phi}\right)^{1/2}\right]. \quad (11.79)$$

This corrected distribution function can now be introduced into the filling factor  $c/a$ , defining the space-charge pipe radius of the dislocations. The state density is

$$\begin{aligned} \frac{1}{a} &= \pi R^2 (N_d - N_a) \\ &= \frac{1}{2c} \left(1 + \exp \frac{E_D - E_F}{kT}\right)^{-1} \left[1 + \left(1 + \frac{eV_e}{\phi}\right)^{1/2}\right], \end{aligned} \quad (11.80)$$

where  $a$  = spacing of added electrons,

$c$  = spacing of free bonds.

Therefore

$$R^2 = \frac{1 + (1 + eV_e/\phi)^{1/2}}{2\pi c(N_d - N_a)\{1 + \exp[(E_D - E_F)/kT]\}}. \quad (11.81)$$

We see that the actual space-charge radius  $R$  depends first on the applied voltage, second on the spacing  $c$  of available states, third on the bulk impurity range, and fourth on the position of the dislocation level  $E_D$  with respect to the Fermi level.

An estimate of the space charge dependence on the dislocation spacing, and the bulk impurity density is of importance in cases where certain boundaries have to be checked with respect to their electrical influence in bulk crystals and devices. As we saw in Section 9.3, the pipe radius can be found on account of the distance  $D$  between dangling bonds;  $D = b/2 \sin(\theta/2)$ , which is equal to  $c$  in this case. Disregarding the  $V_e$  dependence, we have then

$$R = \left\{ \frac{2 \sin(\theta/2)}{\pi b \Delta N} \frac{1}{(1 + \exp(E_D - E_F)/kT)} \right\}^{1/2}, \quad (11.82)$$

where

$$\Delta N = (N_d - N_a).$$

This can also be written

$$R = \left[ f \cdot \frac{2 \sin(\theta/2)}{\pi b} \right]^{1/2} \cdot \Delta N^{-1/2}, \quad (11.83)$$

Assuming now  $f \simeq 0.1$  as before (temperature range  $0 < T < 150^\circ$ ), we get

$$R = \left( \frac{0.1}{\pi} \right)^{1/2} \left[ \frac{2 \sin(\theta/2)}{b} \right]^{1/2} \Delta N^{-1/2}, \quad (11.84)$$

or

$$\log R = \frac{1}{2}(\log 0.1 - \log \pi - \log b) + \frac{1}{2}[\log 2 \sin(\theta/2) - \log \Delta N]. \quad (11.85)$$

For a Burgers vector  $b$  = lattice translation vector, one can readily calculate the dependence of  $R$  on  $\theta$  and  $\Delta N$ . This gives a nomogram of the form shown, in Figure 11.26. Here the tilt angle  $\theta$  is varied from below  $1$  to more than  $25^\circ$  and  $\Delta N$  from  $10^{14}$  to  $10^{19} \text{ cm}^{-3}$ . We see that the pipe radius is between  $10^{-7}$  and  $10^{-4} \text{ cm}$  wide for this range (no consideration of  $V_e$ ). The dislocation spacing  $D$  is also plotted with  $\theta$  as parameter. This depicts the regions in which  $R$  surpasses  $D$  or where the space charge exceeds the dislocation spacing (to the right of the  $D$  line).

In an analysis of the current flow across grain boundaries, R. K. Mueller starts with the expressions for the hole current as main contributor (a) in the direction from the positively biased side to the inversion layer  $I_h^+$  and (b) from the inversion layer to the negatively biased side  $I_h^-$  and expresses these in terms of the applied voltage  $V_e$  and  $\Delta V$ , the difference between the quasi

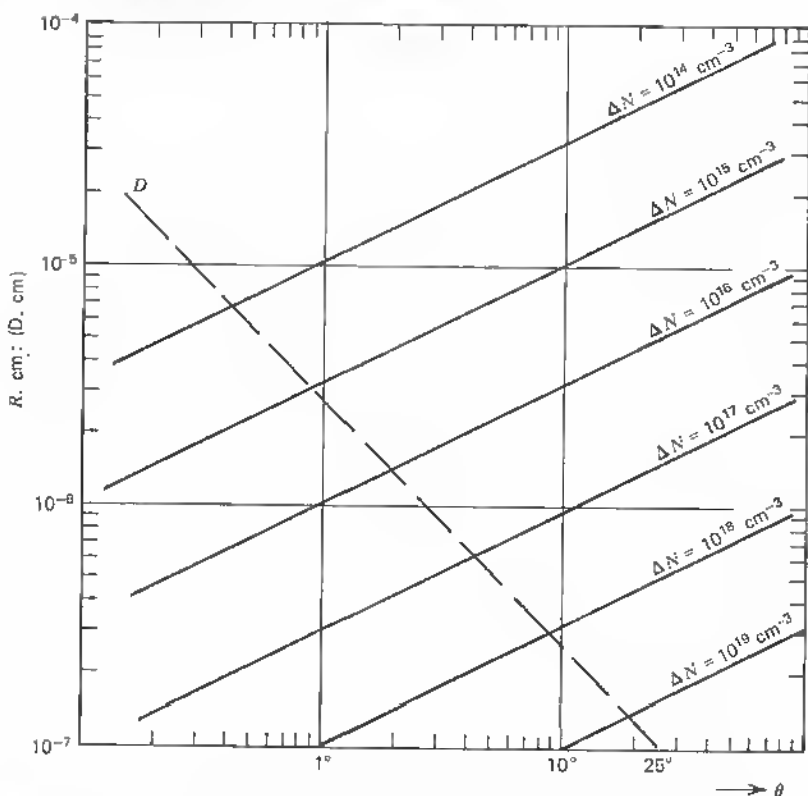


Fig. 11.26 Radius  $R$  of space charge pipe of grain-boundary as  $f(\theta)$  and  $f(\Delta N)$  and dislocation spacing  $D = f(\theta)$ .

Fermi level of electrons in boundary states and the Fermi energy in the negatively biased side of the grain-boundary junction:

$$\left. \begin{aligned} I_h^+ &= I_s(1 - e^{-q(V-\Delta V)/kT}) \\ I_h^- &= I_s(e^{q\Delta V/kT} - 1) \end{aligned} \right\} \text{for holes,}$$

and

$$\left. \begin{aligned} I_r^+ &= I_r e^{-q(V-\Delta V)/kT} \\ I_r^- &= I_r e^{q\Delta V/kT} \end{aligned} \right\} \text{for electrons,} \quad (11.86)$$

$I_s$  = hole saturation current,

$I_r$  = electron saturation current (random current).<sup>9</sup>

Here the boundary is represented as a trapping site with a carrier emitting surface on the other side.

A capture rate  $\gamma$  is defined that has a value of 0.2 to 0.6 for the equilibrium case.

The zero bias conductance  $G_0$  is then derived (equation 18 l.c.):

$$G_0 = \left(1 - \frac{2}{\gamma}\right) \left(\frac{q^2 N_c \bar{v}}{4kT^2}\right) e^{e/kT} e^{-\phi_0/kT}. \quad (11.87)$$

This can be written

$$G_0 = \left(1 - \frac{\gamma}{2}\right) \left(\frac{q^2 N_c \bar{v}}{4kT}\right) \exp\left(-\frac{\phi}{kT}\right), \quad (11.88)$$

where  $\gamma$  = capture rate,

$q$  = electron charge,

$N_c$  = effective number of states,  $= 2 \left(\frac{2\pi m^* kT}{h^2}\right)^{3/2}$

$$= 2.5 \times 10^{19} \left(\frac{T}{300^\circ\text{K}}\right)^{3/2} \left(\frac{m^*}{m}\right)^{3/2} \text{ cm}^{-3},$$

$\bar{v} = \left(\frac{8kT}{\pi m^*}\right)^{1/2}$  = average thermal velocity,

$\phi$  = barrier height (actual),  $m^*$  = effective mass.  $m$  = free mass,

$\phi_0$  = equilibrium barrier height ( $\phi = \phi_0 - eT$ ),

$kT$  = Boltzmann factor.

This expression can be modified by introduction of the expression for  $N_c$  and for  $\bar{v}$  which equals  $\mu E_0$ .

We have therefore

$$G_0 = \left(1 - \frac{\gamma}{2}\right) \left(\frac{q^2}{2kT}\right) \mu E_0 A T^{3/2} \exp\left(-\frac{\phi}{kT}\right), \quad (11.89)$$

$$\text{where } A = \frac{2\pi m^* k}{h^2}.$$

The theory as developed before is based on Fan's model and gives for the conductance

$$G_0 = \frac{q^2}{2kT} \mu E_0 A T^{3/2} \exp\left(-\frac{\phi + \zeta}{kT}\right) \quad (11.90)$$

(see Ref. 1). The difference between Mueller's approach (11.89) and Fan's (11.90) is small.  $\phi$  in the latter case is measured to the lower edge of the conduction band so that  $\phi + \zeta$  is the total height from the Fermi level. Mueller defines  $\phi = E_{cm} - E_F$ , which is the difference measured from the Fermi energy level to the edge of the conduction band  $E_{cm}$  at the maximum of the grain-boundary barriers. The only difference between (11.89) and (11.90) is the factor  $(1 - \gamma/2)$ . Although  $\gamma$  is 0.2 to 0.6 at equilibrium, smaller values are expected for the biased conditions.



Current-voltage relationships for small bias voltages (range of  $kT/q$ ) are in good agreement with measured characteristics.<sup>10</sup> The set of equations used to derive the current voltage relationship is the following:<sup>9</sup>

$$1. \quad I_{em}^+ = I_{em}^- = I_{em} = \gamma I_r. \quad (11.91)$$

This relation expresses essentially that the emission current from the boundary is unaffected by the applied bias and according to the principle of detailed balancing equal to the random current  $I_r$  times the capture rate  $\gamma$ .

2. The set of equations for the electron current as given in (11.86).

3. Assuming that the net rate of holes and electrons captured at the boundary is the same, one can derive a relation between the applied voltage

$$V = \frac{1}{q} (f^- - f^+)$$

where  $q$  = electron charge,

$f^-$ ,  $f^+$  = Fermi energies in bulk on both negative and positive boundary sides,

and the built-in voltage

$$\Delta V = \frac{1}{q} (f^- - f_B), \quad (11.92)$$

where  $f_B$  = quasi Fermi level of electrons in boundary states.

This leads to a third equation:

$$e^{q\Delta V/kT} = 2(1 + e^{-qV/kT})^{-1} *. \quad (11.93)$$

Since the electron current across the boundary is

$$I_e = I_r^- - (1 - \gamma)I_r^+ - I_{em}^- \quad (11.94)$$

see (11.17)—one gets with (11.86) and (11.93):

$$I_e = I_r e^{q\Delta V/kT} - (1 - \gamma)I_r e^{-q(V - \Delta V)/kT} - \gamma I_r. \quad (11.95)$$

With (11.93), this leads to

$$I_e = I_r \left[ \frac{2 - 2(1 - \gamma)e^{-qV/kT} - \gamma - \gamma e^{-qV/kT}}{1 + e^{-qV/kT}} \right] \quad (11.96)$$

or to

$$I_e = I_r (2 - \gamma) \tanh qV/2kT. \quad (11.97)$$

For the hole current one finds similarly

$$I_h = I_r \tanh qV/2kT, \quad (11.98)$$

where  $I_s$  = hole saturation current per unit area.

\* Note that Mueller's equation (16) is misprinted.

The total current across the boundary

$$I_{\text{tot}} = I_e + I_h$$

is given by

$$I_{\text{tot}} = 2I_r \left( 1 - \frac{\gamma}{2} + \beta \right) \tan hqV/2kT, \quad (11.99)$$

where  $\beta = I_s/2I_r$ .

$\beta$  measures the relative importance of the hole versus the electron contribution. It is a significant value only for lightly doped bicrystals and can be disregarded for bulk doping  $N_d \geq 10^{14} \text{ cm}^{-3}$ .

For a wider voltage range, R. Stratton derived expressions on account of the diode theory that can be fitted to the measured data.<sup>11</sup>

Recently, R. H. Glaenzner and A. G. Jordan<sup>12</sup> have measured resistivity and mobility in *n*- and *p*-type silicon crystals with a known amount of dislocations produced by plastic deformation. They found that the conductivity is highly anisotropic, being orders of magnitude higher for current flow parallel to the dislocations. This difference increases as the temperature is lowered and disappears, of course, near the intrinsic conductivity beyond 500°K.

These authors conclude from their measurements that such a large resistivity anisotropy can only be associated with a space charge or, in this case, space-charge cylinders. They also find that in *n*-type silicon the dislocations are acceptors, and in *p*-type silicon the dislocations are donors, in distinction to the case of germanium.

The temperature variation of the resistivity can be represented by the simple space-charge-cylinder model according to which

$$\frac{\sigma_{\parallel}}{\sigma_0} = (1 - \varepsilon) = \frac{\rho_0}{\rho_{\parallel}}, \quad (11.100)$$

in which

$$\varepsilon = \pi R^2 D = fD/a(N_d - N_a), \quad (11.101)$$

where  $\varepsilon$  = fractional volume of space-charge cylinders  
as voids (see Section 9.1 and 9.2),

$R$  = space-charge-cylinder radius

$D$  = dislocation density,  $\text{cm}^{-2}$

$a$  = distance between dangling bonds,

$N_d - N_a$  = net donor density.

These experiments confirm the importance of the broken bond for the behavior of the dislocations. The complications of the impurity atmospheres in the case of silicon obscure somewhat the action of the broken bonds,<sup>13</sup>

see section 12.4, but the experiments of Glaenzer and Jordan<sup>12</sup> confirm significantly the established importance of the lattice defect as it has been developed here.

## REFERENCES

1. Taylor, W. E., N. H. Odell, and H. Y. Fan: Grain Boundary Barriers in Germanium, *Phys. Rev.*, vol. 88, no. 4, pp. 867-875, Nov. 15, 1952.
2. Mataré, H. F.: Electronic Behavior of Certain Grain Boundaries in Perfect Crystals, *Z. f. Naturforschung*, vol. 9a, p. 698, 1954.
3. Mataré, H. F., et al.: Study of Electrical Characteristics of Grain Boundaries, *Phys. Rev.*, vol. 98, p. 1179, 1955.
4. Mataré, H. F.: Grain Boundaries and Transistor Action, *IRE Convention Record*, Nat. Convention 113, 1955.
5. Mataré, H. F.: Grain Boundary Structure and Carrier Transport in Semiconductor Crystals, *Z. f. Naturforschung*, vol. 10a, no. 8, pp. 640-652, 1955.
6. Mataré, H. F.: Electrical Behavior of Bicrystal Interfaces, *Z. f. Physik*, vol. 145, pp. 206-234, 1956.
7. Queisser, H. J.: Failure Mechanisms in Silicon Semiconductors, *Quarterly Status Report* 3, Contract AF30(602)2556, Project 5519, Task 45155, April 10, 1962.
8. Kaiser, W., H. L. Frisch, and H. Reiss: Mechanism of the Formation of Donor States in Heat-treated Silicon, *Phys. Rev.*, vol. 112, pp. 1546-1554 Dec. 1, 1958.
9. Mueller, R. K.: Current Flow across Grain Boundaries in *n*-Type Germanium I, *J. Appl. Phys.*, vol. 32, no. 4, pp. 635-639, April, 1961.
10. Mueller, R. K.: Current Flow across Grain Boundaries in *n*-Type Germanium II, *J. Appl. Phys.*, vol. 32, pp. 640-645, April, 1961.
11. Stratton, R.: Surface Barriers at Semiconductor Contacts, *Proceed. Phys. Society B*, vol. 69, pp. 513-527, 1956.
12. Glaenzer, R. H., and A. G. Jordan: The Electrical Properties of Dislocations in Silicon-II. The Effects on Conductivity, *Solid State Electronics*, vol. 12 pp. 259-266, 1969.
13. Queisser, H. J.: Dislocations in Silicon, "Festkörperprobleme II (Halbleiter-Probleme VIII)," Vieweg, Braunschweig, 1963, edited by F. Sauter, pp. 162-187.

## 11.3 HALL EFFECT DATA

The first point-to-point measurements of the Hall constant and Hall mobilities on bicrystals of a nontwinned nature already displayed values far in excess of the expected ones.<sup>1</sup> Conforming to the theory of high scattering in a region of over  $10^{12} \text{ cm}^{-2}$  dangling-bond states, the mobility was expected to be extremely small. The data first reported by Tweet are close to the bulk

values for germanium near room temperature and diminish slightly from 150°K down to liquid helium temperatures for the pure grain-boundary case, covering values from  $10^4$  to  $5 \times 10^3$  cm<sup>2</sup>/V sec. The probe method used by this author is not well suited for precise measurements, because positioning and surface-contact potential differences can mask the effects, especially since the barrier-layer width is of the same order of magnitude as the probe diameters. There is no doubt, however, that these original tests already revealed the correct fact that carrier transport in these layers is based on a somewhat ordered materials structure.

This was elucidated more clearly by the measurements of Japanese scientists on bicrystals made under controlled growth conditions, using double seed crystals.

Matukura et al.<sup>2,3</sup> reported on measurements made with bicrystal samples of germanium and silicon. Contacts to the grain boundaries were made by microalloy dots. Although photoresponse measurements revealed that germanium grain boundaries are *p*-type and silicon grain boundaries *n*-type, resistivity and Hall constant measurements showed somewhat unexpected high values of the mobility parameter. Since the exact width of the grain-boundary conduction path is not known, these values are plotted as

$$\begin{aligned}\rho^* &= \frac{\rho}{t}, \\ R^* &= \frac{R}{t},\end{aligned}\tag{11.102}$$

where  $t$  = thickness of conduction path.

For the mobility  $\mu = R/\rho = R^*/\rho^*$ , there is no dependence on  $t$ , and  $\mu$ -values can be derived directly if  $R^*$  and  $\rho^*$  are known.

The sample orientation was the one discussed earlier (see Fig. 11.20). In these measurements, two main current flow directions were chosen (see Figure 11.27). In case *A*, the current flow is parallel to the dislocation pipes, and in case *B*, the sample is cut perpendicular to the [010] tilt axis, and current flow is perpendicular to the dislocation arrays.

First measurements in the temperature range 80 to 250°K showed relatively high mobility values for both *A* and *B* orientations, but also erratic results for low-angle boundaries, probably because of contact problems. (If the microjunctions do not rectify properly, essentially bulk properties are measured.) In refined measurements, Y. Hamakawa and J. Yamaguchi<sup>4</sup> showed that there is, in fact, a negligible difference in mobility for the cases  $\mu_{\perp}$  and  $\mu_{\parallel}$  for the same tilt angle  $\theta$  in the medium range (see Figure 11.28). They also showed that the temperature dependence of the mobility can be

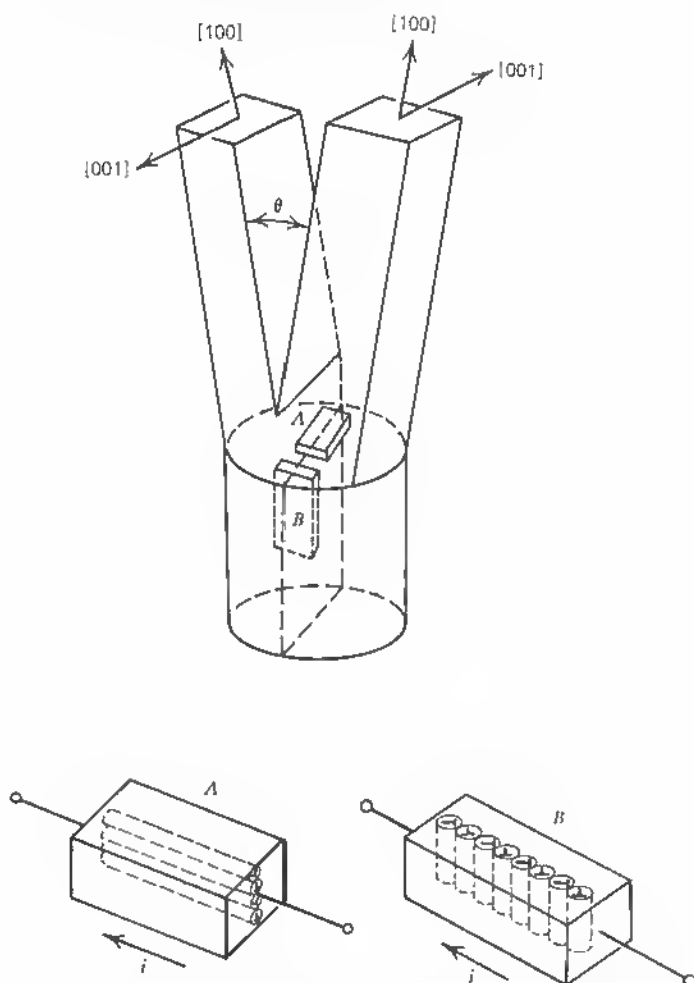


Fig. 11.27 Bicrystal orientation and main current direction in samples: A current parallel to dislocation pipes, B current perpendicular to dislocation pipes.

explained by the super-position law of scattering processes:

$$\mu^{-1} = \mu_{ls}^{-1} + \mu_i^{-1} + \mu_d^{-1}, \quad (11.103)$$

where  $\mu_{ls}$  = mobility due to lattice scattering restricted by a potential well  
 $= \zeta \mu_L$ ,

$\mu_L$  = lattice mobility  $\approx 1.05 \cdot 10^9 \cdot T^{-2.33}$ ,

$\zeta$  = ratio of surface/bulk mobility (Schrieffer),

$\mu_i$  = mobility due to ionized impurity scattering (negligible, small),

$\mu_d$  = mobility due to scattering of carriers in dislocation stress field.

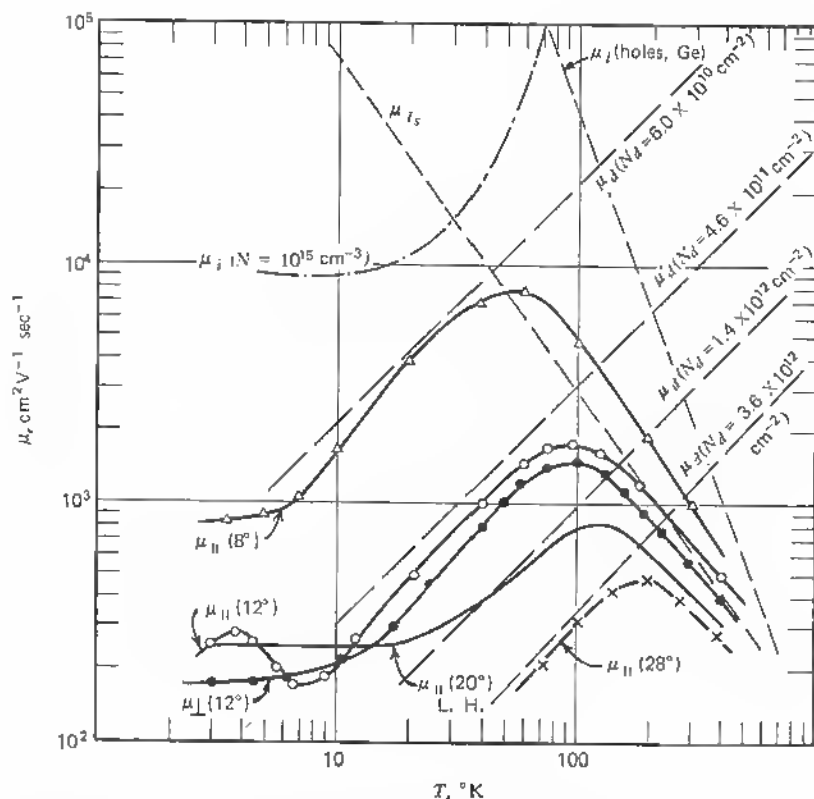


**Fig. 11.28** Mobility of holes in grain boundary plane as a function of temperature.  $\mu_{\parallel}(8^{\circ})$ ,  $\mu_{\parallel}(12^{\circ})$ ,  $\mu_{\parallel}(20^{\circ})$ ,  $\mu_{\parallel}(28^{\circ})$  are the measured mobilities for sample orientation  $A$ .  $\mu_i$  is the mobility for ionized impurity scattering,  $N = 10^{15} \text{ cm}^{-3}$ .  $\mu_d$  = scattering mobility (Dexter-Seitz) calculated for different impurity ranges corresponding roughly to dislocation densities.  $\mu_l$  = lattice mobility for holes in Germanium.  $\mu_{ls}$  = surface corrected mobility  $\mu_l$ .

Using the model by Dexter and Seitz, the authors derive a temperature dependence of  $\mu_d$ :

$$\mu_d = \alpha_d \cdot T, \quad (11.104)$$

in which

$$\alpha_d^{-1} = \frac{300}{32} \frac{3\pi}{k_0} \frac{E_1^2}{\hbar} \lambda^2 \left( \frac{1-2\nu}{1-\nu} \right) N_d \frac{m^*}{e}, \quad (11.105)$$

where  $\lambda$  = unit crystallographic slip distance  $\lambda^2 = 5 \times 10^{-16} \text{ cm}^2$ ,

$\nu$  = Poisson's ratio = 0.4,

$k_0$  = Boltzmann's constant,

$m^*$  = effective mass  $\approx 0.25m$ ,

$E_1$  = experimentally determined field parameter (here = 4.5 eV),

$e$  = electron charge,

one gets

$$\mu_d^{-1} = 0.31 \cdot 10^{-12} \cdot N_d \cdot 0.25T^{-1}. \quad (11.106)$$

The two decisive mobilities in (11.103),  $\mu_{is}$  and  $\mu_d$ , explain, in fact, the form of the measured mobility values as  $f(T)$  (see Figure 11.28). The number of dislocation scattering centers  $N_s$  was calculated from the spacing  $D = b/[2 \sin(\theta/2)]$  and the effective charge carrier concentration in the grain boundary  $p_{eff}$  was derived on account of

$$\frac{p_{eff}(p_{eff} + N_D)}{N_s - N_D} = \frac{N_v}{g} \exp\left(-\frac{\Delta E_i}{kT}\right), \quad (11.107)$$

where  $N_D$  = bulk (compensating) impurity density (donors)  $\approx 10^{13}$  to  $10^{14} \text{ cm}^{-3}$ ,

$N_v$  = effective state density in valence band,

$N_s \approx 10^{17}$  to  $10^{18} \text{ cm}^{-3}$ ,

$g$  = degeneracy factor of dangling-bond levels,

$\Delta E_i$  = activation energy of dislocation acceptor level ( $0.006 \pm 0.002$ ) eV from temperature dependence of reduced Hall coefficient in impurity reserve region.

In Figure 11.29, the relation between the effective hole density  $p_{eff} (\text{cm}^{-3})$  and  $1/D$  is plotted. With these data, the analysis of measured mobility values is quite reasonable (see Figure 11.28, from Ref. 5).

We see that with increasing tilt angle, the mobility decreases in accordance with  $\mu_d$  calculated using the Dexter-Seitz formula, where  $\mu_d$  is essentially proportional to  $1/N_D$ .

$\mu_i$ , the mobility for ionized impurity scattering, is also shown and is well beyond the range of the values in question. The lattice mobility  $\mu_l$  for holes in the valence band is slightly off the asymptotic value beyond room temperature and has to be corrected to  $\zeta\mu_l$ , where  $\zeta$  is the ratio of surface/bulk mobility.

It is doubtful, however, that these values for  $\mu_d$  would explain the grain-boundary conduction mechanism also in the low temperature range ( $T < 10^\circ\text{K}$ ), where total degeneracy exists. We have seen that in this range, the complete overlap of the wave functions more or less eliminates individual doping differences of the bulk. In Figure 11.28, we have also plotted the mobility versus temperature curve derived from values measured and published by Landwehr and Handler (L.H.)<sup>6</sup>

According to these values, the room-temperature mobilities are about equal to those measured at low temperature ( $T < 10^\circ\text{K}$ ) in grain boundaries.

Hamakawa et al.<sup>4</sup> express their surprise that  $\mu_{||} \approx \mu_{\perp}$ , or the mobility in sample A (see Figure 11.27) is not much higher than the mobility  $\mu_{\perp}$  in sample B. From the fact that the space-charge pipes scatter the momentum vector in case B, but not in case A, one should expect a strong effect on the outcome of

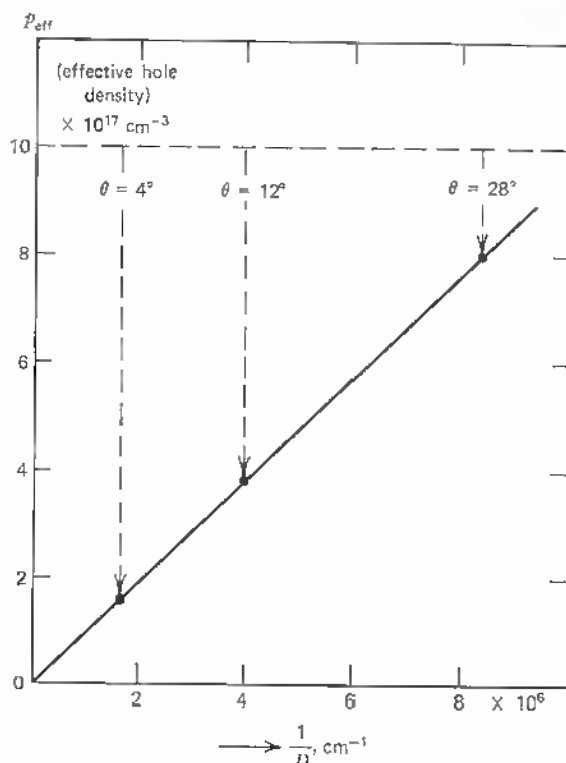


Fig. 11.29 Effective hole density as function of dislocation density (linear). (See [11.3, 4].)

the  $\mu$  values. Here we have to consider that the actual hole transport takes place within the degenerate region bounded on one side by the dislocation arrays and on the other side by the space charge. In either case, *A* or *B*, this region is a planar structure. Because of the wide extension of the space charge (over  $10 \mu$ , compared with the actual grain-boundary disturbed layer width of  $\sim 100 \text{ \AA}$ ), a smoothing of the pipes occurs and for close overlap (tilt angles  $\theta$  of more than a few degrees) no marked difference between case *A* and *B* can be found.<sup>7-8</sup> (Compare Figure 8.14.)

From Figure 11.28, it is apparent that the maximum of the mobility in grain-boundary layers is shifted toward higher temperatures as the tilt angle increases. This is in accordance with the impurity band conduction behavior in highly doped samples. However, the pronounced flattening of the mobility versus temperature curves in bulk samples with increasing impurity content<sup>9</sup> does not occur because of the effect of the preferred conduction in space-charge pipes along the overlapping rows of free bonds.



In bulk crystals with an impurity density of  $10^{19} \text{ cm}^{-3}$ , the linear density of impurity atoms is of the order of  $2.2 \cdot 10^6 \text{ cm}^{-1}$ , which corresponds to  $2 \cdot 10^7$  atoms per cm or roughly to a distance of 10 lattice atoms between impurity atoms, while for grain boundaries of  $10^\circ$  tilt angle and above (see Figure 11.26), the spacing between dangling bonds is also approximately  $2 \cdot 10^{-7} \text{ cm}$ . Therefore, it is clear that the preferred pipe conduction mechanism is responsible for the relatively high mobility values. The flattening of these curves at temperatures below  $30^\circ\text{K}$  shows the transition from Fermi-Dirac to Maxwell-Boltzmann statistics, as it known for degenerate bulk samples, where the distinction between impurity levels and conduction-band levels has practically vanished.

## REFERENCES

1. Tweet, A. G.: Properties of Grain Boundaries in Gold-doped Germanium, *Phys. Rev.*, vol. 99, no. 4, pp. 1182-1189, August 15, 1955.
2. Matukura, Y., and S. Tanaka: Conductivity of Grain Boundaries in Germanium, *J. Phys. Soc. Japan*, vol. 16, pp. 833-834, 1961.
3. Matukura, Y.: Properties of Grain Boundaries in Silicon, *J. Phys. Soc. Japan*, vol. 16, pp. 842-843, 1961.
4. Hamakawa, Y., and J. Yamaguchi: Electrical Conduction in Germanium Grain Boundary Plane, *Jap. Journal of Applied Physics*, vol. 1, no. 6, pp. 334-342, December, 1962.
5. Hamakawa, Y., T. Nishino, and J. Yamaguchi: *Japan J. Appl. Phys.*, vol. 2, pp. 371-372, 1963.
6. Landwehr, G., and P. Handler: Galvanomagnetic Properties of Grain Boundaries in Germanium Bicrystals from 1.25 to  $240^\circ\text{K}$ , *J. Phys. Chem. Solids*, vol. 23, pp. 891-906, 1962.
7. Mataré, H. F., and C. W. Laakso: Scanning Electron Beam Display of Dislocation Space Charge, *Appl. Phys. Letters*, vol. 13, no. 6, pp. 216-218, September 15, 1968.
8. Mataré, H. F., and C. W. Laakso: Space Charge Domains at Dislocation Sites, *J. Appl. Phys.*, vol. 40, no. 2, pp. 476-482, February, 1969.
9. Conwell, E. M.: Impurity Band Conduction in Germanium and Silicon, *Phys. Rev.*, vol. 103, no. 1, pp. 51-61, July, 1, 1956.

## 11.4 MAGNETORESISTANCE EFFECTS

The galvanomagnetic effects in grain-boundary layers show a number of characteristics which add to the picture as derived in the preceding chapter and which establish an interesting correlation between grain-boundary and thin-film conduction. It is well established that the main carrier flow along the grain boundary is carried by the holes in the degenerate valence band bounded on one side by the dangling-bond line and on the other by the space charge in the bulk.

In this sense the grain boundary establishes a thin film and the conductance is dependent on the space-charge extension from the grain boundary into the bulk material. In tests of different kind, the width of the actual disturbed layer was measured to be 100 to 200 Å, if measured from either side of the bulk crystal. Without a bias voltage applied, the pathway for conducting holes in a longitudinal direction parallel to the rows of dangling bonds is about a factor of 10 larger. Scanning-electron replica of the space charge measured without external bias<sup>1</sup> have to be considered as internally biased because of the outer junction shunt as current path and the electron injection in the surface scanning mode. We return to this question at the end of our consideration of carrier flow within grain boundary layers.

There are several ways to measure magnetoresistance effects in these structures. As shown in Figure 11.30, the current flow 1 to 2 through the grain-boundary sheet  $G$  can be monitored in different ways. Contacts 3 and 4 would give the voltage drop along the boundary and the resistivity—contacts 1 through 6 are ohmic to the grain-boundary sheet or carry indium alloy pellets in the case of germanium.

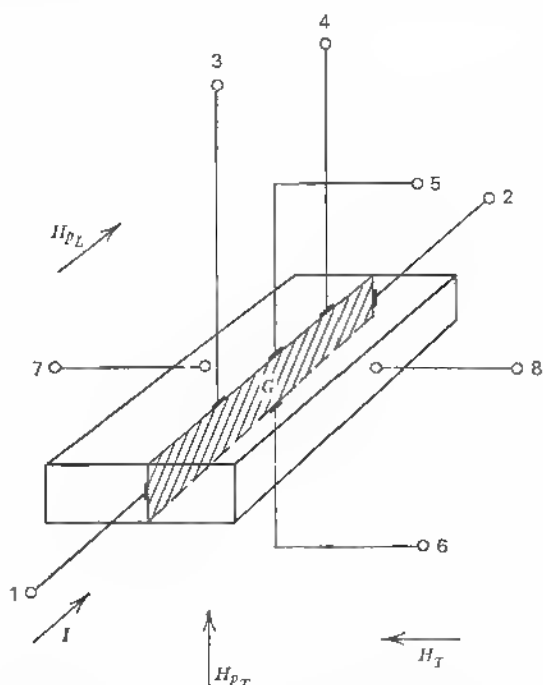


Fig. 11.30 Current and field orientations for magnetoresistance and Hall-measurements on grain boundaries.

Contacts 5 and 6 give the Hall voltage and contacts 7 and 8 to the bulk material sides allow one to apply a bias to the grain-boundary space-charge layers.

In such a geometry there are three magnetic field directions:

1.  $H_T$  = transversal magnetic field.

The magnetic field vector is perpendicular to the current flow but also to the grain-boundary plane.

2.  $H_{pT}$  = parallel-transversal magnetic field.

The magnetic field vector is again perpendicular to the current flow, but parallel to the grain-boundary plane.

3.  $H_{pL}$  = parallel-longitudinal magnetic field.

The usual longitudinal magnetoresistance for the grain-boundary plane is measured.

It seems that the earliest date of publication of the anomalous magnetoresistance in grain boundaries was 1962. G. Landwehr<sup>2</sup> first reported negative magnetoresistance in a germanium bicrystal.

At about the same time Hamakawa and Yamaguchi<sup>3</sup> reported careful measurements on bicrystals. They found negative magnetoresistance values and also oscillatory magnetoresistance at lower temperatures (see Figure 11.31).<sup>4</sup> This is the case of the transversal ( $H_T$ ) magnetoresistance.

The different cases are

$(\Delta\rho_H(\text{transv})/\rho_s)$	transversal,
$(\Delta\rho_{H_p}(\text{transv})/\rho_s)$	parallel-transversal,
$(\Delta\rho_{H_p}(\text{longit})/\rho_s)$	parallel-longitudinal,

where  $\rho_s$  = sheet resistivity.

As we have seen from the Hall data (see Figure 11.28), the mobility values (parallel and transversal case) were defined here with respect to the current flow (parallel or vertical to the dislocation pipes) and showed a decrease toward lower temperatures and a saturation effect below 10°K with a limit value of about 200 to 300 cm/sec/V/cm. The magnetic field in this case corresponded to  $H_{pL}$  in Figure 11.30. The specific sheet resistivity  $\rho_s/t$  ( $t$  = thickness of sheet) was found to decrease clearly at lower temperatures from about 20°K on downward. When a magnetic field was applied (see also Figure 6 in Ref. 3), G. Landwehr found that at  $T = 79^\circ\text{K}$  only the longitudinal  $H_{pL}$  and the transversal  $H_{pT}$  magnetoresistance values showed negative characteristics with increasing magnetic field, and  $H_T$ , the transversal-perpendicular case (see Figure 11.30), showed a positive magnetoresistance. This is the situation under which Hamakawa and Yamaguchi measured the negative magnetoresistance (see Figure 11.31). Here we have to consider that Landwehr did not measure a magnetic field dependence below 79°K. His

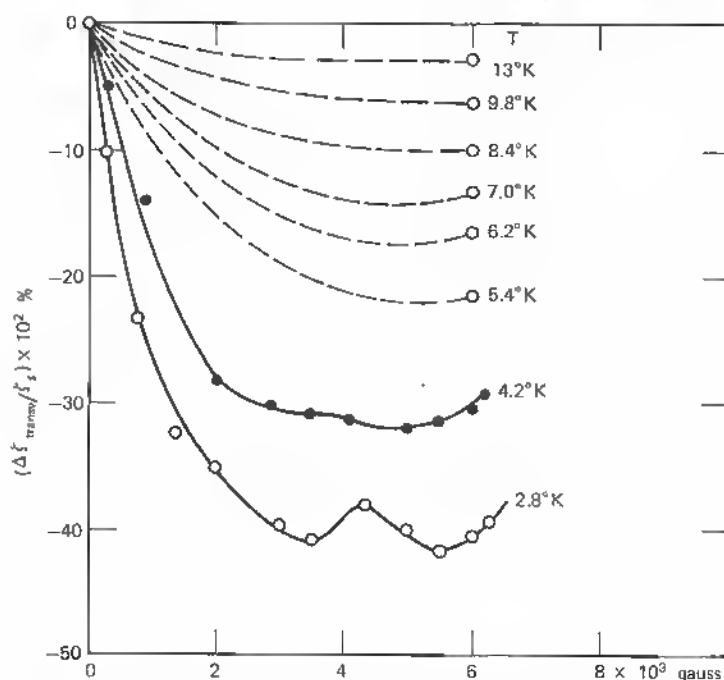


Fig. 11.31 Magnetic field dependence of transverse magnetoresistance as function of temperature (Ge grain-boundary plane). (See [11.4,3].)

measurements were taken at rather high and constant magnetic fields (5,330 and 8,300 gauss) for the lower temperature range. He finds that the transverse  $\perp$  magnetoresistance  $H_T$  has an abrupt change in sign between 10 and 20°K. It changes from a negative to a positive magnetoresistance with decreasing temperature (see Figure 11.32). For the transverse magnetoresistance measured by the Japanese authors, we cannot derive this behavior, since here a lowering of the temperature clearly enhances the negative magnetoresistance. However, a slight change to a positive magnetoresistance can be seen in the curves as the magnetic field increases over 5 kG. These field values, measured by Landwehr, 5,366 and 8,300 gauss respectively, lie in the ascending branch in Figure 11.31. It seems, therefore, that the results are reconcilable with the assumption that for magnetic field strengths beyond 5 kG (Landwehr's values) the magnetoresistance is increasingly positive with decreasing temperature. It would be most revealing to repeat Landwehr's measurements for varied magnetic fields, beginning with low field values. The specific temperature point at 14°K at which the sign change of the magnetoresistance occurs is somehow also the point at which the mobility reaches its minimal value in order to attain a saturation value (see Figure 11.28). It is also the temperature

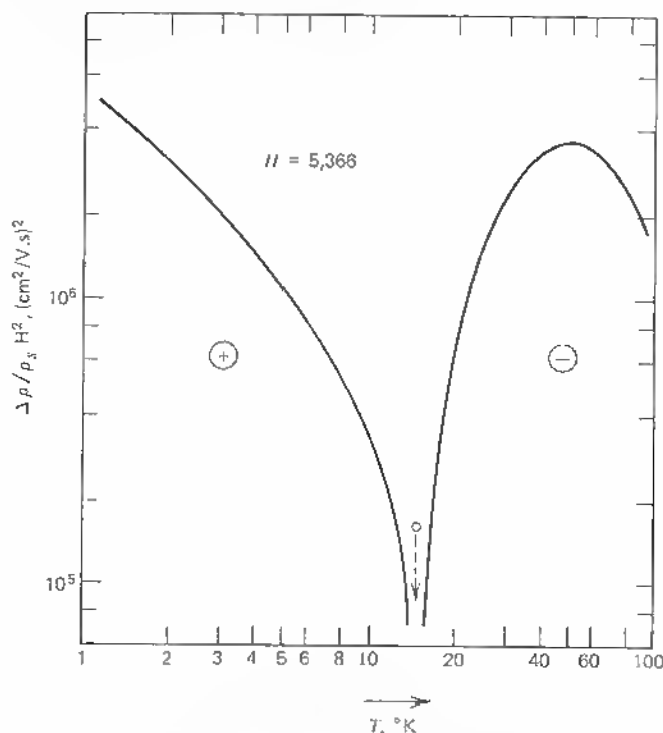


Fig. 11.32 Longitudinal magnetoresistance of Ge-bicrystal as  $f(T)$ . (See Landwehr [11.4,2].)

value at which the Japanese authors found a change from negative to positive behavior (see Figure 11.31). Here we can see a similarity between Landwehr and Hamakawa et al. It is apparent that for field values  $H > 5$  kG, the positive magnetoresistance shows a lesser slope with  $H$ , as Figure 11.32 indicates. Landwehr already discusses the fact that the grain-boundary conduction mechanism is similar to the one in thin films and that a situation of comparable cyclotron radius  $r$  and thickness  $d$  leads to damped oscillations. Since

$$r = \frac{v}{\omega_c} = \frac{vcm^*}{eH}, \quad (11.108)$$

where  $m^*$  = effective mass,  
 $v$  = average drift velocity,  
 $c = 3 \times 10^{10}$  cm/sec,  
 $e$  = electron mass,  
 $H$  = magnetic field,  
 $\omega_c$  = cyclotron frequency,

we can expect a cyclic (trochoidal) path for the electrons when the velocity to magnetic field ratio has certain values in order to bring  $r$  into the range of the mean free path. We shall see that a velocity value of  $4 \times 10^6$  cm/sec and a value of  $\omega_c = 1.5 \times 10^{11}$  radians/sec are reasonable to assume and yield a critical value of

$$r = \frac{v}{\omega_c} \approx 3 \cdot 10^{-5} \text{ cm}, \quad (11.109)$$

or 3,000 Å, in accordance with the grain-boundary barrier-layer thickness to be assumed for the unbiased case (or short-circuited case with optical injection internally biased).

In calculating the cyclotron frequency-relaxation time product (angle between  $E$  and current), one has

$$\beta = \omega_c \cdot \tau = \frac{eH}{m^*c} \tau \quad (11.110)$$

$$= \mu \frac{H}{c} = 10^{-8} \mu [\text{cm}^2/\text{V} \cdot \text{cm}] H [G], \quad (11.111)$$

the sheet mobility being 300 cm<sup>2</sup>/V·cm. We find that for a  $\beta$  value of 1, for example ( $\omega_c \cdot \tau$  has to be of the order of 1 or higher for a resonance to occur),

$$H = \frac{1}{10^{-8} \cdot 300} \approx 0.3 \cdot 10^6. \quad (11.112)$$

Since  $\beta = 10^{-8} \mu H$  applies to a free mass  $m$ , we have to divide by 4 for the case of  $m_e/m_{\text{eff}} = 4$  ( $m_e$  = cyclotron mass,  $m_{\text{eff}}$  = effective mass), which leads to  $\sim 80$  kG. This value was calculated by Hamakawa et al., and their conclusion is that the critical cyclotron field was not reached in their experiment, since the magnetic field was an order of magnitude smaller and therefore de-Haas-Van Alphen oscillations cannot occur. They point out, however, that galvanomagnetomorphic effects (interaction with boundaries) can be responsible for the oscillatory magnetoresistance, as we noted above.

The relation for the Hall angle  $\theta$  or the relaxation time-cyclotron frequency product

$$\theta = \tau \omega_c = 10^{-8} \mu [\text{cm}^2/\text{V} \cdot \text{sec}] H [G] \quad (11.113)$$

$G$  = Gauss

used before is based only on temperature and mass-independent conversion factors.<sup>5</sup>

Detailed derivations to find the cyclotron radius  $r$  make it necessary to know more about the electron velocity at low temperature and the relaxation (mean free) time  $\tau$  in the product for  $\theta$ .

Since the magnetoresistance measurements were carried out at liquid helium temperatures and on germanium as material, we can use the values published by Kittel for the measurements of the effective masses by cyclotron resonance,<sup>6</sup> introducing, however, the mobility value marked for grain-boundary conduction at liquid helium temperatures. For a cyclotron frequency  $f_c = 24$  GHz or  $\omega_c = 1.5 \cdot 10^{11}$  radians/sec, resonance was established for  $H \approx 860$  oersteds and  $m^*/m \approx 0.1$ .

This corresponds to the value for  $\omega_c$  according to the classical formula:

$$\omega_c = \frac{eH}{m^*c} = \frac{4.8 \cdot 10^{-10}}{0.1 \cdot 9 \cdot 10^{-28} \cdot 3 \cdot 10^{10}} H \quad (11.114)$$

$$= 1.8 \cdot 10^8 \cdot H[\text{G}] [\text{radians/sec}], \quad (11.115)$$

which for  $H \approx 10^3$  gauss yields

$$\omega_c = 1.8 \cdot 10^{11} \text{ radians/sec.} \quad (11.116)$$

With (11.113) or

$$\tau = \frac{10^{-8} \mu H}{\omega_c}$$

this value of  $\omega_c$  gives a mean free time of

$$\tau \approx 0.55 \cdot 10^{-13} \text{ sec} \quad (11.117)$$

for  $m^* = 0.1 m$  and  $H = 10^3$  gauss.

Or since velocity and cyclotron radius are related as

$$r\omega_c = v$$

(11.109),

we can replace  $\omega_c$  by (11.113):

$$\omega_c = \frac{\theta}{\tau}$$

and get

$$v = r \frac{\theta}{\tau} \quad (11.118)$$

In calculating  $\theta$  in (11.113), we have not made assumptions regarding the cyclotron radius  $r$ . Using the value here, which we derived from grain-boundary barrier measurements without bias, that is, 3,000 Å, we get for the average drift velocity from (11.118)

$$v = 3,000 \cdot 10^{-8} \frac{10^{-8} \cdot \mu \cdot H}{\tau}. \quad (11.119)$$

Now assuming that

$$\mu = 300 \text{ cm/s V cm},$$

$$H = 10^3 \text{ gauss},$$

and  $\tau$  from (11.117) we have

$$v \simeq 2 \cdot 10^6 \text{ cm/sec},$$

a value close to the normally assumed value under the conditions outlined before.

In further measurements of the transverse magnetoresistance  $H_T$  on bicrystals tilted around the (001) axis (see Figure 11.33 and 11.34), J. J. Busse and H. F. Mataré<sup>7</sup> also found oscillatory behavior at liquid helium temperatures and for magnetic fields between 1,000 and 10,000 gauss (see Figure 11.35) in accordance with the galvanomagnetomorph effects discussed earlier.

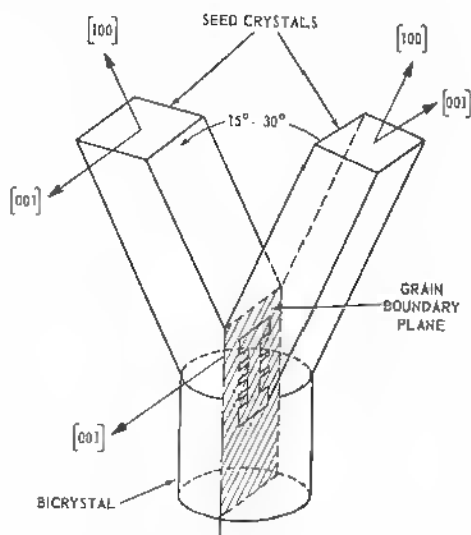


Fig. 11.33 Bicrystal sample orientation.



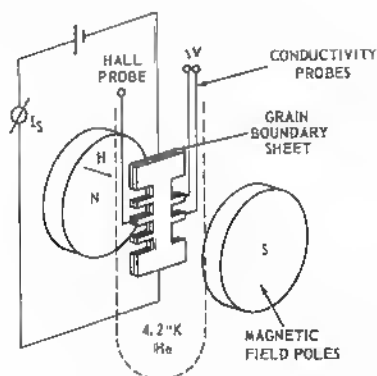


Fig. 11.34 Perspective of bicrystal sample arrangement.

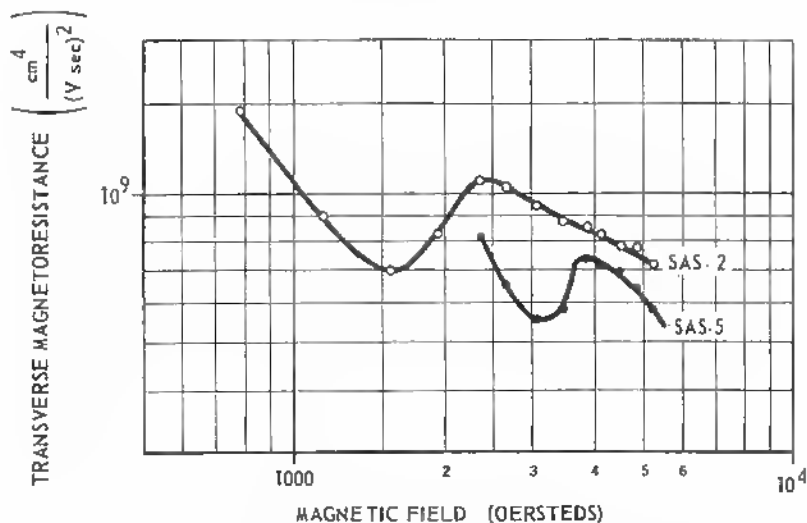


Fig. 11.35 Transverse magnetoresistance ( $\Delta\rho/pH^2$ ) versus magnetic field at 4.2°K.

In a model for the conductivity of thin films such oscillatory effects had been predicted for metals by Sondheimer.<sup>8</sup>

Solution of the Boltzmann equation:

$$4\left(\frac{2\pi e}{h}\right)\left[\mathbf{E} + \left(\frac{1}{c}\right)\mathbf{v} \times \mathbf{H}\right] \text{grad}_k f + \mathbf{v} \text{grad}_r f = -\frac{f - f_0}{\tau}, \quad (11.120)$$

where  $e$  = electronic charge,

$\tau$  = relaxation time of conduction electrons (depending on an absolute value of  $k$ ),

$f = f_0 + f_1(v, z)$  or distribution function (function of wave vector  $k$  and space vector  $r$ ),

$f_0$  = Fermi function =  $[e^{(E-\zeta)/kT} + 1]^{-1}$ ,

$\zeta$  = Fermi energy,

$v$  = electron velocity,

$f_1$  = function of  $v$  and  $z$  to be determined,

leads to an expression for the current density similar to the expression derived by K. Fuchs for thin films.

If the determining parameter

$$\beta = \frac{a}{r},$$

where  $a$  = film thickness,

$r$  = cyclotron radius,

is greater than 1, the resistance of the metallic film is oscillating with the strength of the magnetic field  $H$ .

Without such boundary limitations, the oscillatory character of the magnetoresistance in bulk crystals of larger dimensions does not appear<sup>10</sup> until the magnetic field is so large that the cyclotron frequency  $\omega_c$  is greater than the reciprocal time between collisions in the lattice, or for

$$\omega_c \tau \gg 1 \quad (11.121)$$

(see Ref. 11). Negative magnetoresistance has been found in bulk samples with a major contribution of the surface inversion layer and in samples of higher impurity concentrations. Mikoshiba et al.<sup>12, 13</sup> based their theory on the idea of a localized spin ordering in the impurity band.

For  $n$ -type samples in the impurity conduction range with a phonon-induced hopping conduction mechanism, the effect of a Lorentz force can actually give rise to a spin ordering among the scattering centers and thus decrease the scattering rate, leading to negative magnetoresistance.

A similar process can be active in the degenerate layer of a grain boundary so that the overlapping acceptor wave functions shrink in an increasing magnetic field.

With the mobility values in grain-boundary layers and the relatively low magnetic fields applied in the measurements described earlier, it is to be assumed that, according to (11.111), the  $\omega_c \tau$  product does not reach into the necessary range beyond 1. In III-V compound crystals, like InSb and InAs, however, with electron mobilities of the order of  $10^5$  cm<sup>2</sup>/V sec, we expect this to occur at relatively small magnetic fields. Since

$$\omega_c \tau = 10^{-8} \mu \cdot H,$$

we get for  $\mu = 10^5$ , magnetic fields in the kilogauss range. In fact, oscillatory transverse magnetoresistance was clearly measured in these cases at fields as low as 1 to 10 kG.<sup>14</sup> A number of cycles have been measured corresponding to the different Landau levels in the energy expression for the carriers:

$$E = E_0 + \left(n + \frac{1}{2}\right) \hbar \omega_c, \quad (11.122)$$

where  $E_0 = \frac{\hbar^2 k_H^2}{2m^*}$  and  $k_H$  the wave vector component parallel to  $H$ ,

$n$  = integral quantum number.

In the general expression for the energy change  $\Delta E$  with the magnetic field we get with  $\omega_c = eH/cm^*$

$$\Delta E = \left(n + \frac{1}{2}\right) \frac{\hbar e H}{m^* c} \quad (11.123)$$

or oscillations with a period

$$\Delta\left(\frac{1}{H}\right) = \frac{e \hbar}{m^* c \cdot \Delta E}. \quad (11.124)$$

Such oscillations have now also been found in germanium when the magnetic field strength exceeds  $5 \cdot 10^4$  gauss. In fact

$$\omega_c \tau = 10^{-8} \mu H$$

gives a value of 1 for  $\mu = 2,000$  in this case.<sup>15</sup>

In the case of the grain boundary, we must invoke galvanomagnetomorphic effects, as we have seen. The case of the magnetoresistance of thin semiconductor films and surface layers has been treated by Amith<sup>16</sup> and is applicable here.

Starting with the Boltzmann equation of the kind used by Sondheimer (11.120), Amith defines in the distribution function

$$f = f_0 + f_1 \quad (11.125)$$

the term  $f_0$  as the Maxwell Boltzmann function for thermal equilibrium:

$$f_0 = n_0 \left(\frac{m^*}{2\pi kT}\right)^{3/2} \exp\left(-\frac{\frac{1}{2}m^*v^2 + e\psi}{kT}\right), \quad (11.126)$$

where  $n_0$  = thermal equilibrium density of carriers in bulk,  
 $\psi$  = electrostatic potential.

Amith later assumes  $\psi = 0$ , which is not adequate for the grain boundary, since a high barrier exists across the grain-boundary space-charge layer.

If the electric field  $\mathbf{E}$  is assumed in the  $x$  direction and the magnetic field  $\mathbf{H}$  in the  $z$  direction, and we neglect products of  $f_1$  and components of the applied longitudinal electric field ( $E_x, 0, 0$ ) and the induced Hall field ( $0, E_y, 0$ ), the transport equation reduces to

$$f_1 + \tau v_z \frac{\partial}{\partial z} f_1 + \frac{e\tau}{m^*} E_z \frac{\partial}{\partial v_z} f_1 - \beta \frac{\partial}{\partial \xi} f_1 = \frac{q\tau v f_0}{kT} [E_x \cos \xi + E_y \sin \xi],$$

where

$$\begin{aligned} v_x &= v \cos \xi, \\ v_y &= v \sin \xi, \end{aligned} \quad (11.128)$$

$$\beta = \frac{e\tau}{m^*c} H_z. \quad (11.129)$$

$\beta$  is again introduced as decisive parameter—see (11.110)—and is the variable plotted as abscissa in magnetoresistance measurements. (In this case, the mobility is an unknown factor). For the solution of (11.126) assumptions with regard to the scattering mechanism at the boundaries of the potential will have to be made. If diffuse scattering is assumed at the inner barrier toward the grain boundary, the distribution function for carriers leaving this plane must be independent of direction; that is,  $f_1$  must vanish in (11.125). For specular reflection at the outer potential well (toward the bulk) only the  $z$  component of the velocity is reversed. Therefore, Amith uses two distribution functions to describe this system. From the expression for  $f_1$ , the current densities are expressed by volume integrals:

$$\begin{aligned} J_x &= e \iiint v_x f_1 dv_x dv_y dv_z, \\ J_y &= e \iiint v_y f_1 dv_x dv_y dv_z. \end{aligned} \quad (11.130)$$

Introducing average current densities  $\bar{J}$ , one can finally express

$$\begin{aligned} \bar{J}_x &= E_x \frac{\bar{\sigma}}{1 + \beta^2} (1 - A) + \beta E_y \frac{\bar{\sigma}}{1 + \beta^2} (1 - B), \\ \bar{J}_y &= E_y \frac{\bar{\sigma}}{1 + \beta^2} (1 - A) - \beta E_x \frac{\bar{\sigma}}{1 + \beta^2} (1 - B), \end{aligned} \quad (11.131)$$

where  $A$  and  $B$  are grain-boundary scattering parameters in one case and  $\bar{\sigma}$  is the mean conductivity

$$\bar{\sigma} = \bar{n} e \mu \quad (11.132)$$

where

$$\bar{n} = n_0 S/d, \quad S = \int_0^d dz \exp\left(-\frac{e\psi}{kT}\right).$$

$d$  = space-charge-layer thickness.

From the current densities (11.131), one can derive Hall coefficient and magnetoresistance.

Assuming no net current in the  $y$  direction,  $\bar{J}_y$  in (11.131) is zero, and thus

$$E_y = \beta E_x \frac{1-B}{1-A}. \quad (11.133)$$

With the first equation this yields

$$\bar{J}_x = \frac{\bar{\sigma}}{1+\beta^2} E_x \left[ 1 - A + \beta^2 \frac{(1-B)^2}{1-A} \right]. \quad (11.134)$$

Since the magnetoresistance is given as

$$M = 1 - \frac{\bar{J}_x}{\bar{J}_x(H=0)}, \quad (11.135)$$

we have in this case

$$M = 1 - \frac{1-A+\beta^2(1-B)^2/(1-A)}{(1+\beta^2)(1-A^0)}, \quad (11.136)$$

where  $A^0 = A$  for  $H = 0$ .

The expressions for the scattering parameters  $A$  and  $B$  are complicated functions of  $\beta$  and a factor

$$K = \frac{d}{\tau} \left( \frac{m^*}{2kT} \right)^{1/2} \quad \tau = \text{relaxation time}$$

and have been derived in two sets. Amith assumes two different functions for the two kinds of carriers, since for one the attractive potential may be coupled with diffuse scattering and for the other this potential is coupled with a specular reflection (on the potential incline).

It is by no means certain that the actual path for hole conduction along a grain-boundary sheet would be bounded by two different scattering mechanisms. The layer of a clean and straight line of broken bonds that have accepted electrons may be as flat as an abrupt impurity density change or a surface barrier, and both sides would have to be treated as similar scatterers. In any event, the form of  $M$  (11.136) as a function of  $\beta$ , even under the general assumptions of two different scattering mechanisms, shows clearly oscillatory character for values in excess of

$$\beta = 1 \quad \text{and} \quad K = 1,$$

as shown in Figure 11.36, calculated by J. J. Busse<sup>17</sup>. See also Ref. 16, Figure 2.

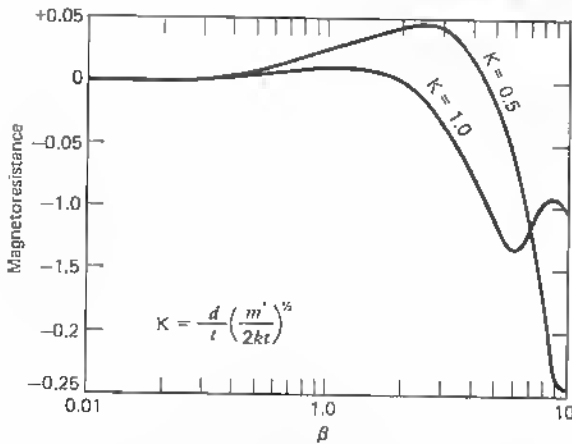


Fig. 11.36 Calculated magnetoresistance for model of grain boundary (J. Busse).

#### REFERENCES

1. Mataré, H. F., and C. W. Laakso: Space Charge Domains at Dislocation Sites, *J. Appl. Phys.*, vol. 40, no. 2, pp. 476-482, February, 1969.
2. Landwehr, G., and P. Handler: Galvanomagnetic Properties of Grain Boundaries in Germanium Bicrystals from 1.25° to 240°K, *J. Phys. Chem. Solids*, vol. 23, pp. 891-906, 1962.  
Landwehr, G.: Negative Magnetoresistance in a Germanium Bicrystal, *Proceedings of the International Conference on the Physics of Semiconductors*, Exeter, England, 1962.
3. Hamakawa, Y., and J. Yamaguchi: Electrical Conduction in Germanium Grain Boundary Plane, *Japanese Journal of Appl. Phys.*, vol. 1, no. 6, pp. 334-342 December, 1962.
4. Hamakawa, Y., and J. Yamaguchi: "Galvanomagnetic Effects in Boundary Layers of Germanium Bicrystals," *Proceedings International Conference on Crystal Lattice Defects*, 1962, *Journal of the Phys. Soc. Japan*, vol. 18, no. 11, pp. 166-171, 1963.
5. Shockley, W.: "Electrons and Holes in Semiconductors," Van Nostrand, Princeton, N.J., 1950, pp. 211ff.
6. Kittel, C.: See, for example, "Solid State Physics," Wiley, New York, 1956, pp. 371ff.
7. Busse, J. J., and H. F. Mataré, Transverse Electric and Magnetic-field Studies of Conduction in Germanium Bicrystals, *Bull. Am. Phys. Soc.*, vol. 8, p. 62, 1963.
8. Sondheimer, E. H.: The Influence of a Transverse Magnetic Field on the Conductivity of Thin Metallic Films, *Phys. Rev.*, vol. 80, no. 3, pp. 401-406, November, 1, 1950.

9. Fuchs, K.: The Conductivity of Thin Metallic Films according to the Electron Theory of Metals, *Proceed. Camb. Phil. Soc.*, vol. 34, pp. 100–108, 1938.
10. Abeles, B., and S. Meiboom: Theory of the Galvanomagnetic Effects in Germanium, *Phys. Rev.*, vol. 95, pp. 31–37, July, 1, 1954.
11. Adams, E. N., and T. D. Holstein: Quantum Theory of Transverse Galvanomagnetic Phenomena, *J. Phys. Chem. Solids*, vol. 10, pp. 254–276, 1959.
12. Mikoshiba, N., and Shun-Ichi Gonda: Weak-field Magnetoresistance of Impurity Conduction in *n*-Type Germanium, *Phys. Rev.*, vol. 127, no. 6, pp. 1954–1961, September, 15, 1962.
13. Mikoshiba, N.: Strong-field Magnetoresistance of Impurity Conduction in *n*-Type Germanium, *Phys. Rev.*, vol. 127, no. 6, pp. 1902–1969, September, 15, 1962.
14. Weiss, H.: Magnetoresistance, in "Semiconductors and Semimetals," R. K. Willardson and A. C. Beer (eds.), Academic, New York, 1966, vol. 1, pp. 315–376.
15. Lutsikii, V. N., A. A. Zhirmov, and M. I. Elinson: Transverse Hall Effect and Magnetoresistivity of Germanium in Strong Magnetic Fields, *Soviet-Physics-Solid State*, vol. 7, no. 2, pp. 415–416, August, 1965.
16. Amith, A.: Galvanomagnetic Properties of Semiconductor Thin Films and Surface Layers, *J. Phys. Chem. Solids*, vol. 14, pp. 271–290, 1960.
17. Busse, J. J.: Transverse Magnetoresistance and Hall Effect in Germanium Bicrystals, *Bendix Report 2357*, Research Laboratories Division, Southfield Mich., June, 1963.

## 11.5 TRANSPORT ANISOTROPY

In this Section another peculiarity of carrier transport across bicrystal interfaces and parallel to the interface is considered. Although the preceding section drew attention to the special aspects of magnetoresistance, we now describe the behavior of these interfaces when minority carriers are injected and lifetime is measured.

In looking at the proposed grain-boundary band models, as discussed in Section 11.1 and shown in Figure 11.3 or 11.23 for the nondegenerate case, it is clear that longitudinal conduction in the sheet is by holes and that a high *n-p-n*-barrier shows the behavior of ordinary *n-p-n* structures when subjected to injection. That one has to take into account the high quantum yield for photon injection at such a dislocation line and a hook effect, that is, carrier multiplication at one *p-n* interface, became clear after extended lifetime measurements. In such measurements, the point of injection has to be variable across the bicrystal surface, and the collector probe should be adjustable. Figure 11.37 shows such an arrangement schematically.

The collector *C* is adjustable at the microscope table. It is also shielded to minimize pickup of noise and other static disturbances. The cable leads to the amplifier and the filter, which passes only the light modulation frequency  $\omega_L$ .

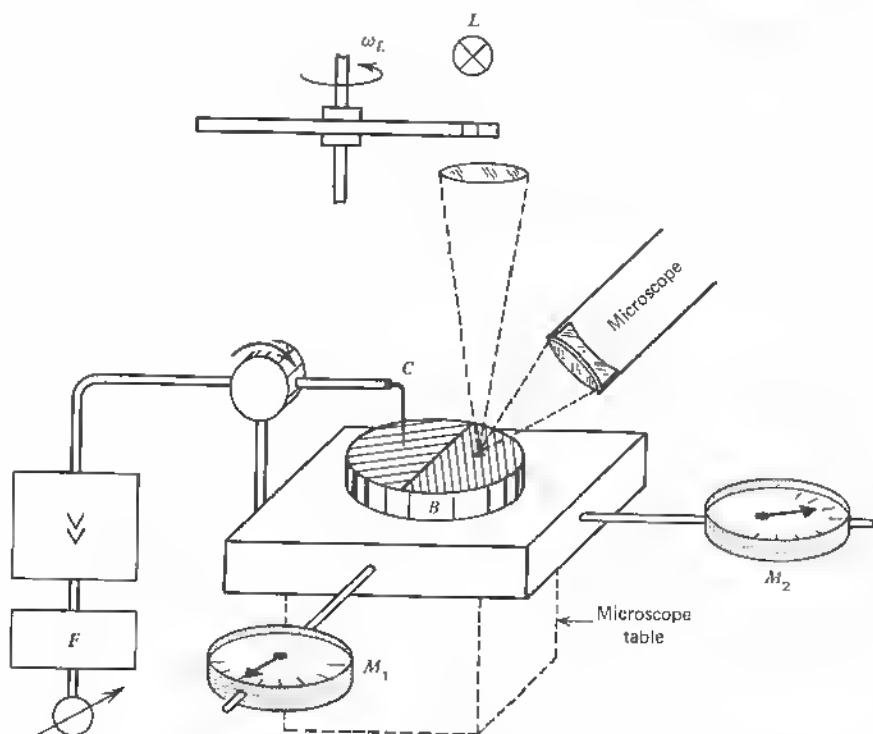


Fig. 11.37 Lifetime measurement equipment scheme.

The illumination source  $L$  is modulated by the usual disk with hole openings. The bicrystal  $B$  fixed to the microscope tabletop can be moved in two directions with the microscope table. This is measured by the micrometers  $M_1$  and  $M_2$ . The microscope is directed toward the bicrystal top to adjust the light injection point or line to specific areas of the bicrystal.

A photograph of this setup is shown in Figure 11.38 (see also Ref. 1). The method is a modification of the known Haynes-Shockley method<sup>2</sup> as applied to a practical equipment built up by Valdes<sup>3</sup> (see also Appendix).

Ordinarily, for monocrystals, the results of lifetime measurements are expressed in terms of a single lifetime parameter  $\tau$ , which is assumed to be a homogeneous parameter of the crystal. The results of such measurements on bicrystals do not lend themselves to this interpretation, since the crystal is subdivided into three distinct areas if the light injection point and the collector probe are on different sides of the grain boundary. These measurements show in an amplified form what can happen to an injected signal within a crystal with a dislocation structure in the pathway of the carriers.



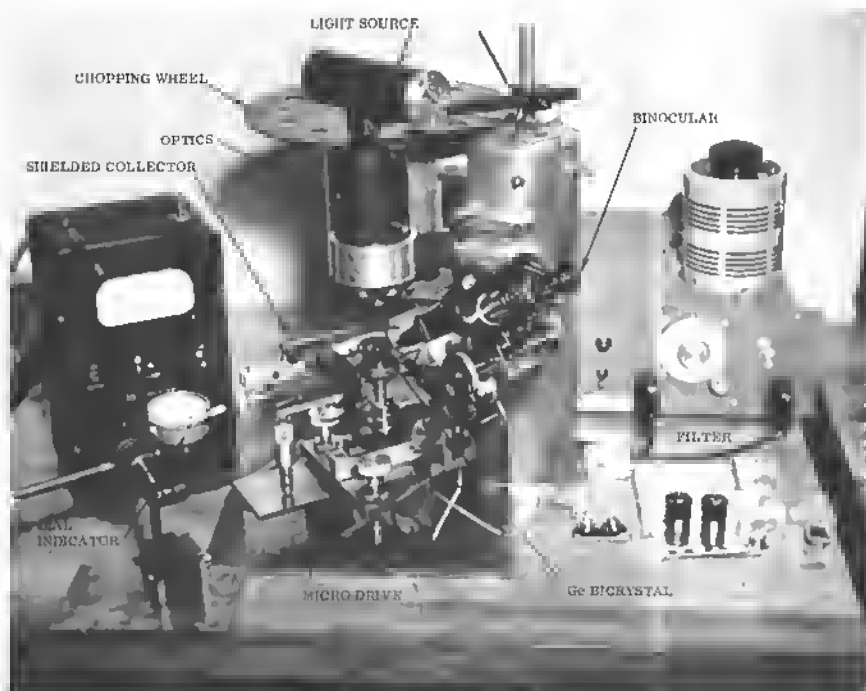


Fig. 11.38 Photograph of set-up for lifetime study on bicrystals.

Figure 11.39 is the typical result of a measurement. The moving light line (or point) passes from its initial position at the collector probe (contact point) away from the collector, and the signal pickup (in millivolts) decreases as is expected. But the slope on semilogarithmic paper does not linearize within a short distance (20 mils) from the grain boundary, because the bulk lifetime of  $\sim \tau_p \approx 20 \mu\text{sec}$  is causing a diffusion length of

$$L_p = \sqrt{D_p \tau_p} \approx 3 \cdot 10^{-2} \text{ cm},$$

or approximately 10 mils ( $D_p = 40 \text{ cm}^2/\text{sec}$ ). Therefore, the hole-sink behavior of the boundary predominates under the light injection. When the light spot reaches the grain-boundary barrier, the signal is strongly increasing until the other side of the  $n$ - $p$ - $n$  barrier is reached, and from here on an apparent lifetime of  $\sim 1,000 \mu\text{sec}$  appears. This is not the real lifetime of injected carriers but a new quantity measuring the photoelectronic yield of the  $n$ - $p$ - $n$  structure under photon injection and carrier multiplication.

The relatively high injection efficiency of the  $n$ - $p$ - $n$  grain-boundary interface explains the often unusually high carrier density with respect to the high

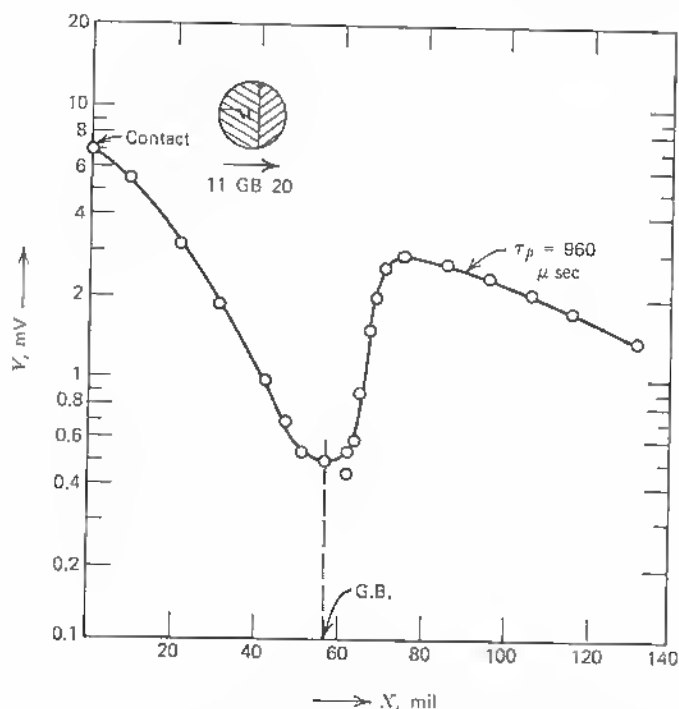


Fig. 11.39 Photovoltage pick-up of collector point with light spot moving across bicrystal boundary (G.B.).

photovoltage when the light reaches the other side of the grain boundary (away from the collector probe). This can give very puzzling results when the collector probe is far away from the boundary, and the signal may increase beyond the value found at the collector side of the boundary (see Figure 11.40). The lifetime  $\tau_p$  is indicated only as a parameter but has to be interpreted here as a measure of the high quantum yield of the grain boundary. That the phenomenon is definitely linked to the light sensitivity of the  $n$ - $p$ - $n$  structure is shown in the next diagram where the photovoltage pickup is plotted for three different collector-positions ( $a, b, c$ ) with respect to the grain boundary. It is clear that the collector field, when penetrating the grain-boundary barrier partially eliminates the carrier enhancement because of the depression of the  $n$ - $p$ - $n$  barrier by the negative collector field (see Figure 11.41). This is similar to the case of varied collector bias. As the bias is increased, the collector field can reach into the grain-boundary barrier field and eliminate the carrier multiplication (see Figure 11.42). Also a quenching of the photosensitivity of the grain boundary by light is visible. Illumination of the moving spot to

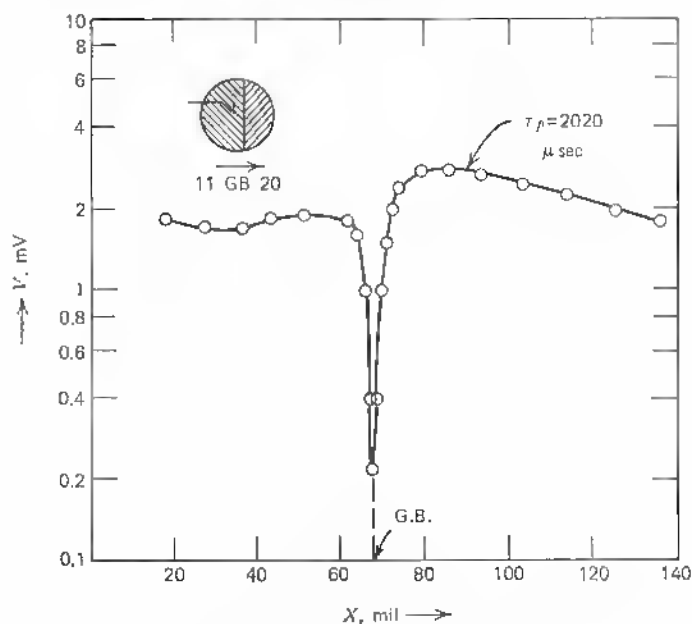


Fig. 11.40 Same as Figure 11.39.

high intensity somehow overshadows the barrier effect and also accounts for a higher apparent lifetime because of hole saturation (see Figure 11.43).

In all these cases, however, the unusually flat decay (long lifetime) when injection point and collector probe are separated by the grain boundary, points to a fact known as the hole-sink behavior of the dislocation line. Since the grain boundary cuts the crystal in halves, the  $n$ - $p$ - $n$  structure operates like a new injection area of large extent, and the decay curve can no longer be compared with the one for a point source. Also the boundary acting as a hole sink, one has to consider the diffusion equation with a sink at  $x = x_1$  ( $x_1$  = center of grain boundary):

$$\text{div grad } n_p = \frac{n_p}{D\tau} \left(1 - \frac{x}{x_1}\right), \quad (11.137)$$

where  $n_p$  = added hole density,

$\tau D = L_p^2$  = (diffusion length)<sup>2</sup>,

$\tau$  = carrier lifetime,

$D$  = carrier diffusion constant.

In cylindrical coordinates and with a light line at  $r = 0$ , this equation reads

$$\frac{d^2 n_p}{dr^2} + \frac{1}{r} \frac{dn_p}{dr} - \frac{n_p}{L_p^2} \left(1 - \frac{r}{r_1}\right) = 0, \quad (11.138)$$

where  $r_1$  = sink coordinate.

Since, by definition,  $r = L_p x$ , this becomes

$$\frac{d^2 n_p}{dx^2} + \frac{1}{x} \frac{dn_p}{dx} - n_p \left(1 - \frac{x}{x_1}\right) = 0, \quad (11.139)$$

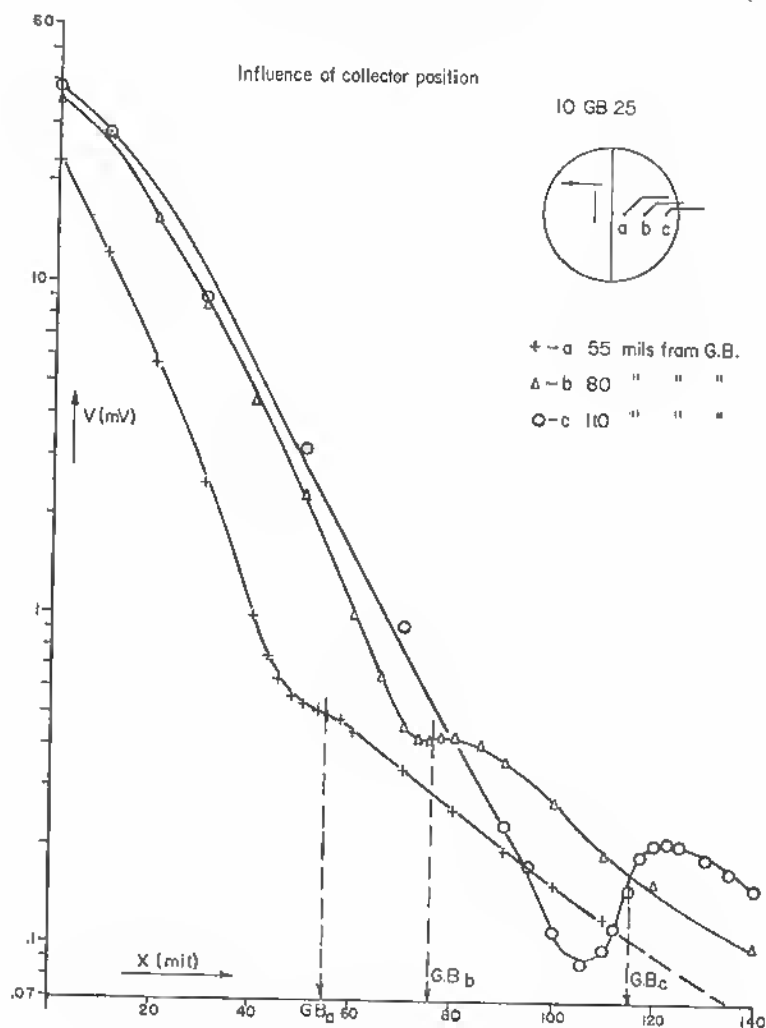


Fig. 11.41 Photovoltage decay curves for three different collector positions with respect to the boundary plane.

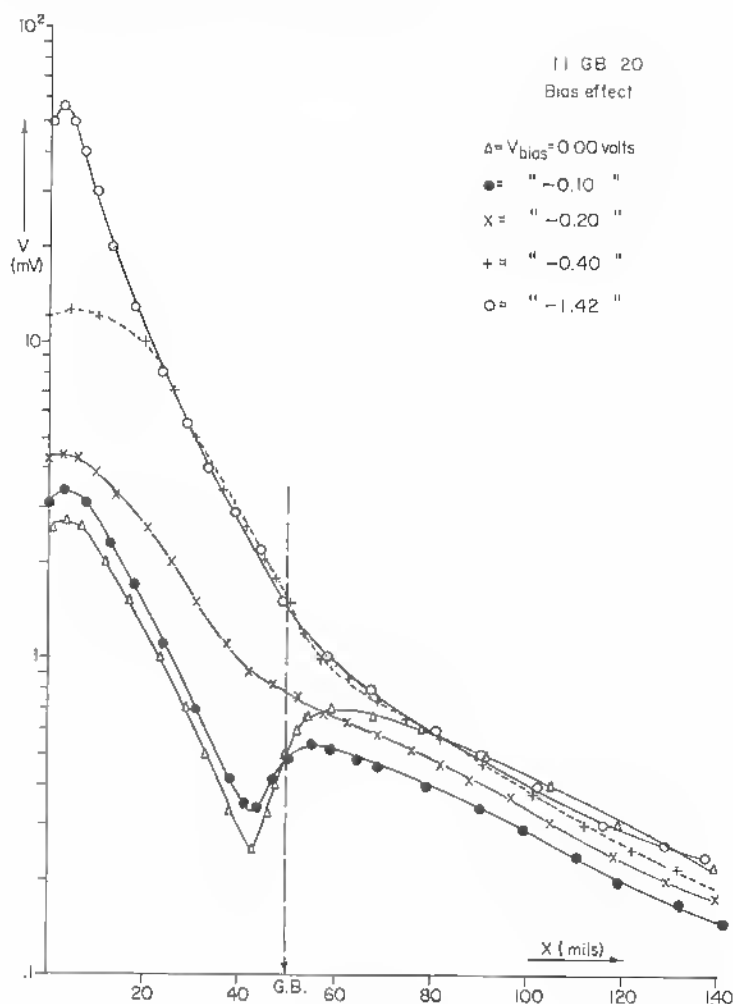


Fig. 11.42 Photovoltage decay curve for moving light spot with five different collector potentials.

or

$$\left[ x \frac{d}{dx} \left( x \frac{d}{dx} \right) - \left( 1 - \frac{x}{x_1} \right) x^2 \right] n_p = 0. \quad (11.140)$$

Now three different ranges for the solution have to be considered:

1.  $x_1 \gg x$ . The boundary location outside of the range is considered. This is the normal case with the solution

$$\frac{\partial \ln V}{\partial r} = \frac{\partial \ln n_p}{\partial r} = - \frac{1}{L_p} \frac{H_1^{(1)}(ix)}{iH_0^{(1)}(ix)}, \quad (11.141)$$

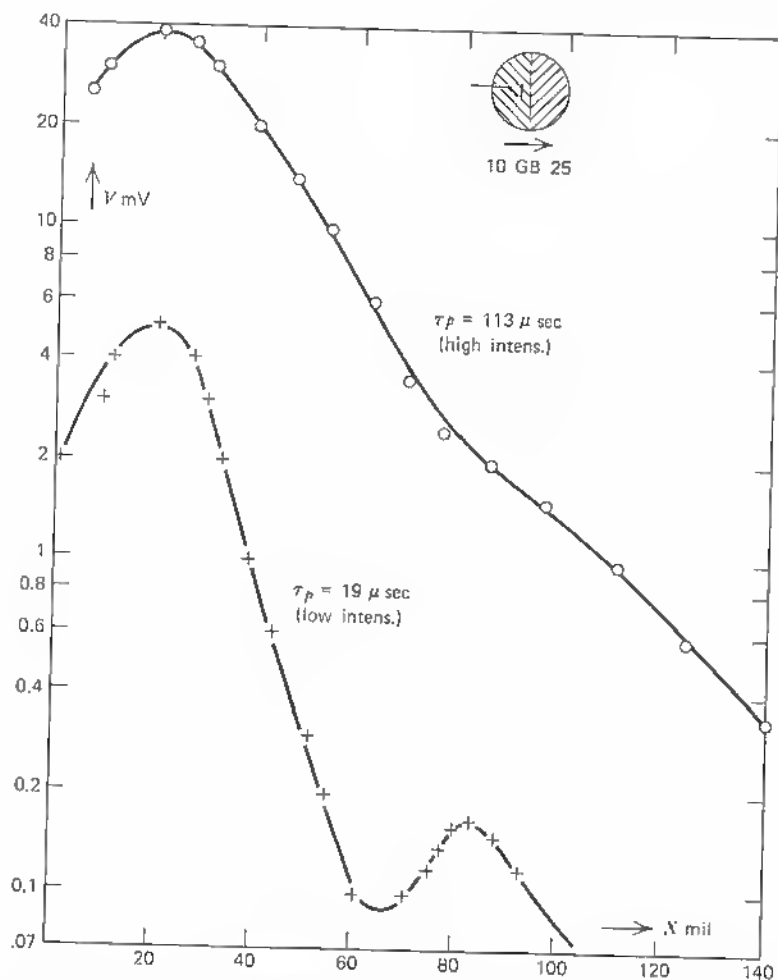


Fig. 11.43 Two photovoltage decay curves for high and low intensity light spots.

where  $H_0^{(1)}$  and  $H_1^{(1)}$  are Hankel functions of first rank and of zero and first order, respectively. A simpler expression can be derived for the point light source.<sup>4</sup> In this case

$$\frac{\partial \ln V}{\partial r} = \frac{\partial \ln n_p}{\partial r} = -\left(\frac{1}{L_p} + \frac{1}{r}\right). \quad (11.142)$$

2.  $x_1 = x$ . The point considered is at the grain boundary. From (11.140) it follows that

$$\frac{\partial \ln n_p}{\partial r} = \ln r. \quad (11.143)$$

For the normally small value of  $r$ , this means that a small or at least decreased value of the slope is found.

3.  $x_1 < x$ . This describes the case where the light point has crossed the grain boundary and is on the other side of the crystal. Here the sink behavior alone cannot give a full explanation, as described earlier, since now the geometry of the set up has changed basically and the collector sees a large source of minority carriers that has a high quantum efficiency also.

In this respect, the dislocation structure with a built-in stress field and a resulting gap widening is an efficient injector area. Conversion of one side to  $p$ -type and application of an ohmic contact result in a structure as shown in Figure 11.44. The gap difference  $E$  adds to the applied bias voltage  $V_e$  between the quasi Fermi levels  $E_F$  and  $E_{F_2}$  and enhances the hole flow toward the  $n$ -type side, increasing at the same time the barrier for electrons toward the  $p$ -type side.

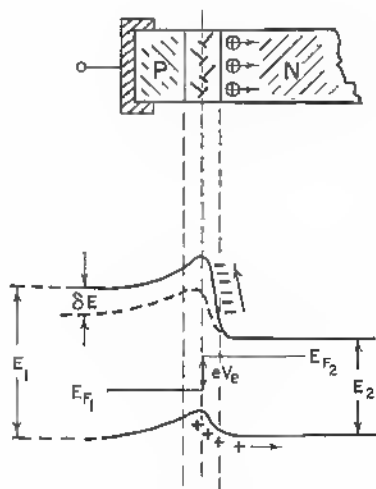


Fig. 11.44 Grain boundary plane as efficient minority carrier injection zone.

In this picture, the barrier height is not taken into account. This barrier height is actually strongly enhanced by an applied voltage because of the filling of available grain-boundary levels, as derived in Section 11.2.

To a great extent, the influence of a grain boundary on carrier transport is defined by:

1. The position of the dislocation acceptor levels
2. The barrier height

As shown earlier (9.26) the fraction of volume occupied by the space-charge tubes can be obtained from the measured carrier density and the distribution function  $f(T)$ :

$$\varepsilon = \frac{N_s}{C} \frac{f(T)}{N_d - N_a} \quad (11.144)$$

and is therefore a function of temperature and the actual acceptor energy  $E_2$ , of the dislocation, since

$$f = \frac{1}{1 + \exp[(E_2 - E_F)/kT]}. \quad (11.145)$$

This energy  $E_2$  varies with the kind of dislocations present and with respect to their density. For a high dilution in bent samples, the level is generally assumed at 0.2 eV below the conduction band (see Chapter 9, Ref. 2). (This would correspond to a value of 0.54 eV from the top of the valence band for an assumed gap of 0.74 eV at 103°K).

For low-angle boundaries, R. K. Mueller<sup>5</sup> finds a level (above the valence band) of  $E_2 = 0.06$  eV for temperatures below 250°K. This value relates to grain boundaries, grown with small tilt angle between 1 and 4°. For grain boundaries of a higher tilt angle,  $\theta = 4^\circ \sim 6^\circ$ , Mueller<sup>6</sup> finds a level  $E_2 \leq 0.04$  eV. For even larger misfit angles (12° and higher), Hamakawa and Yamaguchi<sup>7</sup> find a level roughly a factor of 10 nearer to the valence band. In other words, as the degree of degeneracy increases, the dislocation level approaches the top of the valence band.

The other important quantity, the barrier height  $\phi$ , is a quantity measuring the energy difference from the bottom of the conduction band to the barrier top (see Figure 11.25). We have seen that  $\phi$  is bias-dependent (see Section 11.2). In equilibrium,  $\phi$  is a measure of the intrinsic barrier. With a bias  $V < kT/e$  applied, the apparent barrier height increases. The increase in state density is not considered in Ref. 6 (see Section 11.2), but for higher voltages it remains practically constant.

As we have seen before (Section 11.2), the potential drop across the barrier is

$$V = \frac{kE^2}{8\pi en}, \quad (11.21)$$

where  $E$  = electric field,

$k$  = dielectric constant,

$n$  = impurity density in bulk,

and with (11.23)

$$l = \left( \frac{kV}{2\pi en} \right)^{1/2}, \quad (11.146)$$

where  $l$  = barrier thickness.



The total space charge is then

$$Q = enl = \left( \frac{kenV}{2\pi} \right)^{1/2}. \quad (11.147)$$

Therefore, the capacitance is

$$C = \frac{dQ}{dV} = \left( \frac{ken}{8\pi V} \right)^{1/2}. \quad (11.148)$$

and under the applied bias:

$$V_e = (V_1 - V_2) > 0,$$

where  $V_1 = V_e + \phi_1$ ,  $\phi$  in eV;

$$V_2 = \phi_2,$$

on either boundary side. Thus, the reciprocal capacitance is

$$\frac{1}{C} = \left( \frac{8\pi}{ken} \right)^{1/2} [(V_e + \phi_1)^{1/2} + \phi_2^{1/2}] \quad (11.149)$$

(compare Section 11.2, Ref. 1; here we have neglected a possible difference of  $n$  at either barrier side). Generally,  $\phi_1 = \phi_2 = \phi$ . R. K. Mueller<sup>6</sup> finds  $\phi \geq 0.66$  eV. He also refined these considerations to include the difference between  $\phi_0$  (zero bias) and the height  $\phi'_0$  to the barrier at points where the hole density is equal to the donor concentration  $N_d$ . For zero applied bias

$$\phi'_0 = 2kT \ln \frac{N_d}{n_i},$$

where  $n_i$  = intrinsic density.

If  $\phi_0 - \phi'_0 \approx 0$ , (11.149) is correct. For a difference between  $\phi_0$  and  $\phi'_0$ , the apparent barrier height  $\phi'_0$  has to be used in the  $C$  determination, for which case Mueller derived a set of equations. Measurements of the temperature dependence of grain-boundary capacitance values show that

$$\phi_0 > \phi'_0$$

(see Figure 11.45).

This difference decreases with decreasing temperature, where  $\phi_0 = \phi'_0$ .  $C$ -measurements at lower temperature, however, are difficult because of increase in relaxation time.

The most important fact is that the capacitance values become frequency-independent for temperatures below 280°K and are practically frequency-independent for frequencies in excess of 1 Mc/sec (see Figure 11.46). Taylor, Odell, and Fan (Section 11.2, Ref. 1) measured values between 150 and 600 pF

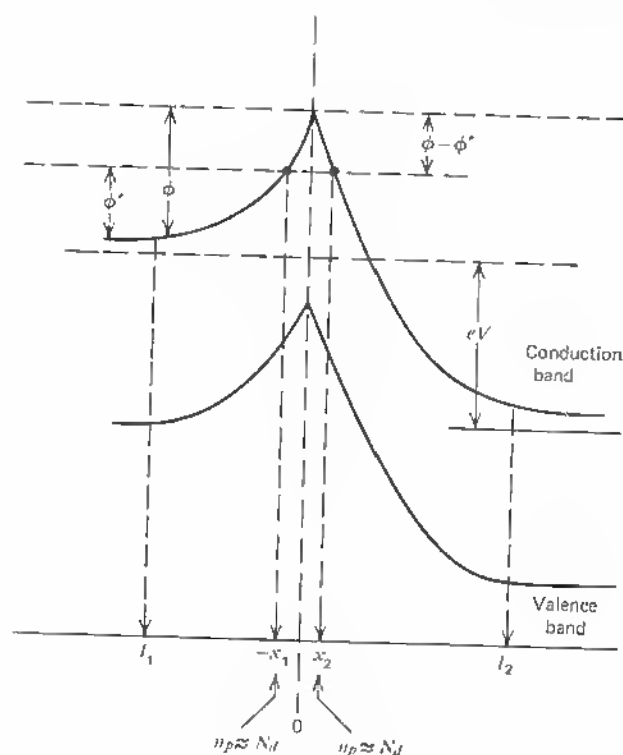


Fig. 11.45 Potential distribution at grain boundary. (After Mueller [11.5,6].)

in the frequency-independent range above 1 Mc/sec. Measured areas were not indicated, but since these measurements were carried out between probes on thin samples, their values seem to agree with those published by Hamakawa et al.,<sup>7</sup> who find values of 2,200 to 3,700 pF/cm<sup>2</sup>, or 22 ÷ 37 pF/mm<sup>2</sup>.

Since the field lines between probes at high-resistivity samples show a considerable spread, a capacitive area of 10 mm<sup>2</sup> and more in the case of Taylor et al. is quite normal.

Table 11.5-1 gives a useful list of properties of grain-boundary samples, measured by Hamakawa et al.<sup>7</sup>

The capacity values for the samples with  $\parallel$  orientation are about twice as large as those measured at the  $\perp$  samples, since, in the first case, the grain-boundary plane was contacted, and, in the second case, measurements were carried out between the  $n$ -type bulk contacts (two  $C$  values in series). The barrier height  $\phi$  was measured by capacity versus voltage readings.

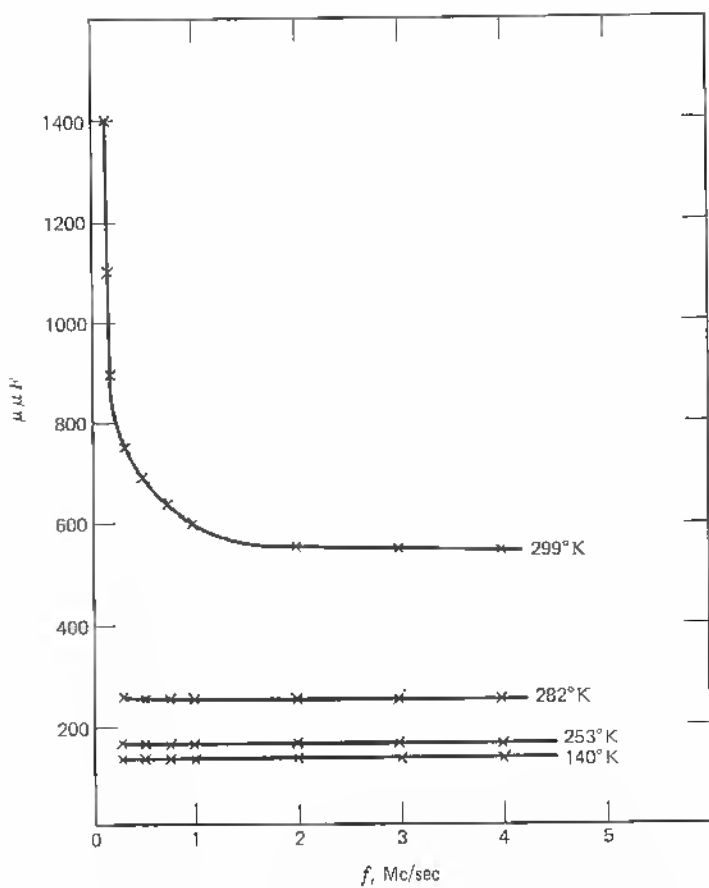


Fig. 11.46 Capacitance versus frequency. (After Taylor, Odell, Fan.)

Table 11.5-1 Properties of the Grain-boundary Barrier

Sample orientation and current flow with respect to dislocations	Donor Concentration in bulk, $\text{cm}^{-3}$	Break-down voltage,	Capacitance, $\text{pF}/\text{cm}^2$	Dislocation level $E_2$ , eV (from valence band)	Barrier height $\phi$ , eV
$4^\circ \parallel$	$1.3 \cdot 10^{14}$	190–220	$2,200 \pm 200$	$0.03 \pm 0.002$	$0.31 \pm 0.015$
$4^\circ \perp$			$900 \pm 80$		
$12^\circ \parallel$	$1.1 \cdot 10^{14}$	160–210	$3,450 \pm 250$	$0.006 \pm 0.002$	$0.32 \pm 0.015$
$12^\circ \perp$			$1,600 \pm 100$	$0.010 \pm 0.002$	
$28^\circ \parallel$	$3.4 \cdot 10^{14}$	120–160	$3,700 \pm 180$	$0.003 \pm 0.002$	$0.34 \pm 0.02$
$28^\circ \perp$			$1,700 \pm 100$	$0.005 \pm 0.002$	

## REFERENCES

1. Mataré, H. F.: Anisotropy of Carrier Transport in Semiconductor Bicrystals, "Solid State Physics in Electronics and Telecommunications," Academic, New York, 1959.
2. Haynes, J. R., and W. Shockley: Mobility and Life of Injected Carriers in Germanium, *Phys. Rev.*, vol. 81, pp. 835–843, March 1, 1951.
3. Valdes, L. B.: Measurement of Minority Carrier Lifetime in Germanium, *Proc. IRE*, vol. 40, no. 11, pp. 1420–1423, November, 1952.
4. Mataré, H. F., and B. Reed: Anomaly of Carrier Lifetime in Germanium Bicrystals, *Zschr. f. Naturf.*, vol. 11a, no. 10, pp. 876–878, 1956.  
Mataré, H. F.: Dislocation Planes in Semiconductors, *Proceed. IRE*, vol. 106, part B, Suppl. 15, pp. 293–302, 1959.
5. Mueller, R. K.: Dislocation Levels in Germanium, *J. Appl. Phys.*, vol. 30, no. 12, pp. 2015–2016, December, 1959.
6. Mueller, R. K.: Capacitance and Barrier Height in Grain Boundaries, *J. Appl. Phys.*, vol. 30, no. 4, pp. 546–550, April, 1959.
7. Hamakawa, Y., and J. Yamaguchi: Electrical Conduction in Germanium Grain Boundary Plane, *Japanese Journal Appl. Phys.*, vol. 1, no. 6, pp. 334–342, December, 1962.

## 11.6 FIELD EFFECT

The field effect is commonly an expression for the conductivity—or, more generally, impedance—modulation of a conducting channel by a variable field or potential. In order to achieve measurable results, the field influence has to affect a major part of the cross section of the current path. As is well known, the early approaches to the field modulation of thin semiconductor films (patents by O. Heil, 1935, and subsequent work by Shockley and Pearson<sup>1, 2</sup>) showed that only a small part of the induced charges ( $\sim 10$  per cent) are effective in changing the conductance. At this point, the well-known Bardeen surface states gave the necessary explanation<sup>3</sup> for the immobilization of charge carriers in centers at the free semiconductor surface. Shockley later described in a classical paper how these surface states can be eliminated by the use of junction space-charge layers within a semiconductor so that essentially a bulk channel is being modulated.<sup>4</sup> This started further work on unipolar transistors and lead to the now commercially important versions of field-effect transistors of all variations. It finally became possible also to field-modulate semiconductor surfaces efficiently when the natural surface inversion layer is made the current-carrying medium, as is the case in many metal-oxide-semiconductor structures (MOS technology).

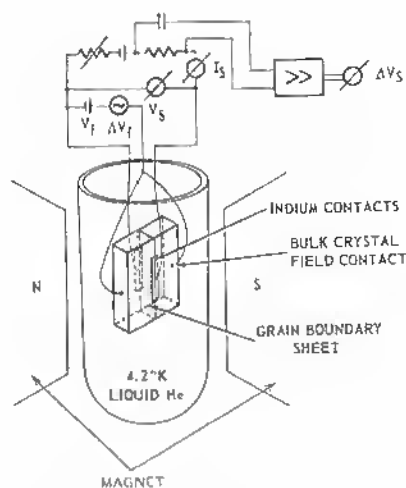


Fig. 11.47 Bicrystal Field Effect measurement. View of Dewar mount and circuit.

In the case of the grain boundary, the  $n$ - $p$ - $n$  structure of grown bicrystals prompted laboratory work to use the inner  $p$  layer directly as a base layer for transistor like devices. This proved inefficient, since in a transverse mode the dislocation array is a layer of high recombination velocity for holes. In early measurements on bicrystals, the dislocation array or the  $p$ -type layer was used, therefore, as emitter contact, and the adjacent  $n$ -type layers were connected as base and collector contacts.<sup>5</sup> In this case, however, the base configuration is poor because of high spreading resistance and does not allow optimization of the current multiplication without complicated diffusion and alloy steps.

In physical measurements on bicrystals, it was found that the sheet conductance shows a remarkable independence of the actual degree and kind of bulk doping (see Section 11.1). This and the fact of the temperature independence suggested a field modulation of the layer conductance by a voltage applied to the bulk sides of a bicrystal (see Figure 11.47). For the geometry and circuitry for such measurements see Figure 11.48. The geometry to maximize the voltage influence on the sheet barrier has to be such that  $dW/l$  is maximized. The voltage  $V_1$  is applied between the bulk crystal in the forward-biased terminal of the slab. Figure 11.49 shows the results for three different bulk doping ranges. Obviously, this modulating voltage decreases the barrier

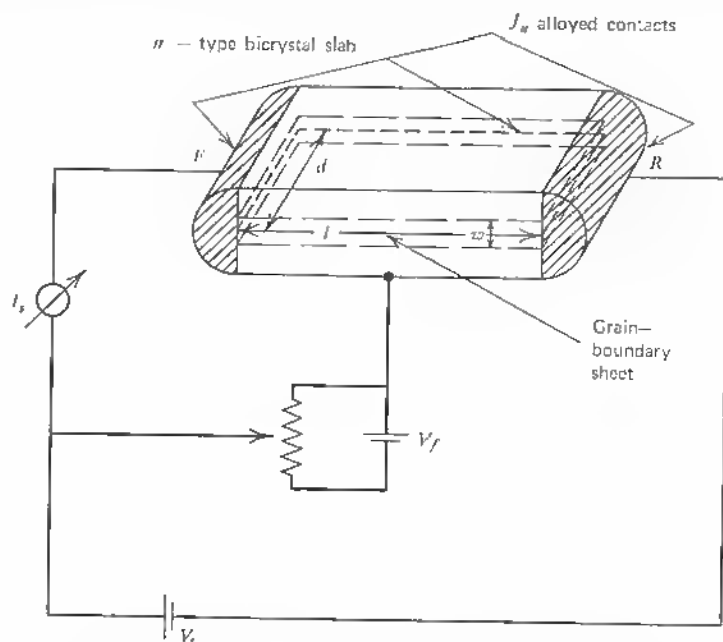


Fig. 11.48 Sample geometry in field modulation studies on bicrystals.

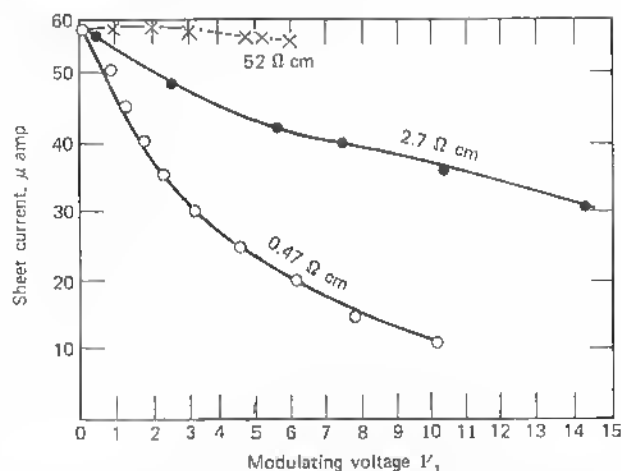


Fig. 11.49 Sheet current  $I_s$  as function of field voltage  $V_f$  for constant sheet voltage  $V_s$  for three resistivity values of Germanium bicrystals (measured at 4.2°K).

width and the sheet current. This effect, however, is more pronounced for lower-resistivity material (junction leakage smaller, measurements at 4.2°K). It is also found that the linearity of the sheet current is better maintained for high-resistivity material (see Figure 11.50). The reason for this can be found in the fact that a self-modulation sets in as a consequence of the nonlinearity of the bulk voltage distribution (see Figure 11.51), which is enhanced in low-resistivity bulk material and because of the nonlinearity of the barrier-layer  $I$ - $V$  characteristics. For the arrangement in Figure 11.47, one finds a sheet current versus field voltage characteristics as given in Figure 11.52. Here the sheet voltage  $V_s$  is parameter (measurements at liquid helium temperature).

Plotting the sheet current versus the sheet voltage (usual plot) with the field voltage  $V_f$  as a parameter gives a graph, as in Figure 11.53. Here the characteristics for liquid nitrogen temperature (a) and liquid helium temperature (b) are plotted. The influence of the field voltage on the sheet current is higher for the low-temperature range because of a minimization of the junction leakage through the bulk (see also absolute value of  $I_s$  in both cases). Although the sheet  $I$ - $V$  characteristics changes little in form for a change in temperature (see Figure 11.54), the spread of the sheet characteristics with the applied field voltage increases with decreasing temperature (see Figure 11.55).

The physical model for this kind of field effect is quite different from that of the field effect described by Shockley.<sup>4</sup> In the usual case, the width of the

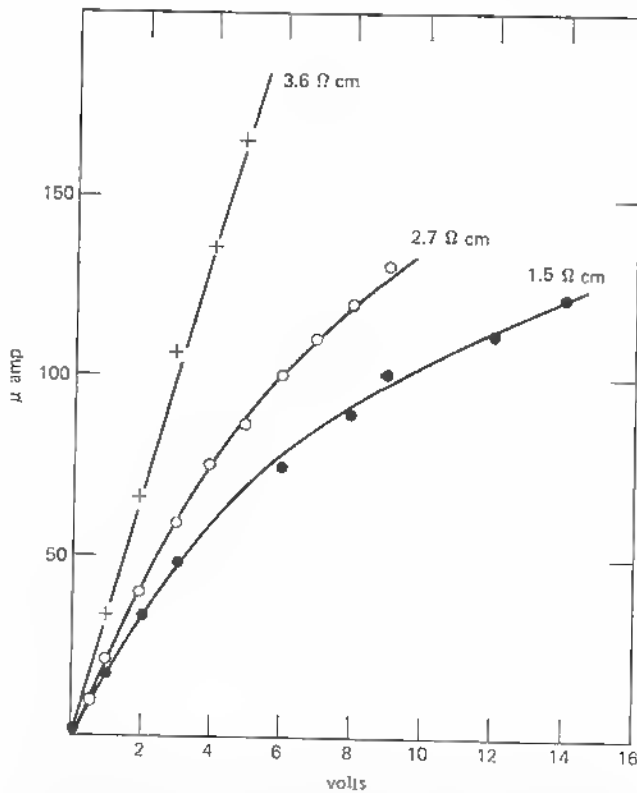


Fig. 11.50 Sheet current versus sheet voltage at 4.2°K for three different resistivities. Saturation effect increases with decreasing resistivity of the N-type bulk.

channel of majority carriers is pinched by a progressing space charge as the field voltage increases. In the bicrystal case, the conduction medium is the space-charge sheet surrounding the sheet of negative charges in boundary states. To analyze this case, a more general approach has been used by Weinreich and carried through by Mataré.<sup>6</sup> With the sample dimension indications in Figure 11.48, the channel conductivity is

$$\sigma_c = \sigma_0 \frac{w \cdot d}{l}, \quad (11.150)$$

where  $\sigma_0$  = conductivity in channel,  
 $w$  = channel width,  
 $d$  = lateral channel extension,  
 $l$  = channel length.



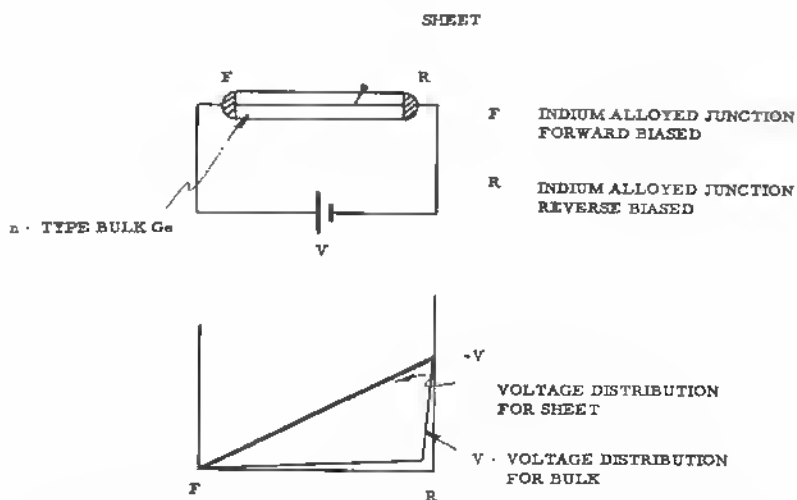


Fig. 11.51 Self-modulation of sheet current due to different voltage distribution along bulk and sheet.

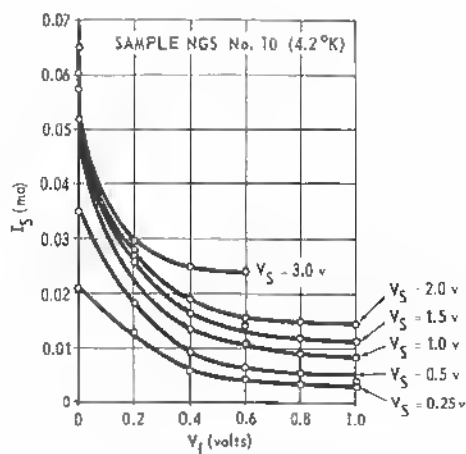


Fig. 11.52 Bicrystal field effect. Sheet current versus field voltage (parameter sheet voltage).  
 $T = 4.2^\circ\text{K}$ .

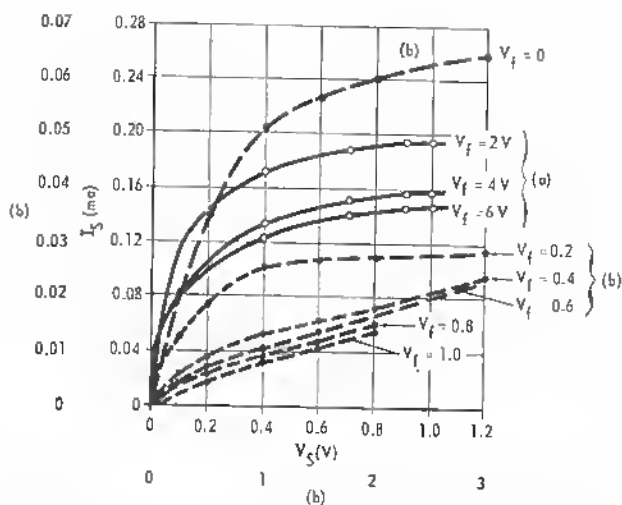


Fig. 11.53 Bicrystal Field Effect. Sheet current versus sheet voltage with field voltage as parameter for 2 different temperatures: (a) liquid Nitrogen, (b) liquid Helium.

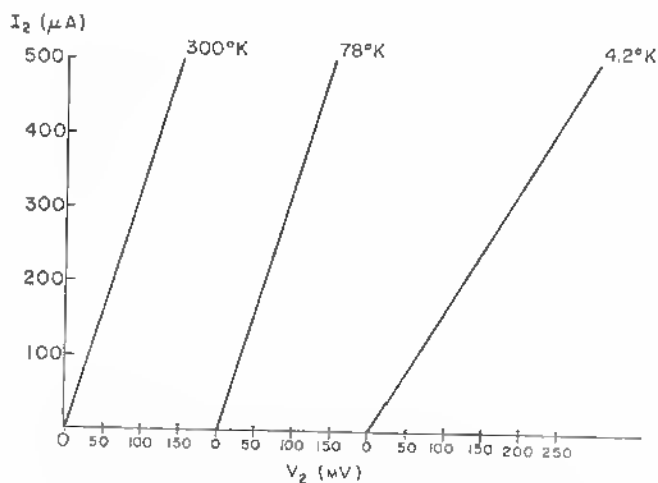


Fig. 11.54  $I$ - $V$  characteristics of a Ge grain boundary at different temperatures. ( $V_1 = 0$ ).

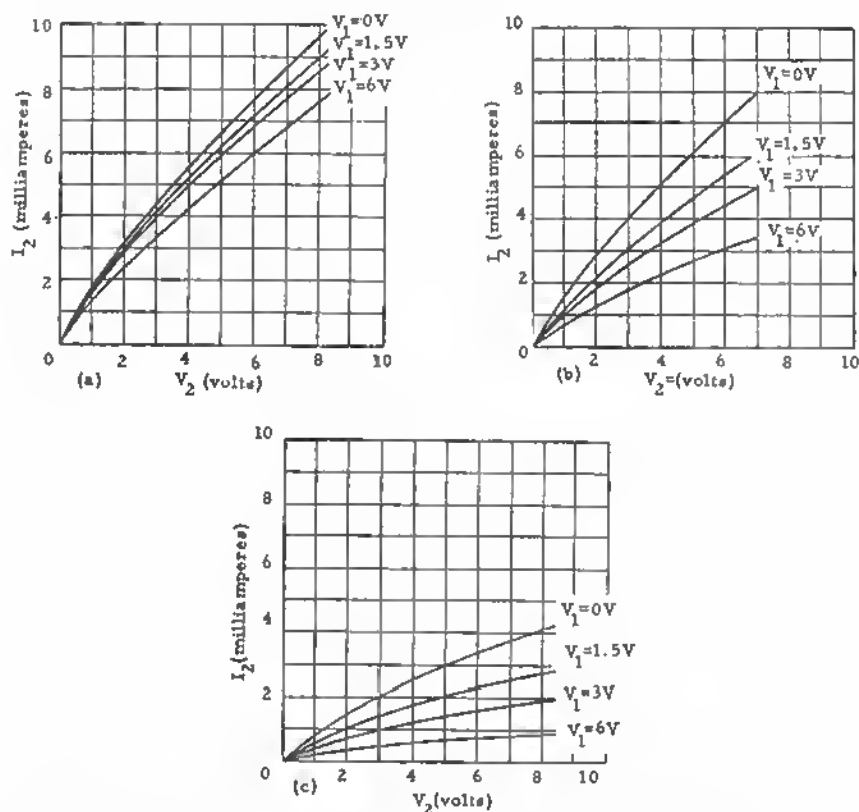


Fig. 11.55 Grain boundary field effect. Sheet current ( $I_2$ ) versus sheet voltage ( $V_2$ ) with field voltage ( $V_1$ ) as parameter for (a) 300°K, (b) 78°K, (c) 4.2°K.

Now

$$\sigma_0 = e\mu n, \quad (11.151)$$

where  $e$  = electron charge,

$\mu$  = mobility in channel,

$n$  = carrier density in channel,  $\text{cm}^{-3}$ .

Thus the total conductance of the channel is

$$\sigma_s = ne\mu \frac{wd}{l}. \quad (11.152)$$

We can also define the total charge  $Q$  within the channel as

$$Q = newd \cdot l \quad (11.153)$$

and write

$$\sigma_s = \mu \frac{Q}{l^2}, \quad (11.154)$$

This form of the conductance is useful in order to describe the grain-boundary sheet conductance when only the charge per square is known and the width  $w$  remains unknown:

$$\sigma_s = \mu \cdot \frac{q}{\square}. \quad (11.155)$$

The sheet current can be expressed by the sheet conductance:

$$I_s = \sigma_s \cdot V_s, \quad (11.156)$$

and with (11.154)

$$I_s = \mu \frac{Q}{l^2} V_s. \quad (11.157)$$

Introducing now the carrier transit time in the channel

$$\tau_s = \frac{l}{v_s} \quad (11.158)$$

and considering that

$$v_s = \frac{\mu V_s}{l}, \quad (11.159)$$

we get:

$$\frac{1}{\tau_s} = \frac{\mu V_s}{l^2} \quad (11.160)$$

or with (11.157)

$$I_s = \frac{Q}{\tau_s} \quad (11.161)$$

for the sheet current as function of total charge and transit time. In this form  $Q$  can be assessed by capacity measurements, since the variation of the current  $I_c$  with the field voltage  $V_f$  is the important quantity here and can be written as transconductance:

$$g_s = \frac{\partial(Q/\tau_s)}{\partial V_f} = \frac{1}{\tau_s} \frac{\partial Q}{\partial V_f} = \frac{\Delta C}{\tau_s}. \quad (11.162)$$

$\Delta C$ , the capacity variation with field voltage, can easily be measured as  $\partial I_s / \partial V_f$ , also resulting in a measurement of  $\tau_s$ .

These equations have been applied in order to assess the actual values in grain boundaries. For example, for the sample with the characteristics in Figure 11.50 and the dimensions

$$d = 0.015 \text{ in.}$$

$$l = 0.015 \text{ in.}$$

a transconductance  $g_c$  of 1 mA/V was measured.  $C$  was found to be  $2 \times 10^{-10}$  farad. This leads to

$$\tau_s = \frac{2 \cdot 10^{-10}}{0.001} = 2 \cdot 10^{-7} \text{ sec.}$$

With (11.161) and a known channel current  $I_c = 5$  mA one finds

$$Q = 2 \cdot 10^{-7} \cdot \frac{5}{10^3} = 10^{-9} \text{ coulomb.}$$

Since 1 coulomb =  $3 \cdot 10^9 \cdot \frac{1}{4.77} \cdot 10^{10}$  electrons,  $Q$  corresponds to  $0.63 \times 10^{19}$  electrons.

Thus  $Q$  corresponds to a carrier density of  $6.3 \times 10^9$  unity charges present in the space charge layer in order to compensate for the electrons in dangling bonds. With a grain-boundary area of the sample in question of  $150 \times 13$  mils or  $0.0125 \text{ cm}^2$ , the charge density  $\text{cm}^{-2}$  is then

$$\frac{q}{\square} = \frac{6.3 \cdot 10^9}{0.0125} = 4.8 \times 10^{11}.$$

This agrees well with the density measurements made by other methods, which all lie in the  $10^{12} \text{ cm}^{-2}$  range (see, for example, Chapter 9, Sect. 4). In comparing the measured values at the dislocation sheet for  $\tau_s$  and  $V_s$  with the resulting mobility value according to (11.160), one finds, for example, for  $V_s = 5$  volt,  $l = 13$  mils =  $3.3 \times 10^{-2} \text{ cm}$ , and  $\tau_s = 2 \times 10^{-7} \text{ sec}$ :

$$\begin{aligned} \mu &= \frac{l^2}{V_s \cdot \tau_s} = \frac{10.5 \times 10^{-4}}{5 \times 2 \times 10^{-7}} \\ &\simeq 10^3 \text{ cm}^2/\text{V sec,} \end{aligned}$$

a value that is on the high side but of the correct order of magnitude (see Section 11.3).

## REFERENCES.

1. Shockley, W., and G. L. Pearson: Modulation of Conductance of Thin Films of Semiconductors by Surface Charges, *Phys. Rev.*, vol. 74, pp. 232-233, 1948.
2. Shockley, W.: "Electrons and Holes in Semiconductors," Van Nostrand, Princeton, N.J., 1950.
3. Bardeen, J.: Surface States and Rectification at Metal-Semiconductor Contact, *Phys. Rev.*, vol. 71, pp. 717-727, 1947.
4. Shockley, W.: A Unipolar Field Effect Transistor, *Proceed. IRE*, vol. 40, pp. 1365-1376, November, 1952.
5. Mataré, H. F.: Electronic Behavior of Certain Grain Boundaries in Perfect Crystals, *Zschr. f. Naturf.*, vol. 9a, no. 7/8, p. 698, 1954.  
Mataré, H. F.: Grain Boundary Structure and Carrier Transport in Semiconductor Crystals, *Zschr. f. Naturf.*, vol. 10a, no. 8, pp. 640-652, 1955.
6. Mataré, H. F.: Low Temperature Field Effect Transistor Using Dislocation Planes, "Colloque International sur les Dispositifs à Semiconducteurs," vol. 1, pp. 499-515, Chiron, Paris, 1961.

## 11.7 PHOTOELECTRIC EFFECTS

As an  $n$ - $p$ - $n$  structure, the grain-boundary layer is a zone of internal electric fields. When a  $p$ - $n$  junction is subject to photon injection, the Fermi level  $\xi$  is shifted from its equilibrium position so that the barrier is lowered, the shift  $\Delta\phi$  of the electrostatic potential corresponding to the difference between the equilibrium value  $\phi_{\text{equil}}$  and the value  $\phi_F$  caused by the injection (see Figure 11.56).  $\phi_F$  corresponds to the case of a forward-biased junction. The relative positions in the energy scale between the Fermi level and the lower edge of the conduction band in the  $n$ -type side ( $\xi_n$ ) and the Fermi level and the upper edge of the valence band in the  $p$ -type side ( $\xi_p$ ) remain unchanged.

As in the case of the normal  $p$ - $n$  junction, electrons have diffused toward the  $p$ -region and holes toward the  $n$  region until equilibrium is set up. This equilibrium state is synonymous with an internal barrier built up to stop further flow of carriers. The remaining ionized donors at the  $n$ -type side and the acceptors at the  $p$ -type side form the blocking layers.

A more detailed description of the dynamic equilibrium involves diffusion and injection of carriers. If no light is injected, the potential barrier of height  $\phi$  does not block a certain number of carriers with sufficient energy to pass over this barrier. Their number is given by the Boltzmann factor. In a closed circuit they give rise to a current

$$I_i = \text{const } e^{-\phi/KT} \quad (11.163)$$

that is balanced out by the thermally freed carriers swept across the barrier,

forming a current

$$I_s = -eD \left( \frac{p_n}{L_p} + \frac{bn_p}{L_n} \right), \quad (11.164)$$

where  $D$  = hole diffusion constant,

$p_n$  = hole concentration at  $n$  side,

$n_p$  = electron concentration at  $p$  side,

$L_p, L_n$  = hole, electron diffusion length,

$b$  = electron/hole mobility ratio.

Thus in equilibrium  $I_i = -I_s$ .

If the junction is now subjected to light, hole-electron pairs are injected, shifting the barrier height for the amount

$$\Delta\phi = \phi_{\text{equil}} - \phi_F \quad (11.165)$$

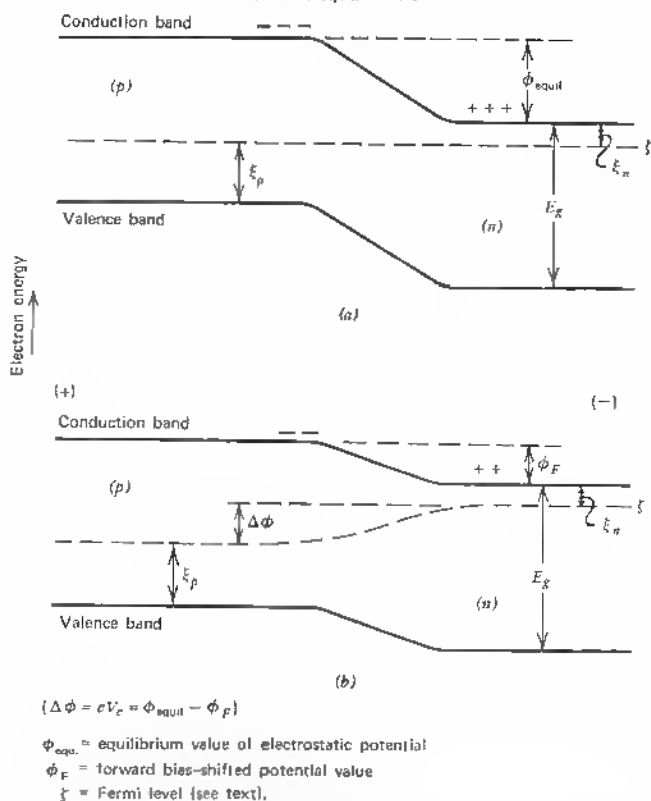


Fig. 11.56 (a)  $p$ - $n$  junction potential distribution at equilibrium. (b)  $p$ - $n$  junction (open circuit) with built-in field generated by a photovoltage due to injected photons.

(see Figure 11.56). This causes a current:

$$I_j = \text{const } e^{-\Delta\phi/kT} \quad (\phi \text{ and } \Delta\phi \text{ in eV}). \quad (11.166)$$

The light generated current in a closed circuit is then

$$I_L = I_j + I_i = I_j - I_s, \quad (11.167)$$

and with (11.164) and (11.165)

$$\begin{aligned} I_L &= \text{const. } e^{-\phi_{\text{equil}}/kT} e^{\phi_F/kT} - I_s \\ I_L &= I_s (e^{-\Delta\phi_F/kT} - 1), \end{aligned} \quad (11.168)$$

where  $\Delta\phi_F$  is the shifted electrostatic potential due to light injection, which corresponds to an external voltage  $V_e = \phi_F/e$ . The carrier injection generates, therefore, a voltage at the junction amounting to

$$V_e = \frac{kT}{e} \ln \left( 1 + \frac{I_L}{I_s} \right). \quad (11.169a)$$

The thermal diffusion current  $I_s$  is proportional to the number of thermally excited minority carriers:

$$I_s \approx g_{th},$$

and the current  $I_L$  is basically proportional to the number of electron-hole pairs  $g_L$  generated by the photon injection. Thus

$$V_e = \frac{kT}{e} \ln \left( 1 + \frac{g_L}{g_{th}} \right) \quad (11.169b)$$

As seen in Figure 11.56, the junction illumination causes a built-in field  $\Delta\phi$ , separating the generated electron-hole pairs. The additional free holes are drawn by the field toward the *p*-type side and the free electrons toward the *n*-type side, thus decreasing the space charge and lowering the barrier. The maximum photovoltage one may induce by injection is therefore given by the original barrier height  $\phi_{\text{equ}}$ . If now the barrier height increases with a reverse voltage applied, as is the case for one side of the grain-boundary *n-p-n* structure, the electron-hole pair generation is enhanced. Even without an additional external voltage applied, the injection-generated internal bias voltage  $V_e$  on one side of the barrier impresses a reverse bias on the other side through the outer circuit and thus increases the number of occupied dangling-bond states to (see equas. 11.40)

$$q = \frac{q_0}{2} \left[ 1 + \left( 1 + \frac{eV_e}{\phi} \right)^{1/2} \right], \quad (11.170)$$



This again leads to an increased barrier height:

$$\phi_0 = eV_B = \frac{k}{8\pi n} \left\{ \frac{\pi q_0}{k} \left[ 1 + \left( 1 + \frac{eV_s}{\phi} \right)^{1/2} \right] \pm \frac{2enV_e}{q_0} \left[ 1 + \left( 1 + \frac{eV_e}{\phi} \right)^{1/2} \right]^{-1} \right\}^2 \quad (11.171)$$

(see Section 11.2). Since both junctions are separated only by the very small innermost dislocation array of about 100 Å width, the injected carriers therefore actually decrease one barrier side while increasing the other. Since the dominating barrier for the carrier separation is the higher one, the injection current causes an increase in quantum efficiency above the one for normal  $n$ - $p$ - $n$  or  $p$ - $p^+$ - $p$  structures.

Before entering the difficult field of the spectral response and quantum efficiency, we describe the barrier and its photo-response. The total barrier shows the spacial potential distribution as given in Figure 11.57. Here the degeneracy is expressed by the fact that the valence-band top crosses the Fermi level at the barrier center. Under an external voltage  $V_e$ , the total potential at the left is the sum of  $V_e$  and the intrinsic barrier potential. If germanium is assumed, a number of levels are introduced in the gap, as we shall see. For the purpose of representation, only a typical mid-band level at 0.42 eV from the top of the valence band is shown, which was

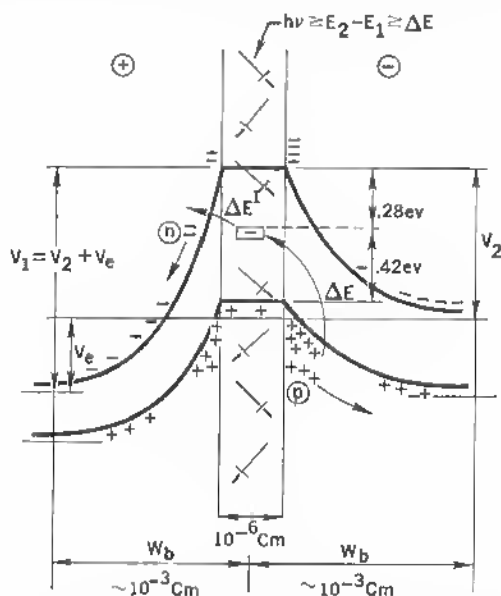


Fig. 11.57 Band scheme at grain boundary layer.  $V_e = V_1 - V_2 =$  external bias voltage.  $\Delta E$  and  $\Delta E' =$  energy differences from valence band to dislocation level respectively from dislocation level to conduction band.

also identified. In the case of injection of photons with energy  $h\nu$  smaller than the band gap but larger than 0.42 eV, electrons may be lifted from the valence band to the interband level, leaving free holes behind (see below). The interesting aspect of this structure is the strongly localized photoelectric sensitivity. The bicrystal represents a left-right discriminating device of highest photoelectric sensitivity. Since the grain-boundary barrier acts as a hole sink, the current flow reverses when the barrier position with respect to the light injection point is changed (see Figure 11.58). This results in a characteristic of the kind shown in Figure 11.59. As the light injection point moves across the bicrystal toward the boundary, the photovoltage increases and reaches a peak where it reverses in a steep fall to a negative peak, fading to zero as the distance increases. Although here monochromatic light was injected, the resolution does not suffer when a normal broad band light source is used that contains the frequency of the basic gap energy. Highest displacement resolution is achieved for minimized space-charge extension. This is seen

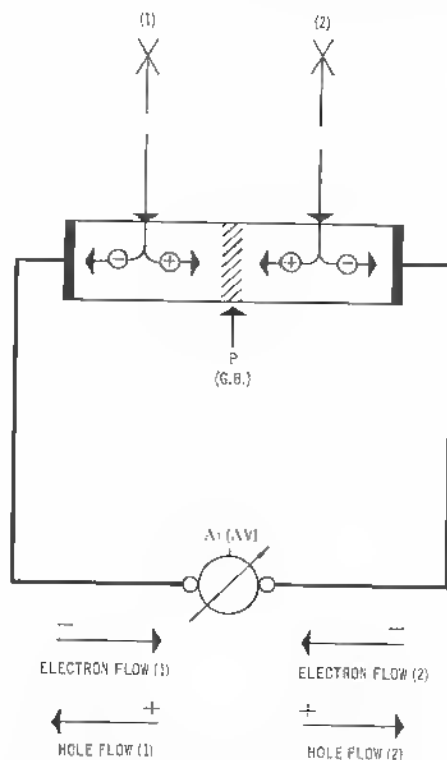


Fig. 11.58 Electron-hole separation in bicrystal under illumination at different sides of grain boundary (closed circuit).

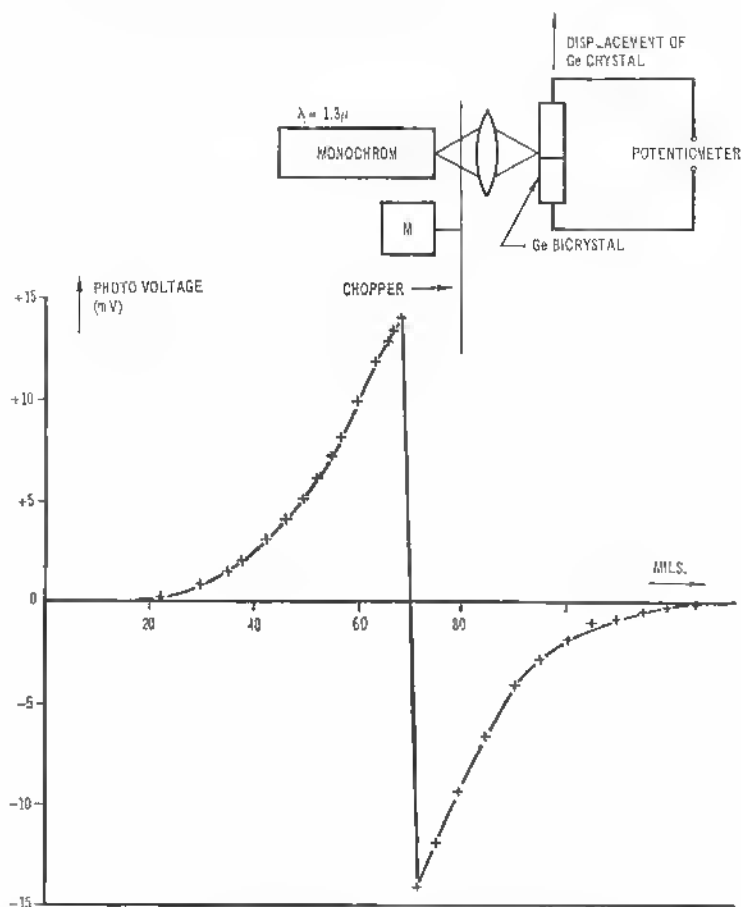


Fig. 11.59 Photovoltage measured at bicrystal for migrating light-injection point.

from measurements on  $p$ - $p^+$ - $p$  structures (bicrystals) grown from  $p$ -type material of a doping not exceeding  $10^{17}$  to  $10^{18} \text{ cm}^{-3}$ . Figure 11.60 is the displacement characteristic (photovoltage versus displacement  $x$ ) for a bicrystal with tilt angle  $\theta = 20^\circ$  of the usual orientation, as indicated before.<sup>1</sup>

R. K. Mueller<sup>2</sup> pointed out that a voltage pulse applied across a grain boundary increases the barrier height to a value practically independent of the height of the barrier before the pulse. At low temperature, slow surface states can maintain this barrier height for a long time. Transient responses to a pulse, however, would depend strongly on the state of the boundary prior to the pulse and therefore provide a signal indicating the boundary condition.

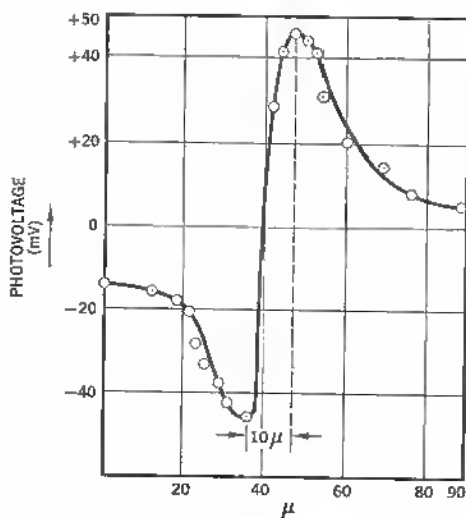


Fig. 11.60 Bicrystal photoresponse curve with displacement resolution of  $0.1 \text{ V}/10 \mu$ .

Such signals may be of small radiative energy. Mueller indicates a minimum radiative detectable power of the order of

$$P = 10^{-13} \text{ to } 10^{-14} \text{ watt}$$

under sensitive conditions.

Such values were later measured<sup>3</sup> at liquid nitrogen temperatures. At this time also anomalies in the spectral response curves were detected. The response curves showed distinct energy levels in the long wavelength region at 1.3, 1.6, and  $1.72 \mu$  and a general extension of the response toward smaller eV numbers.

These measurements were partially confirmed by later measurements on bicrystals, revealing also levels at 1.3 and  $1.6\mu$ , but additional fine structure in the low-wavelength part of the photoresponse curve.<sup>4</sup> More measurements, especially concerning the role of the bias voltage, were started by Mataré, Cronmeyer, and Beaubien on grown  $20^\circ$  bicrystals.<sup>5</sup> The typical equipment setup is shown in Figure 11.61. Preliminary studies of the optical transmission of bicrystals and monocrystals of the same bulk material did not reveal any difference. This study was concerned particularly with (a) the extension of the photoresponse of a bicrystal to both larger and smaller photon energies as compared with single crystals, (b) the change of photoresponse as a function of temperature, and (c) the change of photoresponse as a function of applied bias.

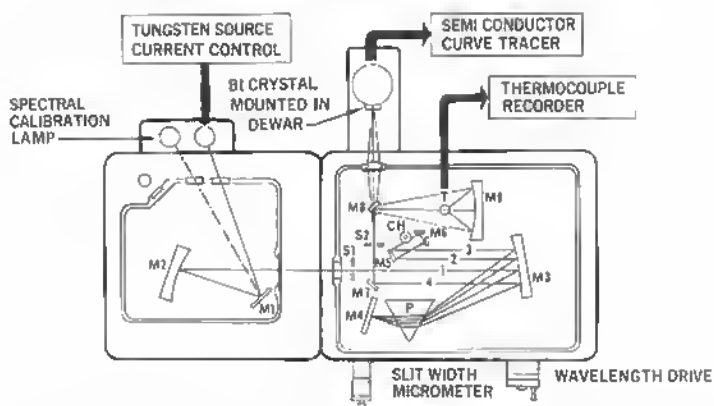


Fig. 11.61. Schematic of photoresponse measurements on bicrystals showing optical path in a Perkin-Elmer model 112 single beam double-path photometer.

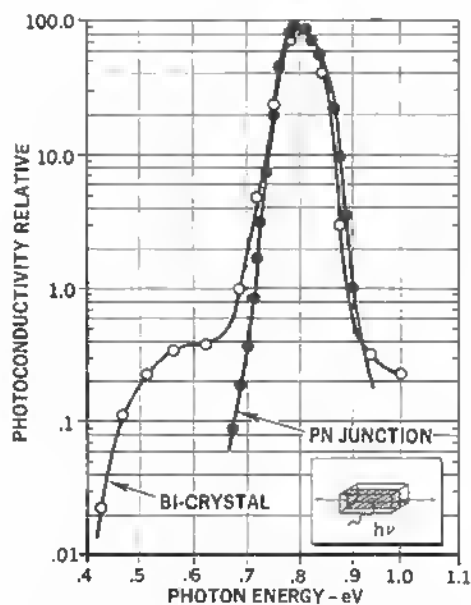


Fig. 11.62 Photoconductivity versus photon energy for germanium bicrystal and a  $p$ - $n$  junction (at liquid nitrogen temperature).

The photoconductive mode (ohmic In contacts to the grain boundary) already revealed a marked difference between a dislocation plane and a  $p$ - $n$  junction. The result is shown in Figure 11.62.

Although the major peak remains at the point typical for germanium (0.7 to 0.8 eV), the fall-off at lower photon energies is quite different. Thresholds appear at 0.65 and 0.42 eV. A similar behavior has been noted by Galacki et al.<sup>6</sup> on plastically bent germanium samples.

The change of the photoresponse of a biased bicrystal with temperature is evident in Figure 11.63. The room-temperature response appears normal (the peak of the response for a germanium monocrystal lies at 0.708 eV for room temperature), but the response at 80°K is considerably enhanced for the long wavelength region. The threshold is the same as in the photoconductive mode (see Figure 11.62).

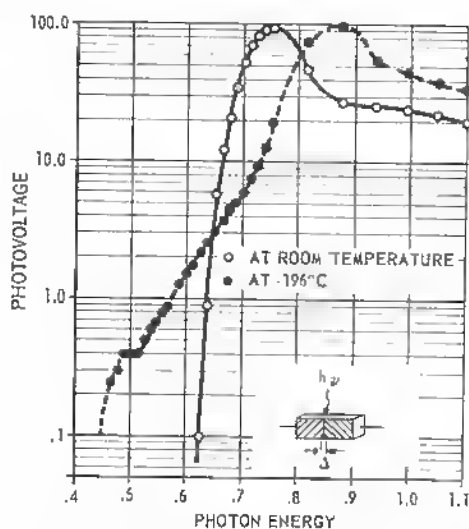


Fig. 11.63 Photovoltage versus photon energy for bicrystal wafer with bias applied at room temperature and liquid nitrogen temperature.

Finally, the extension of the spectral response of a bicrystal due to a bias voltage (increase in effective barrier height) is shown in Figure 11.64. This curve is taken at 80°K. It is thus concluded that the effectiveness of a bias potential is more pronounced for lower temperature.

It is apparent in Figure 11.64 that the extension of the photoresponse due to a bias field (of less than 1 volt) is considerable in both the long- and short-wavelength regions of the spectrum. More detail has been found within the short-wavelength region with thresholds at 0.85 and 1.22 eV at room temperature (0.95 and 1.32 eV at 80°K).<sup>7</sup> The measured photoresponse in the region

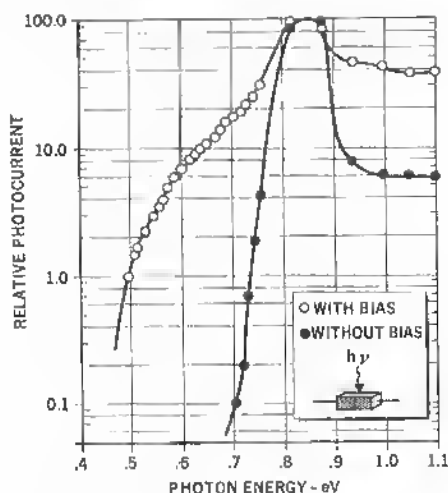


Fig. 11.64 Spectral response of a bicrystal (photovoltage) at liquid nitrogen temperature with and without bias applied.

from .8 to  $1.8\mu$  is shown in Figure 11.65. In all cases, the peak value corresponds to the band-to-band energy for the particular temperature applied. The dislocations introduce additional levels that, in coherent form, as in grain boundaries, can give rise to remarkable sensitivity extensions. It is important to calibrate correctly the spectrometer set for equal incident energy in order to avoid such findings as a decrease in photoresponse toward the fundamental absorption edge, which can produce erroneous readings.<sup>8</sup>

There have been attempts to explain these extensions of the photoresponse curves for bicrystals. Obviously the explanations have to differ fundamentally for the areas beyond and below the fundamental peak value. A more detailed consideration regarding the band structure of a grain boundary is needed to explain also the many response edges that indicate interband and intraband processes.

Starting with the long-wavelength extension, it has to be noted that this result is known also from response measurements on  $p$ - $n$  junctions when amphoteric doping (Zn-As or Zn-Sb) is applied.<sup>9</sup>

Impurities like copper and gold also extend the frequency response, as do random dislocations. The fact that in most diffusion and alloy processes a considerable number of dislocations is generated explains why most  $p$ - $n$  junctions display such a frequency extension even if produced from dislocation-free bulk crystals. As copper introduces a number of interband levels (one at 0.26 eV below the conduction band and two at 0.33 and 0.04 eV above the valence-band edge), so dislocations introduce a series of acceptor levels

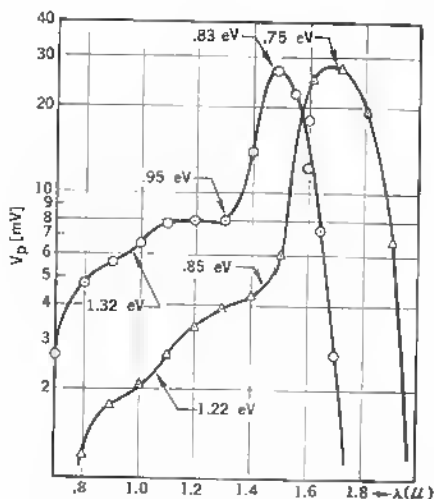


Fig. 11.65 Photoresponse versus optical wavelength for bicrystal:  $\Delta$  at  $T = 300^\circ\text{K}$ ;  $\circ$  at  $T = 77^\circ\text{K}$ .

near the valence band (see Section 11.5) in addition to a midband level at 0.42 eV.

The particular aspect of a bias-induced extension in bicrystals (this refers actually to both the long- and short-wavelength response) can be explained by the increase in electron density in dislocation levels. The incremental photo-voltage is given by

$$\Delta V_p = \frac{kT}{e} \ln \frac{\delta n_e(q)}{\delta V_e}, \quad (11.172)$$

where  $\delta n_e(q)$  = change of number of charges in dislocation levels,  
 $\delta V_e$  = change in external voltage.

As we know from earlier derivations concerning the change of the number of charges at the grain-boundary top with the external voltage applied—see (11.76)—the actual charge density can be represented by

$$n_e(q) \simeq \frac{2n_{e0}}{q_0[1 + (1 + eV_e/\phi)^{1/2}]} \left[ V_2^{1/2} \exp\left(-\frac{eV_2}{kT}\right) - V_1^{1/2} \exp\left(-\frac{eV_1}{kT}\right) \right], \quad (11.173)$$

and the differential  $\frac{\delta n_e(q)}{\delta V_e}$  can be found indicating the rate of change of  $n_e(q)$



with the applied external field. Considering that  $V_1 = V_2 + V_e$ , the external voltage or the injection-generated voltage changes  $V_1$  and leaves  $V_2$  unchanged. Therefore

$$\begin{aligned} \frac{\partial n_e(q)}{\partial V_e} = \frac{2n_{e0}}{q_0} \frac{1}{1 + (1 + eV_e/\phi)^{1/2}} & \left\{ \left( \frac{e}{kT} - \frac{1}{2V_1} \right) V_1^{1/2} \frac{\partial V_1}{\partial V_e} \exp\left(-\frac{eV_1}{kT}\right) \right. \\ & + \frac{e/\phi}{2(1 + eV_e/\phi)^{1/2}} \frac{1}{1 + (1 + eV_e/\phi)^{1/2}} \left[ V_1^{1/2} \exp\left(-\frac{eV_1}{kT}\right) \right. \\ & \left. \left. - V_2^{1/2} \exp\left(-\frac{eV_2}{kT}\right) \right] \right\}. \end{aligned} \quad (11.174)$$

With the conditions  $V_1 \gg V_2$  and  $eV_e/\phi \gg 1$ , we have

$$\begin{aligned} \frac{\partial n_e(q)}{\partial V_e} = \frac{2n_{e0}}{q_0} \left( \frac{\phi}{eV_e} \right)^{1/2} & \left\{ V_1^{1/2} \left( \frac{e}{kT} - \frac{1}{2V_1} \right) \exp\left(-\frac{eV_1}{kT}\right) \right. \\ & \left. + \frac{1}{2V_e} \left[ V_2^{1/2} \exp\left(-\frac{eV_2}{kT}\right) \right] \right\}. \end{aligned} \quad (11.175)$$

Assuming also that  $V_1 \approx V_e \gg kT/e$ , this reduces to

$$\begin{aligned} \frac{\partial n_e(q)}{\partial V_e} = \frac{2n_{e0}}{q_0} \left( \frac{\phi}{eV_e} \right)^{1/2} & \left\{ V_e^{1/2} \frac{e}{kT} \exp\left(-\frac{eV_e}{kT}\right) + \frac{1}{2V_e} \left[ V_2^{1/2} \exp\left(-\frac{eV_2}{kT}\right) \right] \right\}. \end{aligned} \quad (11.176)$$

Since the second term in brackets is small— $V_2 \gg kT/e$ —we can write

$$\frac{\partial n_e(q)}{\partial V_e} \approx \frac{2n_{e0}[e\phi]^{1/2}}{q_0 \cdot kT} \exp\left(-\frac{eV_e}{kT}\right). \quad (11.177)$$

For the photovoltage according to (11.172), this results in

$$\Delta V_p \approx \frac{kT}{e} \ln \left[ \frac{2n_{e0}(e\phi)^{1/2}}{q_0 kT} \exp\left(-\frac{eV_e}{kT}\right) \right] \quad (11.178)$$

$$\approx \frac{kT}{e} \left( \text{const} - \frac{e}{kT} V_e \right). \quad (11.179)$$

We conclude<sup>7</sup> that the photovoltage across the dislocation plane is linearly dependent on the applied voltage within the linearity of the barrier layer characteristics, that is, between the point  $V_e \geq kT/e$  and the avalanche breakdown of the barrier layer. This has actually been found experimentally (see Section 13.1).

There are other causes for the varied frequency response in bicrystals. As stated before, the dislocation plane is under stress (see Chapter 7). Assuming the validity of the classical energy expression for a dislocation pipe,

$$E_{\perp}(D) = \frac{b}{2} \int_0^{\lambda} \sum_n \sigma_{xy}(x, nD) dx, \quad (11.180)$$

where  $D$  = dislocation spacing,

$n$  = number of individual dislocations,

$\sigma_{xy}$  = stress in  $xy$  plane,

$b$  = Burgers vector

$\lambda$  = integration limit (crystal dimension),

one can reduce this by application of the radial stress function  $\sigma_r$  to

$$E_{\perp} = \frac{\mu b^2}{4\pi(1-\nu)} \ln \frac{r_1}{r_0} \quad \text{dyn},$$

where  $\mu$  = shear modulus ( $\sim 10^{12}$  dyn/cm<sup>2</sup> for germanium),

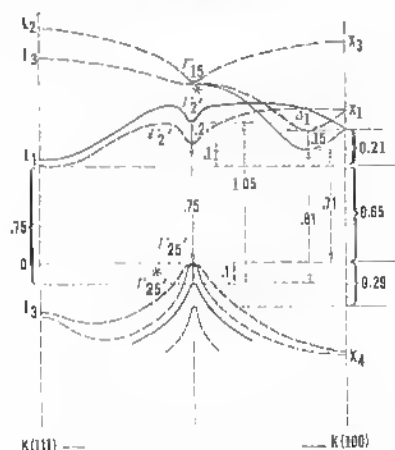
$\nu$  = Poisson's ratio ( $\sim 0.4$  for germanium),

$\ln(r_1/r_0) \simeq \ln(1 \text{ cm}/10^{-7} \text{ cm}) \simeq 16$ ,

for the usual integration limits (see Section 4.5). Calculated values for  $E_{\perp}$  are  $6.4 \times 10^3$  dyn/cm, and with an assumed width of the dislocated area of 100 Å a local stress field of  $10^{11}$  dyn cm<sup>-2</sup> and a band-gap change of 0.15 eV result (see Section 7.1).

This is of the order of magnitude measured in hydrostatic pressure measurements. Since  $10^6$  dyn  $\simeq 1$  kg, the dislocated area is under a strain corresponding to  $10^5$  kg cm<sup>-2</sup>. Actually, the partial overlap of dilation and compression zones cuts this value roughly in half, and one may take readings from Paul's energy gap versus pressure curves<sup>10</sup> to assess the gap changes.

Accordingly, one has to assume that the  $\Gamma_2$  conduction-band minimum at  $k = 0$  moves upward in the energy scale ( $\sim 0.2$  eV) and the [100] minimum  $\Delta_1$  moves downward ( $\sim 0.15$  eV). The  $\Gamma_{25'}$  valence-band edge shifts also in the negative energy direction ( $\sim 0.1$  eV) (see Figure 11.66; shifted values are marked by asterics). For the pressure values considered, the energy at  $\Delta_1$  and the  $L_1$  valleys have crossed, with  $\Delta_1$  lying at a lower value than  $\Gamma_2$ . Considering the small extension of the grain-boundary disturbed layer ( $\sim 100$  Å) compared with the space-charge region responsible for the carrier transport, a superposition of two band structures—one pressure-changed, one normal—must be assumed as far as the photoelectric behavior at the grain boundary is concerned. This may result in new transition values from the valence band to the conduction band.



so that

$$\partial E_c = + \chi \frac{\partial P}{P_0} E_{IC} \quad \text{for the conduction band,}$$

or

$$\partial E_v = + \chi \frac{\partial P}{P_0} E_{IV} \quad \text{for the valence band.}$$

There are examples in the past where anomalous photovoltaic effects in semiconductors have been associated with crystalline defects. Especially in CdTe and ZnS larger than band-gap photovoltages have been found.

A. Lempicki<sup>12</sup> has established a more definite correlation between the defect structure in ZnS crystals and their photovoltaic behavior. The exact model, however, remained to be defined, but the conclusion was that "anomalous photovoltaic effects are connected with crystalline disorder and most probably with stacking faults."

J. Birman<sup>13</sup> has analyzed the energy bands in Zinkblende and Wurtzite structure, applying the tight binding (LCAO) method, and found that, in natural crystals of ZnS and SiC, defects originating from transitions in structure are associated with internal barriers. For example, a ZB-W-ZB (Zinkblende-Wurtzite-Zinkblende) sequence shows a barrier at the Wurtzite face due to the splitting of the  $\Gamma_4$  into the  $\Gamma_5$  and  $\Gamma_1$  states. Other influences like locked-in strain and potential discontinuities have to be considered also, according to Birman.

As an example Birman draws the picture of the band of a rotation-twinned Zinkblende, generating a thin layer of locked-in Wurtzite and a double layer at the twin interface (see Figure 11.67). Here the potential jump at the interface between these structures causes similar effects to those discussed for dislocation planes.

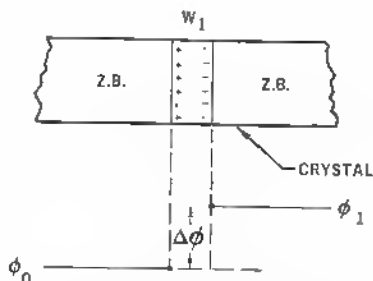


Fig. 11.67 Inner double layer with barrier caused by rotation-twinned Zinkblende (after Birman [11.7,13]).

## REFERENCES

1. Weinreich, O. A., H. F. Mataré, and B. Reed: Electrical and Photoelectrical Properties of Grain Boundary Layers, "Solid State Physics in Electronics and Telecommunications," Academic, New York, 1960, vol. 1, part 1, pp. 97-108.
2. Mueller, R. K.: Transient Response of Grain Boundaries and Its Application for a Novel Light Sensor, *J. Appl. Phys.*, vol. 30, no. 7, pp. 1004-1010, July, 1959.
3. Lindemann, W. W., and R. K. Mueller: Grain Boundary Photoresponse, *J. Appl. Phys.*, vol. 31, no. 10, pp. 1746-1751, October, 1960.
4. Schell, H. A.: Germanium Grain Boundary Photocell, "Colloque International sur les Dispositifs à Semiconducteurs," Chiron, Paris, 1961, vol. 1, pp. 643-649.  
Mataré, H. F.: Germanium Bicrystals and Their Application in Photocells, *Internat. Elektron. Rundschau*, vol. 15, pp. 207-211, 1961.
5. Mataré, H. F., D. C. Cronmeyer, and M. W. Beaubien: Germanium Bicrystal Photoresponse I, *Solid State Electronics*, vol. 7, pp. 583-588, 1964.
6. Galacki, Z., T. Figielski, and M. Jastrzebska: Extrinsic Photoconductivity in Plastically Bent Germanium, *Phys. Stat. Sol.*, vol. 11, p. K35, 1965.
7. Mataré, H. F., and K. S. Cho: Field Dependence of Photoresponse in Germanium Bicrystals, *J. Appl. Phys.*, vol. 36, no. 11, pp. 3427-3431, November, 1965.
8. Miles, M. H.: Extrinsic Photoconductivity from Edge Dislocations in Germanium, *J. Appl. Phys.*, vol. 40, no. 7, pp. 2720-2724, June, 1969.
9. Burstein, E., G. Picus, and N. Sclar: Optical and Photoconductive Properties of Silicon and Germanium, "Photoconductivity Conference Report," Wiley, New York, 1956, p. 253.
10. Paige, E. G. S.: The Electrical Conductivity of Germanium, "Progress in Semiconductors," A. F. Gibson and R. E. Burgess (eds.), Wiley, New York, 1964, vol. 8, pp. 155ff.
11. Muss, D. R.: Injection Luminescence in Germanium, *J. Appl. Phys.*, vol. 35, no. 12, pp. 3529-3531, December, 1964.
12. Lempicki, A.: Anomalous Photovoltaic Effects in ZnS Single Crystals, *Phys. Rev.*, vol. 113, no. 5, pp. 1204-1209, March 1, 1959.
13. Birman, J. L.: Simplified LACO Method for Zincblende, Wurtzite, and Mixed Crystal Structures, *Phys. Rev.*, vol. 115, no. 6, pp. 1493-1505, September 15, 1959.

## Chapter 12 Controlled Growth of Dislocations

### 12.1 PLASTIC DEFORMATION

In Burgers' dislocation model we define the closure failure of a pathway around the dislocation in the undisturbed lattice as the failure vector or Burgers vector  $b$ , which, multiplied by the radius of curvature of a crystal bent under stress is proportional to the dislocation distance. Or the dislocation density is proportional to the reciprocal product of Burgers' vector and radius of curvature:

$$\Delta = \frac{1}{r \cdot b} \quad (12.1)$$

(see Figure 12.1). If the slip plane is inclined at some angle  $\phi$  to the neutral plane of the crystal bar, one has

$$\Delta = \frac{1}{rb \cos \phi}. \quad (12.2)$$

Such bending can be produced when, for example, germanium is heated to approximately 500 to 600°C, where it is easily deformed. When the radius of curvature  $r$  is large compared with the thickness of the bar, the uniform shear stress bends the bar into a circular arc, generating a set of dislocations. F. L. Vogel<sup>1</sup> describes results of such bending with the crystals oriented in the  $(\bar{1}\bar{1}1)$  slip plane inclined at 42° to the neutral plane and a  $\langle 110 \rangle$  slip direction at 42° to the neutral axis. This produces only one set of glide planes and dislocations parallel to the  $\langle \bar{1}12 \rangle$  bent axis. Calculated and observed dislocation densities were in good agreement, considering the uncertainty of the etch-pit count and the possibility of polygonization due to dislocation climb normal to the slip plane.<sup>2</sup>

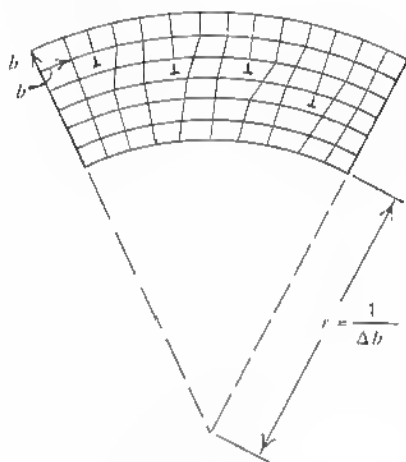


Fig. 12.1 Edge dislocations produced by bending in simple cubic lattice  $b$  = Burgers vector;  $r$  = radius of curvature of slip plane;  $\Delta b$  = density of edge dislocations.

Plastic deformation by torsion at elevated temperatures (germanium at 850°C, silicon at 1180°C) produces similar dislocations. Here screw dislocations may occur in larger quantity, but for the high-twist angles of 230° per inch for germanium (80° per inch for silicon), the formation of broken bonds is likely. No correlation between theoretical density and dislocation count was established.<sup>3</sup>

Plastic deformation of germanium in compression also shows an increase in dislocation density with increasing strain and the appearance of slip lines and polygonization.<sup>4</sup> For high-strain values, domains form that represent crystallographically misoriented regions. This gives rise to low-angle boundaries. It is also found that low-temperature deformation (525°C) produces a higher number of active dislocations (acceptor density) than deformation at higher temperatures (725°C).<sup>5</sup> This is because at the higher temperature annealing can neutralize part of the forming free bonds, as healing of defects can be produced by heat treatment after the crystal has been deformed.

In silicon the initial dislocation density after deformation is somewhat higher than the calculated density. Patel has shown that a much closer fit can be produced by long annealing at 1300°C of the bent crystals.<sup>6</sup>

This points to a difference between germanium and silicon. The silicon lattice is from many indications more flexible than the germanium lattice (twinning; see Section 4.4) and therefore yields more readily to the initial strain, causing piled-up groups of dislocations. These cause secondary slip,

which may lead to the formation of dislocation tangles containing a high density of so-called "forest" dislocations.<sup>7</sup>

Further annealing is effective in dissolving high-energy groups of dislocations.

The study of dislocations produced by plastic deformation has resulted in highly valuable information about materials properties in general, but the method is not suited to the generation of defined and localized arrays of dislocations when their electrical properties are considered. The models developed and the correlation between the degree of deformation and the resultant dislocation density, however, have been very useful, for example, in the evaluation of thin films produced in heteroepitaxy, where local stress fields are generated because of the mismatch of the thermal expansion coefficients of substrate and film (see Chapter 14).

## REFERENCES

1. Vogel, F. L., Jr.: Dislocations in Plastically Bent Germanium Crystals, *Journal of Metals*, pp. 946-949, August, 1956.
2. Vogel, F. L., Jr.: Dislocations in Polygonized Germanium, *Acta Metallurgica*, vol. 3, pp. 95-96, January, 1955.
3. Greiner, E. S.: Plastic Deformation of Germanium and Silicon by Torsion, *Transactions AIME, Journal of Metals*, pp. 203-205, January, 1955.
4. Patel, J. R., and B. H. Alexander: Plastic Deformation of Germanium in Compression, *Acta Metallurgica*, vol. 4, pp. 385-395, July, 1956.
5. Greiner, E. S. P. Breidt, J. N. Hobstetter, and W. C. Ellis: Effects of Compression and Annealing on the Structure and Electrical Properties of Germanium, *Transactions AIME, Journal of Metals*, pp. 813-818, July, 1957.
6. Patel, J. R.: Arrangements of Dislocations in Plastically Bent Silicon Crystals, *J. Appl. Phys.*, vol. 29, no. 2, pp. 170-176, February, 1958.
7. Mitchell, T. E.: The Stress-field around Groups of Dislocations in Face-centered Cubic Metals, *Phil. Magazine*, vol. 10, pp. 301-314, 1964.

## 12.2 DOUBLE-SEED TECHNIQUE

The technique of using bicrystals was apparently first reported by Smoluchowski and coworkers, who studied grain-boundary diffusion in copper crystals.<sup>1</sup> Tweet produced rather undefined bicrystals for his work on grain boundaries,<sup>2</sup> and H. F. Mataré and H. A. R. Wegener described precision production of bicrystals and stability of grain boundaries that prompted extensive studies of these structures.<sup>3</sup> There are numerous ways of performing grain-boundary growth with double seeds. It appeared essential to maintain medium angles of misfit, that is, tilt angles between a few degrees and a maximum of 25°. For smaller misfit than 1°, the boundaries do not produce



compression-dilation overlap sufficient for stabilization (see Section 7.2) and form lineage boundaries, while for misfit angles greater than  $25^\circ$  microcracking destroys the coherency so that preferential diffusion is dominant. Consequently, the bicrystal seeds are generally oriented at  $2\theta < 25^\circ$  (in Figure 12.2). Fundamentally, there are two kinds of grain boundaries that can be created by changing only one parameter of two parallel lattices. In one case, the grain boundary lies at right angles to the plane containing the variable parameter  $\theta$ . In the other, the grain boundary lies in the plane of the variable parameter  $\theta$ , which is the twist angle or the deviation of the seed-crystal axis, for example,  $\langle 100 \rangle$ , out of the orthogonal to the grain-boundary plane. This is equal to a deviation in the  $\langle 100 \rangle$  direction (see Figure 12.2). These two kinds are the extremes of a series of intermediate boundaries with more or less distance between broken bonds because of twist or screw dislocations.

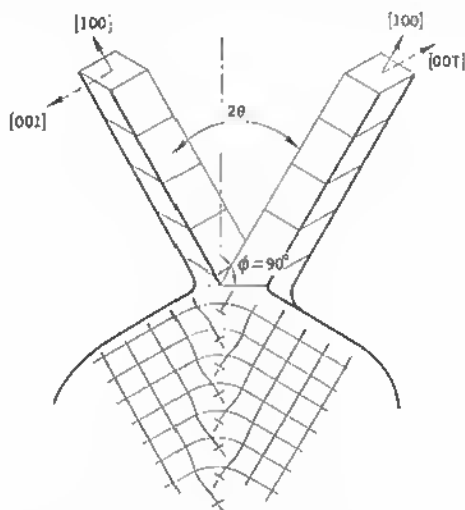


Fig. 12.2 Double seed arrangement with bicrystal boule (schematic).

Seed mounts for tilt boundaries can have varied forms. Figure 12.3 shows the basic arrangement. Each seed is cut along a major crystallographic direction so that the angle  $\theta$  between the seed faces is also the angle between the lattices of the single crystals. For each value of  $\theta$ , a new seed holder is required. For the purpose of varied tilt, a wedge seed holder has been used by researchers (see Figure 12.4). Here, one has to make sure that the seed crystal lattice has the correct orientation with respect to the axis. If the mount allows for screw adjustment, it is commonly fine-adjusted on the x-ray goniometer. The most appropriate form of a double seed is produced by cutting a monocrystalline boule under the desired angle of tilt ( $\theta/2$ ) with respect to the  $[100]$

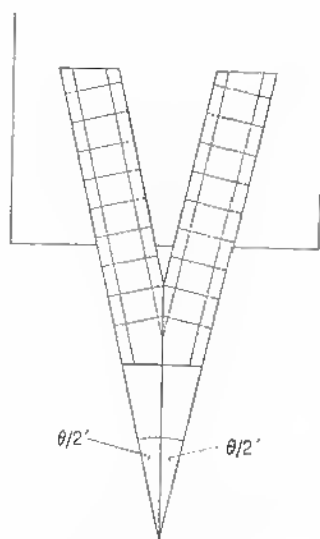


Fig. 12.3 Bicrystal double seed holder (tilted).

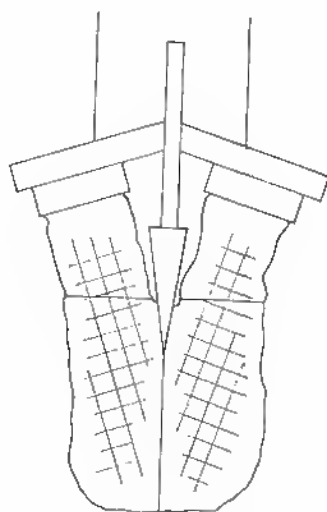


Fig. 12.4 Double seed holder with cone.

axis and rotating one of the seeds before placing them together (see Figure 12.5). In this case, the seed holder is conventional, and there is no need for fine adjustment and complicated holder mechanisms, because all orientation precision is done on the double seed itself. It should be mentioned here that the choice of the tilt around the  $\langle 001 \rangle$  direction for the  $[100]$  seed crystal orientation was made after numerous studies on bicrystals. Expressed in simple form, the result was that all other orientations resulted in less pronounced barrier layers, and measurements revealed that the number of free bonds was not so high as in the case above (screw dislocations and twins). A testing of the effect of the lattice orientation with respect to the pulling direction (see Figure 12.6) showed generally that there is no basic difference between these cases.

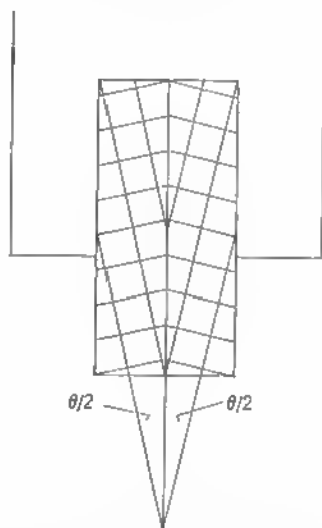


Fig. 12.5 Prepared and assembled bicrystal seed.

A bicrystal seed within its seed holder is shown in Figure 12.7. The screw fixings shown press against the seed rods, which, in turn, are pressed against reference planes in the seed holder. Figure 12.7, shows a bicrystal seed with a portion of a pulled bicrystal. The grain boundary is visible at the top flat.

The result of a successful operation (Czochralski equipment best with floating crucibles)<sup>4</sup> should be a straight boundary line across the crystal boule (see Figure 12.8). Because of the excellent stability of medium-angle boundaries, a greater number of defined grains can be grown by mounting of multi-seed crystals that, for example, are alternatively tilted for  $20^\circ$ . The result of such a pulling operation with eight seeds and seven grain boundaries is shown

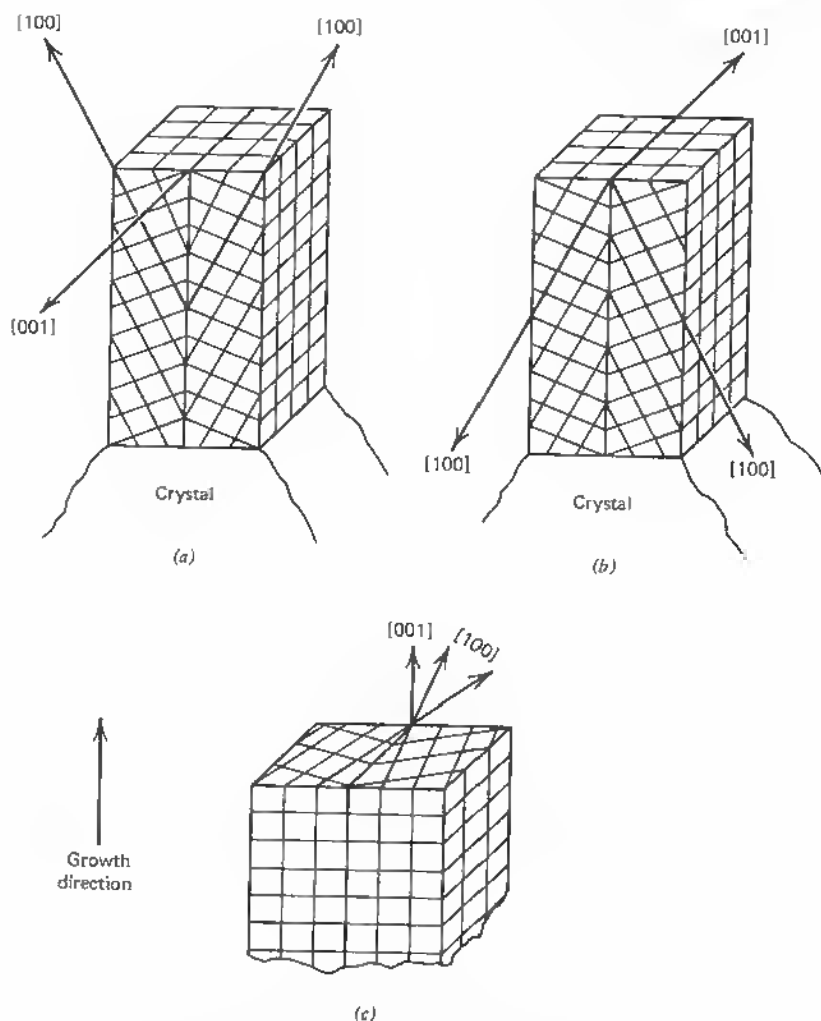


Fig. 12.6 Three different bicrystal-seed arrangements. (a) and (b) tilt axis perpendicular to growth direction; (c) tilt axis in growth direction.

in Figure 12.9. The temperature control is obviously rather critical when the crystal is subjected to varied growth pattern across the diameter. Small deviations occur near the crystal border line, but the center allows cutting out a large number of useful bicrystals (see cut slice).

The orientation of bicrystal proceeds in several steps. First, a single crystal is set by x-ray diffraction Laue patterns, with one  $(100)$  plane parallel to the



Fig. 12.7 Bicrystal seed holder (graphite) and bicrystal seed with first part of pulted crystal.  $2\times$ .

x-ray beam and vertical to the track. The goniometer is then transferred from the x-ray unit to the cutoff machine, and the crystal is sliced into slabs. Each slab is then set by x-ray methods again. This time the slab is oriented so that a (010) plane is parallel to the x-ray beam and the line of intersection of the previous cut and the new plane of cut is also parallel to the x-ray beam. The goniometer is then transferred again to the cutoff wheel, and the slabs are then sliced into square-based columns.

The three angles defining the relative position of the bicrystal boundary are  $\theta$  = tilt angle,  $r$  = angle of rotation, and  $t$  = angle of twist of the seeds. If one wants a dominance of the dangling-bond behavior of the grain boundary,

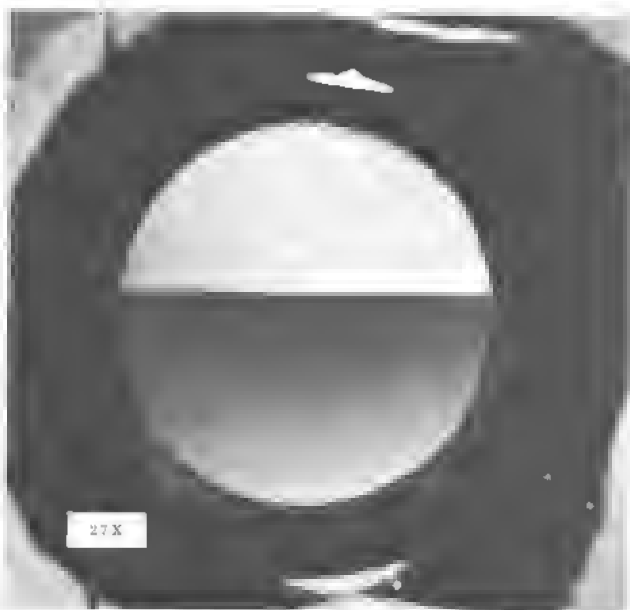


Fig. 12.8 View of surface of germanium bicrystal  $[100] - \theta_1 - [100]$ ,  $\theta_1 = 20^\circ$ .



Fig. 12.9 Multicrystal grown from eight monocrystal-seeds (seven grain boundaries of equal tilt angle  $\theta_1$ ).

$r$  and  $t$  have to be minimized in order to avoid repaired bonds. This requires exacting alignment of the seed crystals. The grain-boundary plane, defined by  $\theta$ ,  $r$ , and  $t$ , has two more degrees of freedom, since it can have different positions with respect to the growth plane: angle  $\phi$ . We consider generally only the symmetric case of a coincidence of the tilt axis into the grain-boundary plane:  $\phi = 90^\circ$  (see Figure 12.2). In terms of crystallographic directions,  $r$  is the rotational angle between both the  $\langle 010 \rangle$  and the  $\langle 001 \rangle$  directions in the  $(100)$  plane.  $\theta$  is the tilt angle between the  $\langle 100 \rangle$  directions in the  $(001)$  plane, and  $t$  (twist) is the angle between the original  $\langle 100 \rangle$  direction and the projection of the second  $\langle 100 \rangle$  direction in the  $(010)$  plane.

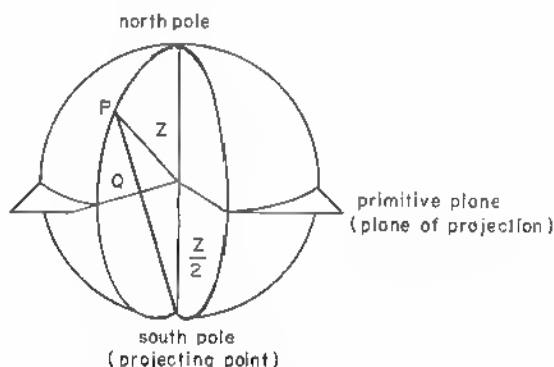
Aside from the two crystal lattices, the grain boundary between the two mutually inclined crystals requires definition.

Since ideally the grain boundary is a plane, only two angles are necessary for its full description. One angle  $b$  lies in the same plane as  $\theta$  and should be kept half its value. The other angle  $g$  is related to  $r$  and should be kept zero.

In general, seven angles are needed to correlate the measured properties of a grain boundary unequivocally with the lattices of the two seed crystals.

The orientation of a bicrystal can be represented in the usual stereographic projection<sup>5</sup> if the following limitations apply: Both monocrystalline components are symmetrical across the grain boundary, and the twist angle  $t$  is zero. Then, if the plane of projection is considered the grain-boundary plane (see Figure 12.10), the pole of the plane is at the center of the stereographic projection. The upper hemisphere can be used to describe the orientation of a single crystal component of the bicrystal.

As it is rotated to indicate its lattice orientation with respect to the grain



P = any spherical-projection point  
Q = the corresponding stereographic-projection point

Fig. 12.10 Stereographic projection of crystal plane upon reference sphere at point P.

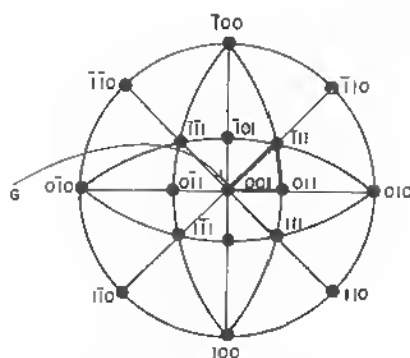


Fig. 12.11 Projection of cubic crystal with cube face parallel to projection plane.  $[001]$  direction is parallel to grain boundary-normal  $G$  (see text)

boundary in terms of  $\theta$  and  $r$ , the grain-boundary pole wanders in the unique triangle of the standard projection of the cubic system. This suggests that any bicrystal property can be plotted on this triangle and that all possible orientations, with the limitations cited, are restricted to this triangle. This is shown in Figure 12.11. Here the crystal at the center is assumed with a cube face parallel to the plane of projection. Possible unique orientations are given by 24 spherical triangles, as for example,  $[001]$   $[011]$   $[\bar{1}11]$ . The  $\langle 001 \rangle$  direction is parallel to the grain boundary normal  $G$ . Increasing  $\theta$  causes pole  $G$  to wander in the  $\langle 100 \rangle$  direction.

### Bicrystal Alignment

The Laue back-reflection technique can be used to measure the five parameters (or seven when the plane of cut is important) necessary to describe the orientation of a bicrystal. The x-ray beam is directed toward the grain boundary so that it is reflected from one crystal, giving rise to its Laue pattern on the film. A part is also reflected from the other crystal, resulting in a second Laue pattern displaced from the first one but on the same photograph. Reflection points belonging to the same crystal side can easily be identified by their shape. Shapes of Laue spots depend on the geometrical conditions.<sup>5</sup> Here the grain boundary dissects the circular spots in halves. Figure 12.12 shows a Laue pattern of a silicon bicrystal (tilt angle is  $\theta_1 = 6^\circ 14' \pm 10'$ , rotational angle  $\theta_2 = 0^\circ \pm 20'$ , and twist angle is  $\theta_3 = 6^\circ 14' \pm 10'$ ). Crystal  $A$  is identifiable by half-moons pointing down and crystal  $B$  by half-moons pointing up. The calculation of the different angles is described in Figure 12.13. Part  $a$  indicates the three main angles for the  $\phi = 90^\circ$  grain orientation and the reflection condition for beam  $x$  onto the boundary. The tangent relations or the ratios of the point distance from the central beam to the screen distance



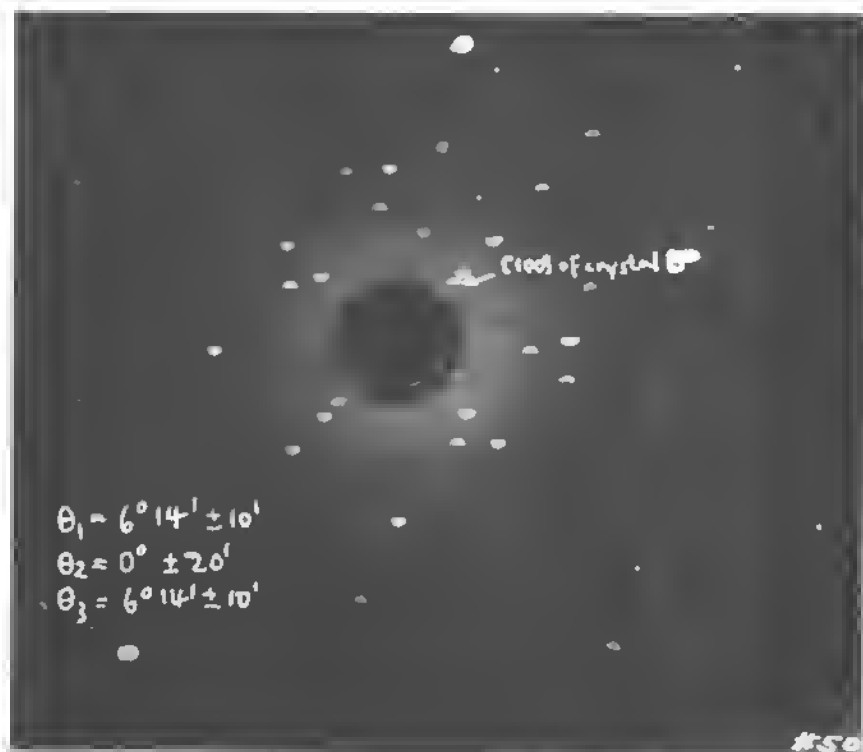


Fig. 12.12 Bicrystal Laue pattern (silicon): Tilt angle  $\theta_1 = 6^\circ 14' \pm 10'$ ; rotational angle  $\theta_2 = 0^\circ \pm 20'$ ; twist angle  $\theta_3 = 6^\circ 14' \pm 10'$ .

give the angle  $\theta_1$  (Figure 12.13b).  $\theta_2$  follows directly from the inclination of two lines connecting equal lattice reflection points, and  $\theta_3$  follows from the vertical distances of the Laue points with respect to the center spot (Figure 12.13c). [See also H. Kedesdy, *Am. Mineralogist* 39, 750 (1954).] If the grain-boundary orientation  $\phi \neq 90^\circ$ , one of the angles  $g$  and  $b$  can be determined by measuring the angle between the straight edge bordering a Laue spot near the center of the photograph and the corresponding reference direction. The other angle cannot simply be determined from the same photograph. For this reason, a second photograph has to be taken at right angle to the previous direction. The same procedure is followed throughout, only that in this case, the other angle of the grain boundary is the parameter.

The grain boundary itself can be used as a plane of reference for measurements. It seems best in practice to align the plane of the grain boundary so that its normal is the independent axis of rotation of the mounted crystal and

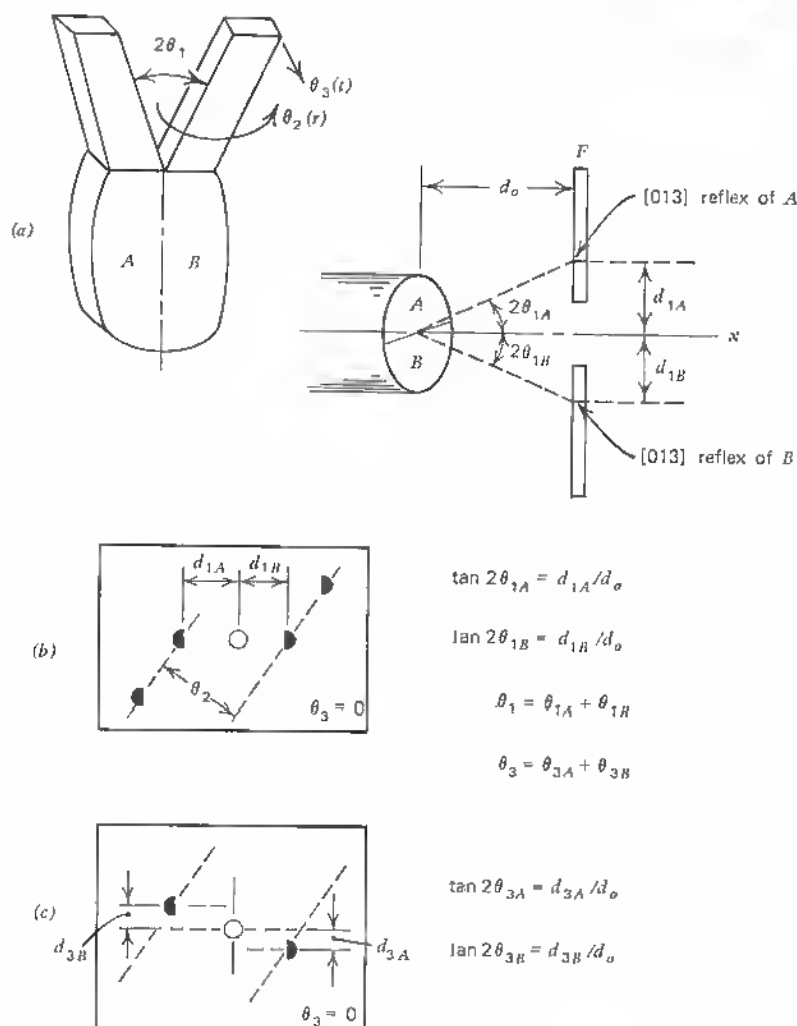


Fig. 12.13 Seed crystal-arrangement for bicrystals (a) and definition of misfit angles from Laue-reflection pattern. (b) (c)—(see text)

the x-ray beam is contained in it. Experimentally, this can be achieved by aligning the axis of a telescope to be coincident with the x-ray beam and then aligning the grain boundary in the goniometer so that full rotation of the bicrystal does not cause any wandering of the grain-boundary line from the cross hairs of the telescope. In this arrangement, only one photograph is required in order to determine the value of all five parameters:  $\theta_1$ ,  $\theta_2$ ,  $\theta_3$ , and  $g$ ,  $b$ .

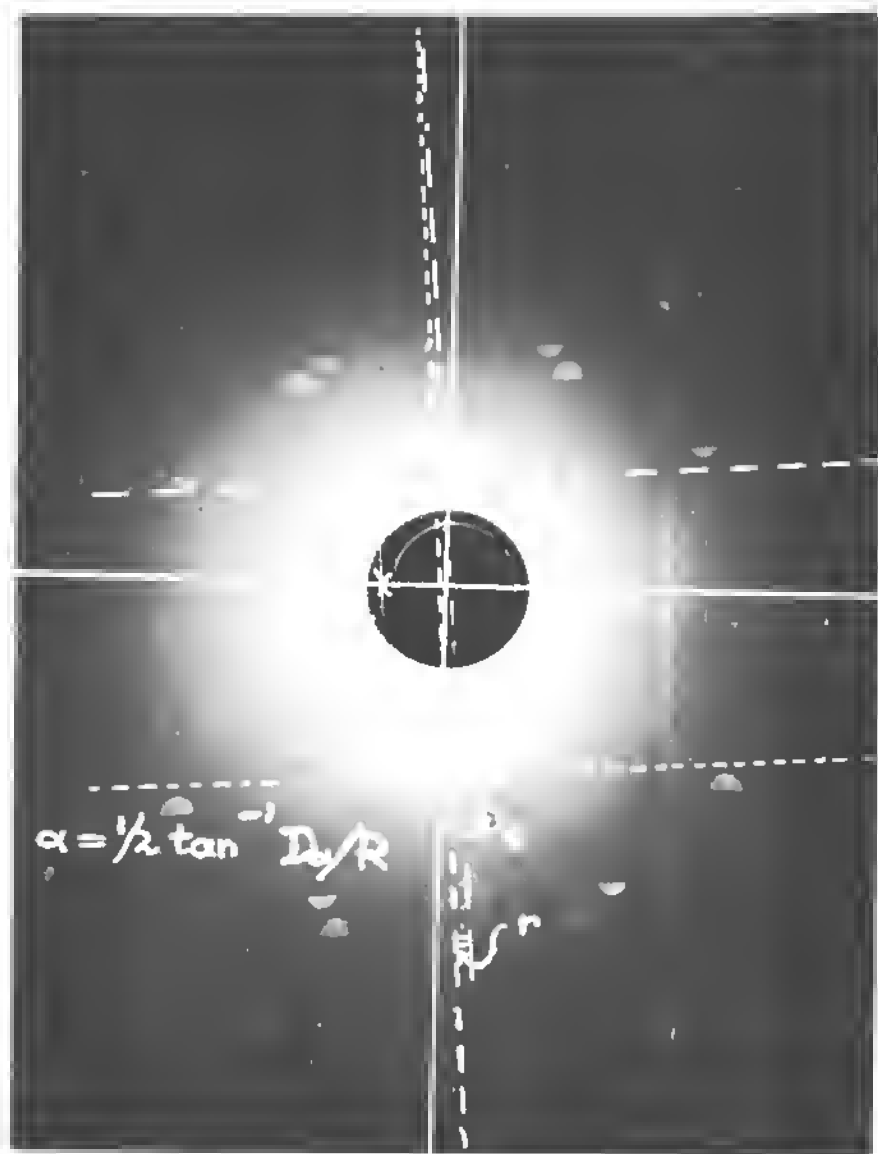


Fig. 12.14 Analysis of Bicrystal Laue pattern. Connection of corresponding Laue points: tilt ( $\theta_1$ ) and twist  $\theta_3$  from

$$\tan 2\theta_{1A} = [D_t/R]_A$$

$$\tan 2\theta_{1B} = [D_t/R]_B$$

tilt

$$\theta_2 = \text{rotation} = \angle r;$$

$$\tan 2\theta_{3A} = [D_t/R]_A$$

$$\tan 2\theta_{3B} = [D_t/R]_B$$

twist

$R$  = distance of bicrystal surface  
to photoplate

Finally, the actual orientation of the plane of cut with respect to the crystal lattice or the grain boundary has to be fixed.

This is most easily done by giving a flat or mirrorlike polish to the surface. The reflection of a light beam can serve as a reference guide in order to bring the normal to the polished plane into coincidence with the x-ray beam. A Laue diagram then reveals the angles between the normal of this plane and two chosen crystallographic directions in one of the single-crystal components of the bicrystal. These values can then be recalculated in terms of the reference previously chosen. An analysis of the angles of misfit is shown on an actual Laue-pattern in Figure 12.14.

The result of the original orientation procedure can easily be verified for each slice of the bicrystal cut from the boule by point-source light reflection (preferably laser light). The orientation difference of small crystallites visible in etch figures corresponds to the seed-crystal orientation (see Figure 12.15). Dark-field microphotography also reveals the tilt angle very clearly between the individual crystalites (see Figure 12.16).

The same methods are applied in the growth of compound bicrystals of the  $A_{III}B_V$  type. For example, R. K. Mueller et al.<sup>8</sup> studied InSb bicrystals grown with [111] seeds. In this case, however, the dangling bonds may appear on either of the two groups of atoms. This leads to two different kinds of boundaries based on either the  $\alpha$  dislocations (group III bonds) or the  $\beta$  dislocations (group V bonds). It is important to define whether dislocations accept electrons in  $p$ -type material. If the dislocations accept electrons, the boundary charges up negatively and presents a barrier to current flow in  $n$ -type material. If the dislocations donate electrons, the boundary becomes positive and presents a more pronounced barrier in  $p$ -type material.

Mueller found, basically, coincidence between the results of his studies on InSb grain boundaries and those of Gatos and coworkers but discrepancies between his results and earlier theoretical studies by Holt, who predicted acceptor character throughout (see Table 12.1). The free bond at the column III element ( $\alpha$ ) is generally acceptor type; and the free bond at the column V element is donor type. This is in line with the established character of these atoms. The higher filling of the  $p$  orbital in the case of antimony suggests donor type. Mueller found, however, that the environment can change this simple rule. Although, the  $\alpha$  boundaries are acceptor type in  $n$ -type doped crystals of InSb, as expected, and the  $\beta$  boundaries donor type, as expected, the  $\alpha$  boundaries are also donor type in  $p$ -type material where acceptor type should be expected (and was measured by Gatos et al.). Here, we have to consider that the degree of doping can play an important role in the relative position of the dislocation levels with respect to the Fermi level. As the dislocation levels are closely spaced, they represent a local band with a finite number of states:  $2N$  ( $N$  = number of dangling bonds). As Mueller dis-

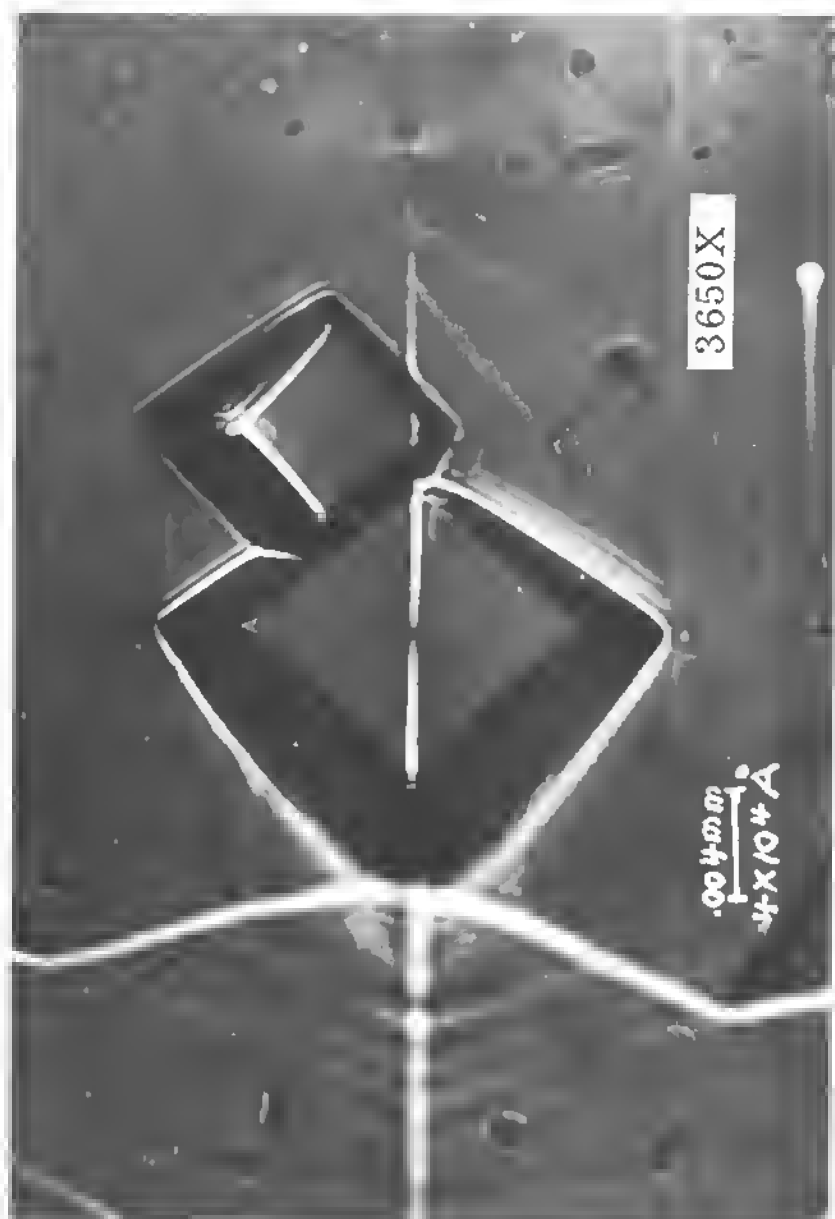


Fig. 12.15 Typical etch figure crossed by grain boundary under oil-immersion microscope; 3650 $\times$  magnification.

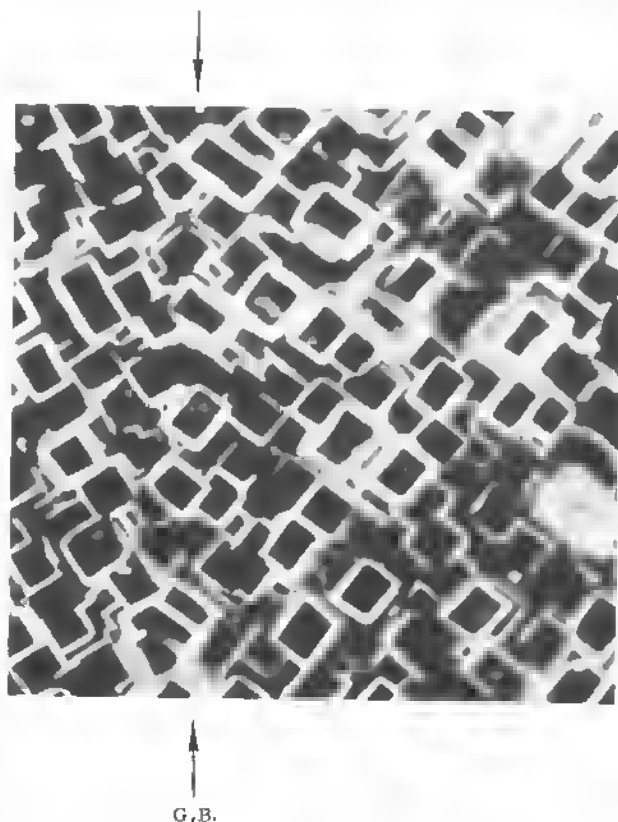


Fig. 12.16 Dark-field photo of etched bicrystal surface ( $\theta_1 = 20^\circ$ ). Line of grain boundary is marked by arrows.

cusses, it can be shown that such bands ideally contain  $3N/4$  ( $\alpha$ ) respectively  $5N/4$  ( $\beta$ ) more electrons than there are states in the valence band. Therefore, dislocations, boundaries, or free surfaces with  $N$  dangling bonds (containing  $2N$  states) are neutral if the boundary band is filled to contain  $3N/4$  and  $5N/4$  electrons, respectively. Whether this structure shows donor or acceptor character, however, depends on the free energy of an electron in the boundary band. The free energy, in turn, can be higher than the Fermi level at a given temperature and doping level, and thus electrons move from the dislocation level into the conduction band (donor character); or in the other case, electrons move into the valence band, and the boundary displays acceptor character. Especially for the  $\alpha$  boundary in  $p$ -type material, it is therefore possible to display donor character also, when the Fermi level is below the  $\frac{3}{4}$  filling level with respect to the valence band (low temperatures).

Table 12-1<sup>a</sup>

Dislocation type	Environment	Experimentally observed type		Behavior predicted from suggested models		
		Mueller	Gatos et al. <sup>a</sup>	Mueller	Gatos, Lavine <sup>b</sup>	Holt <sup>c</sup>
$\alpha$	$n$	Acceptor	Acceptor	Acceptor	Acceptor	Acceptor
$\alpha$	$p$	Donor	...	Donor	Acceptor	Acceptor
$\beta$	$n$	?	Donor	Donor	Donor	Acceptor
$\beta$	$p$	Donor	...	Donor	Donor	Acceptor

<sup>a</sup> H. C. Gatos, M. C. Finn, M. C. Lavine, *J. Appl. Phys.*, **32**:1174 (1961).

<sup>b</sup> H. C. Gatos, M. C. Lavine, *J. Electrochem. Soc.*, **107**:427 (1960).

<sup>c</sup> D. B. Holt, *J. Appl. Phys.*, **31**:2231 (1960).

## REFERENCES

1. Couling, S. R. L., and R. Smoluchowski: Anisotropy of Diffusion in Grain Boundaries, *Phys. Rev.*, vol. 25, no. 12, pp. 1538-1542, December, 1954.
2. Tweet, A. G.: Properties of Grain Boundaries in Gold-doped Germanium, *Phys. Rev.*, vol. 99, no. 4, pp. 1182-1189, Aug. 15, 1955.
3. Mataré, H. F., and H. A. R. Wegener: Oriented Growth and Definition of Medium Angle Semiconductor Bicrystals, *Zschr. f. Phys.*, vol. 148, pp. 631-645, 1957.
4. Mataré, H. F.: General Considerations concerning the Double-crucible Method to Grow Uniformly Doped Germanium Crystals of High Perfection, *Solid State Electronics*, vol. 5, no. 2, pp. 163-167, 1963.
5. Barret, C. S.: "Structure of Metals, Crystallographic Methods, Principles, and Data," McGraw-Hill, New York, pp. 26-44, 1952.
6. *Ibid.*, pp. 88-101.
7. Mataré, H. F.: Grain Boundary Structure and Carrier Transport in Semiconductor Crystals, *Zschr. f. Naturf.*, vol. 10a, no. H8, pp. 640-652, 1955.
8. Mueller, R. K., and R. L. Jacobson: Alpha and Beta Grain Boundaries in Indium Antimonide, *J. Appl. Phys.*, vol. 33, no. 7, pp. 2341-2345, July, 1962.

## 12.3 BICRYSTAL GROWTH AND PERFECTION

With the careful procedures of seed alignment described, one step is taken in order to achieve perfect grain-boundary growth. The other conditions lie in the crystal-growth equipment and are mainly connected with the temperature control during growth.

As in all monocrystal growth, the bicrystal requires horizontal and vertical gradient control to at least  $\frac{1}{10}$  of a degree at the melting point. If a Czochralski crystal pulling unit allows to grow dislocation-free monocrystals, it also allows growing perfect bicrystals. The monocrystalline sides of these bicrystals have the defect number corresponding to the one attained in normal pulling operations. This means that the bicrystal halves must have a perfect Laue pattern for example, the one shown in Figure 12.17 for a silicon bicrystal. The perfection of the boundary itself is established by surface etching and microscopy along the boundary. If the grain boundary does not show any irregular deviations from a perfect line across the crystallites, it can be considered well grown (see Figure 12.18). For a larger bicrystal section (magnification  $500\times$ ) this is shown in Figure 12.19.

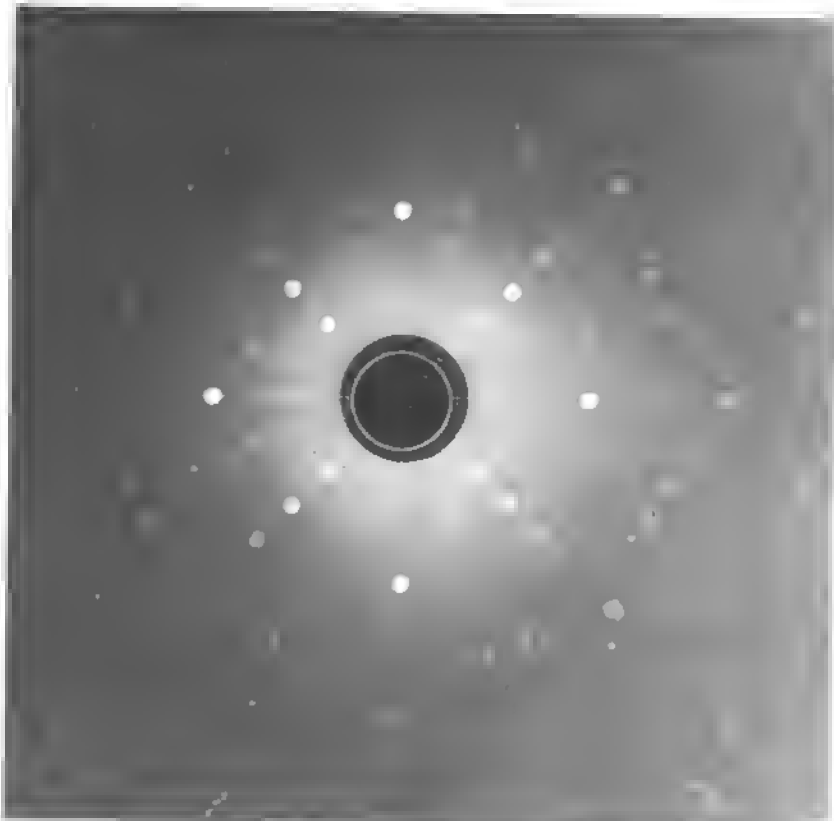


Fig. 12.17 Laue pattern of one side of silicon bicrystal showing perfection of crystal adjacent to grain boundary.



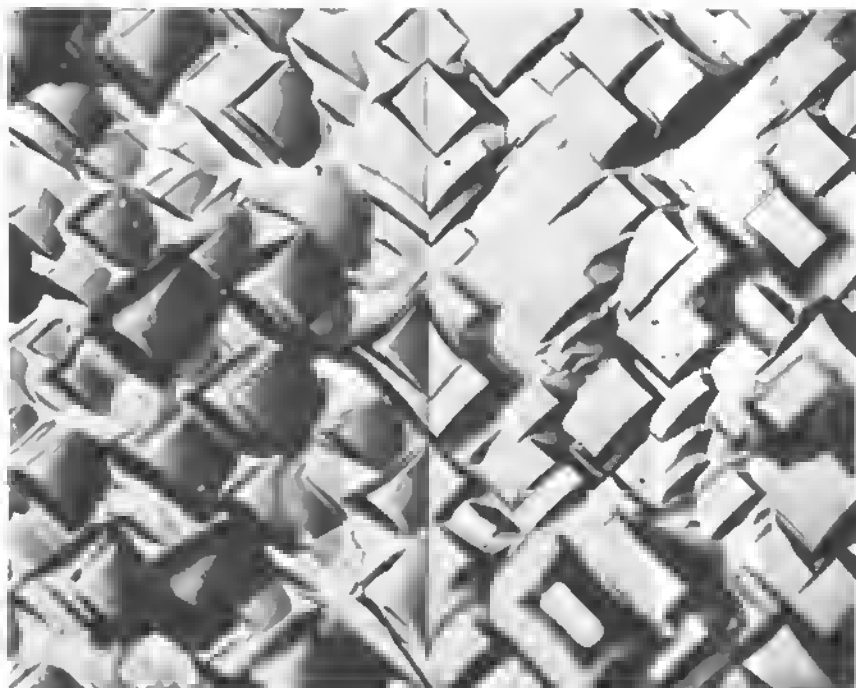


Fig. 12.18 Etch pattern of bicrystal surface: germanium  $[100] - \theta_1 - [100]$ ;  $2\theta_1 = 15^\circ$ .  $1300\times$ .

The errors in the orientation as carried through by the Laue pattern technique given in Section 12.2 are mainly dependent on the precision with which a distance can be measured on the film. For the two angles  $\theta_1$  and  $\theta_3(t)$  defined by  $\theta = \frac{1}{2} \tan^{-1} d/d_0$  ( $d$  = distance between x-ray beam and spot on the film and  $d_0$  = film to specimen distance, see Figure 12.4) the error depends mainly on the precision with which the  $[100]$  reflection can be brought into coincidence with the reference center of the film and the precision with which this center coincides with the point at which the x-ray beam penetrates the film. Both values of  $\theta_1$  and  $\theta_3$  are limited only by the errors with which the distance on the film can be measured. This limit is of the order of 0.05 mm. The most probable error in  $\theta_1$  is  $\Delta\theta_1 \simeq \frac{1}{2} \Delta d/d_0 \simeq 4'$ . The third angle  $\theta_2(r)$  is measured directly on the film. A somewhat similar situation exists as in the previous measurement, except that the reference is a line going vertically through the x-ray beam.

In  $\theta_2 = \tan^{-1} d_1/d_2$  ( $d_1$  = distance between x-ray beam and spot in the direction  $90^\circ$  to the reference line, and  $d_2$  is the distance between the Laue spot and the x-ray beam along the reference line),  $d_1$  is made close to zero.

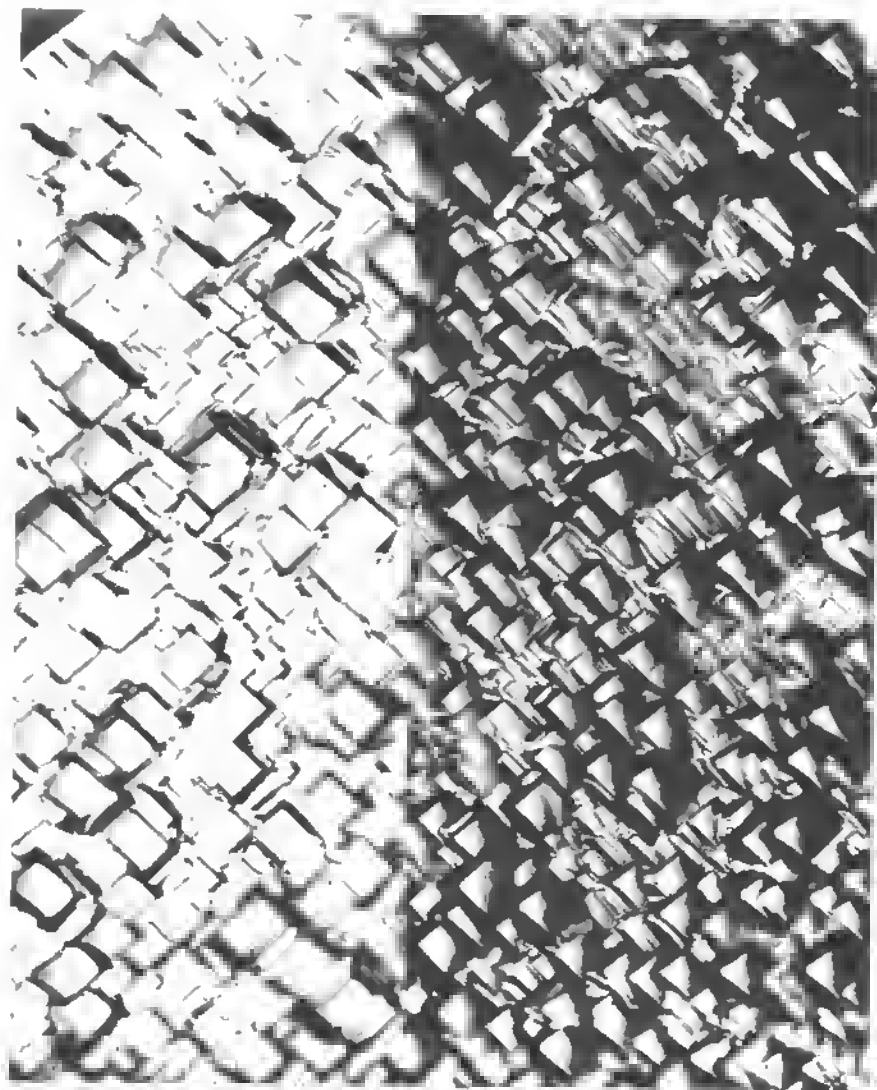


Fig. 12.19 Tilt grain boundary as above. Magnification  $470\times$ .

The error in these measurements is about 7/100 mm.  $d_2$  is generally of the order of 3 cm. This leads by reasoning analogous to the previous calculation to a probable error:

$$\Delta\theta_2 = 0.07 \frac{360}{2\pi \cdot 30} \cdot 60 \simeq 8' \text{ (8 minutes of an arc).}$$

After the crystal is aligned, the goniometer is transferred to the cutoff machine. The saw cuts the crystal in a direction parallel to the x-ray beam and vertical to the goniometer, since the crystal was aligned for this direction. This results at best in an accuracy of 30 minutes of arc. The cutting operation leaves the crystal surface with a roughness of the order of 0.003". Over the smallest dimension of the slab (about 1"), this gives rise to an error of 10'.

Now orientation and cutting are repeated for each slab, resulting in the quarter-square-based-column single crystal seeds. The errors due to the Laue technique and the saw-blade alignment are the same as before.

The effect of surface roughness, however, is magnified, since now the smallest dimension on each side is 0.0250". This increases this error to about 40'. The single crystal seeds are then placed in the pulling fixture. The final alignment of these against the reference surface then gives rise to the last error. If it is assumed that the machining was accurate to at best 0.001", the error is 14'. Since two crystals are required for a bicrystal seed, their errors necessarily combine. This effect may be canceled if it can be assumed that the error is the result of two error components along the crystallographic directions.

Table 12.2 gives a comparison of values determined by the Laue back-reflection technique. The value of  $\theta_1$  tried for is designated as ideal;  $\theta_2(t)$  and  $\theta_3(r)$  should be ideally zero. It is obvious that the alignment of the single

Table 12-2<sup>1</sup>

Ideal $2\theta_1(i)$	Experimental		
	$2\theta_1(t)$	$2\theta_2(t)$	$2\theta_3(r)$
30°	30° 44'	21'	55'
25°	25° 32'	70'	30'
20°	20° 20'	26'	11'
15°	14° 51'	58'	13'
10°	9° 1'	31'	17'
5°	3° 43'	34'	8'
Standard deviation	±46'	±44'	±27'

crystal in its goniometer by x-ray methods causes the smallest error. Improvements, if possible, should be concerned with the various mechanical adjustments during the alignment process.

First the saw blade could be aligned by the use of a mirror and an autocollimator. This could cut down this error to 10'. The surface of the crystal after the cutting action could be improved by polishing and etching.

If a still higher precision is required, additional steps in the preparation of the seed crystals are necessary. After each cutting operation on the saw, the cut slab or column is once more mounted on the goniometer and aligned by the Laue method. Then the goniometer is transferred to the magnetic chuck of a grinder, and the surface is ground flat. Grinders available are capable of reproducing a surface flat to about 0.005". This gives rise to an error of 4' (linear dimensions of the crystal in the 0.500" range). Alignments of chuck and goniometer are accurate to about 0.001" out of 3" or about 1'.

For still higher precision, mechanical problems have to be eliminated. This can be accomplished by the design of a goniometer that can be used directly as a pulling fixture. A device of this nature could be used for alignment of single crystals by Fankuchen's<sup>2</sup> equi-inclination method with attendant improvement in precision.

The precision of alignment by Geiger counter can be made to depend mainly on the slit width of the counter (0.003") and the specimen-to-counter distance (7"). Here the error could decrease to 2', since no cutting and transfer error occur.

It is unlikely that such precision is needed for medium-angle bicrystals. In Table 12.2 we note that the standard variation for  $\theta_1$  represents increasing percentages for decreasing angle values:

$2\theta_1$	Standard deviation, percent
30° 44'	2.40
25° 32'	3.00
20° 20'	3.75
14° 51'	5.10
9° 1'	8.40
3° 43'	20.0

It is therefore extremely doubtful that bicrystal alignment can produce predictable lattice relations for misfit angles smaller than  $\theta_1 \approx 10^\circ$  ( $2\theta_1 \approx 20^\circ$ ).\*

\* Compare Ch. 12.4.



Fig. 12.20 Strong surface etch of bicrystal revealing normal dislocation density around artificial grain boundary. Magnific;  $1000\times$ .

Summarizing the error per bicrystal parameter in the different techniques gives the following possibilities:

Technique	Probable error per bicrystal lattice parameter
Present	52'
Optical Alignment of saw, increase in seed dimension	25'
Addition of a grinding step	11'
Pulling fixture as goniometer	2'

### Perfection

Independently of the orientation precision, the bicrystal perfection plays a role in the electronic properties of the grain-boundary barrier. If, for example, a high dislocation density appears in the neighborhood of the grain boundary, the coherent form of the barrier may be disrupted. Also impurity clusters can produce localized breakdown areas within the barrier layer. Careful growth, however, produces generally perfect bicrystals, and the grain boundary is as such no cause for increased dislocation densities or impurity clustering (the preferred diffusion is discussed in Chapter 13). Figure 12.20 shows that the etch-pit density in the neighborhood of the grain boundary at a bicrystal interface is not abnormal. This was observed in all cases.

As we saw earlier (Section 7.2), lineage boundaries of the usual misfit in the minute-of-an-arc range have a tendency to be disrupted, sometimes by climb, in the stress field of a medium-angle grain boundary.

Revealing more detail of the innermost structure of grain boundaries and assessing the actual width of the dislocation layer has been tried. Because this area is of the order of 20 lattice constants ( $\sim 100 \text{ \AA}$ ), only a developed scanning-beam electron microscope with small beam width and a resolution of  $\sim 20 \text{ \AA}$  could reveal detail. Electron microscopy in transmission has not been successful so far, and replication methods have not revealed any detail. Figure 12.21 shows an electron micrograph of a germanium tilt boundary ( $2\theta_1 \simeq 20^\circ$ ) using a direct carbon replica preshadowed with platinum metal at approximately  $27^\circ$ . The magnification gives the distance of  $1 \mu$  at about  $0.5 \text{ cm}$ .

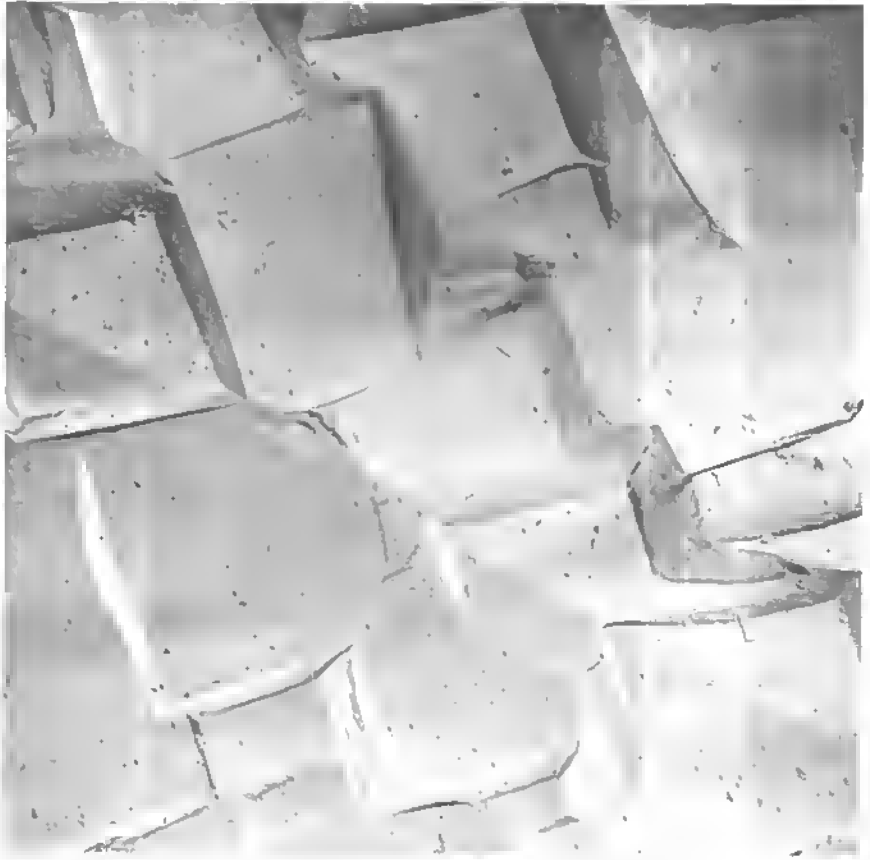


**Fig. 12.21** Electron micrograph of germanium bicrystal. Angle of tilt  $20^\circ$ . Specimen prepared and etched. Direct carbon replica preshadowed by platinum metal at approx.  $27^\circ$ . Magnification  $5000\times$ .

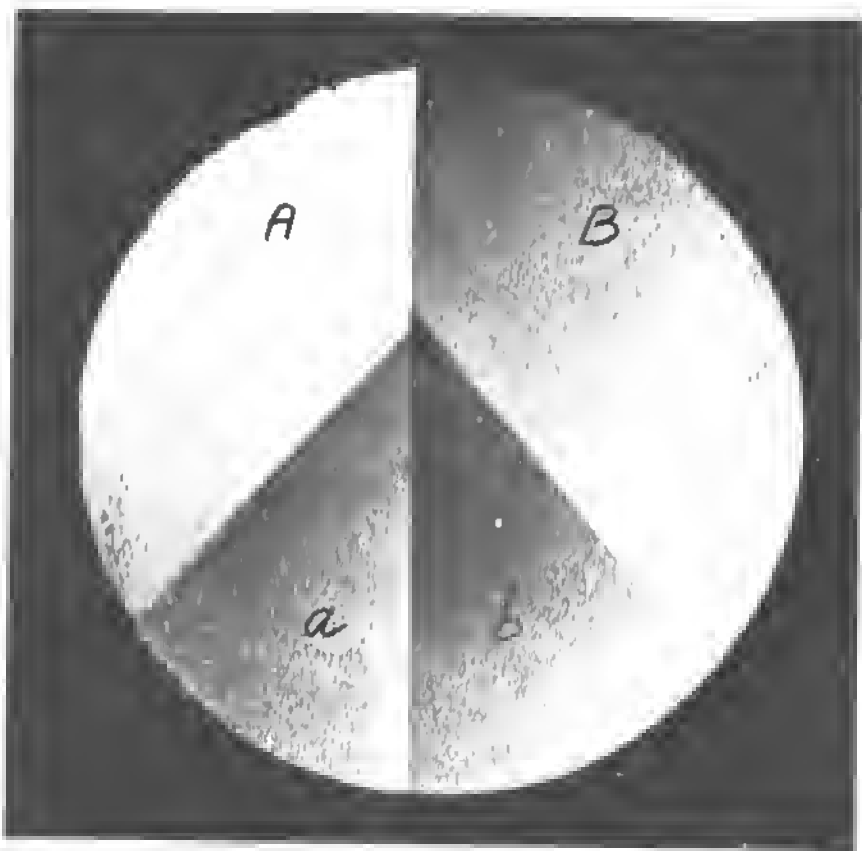


Fig. 12.22 Photo ( $2.8\times$ ) of cut trough grown bicrystal boule with twins generated at grain boundary. Tilt angle  $\theta \approx 20^\circ$  of two  $[100]$  seeds A and B: new grain boundary  $a-b$  is  $[100] - (\theta = 5^\circ) - [100]$ .





Fig. 12.23 Same bicrystal as 12.22 ( $53\times$ ) at twin nucleation points at grain boundary. Twin rotations between A —  $a$  and B —  $b$ .

As we mentioned, the tendency for twinning can eliminate the broken bonds. Especially in silicon, many twinning relations occur, and grain boundaries can act as the source for the formation of twins. A typical example is shown in Figure 12.22. Here the original bicrystal is the A — B structure with a tilt of  $20^\circ$ . First-order twins originate at the boundary and form a new structure between individuals  $a$  and  $b$ , but in a straight-line continuation with the original grains so that the new grain boundary has an angle of tilt of only  $5^\circ$  between  $a$  and  $b$ .

There is no visible disturbance at the points of origin of these twins at magnifications of  $\times 76$  (see Figure 12.23) and at a magnification of  $\times 650$  (see Figure 12.24) where the source of the twin is apparently a low-energy rotation in the lattice, giving rise to a new and stable lattice configuration of lower energy. This kind of disturbance is the most frequent one found in silicon and to a minor degree in germanium and III-V compound bicrystals.

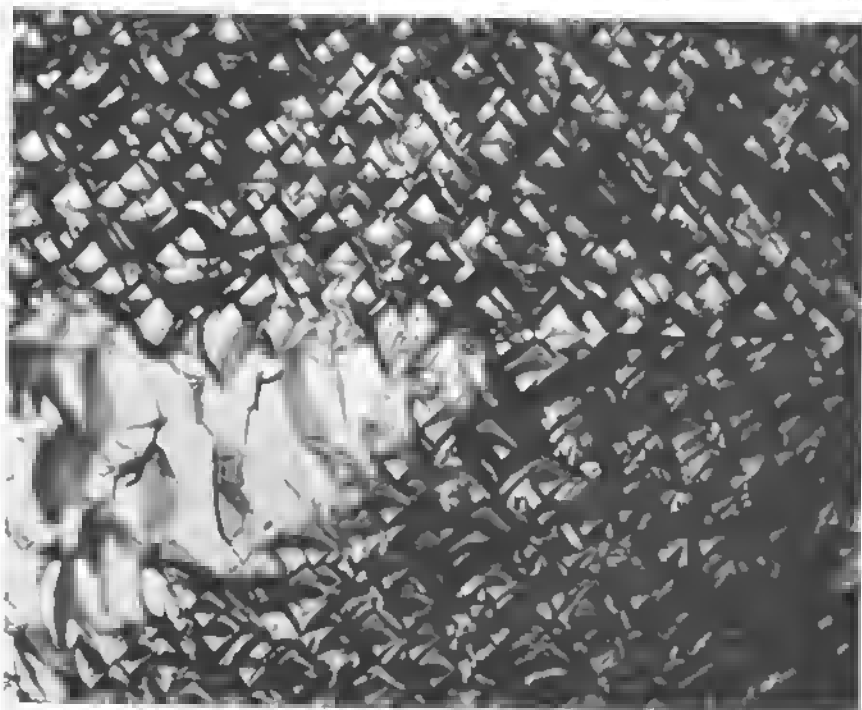


Fig. 12.24 Same bicrystal as 12.22 ( $450\times$ ) focused on twin growth point B — b.

## REFERENCES

1. Mataré, H. F., and H. A. R. Wegener: Oriented Growth and Definition of Medium Angle Semiconductor Bicrystals, *Zschr. f. Phys.*, vol. 148, pp. 631–645, 1957.
2. Fankuchen, I.: U.S. Patent 2, 392, 528, 1942.

## 12.4 GRAIN-BOUNDARY DIFFUSION AND IMPURITY DISTRIBUTION

We have already touched on the questions of the impurity influence on the electronic behavior of dislocations. An isolated edge-dislocation pipe has a pronounced impurity atmosphere (Cottrell atmosphere) because of the far-reaching influence of dilation and compression regions. In Section 7.2 (see especially Figure 7.10) we saw that a narrow spacing of the dislocation pipes leads to a closer overlap of the alternating dilation and compression zones, with some cancellation of the effect on surrounding impurities. A few remarks

concerning the impurity influence in the case of silicon boundaries were made in Section 11.2. However, the issue is important enough to be considered more extensively, because it is a recurring question in all meetings on dislocations and dislocation arrays and an essential part of the structural theory of cold-worked metals, hardening, fracture theory, phase transformation, plastic deformation, and the like.

Detailed work on grain-boundary diffusion was first carried out by S. Smoluchowski and coworkers. At that time, many experimental findings that seemingly contradicted one another had to be explained. The systematic work of Smoluchowski has helped in understanding a number of these results and properly defining the parameters that are significant in grain-boundary diffusion. Several facts are important in this context and have been neglected in a number of studies.

1. The stress field around a dislocation is felt specifically at any free surface. As the grain boundary approaches a free surface, the forces balancing the internal stress field are decreasing, and the material tends to "crack" at the surface in a form described in Section 7.2, specifically in Figure 7.9. Such microcracks form in all cases where bicrystals are polished and etched down, and subsequent diffusion reveals "spike behavior" down into the material for an appreciable distance ( $> 20 \mu$ ) because of the heat treatment.

2. An isolated dislocation line acts as a pipe in a direction parallel to the dislocation. It is not apt to show enhanced diffusion vertically to the pipe or array.

3. The free or dangling bond as a main contributor to the dislocation behavior and its effect on the diffusion are partially eliminated in grain boundaries with paired or rotated bonds (screw or twin dislocations in "repaired" lattice structures). See Sect. 4.4.

4. In medium-angle grain boundaries ( $1^\circ < \theta < 25^\circ$ ), the pipe overlap is complete and properties should not be much different parallel or orthogonal to the dislocations. Small-angle boundaries ( $\theta < 1^\circ$ ) on the contrary show strong differences in directional diffusion experiments.

5. Large-angle boundaries (beyond the Shockley-Read energy maximum) are in all probability rather disordered lattice structures with high-preferential diffusion parallel and orthogonal to the dislocations;  $D_{\parallel}/D_{\perp} \approx 1$ .  $D_{\parallel}$  = diffusion coefficient parallel to dislocation;  $D_{\perp}$  = diffusion coefficient orthogonal to dislocation.

As a consequence, the extreme cases are isolated dislocation pipes of the lineage type with direction-dependent preferential diffusion and high-angle boundaries with strongly enhanced diffusion, not dependent on orientation.

The intermediate case of medium-angle boundaries has caused puzzling effects in diffusion work, because a precise overlap of dilation and compression

regions in adjacent pipes partially cancels the stress field, decreases the Cottrell atmospheres, and shows small diffusion enhancement except near the free surfaces.

We now analyze the major conclusion arrived at by several researchers in this field. R. Smoluchowski<sup>1</sup> in his work with copper bicrystals ( $\theta \approx 15^\circ$ ) makes use of the *rod model* of the dislocations. It is assumed here that the dislocations generate crystal areas of highly distorted form within which the diffusion coefficient and the activation energy are thought independent of orientation (Mott). The assumption that the grain boundary is a uniform (or partially uniform) slab of material of high diffusivity is the basis of the Fisher-Whipple diffusion theory and its application to practical diffusion problems where boundaries are involved.<sup>1, 3, 6, 11, 12</sup>

In applying this theory, Smoluchowski uses also another assumption concerning the flow of the diffusant, namely, that the material diffusing along the grain boundary (direction  $y$  in Figure 12.25a) is being lost into the two adjacent grains by volume diffusion in a direction perpendicular to the grain boundary (direction  $x$ ). Smoluchowski points out that this assumption eliminates the possibility of calculating the shape of the *cusps* for small  $y$ , that is, in the proximity of the intersection of the grain boundary with the original interface where the concentration gradient (and the direction of the diffusion) is approximately perpendicular to the outline of the cusp. Queisser et al.<sup>6</sup> later derived a relation for the spike velocity as a function of  $D_v$  (volume diffusion coefficient) and  $\phi$ , the spike angle (see Figure 12.25b), which allows finding the factors  $W_0$  and  $W_D$  expressing roughly the additional number of impurities and dislocation generated vacancies there, respectively. The main results of Smoluchowski's treatment based on the Fisher-Whipple columnar diffusion are in his formulation:

1. There is a critical misfit angle  $\theta_c$  of the grains where grain-boundary diffusion begins. For smaller misfit angles, pipes do not overlap sufficiently to result in enhanced diffusion (see  $\theta_c$  in Figure 12.25c).
2. As the temperature increases, the relative contribution of the grain boundary to the diffusion is decreased (increase in  $\theta_c$  in Figure 12.25c; curves are normalized in order to give equal penetration at  $\theta = 45^\circ$ ).

In careful measurements of the diffusion of Zn into copper bicrystals, Flanagan and Smoluchowski (see Figure 12.26) measured a rather small shift of  $\theta_c$  with temperature, but in all cases the critical misfit angle is at or about the angle for the energy maximum of the grain boundary according to the Read-Shockley energy expression (see Section 4.1 and Figure 12.25c).

Smoluchowski defines an apparent activation energy  $Q_A$  from the limit penetration in the  $y$  direction in the grain boundary:

$$y_L^2 = f(t, T) \exp\left(-\frac{Q_A}{RT}\right). \quad (12.3)$$

In the bulk  $Q_A = Q_v$ :

$$y_v^2 = \text{const} \cdot t \exp\left(-\frac{Q_v}{RT}\right), \quad (12.4)$$

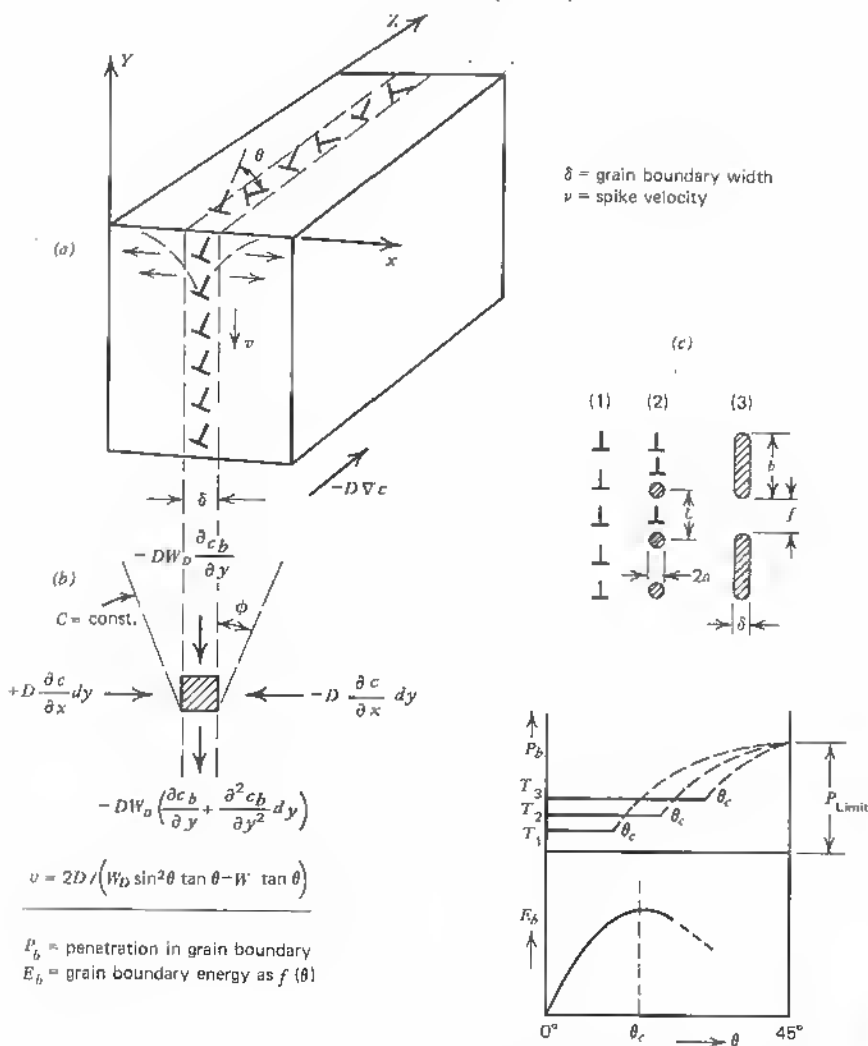


Fig. 12.25 (a) Coordinate system used in the discussion of diffusion in grain boundaries. (b) Boundary conditions along the diffusion spike and velocity expression. (c) Structure of grain boundaries for increased misfit (1)  $\rightarrow$  (2)  $\rightarrow$  (3) and penetration as  $f(\theta)$  for different temperatures according to Smoluchowski.<sup>1</sup>

where  $t$  = time,

$T$  = temperature,  $^{\circ}\text{K}$ ,

$R$  = gas constant  $= 6.06 \cdot 10^{23} \cdot k$ ,

$k$  = Boltzmann constant.

$f(t, T)$  is a slowly varying function of  $T$  or independent of  $T$ .

In conjunction with the usual expressions for the diffusion coefficients  $D_B$  in the grain boundary and  $D_v$  in the bulk:

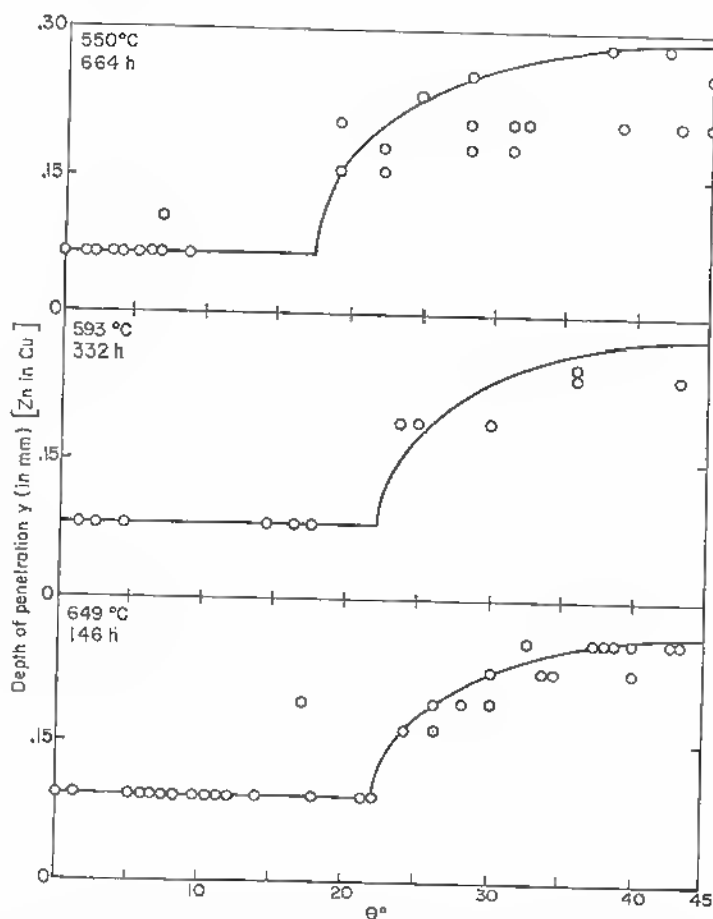


Fig. 12.26 Measured data of penetration (Zn) into copper bicrystals as a function of tilt angle (after Flanagan-Smoluchowski, Phys. Rev. 23, 7 (1952)).

$$D_B = D_{B_0} \exp\left(-\frac{Q_B}{RT}\right), \quad (12.5)$$

$$D_v = D_{v_0} \exp\left(-\frac{Q_v}{RT}\right), \quad (12.6)$$

the apparent activation energy  $Q_A$  can be expressed by  $Q_v$  and  $Q_B$ , the activation energy in the boundary depending on the assumptions for the grain-boundary misfit and the extension of the supposed rod structure, respectively, as the misfit angle increases (see Figure 12.25c). Smoluchowski finds an increase in  $Q_A$  as the misfit increases in accordance with the theoretical model (see Table 12.3).

Table 12.3

Angle		25°	30°	35°	40°	45°
Rod separation	$Q_A$ , cal/mole (experim.)	1960	4050	7210	7500	7500
	$Q_A$ , cal/mole (theoret.)	2160	4000	7200	7500	7500
	$L$ , Å (experim.)	16	8.5	5.2	Slab	
	$L$ , Å (theoret.)	10	6.8	5.1	Slab	

It is striking how well the calculated  $Q_A$  values agree with those measured from penetration values.

Later criticism of Smoluchowski's results by Turnbull and Hoffman<sup>3</sup> concentrates on the assumed vanishing diffusion enhancement for small angles of misfit. It seems that Smoluchowski's assumption of highly distorted areas with activation energy independent of orientation is not realistic. In fact, the more the pipes are separated, the more pronounced their directional influence on diffusion. Diffusion parallel to the pipes (direction  $y$  in Figure 12.25a) is even stronger for isolated pipes than for overlapping pipes with dilation-compression force cancellation. Such force cancellation, with attendant elimination of the Cottrell atmospheres, is most effective for medium-angle grain boundaries, that is, for the range  $1^\circ < \theta < 25^\circ$  or dislocation distances between 10 and 300 Å or 2 to 60 lattice constants. For angles in the range of a few degrees and below, the overlap is incomplete, and the picture of isolated pipes has to be applied. The stress field around a dislocation extends over many lattice constants,<sup>8</sup> and one would expect isolated pipe behavior for separations  $D > 60a_0$ .

Turnbull and Hoffman point out that preferential diffusion parallel to the dislocation pipes should be assumed for lineage and polygonization boundaries.

In careful diffusion runs of silver in copper bicrystals, Couling and Smoluchowski<sup>2</sup> found that the diffusion was enhanced as  $\theta$  increases from about  $10^\circ$  to  $45^\circ$  and decreases again from  $45^\circ$  to  $80^\circ$ . The dependence on the orientation of the boundary was of minor importance. Below  $\theta = 10^\circ$  and above  $\theta = 80^\circ$ , the diffusion in boundaries was unmeasurably small (see Figure 12.27). According to Turnbull and Hoffman<sup>3</sup> separated dislocation pipes would show a diffusion constant variation, as described in Figure 12.28 for small angle  $\theta$ . With increasing overlap ( $\theta$  increasing), the diffusion peaks level off as they get closer together and finally come close to the bulk diffusion value  $D_B$ . (This is at an angle of misfit of  $10$  to  $20^\circ$ ). As the angle increases, the individual pipe diffusion is no longer observed (overlap), and the boundary diffusion increases again to an angle of  $45^\circ$ , as shown in Figure 12.27. The individual pipe diffusion should be about equal to the  $45^\circ$  block diffusion if no microcracking is assumed. Turnbull and Hoffman find an analogous increase in activation energy with increasing misfit angle. These results, although yielding somewhat higher diffusion constants, are consistent with Smoluchowski's results. The grain boundaries were very poorly produced and show large deflections and inhomogeneities responsible for the nonuniform penetration

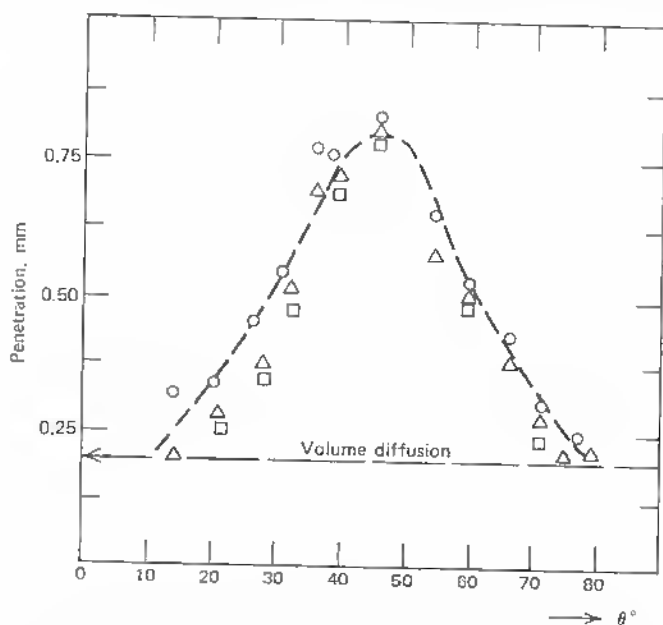


Fig. 12.27 Grain-boundary penetrations as a function of  $\theta$  for  $\phi = 0^\circ$ ,  $45^\circ$ ,  $90^\circ$ , O,  $\Delta$ ,  $\square$ , respectively. (After Couling and Smoluchowski.<sup>2</sup>)



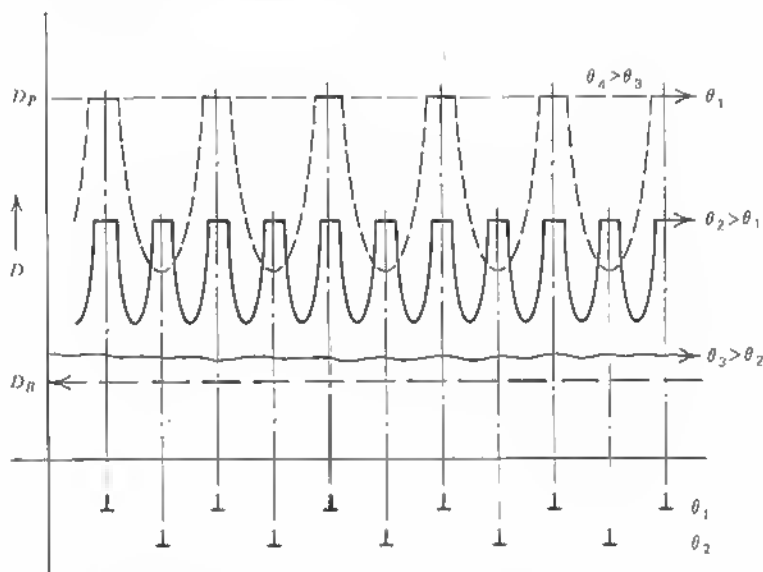


Fig. 12.28 Variation of grain-boundary diffusion coefficient parallel to pipes for small  $\theta$  ( $\theta_1 < 1^\circ$ ),  $\theta_2 > \theta_1$  and  $\theta_3 < 25^\circ$ ,  $\theta_4 > 25^\circ$  ( $\theta_{\max} = 45^\circ$ ).

measured. In a subsequently published paper,<sup>4</sup> the reasons for the partially different results of diffusion experiments on grain boundaries are reviewed, and facts are compiled that give credence to the assumption of a predominance of the dangling bond in accounting for the remarkable electronic properties of grain boundaries. It must be emphasized here that the bicrystals grown from silicon and germanium were specifically made to produce high barriers and that screw dislocations and twin relations were carefully avoided but that low energy boundaries were always used also in grain-boundary diffusion studies. None of the diffusion studies published to our knowledge has specified the electrical characteristics of the boundaries under study. The typical properties of grain boundaries, for example, the strong *p*-type behavior in germanium, cannot be explained by impurity segregation or diffusion. Mataré<sup>4</sup> points out that grain-boundary barriers of *n-p-n* type appear in crystals where the last solidifying parts are *n*-type, for example, antimony doping. Some researchers assume that copper plays a predominant role in these dislocations. But copper has a solubility that is exponentially decreasing at lower temperature (in germanium, the maximum is at  $875^\circ\text{C}$ ). If copper is accumulated in the dislocations during crystal growth, the supersaturation during the slow cooling process inactivates the copper electrically, and rapid cooling activates the copper atoms. This is the reverse of what happens to the

grain boundaries in germanium. Rapid cooling or quenching deactivates the  $p$ -type centers in the grain boundary.

Mention is also made of the proposition that the grain boundary as a region of higher local energy is the last part to freeze during crystal growth and that segregation therefore enhances copper accumulation. But assuming normal segregation constants, we find an unmeasurably small effect. The transition region from  $n$  to  $p$  is located where the fractional recrystallization lies, that is, at

$$g_{PN} = 1 - \left( \frac{K_2 Co_2}{K_1 Co_1} \right)^{1/(K_1 - K_2)}, \quad (12.7)$$

where  $Co_1$  = concentration of copper,

$Co_2$  = concentration of antimony,

$K_1$  = segregation constant for copper =  $1.5 \times 10^{-5}$ ,

$K_2$  = segregation constant for antimony =  $3 \times 10^{-3}$ .

Assuming for the sake of argument that copper is present at the same concentration as antimony,  $Co_1 = Co_2$ , we get

$$g_{PN} = 1 - (2 \times 10^2)^{-10^3/3} \simeq 1.$$

In this extreme case even the  $p$ -type zone due to copper would not develop at a measurable distance from the end of the solid phase. In addition during growth, the boundary is in constant contact with the liquid phase, and so the  $p$ -type layer does not originate on account of copper as an impurity.

Hoffman<sup>5</sup> has shown that, in effect, the penetration (or diffusion constants) parallel and vertical to the dislocations are very different. His results are summarized in Figure 12.29 and show how this difference decreases with increasing  $\theta$  for silver bicrystals. Such a curve cannot be considered a standard, however, because the kind of boundary (pure tilt or partial screw or twin) and the kind of diffusant have a strong influence on the extent of the stress field and the Cottrell atmospheres. As mentioned already, Qucisser et al.<sup>6</sup> applied the Fisher-Whipple formalism to the case of the spike diffusion in Silicon (see Figure 12.25b), but with the assumption of an additional flux of solute atoms from the boundary into the bulk, expressed by

$$W_0 = \theta b \exp \frac{U_i}{kT}, \quad (12.8)$$

where  $b$  = Burgers vector,

$\theta$  = angle of misfit,

$U_i$  = maximum binding energy of a foreign atom with atomic radius

$r_i = r_{Si}(1 + e_i)$ ,  $r_{Si}$  = atomic radius for Silicon.

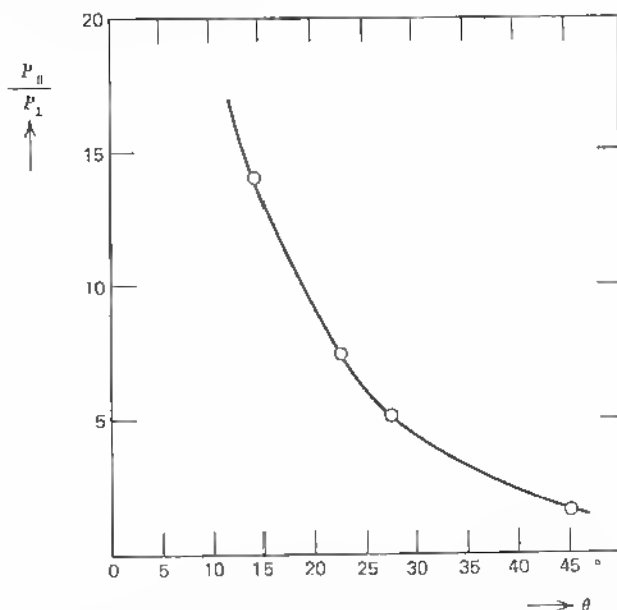


Fig. 12.29 Penetration ratios  $P_{\parallel}/P_{\perp}$  (parallel and perpendicular to dislocations) as a function of  $\theta$ . Measurements by Hoffman<sup>5</sup>.

Similarly a vacancy-controlled diffusion current down the dislocation core is controlled by

$$W_D = b\theta \exp \frac{U_D}{kT} \quad (12.9)$$

when  $U_D$  is the sum of  $U_l$  and the binding energies  $U_v$  and  $U_j$  for vacancies in compression and dilation regions, respectively.

Thus the diffusion process is described from the divergence of flux in the grain boundary plus the inward fluxes from the bulk sides and an additional flux in the  $z$  direction (see Figure 12.25b):

$$W_0 \frac{\partial c_b}{\partial t} = D \left[ \left( \frac{\partial c}{\partial x} \right)_+ - \left( \frac{\partial c}{\partial x} \right)_- \right] + DW_{D,y} \left( \frac{\partial^2 c_b}{\partial y^2} \right) + DW_{D,z} \left( \frac{\partial^2 c_b}{\partial z^2} \right), \quad (12.10)$$

where the derivatives with respect to  $x$  are limits as  $x \rightarrow 0$  from  $x > 0$  and  $x < 0$  sides of the boundary.  $c$  = concentration in the grains,  $c_b$  = concentration in the boundary region.

In assessing the results, Queisser et al. make certain assumptions concerning the dislocation type. For crystals grown isoaxially with a  $[100]$  growth axis

and  $\theta = 4.5 \pm 0.25^\circ$ , the Burgers vector is thought to be  $b_1 = \frac{1}{2}a$  [01 $\bar{1}$ ] along a [100] line. The dislocation spacing is given as

$$D \simeq \frac{b}{\theta} = 55 \text{ \AA}.$$

But the authors point out that their boundaries were not completely symmetrical and that a slight rotation can lead to a [110] main orientation with a Burgers vector  $\frac{1}{2}a$  [110], a case discussed by Hornstra<sup>7</sup> and leading to *pairing* of the dangling bonds. This would eliminate much of the electrical properties (preferred conductance along the boundary) and diminish the compression-dilation misfit used in the calculation of the binding energies.

The higher than usual bulk diffusion constants found near the surface of the samples and the flattening of the spike toward the inner part of the crystal point to a lattice disturbance in the sense of the picture of *microcracking* discussed earlier. It is also significant that the spike velocity decreases strongly toward the inside of the crystal ( $-y$  direction in Figure 12.25a) and the predeposit strength  $Q$  does not decrease but increases slightly.

Table 12.4 gives the interesting values given by Qucisser<sup>6</sup> et al. in this context, with a figure showing the decrease in spike velocity (to  $10^{-2}$  of the initial value) and the decrease of the relative spike depth compared with the junction depth as the spike moves into the crystal.

It is significant that these authors found that the diffusion coefficient  $D$  (at the tip of the spikes) is abnormally high near the free surface and decreases to normal values at a depth  $y_s/y_j$  of about 10  $\mu$ .

It seems, therefore, that an assessment of binding energies by way of  $W_0$

Table 12.4 Diffusion of Phosphorous in Silicon at 1050°C

$t$ (total diffusion time), hr	0.5	1.0	2.0	4.0	16	80.3	133
$y_j$ (junction depth), $\mu$ , smoothed	1.7	2.2	2.8	3.6	6.0	11.0	13.4
$y_s$ (spike depth), $\mu$ , smoothed	10.6	11.6	12.7	13.8	16.4	20.0	21.5
$\tan \phi$	0.147	0.185	0.230	0.290	0.425	0.750	0.900
$v$ (spike velocity), $\mu/\text{hr}$	2.6	1.4	0.8	0.4	0.13	0.03	0.02
$Q$ (predeposit strength), $10^{16} \text{ cm}^{-2}$	4.4	3.8	4.8	6.5	9.7	10.4	8.2
$D$ (diffusion coefficient), $\mu^2/\text{hr}$	0.232	0.174	0.145	0.114	0.070	0.045	0.042
$y_s/y_j$	6.2	5.3	4.5	3.8	2.8	1.8	1.6

and  $W_D$  values expressed by the spike velocity may be doubtful and that a much higher precision in the control of the actual boundary type is needed to correlate electrical behavior and impurity atmospheres clearly. There is no doubt that in silicon the complicated behavior of oxygen gives rise to stronger impurity influence on dislocations. Thermal donors and acceptors acting in conjunction with boundary vacancies and impurities<sup>9</sup> result in variations of the energy-level scheme of dislocations quite at variance to the case of germanium. The tendency of silicon to form higher-order twins and screw dislocations should lead to a lower diffusivity in such cases compared with the edge dislocation. Measurements on silver-twist boundaries by Love et al.<sup>10</sup> have shown that the self-diffusivity is about  $\frac{1}{10}$  of the values found for tilt boundaries. According to Love<sup>11</sup> it is probable that diffusion along random dislocations in the lattice is greatly different from diffusion along a dislocation array in which stabilizing interactions between the individual dislocations exist. This picture is again valid only for medium-angle grain boundaries and breaks down for very small misfit (below a few degrees) and very high misfit ( $\theta > 25^\circ$ ). The extreme stability of grown bicrystal interfaces was apparent in diffusion experiments on copper bicrystals when these were simultaneously subjected to slide.<sup>12</sup> The coefficient of grain-boundary diffusion was found to be only 30 percent higher here than in static boundaries. The formation of cavities, however, was an additional aspect that acts as a retarding mechanism.

In more recent work Pavlov et al.<sup>13</sup> review the available literature on dislocation diffusion. They find a concentration dependence  $\ln c = f(y)$  rather than  $\ln c = f(y^2)$ . In solving the diffusion equation for the boundary, Smoluchowski<sup>1</sup> discarded this case based on the boundary condition  $\partial c / \partial t = 0$  in the grain boundary at time  $t$ . Pavlov et al. used silicon samples subjected to antimony diffusion but used only crystals with random dislocations of varied densities. It is difficult to see how conclusions can be drawn from a statistical average of the effect of a number of very different dislocations, small-angle boundaries (lineage) and block boundaries (microcracks), of different orientation.

Much more refined work is needed apparently to correlate all effects clearly that may play a role in this difficult problem. Summarizing the probable situation with respect to individual dislocation pipes and tilt boundaries, the following scheme seems to be prevalent:<sup>14</sup>

$$0^\circ < \theta < 1^\circ : D_{\parallel} \gg D_{\perp} : D_{\parallel} \simeq 10^6 D_{\perp} : D_{\perp} \simeq D_b,$$

$$1^\circ < \theta < 20^\circ : D_{\parallel} \geq D_{\perp} \Rightarrow D_b,$$

$$20^\circ < \theta < 90^\circ : D_{\parallel} \simeq D_{\perp} \gg D_b,$$

where  $D_b$  = diffusion constant in bulk,

$D_{\parallel}$  = diffusion constant parallel to dislocation,

$D_{\perp}$  = diffusion constant perpendicular to dislocation.

## REFERENCES

1. Smoluchowski, R.: Theory of Grain Boundary Diffusion, *Phys. Rev.*, vol. 87, no. 3, pp. 482-487, Aug. 1, 1952.
2. Couling, S. R. L., and R. Smoluchowski: Anisotropy of Diffusion in Grain Boundaries, *J. Appl. Phys.*, vol. 25, no. 12, pp. 1538-1542, December, 1954.
3. Turnbull, D., and R. E. Hoffman: The Effect of Relative Crystal and Boundary Orientations on Grain Boundary Diffusion Rates, *Acta Metallurgica*, vol. 2, pp. 419-426, May, 1954.
4. Mataré, H. F.: Electrical Properties of Bicrystal Interfaces, *Zschr. f. Phys.*, vol. 145, pp. 206-234, 1956.
5. Hoffman, R. E.: Anisotropy of Grain Boundary Self-diffusion, *Acta Metallurgica*, vol. 4, pp. 97-98, 1956.
6. Queisser, H. J., K. Hubner, and W. Shockley: Diffusion along Small-angle Grain Boundaries in Silicon, *Phys. Rev.*, vol. 123, no. 4, pp. 1245-1254, Aug. 15, 1961. See also: Queisser H. J.: Dislocations in Silicon, *Festkörperprobleme II*, F. Sauter ed. F. Vieweg, 1963, pp. 162-187.
7. Hornstra, J.: Models of Grain Boundaries in the Diamond Lattice: 1. Tilt about  $\langle 110 \rangle$ , *Physica*, vol. 25, pp. 409-422, June, 1959.
8. Mitchell T. E.: The Stress around Groups of Dislocations in Face Centered Cubic Metals, *Phil. Mag.*, vol. 10, pp. 301-314, 1964.
9. Seybolt, A. V., J. H. Westbrook, and D. Turnbull: Mechanism for Grain Boundary Free Surface Hardening by Oxygen and Vacancy Interaction, *Acta Metallurgica*, vol. 12, pp. 1456-1457, 1964.
10. Love, G., and P. G. Shewmon: Self Diffusivity of Silver in Twist Boundaries *Acta Metallurgica*, vol. 11, pp. 899-906, August, 1963.
11. Love, G. R.: Dislocation Pipe Diffusion, *Acta Metallurgica*, vol. 12, pp. 731-737, June, 1964.
12. Blackburn, D. A., and A. F. Brown: Diffusion and Grain Boundary Slide in Copper Bicrystals, *Journal of the Institute of Metals*, vol. 91, pp. 106-113, August-September, 1962.
13. Pavlov, P. V., V. A. Panteleev, and A. V. Maiorov: Diffusion of Antimony along Dislocations in Silicon, *Soviet Physics—Solid State*, vol. 6, no. 2, pp. 305-310, August, 1964.
14. Mataré, H. F.: Grain Boundaries as Imperfections of Planar Extent: Their Model and Electronic Properties, *Proceed. of the Conference on Ultrapurification of Semiconductor Materials*, Boston, April, 1961. M. S. Brook and J. K. Kennedy eds. Macmillan, 1961.

## Chapter 13 Device Applications

The survey of the interesting properties of dislocations, dislocation arrays, and dislocation planes would not be complete without mentioning some device applications that are the consequence of those properties described earlier. In fact, some of the special aspects of dislocation planes have been derived on account of measurements that can be characterized as device type; for example, the photoelectric properties (high localization sensitivity), the extension of the photoresponse under bias, the low-temperature conductance, the field effect, and the like, are all directly applicable to the interpretation of the properties of dislocations and are also useful in device structures.

On the other hand, elucidation of these properties in devices can help in understanding the influence of dislocations on devices where they are contributing but where their influence is unwanted.

We direct our attention to those properties which are well established and have been used in device structures already. Other more speculative device aspects that are based on a number of possible electrooptic interactions on account of the multiple-level scheme, such as upconversion, optical waveguide structures, light-pumped maser applications, are not dealt with in detail in this text.

### 13.1 PHOTOELECTRIC (MICROMETRICAL) APPLICATIONS

In Section 11.7, the localizing sensitivity of a bicrystal as  $n$ - $p$ - $n$  structure and the extension of its optical frequency response with bias are described in detail. The high photoelectric sensitivity for light displacement gives this device an important advantage in cases where utmost precision in micrometrical equipment is desired. Use of bicrystals has been made, therefore, in tracking equipment where a target is pursued optically. The problem generally encountered in such cases is that the high localization sensitivity reaching the

resolution of millivolts per micron displacement with an illumination in the 1,000 lux range (potentially reaching into the angstrom range when amplification is applied, since then the signal strength may be a factor of 1,000 or less smaller), is such that the device would not find a target without a broader fall-in control. This can be achieved by a superposition of a less localizing photocell, and after target acquisition the signal can be processed by the bicrystal. Because of the transparency of germanium in the infrared spectrum, two bicrystals of different resolution may be used in parallel in order to widen the view field. H. A. Schell<sup>1</sup> has indicated relative resolution of bicrystal photocells. It is only necessary to use one bicrystal grown of high resistivity,  $n$ -type bulk material, in conjunction with a second one of low-resistivity  $n$ -type bulk material (see Figure 13.1). The photovoltage  $U_p$  is plotted in absolute value.

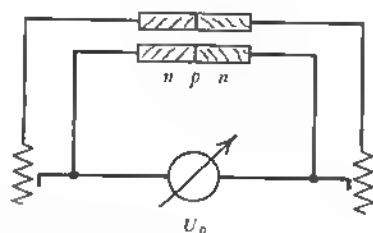
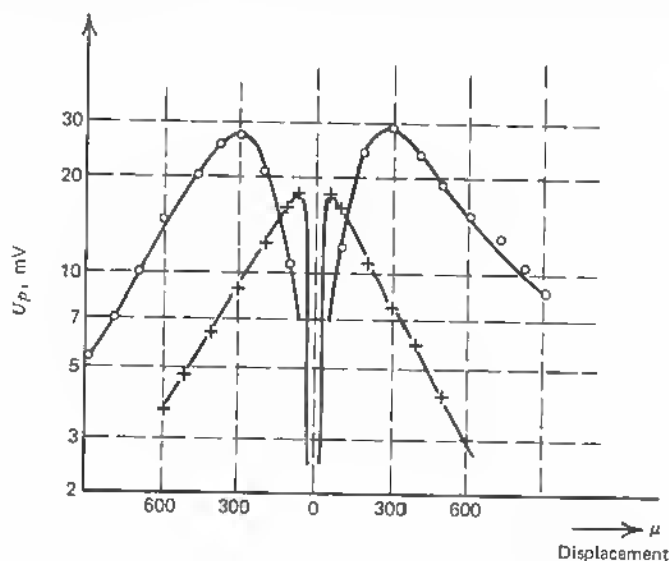
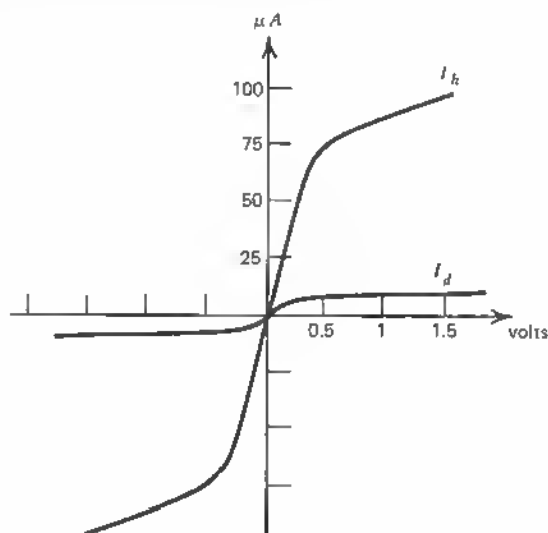


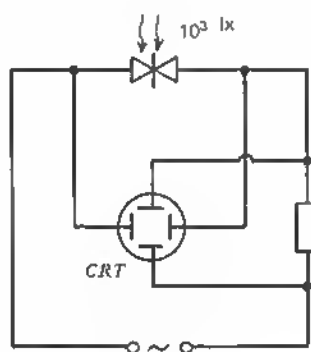
Fig. 13.1 Superposition of photovoltage of two bicrystals (Germanium) of different bulk doping.



If the light beam has an initial local uncertainty of  $\Delta x = 600 \mu$ , it is centered between the peaks of the higher-resistivity bicrystal until it is centered by the peaks of the low-resistivity bicrystal, which may be only a few microns apart. The bicrystal representing a back-to-back connection of two diodes shows a characteristic  $U_d$  as drawn in Figure 13.2. On broad illumination, the current is shifted, as shown by the curve  $I_h$ .



(a)



(b)

Fig. 13.2 (a) Characteristic of bicrystal photocell as viewed in cathode-ray tube without ( $I_d$ ) and with ( $I_h$ ) illumination, (b) CRT-set-up for bicrystal  $I$ - $V$ -characteristic display.

As Figure 13.2*b* shows, this characteristic is easily displayed on the cathode-ray oscilloscope with an ac exploration of small voltage while illumination is applied.

A special aspect of bicrystal photocells is a relatively non saturating photocurrent with applied illumination. For increasing light intensity (lux), the characteristic shifts to higher current values without basically changing its form. Figure 13.3*a* gives the typical result of measurements first published by H. A. Schell<sup>2</sup> and Figure 13.3*b* the form of a grain-boundary photocell.

As the bulk crystal material changes with respect to resistivity and lifetime of minority carriers, certain aspects of these photocells change also. Aside from the narrower minimum at the center of illumination for higher doping, we find a decreasing ratio of blocking resistance  $R^*$  to spreading resistance  $R$  (see Figure 13.4) and with the increased lifetime a generally increased photovoltage until the  $R^*/R$  ratio reaches values below 200<sup>1</sup>. Schell<sup>2</sup> has made a comparison of the different discriminator cells, shown in Table, 13.1.

For special purpose, silicon discriminator cells have been developed also; however, no junction or Schottky barrier combination can produce the sensitivity and localization combined that one finds in grain-boundary barriers.<sup>3</sup>

As pointed out in Section 11.7, the interband states originating from the dislocations can have various effects regarding recombination. As mid-band levels, they are especially efficient in conjunction with amphoteric impurities like gold in enhancing photon-induced hopping from a low-lying level near the valence band into the conduction band by way of the mid-band dislocation levels.

R. K. Mueller<sup>4</sup> showed that these grain-boundary photocells are not only extremely sensitive (to  $10^{-13}$  watt sec) but also very fast. Their recovery time can be drastically reduced by a sweep voltage or pulse applied to the cell while the light pulses or the modulated light is impinging on the junction area. Frequency-response measurements on highly doped bicrystals have shown that for normal geometry the cutoff frequency is beyond 10 MHz.

In a special application where small size and fast photodetectors were needed, laser patterns were measured. The bicrystal was exposed to different zones of the far field pattern in order to measure light intensity, threshold dependence, and time constant within defined areas of the lobe.<sup>5</sup> In this way, it was shown, for example, that the center lobe of the ruby laser has a longer burst duration during the pulse than the peripheral parts of the lobe and that the threshold at the center is lower than at the periphery. Figure 13.5 shows a typical result of the bicrystal output for the lower lobe. The sequence of the pictures of the bicrystal voltage is taken with increasing sweep frequency on the bicrystal. (a) is the far field pattern; (b) shows the burst pattern as viewed on the oscilloscope connected to the bicrystal, with a 200  $\mu$  sec/cm sweep voltage applied; (c) here the sweep frequency is a factor of 10 higher and the

sweep speed correspondingly  $20 \mu \text{ sec/cm}$ ; (d) this is the result of a  $4 \mu \text{ sec/cm}$  sweep speed and shows clearly the individual laser spikes during the pulse; (e) the  $RC$  time constant of the bicrystal circuit is increased by insertion of a resistor (here 24 ohms) in series in order to suppress the individual spikes, leaving the envelope of the total burst.

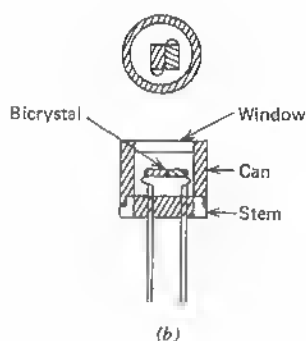
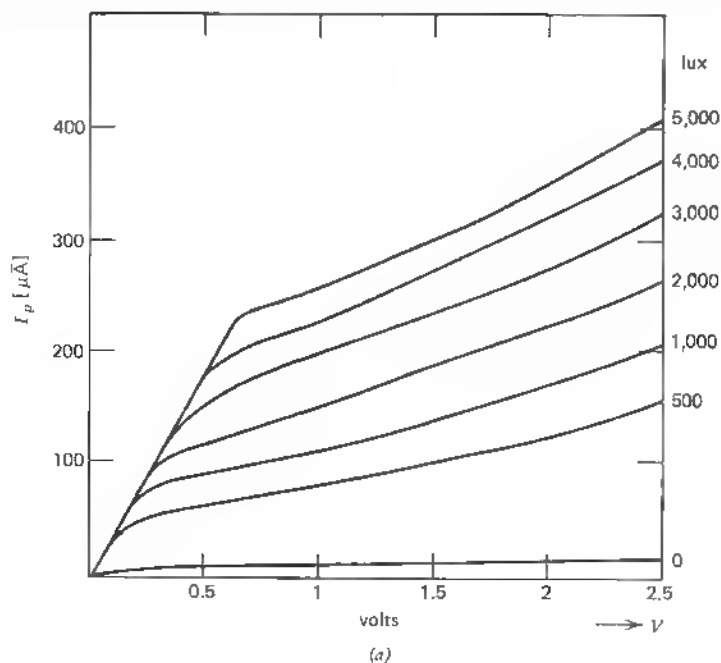


Fig. 13.3 (a)  $I$ - $V$ -characteristic of bicrystal with different illuminations in Lux.  
(b) Bicrystal photocell mount.

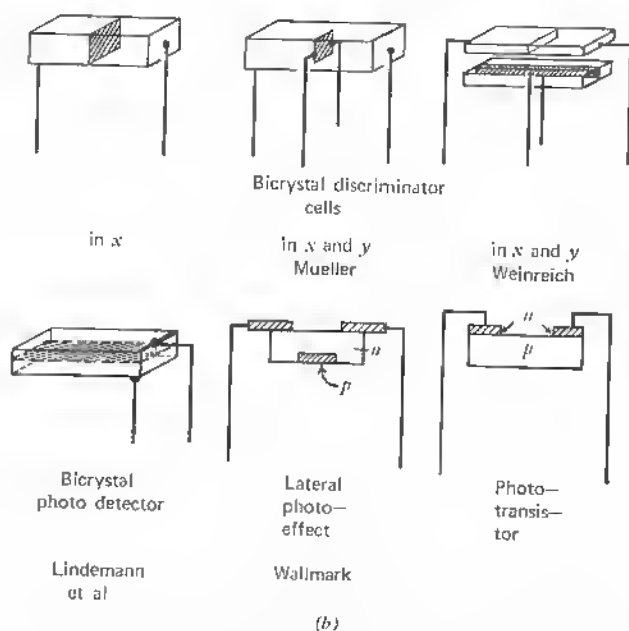
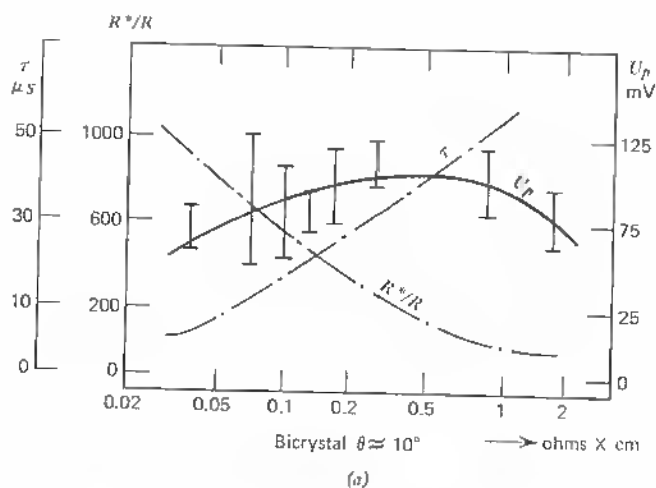
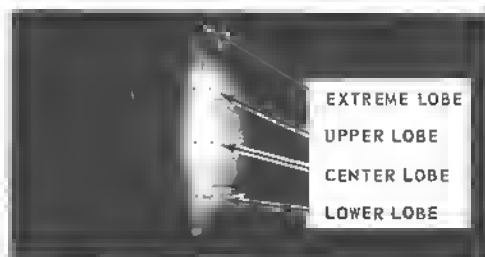


Fig. 13.4 (a) Dependence of  $R^*/R$  (bicrystal blocking resistance/spreading resistance), lifetime  $\tau$ , and photovoltage  $U_p$  on bulk resistivity in ohm cm.  
 (b) Different forms of localizing semiconductor discriminator cells.

Table 13.1

Type	Structure	Sensitive area, mm <sup>2</sup>	$J_{dark}$ $\mu A$	$U_{op}$ , V	$N_{0,100P}$ max, mW	Sensitivity, mA/lm	Frequency limit, MHz	Discrim., mV/ $\mu$ 1,000 lx
Bicrystal	<i>n-p-n</i> germanium	1	10-30	1-5	35	300-1,000	>1	>1
Photo-transistor	<i>n-p-n</i> germanium	1	10-30	10-30	50	300-1,000	0.015	0.1
Photo-diode TP50, Siemens	<i>p-n</i> germanium	1	1-4	<100	50	30-60	0.1	10 <sup>-2</sup>



(a) Positioning of bicrystal photocell in ruby laser far field pattern.



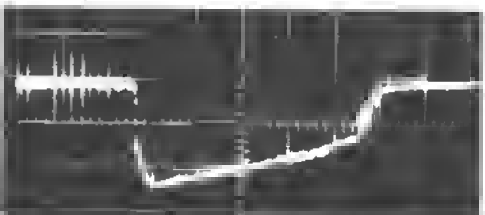
(b) Burst pattern taken at 200  $\mu\text{sec}/\text{cm}$  sweep speed [50 mV/cm] of bicrystal.



(c) Burst pattern taken at 20  $\mu\text{sec}/\text{cm}$  sweep speed of bicrystal.



(d) Burst pattern taken at 4  $\mu\text{sec}/\text{cm}$  sweep speed of bicrystal.



(e) Envelope of burst taken with augmented RC time constant at bicrystal circuit.

Fig. 13.5

The comparison of such localized high-frequency signals permitted showing, as mentioned, that the burst at the central lobe is longer than at the side lobes and that its threshold is considerably smaller.

## REFERENCES

1. Schell, H. A., and H. F. Mataré: Electrical Properties of Semiconductor Grain Boundaries [German], *Zschr. f. Metallkunde*, vol. 52, pp. 86-91, 1961.
2. Schell, H. A.: Germanium Grain Boundary Photocell, "Colloque International sur les Dispositifs à Semiconducteurs," Chiron, Paris, vol. 1, pp. 643-649, Feb. 20-25, 1961.
3. Weinreich, O. A., H. F. Mataré, and B. Reed: Electrical and Photoelectrical Properties of Grain Boundary Layers, *Solid State Physics in Electronics and Telecommunications, Proceed. Int. Conference*, Brussels, June, 1958, pp. 97-108, Academic, New York, 1960.
4. Mueller, R. K.: Transient Response of Grain Boundaries and Its Application for a Novel Light Sensor, *J. Appl. Phys.*, vol. 30, no. 7, pp. 1004-1010, July, 1959.
5. Mataré, H. F., and R. L. Zastrow: Bicrystal Photocells for Measurements on Optical Masers and as Optical Receivers, *Optica Acta*, vol. 10, no. 3, pp. 193-204, July, 1963.

## 13.2 PHOTOELECTRIC FREQUENCY CONVERTERS

The property of bicrystals of changing their optical frequency response with bias applied is mentioned in Section 11.7, and photoresponse curves are shown in Figures 11.62 to 11.65, which reveal a relatively strong variation with bias applied. There is no doubt that the local fields at the grain-boundary barriers at a few volts external bias can reach high internal values and change the normal response because of the enhancement of the binding force and consequent occupation of the free bonds:  $q/q_0 = f(V_e)$ . The number of charges  $q$  in dislocation levels increases with  $V_e$  ( $q_0$  = equilibrium number). We derived from this effect the relation (11.179), namely, that

$$\Delta V_p(v) \approx \text{const } V_e, \quad (13.1)$$

or a linear dependence of the variation of the photovoltage on the external bias voltage. In other words, the bias at the grain boundary increases the capture probability of minorities (holes, in the case of  $n$ -type germanium) and decreases the probability of electron capture. This is the usual effect of imperfections and its influence on optical sensitivity (see, for example, Ref. 1, pp. 130ff). A further effect of the bias voltage was described as a stress-field increase due to increased coulombic repulsive forces in the dislocation arrays. This would lead to a band-gap widening (in germanium) and explains the

high-frequency extension of the photoresponse (see also overlapping band structures, Section 11.7).

For an incident optical frequency somewhat off the band-to-band peak value of germanium (for example,  $\lambda = 1.55 \mu$  or 0.8 eV), a comparison of the sensitivity of a bicrystal with an ordinary  $p-n$  photocell shows a factor of 10 superiority of the photovoltage of the bicrystal (see Figure 13.6).

The pronounced bias dependence of the optical frequency response of a bicrystal device, however, is the important aspect not found, at least to this extent, in ordinary photoelectric devices. This effect can be used in various ways. In Figure 13.7, we have plotted the photovoltage at the peak value of incident optical frequency ( $1.65 \mu$ ) with the bias voltage on the bicrystal as parameter. As one sees, the effect is very strong. According to our earlier

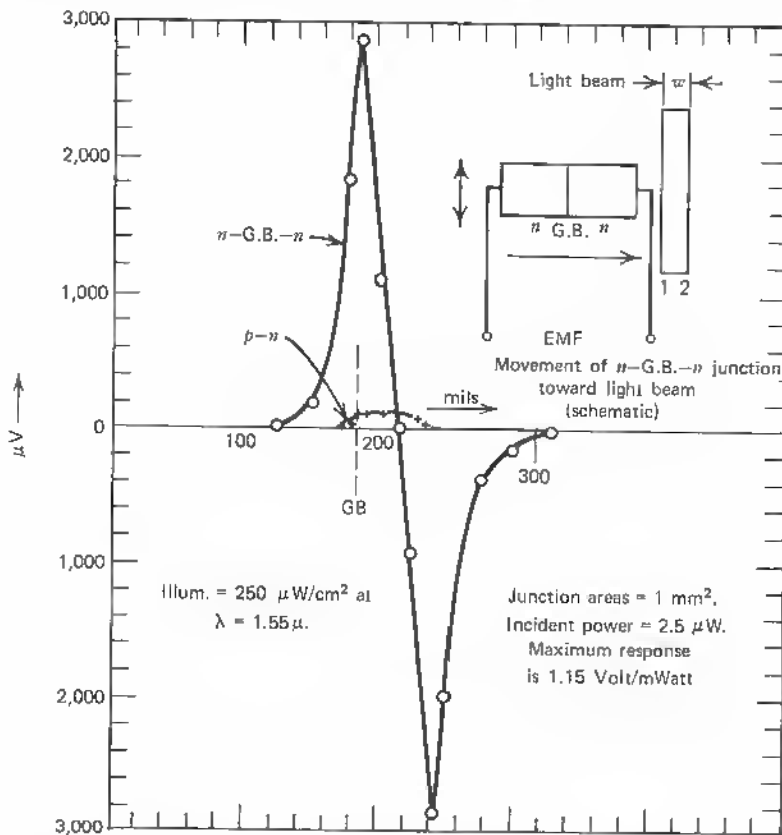


Fig. 13.6 Comparison of photovoltage of a bicrystal and 2P-N junction from same germanium crystal (bicrystal  $\theta = 25^\circ$ ). Width  $w \approx 50$  mils.



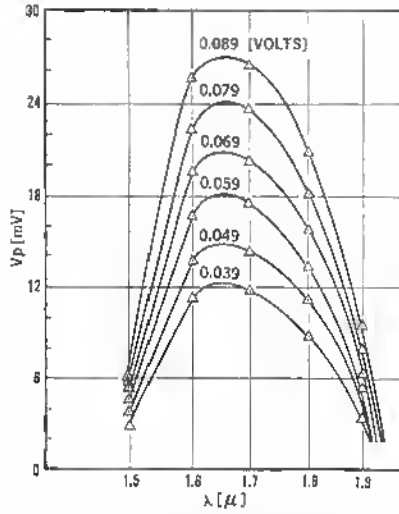


Fig. 13.7 Bias-dependence of bicrystal photoresponse. Photovoltage  $V_p$  (mV) plotted versus incident optical wavelength  $[\mu]$ . Parameter is bias voltage. Bicrystal ( $\theta = 10^\circ$ ), Germanium  $0.01 \sim 0.1 \text{ ohm cm}$ , N-type. Temperature =  $300^\circ\text{K}$ . Circuit resistance  $R_c = 1 \text{ k}\Omega$ .

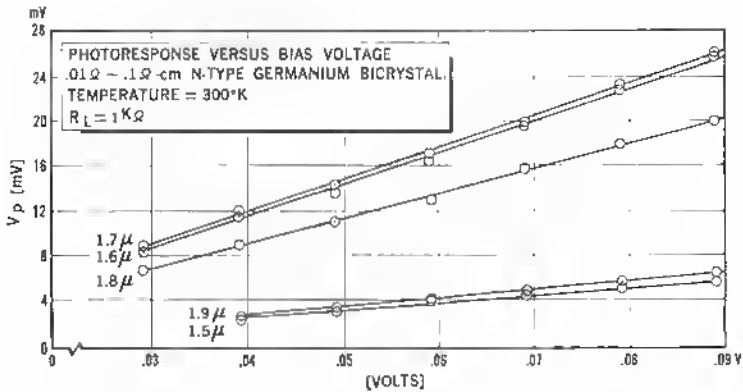


Fig. 13.8 Bicrystal photoresponse versus bias voltage. Parameter is wavelength of incident optical signal. Same bicrystal and circuit as in 13.7.

derivations, the  $V_p = f(V_e)$  function is linear with a slope near to 1. In the complex formula for  $V_p$

$$V_p \approx \frac{kT}{e} \ln \left[ \frac{2n_{e0}(e\phi)^{1/2}}{q_0 kT} \exp\left(-\frac{eV_e}{kT}\right) \right] \quad (13.2)$$

the factor with  $\phi$ , however, is somewhat dependent on the incident frequency, because the comparable equilibrium charge density  $n_{e0}$  is dependent on the incident light frequency, which also influences the barrier height  $\phi$ . For the center frequency ( $\lambda_{opt} = 1.65 \mu$ ), however, a slope of 1 is found. Figure 13.8 gives the results for a limited bias change at room temperature for different incident-light frequencies as parameter. Similar linear relationships are found at 77°K (see Figure 13.9). At higher voltages  $V_e$  a saturation is reached from

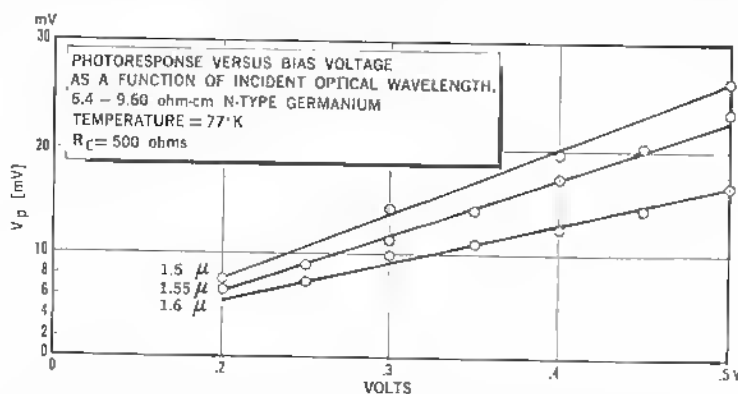


Fig. 13.9 Bicrystal photoresponse versus bias voltage. Parameter is wavelength of incident optical signal. Bicrystal  $\theta = 10^\circ$ , N-type bulk of 6.4–9.6 ohm cm. Temperature 77 K. Circuit resistance  $R_c = 500\Omega$ .

which the photovoltage does not increase but levels off. This is understood because in deriving (11.178), we used the exponential dependence of the carrier density at the barrier top on the voltage (11.76), which obviously has a saturation value. This is seen in Figure 13.10, which shows the photovoltage for a bias swing from 2 to 5 volts. The linear photovoltage bias dependence is similar to the case of photoconductive detectors; but in this case two barriers in opposition are involved, and the device has to be treated as a photovoltaic junction detector operating in the reverse part of its characteristic. The linearity of the photovoltage bias dependence does not, of course, eliminate the non-linear mixing properties, since the  $n$ - $p$ - $n$  junction (Figure 13.11a) current-voltage relation at small bias obeys a Wagner-Schottky  $I$ - $V$  characteristic. In the bicrystal case, one of the two junctions is forward-biased, the other one is operating in the blocking direction. In the series connection, the current-voltage relation is dominated by the reverse-biased side and the composite

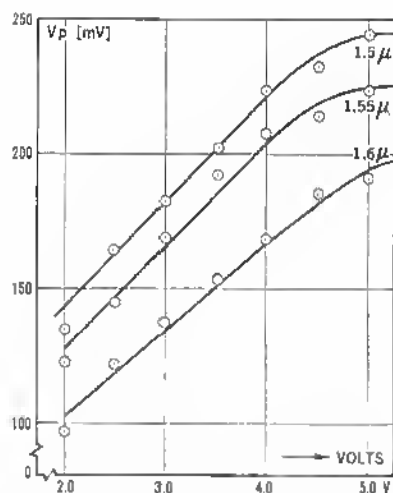


Fig. 13.10 Bicrystal photoresponse as function of bias. Photoresponse versus bias voltage as function of optical wavelength. 6.4-9.6  $\Omega$ -cm *n*-type germanium  $R_c = 500\Omega$ .

#### GRAIN BOUNDARY CURRENTS

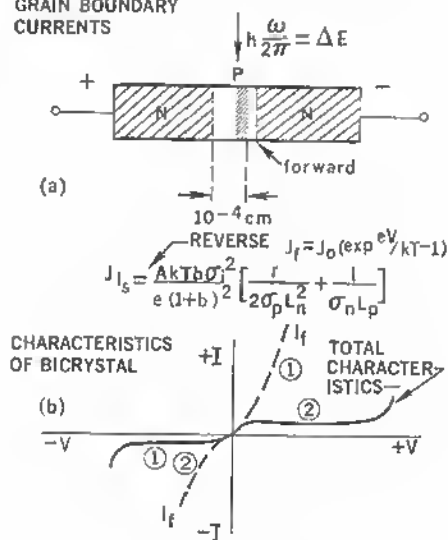


Fig. 13.11 (a) Grain boundary N-P-N structure with forward current characteristic and reverse saturation current (see text).  
(b) Composite  $I$ - $V$  characteristics

characteristic is as shown in Figure 13.11*b*. We consider the Shockley-form of the saturation current of the reverse-biased characteristic, with the wider depletion region:<sup>2</sup>

$$I_s = \frac{kT}{e} \left[ \frac{b\sigma_i^2}{(1+b)^2} \right] \left( \frac{1}{\sigma_n L_p} + \frac{1}{\sigma_p L_n} \right), \quad (13.3)$$

where  $b = \mu_p/\mu_n =$  mobility ratio,

$\sigma_i = e\mu_i n_i =$  intrinsic conductivity,

$n_i^2 = n_n p_n =$  intrinsic carrier density,

$\mu =$  mobility,

$e =$  electronic charge,

$\sigma_n = e\mu_n n_n = n$ -type conductivity,

$\sigma_p = e\mu_p p_p = p$ -type conductivity,

$L_n = \sqrt{D_n \tau_n} =$  diffusion length for electrons,

$L_p = \sqrt{D_p \tau_p} =$  diffusion length for holes,

$D_n =$  diffusion constant for electrons (92 cm<sup>2</sup>/s for germanium),

$D_p =$  diffusion constant for holes (=44 cm<sup>2</sup>/s for germanium),

$\tau_n =$  lifetime for electrons,

$\tau_p =$  lifetime for holes.

In a crystal of the geometry shown in Figure 13.12, the electron saturation current

$$I_{ns} = \frac{kT}{e} \frac{b\sigma_i^2}{(1+b)^2 \sigma_p L_n} \quad (13.4)$$

is decisive, since the barrier layer of width  $r$  is extending into the bulk  $n$ -type material, where the electrons are moving and the holes are attracted toward and kept at the grain boundary, as we have seen (Section 11.7). The contribution to the saturation current therefore is multiplied by  $(r/2)/L_n$  in expressing

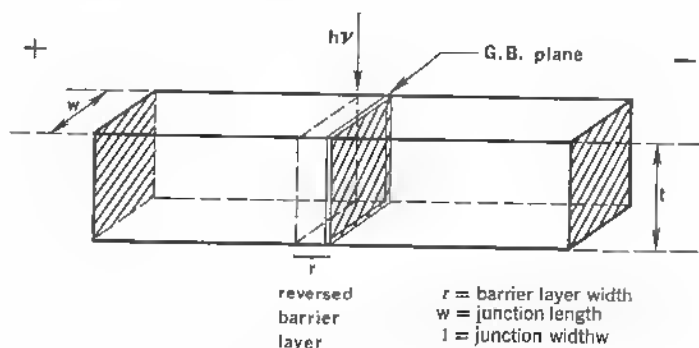


Fig. 13.12 Bicrystal geometry.

the electron contribution across the total depletion layer width  $r$  (see Figure 13.11). Introducing the short-circuit current due to  $N$  hole-electron pairs generated per unit area per second, we have

$$I_s = w \cdot e \cdot N(L_n + L_p), \quad (13.5)$$

where  $w$  = bicrystal width.

Here the area contributing to the current is defined by the diffusion length.<sup>3</sup> Simplifying and assuming that  $L_n \simeq L_p$  and that the depletion layer width is of the order of a diffusion length, we have

$$I_s = weN \cdot 2r. \quad (13.6)$$

The photoresistance or internal cell resistance is now given by

$$R_i = \frac{V_p}{I_s} = \frac{(kT)/e \ln\{[(2n_{e0}(e\phi)^{1/2})/q_0kT] \exp(-(eV_e)/kT)\}}{2rweN}, \quad (13.7)$$

according to (13.2).

The decisive variables are the barrier height  $\phi$ , the external bias voltage  $V_e$ , and the number of electron-hole pairs  $N$ . In (13.7) we have included the specific dependence of the photovoltage on the bias in bicrystals. We are also interested in the fact that bicrystals show the unusual extension of the optical frequency response with bias voltage  $V_e$ . For ordinary  $p$ - $n$  junctions, one derives an expression for the photocurrent at reverse bias and nonnegligible carrier generation in the depletion region,\* which explains a small change of the spectral distribution of the photocurrent with  $V_e$  (a factor of 3 to 6):

$$|I| = e\Psi \left[ 1 - \frac{\exp(-ar)}{1 + aL} \right], \quad (13.8)$$

where  $\Psi$  = light flux density,

$a$  = absorption coefficient,

$r = r_0 \sqrt{V_e}$  = barrier width,

$r_0$  = width constant,

$V_e$  = external voltage on barrier,

$L$  = carrier diffusion length.

This is due to the band-gap variation in the depletion layer, which is subjected to high local fields (Franz-Keldysh shift).

The amount of spectral response change observed in bicrystals goes, however, much beyond the explained changes of a factor 3 to 6; for example, in Figure 11.64 we see that application of a normal bias (a few volts within the

\* W. Gaertner, Phys. Rev. 116, 84, 1959.

saturation range) accounts for a change of two orders of magnitude at a photon energy of 0.7 eV. To account for this effect, we have to include both the light signal input and the bias dependence in the final expression for the photo-voltage.<sup>3</sup>

We start with (13.8) and introduce a light flux

$$\Psi = \Psi_0(1 + M \cos \omega_s t), \quad (13.9)$$

where  $\Psi_0$  = static photon flux,

$\omega_s$  = signal frequency,

$M$  = modulation index of incoming light signal.

At the same time, the bicrystal can be subjected to a small local oscillator voltage  $V_L$ :

$$V = V_0 + V_L \cos \omega_L t, \quad (13.10)$$

where  $V_0$  = back bias voltage,

$V_L$  = local oscillator voltage,

$\omega_L$  = local oscillator frequency.

This yields a photocurrent:

$$|I| = e\Psi_0(1 + M \cos \omega_s t) \left[ 1 - \frac{1}{1 + aL} \exp(-ar_0 \sqrt{V_0 + V_L \cos \omega_L t}) \right]. \quad (13.11)$$

Since in the back-biased case

$$V_0 = -V_B < 0$$

and

$$\frac{V_L}{V_B} \ll 1,$$

it is sufficient to retain only the first-order terms in the binomial expansion of  $(V_0 + V_L \cos \omega_L t)^{1/2}$ , which leads to

$$|I| = e\Psi_0(1 + M \cos \omega_s t) \times \left\{ 1 - \frac{1}{1 + aL} \exp \left[ -ar_0 \sqrt{V_B} \cdot i \left( 1 - \frac{1}{2} \frac{V_L}{V_B} \cos \omega_L t \right) \right] \right\}, \quad (13.12)$$

$$|I| = e\Psi_0(1 + M \cos \omega_s t) \times \left[ 1 - \frac{1}{1 + aL} \exp(-iar_b \sqrt{V_B}) \exp \left( i \frac{ar_0}{2} \frac{V_L}{\sqrt{V_B}} \cos \omega_L t \right) \right]. \quad (13.13)$$

Using the Bessel function expansion formula

$$e^{jz \cos \phi} = \sum_{m=-\infty}^{+\infty} e^{jm(\phi + \frac{1}{2}\pi)} J_m(z), \quad (13.14)$$

where  $J_m(z)$  = Bessel function of order  $m$  and first kind, and its expansion

$$J_m(z) = \frac{1}{m!} \left(\frac{z}{2}\right)^m \left[ 1 - \frac{(z/2)^2}{1!(m+1)} + \frac{(z/2)^4}{2!(m+1)(m+2)} \dots \right], \quad (13.15)$$

and finally the equality

$$J_m(-z) = (-1)^m J_m(z), \quad (13.16)$$

the last term of (13.14) can be expanded in a Bessel function series. Summing up by means of (13.14) and discarding the terms of higher order,<sup>3</sup> one finds

$$|I| = e\Psi_0(1 + M \cos \omega_s t) \left\{ 1 - \frac{\exp(-ar_0 \sqrt{V_B} i)}{1 + aL} \left[ J_0\left(\frac{er_0}{2} \frac{V_L}{\sqrt{V_B}}\right) + 2iJ_1\left(\frac{ar_0}{2} \frac{V_L}{\sqrt{V_B}}\right) \cos \omega_L t \right] \right\}, \quad (13.17)$$

where  $J_0$  and  $J_1$  are the Bessel functions of order zero and one, first kind.

From (13.17) it is obvious that the term responsible for the formation of an intermediate frequency between  $\omega_s$  and  $\omega_L$  is

$$e\Psi_0 M \left[ \frac{1}{1 + aL} \exp(-ar_0 \sqrt{V_B} i) \right] \left[ iJ_1\left(\frac{ar_0}{2} \frac{V_L}{\sqrt{V_B}}\right) \right]. \quad (13.18)$$

Equation (13.18) multiplied by the load resistance  $R_L$  would give the photovoltage.

From (13.18), we can conclude the following with respect to the result of heterodyning of an optical signal with a local oscillator (which is preferably here in the microwave region):

1. The I.F. voltage (amplitude) is proportional to the modulation index  $M$ . This is the case (see measured data in Ref. 4).
2. The I.F. voltage dependence on the local oscillator amplitude and the back-bias voltage are determined as follows: For

$$\frac{er_0}{2} \frac{V_L}{\sqrt{V_B}} \ll 1$$

(always satisfied for small local oscillator voltage in the microwave range),

$$|V|_{IF} = \frac{|R_L e \psi_0 M|}{(1 + aL)} \left| J_1 \left( \frac{ar_0}{2} \frac{V_L}{\sqrt{V_B}} \right) \right| \quad (13.19)$$

$$\approx \frac{R_L e \psi_0 M}{(1 + aL)} \left( \frac{ar_0}{4} \frac{V_L}{\sqrt{V_B}} \right). \quad (13.20)$$

Thus for fixed large back bias, the I.F. voltage should be proportional to the local oscillator voltage amplitude  $V_L$ . This law was also found valid in detailed parameter measurements.<sup>4</sup>

In more detailed measurements on heterodyne receivers, (13.20) was found to be valid inasmuch as local oscillator voltage  $V_L$  and bias voltage  $V_B$  established a characteristic of the form

$$V_{IF} = k \frac{M V_L}{\sqrt{V_B}} \quad (13.21)$$

for the intermediate frequency voltage  $V_{IF}$ .<sup>5</sup>

So far, we have not yet considered that the backward-bias voltage  $V_B$ —in the  $n$ - $p$ - $n$  bicrystal structure any bias voltage  $V_e$  results in a backbias—has a direct effect on the photovoltage according to (13.2). This can be considered by way of the internal cell resistance

$$R_p = \frac{V_p}{I_s}, \quad (13.22)$$

where the photovoltage  $V_p$  is expressed by (13.2) and the saturation current  $I_s$  by (13.6):

$$R_p \approx \frac{kT}{2rNe^2w} \ln \left[ \frac{2n_{e0}(e\phi)^{1/2}}{q_0 kT} \exp \left( -\frac{eV_e}{kT} \right) \right].$$

The actual I.F. photovoltage with a local oscillator applied is

$$V_{IF} = |I| - R_p, \quad (13.23)$$

where  $|I|$  is given according to (13.17), and the static flux  $\psi_0$  is equivalent to

$$\psi_0 = \frac{I_s}{wt} = \frac{\text{saturation current density}}{\text{cross section}}, \quad (13.24)$$

where  $w$  = bicrystal width,

$t$  = bicrystal height

(see Figure 13.12).

With (13.6) this leads to

$$\psi_0 = 2rNe/t. \quad (13.25)$$



Therefore

$$V_{IF} = \frac{kT}{wt} (1 + M \cos w_s t) \left\{ 1 - \frac{\exp(-ar_0 \sqrt{V_e})}{1 + aL} \left[ J_0 \left( \frac{er_0}{2} \frac{V_L}{\sqrt{V_B}} \right) + 2iJ_1 \left( \frac{ar_0}{2} \frac{V_L}{\sqrt{V_e}} \right) \cos w_L t \right] \right\} \ln \left[ \frac{2n_{e0}(e\phi)^{1/2}}{q_0 kT} \exp \left( -\frac{eV_e}{kT} \right) \right]. \quad (13.26)$$

As we discussed in connection with (13.17), there are ways to reduce this expression in practical cases because of the relative importance of the parameters used. Generally,  $V_L/\sqrt{V_B}$  or  $V_L/\sqrt{V_e} \ll 1$ , and the Bessel functions  $J_0$  and  $J_1$  can be reduced for small argument  $(ar_0/2) \cdot (V_L/\sqrt{V_e})$  by the series expansion (13.15).

The interesting relation among photoresponse, bias voltage, and optical frequency response has other important consequences. In Figure 13.13, three different positions of the response edge are drawn, that is, three different bias conditions in the characteristic as measured and shown, for example, in Figure 11.64. This leads to a possibility of mixing the voltages resulting from

1. A bias variation  $\Delta V_e$  and an incident light amplitude variation  $\Delta \psi$ ,
2. A bias variation  $\Delta V_e$  and a variation  $\Delta f$  of the incident light frequency.

We see in Figure 13.13 that a change in photovoltage can be effected by either a bias change  $\Delta V_e$  or a frequency change. By a  $\Delta V_e$  the operating point moves from characteristic *b* to *c* and changes the photovoltage for an amount  $\Delta V_p'$  correspondingly.

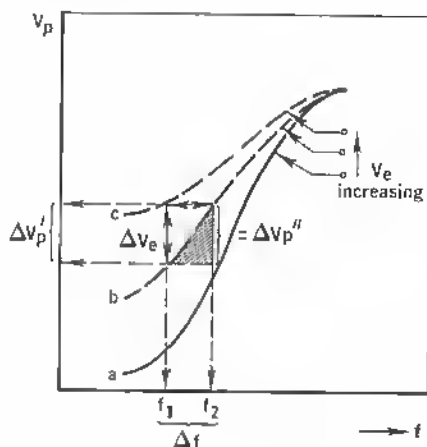


Fig. 13.13 Bicrystal photoresponse and exploration.

A frequency change of the light signal from  $f_1$  to  $f_2$  results in a photovoltage change along characteristic  $b$  and yields a difference  $\Delta V_p'$ . Thus either  $\Delta V_e$  (by way of the local oscillator) can cause  $\Delta V_p'$  for a fixed light-signal frequency or a change  $\Delta f = f_2 - f_1$  in the signal frequency causes a change  $\Delta V_p''$ . Therefore, a mixing between a frequency-modulated light signal (via  $\Delta f$ ) and an amplitude-modulated local oscillator (via  $\Delta V_e$ ) results in an amplitude-modulated intermediate frequency. In other words, frequency variations induce resistance variations, which are then superimposed on local oscillator-induced resistance variations.

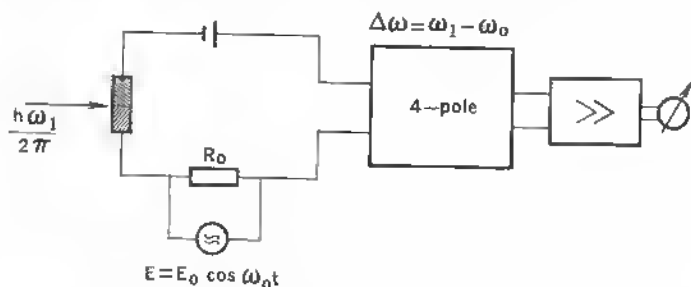


Fig. 13.14 Bicrystal mixer. Local oscillator voltage:  $E_0 \cos \omega_0 t$ ;  $\Delta\omega = \omega_1 - \omega_0 =$  intermediate frequency,  $\omega_1 =$  subcarrier frequency

In summary, it can be stated that the bicrystal is not only a light-sensitive detector but well suited to the detection of frequency-modulated light signals. Other important questions in this respect have to do with the signal-to-noise ratio of such a light receiver. Since the bicrystal is not a quantum counter, but a junction detector and mixer, a light frequency conversion with a local light oscillator generates additional quantum noise that degrades the sensitivity. Therefore, the best use of these devices in optical communication is in connection with subcarrier demodulation when a light beam carries frequency-modulated signals (see for example, Figure 13.14). With several local oscillator frequencies, several intermediate frequencies can be derived and extracted by separated tuned circuits. The equivalent noise-source schemes for such light mixers have been derived and signal-to-noise ratios given.<sup>3</sup>

## REFERENCES

1. Bube, R. H.: "Photoconductivity of Solids," Wiley, New York, 1960.
2. Shockley, W.: The Theory of  $p$ - $n$  Junctions in Semiconductors and  $p$ - $n$  Junction Transistors, *Bell System Techn. Journal*, no. 3, pp. 435-489, July, 1949.
3. Mataré, H. F.: Field Dependence of Photoresponse and Heterodyning of Optical Signals, *Internat. Journal of Electronics*, vol. 19, no. 5, pp. 405-437, November 1965.

4. Cho, K. S., H. F. Mataré, A. H. Solomonian: Parameter Dependence of I.F. Voltage in Optical Mixers, *Internat. Journal of Electronics*, vol. 19, no. 6, pp. 549-554, December, 1965.
- Mataré, H. F., and K. S. Cho: Parameter Dependence of I.F. Voltage in Optical Mixers and Bias Dependence of Photoconductivity in Bicrystals, *Proceed. Electronic Components Conference, IEEE*, Washington, pp. 415-425, 1966.
5. Cho, K. S., and H. F. Mataré: Parameter Optimization in Frequency Conversion of Optical Signal Demodulation in PIN Silicon Photodiodes, *Solid State Electronics Journal*, vol. 10, pp. 365-367, 1967.
6. Mataré, H. F.: Dislocation Plane Devices in Optical Communication, *Advance in Electronics*, *Proceed. of the XIIIth International Scientific Congress on Electronics*, Rome, Italy, 1966, vol. 1.

### 13.3 THE DISLOCATION FIELD-EFFECT TRANSISTOR

Early studies of grain-boundary barriers in transistor structures showed that the reverse (saturation) characteristic of the bicrystal can be shifted considerably by a bias to the grain-boundary sheet when an ohmic contact to the latter is established.<sup>1</sup>

In further measurements on such *grain-boundary transistors* power gains of 20 db and more were measured,<sup>2-4</sup> especially when the grain-boundary sheet was used as emitter, one *n*-type bulk side as collector and the other as base contact.

In such a structure, the geometry for high-frequency performance is not optimal and suffers from relatively high emitter-to-base capacitance. Also, the degenerate sheet conductance is not used as such, and the advantage of its temperature-independent conductivity is not fully exploited. If, however, the dislocation sheet is used as the source-drain channel in a unipolar transistor structure, it seems that the interesting properties of the sheet can be exploited.<sup>5,6</sup> Figure 13.15 shows how, at room temperature, the current-voltage relation across the bicrystal interface  $I_2/V_2$  changes when a voltage  $V_1$  (leakage current  $I_1$ ) is applied to the bulk crystal sides. As  $V_1$ , the voltage across the space-charge layer, increases (positive), the current  $I_2$  through the dislocation sheet decreases. The sheet conduction is carried mainly by holes in the space-charge layer, as discussed earlier. A bias between sheet and bulk, therefore, acts as the gate voltage in a normal field-effect structure or surface-barrier transistor. The geometry of the device is shown in Figure 13.16, where the dimensions of the test samples are also indicated. The actual transistor is shown in Figure 13.17 in  $\times 30$  magnification. The grain-boundary contact (indium alloy) is in the center (source-drain contacts), and the gate connections to the monocrystalline sides are visible on either side of the bicrystal wafer. A simple equivalent circuit of this field-effect amplifier is shown in Figure 13.18. The input is the gate circuit with its relatively high

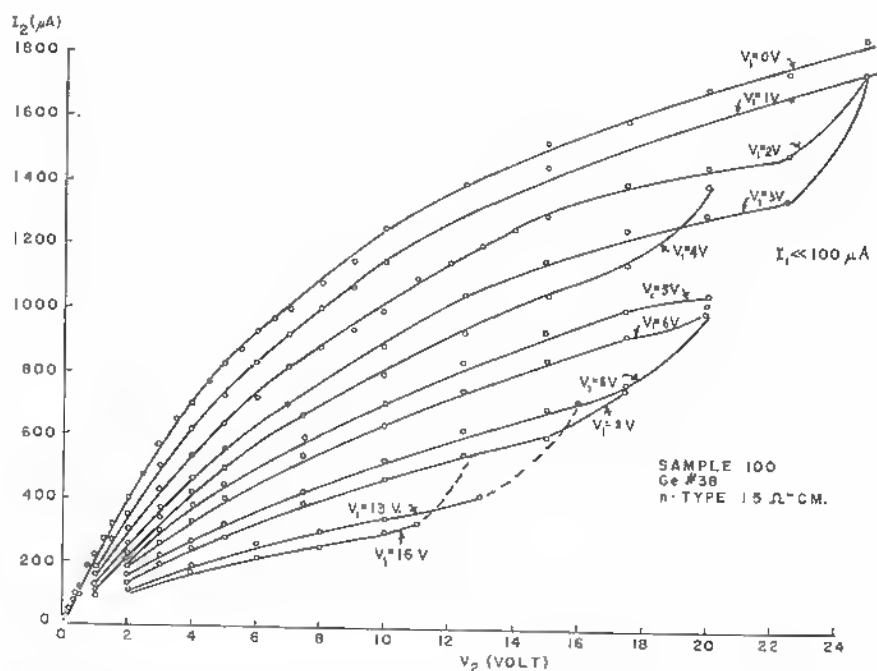


Fig. 13.15 Dislocation field effect transistor-characteristics. Sheet current versus sheet voltage with gate voltage as parameter (room temperature)

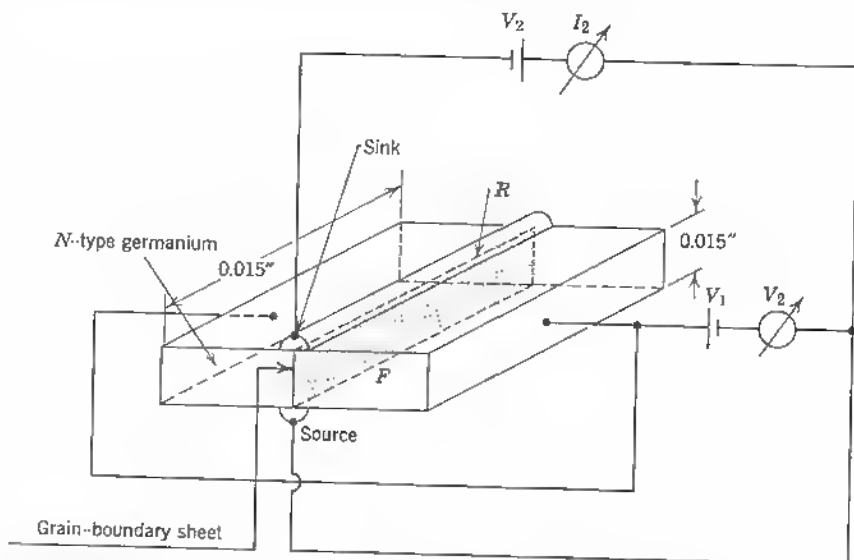


Fig. 13.16 Dimensions and circuit of grain-boundary amplifier sample. Note.  $F$  = indium alloyed junction forward biased;  $R$  = indium alloyed junction reverse biased.

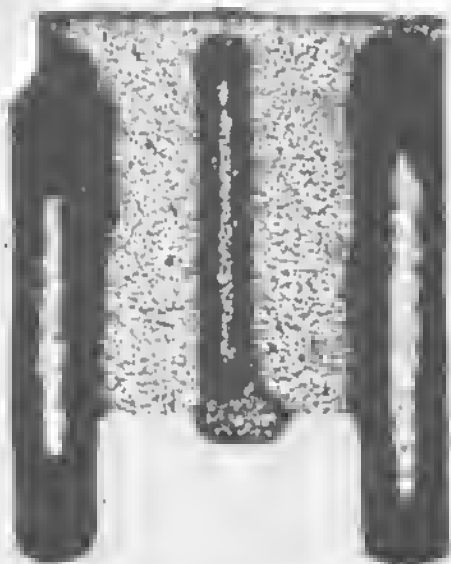


Fig. 13.17 Grain-boundary field-effect transistor. Bi-crystal side contacts *Pb-Sb*; center contact to G.B. line is indium.  $30\times$ .

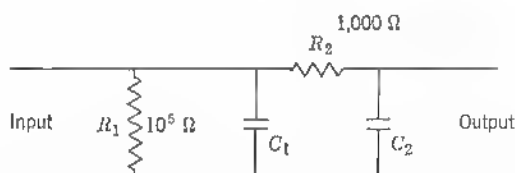


Fig. 13.18 Grain-boundary amplifier simplified equivalent circuit;  $C_1 \sim 100 \mu\text{F}$  due to contact capacity;  $C_2 \sim 100 \mu\text{F}$  grain boundary capacity;  $R_2$  channel resistance;  $R_1$  leakage resistance.

impedance of  $10^5$  ohm due to the barrier-layer separation. The gate-source or gate-drain capacitance is in the  $100 \mu\text{F}$  or  $100 \text{ pF} \approx 100 \text{ cm}$  range, which is high because of the large samples and the use of relatively highly doped bulk material ( $N > 10^{17} \text{ cm}^{-3}$ ). The same applies to the output capacitance. The actual grain-boundary-plane resistance (channel resistance) is 1000 ohms in this case.

From the expression for the conductance  $\sigma_s$  derived in Section 11.6, equation (11.154), one can derive a dynamic conductance due to a charge modulation  $\pm \Delta Q$  at the gate:

$$\sigma_s = \mu \frac{Q \pm \Delta Q}{l^2} \quad (13.27)$$

see (11.154).

This leads to a sheet current  $I_s$ :

$$I_s = \mu \frac{Q \pm \Delta Q}{l^2} V_s, \quad (13.28)$$

where  $V_s$  = sheet voltage.

The transconductance of the device follows from the differential of the channel or sheet current  $I_s$  with respect to the input or gate voltage  $V_g$  for constant drain or channel voltage  $V_s$ :

$$g_s = \left( \frac{\partial I_s}{\partial V_g} \right)_{V_s = \text{const}}. \quad (13.29)$$

As derived in Section 11.6, the sheet or channel current can be found as the ratio between charge and transit time in the channel. Therefore

$$g_s = \frac{\partial(Q/\tau_s)}{\partial V_g} = \frac{\Delta C(f)}{\tau_s}. \quad (13.30)$$

The gate-electrode capacity variation is a function of the operating frequency  $f$  at high frequencies.

A maximum voltage amplification  $G_{\max}$  can also be defined<sup>10</sup> on this basis:

$$G_{\max} = \frac{\Delta C(f)}{\tau_s} \left[ \frac{1}{\tau_c} \frac{\partial Q}{\partial V_g} + Q \frac{\partial(1/\tau_s)}{\partial V_g} \right]_{V_s = \text{const}}^{-1}. \quad (13.31)$$

Here  $G_{\max}$  is essentially expressed by the capacity variation with gate voltage. If the gate electrode also has an inductive component, one gets

$$G_{\max} = \frac{\Delta C(f) \cdot \tau_s}{\Delta C(f) \cdot L_g + \tau_s^2} \left[ \frac{1}{\tau_c} \frac{\partial Q}{\partial V_g} + Q \frac{\partial(1/\tau_s)}{\partial V_g} \right]_{V_s = \text{const}}^{-1}. \quad (13.32)$$

Amplifiers of this kind have been investigated<sup>7</sup> at room temperature, liquid nitrogen temperature (78°K), and liquid helium temperature (4.2°K) and have been found to improve in transconductance as the temperature is lowered. A typical characteristic is seen in Figure 13.19. As the insert shows, the sheet current is plotted along the ordinate, the sheet voltage along the abscissa. Parameter is the gate voltage. The gate current is negligible at liquid helium temperature and is of the order of

$$I_1 < 10^{-7} \text{ A}.$$

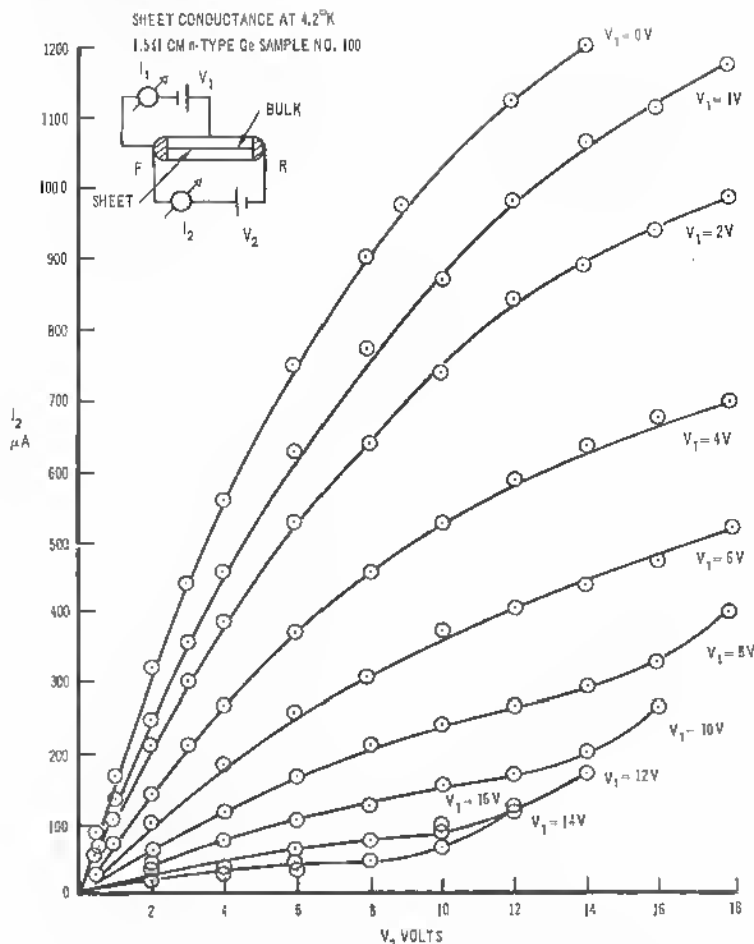


Fig. 13.19  $I/V$ -characteristic of a grain boundary field-effect transistor at liquid Helium temperature.

It is seen that the field changes of the degenerate sheet conductance are rather strong. This has been difficult to explain.<sup>8</sup> The reason seems to be the low activation energy of the dangling-bond levels filled with electrons that are not deactivated even at very low temperatures and are compensated by free holes in the space charge around the dislocation sheet (at about  $10^{-5}$  cm from the core). A potential change at the space-charge layer (about  $10^{-4}$  cm wide) then affects the number of holes and, therefore, the sheet conductance. Practical devices have been built and used in low-temperature experiments.<sup>9</sup> It is worthwhile to mention a few aspects that may lend this device a certain importance in future high-sensitivity optical and microwave equipment. The

problem of amplifying faint signals derived from photodetectors is acute. In the far infrared, amphoteric doped germanium monocrystals are used to detect faint optical signals. In all cases, optical detection beyond  $10\ \mu$  has to be carried out at low temperature. Crystals with good sensitivity between  $10$  and  $20\ \mu$  wavelength are germanium-silicon, zinc-doped; germanium, mercury-doped; germanium-silicon, gold-doped; germanium, cadmium-doped; and for the wavelength range beyond  $20$  to  $40\ \mu$ , germanium, copper-doped, and germanium, zinc-doped.

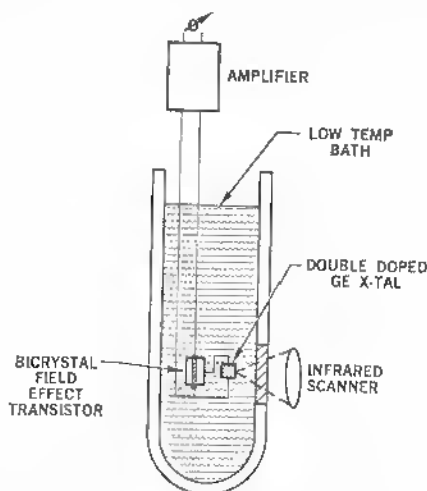


Fig. 13.20 Bicrystal field-effect transistor as low temperature amplifier in infrared sensing equipment.

Sensitivity of such photoconductors is highest at liquid helium temperature, where  $kT$  is kept below the signal noise level. It is important to amplify the small signals emanating from the quantum counter without adding thermal noise. A cable connection from such an infrared detector in the cryostat to a room-temperature amplifier adds generally of the order of  $20\text{ db}$  to the noise level and deteriorates the detector sensitivity. Here a low-temperature amplifier connected to the photodetector right within the cryostat is the ideal configuration. After the signal level is sufficiently amplified, a cable connection can bring the signal out into the room-temperature amplifier without diminishing the signal-to-noise ratio (schematically shown in Figure 13.20). If the bicrystal amplifier is made small enough to respond to higher frequencies, it may also be used in connection with MASER receivers. In the usual expression for the transconductance

$$g = 2\sigma_0 \frac{d \cdot w}{l} \quad (13.33)$$



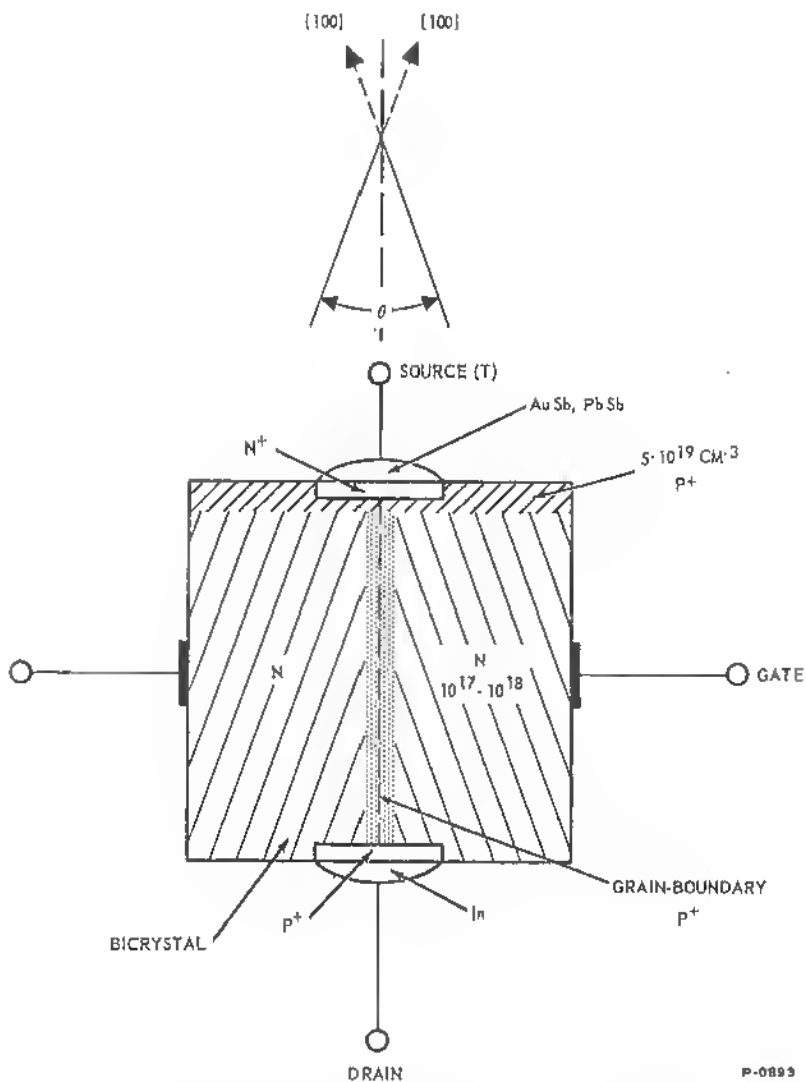


Fig. 13.21 Scheme of grain boundary tunnel transistor (see text).

see e.g. Ref. 13.8—the space-charge width is given by the crystal properties, but the ratio  $d/l$  can be made large by increasing the channel extension  $d$  and decreasing the channel length  $l$  (thin bicrystal samples). See also Figure 13.16.

It has also been shown that an additional inductive component in the gate circuit (generally present because of contact leads) in this case may increase the limiting frequency.<sup>8</sup>

Finally, the noise figure of this device should be mentioned, because it seems that this alone can justify the application of low-temperature field-effect transistors. As the field-effect transistor is, already at room temperature, a low-noise device, it should be a very excellent low-noise amplifier at liquid helium temperatures. As shown for ordinary field-effect transistors,<sup>11</sup> the resulting noise resistance is very low and caused by the thermal noise of the conducting channel, with a minor contribution from the gate junctions that are causing shot noise.<sup>10</sup> According to van der Ziel, the equivalent noise resistance  $R_e$  (in  $i^2 = 4kTR_e \Delta f g_m^2$ ),

$g_m$  = mean value of transconductance

$$\text{can be represented by} \quad R_e \simeq \frac{g_{\max}}{g_s^2}, \quad (13.34)$$

$$\text{where} \quad g_s = -\left(\frac{\partial I_s}{\partial V_g}\right)_{V_d=\text{const}}, \quad \text{source transconductance} \quad (13.35)$$

$$g_d = -\left(\frac{\partial I_s}{\partial V_d}\right)_{V_g=\text{const}}, \quad \text{drain transconductance} \quad (13.36)$$

$$g_{\max} = g_d + g_s. \quad (13.37)$$

This results in values close to  $1/g_{\max}$  when the saturation range is considered ( $g_s \approx g_{\max}$  and  $g_d \approx 0$ ). In this range, the noise resistance can be equalled to the reciprocal transconductance value.

Considering, however, the junction leakage current with its shot-noise component, the noise depends rather on the ratio of the load impedance  $g_0$  to the square of the junction or gate conductance,  $g_0/g_g^2$ .<sup>10</sup>

There have also been attempts to use the grain boundary as a low-resistance sheet in connection with the base modulation in tunnel transistors.<sup>12</sup> Because the problem is the efficient base current modulation, the grain-boundary sheet serves as a base extension that can be subjected to field changes (see Figure 13.21). The degenerately doped layer at one bicrystal surface ( $P^+ : 5 \cdot 10^{19} \text{ cm}^{-3}$ ) serves as base layer for the tunnel junction. But the base contact is attached to a ( $p^+$ -type) contact layer to the grain-boundary sheet at the other side of the sample. Gate electrodes to the bulk are foreseen to effect a sheet modulation.

## REFERENCES

1. Mataré, H. F.: Grain Boundaries and Transistor Action, *IRE Record of New York Convention*, pp. 113-124, March 21-24, 1955.
2. Mataré, H. F.: Grain Boundary Structure and Carrier Transport in Semiconductor Crystals, *Zschr. f. Naturf.*, vol. 10a, pp. 640-652, 1955.
3. Mataré, H. F.: Study of Electrical Characteristics of Grain Boundaries, *Phys. Rev.*, vol. 98, p. 1179, 1955.
4. Mataré, H. F.: Grain Boundary Transistors, *Internationale Elektronische Rundschau*, vol. 10, no. 8, pp. 209-211, 1956, and vol. 10, no. 9, pp. 253-255, 1956.
5. Mataré, H. F.: Anisotropy of Carrier Transport in Semiconductor Bicrystals, "Solid State Physics in Electronics and Telecommunications," Academic, New York, pp. 73-96, 1959.
6. Mataré, H. F.: Dislocation Planes in Semiconductors, *The Proc. of the Institute of Electrical Engineers (British)*, vol. 106, part B, suppl. 15, pp. 293-302, 1959.
7. Weinreich, O. A., H. F. Mataré, and B. Reed: The Grain Boundary Amplifier, *Proc. of the Phys. Soc. (British)*, vol. 73, pp. 969-972, 1959.
8. Mataré, H. F.: Recent Development in the Field of Semiconductor Devices for High-frequency, *Fortschritte der Hochfrequenztechnik*, vol. 5, pp. 347-412, 1960.
9. U.S. Patent 2,970,229 of Jan. 31, 1961, filed Oct. 10, 1958, Temperature Independent Transistor with Grain Boundary, H. F. Mataré, B. Reed, and O. A. Weinreich.
10. Mataré, H. F.: Low Temperature Field-effect Transistor Using Dislocation Planes, *Direct Current Journal (British)*, vol. 6, no. 5, pp. 1-8, August, 1961.
11. Van der Ziel, A.: Thermal Noise in Field Effect Transistors, *Proceed. IRE*, vol. 50, no. 8, pp. 1808-1812, 1962.
12. U.S. Patent 3,171,042 of Feb. 23, 1965, filed Sept. 8, 1961, Device with Combination of Unipolar Means and Tunnel Diode Means, H. F. Mataré.

## 13.4 STRESS-STRAIN TRANSDUCERS

In connection with the devices based on dislocations, we briefly describe an application that makes use of the unusual lattice configuration in a dislocation sheet and of the fact that this sheet is separated from the surrounding crystal material by junctions.

Conventional semiconductor stress transducers operate on account of the piezo-resistive effect, that is, the interaction between the stress tensor and the electrical resistance tensor.<sup>1</sup> In material of symmetrical cubic structure, like silicon, only the basic piezo-resistance coefficients  $\pi_{11}$ ,  $\pi_{12}$ , and  $\pi_{44}$  ( $\pi_{44} = \pi_{55} = \pi_{66}$ ) are important. All other shear components vanish for cubic symmetry.

It can be shown that for cubic crystals like silicon and germanium, with the orthogonal axes along the crystal axes, the piezo-resistance coefficients

$\pi'_{pq} \Rightarrow \pi_{pq}$  ( $\pi'$  refers to the arbitrarily oriented set of rectangular axes and is replaced here by a set along the major crystal axes) take the form<sup>2</sup>

$$\pi_{qp} \equiv \begin{bmatrix} \pi_{11} & \pi_{12} & \pi_{12} & 0 & 0 & 0 \\ \pi_{12} & \pi_{11} & \pi_{12} & 0 & 0 & 0 \\ \pi_{12} & \pi_{12} & \pi_{11} & 0 & 0 & 0 \\ 0 & 0 & 0 & \pi_{44} & 0 & 0 \\ 0 & 0 & 0 & 0 & \pi_{44} & 0 \\ 0 & 0 & 0 & 0 & 0 & \pi_{44} \end{bmatrix}. \quad (13.43)$$

Therefore  $\pi_{11}$ ,  $\pi_{12}$ ,  $\pi_{44}$  only are the basic piezo-resistance coefficients corresponding to the crystal axes.

If a filament of silicon is subjected to tension while subjected to an electric field  $E$  and a current  $i$ , the current density can be described by

$$\frac{E}{\rho} = i(1 + \pi_i \sigma), \quad (13.38)$$

where  $E$ , V/cm,

$\rho$ , ohm cm,

$i$ , amp,

$\pi_i$  = longitudinal stress gage factor (coefficient),

$\sigma$  = longitudinal stress.

Defining the current flow in the longitudinal axis of the element and using direction cosines  $l_1$ ,  $m_1$ ,  $n_1$  from the cubic crystal axis to the longitudinal axis of the element, one may express the longitudinal stress gage factor as

$$\pi_i = \pi_{11} - 2(\pi_{11} - \pi_{12} - \pi_{44})(l_1^2 m_1^2 + l_1^2 n_1^2 + m_1^2 n_1^2). \quad (13.39)$$

The gage factor can also be expressed in terms of the piezo-resistive coefficients and the Miller indices  $h$ ,  $k$ ,  $l$ :

$$\pi_i = \pi_{11} + 2(\pi_{44} + \pi_{12} - \pi_{11}) \frac{h^2 k^2 + h^2 l^2 + k^2 l^2}{(h^2 + k^2 + l^2)^2}. \quad (13.40)$$

In terms of the change in resistivity, the simple relation can be used:

$$\frac{\Delta \rho}{\rho_0} = \pi_i \cdot \sigma, \quad (13.41)$$

where  $\rho_0$  = zero stress resistivity,

$\Delta \rho = \rho - \rho_0$ .

It is well known that the changes in resistivity with a stress component  $\sigma$ —(13.41)—are larger when several orientations are involved, since piezo-resistance components add up when different combinations of electric field vectors,

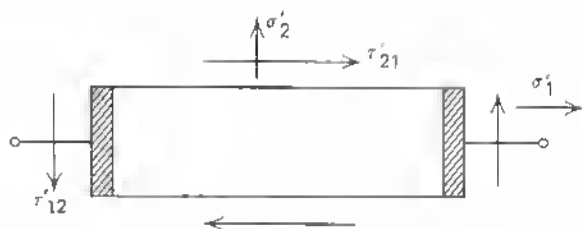


Fig. 13.22 Semiconductor strain gage, and stress components  $\sigma'_1$ ,  $\sigma'_2$  as well as shear stresses  $\tau'_{12}$  and  $\tau'_{21}$

current directions, and piezo-resistance coefficients are combined. For example, consider a semiconductor strain gage, as shown in Figure 13.22, with current in the longitudinal direction. If subjected to a longitudinal stress  $\sigma'_1$ , a transverse stress  $\sigma'_2$ , and a shear stress  $\tau'_{12} = \tau'_{21}$ , the relative resistance change is given by

$$\frac{\Delta R}{R_0} = \pi'_{11} \sigma'_1 + \pi'_{12} \sigma'_2 + \pi'_{44} \tau'_{12}, \quad (13.42)$$

where  $R_0$  = zero stress resistance,

$\Delta R = R - R_0$  = resistance change,

$R$  = resistance under stress.

On a micron scale three major stress components in the crystal may appear as only one external stress component in the expression for the resistance variation  $\Delta R$ .

Numerically, the important piezo-resistance coefficients for silicon at 300°K are, for example:<sup>3</sup>

Type	Resistivity, ohm cm	$\pi_{11}$	$\pi_{12}$	$\pi_{44}$	$\pi_1$
<i>n</i>	11.7	-102.2	53.4	-13.6	-142.0
<i>p</i>	7.8	6.6	-1.1	138.1	-130.4
$\underbrace{\hspace{10em}}_{\times 10^{-2} \text{ cm}^2/\text{dyn}}$					

$$\pi_1 = \pi_{11} - \pi_{12} - \pi_{44}.$$

To maximize  $\Delta \rho / \rho_0$  in (13.41), the gage factor  $\pi_1$  has to be maximized, which results in particular choices of crystallographic orientations with respect to the stress direction.

The saturation character of a single  $\Delta R / R_0$  versus stress component relation limits the efficiency of gauges made of monocrystalline material if they are subjected to uniaxial strain. Therefore, the use of a sample geometry favoring

a summing up of principle strain in several crystallographic directions is desirable. A current direction normal to the plane of gauge fulfills this condition, as shown in Figure 13.23. However, in the case of one major crystallographic direction of the current flow, only multiple components of an essentially unstrained lattice contribute to the piezo-resistance, as shown in Figure 13.24.

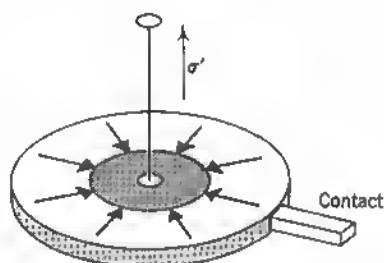


Fig. 13.23 Current direction normal to the plane of gage of a stress-strain transducer.

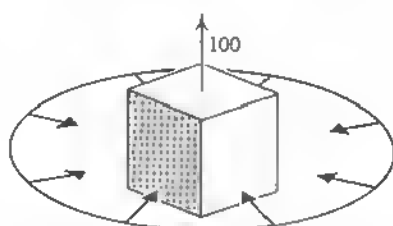


Fig. 13.24 Major current flow in [100] direction within a concentric strain gage.

In bicrystals an originally multioriented crystal sheet gives the possibility of a  $\Delta R/R$  overlap due to stress-component overlap. For example, consider the external stress  $\sigma_a$  acting on a dislocation plane (see Figure 13.25). It is vectorially decomposed at point *A* within the dislocation sheet into two components: a vector  $\sigma_b$  acting perpendicular to the (100) plane of individual crystal one (right bulk crystal) and  $\sigma_c$  perpendicular to the dislocation plane. The relative resistance change in the direction of the dislocation sheet is therefore a function of two basic piezoelectric coefficients. Resulting lattice deformation forces especially on the offset (tangent *t*) lattice planes in the strained crystal induce piezo-resistance changes in the disturbed layer of the bicrystal,  $\Delta$ .

Contacts with the dislocation plane have been discussed and are generally *p*-type in order to make ohmic contact to the *p*-type acceptor layer around the dislocation sheet.



Thus

$$E_{\perp} = \frac{\mu_b^2}{4\pi(1-\nu)} \log\left(\frac{r_1}{r_0}\right) + \frac{b}{2} \int_{r_0}^{r_1} \sigma_a dr. \quad (13.46)$$

There are several ways to use the junction in connection with the bicrystal sheet in stress-strain transducers. Figure 13.26 shows an example of a bicrystal where the junction current is monitored while the pressure  $\Delta p$  is applied orthogonal to the grain-boundary plane. The sensitivity of the junction to light can also be used as shown in Figure 13.27 with the pressure  $\Delta p$  applied parallel

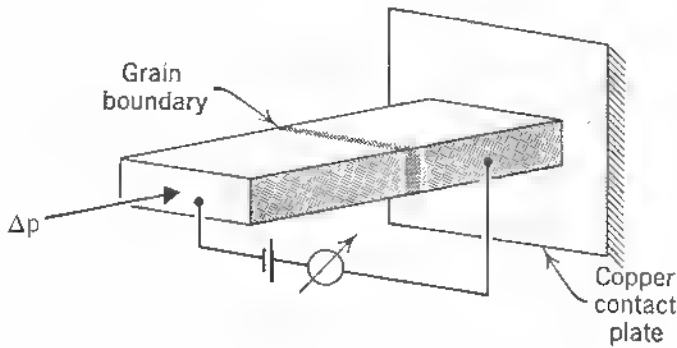


Fig. 13.26 Bicrystal transducer.

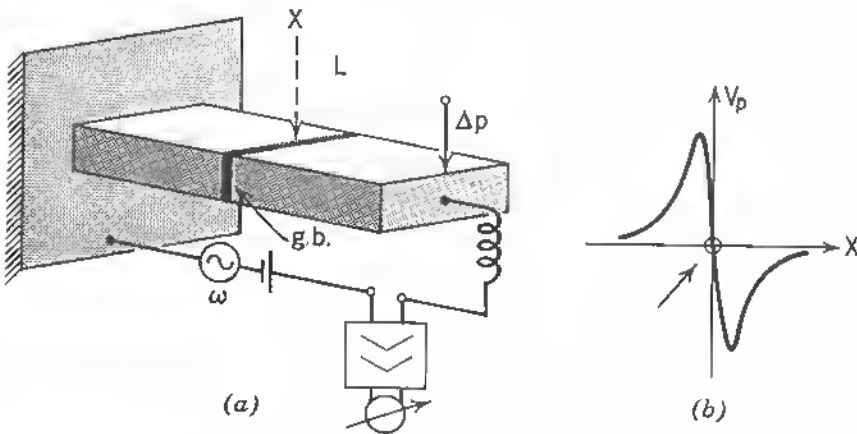


Fig. 13.27 Bicrystal transducer as phototransistor structure with a.c. bias.



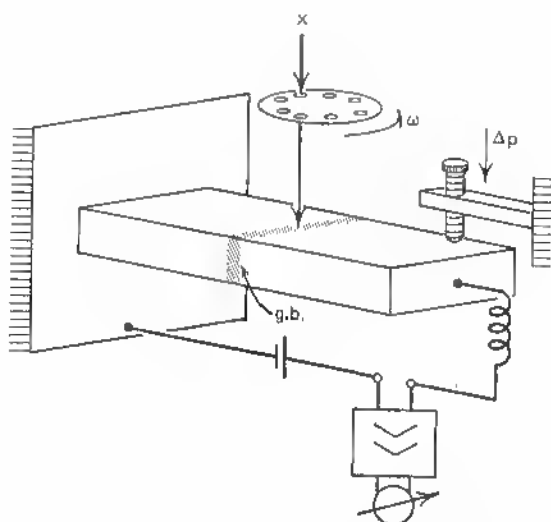


Fig. 13.28 Bicrystal transducer as a.c. light amplifier.

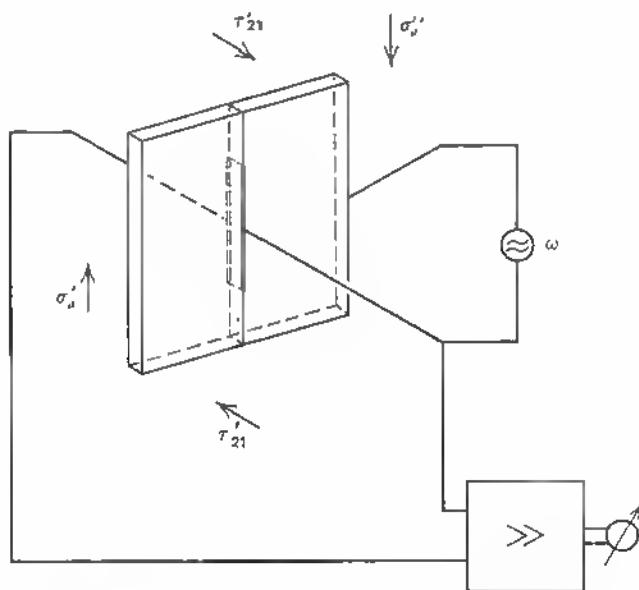


Fig. 13.29 Bicrystal field effect transistor as stress strain transducer.

to the dislocation sheet. Here an alternating bias supply facilitates amplification. In a similar fashion the light intensity can be modulated and the resulting current variations amplified (see Figure 13.28). The most sensitive application without the use of light (phototransistor) is in the form of the field-effect transistor structure described in Section 13.3. In this case, the bicrystal field-effect transistor plate is mounted on the membrane, and a small ac voltage is fed into the gate contact while source and drain contacts (to the grain boundary) are connected to the amplifier (see Figure 13.29). The manifold orientation relations possible for bicrystals to enhance the sensitivity as stress-strain transducers have not yet been considered in detail, but it seems worthwhile to consider this case of especially combined piezo-resistance overlap for particularly sensitive transducers.

### REFERENCES

1. "Semiconductor and Conventional Strain Gages," Mills Dean III and R. D. Douglas (eds.), Academic, New York, 1962.
2. Integrated Silicon Device Technology, vol. V, Physical-Electrical Properties of Silicon, *Techn. Report ASD-TDR-63-316*, Research Triangle Institute, Project 4159, Task 415905.
3. Smith, C. S.: Piezo-resistance in Germanium and Silicon, *Phys. Rev.*, vol. 94, pp. 42-49, April, 1954.

## Chapter 14 Dislocations and the Electronic Properties of Semiconductor Devices

The main application of the knowledge of the properties of dislocations and dislocation arrays lies in the fields of device performance, device yield, device reliability, and reproducibility. Because devices are integrated and are supposed to maintain a high degree of performance, the materials qualities gain increasing importance.

In microelectronics, where device size decreases and device density increases, the bulk material is the key to the definition of device yield when process parameters are well controlled.

How "good" a given crystal material is, however, is a complicated function of device type, operational conditions, density, process parameters, and cost. It is impossible to define the materials quality independent of these parameters. On the other hand, modern high-density microcircuitry has pushed crystal quality control to the point where monocrystals with diameters of several inches are mass-produced for which not only the dislocation density is guaranteed within narrow limits down to zero but where also radial and longitudinal resistivity gradients in the 0.1 per cent range are maintained for material in the ordinary doping ranges.

The control becomes extremely difficult in all cases where process-induced dislocations have to be considered, as in diffusion and ion implantation.

This field is of utmost importance to the industrial device development and production, and we therefore add some considerations that may be useful in the quest for better control of all parameters.

We first summarize some basic effects due to dislocations in devices and then direct our attention to the important field of thin films. Here the limitations are reviewed when structural imperfections are considered. A buildup of a crystal base by homoepitaxial and heteroepitaxial processes is also very important in modern devices and can be combined with the device con-

struction itself. It is imperative to know the constraints in these methods in order to avoid the well-known problem of good laboratory samples but prohibitively low production yields or high costs.

## 14.1 DISLOCATIONS IN JUNCTION DEVICES IN GENERAL

The effects of the dislocations measured in bulk crystals regarding resistivity, mobility, and lifetime have been described earlier. In general, dislocations do not add free electrons to the amount of free carriers available, as had been assumed originally (W. T. Read), but they actually withdraw free electrons from the free carrier pool to form a space charge. As we have seen in the case of III-V compounds, there are, however, situations where dislocations act as donors.

The work on silicon has also shown that both cases can be realized, depending on the environment of the dislocation with respect to doping.

Much literature is available on imperfections, predominantly point defects and statistically distributed dislocations and their behavior in bulk crystals.<sup>1</sup> As a general rule, the resistivity is basically affected only for dislocation densities in excess of  $10^5$  to  $10^6$   $\text{cm}^{-2}$ , which corresponds to an equivalent bulk ratio in intrinsic germanium ( $n_i \approx 10^{13}$   $\text{cm}^{-3}$ ) of  $10^{-4}$  and in silicon ( $n_i \approx 10^{12}$   $\text{cm}^{-3}$ ) to an equivalent of  $10^{-3}$ . It is known, however, that the radial resistivity gradient in Czochralski grown crystals can be kept smaller when such "normal" dislocation density is counted, compared with dislocation-free crystals. This is certainly due to the Cottrell atmospheres around the dislocations. A regular distribution of dislocations across the horizontal crystal axis enhances a more regular impurity distribution and diminishes the effects of the temperature gradient, segregation differences due to rotation (angular velocity gradient), and coring in particular.

A property really sensitive also to small amounts of dislocations is the lifetime of minority carriers. For germanium, the simple rule can be used:

$$N_d(\text{cm}^{-2}) = (\tau[\text{in sec}])^{-1};$$

for example, a dislocation density of  $10^4$   $\text{cm}^{-2}$  allows a lifetime of  $10^{-4}$  sec. Considerable influence on resistivity and mobility values was found in materials where defects were generated by nucleon bombardment. If neutrons of a density approaching the doping range are injected, strong changes and rapid annealing are found.<sup>1</sup> To judge from these figures of the behavior of bulk crystals, one would not consider dislocations a basic impediment for device performance when "normal" densities are considered. This point of view was originally the basis for controversial arguments at the time when mobility and resistivity were considered the most important defining factors for the device potential of a semiconductor material (1948 to 1952). Later it became apparent

that these magnitudes may have excellent values, although the greater number of devices produced from these crystals are useless. This is simply because a device operates on account of steep impurity gradients and high-field regions within a crystal and dislocations, especially within these areas, are able to degrade such devices in a way recognized much later and to be described here. But even today, many researchers predict device potential of materials (e.g., epitaxially grown semiconductors on insulator substrates of other materials) on account of measured resistivity and mobility data only. We discuss the pitfalls of such arguments in Section 14.4.

The modern trend to decrease the individual device size in order to accommodate many devices on one wafer and to accomplish multiple device functions in a "large-scale integration" has produced interesting consequences with respect to yield, performance, reproducibility, and reliability. On the one hand, decreased device size in itself improves the chances of high performance, since more devices are free of dislocations. For example, in material of  $10^6$  dislocations  $\text{cm}^{-2}$ , devices of  $100\mu^2$  active area parallel to the crystal surface would find one dislocation each at an average. In the same material, power transistors of a few  $\text{mm}^2$  surface, however, would find  $10^4$  dislocations per junction area, a prohibitively high amount for reasonable yield.

As device size decreases the use of the available crystal surface increases simply because of a now higher device density. But, judged from an overall point of view of yield, the importance of highly perfect material is the same for large and small area devices. As high-density micro-circuitry with simultaneous deposition of active and passive devices progresses, an ever-increasing emphasis is placed on the perfection of crystals. Dislocations and other large defects, such as impurity clusters or combinations of these, are well-known causes for device performance failure, device deterioration, low reproducibility, and yield, and deviations from design specifications. Therefore, crystal production has developed for years in order to produce more perfect crystals. Czochralski and floating-zone growth equipment has been developed continuously in this direction, and also radial and vertical resistivity gradients have been decreased. The "Dash" seed-crystal diameter-reduction method in Czochralski growth and in modified floating-zone equipment can yield dislocation-free material, and the growth methods (speed of rotation and lift) are so well in hand today that almost any desired dislocation density can be achieved. The use of dislocation-free crystals has increased greatly during the last years in spite of the fact that process-generated dislocation densities are often even higher than the figure of  $10^3 \text{ cm}^{-2}$  quoted for good "ordinary crystals." Much work has been done in order to identify the process characteristics responsible for the generation of dislocations and corresponding device failure and degradation. G. Schwuttke has made important contributions in this field and has shown that diffusion, heat treatment, alloying, and formation of oxide layers generate crystallographic disturbances that are altering if not

destroying device characteristics (see Ref. 2, with main literature cited in the text). An important tool developed to "see" such crystallographic changes is the SOT technology of producing x-ray diffraction topographs of larger crystal areas. SOT, scanning oscillator technique, describes a modified x-ray diffraction method originally described by A. R. Lang [*J. Appl. Phys.*, **30**, 1748 (1959)], in which the primary x-ray beam is shielded and only the diffracted beam reaches the photoplate. In trying to apply this method of a very refined structural analysis to larger crystal areas and even complete wafers, G. Schwuttke introduced the scanning mode, in which the incoming x-ray beam oscillates around a central position of incidence by slight angular deflections.

A large amount of pictures of crystals before and after processing through typical microelectronic production steps shows that dislocations and dislocation networks (lineage) are generated by the following:\*

1. Surface damage (handling)
2. Thermal oxidation
3. Diffusion of impurities like phosphorous and boron (within the diffused areas)
4. Diffusion-generated strain in adjacent areas not subject to the diffusion (stress jumping especially in the case of emitter edge dislocations)
5. Ion implantation
6. Alloying
7. Metal deposition

The original project of the growth of silicon web dendrite crystals was concerned with the growth of perfect crystals by a cheaper method than Czochralski growth in order to avoid the cutting and subsequent losses of crystal boules when tailored into wafers.

Such dendrites have been found to abound with crystallographically strained regions that, on thermal processing, convert into dislocation networks and make these crystals highly imperfect.<sup>2</sup>

As far as the actual influence of dislocations on devices is concerned, experimental work shows clearly their effect of increasing diode leakage current and causing microplasma breakdown.<sup>3, 4</sup> It has been found, however, that their direct electronic effects in silicon are less apparent than in germanium and gallium arsenide. As we have seen, silicon has a tendency to form twin lattice structures without dangling bonds, and most often the free bonds of dislocations are neutralized by surrounding point defects.<sup>5</sup> The Cottrell atmosphere can directly serve as a neutralizing agent. Here foreign atoms with smaller radii than the host atoms find their appropriate place in the compression regions, and larger impurity atoms are drawn into the dilation

\* For an excellent treatise on the microscopy of dislocations, see: S. Amelinckx: "The Direct Observation of Dislocations", Solid State Physics Suppl. 6, Academic Press 1964.

regions surrounding the dislocations. Also metal deposits can cluster in or around dislocations as nucleation centers.

Complex interactions among impurities, defects, and surfaces are possible in device production, where many different doping agents and metals can act in conjunction. The accumulation of copper as a precipitate in the junction area may be less strong for a higher dislocation density in the bulk so that for the particular temperature treatment the copper atoms are drawn into these sites instead of precipitating near the space charge, where they degrade the junction of a device. This is a special case of a useful role of some dislocations in the bulk.

Also the statement that stable dislocations are less damaging than moving dislocations is correct, since in device production such strain-propelled cluster centers easily concentrate because of a stress field in one direction. But it is at least a simplistic generalization, therefore, to consider the dislocation a useful part of the bulk.<sup>6</sup> Whelan<sup>3</sup> has clearly shown that the measurements of the leakage current of diodes can be correlated with the dominant recombination generation level of the dislocations.

Plotting the reverse current versus temperature (actually  $I/n_i$  versus  $10^3/T$ ) and comparing with the current expression as derived for a recombination center near the center of the energy gap,

$$I_{sp} = -AWqn_i/[\tau_{p0}e^{\beta(\phi_i - \phi_c)} + \tau_{n0}e^{-\beta(\phi_i - \phi_v)}], \quad (\text{Sah-Noyce-Shockley})^*$$

where  $A$  = constant (area),

$q$  = electronic charge,

$n_i$  = intrinsic carrier density,

$W$  = space-charge width,

$\beta = 1/kT$ ,

$\tau_{p0} \equiv (N_t \sigma_n v)^{-1}$ ,

$\tau_{n0} \equiv (N_t \sigma_p v)^{-1}$ ,

$N_t$  = density of bulk recombination generation centers,  $\text{cm}^{-3}$ ,

$\sigma_n, \sigma_p$  = capture cross sections of defect for electrons, holes,

$v$  = thermal velocity of free holes and electrons,

gives a reasonable value for  $\phi_i - \phi_c = \pm 0.055$  eV for the dislocation level, compared with the center of the gap energy  $\phi_i$  (0.585 eV). (Silicon)

Whelan argues that in his case  $\phi_i - \phi_c$  is negative, because a positive value would lead to electron lifetimes higher in the space-charge region than in the bulk, which is unlikely because of the defects present near his  $n^+$  regions for MOS transistors. With the silicon mid-band value  $\phi_i = 0.585$  eV from the valence band,  $\phi_i - \phi_c = -0.055$  gives a value of

$$\phi_c = 0.640 \text{ eV}$$

\* Proceed. IRE; 45, p. t228 (1957).

in accordance with the dislocation level in silicon measured by other methods (see Section 9.1).

Measurements of the conduction anisotropy in deformed samples have generally established the fact that the space-charge cylinders around dislocations are the main factor to consider<sup>7</sup> (see also Section 11.2 and Figure 14.1).

Sometimes the explanation for the increased leakage current is based on the Cottrell atmospheres around dislocations. Here foreign atoms with smaller ionic radii than the host concentrate within the compression regions and impurities with larger ionic radii find their appropriate places in the dilation regions around the dislocation. We mentioned also that metal deposits can form in or around dislocations as nucleation sites.

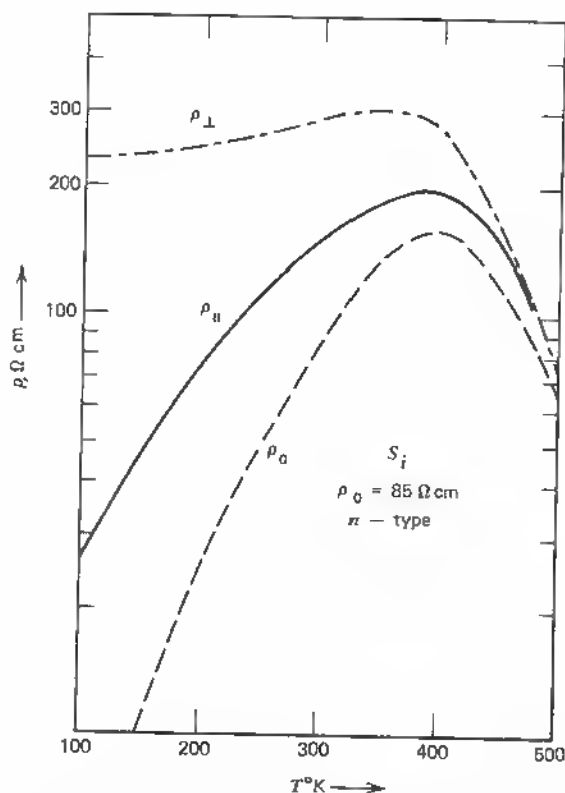


Fig. 14.1 Temperature dependence of resistivity parallel ( $\rho_{\parallel}$ ) and perpendicular ( $\rho_{\perp}$ ) to dislocation pipes ( $\rho_0$  unbent sample) (after Glaenger-Jordan<sup>7</sup>).



All these effects are certainly deleterious for device properties. It is, however, an important question to what degree these effects influence the device performance in actual cases of device production and in microcircuits and if effects of isolated dislocations in statistical distribution are as important a cause for failure as dislocation agglomerations or lineage, for example, where the Cottrell atmospheres are of lesser importance than in the case of individual dislocations.

The impurity atom has a radius that may be represented as

$$r_h = r(1 + \epsilon_i),$$

where  $r_h$  = host atomic radius,

$\epsilon_i$  = correction factor or proportionality constant of impurity atom with respect to host atom radius:  $\epsilon_i = (r_i - r_h)/r_h$ .

If  $\epsilon_i$  is negative, the compression side of the dislocation is occupied; if  $\epsilon_i$  is positive, the dilation side is involved.

Queisser et al.<sup>8</sup> estimate that for phosphorous

$$\epsilon(P^+) = -0.055 \text{ to } -0.09.$$

The higher value is an estimate based on tetrahedral radii and ionization of the phosphor atoms. Using the mean value of

$$\epsilon(P^+) = -0.07,$$

we have for the impurity radius

$$r_i = r_h \times 0.93.$$

Since, for example, in silicon  $r(\text{Si}) = 1.17 \text{ \AA}$ , the impurity radius is

$$r_i = 1.17 \cdot 0.93 \text{ \AA} = 1.088 \text{ \AA},$$

while  $r(P) = 1.10 \text{ \AA}$ .

This would actually correspond to a reduction of the ionic radii in dislocation sites when the compression regions are occupied.

Experience tends to give preponderance to the actual space charge originating from the free bonds. Only in extreme cases of impurity clustering around dislocation sites acting as nucleation centers, do strong electronic effects result (for example, in copper decoration). These cases are relatively rare in devices produced with ordinarily moderate impurity densities.

As shown in the preceding chapters on the electronic properties of dislocations, our main concern should be the actual array of dangling bonds and the resulting space-charge pipe.

As we have seen, such a pipe acts as a highly conducting path because of wave function overlap but establishes blocking properties in a direction perpendicular to the pipe.

Therefore the orientation of the dislocation is of importance for its behavior in depletion layers where its influence is mostly felt.

The high field region in all junction devices or the intrinsic layers are most sensitive in this respect. If the array is located (*a*) in the direction of the field lines between the *n* and *p* layer, it establishes an efficient breakdown region and forms the origin for microplasma excitation (case *a* in Figure 14.2). If the dislocation is (*b*) running parallel to the *p-n* layer, it may not interfere with the junction properties, but its space charge widens considerably because of the bias effect (see Section 9.3).

In case *a*, a high current density also leads to local heating effects and eventually to a destruction of the crystal properties (segregation, second phase formation, melting, and the like).

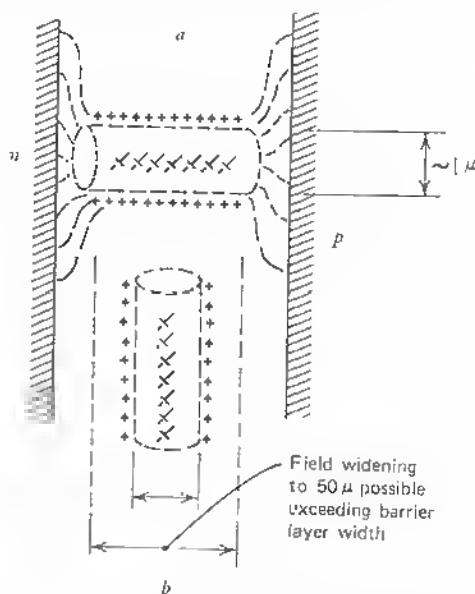


Fig. 14.2 Dislocation arrays with space charge pipe in two positions within barrier layer region.

It is due to these effects of dislocations, especially of the lineage type, that bipolar devices are extremely dependent on the dislocation density.

Process-induced dislocations have the same effects as in-grown defects when they are located within the high field regions of the devices. But this does not mean that the original wafer perfection is less important. All causes contributing to the dislocation density should be avoided. If, however, the original wafer has a dislocation density  $N_A \leq 10^3 \text{ cm}^{-2}$  and a high concentration

phosphorous diffusion, for example, generates  $N_A = 10^6 \text{ cm}^{-2}$ , the wafer quality can be lowered to  $N_A = 10^4 \text{ cm}^{-2}$  without a major loss in device yield, because the number of dislocations per given device or junction area on account of grown-in dislocations is only 1 per cent of the generated dislocation density.

We have already mentioned that dislocations and their effect on the lifetime of minorities are a specific reason of failure in bipolar transistor structures.

In unipolar devices like field-effect transistors, this dependence on the bulk crystal properties does not exist to such degree because only majority carriers move across the source-drain channel and the device works satisfactorily as long as the gate electrode is not drawing appreciable leakage current through the channel isolation (a dielectric layer, a depletion layer, or a surface barrier layer). However, the last condition is no longer fulfilled when dislocations

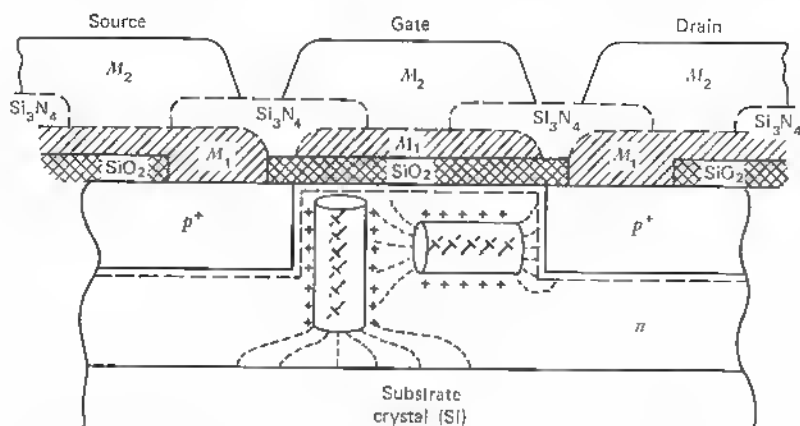


Fig. 14.3 MOS (FET) cross section, and effect of dislocation pipes on current flow in channel region.

are orientated perpendicularly to the gate surface within the gate depletion region. This is an occurrence of great probability in all surface barrier (MOS, FET) devices, since the surface-generated dislocations, due to the  $\text{SiO}_2$  deposition, for example, are in the proper direction as they are generated by tensile stress due to the difference in expansion coefficient. In Figure 14.3, we show how the dislocation array can interfere with the operation of an MOS structure.

In the case of random distribution of dislocation networks, the approach to the problem is generally to define two sets of transport parameters (as carrier density, mobility, resistivity, etc.), one within the space charge pipe, the other one in the bulk. If the width of the dislocation space charge is  $l_d$

and the remaining bulk is  $l_o$ , the ratio

$$\gamma \equiv l_d/l_o \quad (14.1)$$

defines the relative importance of the dislocations or  $\varepsilon = (1 + \gamma)^{-2}$  the relative area of bulk material per surface area. Then e.g., the number of free plus trapped carriers per unit area is given by:

$$\bar{n} = \varepsilon n_o + (1 - \varepsilon) n_d \quad (14.2)$$

where  $n_d$  = carrier density within dislocation region

$n_o$  = carrier density within bulk region

(for more detailed parameter-evaluation, see Chapter 9.2).

It has been found that dislocation networks at the surface of unipolar devices result in a strong field dependence of the surface mobility. The increase in surface mobility with the cross-field applied was first reported by Waxman et al.<sup>9</sup> for vapor-deposited CdS-films when used in MOS-structures. To explain the measured strong increase in Hall- and field-effect mobilities (by as much as a factor of 12) by application of the field voltage, these authors assume a mosaic structure with barriers between the different crystal regions. The origin of these barriers was supposed to be a variable impurity density caused by stoichiometric variations within the film. It is easy to show, however, that the necessary barrier height of a few tenth of an eV would require doping differences which are unlikely to occur even in vapor deposition of II-VI compound semiconductors: The barrier height  $\phi$  expressed as a function of the carrier densities  $n_1$  and  $n_2$  in adjacent regions is:

$$\phi = kT \ln(n_1/n_2). \quad (14.3)$$

At room temperature 1 eV  $\simeq 40 kT$ . Assuming a barrier of 0.1 eV only, we would have:

$$n_2/n_1 = e^4 \simeq 55.$$

Such resistivity changes are unlikely. Grain boundary barriers on the other hand will have a sufficient barrier height due to the broken bonds as we have seen (See Chapter 11.2).

The number of charges in grain boundary states is:

$$q/q_o = \frac{1}{2} [1 + (1 + eV_e/\phi)^{1/2}] \quad (14.4)$$

(see Chapter 11.2, Equ. 11.40)

$q_o$  = equilibrium number of charge carriers

$q$  = charge number due to  $V_e$

$V_e$  = external voltage applied across space charge pipe

$e$  = electron charge

$\phi$  = barrier height

(14.4) allows to express the barrier height  $\phi$  in terms of the applied voltage  $V_e$ :

$$\phi = \frac{eV_e}{4 \, q/q_o(q/q_o - 1)}. \quad (14.5)$$

Now the relative number of boundary charges can be represented by a vertical field gradient resulting in

$$\phi_{\perp} = e\Delta V_{\perp} = kT \ln q/q_o. \quad (14.6)$$

Therefore, the barrier height can be represented by:

$$\phi = eV_e/[4 \exp(e\Delta V_{\perp}/kT)][\exp(e\Delta V_{\perp}/kT) - 1] \quad (14.7)$$

(14.7) shows that the vertical field has a strong influence on the barrier within the surfacelayer or film depressing the barrier height at small field voltages  $V_{\perp}$  and accounting for the mobility increase. The mobility expression derived by Waxman et al.<sup>9</sup> is based on (14.3) with the provision that the surface potential is increased by the field plate inducing a change in carrier density:  $\Delta n$ . Therefore:

$$\phi_{\perp} = kT \ln[(n_i + \Delta n/L_c)/(n_2 + \Delta n/L_c)] \quad (14.8)$$

with  $L_c$  = width of accumulation layer.

In the grain boundary case we can replace the carrier densities by the charges in surface states  $q$  and  $q_o$  as in (14.6). For a change  $\Delta q$ , we have:

$$\phi'_{\perp} = kT \ln[(q + \Delta q/d)/(q_o + \Delta q/d)] \quad (14.9)$$

where  $d$  = width of grain boundary barrier

and the change in barrier height is:

$$\Delta\phi = \phi - \phi_{\perp} = kT \ln[(1 + \Delta q/dq_o)/(1 + \Delta q/dq)] \quad (14.10)$$

The change  $\Delta q$  can be expressed by a field voltage:

$$V_{\perp} \, \theta \epsilon_i / t_i = e\Delta q \quad (14.11)$$

$\theta$  = ratio of induced free charges to trapped charges

$\epsilon_i$  = permittivity  
 $t_i$  = thickness } of the insulator layer

$e$  = electron charge

Introducing the expressions:

$$\left. \begin{aligned} \alpha &= \theta \epsilon_i / e t_i d \cdot q \\ \beta &= \theta \epsilon_i / e t_i d \cdot q \end{aligned} \right\} \quad (14.12)$$

Equation (14.10) writes:

$$\Delta\phi/kY = -\ln[(1 + \alpha V_{\perp})/(1 + \beta V_{\perp})] \quad (14.13)$$

The Hall mobility for the granular surface layer can be expressed as:

$$\mu_H = e\langle v \rangle e^{-\Delta\phi/kT} / 4NkT \quad (14.14)$$

(see [14.9])

where  $\langle v \rangle$  = mean carrier velocity

$N$  = number of grain boundary barriers

and following (14.13):

$$\mu_H = \frac{e\langle v \rangle}{4NkT} \cdot \frac{1 + \beta V_{\perp}}{1 + \alpha V_{\perp}}, \quad (14.15)$$

(See Reference 14.10)

The case considered by Waxman et al. is based on a difference between  $n_1$  and  $n_2$  in the film-domain and leads to a mobility:

$$\mu_H = \frac{e(v)}{4kTN} \cdot \frac{n_2 + \text{const} \frac{n_2}{n_1} V_{\perp}}{n_2 + \text{const} V_{\perp}} \quad (14.16)$$

increasing rapidly for small field voltages  $V_{\perp}$  and reaching saturation at about half a volt for  $V_{\perp}$ .

The values chosen for  $\theta$ , the ratio of induced free to trapped charges, was varied between  $10^{-1}$  and  $10^{-2}$ .

Instead of (14.16), we have in this case (14.12) a mobility:

$$\mu_H = \frac{e(v)}{4kTN} \frac{1 + \text{const} \frac{q}{q_0} V_{\perp}}{q + \text{const} V_{\perp}} \quad (14.17)$$

which results in a similar increase of  $\mu_H$  for small field voltages  $V_{\perp}$  but for  $n_1 = n_2$ .

The influence of misfit dislocations on the interfacial mobility has been derived in a more general form by G. F. Neumark<sup>11</sup> starting with the void model mentioned. From the average carrier concentration  $\bar{n}$  (Equation 14.2) and the bulk density  $n_0$  the effective mobility is defined as:

$$\bar{\mu} = \mu_0 \cdot \bar{\sigma} n_0 / \sigma_0 \bar{n} \quad (14.18)$$

$\bar{\sigma}$  = average conductivity,  $\mu_0$  = bulk mobility

$\sigma_0$  = bulk conductivity

and can be developed further by appropriately expressing  $\bar{\sigma}$  and  $\sigma_0$ . This leads to a similar law for the mobility as a function of the carrier density ratio  $n_0/n_d$  and with the parameter  $\gamma$  (14.1) which corresponds to our parameter  $q/q_0$ .

In this more statistical approach to the problem, the conduction along dislocation lines is equated to the one perpendicular across the pipes. While this may be representative for random dislocations, any preferred orientation of

the space charge pipes would, however, lead to a clear anisotropy of conduction such that carrier mobility values would be higher parallel to the pipes.

In MOS devices we find less of an influence in terms of catastrophic failures as is known from bipolar devices; however, the critical device parameters may change from device to device and from batch to batch so that no reproducibility or yield within reasonable cost limits can be achieved.

Here we have the outstanding problem caused by defect crystals. Although interesting device properties can be found on a laboratory scale, no reliable production can be based on material which is defect to a degree that interferes with the device yield expected. That this consideration is of great importance in the evaluation of new materials and materials combinations has been found in many cases in the past. Especially devices produced from heteroepitaxial material of low crystallographic perfection generally have to be considered production hazards (see Section 14.4).

We also want to mention the case of ion implantation. It is a preferred method in modern device technology, especially in the construction of MOS devices. Here the source and drain regions are produced by ion implantation while the gate metal serves as mask,<sup>12</sup> and thus optimum alignment is achieved and parasitic gate capacities can be minimized.

As elegant as this method is—it can be combined with vacuum evaporation of contacts and sputtering—as certain is a destructive influence on the crystal, especially when deeper penetration has to be achieved. The case of a shallow  $p^+$  layer in the case of an MOS-FET structure is especially suited; however, the junction interfaces of ion implanted junctions always have a high dislocation density. In fact, earlier studies showed that ion implantation has to be followed by a diffusion step in order to carry the doping layer beyond the final damage point into the undamaged crystal material or to subject the crystal to strong annealing<sup>13</sup> in order to achieve a flat  $p$ - $n$  junction.

The damage to the crystal is a function of the energy of the ions on implantation. Therefore, deep implantation, as needed in bipolar devices, has proved impracticable. To some extent, the relatively open lattice of the major semiconductors in certain crystallographic directions can be used to “channel” the ions deeper into the material.<sup>14</sup> In a junction formation, one wants, however, to produce a flat front of impurities, which is a problem when channeling is used. Especially energetic ions, used to form a doped layer, for example,  $2\ \mu$  deep, have damaging effects in the crystal<sup>15</sup> because of the spiking phenomenon, that is, the final path is marked by a thermal spike where the energy of the moving particle or ion is converted into heat and attendant damage to the lattice.<sup>16</sup>

In modern device technology, the heterojunction plays an important role. Since Kroemer's original proposition<sup>17</sup>, many applications have been made

of the interface-field either to enhance injection of carriers or to confine injected carriers or both. (See Figure 14.4a.)

The injection gain due to a wide-to-low gap transition is considerable. Kroemer has shown that the injection efficiency  $\gamma$  in this case increases exponentially with the band gap difference for injection from high-to-low gap. In terms of the hole and electron current densities,  $j_p$  and  $j_n$  at the junction:

$$\gamma = \frac{j_p}{j_n + j_p}$$

or the injection deficiency

$$D_i = \frac{1 - \gamma}{\gamma}$$

is simply

$$D_i = \frac{j_n}{j_p} \quad (14.19)$$

Using the well-known relations for the junction current

$$j_{p,n} = j_{\text{sat}} \left( \exp \frac{qV}{kT} - 1 \right)$$

$j_{\text{sat}}$  = saturation current

$q$  = electron charge

$V$  = voltage applied

$kT$  = Boltzmann factor

one shows easily<sup>17</sup> that

$$D_i = \frac{j_n}{j_p} = \frac{D_{ne} L_{pb}}{D_{nb} L_{pe}} \frac{N_b}{P_e} \left( \frac{m_{ne}^* m_{pe}^*}{m_{nb}^* m_{pb}^*} \right)^{3/2} \exp(-\Delta E/kT)^* \quad (14.20)$$

$D_{ne}$ ,  $D_{pe}$  = diffusion constants for electrons in the emitter and holes in the base

$L_{ne}$ ,  $L_{pe}$  = corresponding diffusion lengths

$N_b$ ,  $P_e$  = net donor density in base ( $N$ -side in Figure 14.4) and net acceptor density in emitter ( $P$ -side in Figure 14.4).

$\frac{m_{ne}^* m_{pe}^*}{m_{nb}^* m_{pb}^*}$  = effective masses of electrons of electrons ( $n$ ) and holes ( $p$ ) in emitter ( $e$ ) and base ( $b$ )

$\Delta E = E_e - E_b$  = energy band difference.

\* The electron and hole current densities at the junction (Equation 14.3) are given explicitly by:

$$j_n = \frac{q D_{ne} n_{oe}}{L_{ne}} \left( \exp \frac{qV}{kT} - 1 \right)$$



$$j_p = \frac{q D_{pb} p_{ob}}{L_{pb}} \left( \exp \frac{qV}{kT} - 1 \right)$$

Here  $n_{oe}$ ,  $p_{ob}$  = equilibrium minority carrier densities in emitter (electrons) and base (holes).

Therefore with (14.19)

$$D_1 = \frac{D_{ne}}{D_{pb}} \frac{L_{pb}}{L_{ne}} \frac{H_{oe}}{p_{ob}}$$

Now the equilibrium minority carrier densities can be expressed by the intrinsic carrier densities  $n_{ie}$  and  $n_{ib}$  in emitter and base:

$$n_{oe} = \frac{n_{ie}^2}{p_e}; \quad p_{ob} = \frac{n_{ib}^2}{n_b}$$

On the other hand the intrinsic carrier densities are given by the state density equations:

$$n_{ie}^2 = \{N_c N_v \exp[-(E_c - E_v)/kT]\} \text{ emitter}$$

$$n_{ib}^2 = \{N_c N_v \exp[-(E_c - E_v)/kT]\} \text{ base}$$

According to the usual Fermi statistics, the effective state densities are:

$$\begin{aligned} \text{emitter} \quad & \begin{cases} N_{ce} = 2 \left( \frac{2\pi m_{ne}^* kT}{h^2} \right)^{3/2} = 2.5 \cdot 10^{19} \left( \frac{m_{ne}^*}{m_0} \right)^{3/2} \left( \frac{T}{T_0} \right)^{3/2} \\ N_{ce} = 2 \left( \frac{2\pi m_{pe}^* kT}{h^2} \right)^{3/2} = 2.5 \cdot 10^{19} \left( \frac{m_{pe}^*}{m_0} \right)^{3/2} \left( \frac{T}{T_0} \right)^{3/2} \end{cases} \\ \text{base} \quad & \begin{cases} N_{cb} = 2 \left( \frac{2\pi m_{nb}^* kT}{h^2} \right)^{3/2} = 2.5 \cdot 10^{19} \left( \frac{m_{nb}^*}{m_0} \right)^{3/2} \left( \frac{T}{T_0} \right)^{3/2} \\ N_{cb} = 2 \left( \frac{2\pi m_{pb}^* kT}{h^2} \right)^{3/2} = 2.5 \cdot 10^{19} \left( \frac{m_{pb}^*}{m_0} \right)^{3/2} \left( \frac{T}{T_0} \right)^{3/2} \end{cases} \end{aligned}$$

$h$  = Planck's constant  
 $T_0 = 300^\circ K$

With these values, the intrinsic carrier densities are:

$$n_{ie}^2 = (m_{ne}^* m_{pe}^*)^{3/2} \exp[-(E_{ce} - E_{ve})/kT]$$

$$n_{ib}^2 = (m_{nb}^* m_{pb}^*)^{3/2} \exp[-(E_{cb} - E_{vb})/kT]$$

To evaluate  $D_1$ , we need an expression for the ratio  $n_{ie}^2/n_{ib}^2$ :

$$\frac{n_{ie}^2}{n_{ib}^2} = \left( \frac{m_{ne}^* m_{pe}^*}{m_{nb}^* m_{pb}^*} \right)^{3/2} \{ \exp(-E_{ce} + E_{ve} + E_{cb} - E_{vb})/kT \}$$

and since: (See Figure 14.4a)

$$E_{ce} - E_{cb} = \Delta E; \quad E_{ve} - E_{vb} = 0;$$

we have

$$\frac{n_{Te}^2}{n_{Tb}^2} = \left( \frac{m_{ne}^* m_{pe}^*}{m_{nb}^* m_{pb}^*} \right)^{3/2} \exp(-\Delta E/kT)$$

or for  $D_I$ , Equation (14.20)

q.c.d.

In (14.20) the factor characterizing the heterojunction is:

$$F = \left( \frac{m_{ne}^* m_{pe}^*}{m_{nb}^* m_{pb}^*} \right)^{3/2} \exp(-\Delta E/kT) \quad (14.21)$$

Assuming equal effective masses of electrons in the emitter and base and holes in emitter and base, the main influence on the injection deficiency is given by the factor

$$\exp(-\Delta E/kT)$$

which for only  $\Delta E = 0.2$  eV and for  $kT = 0.025$  eV at room temperature yields.

$$\exp(-\Delta E/kT) = 3.3 \cdot 10^{-4}$$

or a correspondingly increased injection efficiency  $\gamma$ .

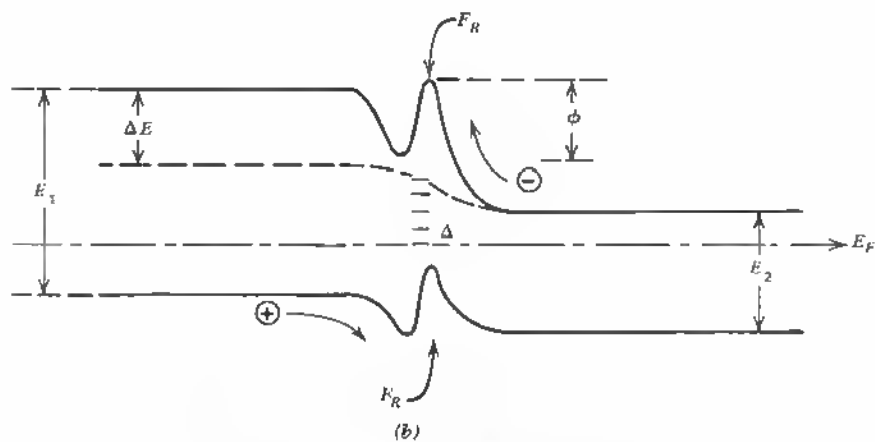
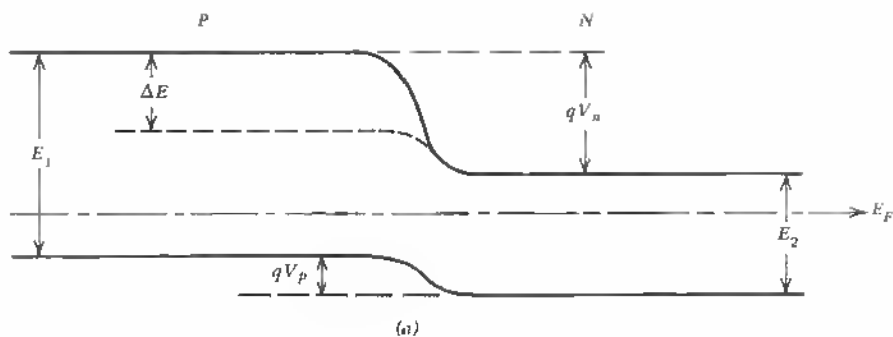
The assumption of equal effective masses on either junction side cannot be assumed for very different semiconductors and strong doping differences ( $m^*$  increases e.g. in GaAs for a factor between 2 and 3 in the range  $10^{16}$  to  $10^{19}$  cm $^{-3}$  doping<sup>18</sup>). The most significant cases are, however, combinations like:

$$\text{GaAs} \sim \text{Ga}_x\text{Al}_{1-x}\text{As}$$

(with  $x \simeq 0.3$ ).

used in light emitting structures. Here the injection efficiency and the carrier confinement due to the interface barriers (see<sup>19</sup>) have given great importance to the heterojunction. A close lattice match is of great importance because the junction interface has to be as perfect as possible to eliminate low threshold spots and nonradiative recombination centers. Interface dislocations will change the band structure as shown in Figure 14.4b (see also<sup>20</sup>). Here the the recombination flux  $F_R$  through the interface is an unwanted feature decreasing the injection efficiency.

Progress in this field has been made however especially when implantation is used for lower doping densities with subsequent annealing and diffusion.<sup>21</sup>



$E_1$  = Gap in eV at emitter side  
 $E_2$  = Gap in eV at base  
 $E_F$  = Fermi level  
 $\phi$  = Barrier height due to  $\Delta$

$V_n, V_p$  = Barrier voltage for electrons, holes  
 $\Delta$  = Dislocation levels  
 $F_R$  = Recombination flux

Fig. 14.4 (a) Band Structure of heterojunction:  $E_1 > E_2$  assuming no interface distortions and no doping differences (b) Band structure of heterojunction:  $E_1 > E_2$  but with interface distortions (no doping difference)  $F_R$  = recombination flux through interface states.

## REFERENCES

1. Rhodes, R. G.: "Imperfections and Active Centres in Semiconductors," Pergamon, New York, 1964.
2. Schwuttke, G.: Semiconductor Junction Properties as Influenced by Crystallographic Imperfections, Report 2, Report AFCRL-67-0564, Contract AF19(628)—5059, Project 5621, Task 562104, 1967.
3. Whelan, M. V.: Leakage Currents of  $n^+p$  Silicon Diodes with Different Amounts of Dislocations, *Solid State Electronics*, vol. 12, pp. 963-968, 1969.
4. Chynoweth, A. G.: Internal Field Emission, in "Progress in Semiconductors," A. F. Gibson, F. A. Kröger, and R. E. Burgess, (eds.), Wiley, New York, pp. 97-123, 1960.
5. Queisser, H. J.: Observations and Properties of Lattice Defects in Silicon, in "Semiconductor Silicon," R. R. Haberecht and E. L. Kern (eds.), The Electrochemical Society, pp. 585-595, 1969.
6. Lawrence, J. H.: On Lattice Disorders, Solute Diffusion, Precipitation and Gettering Silicon Devices, in "Semiconductor Silicon," R. R. Haberecht and E. L. Kern (eds.), The Electrochemical Society, pp. 596-607, 1969.
7. Glaeser, R. H.: and A. G. Jordan: The Electrical Properties of Dislocations in Silicon II, *Solid State Electronics*, vol. 12, pp. 259-266, 1969.
8. Queisser, H. J., K. Hubner, and W. Shockley: Diffusion along Small-angle Grain Boundaries in Silicon, *Phys. Rev.*, vol. 123, no. 4, pp. 1245-1254, Aug. 15, 1961.
9. Waxman, A., V. E. Henrich, F. V. Shall-Cross, H. Borkan, and P. K. Weimer, "Electron Mobility Studies in Surface Space Charge Layers in Vapor-Deposited CdS Films," *J. Appl. Phys.* Vol. 36, No. 1, 168-175, January (1964)
10. Mataré, H. F. and J. J. Grossman, "Thin Film Semiconductors," Proceed. 3rd International Vacuum Congress, Vol. 2 (Parts 1-3), 317-327, Pergamon Press, 1966
11. Neumark, G. F., "Theory of the Influence of Misfit Dislocations on Interfacial Mobility and Hall Effect," *Phys. Rev. B.*, Vol. 1, No. 6, 2613-2622, March 15, 1970
12. Bower, R. W., G. H. Dill, K. G. Aubuchon, and S. A. Thompson: MOS-Field Effect Transistors Formed by Gate Masked Ion Implantation, *IEEE Transactions on Electron Devices*, vol. ED15, no. 10, pp. 757-761, October, 1968.
13. Itoh, T., T. Iuada, and K. Kanekawa: Doping of Silicon by Ion Implantation, *Appl. Phys. Letters*, vol. 12, no. 8, pp. 244-246, Apr. 15, 1968.
14. Brice, D. K.: A Survey of Channelling Theories, in "Radiation Effects in Semiconductors," F. L. Vook (ed.), Plenum, New York, pp. 386-397, 1968.
15. Schwuttke, G. H., K. Brack, E. E. Gardner, and H. M. DeAngelis: High Energy Nitrogen Doping of Single Crystal Silicon, in "Radiation Effects in Semiconductors," F. L. Vook (ed.), Plenum, New York, pp. 406-417, 1968.
16. Brinkman, J. A.: On the Nature of Radiation Damage in Metals, *J. Appl. Phys.* vol. 25, p. 961, 1954.

17. Kroemer, H., Theory of a Wide-Gap Emitter for Transistors, *Proceed. IRE*, Vol. 54, No. 11, 1535-1537, 1957.
18. Nasledov, D. N., Energy Spectrum and Scattering of Current Carriers in GaAs, *J. Appl. Phys., Suppl.* Vol. 32, No. 10, 2140-2145, October (1965).
19. Kroemer, H., "A Proposed Class of Heterojunction Injection Lasers," *Proceed. IEEE*, Vol. 51, No. 12, 1782-1783, 1963.
20. Oldham, W. G. and G. A. Milnes, Interface States in Abrupt Semiconductor Heterojunctions, *Solid State Electronics*, Vol. 7, No. 2, 153-165, 1964.
21. Mayer J. W., L. Erikson, J. A. Davies: *Ion Implantation in Semiconductors*, Academic Press, New York 1970.

## 14.2 DISLOCATIONS AND SEMICONDUCTOR LASER DEGRADATION

The noncatastrophic degradation of semiconductor lasers is an important cause for limitation of their application at a larger scale. It is known that the degree of degradation is coupled with the degree of lasing inhomogeneities. This means that a laser diode showing strong localization of light output just below threshold burns out gradually at a lower current density than diodes with a more regular, that is, distributed, light output over the full extension of their junction.

There is no doubt that light output at localized points below the threshold is associated with interband levels mainly caused by dislocations.<sup>1, 2</sup> As described, a dislocation consists of a core or dangling-bond array and a space charge surrounding it. Such a structure is rather complex in its behavior in electric fields in that more electrons can be associated with the free bonds as the field across the space-charge cylinder increases. This is the case when the dislocation is running parallel to the laser junction. This orientation is prevalent when, for example, liquid epitaxy is applied and a lattice mismatch arises because of the dopant in the grown-on part of the junction during liquid homoepitaxy. If one assumes a lattice mismatch  $\delta = a_0 - a_1$ ,  $a_0$  = lattice constant of host crystal,  $a_1$  = lattice constant of, for example,  $n$ -type doped layer, then the distance between the dislocations generated is

$$\Delta = \frac{S a_0^2}{\delta}, \quad (14.22)$$

where  $S$  is the geometric relation between the  $\langle uvw \rangle$  direction for the lattice translation, resulting in  $\delta$ , and the  $\langle 100 \rangle$  direction. Assuming a  $\langle 100 \rangle$  direction of the epitaxial plane or  $S = 1$ , the number of dislocations generated is then

$$N_D [\text{cm}^{-2}] = \left( \frac{1}{\Delta} \right)^2 = \frac{\delta^2}{a_0^4} \cdot 10^{16}, \quad (14.23)$$

where  $\delta$  and  $a_0$  are in Å.

For a lattice mismatch of, for example, only  $\delta = 10^{-2}$  Å, one has then a dislocation density

$$N_D[\text{cm}^{-2}] \simeq \frac{10^{12}}{a_0^2}. \quad (14.24)$$

If we choose a normal lattice constant, 5 Å, we get

$$N_D = 1.6 \cdot 10^9 \text{ cm}^{-2}.$$

This result shows that even very small differences in lattice spacing cause a considerable density of dislocations. Equations (14.22) to (14.24) have been shown to be correct by measurements of Gatot et al. (see Section 14.4).

Outgrowing layers in epitaxial growth have a tendency to improve in perfection, but the actual interface remains generally disordered.<sup>3</sup> The preferred light output from certain spots has been shown to coincide with dislocations.  $\alpha$  and  $\beta$  dislocations can have different effects on the emitter power; for example,  $\alpha$  dislocations, vertically arranged with respect to the junction field, have stronger light output than those parallel to the junction, and it is the opposite with  $\beta$  dislocations.<sup>4</sup> There is certainly an influence on the junction width and quality because of dislocation-induced diffusion-profile changes; however, the systematic finding of preferential light output at dislocation pipes points to the influence of the interband levels. It is well known that the recombination radiation efficiency for small injection current is much higher in dislocation-rich material.<sup>5</sup>

It is in all probability not the dislocation-induced diffusion profile that causes the low threshold output at localized spots, rather the diffusion-induced dislocations are introducing high field regions and mid-band recombination levels.

Measurements on laser spots in diode structures and their correlation within microscope pictures, transmission electron microscopy, and electron-probe microanalysis have shown that these spots correspond to the regular pattern of dislocation arrays aligned within the junction plane.<sup>6</sup>

Localized microplasma breakdown regions form when the local threshold field value is exceeded, because the space-charge tube is highly conducting and carriers entering the space-charge tube of a dislocation are easily moving within the space-charge pipe and recombine within the dislocation space charge.

Precipitates and striations as well as surface damage can have similar effects but do not basically lower the laser threshold.<sup>7</sup>

Although  $\alpha_{\perp}$  dislocations enhance the light output for laser emission vertical to the surface,  $\alpha_{\parallel}$  dislocations are not efficient in this direction, but only in a plane vertical to the junction. The case of  $\beta_{\parallel}$  dislocations is different inasmuch as here another electronic model applies. The core charge is positive in this

case, and the donor character of the  $\beta$  dislocation is less effective in the  $n$ -type material.

Although the known degradation discussions<sup>8</sup> center on the effects of junction delineation and surface problems, there is an additional basic relation between low-threshold recombination spots and dislocations with strong mid-band recombination efficiency.

Since the number of dislocations in the junction area can be controlled by the lattice misfit in epitaxy, one can study the influence of the dislocation density on the degradation. Furthermore, one can study the influence of the dislocation direction.

In diffused junctions it may be difficult to separate the effect of diffusion-induced dislocations from the natural doping inhomogeneities. But it should be possible to assess the relative effect of either cause. Finally, GaAs bicrystals could be grown with  $\alpha$  and  $\beta$  grain boundaries in order to study the effect of a complete planar arrangement of one kind of dislocation on degradation.

A number of interesting research projects can be grouped around these problems:

1. Grow  $p$ - $n$  homo-junctions in liquid epitaxy with light doping in order to keep  $N_D$  at low values. Measure threshold and light distribution.
2. Change gradually doping and orientation of substrate in order to study dislocation and orientation influence.
3. Bend GaAs samples in order to confirm influence of dislocations independent of doping changes.
4. Assess quantum efficiency as a function of  $N_D$  for fixed current levels.
5. Produce junctions with regular distribution of dislocations over entire cross section by bicrystal growth in order to confirm the regular light output, in this case at low threshold.

The probable outcome of this study is that there are two cases of high efficiency:

1. No dislocations within  $p$ - $n$  layer.
2. Regularly distributed arrays of dislocations over entire junction, lowering the threshold but causing a regularly distributed light output at low current densities (lowering of threshold) due to the pipe field.

## REFERENCES

1. Chynoweth, A. G.: Internal Field Emission, in "Progress in Semiconductors," A. F. Gibson, F. A. Kröger, and R. E. Burgess (eds.), Wiley, New York, pp. 97-123 (with literature), 1960.
2. Gunn, J. B.: High Electric Field Effects in Semiconductors, in "Progress in Semiconductors," A. F. Gibson, P. Aigrain, and R. E. Burgess (eds.), Wiley, New York, pp. 213-247, 1957.

3. Williams, F. V.: Structural Defects in Epitaxial GaAs, Symposium on GaAs, Reading, England, 1966, *Institute of Physics and Physical Society Conference Series* 3, 1967.
4. Osvenskii, V. B., et al.: Effect of Dislocations on the Structure of Diffused  $p$ - $n$  Junctions in GaAs and on Recombination Radiation Parameters, *Soviet Physics—Semiconductors*, vol. 1, no. 6, pp. 755–760, December, 1967.
5. Gippins, A. A.: and V. S. Vavilov, Radiative Recombination at Dislocations in Germanium, *Soviet Physics—Solid State*, vol. 4, no. 9, pp. 1777–1782, March, 1963.
6. Hill, M. J., and D. B. Holt: Defects and Laser Action in GaAs-Diodes, *Journal of Materials Science*, vol. 3, no. 3, pp. 244–258, May, 1968.
7. Holt, D. B., and B. D. Chase: Scanning and Electron Beam-excited Charge Collection Micrography of GaAs Lasers, *Journal of Materials Science*, vol. 3, no. 2, pp. 178–182, March, 1968.
8. Gallium Arsenide, *Proceedings of the International Symposium in Reading*, England, September, 1966, University of Reading.

### 14.3 DISLOCATIONS IN BULK DEVICES

Photoconductors and stress-strain transducers are examples of bulk devices that are less sensitive to crystal perfection in the detailed sense described so far. Obviously gross inhomogeneities interfere with device properties and limit reproducibility and yield of a specific performance, but since no detailed carrier-transport mechanism is required, we can use monocrystals of reasonable perfection and doping regularity. Light impinges on the whole sample surface, and carrier generation changes the resistance that is automatically integrated from one contact to another. In stress-strain transducers, the orientation is of importance; but also here the effect measured is an integral of the individual lattice deformation potentials, and no major changes are derived, for example, from dislocations present in a moderate density, say, up to  $10^5 \text{ cm}^{-2}$ .

A case of importance, however, is the materials property in semiconductor plasma devices where negative differential mobility by intervalley electron transfer is exploited. These devices, called briefly Gunn devices, are very sensitive to crystalline defects, impurity gradients, and defects at the metal-semiconductor interfaces. Kroemer was apparently the first to point out clearly the actual effect of doping inhomogeneities and the initial formation of multiple space-charge layers.<sup>1</sup> Kroemer has discussed the influence of four main non uniformities that can cause a breakup of a single high-field domain of the pure accumulation mode:

1. Noise fluctuations
2. Macroscopic resistivity gradients with a higher resistivity near the source electrode



3. Local field concentrations at the source-electrode interface due to interface irregularities

4. Microscopic spatial fluctuations of the donor distribution. These are thought to be the most fundamental reason for high-field domain breakup.

The model used in the computer program in order to calculate electron energy versus  $x$  (sample length), the total electron number versus  $x$ , and the current waveshape ( $j$  versus time) is based on the set of equations:

$$(a) \quad b = \frac{\mu_2}{\mu_1} < 1 \quad \text{Mobility ratio for populations } n_1 \text{ and } n_2 \quad (14.25)$$

$$(b) \quad \frac{n_2}{n_1} = r(E) \quad \text{Electron density ratio as a function of the field ratio } E = \frac{F}{F_0} = \frac{\text{local field}}{\text{reference field}} \quad (14.26)$$

$$(c) \quad j_{1/2} = q\mu_{1/2} \left( n_{1/2} F - \frac{k\theta_{1/2}}{q} \frac{dn_{1/2}}{dx} \right) \quad (14.27)$$

Double equation for drift and diffusion current for the two carriers, with mobility  $\mu_1$  and  $\mu_2$ ;  $\theta_1$  and  $\theta_2$  electron temperatures)

$$(d) \quad \frac{n_2}{n_1} = r(E) \quad \text{Represented as a power law: } \frac{n_2}{n_1} = E^k \quad (14.28)$$

$$(e) \quad \frac{\partial n}{\partial t} = -\frac{1}{q} \left( \frac{\partial j_1}{\partial x} + \frac{\partial j_2}{\partial x} \right) \quad \text{Continuity equation} \quad (14.29)$$

$j_1; j_2$  = current densities for populations  $n_1; n_2$

$$(f) \quad \varepsilon \frac{\partial F}{\partial x} = q(n_1 + n_2 - n_d) \quad \text{Poisson's equation, where } n_d = \text{donor density} \quad (14.30)$$

This set of conditions gives reasonable results for the electronic energy versus  $x$  and the current waveshapes. If now doping density fluctuations of 10 per cent are assumed, these relations are altered very strongly. Kroemer emphasizes that 10 per cent is a normally expected fluctuation, since, for example, in a doping range of  $10^{14} \text{ cm}^{-3}$  a reference cell of  $(1\mu)^3$  contains 100 donors and the mean square deviation between adjacent cells is  $\sqrt{100} = 10$  per cent of the average. Introducing, therefore, a cell subdivision of the crystal under consideration so that each group, say, 200 cells of  $0.5 \mu$  thickness, has a donor density of

$$n_{d,i} = n_d(0.9 + 0.002r_i) \quad (i = 1, \dots, 200),$$

where  $r_1$  are random two-digit decimal integers read from a table of random numbers, leads to results similar to those based on the equation set (a) to (f) for constant donor density across the sample.

However, in plotting the initial formation of the space-charge layer, it is found that multiple layers form and that the current waveshape for randomized doping is quite different from the case of equal doping (see Figure 14.5).

As a result of randomized doping, the field near the source electrode may never get up to the critical field, and the current versus time shows a disturbed waveshape of reduced amplitude, losing even its periodicity to a large degree. The influence of trapping centers on space-charge waves was discussed by Ridley,<sup>2</sup> who showed that trapping can drastically reduce the velocity of space-charge waves. Ridley's model assumes interaction between a lower and a higher valley (in energy scale) and an impurity center. If the capture rate from the upper valley greatly exceeds that from the lower valley, the negative differential conductivity on account of a mobility ratio for the two valleys is enhanced.

If the capture rate from the upper valley is much less than that from the lower valley, this could result in a destructive influence on the formation of the Gunn effect if the growth rate of these instabilities does not exceed the trapping rate.

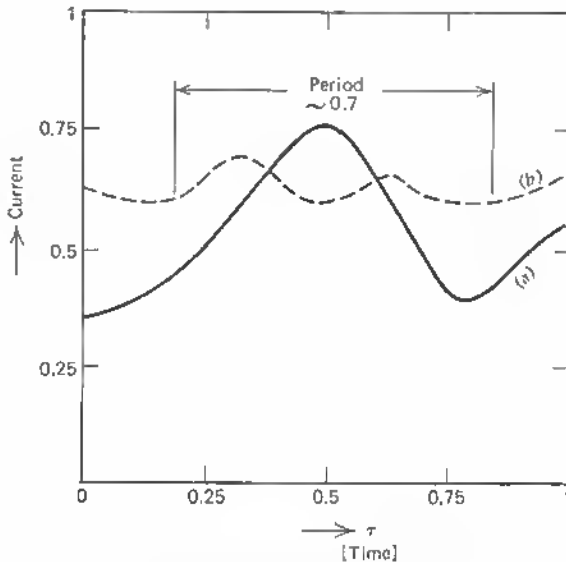


Fig. 14.5 Current wave-shape for pure accumulation mode: (a) for constant doping; (b) for randomized doping, after Kroemer<sup>1</sup>.

Ridley explains the observed presence of slow domains in GaAs of high resistivity on account of this model.

In connection with the suppression of the space-charge waves to couple the carriers directly in the negative conductance mode to the microwave circuit (limited space-charge accumulation = LSA mode), Copeland suggested that doping uniformity is very important because it introduces space-charge fluctuations.<sup>3</sup> In an analysis similar to Kroemer's<sup>1</sup> Copeland calculates the efficiency as a function of relative doping fluctuation. A fluctuation of 10 per cent may already account for a lowering of the efficiency of the device from a theoretical 18 per cent to less than 10 per cent.

An approximate numerical field variation for doping variations is

$$\Delta E_{1/2} = 6 \times 10^4 \text{ V/cm} \left( \frac{\Delta n_{1/2}}{\bar{n}_0} \right), \quad (14.31)$$

so that for  $\Delta n_{1/2}/\bar{n}_0 = 0.1$  a field variation of 6000 V/cm results, which is sufficient to distort the electrical field within the Gunn diode seriously.

Copeland's values of doping variations for the usual efficiencies (below 5 per cent) suggest, however, that doping variations of 80 per cent and more are present in usual cases. This is unlikely, and it must be assumed that the contact (metal semiconductor) and here especially the cathode interface are responsible for a large part of the anomalies and the lower efficiencies. This was shown more recently by Kroemer.<sup>4</sup>

In this paper, Kroemer assumes that the important depletion mode measured by Gunn et al., which appears as a stationary high field domain (*cathode fall*) ahead of the cathode is due to a local excess of acceptors. Such a "faulty" cathode can also cause a shift between high field region and the medium of negative mobility.

Kroemer superimposes the characteristics (current versus field) of the control section *c* and the main section *l*. The control section is assumed not to exhibit a negative mobility and a higher low field resistivity than the bulk semiconductor. In analyzing this model, it seems that the decisive effect is not so much an increase in the local resistivity but the fixed negative charge there and a quasi abrupt discontinuity:

$$\Delta F = \frac{Q}{\epsilon}, \quad (14.32)$$

where *Q* is the amount of the negative fixed charge per unit area ( $\epsilon$  = dielectric constant). As long as the field adjacent to the control section toward the anode is below  $\Delta F$ , the cathode field opposes the electron flow. For increased field strength, the drift current dominates the overall sample current. The crossover point between the control characteristic and the main characteristic (see Figure 14.6) defines the degree of deviation from the ideal Gunn sample. The

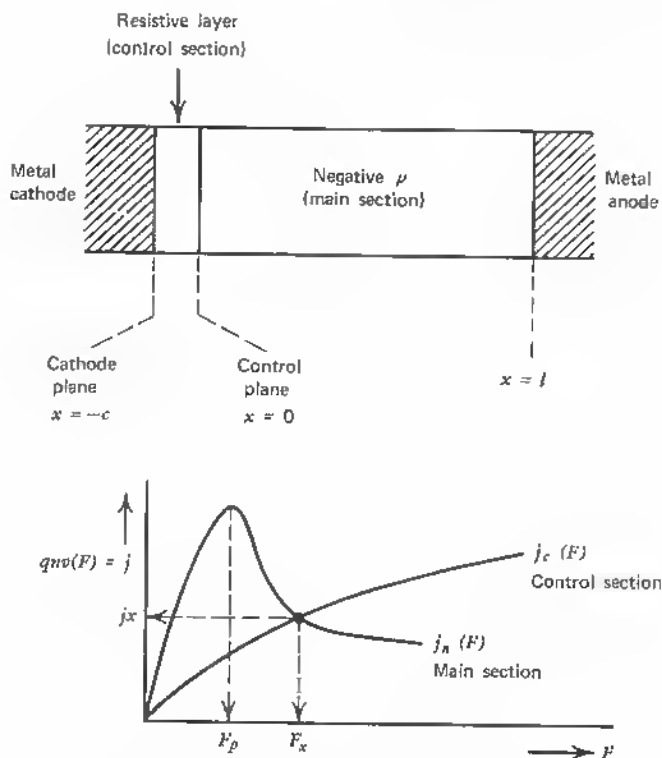


Fig. 14.6 Crystal with resistivity layer at cathode-side and characteristic of control and main section ( $F_x$  = crossover field)\*.

higher the crossover field  $F_x$ , the more pronounced the deviation from the normal Gunn effect.

In calculating detailed examples, Kroemer finds the even very weak built-in depletion layers at the cathodic plane lead to a behavior entirely different from the one with a built-in weak accumulation layer at the cathode. Computrized curves for the electron density, field distribution, and potential across the sample show that such a model can well explain the "pathological" cases observed where much higher fields are needed in order to start oscillation or where oscillation is not obtained at all. For instance, for an assumed acceptor density in the control section of  $10^{11} \text{ cm}^{-2}$  and an impurity density

$$N(x) \begin{cases} N = 2 \cdot 10^{15} \text{ cm}^{-3} & \text{for } x < 0 \\ N = 10^{15} \text{ cm}^{-3} & \text{for } x > 0 \end{cases}$$

and

$$l + c = 20 \mu$$

$$c = 1 \mu$$

$l$  = length of main sample section

$c$  = cathode layer thickness

(see Figure 14.6) the built-in field difference  $\Delta F$  is

$$\Delta F = 14.4 \text{ kV/cm},$$

or four times the threshold field of 3.4 kV/cm for the case considered.

Kroemer mentions that such control layers at the contacts can originate from thin striations in the epitaxial growth, out-diffusion of acceptors from an epitaxial layer, or from an alloy contact where these acceptors were hidden under a high donor density. "Alternately the charge may be thought of as electrons trapped in interface states at small angle grain boundaries or at lattice misfit dislocations ahead of an alloy regrown region".

Here is the actual problem. It is known that metallization at a semiconductor surface results in a strained region and a consequent higher dislocation density at the contact interface. This is especially the case when thermal treatment is involved in producing contacts. The difference in the coefficients of expansion results in a high number of interface dislocations usually of the order of  $10^8 \text{ cm}^{-2}$ . It depends to some extent on the orientation of the GaAs sample if  $\alpha$  or  $\beta$  dislocations predominate (see Chapter 3). In any case, either a depletion or an accumulation layer at the cathode contact strongly interferes with the Gunn mode and greatly increases the threshold field.

Recently, G. L. Pearson and coworkers<sup>5</sup> investigated the oscillator efficiency in connection with the contact problem. They indicate again the well-known fact that ohmic contacts for a wider range of current densities are formed when the metal layer is applied to a heavily doped  $n^+$  layer on the active semiconductor layer. But here also the danger exists that the differently doped layer has a different lattice spacing and that interface dislocations form, leading to another higher resistance layer (see Section 14.4).

These authors found that evaporated Au—Ge—Ni layers, alloyed directly to the  $n$ -type GaAs layers, are best for fabricating reliable Gunn oscillators, producing more than 100 mW of cw-microwave power at 25 GHz.

A distinct difference with respect to contacts was found between boat-grown and solution-grown crystals. No intrinsic layers form at the contacts on boat-grown GaAs. The explanation given for this behavior is that boat-grown material contains deep donor levels that compensate for the acceptors originating at the interface because of lattice mismatch.

We see from all this that material with a high amount of dislocations, which represent microscopic doping changes because of their extended space charge, is poor or unusable for bulk devices of the Gunn variety for microwave generation. In particular, material with a layer arrangement of dislocations as it appears in alloy, diffusion, and especially heteroepitaxial processes cannot be used for devices operating with reasonable efficiency on the principle of negative differential mobility. Homoepitaxy, however, yields the best layer structure (see Section 14.4).

## REFERENCES

1. Kroemer, H.: Nonlinear Space-charge Domain Dynamics in a Semiconductor with Negative Differential Mobility, *IEEE Transactions on Electron Devices*, vol. ED-13, no. 1, pp. 27-40, January, 1966. Also: vol. ED-14, no. 9, pp. 476-492, September, 1967.
2. Ridley B. K.: The Influence of Traps on the Watkins-Gunn Effect, *Brit. J. Appl. Phys.*, vol. 17, pp. 595-602, 1966.
3. Copeland, J. A.: Doping Uniformity and Geometry of LSA Oscillator Diodes, *IEEE Transactions on Electron Devices*, vol. ED-14, no. 9, pp. 497-500, September, 1967.
4. Kroemer, H.: The Gunn Effect under Imperfect Cathode Boundary Conditions, *IEEE Transactions on Electron Devices*, vol. ED-15, no. 11, pp. 819-837, November, 1968.
5. Harris, J. S., Y. Naunichi, and G. L. Pearson: Ohmic Contacts to Solution-grown Gallium Arsenide, *J. Appl. Phys.*, vol. 40, no. 11, pp. 4575-4581, October, 1969.

## 14.4 DISLOCATION GENERATION IN HOMOEPITAXY AND HETERO-EPITAXY

Considering the importance of homoeptaxy, it is appropriate in this context to make a thorough evaluation of the perfection of such layer structures.

In a sense, heteroeptaxy is but a limiting case of homoeptaxy. Isomorphous conditions are not sufficient guarantee of high perfection in homoeptaxy when, for example, strong doping differences prevail. The influence of the doping on lattice spacing and expansion coefficient can be so strong that interface dislocations are generated in analogy to the nonisomorphous case. However, within the normal ranges of doping differences, the lattice constant varies only in the  $10^{-2}$  to  $10^{-3}$  per cent range, and the relatively low dislocation density originating at the interface ( $\sim 10^4$  to  $10^5 \text{ cm}^{-2}$ ) can be grown out during the building up of subsequent layers. It is well known that the perfection of epitaxial layers can be better than that of the substrate. Modern III-V compound semiconductors are available in highest perfection (highest mobility and lowest dislocation values) only in the form of homoeptaxial layers.

As the difference between the substrate and the grown surface layer increases, the conditions for high perfection are less favorable. In the production of  $\text{GaAs}_x\text{P}_{1-x}$  layers on GaAs substrates, for example, it is important to grow sufficiently thick layers to achieve perfection especially for smaller values of  $x$ .

One may also introduce a grading from high to low  $x$  values as the layer grows out from the substrate in order to minimize the difference between the two lattice constants at the interface. This can be achieved in liquid-solid vapor growth by a gradual increase of the vapor pressure of the phosphorous.

In heteroepitaxial cases, the original lattice mismatch is quite large, and growth conditions are very involved, especially when no melt-back is feasible for instance in vapor deposition and therefore one starts with a contaminated surface layer. Without melt-back even pure homoepitaxy shows poor results. For this reason, liquid epitaxy is the preferred method in homoepitaxy. We emphasize, in the following the case of heteroepitaxy by vapor deposition starting from the case of homoepitaxy, with appreciable lattice difference and discuss the various causes of dislocation generation.

Finally, a number of schemes and technical solutions are reviewed that are of interest in this context.

It is a fact that despite many difficulties, a solution to the problem of non-isomorphous growth is desirable, since this would finally enable one to vapor-deposit different device-grade semiconductor layers together on one insulator substrate.

This achievement would solve a major problem in monolithic microcircuitry. In complex circuits for very high frequencies, GaAs and silicon have to be used along with other semiconductors such as germanium in order to optimize device properties. Also all passive circuit components could be deposited on the insulator substrate, and stripline circuits could be positioned on the same surface.

#### Nucleation Catalysis in thin film deposition

That *single crystals*, that is, oriented large films with distinct Laue pattern, can be grown in heteroepitaxy or, in other words, that oriented growth of crystals can be realized between nonisomorphous materials, when only a relatively "close" lattice match prevails, is the consequence of the formation of liquid nuclei at matching points in oriented form and their merger into larger oriented areas. This can be seen from the classical treatment of heterogeneous nucleation using the drop model (see Figure 14.7).

$$\sigma_{cv} = \sigma_{cl} : \theta = 90^\circ$$

$$\sigma_{cv} > \sigma_{cl} : \theta < 90^\circ$$

$$\sigma_{cl} > \sigma_{cv} : \theta > 90^\circ$$

$$\cos \theta = \frac{\sigma_{cv} - \sigma_{cl}}{\sigma_{lv}} \begin{cases} \sigma_{cv} = \text{interfacial energy per area, catalyst/vapor} \\ \sigma_{cl} = \text{interfacial energy per area, catalyst/liquid} \\ \sigma_{lv} = \text{interfacial energy per area, liquid/vapor} \end{cases}$$

$$\cos \theta' = \frac{\sigma_{cl} - \sigma_{cs}}{\sigma_{ls}} \begin{cases} \sigma_{cl} = \text{interfacial energy per area, catalyst/liquid} \\ \sigma_{cs} = \text{interfacial energy per area, catalyst/solid} \\ \sigma_{ls} = \text{interfacial energy per area, liquid/solid} \end{cases}$$

A comparison between the Becker-Döring<sup>1</sup> frequency of nuclei formation

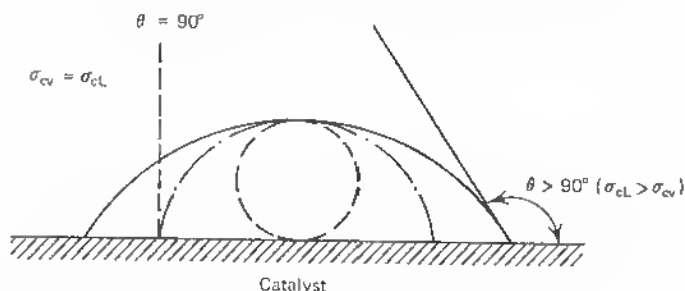


Fig. 14.7 Contact angle for drop model on catalyst in the case: (a) vapor-liquid; (b) liquid-solid.

$I$  in supersaturated vapor and the catalytic case of nucleation ( $I_c$ ) shows that the presence of the catalyst increases this frequency (see Table 14.1).

The classical treatment of heterogeneous nucleation by Volmer<sup>2</sup> is still the basis for more sophisticated treatments. The drop model, as outlined in Figures 14.7 and Table 14.1 has also been used by Turnbull and Fisher<sup>3</sup> to describe heterogeneous nucleation of crystals from supercooled liquids.

As we see from Table 14.1,  $\theta$  is differently defined here, but the frequency of formation has the same analytical form as in homogeneous nucleation. The formulas have been confirmed by measurements on stearate-coated mercury droplets, on oxide-coated mercury droplets and on oxide-coated tin droplets. Although the drop model is also applicable to the possibility of oriented overgrowth under nonisomorphous conditions, there is generally an orientation relation. Planes and directions in the two crystals in which the atomic arrangement is most similar are parallel. Defining  $\delta$  as the disregistry on a low-index plane:

$$\delta = \left| \frac{\Delta a}{a_0} \right|, \quad (14.33)$$

with  $\Delta a = a - a_0$  ( $a_0$  = substrate lattice constant,  $a$  = film lattice constant), it was generally assumed that oriented overgrowth occurs only for<sup>4, 5</sup>

$$\delta \lesssim 0.1 \div 0.2.$$

In some cases, oriented overgrowth was found for values of  $\delta$  as large as 0.5.<sup>6</sup> That such strong misfit still leads to a generally oriented overgrowth is considered to be the consequence of a possible strain of the nuclei. The lattice parameter of a nucleus assumes a value necessary to minimize the free energy of the system. If the strain  $\varepsilon$  is assumed smaller than  $\delta$ , it can be written

$$\varepsilon = \left| \frac{x - a_0}{a_0} \right|, \quad (14.34)$$



Table 14.1

Homogeneous nucleation	Homogeneous catalytic nucleation	Heterogeneous catalytic nucleation
Free-energy difference between a liquid nucleus (critical size) and supersaturated vapor:	Free energy of formation of a liquid nucleus on catalytic surface in supersaturated vapor:	Free energy of formation of a solid nucleus on a catalyst surface in supersaturated liquid:
$\Delta F = \frac{16\pi\sigma L_o^3}{3(\Delta F_c)^2}$	$\Delta F_c = \Delta F \cdot f(\theta)$	$\Delta F_c = \Delta F \cdot f(\theta')$
$\sigma_{L_o} = \text{interfacial energy per area between liquid and vapor}$	$f(\theta) = \frac{(2 + \cos \theta)(1 - \cos \theta)^2}{4}$	$\cos \theta' = \frac{\sigma_{cL} - \sigma_{cS}}{\sigma_{L_S}}$
$\Delta F_s = \text{free-energy difference per volume between vapor and liquid phase } (\infty \text{ extend})$	$(\theta = \text{contact angle})$	Same for $\theta'$
Becker-Döring frequency of nuclei formation	For $\theta \lesssim 90^\circ$ : $f(\theta) \ll 1$ ( $\Delta F \gg \Delta F_c$ )	
$I = A \exp(-\Delta F/kT)$	For $\theta < 180^\circ$ : $f(\theta) < 1$ ( $\Delta F > \Delta F_c$ )	$I_c = 10^{-8} A' \exp\left[\frac{-\Delta F \cdot f(\theta')}{kT}\right]$
$A = \text{kinetic coefficient}$	$I_c = 10^{-8} A' \exp\left[\frac{-\Delta F \cdot f(\theta)}{kT}\right]$ (Volmer)	(Volmer-Turnbull-Fisher) $I_c \gg I$

where  $a_0$  and  $x$  are the lattice parameters of the nucleus in the strain-free and strained conditions, respectively. Thus the actual disregistry between a nucleus and the catalyst is

$$\delta - \varepsilon. \quad (14.35)$$

There are some heuristic assumptions about the limits of this disregistry for good crystal growth. Van der Merwe<sup>7</sup> and Brooks<sup>8</sup> have directly associated the formation of dislocations with the actual disregistry:

$$\Delta[\text{cm}^{-2}] \approx \delta - \varepsilon. \quad (14.36)$$

The dislocation density  $\Delta$  represents an amount of energy that has to be added to the interfacial energy:

$$\sigma_{sc} = \gamma + \alpha(\delta - \varepsilon) \quad (\alpha = \text{constant}), \quad (14.37)$$

where  $\gamma$  is the interaction term due to bond type, chemistry, and the like, and  $\alpha(\delta - \varepsilon)$  is the structural term that is directly proportional to the dislocation density  $\Delta$ .

A resulting dislocation pattern (see Figure 14.8) takes care of the lattice

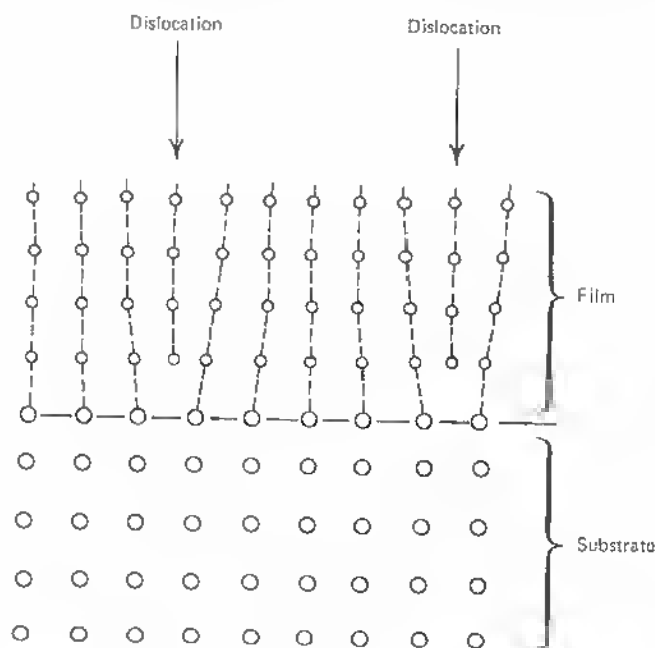


Fig. 14.8 Cross section  $\perp$   $[100]$ -plane of two misfitting simple cubic lattices.

misfit, and the film is still a *single* or monocrystal in the sense of a Laue back-reflection pattern. In fact, the dislocation formation maintains monocrystallinity in the presence of disruptive forces between the two lattices during growth.

To assess the materials quality above monocrystallinity, it is necessary to know how many dislocations per square centimeter are counted. Material for use in microcircuits generally has a dislocation density

$$\Delta[\text{cm}^{-2}] < 10^3$$

and in best cases

$$\Delta[\text{cm}^{-2}] = 0.$$

It is, therefore, of interest to know the exact number of dislocations for films grown by epitaxy. There are many reasons for the formation of dislocations, but we assess here first the one reason: lattice mismatch.

Recently, the MIT group under H. Gatos<sup>9</sup> carried through careful measurements in order to assess the dislocation density of different lattice matchings. Using a melt-back process that yields perfect crystals in homoeptitaxy, the authors measured the dislocation spacing as a function of varied lattice mismatch due to variable percentage increase of the alternate component in the  $A_3B_5$  system:  $\text{Ga}_x\text{In}_{1-x}\text{Sb}$ . With  $x = 1$  (no indium), a complete match with the substrate (GaSb) in the melt-back process was achieved (no dislocations), and with small percentage additions of In, a variable lattice mismatch was obtained.

For the case of a [211] surface with the melt interface parallel to [110], Gatos et al. used a dislocation distance expression:

$$d = \frac{\sqrt{2}a_0^2}{\delta}, * \quad (14.38)$$

where  $a_0$  = lattice constant,

$\delta$  = increment of lattice constant change,

$$\delta = a'_{0(\text{InSb})} - a_{0(\text{GaSb})} = 6.485 - 6.095 = 0.390 \text{ \AA}$$

or

$$\begin{aligned} \delta &= \frac{|a'_0 - a_0|}{a_0} \\ &= 6.4 \text{ per cent.} \end{aligned}$$

\* Actually:  $d = \sqrt{\frac{3}{10}} \sqrt{2} a_0 / \delta$ . The factor of  $\sim \frac{1}{2}$ , however, is compensated for in the measurements because the dislocation count was carried out in the [111] direction and the crystal was grown in the [211] direction.

The only assumption in (14.18) is that the dislocation spacing is proportional to the lattice translation vector  $a_{new}$  times the ratio  $n = a_0/\delta$ . The nucleus strain  $\epsilon$  is considered zero. For convenience, we express the dislocation density  $\Delta(\text{cm}^{-2})$  here as

$$\Delta(\text{cm}^{-2}) = \frac{10^8}{d^2} \quad (d \text{ in } \mu) \quad (14.39)$$

or with (14.38)

$$\begin{aligned} &= \frac{\delta^2}{2a_0^4} \cdot 10^{16} \quad (\delta \text{ in } \text{\AA}) \\ &= 3.9 \cdot 10^{12} \delta^2 \end{aligned} \quad (14.40)$$

In a double logarithmic scale, this gives the relation plotted in Figure 14.9. We see that for lattice misfits of the order  $\delta$  of only  $10^{-1}$  per cent of  $a_0$ , dislocation densities of the order of  $10^8$  result.

The densities, measured by Gatos' group, are shown. They correspond to small amounts of indium added or small InSb percentages (0.25 to 1.4 per cent), and their position is in good agreement with the derived relationship between dislocation density and misfit  $\delta$ . The abscissa is in per cent  $a_0$ , where  $a_0$  is the lattice constant for the substrate GaSb.

In the best cases of heteroepitaxy, one may achieve  $10^{-1}$  to  $10^{-2}$  per cent, and nonregistry then contributes between  $10^8$  and  $10^6$  dislocations  $\text{cm}^{-2}$ . For instance in the case of silicon on chrysoberyl:

$$\begin{aligned} a_{\text{Si}} &= 5.43 \text{\AA}, \\ a_{\text{Al}_2\text{BeO}_4} &= 5.47 \text{\AA}, \\ \delta &= 0.73 \text{ per cent}, \\ \Delta[\text{cm}^{-2}] &> 10^9 \text{ cm}^{-2}. \end{aligned}$$

It should be stated that, in careful crystal growth, the dislocation density may decrease as one moves out from the heterointerface. Gatos et al. point out that the addition of indium also changes the thermal-expansion coefficient of the crystal with regard to the substrate, which is probably the reason for the somewhat higher count, compared with the theoretical curve (see Figure 14.9).

In summary, a lattice mismatch of  $10^{-1}$  per cent ( $\text{Ga}_{0.996}\text{In}_{0.004}\text{Sb}$  on GaSb) originally gives rise to  $10^8$  dislocations  $\text{cm}^{-2}$ .

We note that in epitaxial growth of compound crystals of similar structure (like  $\text{Ga}_x\text{In}_{1-x}\text{Sb}$  on GaSb), the dislocation density is high at the interface. But here we have the means to improve perfection by a graded decrease in  $x$

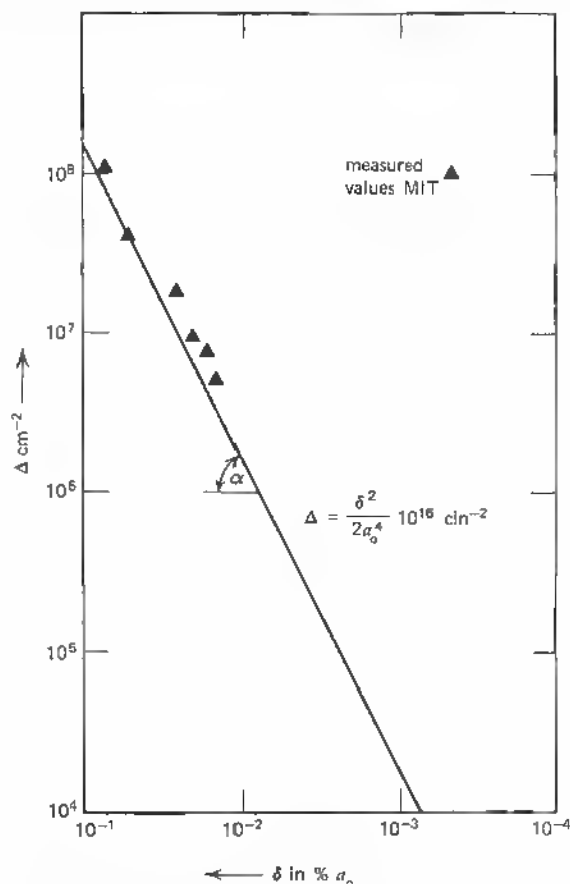


Fig. 14.9  $\Delta \text{ cm}^{-2}$  (dislocation density) as  $f$  (misfit in % of lattice constant).

as we grow the layer. In systems with small interfacial misfit, for example,  $\delta \approx 10^{-2}$  per cent, a minimum thickness of the order of 2 to 3  $\mu$  is needed in order to form misfit dislocations while the interface portion of the film is under some stress.<sup>10</sup>

#### Perfection Limits in Heterogeneous Growth

As we have concluded from the drop model for nucleation catalysis, a wide range of lattice mismatch can be accommodated without losing monocrystallinity, but we have already noted the existence of a high density of misfit dislocations at the substrate interface.

There are unfortunately other reasons why such heteroepitaxial layers have a high degree of imperfection:

1. Nuclei misalignment
2. Difference in expansion coefficient
3. Chemical changes

#### *Nuclei Misalignment.*

We now discuss the effect of the high mobility of the nuclei at deposition. The drop model mentioned earlier, under nucleation catalysis, is doubtful when small nuclei of only a few atoms are considered. In this case,  $\epsilon$  in (14.16) can certainly be disregarded,<sup>11</sup> but new questions arise because of the non-applicability of the concept of surface energy as used in the treatments of Volmer and Becker-Döring. Walton<sup>12</sup> has considered the case of small nuclei (a few instead of 100 atoms, for example) and finds that in this case a *critical nucleus* is no longer defined by the equal probability of growing larger or smaller but that a critical nucleus here is that cluster whose probability of growing is  $\geq \frac{1}{2}$  if one single atom is added in the appropriate position.

The arguments about the form of the nuclei and their influence on the perfection of the film go in different directions, depending on the most recent study of their form. In situ observation under the electron microscope is carried through with a continuously better resolution, and nuclei orientation and movement are studied. Recently, H. Reiss<sup>13</sup> has analyzed the behavior of nuclei, starting from a simple but valid model of a nucleus on a substrate (see Figure 14.10). Without assuming lattice mismatch, a rotational misfit  $\theta$  is introduced, and finally translational misfit is also considered; and it is shown that the nucleus (for example, 25 atoms) in registry has a potential  $V(\theta)$  given by

$$V(\theta) = 4V_1N^2[1 - \sin^2(\theta/\theta^2)], \quad (14.41)$$

where  $V_1 \div$  amplitude of periodic potential function due to substrate,

$N \div$  integer in  $(2N + 1)^2 =$  number of clustered atoms  $\simeq n$ , (nucleus size)

$\theta \div$  angle of rotation between island and substrate,

which has the form of the Fraunhofer diffraction pattern from a square aperture. For increasing number of atoms ( $N \rightarrow \infty$ ), the part of rotational energy surface is smoothened; that is, the maxima and minima become more shallow, especially for increased angle  $\theta$  (see Figure 14.11). The rotational jump distance in terms of  $\theta$  is shown to be  $\sim 1/2N$ , meaning that for growing islands the jump distance becomes smaller. Since it is certain that for lattice mismatch in the percent  $a_0$  range nuclei of larger size have to grow from nuclei in the correct lattice position at the expense of the "wrong" nuclei, there is a good reason

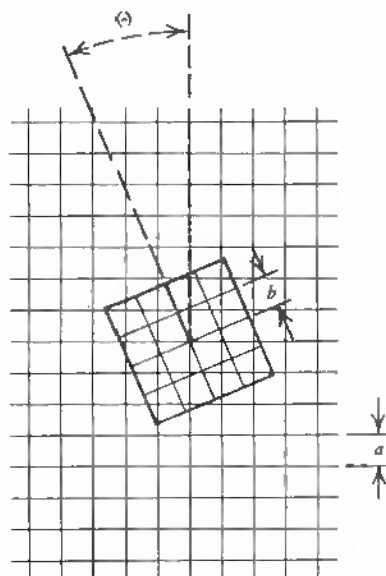


Fig. 14.10 Square island of lattice parameter  $b/\sqrt{2}$  on substrate parameter  $a/\sqrt{2}$ ;  $\theta$  = misorientation. For  $a \neq b$  preferential  $\theta$ -values occur, not only phase factors.

to assume that the case of  $N = 1$  or 2 (only a few maxima or minima of the potential function, no smoothing) is irrelevant. H. Reiss shows, furthermore, that large enough islands under misfit orientations ( $\theta \neq 0$ ) not only rotate easily but also translate easily. In effect, the translational activation energy seems of the same order of magnitude as for a single atom. These two facts agree well with in situ observations of G. A. Bassett on nuclei.<sup>14</sup> Considering further the growth of nuclei and the possibility of their alignment on coalescence, Reiss finds that the maximum nuclei concentration is of the order of  $10^7 \text{ cm}^{-2}$ . Since there are  $\sim 10^{15}$  surface sites available per  $\text{cm}^2$ , this represents an atom fraction of  $10^{-8}$ , low enough to prevent further nucleation.

In considering the rotational diffusion problem for nuclei, one may first derive the amount of inertia of the growing nuclei and the force constant due to the substrate force field and then form an expression for the jumping frequency and its amplitude. Reiss derives that the amplitude of the oscillations is given by:

$$A_0 = \frac{V_1}{\pi^2} \cdot \theta^2 \quad (14.42)$$

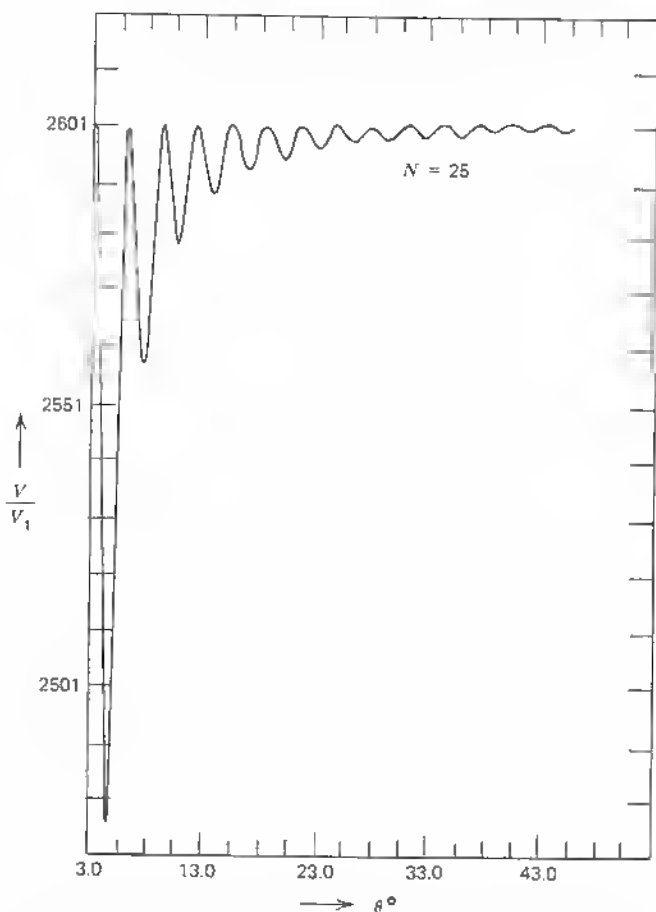


Fig. 14.11 Portion of rotational energy surface for an island containing 2601 atoms, with  $N = 25$  as a function of misorientation  $\theta$ . (After Reiss, [Reference 13].)

within the bounds of (14.41), thus inversely proportional to  $\theta^2$ . For the inner potential valleys, the force constant is

$$G(\theta) = V_1 \cdot \frac{n}{\theta^2}, \quad (14.43)$$

that is, dependent on the size  $n$  of the island. As amplitude and force decrease strongly with increasing  $\theta$ , the jumping frequency increases. Islands of  $n \approx 600$  or about 100 Å in diameter have a typical jump frequency of  $\nu = 1 \text{ sec}^{-1}$ , corresponding to Bassett's observations.



The assumption of a local equilibrium then allows computing an upper limit to the rate of realignment of islands as they fall into the central depression of the substrate potential. As the nuclei grow ( $n \rightarrow \infty$ ), they develop a tendency to get "stuck" in their misaligned positions. An estimation of the resultant dislocation density for an island density of  $10^{10}$  to  $10^{11} \text{ cm}^{-2}$  gives an equal number.

$$\Delta[\text{cm}^{-2}] \approx 10^{11}.$$

Although Reiss' model gives an excellent insight into the actual mechanism of growth, some assumptions are still debatable. For example, the lattice parameter of the islands has been assumed equal to the substrate, and therefore the homepitaxial case must appear as a limit where no other minimum than the central depression is decisive. In fact, the heteroepitaxial case would apparently result in a preferential orientation in side minima because of the different lattice configurations. Since only small nuclei tend to settle in a correct orientation, Reiss proposes a *pulsed* deposition, in which initially a fast delivery of vapor covers the substrate with a layer of small nuclei of higher temperature upon which a slow delivery or slow growth follows. This method, incidentally, had been applied with some success already by several workers in the field. Another problem is the actual magnitude of  $\theta$ . Values of several degrees ( $3^\circ$ , for example) are indicated (Bassett), but even smaller misfit angles in the range  $\ll 1^\circ$  are sufficient to create lineage boundaries between the coalescing nuclei with a resulting dislocation density of the order of

$$\Delta = \frac{1}{D^2} = \left[ \frac{2 \sin(\theta/2)}{5 \cdot 10^{-8}} \right]^2 \text{ cm}^{-2}, \quad (14.44)$$

which for  $\theta/2 \approx .1^\circ$  leads to  $\Delta \approx 10^{10} \text{ cm}^{-2}$ .

#### *Difference in Expansion Coefficient.*

The second cause for imperfections results from the cooling process. There are several steps during deposition:

1. High-mobility prenucleation phase
2. Decreased-mobility nucleation phase
3. Nuclei merger and viscous-liquid growth range
4. Elastic-plastic solid range
5. Solid range

Step 1 is essentially the atomic impact stage, with an equilibrium of cohesive forces between depositing atoms and adhesive forces between depositing atoms and the surface.

Step 2 is defined by the clustering of atoms from the vapor phase and formation of nuclei for which cohesive forces are larger than adhesive forces.

As Step 3 is reached, differences in lattice constant and thermal-expansion coefficient are becoming decisive. Because the forming layer is bound to the

substrate, viscous yield cannot be carried through, as in free material, and residual stress builds up.

In Step 4, where the elastic range leads into a plastic range, limited plastic flow can accommodate the film to the substrate. Here we must apply the known facts about dislocations formed by strain. This strain in dynes per centimeter is given by

$$\sigma = \mu_f \left[ \int_{T_1}^{T_2} \alpha_s(T) dT - \int_{T_1}^{T_2} \alpha_f(T) dT \right], \quad (14.45)$$

where  $\mu_f$  = elasticity modulus of film (for silicon,  $1.87 \cdot 10^{12}$  dyn/cm<sup>2</sup>),  
 $\alpha_s$  = substrate expansion coefficient (for Al<sub>2</sub>O<sub>3</sub>,  $8.31 \cdot 10^{-6}$  cm/°C),  
 $\alpha_f$  = film expansion coefficient (for silicon,  $4.24 \cdot 10^{-6}$  cm/°C at 110°C),

$\alpha$  is generally a function of  $T$ . For the range of deposition temperature to room temperature,  $\Delta T \simeq 800^\circ\text{C}$ , and the  $\alpha$  values given, one obtains

$$\sigma_f \simeq 10^{10} \text{ dyn/cm}^2.$$

If this strain would operate without release on the silicon film, it would already have a strongly diminishing influence on the mobility because of intervalley scattering. The pressure-band-gap coefficient of silicon is positive (germanium negative) and of the magnitude

$$E_m = 1.5 \cdot 10^{-12} \text{ eV dyn}^{-1} \text{ cm}^2$$

for the [100] minimum.<sup>15</sup>

This would result in a gap change of

$$\Delta E_g = 1.5 \cdot 10^{-2} \text{ eV},$$

a value corresponding to a hydrostatic pressure of  $10^5$  kg/cm<sup>2</sup>. At this pressure, the mobility is about 10 per cent of the value at atmospheric pressure.<sup>15</sup> But actually the formation of dislocations relieves the stress to a large extent. That stresses of this order of magnitude are generated has been shown by deposition on a cantilever beam.<sup>16</sup> Ang et al. calculated the stress from the cantilever deflection and found a value for  $\sigma$  in agreement with the value derived from (14.45).

If we assume that a silicon crystal is plastically deformed with the radius of curvature of the order of magnitude measured here ( $\sim 1$  cm), we generate a number of dislocations:

$$\Delta = (r \cdot b)^{-1} \text{ cm}^{-2}, \quad (14.46)$$

where  $r$  = radius of curvature,

$b$  = Burgers vector. (See Figure 12.1)

This corresponds to a dislocation density of

$$\Delta = 0.2 \cdot 10^8 \text{ cm}^{-2},$$

a value measured on the best films.

There has been much argument about the possible use of annealing steps to eliminate strain and strain-induced dislocations in films. It is generally known that slow cooling in crystal growth is essential for perfection. But this relates to step 3 in the list of sequences where the viscous-liquid growth occurs. In this range, the problem is similar to the single- or multistage annealing of glasses.<sup>17</sup> In this case, the standard equation for predicting residual stress is

$$\sigma(\infty) = 1.25 \cdot d^2 \cdot h [\text{kg/cm}^2]^2 \quad (14.47)$$

or

$$\sigma(\infty) = 1.25 \cdot 10^6 d^2 \cdot h [\text{dyn/cm}^2],$$

$d$  = plate (specimen) thickness, cm,

$h$  = cooling rate, °C/min.

Expressing (14.47) in the usual dimensions considered in semiconductor-stress problems, one has

$$\sigma(\infty) = 1.25 \cdot 10^{-2} d^2 [\mu^2] h [^\circ\text{C/min}]. \quad (14.48)$$

This indicates that in the range of film thicknesses of microns, the cooling rate  $h$  may be correspondingly faster in producing the same result as in material of centimeter dimensions. In other words, a cooling rate of 100°C/min, as is the range in epitaxial growth, is still largely sufficient in order to anneal a film down to the same level of residual stress as a layer of centimeter thickness would retain after about one year of annealing.

Thus annealing rates of 1000°C/min would be slow from the point of view of viscous yield in freely suspended layers of the thickness of semiconductor films.

But since these layers are bound to the substrate, viscous yield cannot be carried through as is done in free material layers and residual stress must build up when the material goes into step 4, where the elastic range leads into the plastic solid range. It is a property of the material in step 3 to relieve strain by viscous flow. As soon as nuclei merge together and interatomic crystal-lattice forces become predominant and so form a single crystal, viscous flow stops and only plastic flow can take place. We have to consider here that, once edge dislocations have formed, their activation energy lies in the electron-volt range. The temperature for annealing would follow from

$$\frac{T}{T_0} \simeq \exp \frac{e}{kT_0}, \quad (14.49)$$

where  $e/kT_0 \simeq 40 \text{ V}^{-1}$ ,

$$T_0 = 300^\circ\text{K},$$

indicating that  $T \gg T_m$ ,  $T_m$  = melting temperature.

It could be argued that in the plasticity range, dislocation movement could be aided by local stress fields or by external strain caused by bending. Since the stress field around a dislocation (germanium or silicon) is of the order of

$$E_e \simeq \frac{1}{2} \int_{r_0}^{r_1} \sigma_{\theta z} b \, dr = \frac{\mu b^2}{4\pi} \log\left(\frac{r_1}{r_0}\right), \quad (14.50)$$

where  $\sigma_{\theta z}$  = stress component in slip plane (spherical coordinates),

$b$  = Burgers vector  $\simeq 2.5 \cdot 10^{-8}$  cm,

$r_0 = 10^{-7}$  cm (bad region), (See Chapter 4)

$r_1 \gg r_0$ , for example,  $r_1 = 1$  cm,

$\mu$  = Poisson's ratio,

one obtains

$$E_e = 5 \cdot 10^{-3} \text{ erg/cm.}$$

For each atom plane threaded by the dislocation line, this is an amount of  $2 \cdot 10^{-11}$  erg/atom plane for metals, or 8 eV. (See Ch. 7 and Cottrell.<sup>18</sup>)

This high amount of energy must be overcome in plastic flow when dislocations of different sign are neighbors or when a stress field is brought to bear in order to bring about dislocation movement. In the case of well-oriented dislocation lines, one may improve perfection in a central region by dislocation movement, but if the dislocations are oriented at random (see, for example, Figure 10.1), this seems impossible, since moving deformation bands, twins, and grain boundaries are not maintaining their structure in the presence of other defects and form new dislocations. Nucleation of dislocations is well known in these cases and has been found experimentally in aluminum and silicon crystals under direct microscopic observation.<sup>19</sup>

There is, however, a distinct possibility of improving perfection with layer thickness. Film perfection is much higher at a distance of a few microns from the interface. The layer may improve gradually as it builds up by dislocation outgrowth.

Other considerations, like the induction of creep of different kinds to relieve the localized stress, also lead to the conclusion that high temperatures are necessary. If, for example, exhaustion creep (Mott-Nabarro) or Andrade creep are considered, very long time constants are involved if the film is not brought to a temperature at which the coefficient for self-diffusion is of the order of

$$D \simeq 10^{-13} \text{ to } 10^{-14} \text{ cm}^2/\text{sec},$$

(1100 to 1200°C).

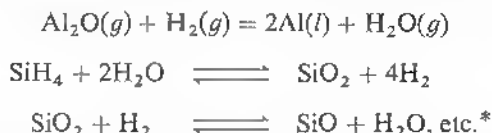
It is also unlikely that vacancy diffusion would be sufficient to restore the film perfection. As we have seen, the nuclei misalignment results directly in dislocations, as does the expansion misfit.

In the case of silicon there is another problem. Silicon, more than germanium, has the tendency to form many kinds of twins. Not only first-order twins,

but above all, second-order twin joins. These joins run in varied crystallographic directions and do not lend themselves to preferred motion in annealing (see, for example, Section 4.4). As discussed, a second-order twin join is formed by rotating superposed  $[110]$  projections by  $38^\circ 57'$  around  $[110]$  (see Figures 4.10 and 4.11) (white points are below projection plane). The second-order join has a resultant direction along  $[\bar{2}21]$  for individual  $A$  and  $[\bar{2}21]$  for individual  $B$ . At points  $b$ , bonds have been combined, at points  $d$  bonds have been rotated. J. A. Kohn<sup>20</sup> has analyzed the first- and second-order twin joins in silicon and established their existence.

#### *Chemical Changes.*

At the deposition temperature in excess of  $1000^\circ\text{C}$  for silicon, the  $\text{Al}_2\text{O}_3$  surface reacts with the atomic silicon. Silicon atoms deposit preferentially at Al sites, as we know, but reactions of the hydrogen carrier gas also take place. In addition, the presence of  $\text{SiO}$  and  $\text{SiO}_2$  leads to localized reactions of the type



Many silica-glass structures are known and have been described in detail.<sup>21</sup> The multiplicity of the  $\text{SiO}$  bond structure is responsible for many variations. Assessing the thermal behavior of these complex structures seems to depend largely on the  $\text{SiO}$  stretching bond vibrations, which again vary with the crystallographic direction.

Another point of uncertainty is the polymerization tendency of the  $[\text{SiO}_4]$  and  $[(\text{Si}, \text{Al})\text{O}_4]$  groups, which are in no way restricted to tetrahedral coordination. Interlinkage of  $[\text{SiO}_4]$  and  $[\text{AlO}_4]$  tetrahedra occurs, for example, in sillimanite. The multiplicity of the  $[\text{Si}_x\text{O}_y]$  chains is important here. Possible different degrees of ionization of the Si atom give rise to different  $\text{SiO}$  distances and the formation of double chains,  $[\text{SiO}_4]-[\text{AlO}_4]$  tetrahedra, and  $[\text{AlSiO}_5]$  double chains.

Variations of cell content of the  $x[\text{Al}_2\text{O}_3] \cdot y[\text{SiO}_2]$  chains and consequent density variations make an estimation of thermal expansion and the effect of annealing more uncertain. Rather difficult situations arise from "quartz" chains,  $\text{Si}-\text{Si}-\text{Si}$ , and "amortite" chains,  $\text{Si}-\text{Al}-\text{Si}-\text{Al}$ . Polymorphism of  $\text{Al}_2\text{SiO}_5$  is known and has strong pressure dependence.<sup>21</sup>

It is known that the sapphire substrate is strongly attacked and transformed after deposition.<sup>16\*</sup> It is also known that the  $\text{Si}-\text{Al}_2\text{O}_3$  interface has electronic

\* For detail on substrate-film reactions, see: J. Mercier, J. Electrochem. Soc. 117, No 5, p. 666, May 1970; 117, No 6, p. 812, June 1970.

properties at variance with either the silicon layer or the  $\text{Al}_2\text{O}_3$  substrate.<sup>22</sup> It has been found that this glassy interface has a trap density of  $10^{16} \text{ cm}^{-3}$  and acts as a strongly ionizable layer that generates an inversion layer next to it in the silicon overgrowth.<sup>22</sup>

Even assuming that thermal treatment for prolonged periods of time would improve the silicon layer perfection, other problems arise from the doping changes that are tied to the annealing process itself. These problems center on the formation of thermal donors and acceptors. These are variations in the electric character of the  $\text{SiO}$  bonds with temperature treatment.

Silicon in contact with oxygen-carrying media (quartz, sapphire, etc.) shows a high degree of oxygen concentration. Oxygen, in turn, can act as a doping agent. A heat treatment as low as  $450^\circ\text{C}$  of silicon with oxygen present shows donor formation to the point that  $p$ - $n$  junctions can be grown into silicon by a  $450^\circ\text{C}$  heat treatment, when an oxygen content of  $10^{17} \text{ cm}^{-3}$  is measured.<sup>23</sup>

Although the maximum donor formation occurs during many hours of heat treatment at around  $450^\circ\text{C}$ , donor formation is already measured after a few hours annealing. Some general laws of heat treatment have been derived for silicon.<sup>24</sup>

1. The initial donor formation is proportional to the fourth power of the oxygen content.
2. The content can be as high as  $10^{19} \text{ cm}^{-3}$ .<sup>23-25</sup>
3. Heating above  $500^\circ\text{C}$  for longer periods of time decreases the donor concentration, and a heat treatment at  $1000^\circ\text{C}$  stabilizes the crystals so that subsequent heat treatment at  $450^\circ\text{C}$  shows reduced donor formation.
4. The solid solubility for oxygen decreases with decreasing temperature (heat of solution = 1 eV).
5. Prolonged heating creates  $\text{SiO}_2$  as a second phase (Tyndall effect, high scattering center density, low mobility).

It has also been found that  $\text{SiO}_4$  tetrahedric formation changes the local dielectric constant of silicon crystals. These facts have not been clearly correlated, since in  $p$ -type silicon the  $450^\circ\text{C}$  cycle can also form thermal acceptors and the  $1000^\circ\text{C}$  cycle can form donor states.<sup>26</sup>

It is well known from bulk crystal growth that prolonged heat treatment can decrease both thermal impurities but that the mobility values (also lifetime) suffer severely because of the above-mentioned neutral scattering centers.

Moreover, it is well established that a lowering of stresses around inclusions, mainly oxygen and oxides, is realized by the formation of separated or paired nonclosed configurations of stacking faults.<sup>27, 28</sup>

For all these reasons, there seems little room for thermal improvements by annealing of silicon films on sapphire or other insulator substrates.

Table 14.2

Material	Silicon Si	Sapphire $\text{Al}_2\text{O}_3$	Spinel $\text{MgO} \cdot \text{Al}_2\text{O}_3$	Crysoberyl $\text{BeO} \cdot x \cdot \text{Al}_2\text{O}_3$
Structure	Diamond cubic	Hexagonal	Cubic	Orthorhombic
Lattice constant	$a_0 = 5.43 \text{ \AA}$	$a_0 = 4.75 \text{ \AA}$	$a_0 = 8.02 \text{ \AA}$ $= 7.96 \text{ \AA}$ ( $\text{MgO} \cdot 3.31\text{Al}_2\text{O}_3$ )	$a = 9.404 \text{ \AA}$ $b = 5.476 \text{ \AA}^{a)}$ $c = 4.427 \text{ \AA}$
Thermal conductivity $\text{cal/cm}^2/\text{cm/sec}/^\circ\text{C}$	0.2 (20°C) 0.39 (40°C)	0.065 (100°C)	0.03 (35°C)	0.2–0.5 ( $\eta$ ) <sup>b)</sup> (dependent on $x$ )
Linear thermal- expansion coefficient, per °C	$4.2 \cdot 10^{-6}$	$9.5 \cdot 10^{-6}$ (20–1200°C)	$8.83 \cdot 10^{-6}$ (20–1200°C)	$10 \div 15 \cdot 10^{-6} (?)^{c)}$ (20–1200°C)

<sup>a)</sup> Crystal structure, Synthesis, and Magnetic Properties of Crysoberyl, R. E. Newnham. *MIT-Techn. Report* 183, Laboratory of Insulation Research, November, 1963.

<sup>b)</sup> An Intermediate Compound in the System  $\text{BeO} \cdot \text{Al}_2\text{O}_3$ , W. R. Foster and H. F. Royal. *Amer. Cer. Soc. Journal*, vol. 32, pp. 26–35, 1949.

<sup>c)</sup> Relative Enthalpy of Beryllium 1 : 3 Aluminate, D. A. Ditmars and T. B. Douglas, *Journ. of Research. Nat. Bureau of Standards A*, vol. 71A, no. 2, pp. 97–103, March-April, 1967.

## Experimental Achievements

### Vapor Deposition.

Much of the experience in heteroepitaxy was gained on silicon as deposition material, and we refer mostly to this work, but many of the conclusions are of a general nature and can be applied to other materials combinations.

Also, the method of chemical deposition ( $\text{SiCl}_4$  and  $\text{SiH}_4$  reduction), as first successfully applied by H. C. Theuerer of Bell Laboratories (1958) in homoepitaxial growth, has been predominant in heteroepitaxy of silicon since then.

As in vacuum deposition, the process of nucleation is decisive for the layer formation, but the fact that surface precleaning immediately preceding deposition is so much easier and equipment cost lower in chemical-vapor deposition than in vacuum deposition has given the first method a much wider industrial use.

Substrate material for silicon is usually sapphire ( $\text{Al}_2\text{O}_3$ ) in varied orientations.<sup>29</sup> Spinel,  $\text{MgAl}_2\text{O}_4$ , has been used also,<sup>30</sup> as well as beryllium oxide,<sup>31</sup> and in moving-mask deposition, SiC was also used.<sup>32</sup> Orientation of films has been achieved on silica,<sup>33</sup> and a better crystallographic and thermal match is expected with crysoberyl,  $\text{Al}_2\text{BeO}_4$ , as substrate. The different substrate structural parameters and thermal constants are compared with silicon Table 14.2.

The sapphire orientation commonly used is  $[1\bar{1}02]$  or  $[\bar{1}012]$  (see Figure 14.12). Here the silicon atoms can find approximate register for a number of film orientations, mostly the  $[111]$  species. In spinel, a wider lattice mismatch is observed.

At first glance, it would seem obvious that a precise match in lattice constant and thermal-expansion coefficient would be most important. In nucleation theory, it seems, however, that more or less of a difference in these parameters, at least within the range of the buildup of the nuclei before cluster formation, is not critical. There is, of course, a fallacy in this argument, which is based on the assumption of perfect growth due to basic nuclei alignment (see our preceding arguments).

In all cases *single crystal* films were produced under careful growth conditions, because in fact a certain register of the silicon atoms with the Al atoms (see Figure 14.13) is sufficient to start an oriented overgrowth yielding near perfect or perfect Laue-back reflection pattern. The perfection increases markedly if thicker layers are grown. It is well known that in homoepitaxy the epitaxial film can have a significantly higher perfection than the original seed crystal.<sup>34</sup>

Therefore, good device characteristics have been achieved with thicker ( $> 1\ \mu$ ) films, especially for devices on a microscale like Schottky barrier diodes for high frequency, mixer diodes, FET devices, tunnel diodes. Vertically



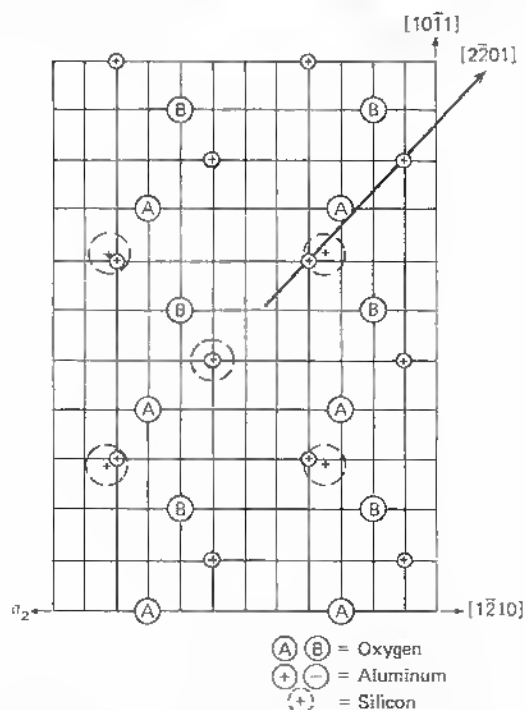


Fig. 14.12 Superposition of silicon-on-sapphire. Aluminum atoms on  $(1\bar{1}02)$ -plane of sapphire. Oxygen atoms on plane below. Silicon atoms in epitaxial layer are larger circles superimposed. After Manasevit<sup>29</sup>

emplaced junctions, as they are used in diode arrays and MOS structures, suffer from a yield problem because of the interface action that is shunting a part of the  $p$ - $n$  junctions formed.<sup>21, 35</sup> If diffusion steps are involved, as in bipolar transistor structures, the high dislocation density is a production hazard and limits yield because of preferential diffusion along dislocations.<sup>36, 37</sup> Also, ion implantation does not basically eliminate this difficulty, since it is operating on the principle of the open lattice in chosen crystallographic directions. Thus dislocations result in punched emitter-collector junctions and uneven  $p$ - $n$  layers.<sup>37</sup>

For device sizes, even as small as a few square microns, a dislocation density of  $10^8 \text{ cm}^{-2}$  puts one dislocation on every 1-micron-square area, thus on any junction fabricated.

Experience shows, therefore, that a careful evaluation has to be made for each case of device chosen with respect to yield, performance, and price if the SOS technology is desired for one reason or another (for example, radiation resistance).

There are numerous efforts to improve layer perfection in chemical vapor deposition. It is known, for example, that codiffusion of two impurities, one with a smaller, the other one with a larger tetrahedral covalent radius (Pauling), can compensate each other and that no lattice strain and subsequent dislocation formation occur. For example, a codiffusion of tin (small Pauling's radius) and boron or phosphorous has been found to compensate each other's lattice strain to a large extent.<sup>38</sup> It is therefore possible that the positive strain in silicon on sapphire is compensated, at least partially, by a coevaporation of Sn in the early deposition stages. But here again the first layer adjacent to the insulator substrate must be degenerate, at least  $10^{19} \text{ cm}^{-3}$  Sn, and vertical junctions are not possible.

*Hall Data.* The reduction in mobility in epitaxial silicon compared with bulk silicon is not only due to dislocation scattering (and neutral scattering) but is mainly caused by the space charge around edge dislocations.<sup>39</sup> Careful measurements of electron and hole mobilities have been compared with those measured on equally doped bulk silicon subjected to the strain calculated for the films.<sup>40\*</sup>

Measurement results are shown in Figure 14.13 for electrons. The maximum values lie at 500 to 600  $\text{cm}^2/\text{V}\cdot\text{cm}$  at  $10^{16} \text{ cm}^{-3}$  and decrease at both sides toward smaller and higher doping values. For bulk silicon (strained), however, the values increase as usual for lower impurity content. The same situation is found for holes (see Figure 14.14). There is one obvious explanation for the striking mobility loss with lower carrier concentration, namely, that compensation takes place between substrate surface impurities and the dopant, increasing the number of neutral scattering centers. This is also true for *p*-type films, showing that other influences than the aluminum autodoping are involved. The effect, however, is more pronounced in *n*-type films. One has to consider here the mosaic structure of these films, which are subdivided into crystallites separated by grain-boundary barriers. This increases the measured resistivity (decrease of  $\sigma$  in  $\mu = \sigma \cdot R_H$ ) and lowers the mobility.<sup>41</sup> In Figure 14.15, a comparison is made of the temperature dependence of the Hall mobility for silicon films with an intentionally high dislocation count (doping range  $10^{18} \text{ cm}^{-3}$ ) and silicon on spinel. Although the influence of the dislocations is striking, there is still a difference between homo- and heteroepitaxial films.

\* The hole mobility actually can increase by strain when the band changes cause a shift at the top of the valence band toward smaller effective mass holes (Figure 14.14 see also: G. Dorda: Appl. Phys. Letters, Vol. 17 No 9, pp. 406-408, 1. Nov. 1970 for quantization effects in the conduction band), but this effect does not make such layers more suitable for devices. Upon heat treatment the strain will relax and diffusion may have erratic results.

Important is also the high density ( $10^{16} \text{ cm}^{-3}$ ) of deep levels in the forbidden gap of silicon on sapphire. (See D. J. Dumin, Solid State Electronics, Vol. 13 No. 4, pp. 415-424, April 1970.)

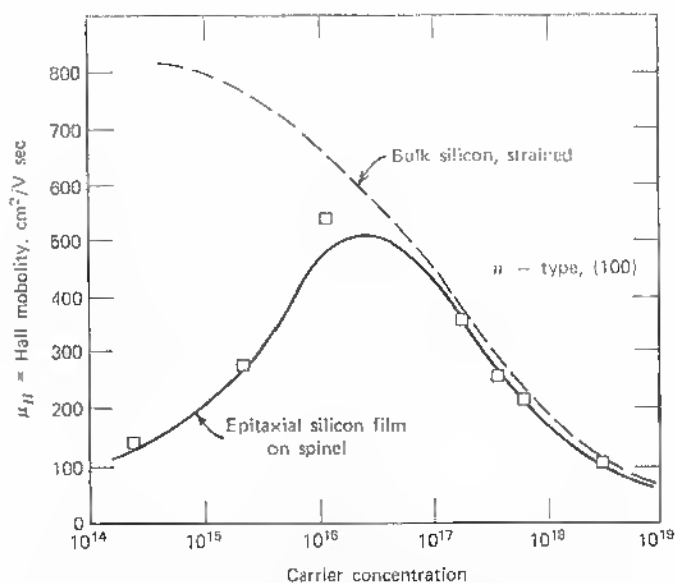


Fig. 14.13 Hall mobility as a function of carrier concentration for bulk silicon and epitaxial silicon on spinel (after Schlötterer<sup>40</sup>)

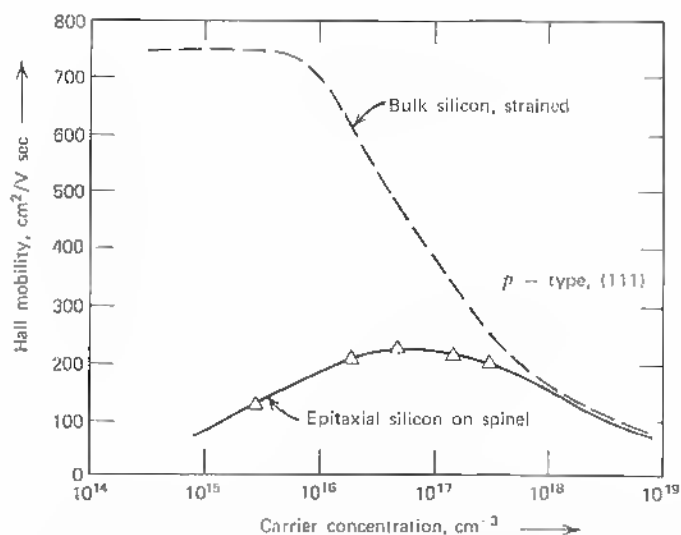


Fig. 14.14 Hall mobility as a function of carrier concentration for bulk silicon and epitaxial silicon on spinel. (After Schlötterer [40].)

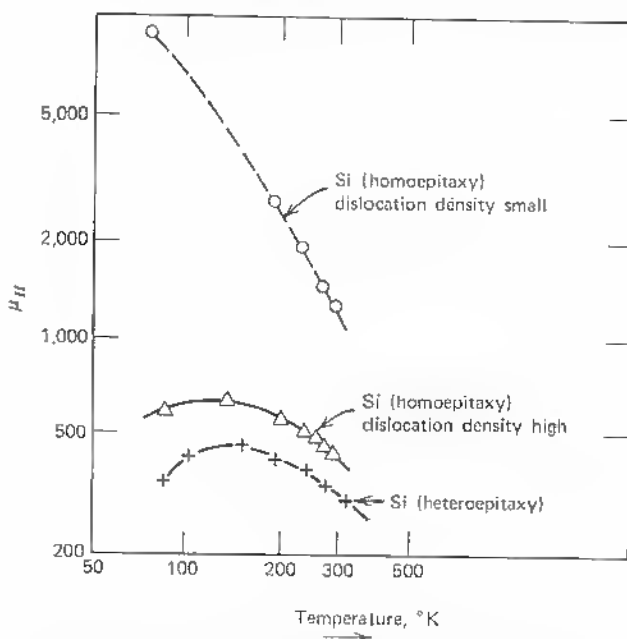


Fig. 14.15 Comparison of Hall-mobilities for holes versus temperature for homoepitaxial silicon with small dislocation density ( $< 10^3 \text{ cm}^{-2}$ ), homoepitaxial silicon with high dislocation density ( $> 10^6 \text{ cm}^{-2}$ ) and heteroepitaxial silicon.

There are, therefore, a number of influences due to the heterogeneous growth conditions, and it seems doubtful that two-dimensional deposition methods will solve this problem without recourse to improved parameter control.

#### *Vacuum Deposition.*

From early experiments in vacuum systems, we know that the growth of device-grade films was not achieved because of the oxygen loading of the deposited films and that even homoepitaxial vacuum deposition suffered from unclean surface conditions that seemed to be independent of the degree of vacuum achieved. With the development of doping methods, the original difficulties ( $p$ - $n$  mosaic structure) can be overcome at least for higher concentrations ( $N_d > 10^{16} \text{ cm}^{-3}$ ). This was shown recently in a system where antimony is coevaporated from a source with the deposition of high resistivity (2,400 ohm cm) silicon.<sup>42</sup> Room-temperature Hall mobilities in excess of 500 cm<sup>2</sup>/V/cm were achieved here at a  $10^{-7}$  Torr initial vacuum range.

An interesting effect was found, namely, a remarkable improvement in mobility (40 per cent) when the grown films were subjected to oxidation

(oxidation in steam and annealing in argon). Itoh et al.<sup>42</sup> explain this effect by the neutralization of the Al atoms freed by autodoping. This effect is also known from the treatment of vapor-deposited films.<sup>43</sup> Similar effects and a redistribution of impurities have been reported in work on hydride dopant sources ( $B_2H_6$ ,  $PH_3$ ) in silicon on sapphire.<sup>44</sup>

At this stage, the results in vacuum deposition do not seem to justify the greater amount of equipment cost and control needed. There is, however, progress in ultrahigh vacuum deposition or sublimation at low substrate temperatures. At a vacuum of  $10^{-10}$  Torr and a substrate temperature of only  $550^\circ\text{C}$ , Thomas and Fracombe<sup>45</sup> have sublimated  $p$ -type silicon on  $n$ -type silicon and produced sharp  $p$ - $n$  interface and good junctions. Such methods could conceivably be applied to heteroepitaxial deposition also, decreasing substrate-film interference, autodoping, chemical changes, thermal stress, and the like. But there is certainly still a long way to go to the successful deposition of device-grade layers below  $1\ \mu$  thickness on insulators.

*Microzone Melting, Traveling Solvent Recrystallization, Directional Growth, and Other Methods.*

We have discussed how four main effects combine to make two-dimensional heterodeposition inefficient as a method to grow device-grade semiconductor material. We have also discussed the problems of heat treatment. With these limitations in mind, it seems desirable to minimize a priori the layer defect formation by a monocrystallizing step independently of the original deposition process or to form a layer by localized deposition under the influence of crystallographic growth forces in a microscopic homoepitaxial process. In such a process, local stress is relieved during growth, since only a microscopic (monoatomic) layer builds up at a time and no large area deposition occurs. Several methods to achieve microscopic growth planes have shown promise and are discussed briefly.

*Microzone Melting.* J. Masujian<sup>46</sup> has applied localized remelting of deposited films. Remelting was achieved by localized exposure to an electron beam (see Figure 14.16). Hall mobility data were improved by more than a

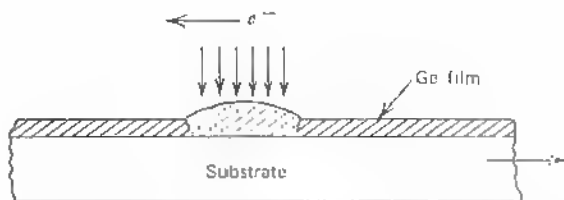


Fig. 14.16 Schematic of electron-beam recrystallization (see text).

factor of 2 this way. The relatively high local temperatures, reaching the melting point, may cause undesirable effects, so that methods using eutectic liquid zones are often preferable when doping effects can be controlled.

*Traveling Solvent Recrystallization.* Instead of moving the heated zone by a moving source, the zone movement can also be effected by a temperature gradient along the substrate. A liquid interface can be formed either by heating or by lowering the melt temperature with an appropriate eutectic layer. This layer may have a cylindrical shape (see Figure 14.17) and is forced to move under a temperature gradient  $\Delta T$  or Peltier heating, reinforcing a gradient already present. W. G. Pfann et al.<sup>47</sup> have extensively analyzed such recrystallization procedures, which are very common in zone refining processes. In a system, such as that shown in Figure 14.18, the liquid-solid interface is directed in different ways at each side with respect to current flow or polarity.

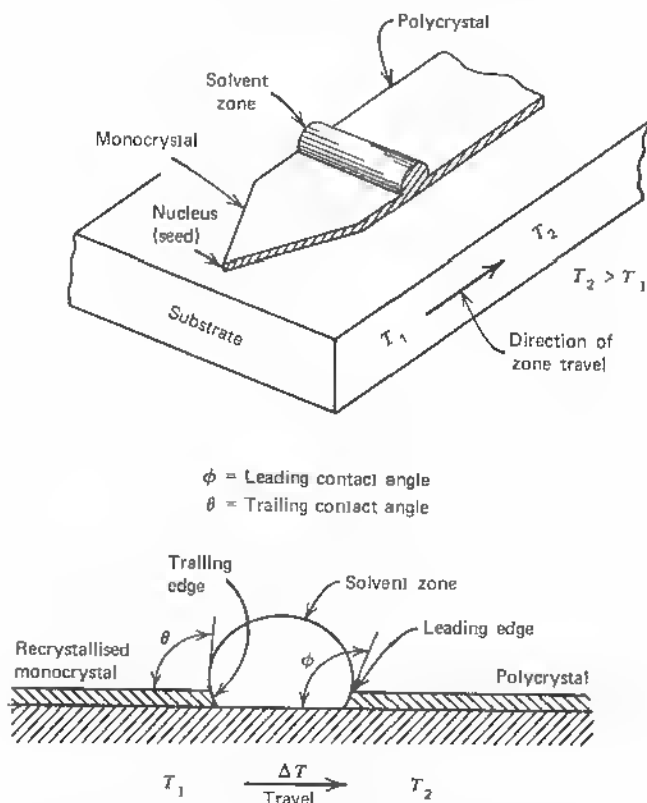


Fig. 14.17 Traveling solvent recrystallization. Solvent zone subjected to temperature gradient  $T_1 \rightarrow T_2$  and cross-section of liquid layer with leading and trailing edge.

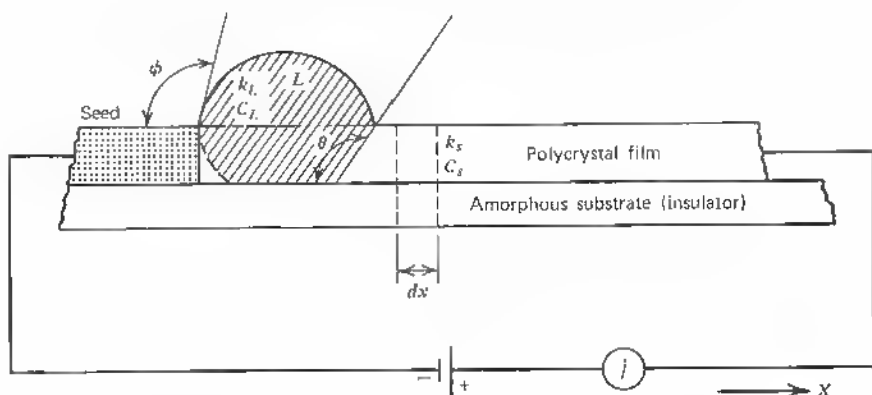


Fig. 14.18 Liquid interface motion due to current flow and Peltier-effect. Heat flow equation after Reiss (see text).

This causes the effects at those interfaces to add together to a total lateral force on the liquid layer.

H. Reiss<sup>47</sup> has derived relations for the velocity of the interface motion.

If a horizontal cylindrical cross section is assumed and the solid part is at the left of the liquid part, with the  $+x$  direction to the right, the interface may move for  $dx$  in time  $dt$  at a current  $j$ . Then the heat absorbed is  $Pj dt$ , with  $P$  = Peltier coefficient in volts, and the heat of fusion (freezing) is  $Hdx$  in cal ( $H$  in cal/cm<sup>3</sup>).

With the temperature gradients  $\Delta T_s$  and  $\Delta T_L$  in the solid and liquid and  $k_s$  and  $k_L$  their respective thermal conductivities, the heat leaving the interface (in the direction of the temperature gradient) is

$$(k_s \Delta T_s - k_L \Delta T_L) dt [\text{cal}].$$

The heat absorbed because of internal energy difference in liquid and solid is

$$(C_L - C_s) T dx,$$

where  $C_L$ ,  $C_s$  = respective heat capacities, cal/cm<sup>3</sup>,

$T$  = melting temperature, °K.

In the heat balance the Peltier heat and the heat leaving the interface must be equated to the heat of fusion  $Hdx$  and the heat absorbed  $(C_L - C_s)Tdx$ . This leads to Reiss' formula:

$$v = \frac{dx}{dt} = \frac{(P \cdot j / 4.186) + (k_s \Delta T_s - k_L \Delta T_L)}{H + (C_L - C_s)T}, \quad (14.51)$$

where 4.186 = dimensional factor, watt sec cal<sup>-1</sup> (see Figure 14.18).

With modest current densities of the order of  $10 \text{ amp cm}^{-2}$ , such interfaces have been moved with speeds of 2 to  $3 \mu\text{sec}^{-1}$ . This is largely sufficient for thin-film recrystallization work. If the Peltier heating is combined with a localized optical heating and an additional temperature gradient, an efficient localization and minimization of convection should enable one to carry through efficient monocrystallization of originally polycrystalline or highly imperfect deposits.

Such schemes have worked, for example, with GaAs when a Ga-rich zone was used. It was established that:

1. The Ga-rich liquid layer was contained because of surface tension at the liquid state.
2. The Ga-rich layer moved under an applicable temperature gradient  $T_2 \rightarrow T_1$ .
3. The film does not detach from the substrate. (e.g. a  $\text{Al}_2\text{O}_3$ -surface).

It turns out that a cleaned substrate surface, even if amorphous, can be used, since no heteroepitaxial relations are required, the crystal is growing out of a seed.

In silicon material, a liquid zone based on indium has also been used. In InSb and InAs, traveling solvent growth has been investigated in bulk crystals, and conditions for preparing *p-n-p* and *n-p-n* structures have been worked out without disturbing the monocrystallinity.<sup>48</sup> For silicon, in particular, low-melting eutectics can also be established by a gold-silicon alloy zone ( $370^\circ\text{C}$ ). Thin alloy zones of this kind have been made in order to assume a liquid-solid substrate-film contact that would diminish the influence of the surface on defect growth.<sup>49</sup> The assurance of a liquid-solid interface, as in the traveling solvent method, has produced improvement of perfection when applied to crystal growth.<sup>50</sup> It is a particular point of the application of this method to thin-film growth that the localized liquid-solid growth mechanisms eliminate the problem of large-area growth and thus the problems of nuclei alignment. In the growth of monomolecular interfaces in contact with a laterally moving liquid-solid interface at a seed crystal, the substrate forces are minimized, since only very small (two-dimensional) layers crystallize under application of the 60-times stronger cohesive forces of the seed-liquid contact. As the layer builds up, the small disturbance introduced at the substrate surface grows out into the perfect upper crystal layers ( $> 1 \mu$ ) of the epitaxial film under dominance of the lateral seeding forces. In two-dimensional growth, interface velocities as large as  $2 \times 10^{-6} \text{ cm/sec}$  for In-InSb systems and for a temperature gradient  $\Delta T \approx 30^\circ\text{C/cm}$  have been measured. In Pb-InSb systems, interface velocities of  $0.9 \times 10^{-6} \text{ cm/sec}$  were found for liquid zones with  $\Delta T \approx 60^\circ\text{C/cm}$ .<sup>51</sup>



*Directional Growth of Single Crystals by a Moving Deposition Zone.* In this technique, CVD can be employed in the usual sense, but the deposition is confined to an edge of the substrate in order to build up a monocrystalline surface by continuous lateral outgrowth under application of a seeding process. Figure 14.19 describes this system.<sup>52</sup> Although the original nucleus is oriented in some preferential direction, the system allows the use of lateral growth forces, as in a zone-leveling equipment,<sup>47</sup> and has shown promise of film-perfection improvements even for film thickness around  $1\ \mu$ . For thicker films, the chances of an upper, more perfect layer are good, but in the immediate neighborhood of the substrate surface one has a disturbed layer. Substrate-film relations are less important than in CVD without seeding. Amorphous substrates can be used in principle.

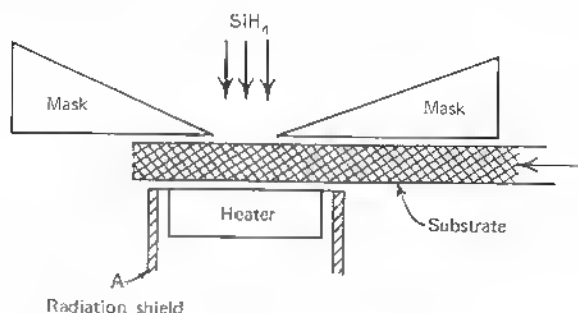


Fig. 14.19 Moving mask deposition with silane vapor.

The same method can be applied to vacuum deposition and is being studied by M. Braunstein (Hughes).<sup>53</sup> There is, however, a use of a low-melting eutectic (Si-Au). In this "vapor-liquid-solid-moving-mask-growth" the silicon evaporation is concentrated on a slit in the moving mask and causes this part to be liquid at the substrate temperature of 800 to 900°C. Single crystal regions of  $20 \times 30\ \mu$  size and some as large as  $50 \times 300\ \mu$  have been achieved. Preferred orientation was [111]. There was no use of a seed. Seeding occurs at a fine point of the triangular mask opening as in a modified Bridgman method, and the outgrowth is oriented along the direction of the original nucleus (see Figure 14.17). The movable, slotted mask, placed between the fixed mask and the evaporation source, gradually uncovers the apex of the acute angle of the fixed mask. The problem of the fine movement of the mask is solved by an hydraulic drive mechanism with bellows. Although silicon single-crystal regions have been formed (clear Laue pattern), no larger films have been grown, and the method at present does not yet yield the perfection reached with CVD.

Aside from the deleterious effects of the gold as a trap center and lifetime killer, the seeding at a triangular point is undefined.

A somewhat more elegant version was reported by Clark et al.,<sup>54</sup> who used the method above, but the silicon is deposited by *sputtering* at 200°C substrate temperature (local temperature is certainly higher). First results are, of course, not yet comparable with CVD, but it seems that if truly lateral growth can be achieved, this method gives a possibility of finally meeting all quality requirements that are attached to the production of bulk mono crystals from the solid-liquid growth in Czochralski methods. It remains a problem here to force the sputtered atoms or molecules to deposit two-dimensionally at the growing crystal surface *A* (see Figure 14.20) and linearly on the substrate surface *B* each time a layer on the growing crystal is formed. A seed would facilitate the original direction and quality of the growing crystal. The contact with the substrate surface would be one-dimensional, but two-dimensional with the seed for each layer formed. Therefore, the substrate would not essentially influence the layer perfection. The cohesive forces within the crystal dominate the adhesive forces along the surface and only a limited thin layer

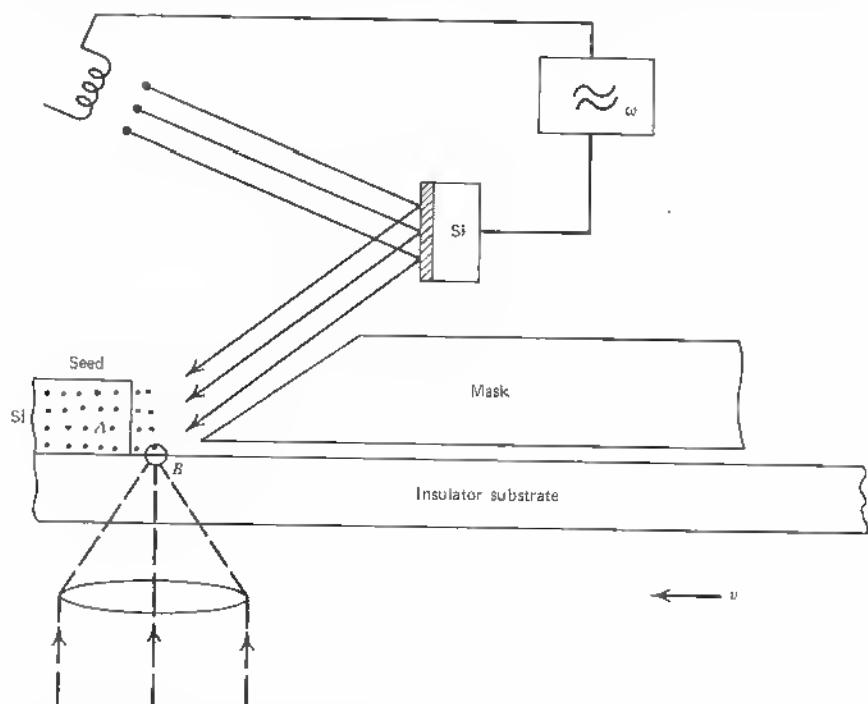


Fig. 14.20 System for mask movement in triangular moving mask deposition and in localized sputtering with optical heating (argon,  $10^{-4}$  Torr).

directly along the substrate surface figures as a contact zone between the substrate and the perfect crystal. The model of the traveling liquid-solid interface is obviously the best conceivable way to form perfect crystals, because here the mobility of the depositing atoms is much higher than in a sputtering process and cohesive forces form the monocrystal in the normal way from the melt.

By localized heating (optically, eventually with laser light), one may be able to sputter new atoms into the liquid surface layer and then move the mask and heat source according to the buildup of the crystal. This method has been described in patent applications (H. F. Mataré—A. deRudnay) and is sketched in Figures 14.21 to 14.23. In a precise ion-sputtering process with electrostatic focusing, a localized deposition at the front of the growing crystal should occur, and the substrate interface should be kept plastic and should finally secure contact with the substrate only.

Such a selective deposition, for example, is made to occur by focusing ionized semiconductor molecules or atoms on the leading edge or by electrostatically attracting them by the leading edge, where they are discharged and

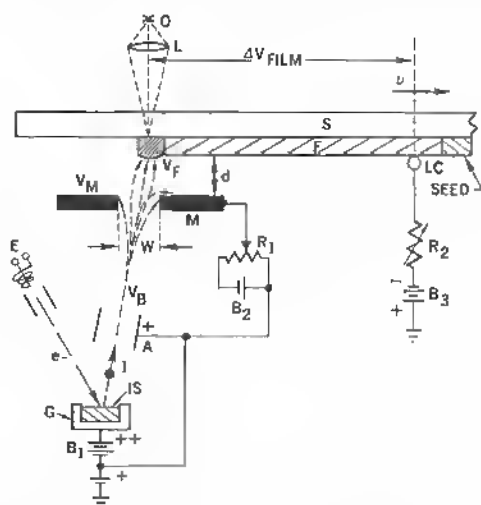


Fig. 14.21 Lateral film-growth by ion deposition from a seed on insulator substrates:  $A$  = accel. electrode;  $v$  = const. velocity;  $L$  = lens;  $M$  = mask;  $V_M$  = mask-potential;  $V_F$  = film-potential;  $V_B$  = beam-potential;  $LC$  = liquid metal contact;  $I$  = semicond. ion;  $S$  = substrate;  $F$  = film;  $G$  = ion gun;  $IS$  = ion source (semi-cond.);  $E$  = electron gun.

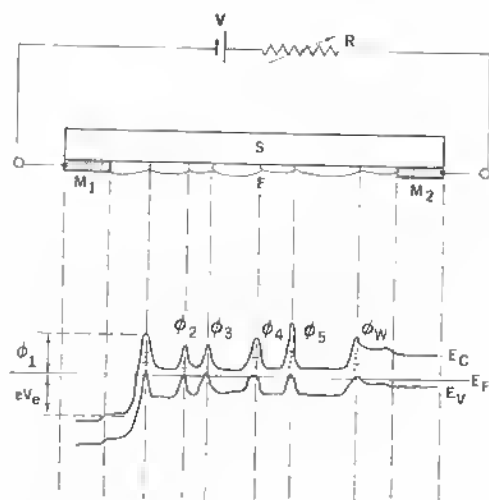


Fig. 14.22 Thin film grains and grain boundary barriers under voltage.

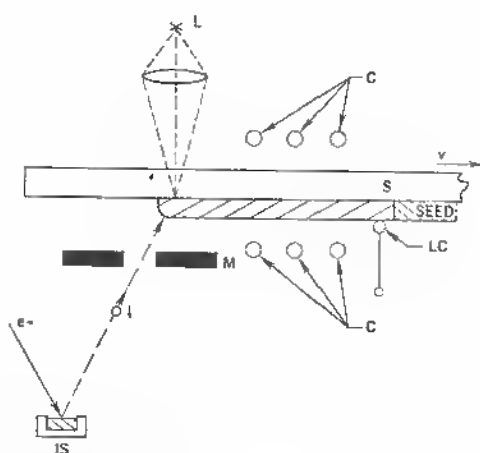


Fig. 14.23 Thin film ion beam deposition with optical heating and rf annealing:  $L$  — light source;  $IS$  = ion source;  $C$  = annealing coil;  $S$  = substrate;  $LC$  = liquid metal contact;  $M$  = mask.

condensed, or by heating the leading edge to a higher temperature than the substrate so that the vapor of volatile compounds of the semiconductor more readily dissociates and deposits semiconductor material on the leading edge rather than on the naked substrate not yet covered by the advancing oriented monocrystalline film. It is known that reactive gas loading can be reduced in vacuum deposition of oriented continuous monocrystalline films by depositing out of a collimated beam. In fact, it is known that in high-vacuum evaporation systems, where the pressure of the residual gas is  $10^{-5}$  mm Hg or less, so that the mean free path of the residual gas molecules is much greater than normal source-to-target distance, most or practically all the reaction between evaporant and residual gas occurs after condensation of the evaporant on the target or substrate. Other deposition parameters remaining constant, reactive gas loading in a vacuum-deposited film or a reactive element or compound, such as Ti, Si, GaAs, is thus inversely proportional to the number of molecules condensing in unit time on a unit surface, and it is, therefore, customary to evaporate Ti, and the like, at a fast rate if gas-free deposits are required. By using collimated beams of the ionized molecules to be deposited, vapor density over the small condensation area is considerably increased, and reactive gas loading consequently reduced. Since absorbed reactive gas, such as oxygen or nitrogen, decreases absorbate diffusion length, thus increasing nucleation rate of polycrystals, it is also responsible for other defects in the growing semiconductor film. By using collimated ion beams for deposition of semiconductor molecules, one can achieve a major improvement in semiconductor filming, particularly in the production of oriented monocrystalline semiconductor films.

Another advantage of the use of an ion beam for depositing oriented single crystals is the possibility of heating the very area of deposition, that is, the leading edge, to higher temperature than the adjoining areas. This selective heating of the leading edge is accomplished by suitably regulating ion-beam density and acceleration potential and should greatly facilitate epitaxy in the growing film.

Figure 14.21 schematically illustrates the process. A moving substrate such as sapphire, a glass ribbon, or a metal foil enameled on one side, moves, with constant speed over an ion gun that deposits an elementary or compound semiconductor film of constant thickness on the moving substrate. The semiconductor can be heated by an electron beam  $e^-$ . The initial deposition is made to occur on the heated left edge of an oriented monocrystalline seed attached to the moving substrate. By conveniently focusing and regulating the density of the ion beam the edge of the crystal seed is heated to the temperature required for epitaxial growth of the film built up by positively charged condensing semiconductor ions that are attracted and discharged respectively by the seed edge and the leading edge of the film that progressively

condenses. Both seed and film are being kept at a suitable potential by means of a liquid metal contact that first contacts the semiconductor film as the deposition proceeds. The condensing film thus takes over both the orientation and the single-crystal structure of the seed and keeps them all through its length. Since the ion beam is focused on and electrostatically attracted by the leading edge of the condensing semiconductor film, only a few scattered ions of the semiconductor can condense ahead of the leading edge, and the danger of heterogeneous nucleation is correspondingly reduced. As an additional precaution against condensing molecules, a positively charged mask with a fine slit opening, or having the shape of a knife covering the part of the substrate that has to be kept free of condensing molecules, can be placed between ion gun and moving substrate.

More detail about the electrical setup is evident in Figure 14.21. The semiconductor ions  $I$  are accelerated by an electrode system  $A$  and pass through the slit mask  $M$  so that the ion beam is congested because of a repulsive voltage  $V_M$  on  $M$  (battery:  $B_2$  and  $R_1$  for regulation). A battery  $B_3$  connected across resistor  $R_2$  to a liquid metal contact gives the film a negative bias with respect to the ion-beam potential. The relations among these different bias potentials are dependent on beam ionization, particle acceleration due to  $V_F$ , and initial particle heating by the electron beam  $E$ .

It is essential that the mask  $M$  eliminate all particles of slow speed that could deviate from the directed path toward the heated point of the thin film advancing with velocity  $v$  and maintaining liquid contact to the frozen mono-crystal. To assess the voltage ratio mainly between bias  $B_2$  and  $B_3$  a simple consideration of the forces acting on the beam particles gives a first approximation.

If  $q$  is the beam particle charge,  $E$  the local field in the mask plane  $M$ , the force on the particles is

$$f = \sum_n \sum_m q_n E_m = \sum_n \sum_m q_n (-\text{grad } V_m). \quad (14.52)$$

For one particle, the decisive is

$$f = \left| q \frac{V}{r} \right| \quad \text{or} \quad f = q \left( \frac{V_F}{d} - \frac{V_M}{w/2} \right), \quad (14.53)$$

where  $V_F$  = film potential,  
 $V_M$  = mask potential,  
 $d$  = film mask distance,  
 $w$  = mask slit width,

In order to minimize beam particles that are not focused and side-tracked, the following condition has to be satisfied:

$$\frac{V_B - V_M}{w/2} \ll \frac{V_B - V_F}{d}, \quad (14.54)$$

where  $V_B$  = beam potential.

This means that

$$\frac{V_B - V_M}{V_B - V_F} \ll \frac{w}{2d}$$

or

$$\frac{V_{B2}}{V_{B3}} \ll \frac{w}{2d}. \quad (14.55)$$

In adjusting the respective film and mask potentials, such a condition can be met.

Another advantage of a relatively high potential from bias  $B_3$  is the establishment of a potential drop across the forming thin film. A dense ion beam can draw a current sufficient to form a lower impedance path than the forming and nucleating thin film. This establishes a voltage drop across the film that is desired in order to merge the forming crystallites. A lateral potential drop exerts ponderomotoric forces on the individual grain-boundary junctions when they form during nucleation. Although such a potential drop is effective only for the total film in case of a deposition under bias (see Figure 14.22), the ion-beam deposition allows the exertion of the field force directly during formation of the film structure and, therefore, eliminates forming grain structures more efficiently. As seen in Figure 14.22, the connection in series of all individual grains leads to a very high impedance and necessary voltage drop although the field required for one barrier of height  $\phi$  is small.

The potential difference across the entire film is

$$\Delta V_{film} = R_{film} \times i_{film}.$$

(We only take into account grain-boundary barriers orthogonal or nearly orthogonal to the current flow.) Thus, in the case of the ion beam (see Figure 14.21),

$$i_{film} = \frac{V_{B3} - V_{beam}}{\rho_F \cdot l_F / q_F}, \quad (14.56)$$

where  $l_F$  = film length,

$q_F$  = film cross section,

$\rho_F$  = resistivity of film.

To assess the ponderomotoric forces on the thin-film grain boundaries under bias, we calculate the electrostrictive forces acting on the forming depletion region of the  $n$ - $p$ - $n$  structures of grain boundaries in analogy to electrostrictive forces in liquids.

It is well known that grain-boundary barriers generate a voltage drop:<sup>55</sup>

$$\Delta V = V_1 - V_2 = \frac{\epsilon}{8\pi e} \left( \frac{E_1^2}{N_1} - \frac{E_2^2}{N_2} \right), \quad (14.57)$$

(See Sect. 11.2)

where  $V_1, V_2$  = potential drop on either boundary side,

$\Delta V = V_1 - V_2$  = external voltage,

$\epsilon$  = dielectric constant,

$e$  = electronic charge,

$N_1, N_2$  = impurity densities on either boundary side,

$E_1, E_2$  = local fields on either boundary side.

Putting  $N_1 = N_2$  and assuming that at nucleation temperature the boundary field forms already, we can derive an expression for the pressure on the dielectric barrier layer in the field  $\Delta V$  as formed by the external bias:

$$\int_{p_0}^{p_1} \frac{dp}{\sigma} = \frac{1}{8\pi} (E_1^2 - E_2^2) \left( \frac{d\epsilon}{d\sigma} \right)_{\sigma=\sigma_1}, \quad (14.58)$$

where  $p$  = pressure component,

$\sigma$  = density of film.

For assumed constant density (low compressibility liquid) it follows that

$$p_1 - p_0 = \frac{1}{8\pi} (E_1^2 - E_2^2) \sigma \frac{d\epsilon}{d\sigma} \quad (\text{pressure increment}). \quad (14.59)$$

Using Clausius-Mosotti's formula

$$\frac{\epsilon - 1}{\epsilon + 2} = C\sigma, \quad (14.60)$$

with  $C$  independent of  $\sigma$ , and differentiating yields

$$\frac{3}{(\epsilon + 2)^2} d\epsilon = C d\sigma \quad (14.61)$$

or

$$\sigma \frac{d\epsilon}{d\sigma} = \sigma C \frac{(\epsilon + 2)^2}{3} = \frac{\epsilon + 2}{3} (\epsilon - 1);$$

thus, it follows from (14.39) to (14.41) that

$$p_1 - p_0 = \frac{1}{2} \Delta E^2 \frac{\epsilon + 2}{3} \cdot \frac{\epsilon - 1}{4\pi}. \quad (14.62)$$



Assuming now  $\epsilon = 10$  and  $\Delta E \approx 10^5$  V/cm, a value easily achieved by a few volts drop across the barrier of  $10^{-4}$  to  $10^{-5}$  cm of thickness, we have

$$\Delta p = \frac{2}{3} \left( \frac{1}{9} \cdot 10^{-4} \right) \cdot 10^{10} = \frac{1}{6} \cdot 10^6 \text{ dyn/cm}^2.$$

Assuming a cross section of the growing film

$$1 \mu \times 1 \text{ mm},$$

the pressure on this interface if a grain boundary formed would amount to

$$1 \text{ dyn or roughly } 10^{-3} \text{ Torr}.$$

In a vacuum of better than  $10^{-5}$  Torr the differential is better than 100. This is a sufficient pressure gradient to force merger of nuclei in the quasi-liquid state.

In order to increase the local particle mobility at the forming film edge additional film heaters can also be provided. As an example, an optical or electron beam heater can be positioned in the vicinity of the ion gun, on either side of the substrate, and a radiation heater can supply radiated heat between ion gun and ground contact of the film. The optical beam or electron beam heater can be used for sharply defined local heating in order to promote epitaxial growth or thermal stress relief, and the radiation heater between ion gun and ground contact may be used for annealing the film and also for raising the semiconductor film temperature to a point where it becomes more conductive and thus provides a sufficient electrically conductive path for the ion discharge current (see Figure 14.23). A need for high-purity-material deposition may demand compound formation in situ. This can be solved by adopting the present technique to the case of a two-source deposition (see Figure 14.24). Although a two-source deposition is known as such, ion-beam deposition in this case is new and should lead to a combination of better materials control with higher film perfection. It is known that the usual flash evaporation used for homopolar and heteropolar semiconductors is rather crude because of particle clustering and consequent film growth defects.

It is also known that in the vacuum deposition of compounds, such as GaAs, the partial pressure of the vapor of the more volatile component must be higher than prescribed by stoichiometry. It is also known that partial pressure and evaporation rate of ionized molecules can be monitored with great accuracy. By using separate ion sources for the vacuum deposition of a compound semiconductor film, we can thus very accurately monitor vapor composition and maintain conditions ideal for film deposition. By separate ion sources we do not only mean separate ion guns for each component but also separate sources of ionized vapors with a common ion optical system for uniting and collimating the originally separate vapors.

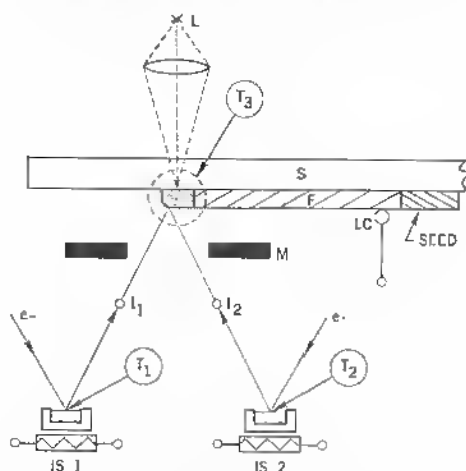


Fig. 14.24 Two source compound film deposition by ion beams: *IS 1* = ion source 1 (e.g. gallium); *IS 2* = ion source 2 (e.g. arsenic); *S* = substrate; *LC* = liquid metal contact; *T*<sub>1</sub>, *T*<sub>2</sub>, *T*<sub>3</sub> controlled temperatures.

Films built up according to this description can be used to deposit contacts and insulators for the formation of active devices like MOS and FET devices. Because of the substrate movement, a part of the film, formed as a monocrystal, can immediately be processed into device structure or parts thereof.

### Conclusions

A number of the techniques have been used to improve perfection of silicon-on-sapphire layers: Improved substrate surface polish and etching, gas-phase etching, deposition-temperature cycling, initial fast delivery followed by slow deposition, vapor-pressure variations, annealing steps, and other methods, such as laser recrystallization. But in considering the systems limitations in two-dimensional chemical-vapor deposition, it occurs that little can be done in order to achieve the desirable device-grade perfection needed for reproducible, predictable, and reliable device performance at larger scale. Also heat treatment has a very limited chance to enhance perfection, as we have seen.

Since the basic limitations derive from the crystal-substrate interface as the origin of growth, methods are being tried and proposed that make the film growth more independent from the substrate and use the 60 times stronger crystallographic growth forces acting in isomorphous growth. The best road of attack seems to be the one that yields new parameters for film growth control:

1. The formation of a localized solid-liquid interface
2. Employing moving forces on such an interface by temperature gradient zone leveling and piezoelectric effects
3. Deposition of materials from the source only at the leading edge of a seed crystal
4. Beam direction by ionized deposition techniques.\*

## REFERENCES

1. Becker, R., and W. Döring: *Ann. Phys.*, vol. 5, no. 24, p. 719, 1935.
2. Volmer, M.: *Z. Elektrochemie*, vol. 35, p. 555, 1929.
3. Turnbull, D., and J. C. Fisher: *J. Chem. Phys.*, vol. 17, p. 71, 1949.
4. Thomson, G. P.: *Proc. Phys. Soc.*, vol. 61, p. 403, 1948.
5. Van der Merwe: J. H.: *Discussions Faraday Soc.*, no. 5, p. 201, 1949.
6. Johnson, G. W.: *J. Appl. Phys.*, vol. 21, p. 1057, 1950; vol. 22, p. 797, 1951.
7. Van der Merwe: J. H.: *Proc. Phys. Soc.*, vol. 63A, p. 616, 1950.
8. Brooks, H.: Metal Interfaces, *Cleveland, Am. Soc. Metals.*, 1952.
9. Mroczkowski, R. S., A. F. Witt, and H. C. Gatos: *J. Electrochem. Soc.*, vol. 115, no. 7, pp. 750-752, July, 1968.  
Morizana, K., A. F. Witt, and H. C. Gatos: *J. Electrochem. Soc.*, vol. 115, no. 7 pp. 747-749, July, 1968.
10. Sugita, Y., M. Tamura, K. Sugawara: *J. Appl. Phys.* vol. 40, no. 8, pp. 3089-3094, July, 1969.
11. Turnbull, D., and B. Vonngat: *Industrial Engineering Chemistry*, vol. 44, no. 7 pp. 1292-1298, 1952.
12. Walton, D.: *J. Chem. Phys.*, vol. 37, no. 10, pp. 2182-2188, Nov. 15, 1962.
13. Reiss, H.: *J. Appl. Phys.*, vol. 39, no. 11, pp. 5045-5061, October, 1968.
14. Bassett, G. A.: "Proceedings of the International Symposium on Condensation and Evaporation of Solids," E. Rutner, P. Goldfinger, and J. P. Hirth (eds.), Gordon and Breach Science Publishers, Inc., p. 599, New York, 1964.
15. Paul, W.: *J. Phys. Chem. Solids*, vol. 8, pp. 196-204, 1959.
16. Ang, C. Y., and H. M. Manasevit: *Solid State Electronics*, vol. 8, no. 12, pp. 994-996, 1965.
17. Woo, T. C.: *J. Appl. Phys.*, vol. 30, no. 4, pp. 2082-2087, March, 1968.
18. Cottrell, A. H.: "Dislocations and Plastic Flow in Crystals," Clarendon Press, Oxford, p.38, 1953.
19. Berghezan, A., and A. Fourdeux: *J. Appl. Phys.*, vol. 30, no. 12, pp. 1913-1922, December, 1959.
20. Kohn, J. A.: *The Am. Mineralogist*, vol. 43, pp. 263-284, March-April, 1958.
21. Eitel, W.: "Silicate Science," Academic, vol. 1, New York, 1964.

\* These conclusions relate quite generally to materials other than silicon as CdS, CdTe, CdSe, etc. on insulator substrates. Progress in the active device field (See Ref. 56) will be possible only when higher film perfection is achieved.

22. Heiman, F. P.: *Appl. Phys. Letters*, vol. 11, no. 4, p. 132, Aug. 15, 1967.
- Neumark, G. F.: *Phys. Rev. Letters*, vol. 21, no. 17, pp. 1252-1256, October, 1968.
23. Kaiser, W.: and P. H. Keck: *J. Appl. Phys.*, vol. 28, no. 8, p. 882, August, 1957 (with additional literature).
- Kaiser, W., and J. Breslin: *J. Appl. Phys.*, vol. 29, no. 9, p. 1292, September, 1958.
24. Kaiser, W., H. L. Frisch, and H. Reiss: *Phys. Rev.*, vol. 112, no. 5, p. 1546, Dec. 1, 1958.
25. Boltaks, B. I.: "Diffusion in Semiconductors," Fizmatgiz (Russian), Moscow, 1961.
- Postnikov, V. V., et al.: *Crystallography, Soviet Physics*, vol. 10, no. 4, pp. 495-496, January-February, 1966.
26. Mataré, H. F.: *Internationale Elektronische Rundschau*, vol. 10, no. 11, p. 293, October, 1957.
27. Rozhanskii, V. N., et al.: *Soviet Physics, Solid State*, vol. 7, no. 4, pp. 937-941, October, 1965.
28. Givargizov, E. I.: *Soviet Physics, Solid State*, vol. 6, no. 6, pp. 1415-1424, December, 1964.
29. Manasevit, H. M., and W. J. Simpson: *J. Appl. Phys.*, vol. 35, p. 1349, 1964.
- Nolder, R. L., D. J. Klein, and D. H. Forbes: *J. Appl. Phys.*, vol. 36, p. 3444, 1965.
- Manasevit, H. M., A. Miller, F. L. Morritz, and R. Nolder: *Transact. AIME*, vol. 233, p. 540, March, 1965.
30. Cullen, G. W., O. E. Gottlieb, C. C. Wang, and K. H. Zaininger: "Semiconductor Silicon," R. Haberecht and E. Kern (eds.), *Electrochemical Society Conference Proceedings*, May 4-9, New York, 1969.
31. Manasevit, H. M., D. H. Forbes, and I. B. Cadoff: *Transact. AIME*, vol. 236, p. 275, March, 1966.
32. Tallman, R. L., T. L. Chu, and J. J. Oberly: *Solid State Electronics*, vol. 9, p. 327, 1966.
33. DeLuca, R. D.: *Semiconductor Silicon*, R. Haberecht and E. Kern (eds.), *Electrochemical Society Conference*, New York, May 4-9, 1969.
34. Williams, F. V.: *Proceed. Internat. Sympos. on Gallium Arsenide*, Reading, England, (paper 5), p. 27, September, 1966.
35. Wrigley, C.: "Semiconductor Silicon," R. Haberecht and E. Kern, (eds.), *Electrochemical Society Conference*, May 4-9, New York, 1969.
36. Single Crystal Silicon Films on Insulating Substrates, *Final Report*, Autonetics Division, NAR to Dept. of Navy Electronic Systems Command, Task 9356, Contract No. 93145, May 1, 1965, to Apr. 30, 1966.
37. *Ibid.*, follow-on program, Nov. 1, 1967, Jan. 31, 1968.
- Hunsperger, R. G. H., O. J. Marsh, and C. A. Mead: *Appl. Phys. Letters*, vol. 13, no. 9, pp. 295-297, Nov. 1, 1968.
38. Yeh, T. H., and M. L. Joshi: *Journal of Electrochem. Soc.*, vol. 116, no. 1, pp. 73-77, January, 1969.

39. Mataré, H. F., and R. W. Laakso: *Appl. Phys. Letters*, vol. 13, no. 6, pp. 216-218, Sept. 15, 1968; *J. Appl. Phys.*, vol. 40, pp. 476-482, February, 1969.
40. Schlötterer, H.: Mechanical and Electrical Properties of Epitaxial Silicon on Spincl, IEEE European Meeting, Semiconductor Device Research, Bad Nauheim, Germany, Apr. 19-22, 1967, and *Solid State Electronics Journal*, 1968.
41. Mataré, H. F., and J. J. Grossman: Transactions of the 3rd International Vacuum Congress, Jun. 28 to Jul. 2, 1965, Stuttgart, Germany; H. Adam (ed.), Pergamon, New York, vol. 2, part II, sessions 5-8, pp. 317-327.
42. Itoh, T., et al.: *J. Appl. Phys.*, vol. 39, no. 11, pp. 5310-5313, October, 1968.
43. Edagawa, H., and Y. Morita: *J. Phys. Soc. Japan*, vol. 18, p. 460, 1963.
44. Grove, A. S., O. Leistico, Jr., and C. T. Sah: *J. Appl. Phys.*, vol. 35, p. 2695, 1964.
45. Fuller, C. S., and F. H. Dolciden: *J. Appl. Phys.*, vol. 29, p. 1264, 1958.
46. Dumin, D. J.: *J. Electrochem. Soc.*, vol. 116, no. 1, pp. 133-137, January, 1969.
47. Thomas, R. N., and M. H. Fracombe: *Appl. Phys. Letters*, vol. 13, no. 8, pp. 270-272, Oct. 15, 1968.
48. Masujian, J.: *Solid State Electronics Journal*, vol. 6, p. 477, 1963.
49. Pfann, W. G.: "Temperature Gradient Zone Melting," *Transact. AIME*, September, 1955; *Journal of Metals*, pp. 961-964; "Zone Melting," Wiley, New York, 1958.
50. Kleinknecht, H. B.: *J. Appl. Phys.*, vol. 37, p. 5, April, 1966.
51. Filby, J. D., and S. Nielsen: *British Journal of Appl. Phys.*, vol. 17, pp. 81-86, 1966.
52. Wolff, G. A., and B. N. Das: *J. Electrochem. Soc.*, vol. 113, no. 3, pp. 299-301, March, 1966.
53. Seidensticker, R. G.: *J. Electrochem. Soc.*, vol. 113, no. 2, pp. 152-156, 1966.
54. Hamaker, R. W., and W. B. White: *J. Appl. Phys.*, vol. 39, no. 3, 1758-1765, February, 1968.
55. Tallman, R. L., T. L. Chu, and J. J. Oberly: *Solid State Electronics Journal*, vol. 9, p. 327, 1966.
56. Braunstein, M.: Moving Mask Growth of Single Crystal Silicon Films on Amorphous Quartz Substrates, *Conference Proceed. Am. Vacuum Soc.*, May 1-3, 1968.
57. Clark, A. H., and R. G. Alibozek: *J. Appl. Phys.*, vol. 39, no. 4, pp. 2156-2157, March, 1968.
58. Mataré, H. F.: *J. Appl. Phys.*, vol. 30, p. 581, 1959.
59. Weimer P.K.: "Thin Film active Devices" in *Handbook of Thin Film Technology* ed. I. Maissel and R. Glang, McGraw Hill, pp. 20.1-20.18, 1970.

## Chapter 15 Dislocations and Channel-Conduction in Amorphous Semiconductors

In a treatise on the electronic properties of defects of the dislocation type, the free or dangling bond plays an important part, as we have seen. The recently much discussed field of amorphous semiconductors and the famous switching phenomenon are in one way or another connected with a change in bonding, and it is, in fact, useful to study some of the aspects of this field in the context of the present material on dislocations and their electronic behavior.

The effect of an abrupt breakdown in resistance of dielectric materials with metallic inclusions or of amorphous semiconductor compounds is a very widely known phenomenon, and many descriptions of such switching phenomena became known when the efforts for publicity of application-oriented groups contracted funds from government agencies and devices were produced that attracted the attention of many workers in the solid-state field.

There is no doubt that the switching phenomenon in disordered structures is an important fact and, if brought to reproducible, reliable, and predictable functioning, can decisively enrich the state of the art in electronics. A specific advantage above ordinary semiconductor thyristors is, for example, the radiation hardness of material with short-range order only. Other aspects are power-handling capability and relative low cost (no purification and mono-crystallization in the usual sense). Without dealing with the controversial history of the switch itself, our attention is focussed on the questions:

1. Long-range versus short-range order
2. Electronic versus ionic and thermal processes
3. Reproducibility and possible applications

Most known semiconductor devices used for basic circuit functions, such as rectification, amplification, generation of frequencies, switching, are based on

the fact that electronic changes in one part of the device are transferred with minimum loss and delay to other parts of the device and that electrodes can be built into the device at macroscopic distances. "Macroscopic" is meant here with respect to the lattice parameter, that is, over distances involving thousands of lattice constants (which still allows microminiaturization in the usual sense or  $\mu$  dimensions:  $1\mu = 2,000$  lattice parameters). A fundamental notion for the solid-state physicist and semiconductor engineer is the Bloch wave function describing the properties of quasi-free electrons in a crystal and allowing charge-transfer velocities of only one or two orders of magnitude below the speed of light if the crystal is an ordered structure.

In the solution of the Schroedinger equation

$$\psi(\mathbf{r}) = Ae^{i\mathbf{k}\cdot\mathbf{r}}, \quad (15.1)$$

where  $\psi(\mathbf{r})$  = localized wave function,

$$\mathbf{k} = \frac{2\pi}{\lambda} \text{ (wave vector),}$$

$$\lambda = \text{DeBroglie wavelength,}$$

for the periodic structure  $A$  is replaced by the lattice-modulated amplitude  $A(\mathbf{r})$ , which is dependent on the atomic configuration.

The solution for the three-dimensional case is essentially a Fourier sum and may be written

$$\psi(\mathbf{r}) = \sum A_{m_1 m_2 m_3} e^{2\pi i[m_1(b_1 r) + m_2(b_2 r) + m_3(b_3 r)]} \times e^{i[2\pi \nu t - (\mathbf{k} \cdot \mathbf{r})]}, \quad (15.2)$$

where  $b_1, b_2, b_3$  = basic vectors of reciprocal lattice,

$$m_1, m_2, m_3 = \text{integers,}$$

$$\nu = \text{frequency.}$$

As discussed in Section 2.2, periodicity deviations lead to nonharmonic terms in  $\psi(\mathbf{r})$  and affect the propagation velocity of the wave.

As we know from the energy balance

$$\Delta E = \frac{1}{2}mv^2, \quad (15.3)$$

the chemical potential  $\zeta = E_F - E_c$  or the energy difference between Fermi level and conduction band can be equated to the kinetic electron energy (see also Chapter 2). In this case,  $m$  is equivalent to the effective mass and  $v$  is the thermal velocity.

For high carrier densities,  $n \gg N_c$  ( $N_c$  = effective density of states in the conduction band),  $\zeta$  can be represented by

$$\zeta = \frac{1}{2} \left( \frac{3}{8\pi} \right)^{2/3} \frac{h^2}{m_{e\pi}} n^{2/3}, \quad (15.4)$$

where  $n$  = electron concentration,

$h$  = Planck's constant,

and therefore

$$v = 7.7 \cdot 10^7 \left( \frac{m}{m_{\text{eff}}} \right) \left[ \frac{n}{10^{22} \text{ cm}^{-3}} \right]^{1/3}. \quad (15.5)$$

For high doping  $n$  and small effective-mass values, the velocity can be a factor of 1/10 to 1/100 near the velocity of light, an important fact for the operation of devices. In the case of energy transfer from optical photons, one may also express

$$\Delta E = \hbar \omega. \quad (15.6)$$

An additional condition for the energy transfer is the momentum equation

$$\hbar |\Delta k| = \hbar \frac{\omega}{c} \quad (15.7)$$

Applying these two equations to the velocity expression by the field gradient in the wave vector plane

$$v = \frac{1}{\hbar} \text{grad}_{(k)} E(k) \quad (15.8)$$

leads to

$$v = \frac{\Delta E}{\hbar |\Delta k|} = c. \quad (15.9)$$

For such a process, the electron, however, is transferred into a higher-energy band with unchanged wavenumber, but it is significant that such transitions occur with light speed.

In amorphous structures, this long-range order is inexistent. The crystal momentum

$$P_x = \pm \hbar k = \pm \frac{h}{\lambda} \quad (15.10)$$

is not a quantum number throughout, but around a chosen atom the distribution of other atoms shows the typical densities known from ordered crystals (to distances of a few angstroms, for example, in germanium to 7 Å); further out densities are smeared out. This is also the reason for broadened optical reflectivity and smeared-out conduction and valence band edges.

We owe to N. F. Mott penetrating work on disordered (amorphous) structures (see especially Ref. 1 and 19 with literature) that has helped much in understanding some of the implications in this difficult field. In many respects, understanding was gained by a study of liquid metals and semiconductors of crystals with compensating impurities (temperature activated hopping) and of



degenerately doped crystals when the electrons behave like an electron gas (finite value of  $\sigma$  at zero°K temperature).

In fact, the model for the density of states,  $N(E)$  versus  $E$ , for a liquid semiconductor (Figure 15.1a) is very similar to the model found for amorphous germanium derived from measurements of the temperature dependence of resistance, thermoelectric power, and reflectivity, (see Figure 15.1b).<sup>2</sup> A

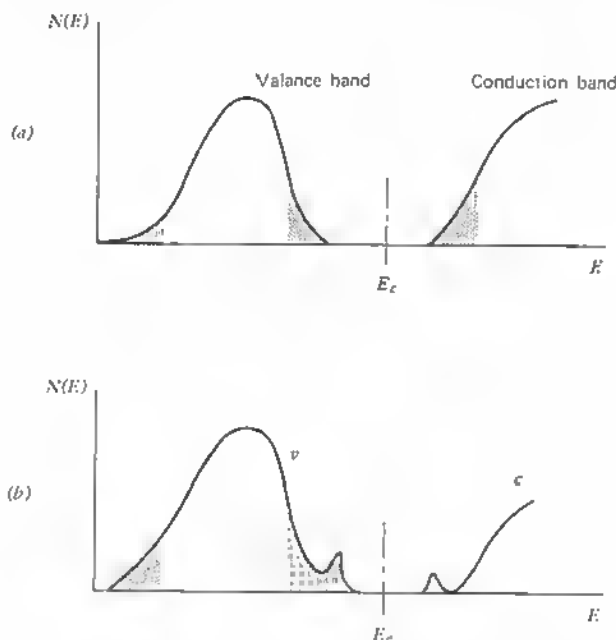


Fig. 15.1 Density of states of a three-dimensional lattice: (a) for a liquid semiconductor (Mott); (b) for amorphous germanium (Tauc).

recurring suggestion in regard to the transport properties of amorphous structures is that localized states exist in the region of forbidden energy.

This means that the Schrödinger equation

$$\frac{d^2\psi}{dx^2} + \frac{2m}{\hbar^2} (E - \bar{V})\psi = 0 \quad (15.11)$$

where  $\bar{V}$  = disordered crystal potential

has for each solution  $\psi_n$  a characteristic energy value  $E_n$  and that their number increases as  $l$  increases (spacing  $1/l$ ), where  $l$  is the length of the atomic chain considered. In Figure 15.1, such localized states would be found in the shaded regions of the density curves. There are defined energy levels  $E$  that separate

localized from nonlocalized states. For liquid or amorphous material  $N(E)$  is found from

$$N(E) = \frac{4\pi k^2}{8\pi^3} \frac{dE}{dk}, \quad (15.12)$$

where  $k$  = wave vector, when  $E$  is derived from second-order perturbation theory for wave functions of the type  $u(v) \exp(ikr)$  and adapted to the amorphous case by a replacement of the scattering matrix by a volume integral, including the Fourier transform of the pair distribution function.<sup>1</sup>

The model for the state density in the case of strong interaction with the lattice (see Figure 15.1) allows some predictions with respect to carrier transport. If the Fermi energy lies in the nonshaded regions of  $E$ , the material is a metal, and the resistivity tends to a finite value as  $T \rightarrow 0$ . Ordinary transport theory is applicable as long as the mean free path  $L$  is large, compared with the electron wavelength  $\lambda$ . If the Fermi energy for low temperatures lies in the shaded regions, the material is a semiconductor or insulator. In this case, current is then carried either by excitation into the unshaded region or by hopping from one localized state to another. Gubanov<sup>3</sup> has pointed out that this model predicts a lesser sensitivity to doping of amorphous semiconductors, compared with crystalline structures.

When the self-consistent potential as a periodic function of the cartesian coordinates  $x_1, x_2, x_3$  has to be replaced by a system of new (deformed) coordinates  $\xi_1, \xi_2, \xi_3$ , the basic form of the Bloch wave function is maintained; however, its characteristic lattice modulated amplitude  $A(x)$  is a quasi-periodic function of the deformed coordinates;

$$U_k(\xi_1, \xi_2, \xi_3)$$

and

$$\sum_{\alpha=1}^3 x_{\alpha} \xi_{\alpha} \neq kr \quad (15.13)$$

(see Ref. 3, pp. 131ff).

It is obvious that, on account of this missing long-range order, doping affects the transport properties at a lesser degree than in monocrystals.<sup>3</sup> It is important to define here that this lesser sensitivity to doping changes and, of course, also defects, originating, for example, from nuclear radiation, does not mean higher stability of a particularly important parameter. One may not bring about measurable changes of the conductivity of an amorphous structure with the usual amounts of dopants, as in the case of crystalline semiconductors, but this may mean that transport properties are undefined to a similar extent so that a conduction process may have a random character built in of a magnitude that is equal to the doping latitude. This would not represent a net gain. Only very uncritical applications would allow the use of devices based on this material (see further below).

Mott considers in detail the conductivity by hopping but does not outrule the influence of barriers within the material and thus tunneling effects. In particular the abnormal properties of selenium (dependence of  $\rho_B$  on the electric field) have been explained by B. Gudden and W. Schottky,<sup>4</sup> who already, as early as 1935, postulated localized states and electronic transport across such "barriers" by tunneling.\* Cold work increases the height and number of such barriers within the structure, especially in selenium, and decreases the mobility further. The barriers formed are, in fact, of the grain-boundary type and represent Schottky barriers only in the sense that the dangling-bond-acceptor density is so high that this  $p^+$ -type side of the barrier can be considered degenerate (see Section 11.2). Mott's assumption that such barriers do not affect the minority carrier has to be corrected, as we know from lifetime measurements on bicrystals (see Section 11.5). We also know that Hall data are dependent on the direction of carrier flow within the space-charge pipe around the barrier-forming dangling bonds.

As we have seen, the important charge carrier transport magnitudes, such as mobility, diffusion length, lifetime of minority carriers, are very small and more or less undefined, and such material, therefore, is useless for the construction of semiconductor devices in the usual sense. However, one aspect must be considered that has given results during the last years with amorphous materials in electronic devices: In situations, for example, where no carrier transport through ordered lattice structures is needed but where only localized energy transitions are of the essence, one does not need macroscopic order. A device of this kind is, for example, a glass laser. The doping with rare earth elements, for instance, neodymium, means locally the same as the doping of a ruby monocrystal. The microscopic order in the glass rod allows the building in of the paramagnetic impurities and the establishment of the energy bands with their different relaxation times. The pumping with light that takes place over the entire glass rod fills the higher-energy bands of the paramagnetic impurity in the field of the glass atoms, and selective transitions are possible within the Farby-Perot cavity. In this process, no macroscopic order is necessary, but only microscopic or local energy transitions. No charge carriers are moving, and the sum of all localized transition processes adds up to the total energy of the emitted light beam. Here we have a typical case of usefulness of microscopic order only. Other examples for limited requirements with respect to macroscopic order can be found in a number of applications of glasses as dielectricum in condensers, in microelectronics at the place of the gate isolation in MOS transistors, in infrared optics, and the like.

The use of  $\text{SiO}_2$  in the field electrode of MOS transistors has caused difficulties, since this glass easily absorbs foreign ions that can move under field

\* Private communication by W. Schottky.

influence. For instance, sodium ions can easily move within the glass if outside fields are applied, and, therefore, a change in conductivity and dielectric constant cause a change in impedance and capacity values. From the beginning of the application of oxidic glasses in semiconductor technology, it was obvious that one had to deal with a complicated case of field-dependent ionic conduction. For example, the fact that a tunnel current could be drawn through a metal-metal-oxide-metal sandwich has been published as a principle for transistor synthesis.\* The then existing Al-Al<sub>2</sub>O<sub>3</sub>-Al tunnel emitters enabled something like transistor action if a collector electrode was used in conjunction with this emitter. But, the Al<sub>2</sub>O<sub>3</sub> did not allow for reproducible devices. The tunnel current did not follow the expected current-voltage characteristics, and, in addition, irreversible changes were noticed. As in the case of capacitors, the applied voltage changes the capacity value, increasing with increased voltage and decreasing again for decreasing voltage; also the tunnel current shows corresponding irreversible changes. These results have moved into the background all work on thin oxide layers for tunnel transistor devices. In the meantime, the problem of the gate isolation in MOS technology has found some solution so that stable gate capacity values can be produced (application of very pure SiO<sub>2</sub>, elimination of earth alkali ions, and the use of Si<sub>3</sub>N<sub>4</sub>). We see that the problems of the insulator become difficult to solve when variable fields are applied. This is especially the case when two orthogonal fields are present in the insulator, as is generally the case in field-effect transistors. Solving the problem of the pure insulator seems, however, easier than the defined doping of an electronically active glass semiconductor with exactly reproducible properties if brought into electric fields. As the doping by a small number of earth alkali ions (about  $10^{12}$  cm<sup>-2</sup> are sufficient) already produces nonreversible capacity-voltage characteristics, the behavior of glass in a current-variable switching device must be especially sensitive to impurities if reliable and reproducible current-voltage characteristics are desired.

A. D. Pearson and collaborators<sup>5</sup> indicated in 1962 that a nonoxidic glass, As-Te-I, can be used in a switching device. The characteristics of such a device are given in Figure 15.2. When initially the voltage across the layer is increased, high resistance is measured (branch 1) up to a voltage point  $V_s$ . Here the increased field causes a drastic change within the glass (2) and switches the material into the high conducting state (in less than  $1 \mu$  sec) to branch (3). Upon regression to the voltage zero point, the process is repeated in a mirror-like shape. If, however, the current at some point on branch (3) is increased, its value drops back to the high resistance branch (1). The material maintains its initial state on under critical voltage swing and, therefore, displays memory. Aside from a number of other possible applications of glasses that will be

\* Originally proposed by C. A. Mead; J. Appl. Phys., Vol. 32, No. 4 pp. 646-652, April 1961.

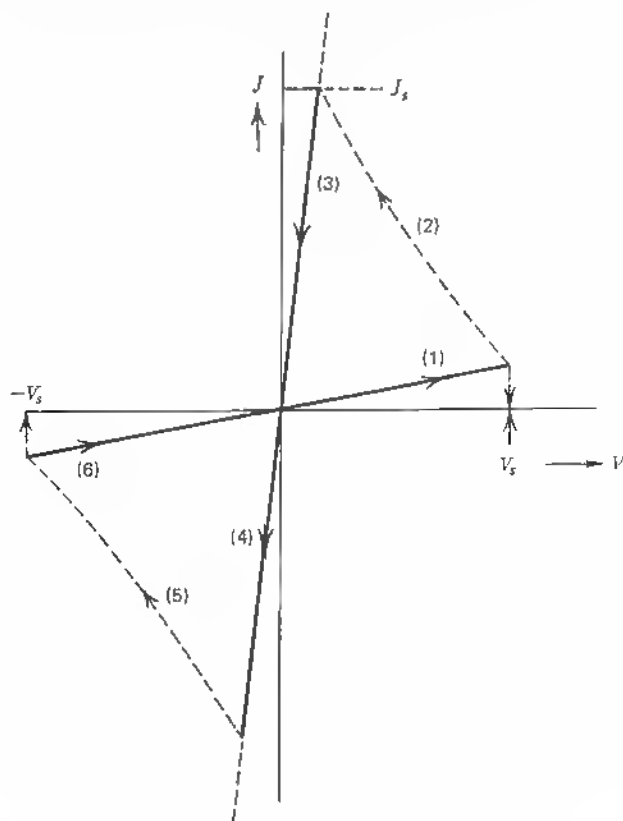


Fig. 15.2  $I$ - $V$  characteristics of glass switch.

mentioned shortly, this effect has attracted much attention, especially since 1963, when S. R. Ovshinsky applied for a patent<sup>6</sup> based on this effect, in which he protected a number of device applications for semiconducting glasses. Some of the patented configurations are shown in Figure 15.3.  $M$  designates the metal electrodes that may be arranged concentrically or laterally (Figure 15.3 (a) and (b)).

One can also generate the active layer at the surface of the glass only and use the remainder of the glass layer as a conductor. This leads to arrangements as shown in Figure 15.3c to f. The layers 2 and 3 respectively are each especially doped to show the switching effect. In (d) through (f) we also assume that one or two additional electrodes influence the active layer in order to bring about a voltage-dependent avalanche. In this case, one may change the necessary saturation voltage by the additional voltage on the side electrodes

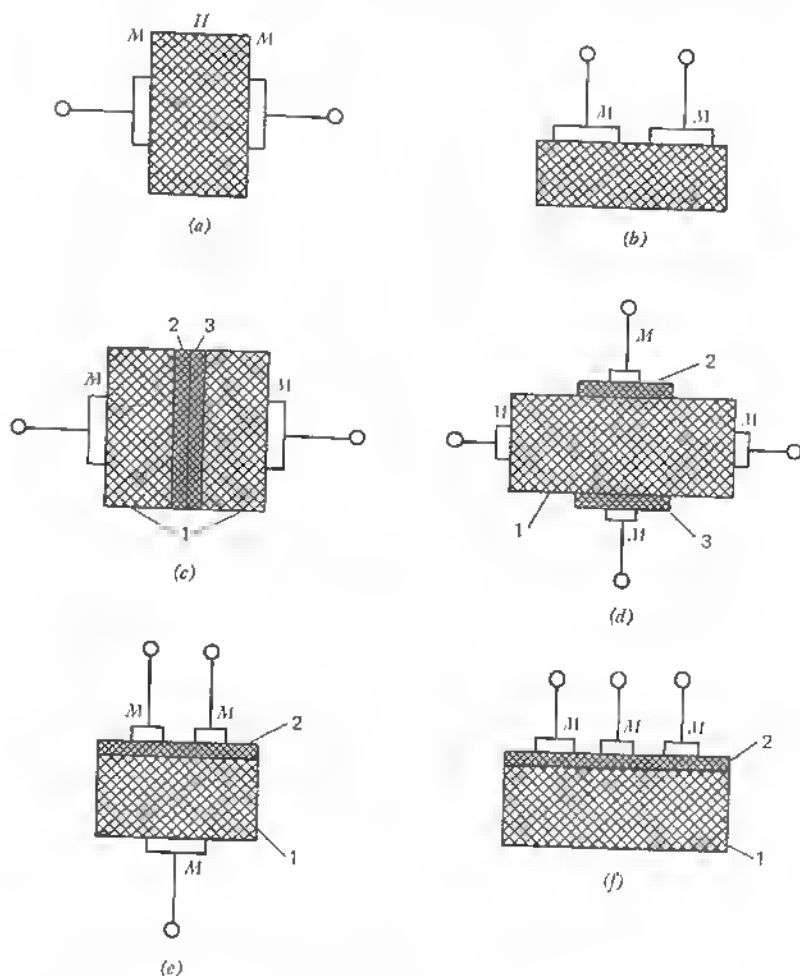


Fig. 15.3 Several different forms of semiconductor glass switches, some with active layers (2, 3) different from conducting layer (1).

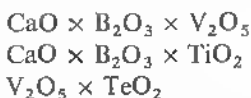
and also change the slope of the current voltage characteristics ((branch 2) in Figure 15.2) by changing the load resistance.

There is no doubt that switching devices are of importance especially if resistance values can be changed for a factor of  $10^8$  and with small time constants.<sup>7</sup> Ovshinsky has indicated quite a number of device applications and even talks about a new microelectronics in the watt dissipation range.<sup>8</sup> We must remind the reader here, however, of the fact that the transition from a

laboratory device to industrial production can be a major hurdle. If materials properties for producing a laboratory effect are not clear, production methods are still vague and, therefore, reproducibility, planning of device characteristics, and reliability constitute a great problem. Although it is stated that all material combinations are workable in the form of tellurides, selenides, sulfides, and oxides, mention is also made of stoichiometric combinations of Te, Ge,  $V_2O_5$ , or Te + GaSb (50/60), or Te (47%) + Ge (47%) + GaAs (5%) + Fe (1%), or Te (50%) + Ni (50%); Te (50%) + Si (50%); Te (50%) + InSb (50%). Other combinations are layers like the following: TeO- $Al_2Te_3$ -TeO. In addition, it is indicated that two pieces of iron wire superficially oxidized and brought into contact would result in a switch. The same is indicated for copper and aluminum wire and the combinations:

Te (90%) Ge (5%) Si (5%)  
 Te (50%) Ge (50%) + Cs (diffusion-doped)  
 Te (50%) Ge (50%) coated with 71.87% Te  
 14.05% As, 13.06% Ga, and 1% PbS

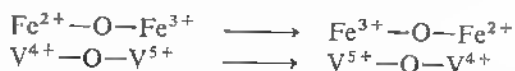
when brought between metallic contacts. Other percentage combinations of arsenic, tellurium, germanium, gallium, indium-antimonide, silicon are possible. The combination of 40 atomic % Te, 30 at % As, 12 at % Si, and 10% Ge is frequently used.<sup>7</sup> Here we face the question of a guiding principle, since the multitude of combinations points to a general scheme, but on the other hand, reproducible electronic properties can only be expected if the reasons for the switching property are better known. Mackenzie<sup>9</sup> recently has written a survey of the field of semiconductor glasses, emphasizing the special importance of oxide glasses as dielectrics. High dielectric constants yield high-capacity values for application in microelectronics. Certain combinations like



have high Seebeck coefficients and are thermoelectrically applicable. On the other hand, nonoxidic glasses like  $As_2S_3$  are very useful for infrared applications. As-S-Se is a low temperature-melting insulator; As-Te-I, already mentioned, is applicable for switches. As-Se-Te is a photoconductor, and As-Ge-Si-Te is a material transparent to infrared but resistant to higher temperatures.

New glasses with semiconductor properties are constantly being found, and a more recent one is the bismuth-selenium combination (Se + 3 to 30%Bi).<sup>10</sup> These glass types are obviously all of a similar nature at least with respect to their electronic properties when brought into electric fields. In oxide glasses

as well as nonoxidic glasses the charge carrier mobilities are very low, below 1 cm/sec/V/cm. Therefore, the mentioned microscopic transport phenomena we know from ordered crystal structures cannot be responsible for a charge exchange taking place in less than a microsecond across measurable distances of 1,000 to 100,000 lattice constants. Mackenzie describes charge transfer within the oxide chain in the following manner:



The moving charge in the microscopic-order range leads to a changed polarization of the oxide chains, which, in turn, cause a charge transfer in the neighboring chain, and so on. The oxides, sulfides, and halides of the transition metals like vanadium, titanium, chromium, and manganese have been discussed earlier with respect to their electronic conduction properties, since they show insulator as well as metal character. F. J. Morin<sup>11</sup> has looked into the correlation between electrical conduction and wave function overlap for the  $d-p$  electrons in the hydrogenic approximation of these materials. It can be shown that a compound changes from insulator to metallic character for increased value of the overlap integral. It is natural, therefore, that semiconductor properties can also be assumed. However, it is not so much the semiconductor property that is realized in a switching application, but more an insulator breakdown, since the mobilities in all these materials are very small (Morin indicates values below  $10^{-2}$  cm/sec/V/cm). To understand this behavior we can go back to the above-mentioned possibility of a hopping charge transfer. It is known, for instance, from research done on diamond that a wide range for the specific resistivity can be measured from undoped pure diamond, with values in excess of  $10^{14}$  ohm cm, down to values of  $10^{-2}$  ohm cm for heavily doped diamond.

Wilson<sup>12</sup> shows that activation energies measured on differently doped diamond crystals are best explained by a hopping process in which electronic exchange between impurity centers occurs. This model of Mott's<sup>1</sup> can be used in modified form for the explanation of the effects in glasses under assumption of the charge exchange principle in the microscopic ordered state or within the individual chains. In all cases the externally applied electric field seems to induce an "alignment" of originally, statistically distributed metal oxide chains. As shown in Figure 15.4a, the compound chain  $\text{V}^{4+}-\text{O}-\text{V}^{5+}$  may originally be in a statistical distribution. In the field (Figure 15.4b) the sequence of the chain arrangement is influenced so that the electron flow within the individual chains can proceed in the direction of the field. On change or polarization the oxidic chains must be reversed in their order to bring about the necessary charge distribution before the critical voltage point  $-V_s$  (see Figure 15.2) is reached, at which point the system enters into the highly



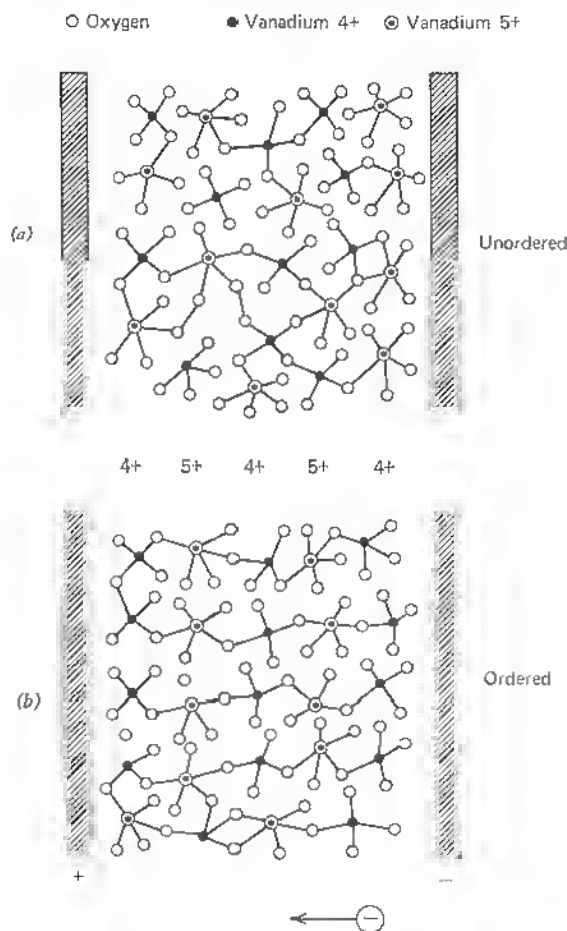


**Fig. 15.4** Proposed scheme of charge transfer through glass due to field ordering.\*

conducting state ( $-I$ ). If, additionally, ions are present in the glass, they can contribute to the current. This contribution, however, is not a desired one and would constitute a loss current as expressed by the slope of lines 1 and 6 in Figure 15.2. Foreign atoms of stronger lattice binding—for instance, calcium—may, however, block mobile ions and, therefore, essentially help give predominance to a directed charge exchange.

\* See also: H. F. Mataré, Semiconductor glasses; Solid State Technology pp. 43-46, Jan. 1969.

As glass switches are produced where  $\text{SiO}_2$  matrices doped with metal combinations are specifically active and show improved reproducibility, the number of conferences and publications has increased remarkably during the last years. It seems that the hopping theory as well as the field ordering may have to be invoked in order to explain the results. Mott feels that the activation energy for hopping is likely to be mainly that for polaron formation in the ion atmosphere of the glass and that impurity band conduction may not be involved in cases like vanadium oxide ( $\text{V}_2\text{O}_5$ ).

In more recent work, a number of facts have been elaborated that leave room for different theories. The nonoxidic glass combinations of the chalcogenide type have found predominant interest in the Joffe Institute in Leningrad for many years. B. Kolomijets<sup>13</sup> emphasizes the electronic and not ionic conduction mechanism in such materials as:

As-S	Ge-S	S-Se	} two-component systems
As-Se	Ge-Se	Se-Te	

and

Cu-As-Se	Zn-As-Se	In-As-Se	} three- component systems
Cu-As-S	Zn-As-S	In-As-S	
Cu-As-Se	Cd-As-Se	Ga-As-Se	
Au-As-S	Cd-As-S	Ga-As-S	
Au-As-Se	Hg-As-Se	Tl-As-Se	
Au-Ss-S	Hg-As-S	Tl-As-S	
Ge-As-Se	<i>Si-Se-Sb</i>	<i>P-As-Se</i>	
Ge-As-S	Si-S-Sb	As-Sb-S	
Ge-Sb-S	Ge-Se-Sb	<i>As-Sb-Se</i>	
<i>Ge-As-Te</i>	<i>Si-Te-As</i>	As-S-Te	
<i>Ga-P-Te</i>	Ge-Se-P	As-Se-Bi	
Ge-Se-Te	Ge-S-P		
<i>Si-P-Te</i>	As-S-J		
S-Se-Te	As-S-Br		
	As-S-Cl		

In the italicized cases stabler compounds are feasible and in the case of SiO a coevaporation of either Te or Se with Sb and As should reveal low switching threshold voltages.

The mixed materials in which oxidic and nonoxidic glasses combine have also been studied by the Leningrad school. Figure 15.5 shows a few combinations where the shaded regions within the stoichiometric triangle are stabler ratios.

From the point of view of device potential, the switching phenomenon and the memory effect deserve attention, and their understanding may lead to the

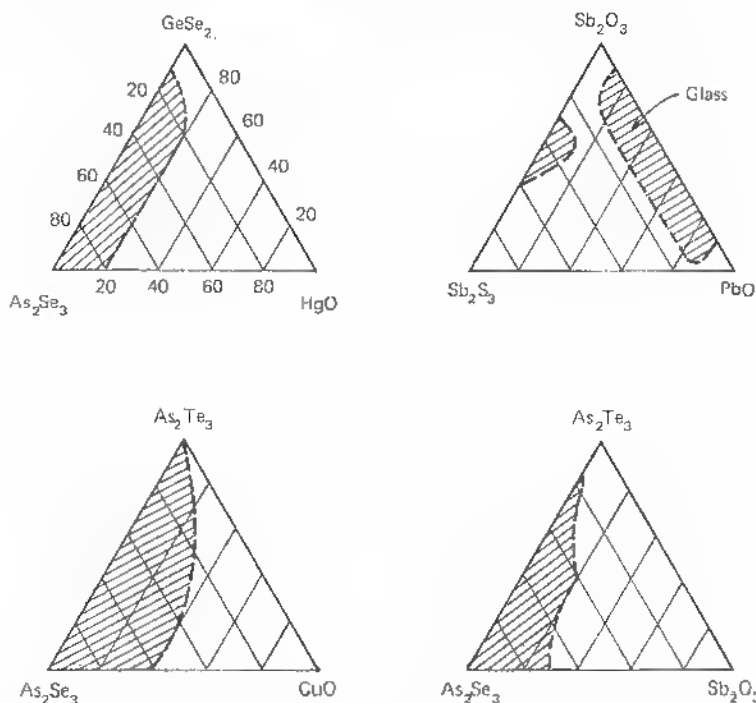


Fig. 15.5 Stoichiometric ratios of chalcogenide and oxidic glasses. Shaded areas are stable compounds, (Kolomijets)

ultimate clarification of the process involved in amorphous conduction. The channel phenomenon has been studied in more detail recently. A. D. Pearson et. al.<sup>14</sup> described how a small channel or filament of about 1 to 10  $\mu$  in diameter grows into the glass of the  $\text{As}_2\text{Se}_3\text{Te}_2$  type. Microphotos show clearly that the breakdown cycles cause darkened areas in which a high-conductance channel has formed. These switches were made by evaporation of small glass disks and evaporation of contacts to them. It was even observed that on reaching the high-current mode (5,000  $\text{A cm}^{-2}$ ), a liquid phase of the material around the central dark channel is in a pivoting movement because of heat circulation. S. Ovshinsky would call the heat generated channel and its electrical effects an "artefact,"<sup>15</sup> because only an electronic change can give a reliable, reproducible device. This is basically true, but if one states "where no structural changes occur, the process is an electronic one," the situation is oversimplified. In effect, electronic processes can also cause structural changes. H. J. Stocker<sup>16</sup> has clearly demonstrated how a  $\text{Ge}_{12}\text{As}_{19}\text{Te}_{69}$  glass and 30 different compositions of the form  $\text{Si}_a\text{Ge}_b\text{As}_c\text{Te}_d$  ( $a + b + c + d = 100$  per

cent) form molten channels when subjected to critical fields while operating as a switch

He shows an important aspect of this channel, namely, that the active region is surrounded by a potential well. The entire voltage drop across a sample, with a channel running orthogonal to the applied voltage, is across the small region in which the switching occurs. In other words, the high-conductivity path is surrounded by a region of higher resistance than the bulk. This reminds us of the preferred conduction in a grain boundary or a dislocation array where the row of overlapping bonds has caused a space charge to be set up with respect to the bulk, the space-charge cylinder. This similarity is discussed in more detail further on. The central question is: Are there channels other than those formed by thermally induced phase transitions? If so, can the memory effect (lasting changes) be clearly separated from the switching phenomenon? C. N. Berglund<sup>17</sup> shows the existence of thermal filaments in thin  $\text{VO}_2$  films and develops a theory for the spatial variation of its temperature, its current-voltage behavior, and its lateral motion under static electric bias.

Clear indication of "burnt-in" spots or filaments is also found by T. W. Hickmott.<sup>18</sup> Here electroluminescence and switching in  $\text{Nb-Nb}_2\text{O}_5\text{-Au}$  diodes are correlated.

As it stands after the latest summary reports and meetings on amorphous semiconductors (see *Physics Today*, August 1969 and October 1969), it is at the time of this writing still a puzzling fact that an induced channel can be formed with such rapidity ( $\sim 10^{-10}$  sec) and can form a current path for such densities as 5,000 to 100,000 A/cm<sup>2</sup>. It is perhaps less astonishing that a channel once formed can have a lasting effect (memory) until it is "burnt."

That, for example, the amorphous mixture of 55 per cent As, 35 per cent Te and 10 per cent Ge changed to a germanium-free  $\text{As}_2\text{Te}_3$  channel structure after application of  $V_c$ , points to an interesting fact. A V-VI compound like  $\text{As}_2\text{Te}_3$  would scarcely form a material of high conductance if it were not for the fact that not all tellurium bonds are saturated and that the chain of As-Te atoms presents a semioordered structure, establishing a quasi-long-range order within the amorphous matrix. This quasi-long-range order is understood in the sense postulated earlier that a bond rotation accounts for a sufficient number of free bonds to form a channel. Such bonds would have an arrangement as is known from silicon grain boundaries, which have either a strong barrier (free bond case) or are almost imperceptible electrically (saturated twin case). J. Kohn<sup>19</sup> has already associated broken-bond adjustment and twinned interfaces for different crystal orientations. In Figure 4.11, we have shown the case of the  $\{2\bar{2}1\} - \{\bar{2}21\}$  second-order joint in silicon. A rotation for  $38^\circ 57'$  of individual  $A$  about the normal to the figure,  $[110]$ , results in a twin boundary (zigzag line). A back rotation for  $38^\circ 57'$  liberates bonds  $d$  and

eventually also opens the bonds at  $b$ . Such rotations can be in the energy range well below 1 eV, and therefore a field of  $10^5$  V/cm is sufficient to effect such changes.

Once the free bonds are established, we have the high-conductance situation known from grain boundaries, especially in III-V compounds (see Figure 11.16).

Mott has recently discussed the switching phenomenon from the point of view of the density gap model (see Figure 15.1). Under the assumption that Schottky barriers form at the metal-contact-glass interfaces when the high-current state is set up, a high-field region at the contacts is postulated. It is furthermore postulated that the barrier is thin and that electrons and holes can tunnel through the barriers.

It is somewhat strange to postulate "high-fields" at the electrodes in the low-field-high-current mode for the filament.

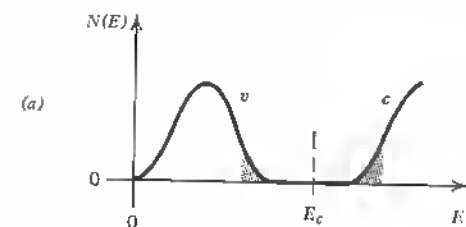
If we assume, however, that the high-current mode is initiated by bond rotation (bonds are set free), the pseudogap in the state density for a particular energy is filled by overlapping wave functions of the broken bonds, and grain-boundary conduction of the degenerate type sets in.

It is of minor importance if such bond rotation is induced by field influence at the contact area or within the molecular gaps. It is concluded, however, from experiments that the channel within the glass structure forms first on the positive electrode and grows from here out to the cathode. Mott invokes slightly overlapping wave functions, as is known from strongly doped and compensated semiconductors.

Thus Figure 15.6a would lead to Figure 15.6b as the state density near energy  $E_c$  increases. It is quite probable that the electrodes to the glass form Schottky barriers, especially as the critical voltage is reached and the number of trapped electrons near the positive metal contact (Figure 15.6c) increases until a channel is formed. It is thought, however, that the bond rotation and the creation of the dangling bonds facilitate the carrier motion from the contact area into the amorphous structure so that under the combined influence of external field and the increase in  $N(E)$ , a highly conducting channel forms.

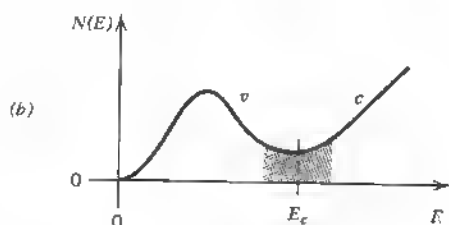
It is most revealing for an exact theory to study the conductance of once-formed channels at liquid helium temperatures. As is known from earlier work on grain boundaries (see Chapter 11), these channels are so degenerate that the specific resistivity does not change at low temperatures. The occurrence of the switching effect in  $\text{Nb}_2\text{O}_5$  combined with an Esaki diode kind of inflection for low-work-function metal contacts points to a tunnel effect at the metal-glass barrier.<sup>18</sup>

We believe, however, that once the channel is formed, a quasi-long-range order through bond overlap is established. This model has great similarity to

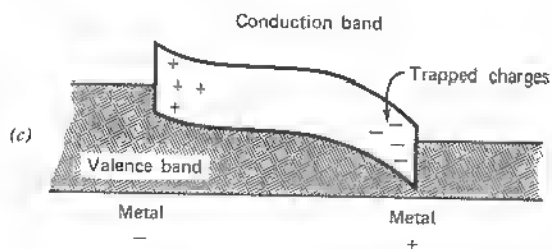


(a) for a liquid semiconductor with weak interaction.

The curved lines show the potential energy of an electron as it moves from the top of the valence band to the bottom of the conduction band under the influence of the field produced by trapped charges.



(b) for a liquid semiconductor with strong interaction (e.g., Tellurium).



(c) suggested band structure for a switch in its low impedance state (MOTT).

Fig. 15.6 State density versus energy

the grain-boundary model. The characteristics of an  $n-p^+-n$  structure where the grain boundary establishes the  $p$  layer also shows a switching behavior (see Figure 15.7). This was found by Hamakawa et al.<sup>20</sup> and had been measured earlier by Taylor et al.<sup>21</sup> The breakdown through the space-charge cylinder is similar to the glass breakdown.

Stocker's model of the low-resistance path surrounded by higher-resistivity material is quite similar to the model for a grain boundary, as described in detail in Chapter 11.

Here we have a well-studied analogon to the channel conduction that allows us somehow to reconcile Mott's suggested conduction in glasses and the structure of a grain boundary that is based on the overlapping wave functions of the broken bonds.

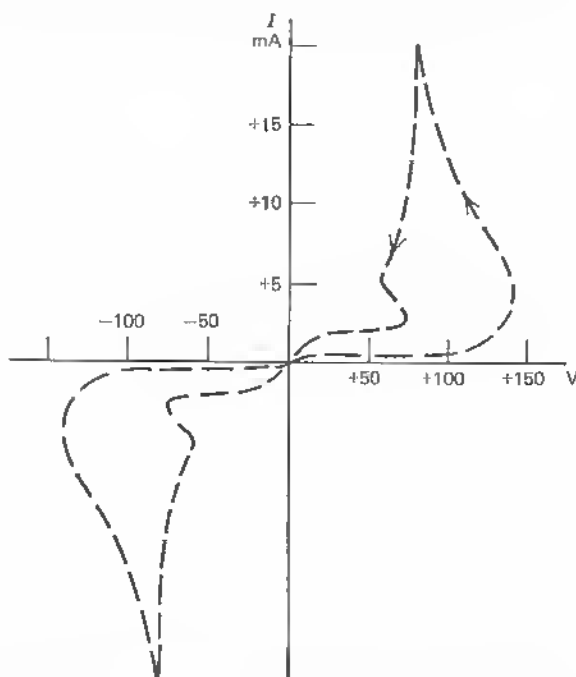


Fig. 15.7 Grain boundary characteristics; saturation range and punch-through!<sup>20</sup> Lower scale refers to saturation range, upper scale to breakdown.

At this point, the question arises how a channel a few microns long and about  $50\ \mu$  in diameter can support the currents in question. Not in all cases have current densities reached values so high as  $10^5\ \text{A cm}^{-2}$ . Ovshinsky claims  $10^3\ \text{A cm}^{-2}$  at one point. But even such densities are difficult to support by ordinary materials without strong heating effects. A major effect that can explain high current densities is the dangling-bond wave-function overlap and the near-zero activation energy or complete degeneracy. As we have seen, the degenerate conduction is especially pronounced in III-V compounds, like InSb.

If the conducting channel is formed by metal oxides in which bonds are rotated or set free because of a critical field so that carriers can move in a degenerate path along the line of broken bonds, but within a space-charge layer, the critical filament thickness is actually 100 times greater than the thickness of the path of broken bonds (see grain-boundary model).

This theory may be tested by the field effect. A field applied perpendicularly

to the current path should result in changes of the current through the filament (see Section 11.6).

The field influence establishes the actual channel width and its blocking layer toward the bulk. This structure also forms a three-terminal device.

Measurements of the resistivity variation with temperature and the change in dielectric constant (capacity) of  $\text{Te}_{48}\text{As}_{30}\text{Si}_{12}\text{Ge}_{10}$  compounds have been carried out that show that in the near-room-temperature range strong phase changes take place as they are known to exist in  $\text{BaTiO}_3$  or  $\text{KH}_2\text{PO}_4$  (see Figure 15.8). This points to an easy molecular reorientation of this compound. Other switching materials, like  $\text{SiO}_2$  with metal additions, seem to be much less sensitive in this respect and promise to be less prone to thermal decomposition.

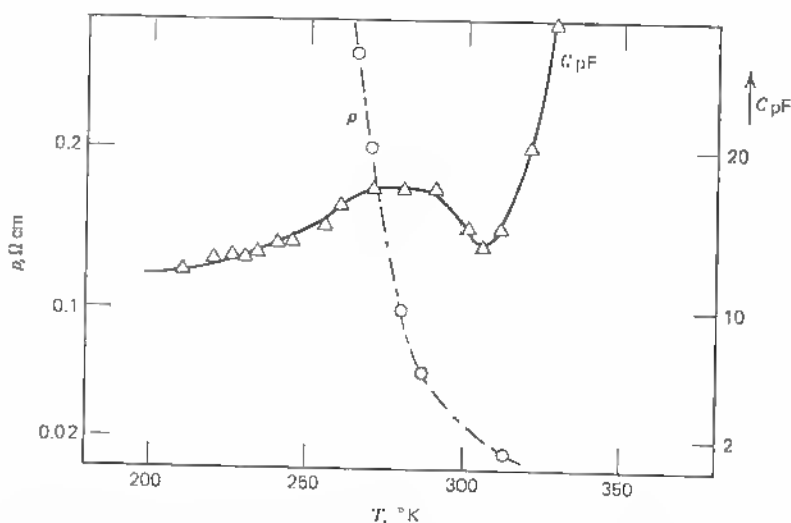


Fig. 15.8 Result of measurements of resistivity and capacity versus temperature for the  $\text{Te}_{48}\text{As}_{30}\text{Si}_{12}\text{Ge}_{10}$ -glass.\*

Important findings with respect to the capacity variation at switching and with respect to the influence of the frequency of the signal voltage have been published recently. R. Vogel has shown<sup>22</sup> that negative capacity values are combined with the switching phenomenon. An original capacity of, for example, 2 pF, before channel formation, decreases rapidly at the threshold voltage and is turning into  $-3$  to  $-4$  pF after breakdown.

\* See H. F. Malaré: Zur Frage der Glassehalter, Internat. Elektr. Rundschau, Vol. 24 No. 7, pp. 171-176, Berlin 1970.



The conclusion of Vogel that no inductive behavior is involved is due to the fact that he measured the variation of the impedance between 15 MHz and 100 kHz only. It is correct that according to

$$C = \frac{1}{L\omega^2}$$

the capacity should vary with frequency. However, this is an appreciable effect only in the range of the resonance frequency  $\omega$ .

The capacity lies in the range measured by Vogel according to estimates based on switching path thickness  $\sim 1.2 \mu$  and nominal circular area:  $3 \cdot 10^{-5} \text{ cm}^2$ :

$$C = \frac{\epsilon F}{4\pi d} = 0.3 \text{ to } 0.5 \text{ pF,}$$

depending on the value of the dielectric constant, here assumed equal to 16. When a channel of high conductivity forms, the current density increases enormously and the current path represents an inductive impedance of the value

$$L = \frac{0.4\pi^2 \cdot r^2}{l} \cdot 10^{-8} \text{ henry.}$$

For our values of

$$\begin{aligned} r^2 &= 10^{-5} \text{ cm}^2, \\ l &= 1.2 \cdot 10^{-4} \text{ cm,} \end{aligned}$$

we have then

$$L = 3 \cdot 10^{-9} \text{ henry} = 3 \text{ nH.}$$

For such a structure the resonance frequency lies at

$$\omega = \frac{1}{\sqrt{LC}} = \frac{1}{\sqrt{3 \cdot 10^{-9} \cdot 2 \cdot 10^{-12}}} = 1.2 \cdot 10^{10}$$

or

$$f = 2 \text{ GHz,}$$

well beyond the range of the measurements by Vogel. An impedance change from capacitive to inductive for increasing bias in the forward and also in the reverse direction near breakdown is well known from measurements on point contact diodes.<sup>24</sup>

The sensitivity of the switch characteristic to the frequency of the switching signal is known from measurements by Holstrom.<sup>23</sup>

Figure 15.9 shows the effect of the frequency. As the signal frequency increases from 0.5 to 5 MHz, the threshold voltage decreases from beyond 10

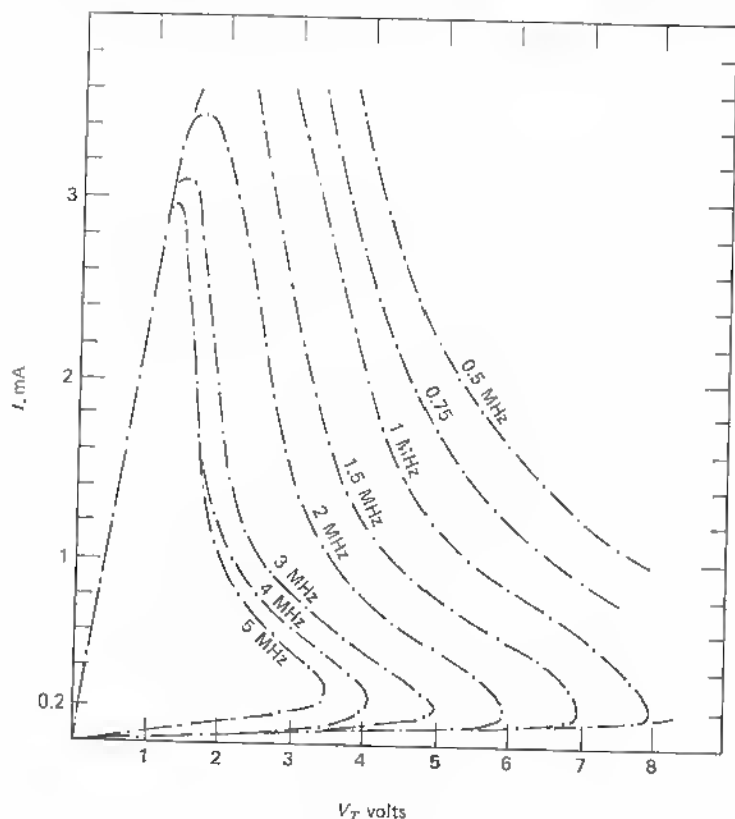


Fig. 15.9 Variation of switching threshold voltage with frequency of reset signal.

to below 4V, and the negative portion of the characteristic becomes steeper.

This behavior can be understood based on the frequency dependence of the conductivity of the transition metal oxides studied by A. P. Schmid.<sup>26</sup> Schmid has shown that the conductivity, for example, of  $V_2O_5$ - $P_2O_5$  glass has two separable branches of the conductivity versus  $1/T$  curve (see Figure 15.10).

One branch has strong temperature dependence and is independent of frequency. This is the limiting curve measured for low frequency (0.1 Hz). The other branch has activation energy zero and is therefore dominant at low temperature but is strongly dependent on the frequency. In effect the conductivity increases with frequency increase. It can be shown also that these two branches and the general behavior as described by Figure 15.10 can be derived from the Polaron theory. Assuming a small Polaron formed from the

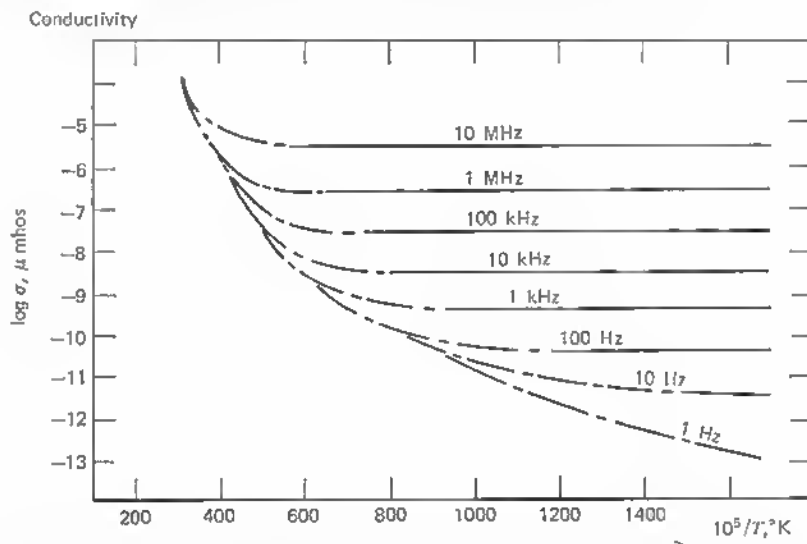


Fig. 15.10 Conductivity as a function of inverse temperature. Parameter is frequency of the conduction current. Model based on sum of hopping and tunneling conductivities. (A.P. Schmid)<sup>26</sup>

moving electron and the lattice distortion it carries, one can derive expressions for a frequency-dependent conductivity

$$\sigma_1(f, T)$$

and a frequency-independent part

$$\sigma_2(T).$$

The sum of these has the form shown in Figure 15.10.<sup>26</sup>

At temperatures below about half the Debye temperature, the dominant conduction mechanism is that of a charge transfer with conservation of lattice energy. At low enough temperatures, the charge transfer is that of tunneling between equivalent sites, and for higher temperatures the dominant conduction mechanism is "phonon-assisted hopping."

This latter process is the one assumed by Cohen et al.<sup>27</sup> The *mobility gap*, which is coincident with the density gap in Figure 15.6a, is activated by such a hopping process initiated by a tunneling current at the electrodes. Filling of the traps by such charges then converts the scheme in Figure 15.6a into Figure 15.6b. Using tunnel contacts to amorphous germanium (Al-Al<sub>2</sub>O<sub>3</sub>-Ge), Osmun and Fritzsche<sup>28</sup> have shown that the conductivity is symmetric with polarization. Mott concluded from measurements of the decreased

activation energy of the resistance with decreasing temperature that a higher-state density is found near the valence-band edge. Osmun and Fritzsche point out, however, that the tunnel effect is concentrated only within a small surface layer and therefore is not representative of the bulk crystal properties.

It is well known that the high-current path originates at the positive electrode and propagates to the cathode. A number of tests under pulsed operation have been made by Haberland<sup>29</sup> showing that:

1. A certain minimum pulse length or duration is needed to switch the material into the low resistance (on) state.
2. The pulse height (voltage) defines the delay time for the material to switch into the "on state." This time is shorter for higher-pulse voltage.
3. The delay time for switching is dependent on the history of the material and decreases for repeated switching (memory effect).
4. The delay time for switching increases with temperature.
5. An increase in pulse repetition rate (frequency) decreases the switching time (high-conductance mode.)

Haberland concludes that these conditions are typical of a process governed by a charge density built up, and he proposes to use  $\int_0^\tau i_p dt$  as a parameter for the switch ( $\tau$  = pulse time,  $i_p$  = pulse current). In fact the forming channel is based on electrons filling the traps in the state density gap. The linear discharge process, working against the charge accumulation, is the usual dissipation of charges in the glass as a conductor, which increases with the temperature.

In summary, the behavior of the glass switch is of a somewhat statistical nature, since individual states have to be filled in material with only short-range order. The long-range effect is an abrupt lowering of the resistance because of trap filling and wave function overlap, with subsequent heating. But since the channel is not exactly formed and reformed at the same points, a statistical variation of threshold and current values ensues.

It has been found that glass switches induce a high amount of Fourier components during the low-impedance cycle. It has also been found that an appropriate impedance or merely a shielding of the device can improve switching reproducibility.

Here is an important area for further studies. It may well be that because of its nature, a glass switch does not allow for exactly reproducible threshold voltage and reset currents but that appropriate application within a resonant structure or within a redundant circuitry can yield reproducible results. Gas-discharge tubes or spark gaps are also microscopically undefined but can still be used in appropriate applications as reliable devices.

## APPENDIX

## Derivation of Field Dependence of Dipole Ordering

For a system of dipoles within a neutral lattice matrix, a field calculation can be carried out when the crystal structure is known. In general terms, the potential energy of a dipole of strength  $p_0$  in an electric field  $E$  is

$$U = -p_0 E \cos \alpha, \quad (1)$$

where  $\alpha$  = angle between dipole axis and field.

In a random situation of  $n_0$  dipoles in a field, the polarization of a substance arising from orientation polarisability is

$$p_0 = n_0 p_0 \overline{\cos \alpha}, \quad (2)$$

where  $\overline{\cos \alpha}$  = mean value for all dipoles in field.

By thermal motion, this mean value is given by the Langevin function  $L(x)$ :

$$\overline{\cos \alpha} = L(x) = \cot x - \frac{1}{x}, \quad (3)$$

in which

$$x = \frac{p_0 E}{kT}, \quad (4)$$

where  $kT$  = Boltzmann factor.

As an estimate, if  $p_0 = 10^{-18}$  cgs. units in a field of

$$E = 18 \cdot 10^3 \text{ V/cm} = 60 \text{ cgs/cm},$$

$$p_0 E = 6 \cdot 10^{-17} \text{ erg.}$$

But the mean thermal energy of a molecule at 300°K is  $\frac{3}{2} kT \sim 6 \cdot 10^{-14}$  erg, or according to (4),  $x \approx 10^{-3}$ .

If  $x < 1$ ,  $L(x)$  can be approximated:

$$L(x) \approx \frac{x}{3}. \quad (5)$$

This into (2) gives

$$p_{or} = \frac{n_0 p_0^2 E}{3kT},$$

the orientation polarization in a field  $E$  as a function of temperature.

Depending on structure and the relative freedom of dipole rotation, the dielectric constant of crystals changes with temperature, sometimes in abrupt steps because of reorientation (see, for example,  $H_2S$  in solid form below 200°K).

That is why measurements of  $\epsilon(T)$  are very informative as to the character of dipole reorientation and dipole strength within a crystal. (See Fig. 15.8).

In a matrix of glass, the insulator character can be changed drastically by a field-induced reorientation of individual metal oxide chains or ions within the neutral structure. A long-range conduction can be established if a simultaneous rotation of dipole molecules affects a continuous charge exchange across the entire crystal length. This is the reason why ordinary glass begins to conduct when subjected to high fields and moderate temperatures ("welding" of glass at 200° to 500°C, but at fields of 3,000 to 7,000 V/cm)\*.

### Field Strength of a System of Point Dipoles

In the general analysis of the effects, it is important to assess the field of a system of dipoles.

Consider the dipole length small, compared with their mutual distance (point dipoles). Then we can derive the field on account of all interesting dipole moments by two radius vectors: the dipole-position vectors  $\mathbf{r}_j$  and the dipole-strength vectors  $\mathbf{p}_j$  ( $j = 1, 2, 3, \dots, N = \text{number of dipoles}$ ). At a point  $k$  in space, the field of all dipoles is then

$$E(\mathbf{r}_k) = \sum_{j=1}^N E_j(\mathbf{r}_{kj}) \quad (6)$$

$$= \sum_{j=1}^N \frac{3\mathbf{r}_{kj}(\mathbf{p}_j \cdot \mathbf{r}_{kj}) - \mathbf{p}_j r_{kj}^2}{r_{kj}^5}, \quad (7)$$

$$\mathbf{r}_{kj} = \mathbf{r}_j - \mathbf{r}_k. \quad (8)$$

In a real crystal, the structural dipole arrangement gives a definite expression for the right-hand side of this equation. For example, if a unit cell contains only one dipole and the dipole moment is defined by the unit vector  $\mathbf{l}$ , the sum (7) can be expressed by the structural sum of the lattice:

$$E(\mathbf{r}_k \cdot \mathbf{a}_1) = pS(\mathbf{r}_k \cdot \mathbf{l}_1) = p \sum_l \sum_m \sum_n \frac{3(R_{lmn} - r_k)(\mathbf{l} \cdot \mathbf{R}_{lmn} - r_k) - l_1(R_{lmn} - r_k)^2}{|R_{lmn} - r_k|^5}.$$

The components of  $S$  along the coordinate axis ( $S_x, S_y, S_z$ ) are the structural coefficients.

$$R_{lmn} = lx + my + nz = \text{operator for parallel vector translation}$$

\* See, for example, G. Wallis and D. I. Pomerantz, Field Assisted Glass-Metal sealing, *J. Appl. Phys.*, vol. 40, no. 10, pp. 3946-3949, September, 1969.

With these, the field in any direction of polarization is known. For example, for a cubic crystal

$$S_x^{110}(x, y, z) = \frac{1}{\sqrt{2}} [S_x^{100}(x, y, z) + S_x^{010}(x, y, z)].$$

Since the structural coefficients of the cubic dipole lattice and other lattices are known, numerical values of  $E(\mathbf{r}_k)$  can be found when the lattice type and the dipole arrangements are known.

In the glass switch, the hopping process is enhanced by a field ordering of the dipoles. It is important, therefore, to measure structural parameters related to the dipole lattice in order to find the field necessary for dipole rotation. It is hoped that some model material can be found that allows comparison of this dipole field with the switching field.

## REFERENCES

1. Mott, N. F.: Electrons in Disordered Structures, *Advances in Physics (British)*, vol. 16, pp. 49-144, 1967.
2. Tauc, J., et al.: Optical Properties and Electronic Structure of Amorphous Germanium, *Physica Status Solidi*, vol. 15, p. 627, 1966.  
Tauc, J.: Electronic Properties of Amorphous Materials, *Science*, vol. 158, pp. 1543-1548, December 22, 1967.
3. Gubanov, A.: "Quantum Theory of Amorphous Semiconductors," Consultants Bureau, New York, 1965.
4. Gudden, B., and W. Schottky: Ionic and Electronic Conduction in Non-metallic Solids, *Zschr. f. Techn. Phys.*, vol. 11, pp. 323ff, 1935.
5. Pearson, A. D., W. R. Northover, J. F. Dewald, and W. F. Peck, Jr.: Chemical Physics and Electrical Properties of Some Unusual Inorganic Glasses, "Advances in Glass Technology," Plenum, New York, p. 357, 1962.
6. Ovshinsky, S. R.: U. S. Patent 3,271,591 (Symmetrical Current Controlling Device), September 6, 1966.
7. Ovshinsky, S. R.: Reversible Electrical Switching Phenomena in Disordered Structures, *Phys. Rev. Letters*, vol. 21, no. 20, pp. 1450-1453, November 11, 1968.
8. Sideris, G.: Transistors Face an Invisible Foe, *Electronics*, pp. 191-195, September 19, 1966.
9. Mackenzie, J. D.: Looking through Glasses for New Active Components, *Electronics*, pp. 129-136, September 19, 1966.
10. Schottmiller, J. S., et al.: New Vitreous Semiconductors, *J. Appl. Phys.*, vol. 39, no. 3, pp. 1663-1669, February 15, 1968.
11. Morin, F. J.: Halides, Oxides and Sulfides of the Transition Metals, *J. Appl. Phys.*, suppl. vol. 32, no. 10, pp. 2195-2197, October, 1961.
12. Wilson, W. B.: Evidence for Hopping Transport in Boron-doped Diamond, *Phys. Rev.*, vol. 127, no. 5, pp. 1549-1550, September 1, 1962.

13. Kolomijets, B.: Glassy Semiconductors, *Ideen des Exakten Wissens*, no. 8, pp. 505-511, 1969.
14. Pearson, A. D., and C. E. Miller: Filamentary Conduction in Semiconductor Glass Diodes, *Appl. Phys. Letters*, vol. 14, no. 9, pp. 280-282, May 1, 1969.
15. Ovshinsky, S. R.: Amorphous Semiconductors, *Science Journal (British)*, pp. 73-78, August, 1969.
16. Stocker, H. J.: Bulk and Thin Film Switching and Memory Effects in Semiconducting Chalcogenide Glasses, *Appl. Phys. Letters*, vol. 15, no. 2, pp. 55-57, July 15, 1969.
17. Berglund, C. N.: Thermal Filaments in Vanadium Dioxide, *IEEE Transactions on Electron Devices*, vol. ED-16, no. 5, pp. 432-437, May, 1969.
18. Hickmott, T. W.: Electroluminescence, Bistable Switching and Dielectric Breakdown of  $\text{Nb}_2\text{O}_5$ -Diodes, *The Journal of Vacuum Science and Technology*, vol. 6, no. 5, pp. 828-833, September-October, 1969.
19. Mott, N. F.: Conduction and Switching in Non-crystalline Materials, *Contemp. Physics*, vol. 10, no. 2, pp. 125-138, 1969.
20. Hamakawa, Y., and J. Yamaguchi: Electrical Conduction in Germanium Grain Boundary Plane, *Jap. Journal of Appl. Phys.*, vol. 1, no. 6, pp. 334-342, December, 1962.
21. Taylor, W. F., N. H. Odell, and H. Y. Fan: Grain Boundary Barriers in Germanium, *Phys. Rev.*, vol. 88, pp. 867-875, 1952.
22. Vogel, R.: Negative Capacitance in Amorphous Semiconductor Chalcogenide Thin Films, *Appl. Phys. Letters*, vol. 14, no. 7, pp. 216-218, April 1, 1969.
23. Holstrom, R.: Switching and Conduction Behavior of Amorphous Semiconductor Diodes, *Proc. IEEE*, vol. 57, no. 8, pp. 1451-1453, August, 1969.
24. Mataré, H. F.: "Receiver Problems in the Ultrahigh Frequency Range," Oldenbourg, München, pp. 151ff, 1951.
25. Bruyere, J. C., and B. K. Chakraverty: Switching and Negative Resistance in Thin Films of Nickel-Oxide, *Appl. Phys. Letters*, vol. 16, no. 1, pp. 40-43, January 1, 1970.
26. Schmid, A. P.: Small Polarons as a Source of the Frequency-dependent Conductivity in Glasses Containing Transition Metal Oxides, *J. Appl. Phys.*, vol. 40, pp. 4128-4136, September, 1969.
27. Cohen, M. H., H. Fritzsche, and S. R. Ovshinsky: Simple Band Model for Amorphous Semiconducting Alloys, *Phys. Rev. Letters*, vol. 22, p. 1065, 1969.
28. Osmun, J. W., and H. Fritzsche: Electron Tunneling into Amorphous Germanium, *Appl. Phys. Letters*, pp. 87-89, February 1, 1970.
29. Haberland, D. R.: Ladungsbedingter Schaltmechanismus in Glashalbleitern, *Solid State Electronics*, vol. 13, pp. 207-217, February, 1970.



## Chapter 16 Conclusions

Starting with the classical carrier transport in periodic structures, we have introduced the influence of defects on the electronic properties of crystals. In a gradual approach to the problem of the deformed lattice, the free bond and the array of dangling bonds as the most important lattice disturbances are dealt with, but other imperfections of a lesser influence are only mentioned.

After a short review of continuum theory and the generation of dislocations by nucleons and also their influence on electronic properties under radiation, the main topic of the book is introduced: the electrical properties of dislocations.

In dealing with the different kinds of dislocations, a number of methods are introduced that help in understanding the following chapters, where a transition from the individual dislocation to the array is made.

Under the heading "Anisotropy of Charge Carrier Transport," we have tried to summarize the various effects of dislocations on the important transport parameters. This opens the way for a description of the electronic properties of grain boundaries, the most important large-area disturbance in crystals.

From here, there is a straight development to the intentional growth of these interesting structures and to applying them in devices.

Finally, the knowledge gained can be applied to assess the effect of dislocations on devices and special materials combinations for devices.

At the time of writing, the field of amorphous semiconductors or disordered structures had gained such importance that it was felt necessary to add Chapter 15 on the channel conduction or the switching phenomenon in amorphous semiconductors.

Without going deeply into the problems of the phenomenon itself, it seemed necessary in this context to describe recent experimental facts in the light of the insight gained by the study of dislocations.

While Chapter 2 introduces the basic point defects of the Scitz list, we have not dealt with the numerous complex point defects to limit the text and concentrate on the most important defect-electronics for the semiconductor device physicist and engineer.

As we have already mentioned, many complex forms of defects are known from the work on radiation damage. It was felt, however, that the status in this field is still too undefined to be included in extenso.

When electronic features of a particular defect are analyzed, there is still considerable discussion as to the effects of the impurities present in the crystal. There is no understanding as yet, how certain defects associate with impurities under the impact of nuclear radiation. Recovery processes, especially, can be quite complex as the introduction of such steps as "diffusion controlled recovery of correlated pairs"<sup>1</sup> shows.

Recovery is a function of defect concentration and also an independent function of the trap concentration. However, how certain defects migrate and separate from their correlated "pair companion" is unknown.

Long distance vacancy migration in silicon and germanium takes place even at low temperatures. As electron paramagnetic resonance studies have shown, interstitials can move at 4°K such that multiple interactions with complex results regarding the electronic states are the consequence, even at low temperatures.

The concept of the divacancy has been invoked to explain certain features of defect level formation and the "divacancy locked to a defect" was introduced on account of EPR studies. The electronic structure of a vacancy in the diamond lattice is already a complex problem for a perfect crystal environment<sup>2</sup> and presents formidable complexity in real crystals. All results, on even the purest silicon crystals grown by a floating zone technique (oxygen free), suffer from uncertainty with respect to the role of the ever present carbon. In its original state a vacancy in silicon is an acceptor (negative core charge) when embedded in *n*-type material and a donor (positively charged) in *p*-type environment.<sup>3</sup> This corresponds to our simple model of the role of broken bonds. However, any detail concerning the impurity defect associations is a complex new project.

This field is a stimulating research area for the semiconductor physicist and is also a rewarding field of endeavor due to the important practical implications. All modern research methods from optical absorption studies to EPR measurements are useful tools in defining the processes so important for the understanding of the electronic features of damaged materials.<sup>4</sup>

We have mentioned a number of research topics concerned with the study of line defects and planar defects in the introduction. It goes without mentioning that beyond this there is a wealth of further questions related to thermoelectric effects and quantum-electronic effects that are worth pursuing.

## REFERENCES

1. R. C. Fletcher and W. L. Brown: Phys. Rev. 92, 585 1953.
2. Lannoo, M., G. Leman and J. Friedel in "Radiation Effects in Semiconductors," F. L. Vook, ed., Plenum 1968.
3. Watkins, G. D., "Radiation Damage in Semiconductors," Dunod, Paris, p. 97, 1965.
4. For a review of these questions see: "Radiation Effects in Semiconductors," F. L. Vook, ed., Plenum 1968.

## Appendix    Measurements of Electronic Properties                  of Semiconductor Crystals and Films

### INTRODUCTION

The determination of semiconductor materials properties has developed from simple resistivity and Hall effect measurements and their temperature dependence, to sophisticated measurements of magnetoresistance changes and cyclotron resonance studies at microwave frequencies. The latter methods have lead to direct measurements of the band structure and effective mass values. But while the elaborate methods are applicable mostly in cases of complete structural perfection, the simple methods are still of great importance for the determination of basic properties of not so perfect crystal material as is encountered especially when we work with III-V or other compound crystals and, above all, when materials in thin-film form are under scrutiny.

Hall effect studies and generally mobility measurements can give an indication of the purity and perfection of materials and of the important collision and scattering processes so decisive for all carrier transport problems in devices.

As such problems have been referred to frequently in this text this review is intended to put together the basic methods known today for materials evaluation. Emphasis is placed on the four fundamental magnitudes ( $\rho$ ,  $\Delta\rho/\Delta x$ ,  $\mu$ ,  $\tau$ ), and in all cases the extension of the bulk methods to measurements on thin films (thick films, epitaxial films, or layers, etc.) is considered in extenso.

### I    RESISTIVITY

#### A.    Resistivity Measurements (General)

Two very important magnitudes relating to carrier transport in solids are resistivity and mobility. The conductivity of a crystal is given by

$$\sigma = \frac{1}{\rho} = ne\mu, \quad (1.1)$$

where  $\rho$  = resistivity,

$e$  = electronic charge,

$n$  = carrier density,

if only one type of carrier (mobility  $\mu$ ) is present. Equation (1.1) shows that resistivity and mobility define each other if the carrier density is known. Here  $n$  is the density of the untrapped excess carriers and  $\mu$  the microscopic mobility. In most cases, however, the carrier density is not exactly known, and independent measurements of  $\sigma(\rho)$  and  $\mu$  are necessary.

We first describe resistivity measurements using various methods and then homogeneity and lifetime measurements and thereafter mobility measurements.

In a very general sense the current through a piece of material, like a semiconductor crystal, can be defined in terms of the electronic distribution function

$$f(x, y, z, v_x, v_y, v_z) \partial x \partial y \partial z \partial v_x \partial v_y \partial v_z$$

in three coordinates  $x, y, z$  with their local carrier velocity vectors  $v_x, v_y, v_z$  if a stationary distribution ( $t = 0$ ) is considered and if the charge carriers are comprised in the volume elements  $x + \partial x, y + \partial y, z + \partial z$  with the respective velocity changes  $v_x + \partial v_x, v_y + \partial v_y, v_z + \partial v_z$ . If no detailed carrier motion is considered, but only the  $i$  versus  $V$  relation at the contacts is considered, one may write the current in the direction chosen, for example,  $y$ , as the triple integral:

$$i = e \iiint v_y f(v_x, v_y, v_z) \partial v_x \partial v_y \partial v_z. \quad (1.2)$$

In a steady-state condition,  $v_y$  is considered constant, and the integral of the distribution function represents  $n$ , the total number of charge carriers:

$$i = ev_y \iiint f \cdot \partial v_x \partial v_y \partial v_z = ev_y \cdot n. \quad (1.3)$$

The velocity is a function of the local field strength  $\partial V/\partial y$  in volts per centimeter, and the mobility is the proportionality factor:

$$i = en\bar{\mu} \frac{\partial V}{\partial y}, \quad (1.4)$$

$$i = en\bar{\mu} E, \quad (1.5)$$

where  $\bar{\mu}$  = mean mobility value.

$E$  is now the resultant field across the sample. As seen in Figure A1.1, a local inhomogeneity in the sample, like a lineage boundary, might completely

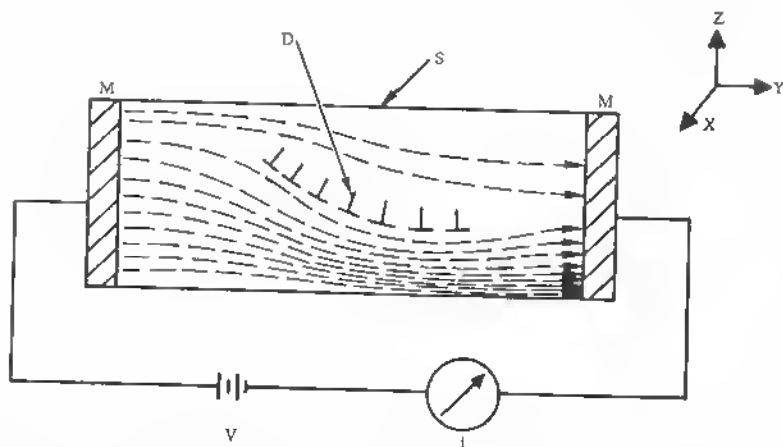


Fig. AL1 Model of current flow in semiconductor crystal with anisotropic carrier flow.

change the carrier flow lines. Macroscopic conductance of the sample, however, is still given by

$$\frac{i}{V} = \frac{Q}{L} \cdot ne\bar{\mu}, \quad (\text{I.6})$$

where  $Q$  = cross section of sample,  
 $L$  = length of sample.

$ne\bar{\mu}$  represents the conductivity  $\sigma$  ( $1/\sigma = \rho$ ) as distinguished from the conductance:

$$\begin{aligned} \frac{1}{R} &= \frac{1}{V} \quad \text{ohm}^{-1} \\ &= \frac{Q}{L} \cdot ne\bar{\mu}, \\ \sigma &= e\mu n \quad \text{ohm}^{-1} \text{ cm}^{-1}, \\ \rho &= \frac{1}{e\mu n} = \frac{V Q}{i L} \quad \text{ohm cm} \end{aligned} \quad (\text{I.7})$$

( $\mu$  is always assumed to be a mean value across the sample from here on).

#### Application to Thin Films

The application of additional contacts being difficult and undesirable in thin-film characterization measurements, (I.7) applies in all cases where two evaporated end contacts  $M$  can be made to a film and the film thickness is

known by either infrared studies (absorption measurements, etc.) or by deposition calibration. If by such methods  $Q$  and  $L$  are known, the resistivity is easy to calculate. In cases of *in situ* measurements, the films remain under vacuum while the resistivity is checked. If in these cases the deposition rate and thus  $Q$  of the film are known, a measurement of the resistance  $V/i$  gives immediately  $\rho$ . Such *in situ* techniques apply especially to mobility checks in which the magnetic field is switched in for additional measurements of the Hall constant (see under Mobility). In the case of films of thickness below  $1\ \mu$  care has to be taken to make sure that the carrier flow is not subjected to strong influence of defect zones or grain boundaries (see below). Equation (1.7) can be applied directly in two-probe measurement techniques. As shown in Figure A1.2, the end contacts are applied to the sample in the form of metallized surfaces of ohmic character. (In the case of *n*-type crystals, a layer of

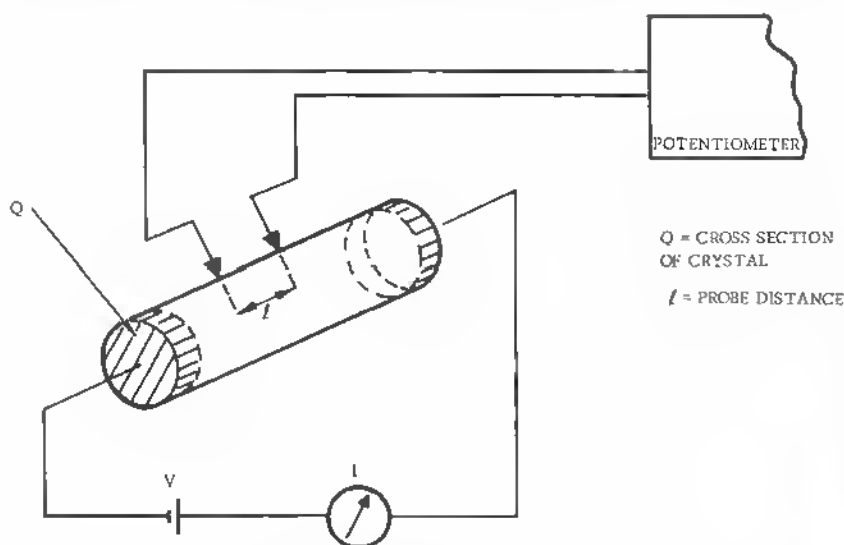


Fig. A1.2 Two-probe method for resistivity measurement.

$n^+$  diffused material is useful underneath the metallization. The same is true for *p*-type crystals, where  $p^+$  diffused regions, if possible to degeneracy, are desirable.) To calculate the resistivity in ohm centimeters from

$$\rho = \frac{V \cdot Q}{i \cdot l}, \quad (1.8)$$

where  $l$  = electrode spacing,

we introduce  $V$  in volts,  $Q$  in square centimeters,  $l$  in centimeters,  $i$  in amperes.

With this method, a certain local resistivity distribution can be measured since  $l$  can be made as small as allowed for by the potentiometer sensitivity. A considerable increase in sensitivity results from application of ac methods. In Figure A1.3, the scheme is shown.  $F$  is a filter passing a band  $\Delta\omega$  around the center frequency  $\omega$  injected into the crystal sample. The distance between the points can be made extremely small if the amplifier  $A$  increases the amplitude correspondingly (for example,  $10^6$  in voltage amplification).

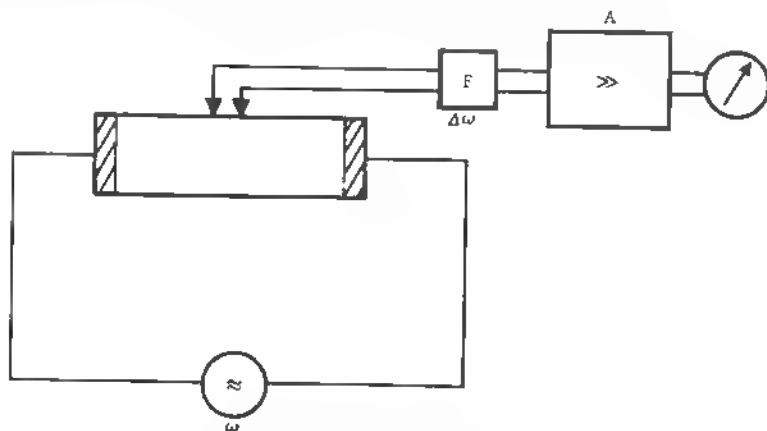


Fig. A1.3 Ac method for resistivity measurement.

#### B. Four-Point Probe Method

A class of very generally applied resistivity sets is based on this method because no application of large-area contacts by plating or other type of deposition is needed. Here, two pressure contacts are used to deliver a current through the sample while another contact pair measures the voltage developed across the semiconductor path used for the current flow (Figure A1.4). In this method, the cross section of the crystal is not needed in the resistivity calculation. Therefore, the method has very general applicability with the main limitation that contacts have to be ohmic at least within the measurement range of currents (probes 1 and 4) and that probes 2 and 3 see a high impedance (toward high impedance voltmeter). Generally written, the voltage at a point  $x, y, z$  is related to the local field  $E$  by

$$V(x, y, z) = - \int_{\infty}^{x, y, z} E \, dr. \quad (1.9)$$

Since  $\text{grad } V = -E$  and  $V = q/r$ ,  $q$  = local charge, we may write for the potential variation with distance  $r$



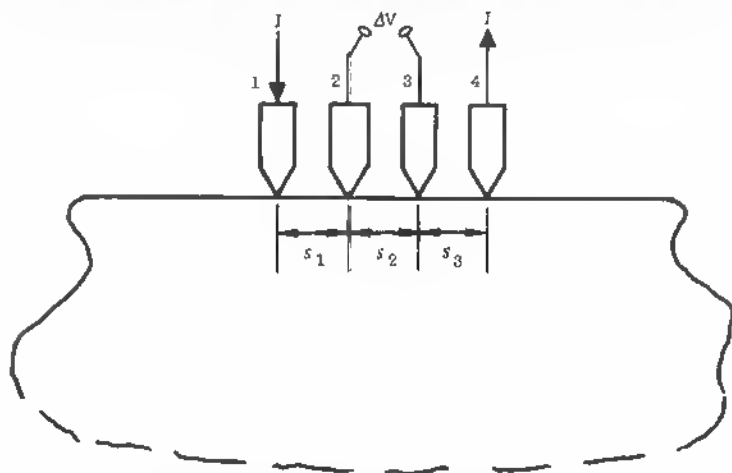


Fig. A1.4 Four-point probe geometry.

$$\frac{\partial V(r)}{\partial r} = -E = \frac{q}{r^2}. \quad (\text{I.10})$$

With this in mind, the potentials at probes 2 and 3 are

$$\begin{aligned} V_2 &= \frac{q}{s_1} - \frac{q}{s_2 + s_3}, \\ V_3 &= \frac{q}{s_1 + s_2} - \frac{q}{s_3}. \end{aligned} \quad (\text{I.11})$$

Here we assume that a continuous charge distribution has been built up because of current  $J$ . The potential difference  $\Delta V$  between probes 2 and 3 is then

$$\Delta V = q \left( \frac{1}{s_1} + \frac{1}{s_3} - \frac{1}{s_2 + s_3} - \frac{1}{s_1 + s_2} \right).$$

This simplifies for  $s_1 = s_2 = s_3 = s$  to

$$\Delta V = \frac{q}{s},$$

or

$$q = \Delta V \cdot s. \quad (\text{I.12})$$

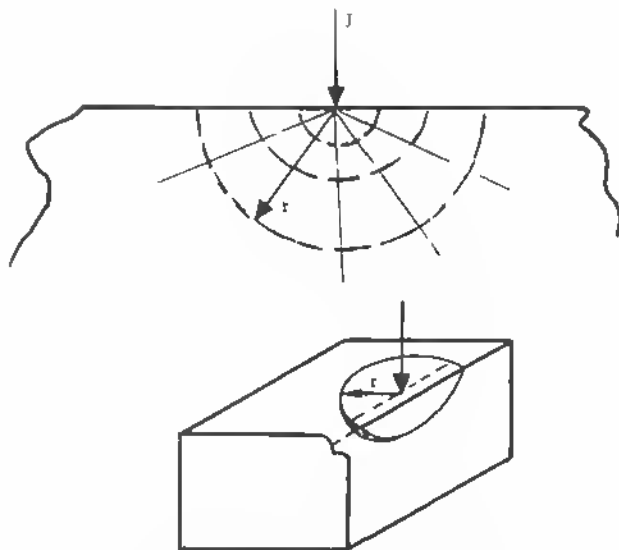


Fig. A1.5 Point probe and radial geometry.

To calculate the resistivity from the voltage at the inner probes, we have to consider the current density in the sample. The equipotential surfaces around a point injector being semispheres (Figure A1.5), the relation

$$\frac{I}{2\pi r^2} = \frac{E}{\rho}, \quad (\text{I.13})$$

where  $I$  = current,  
 $E$  = local field,

holds ( $\rho$  = resistivity of material). Since the field is given by

$$E = V'(r) = \frac{q}{r^2}, \quad (\text{I.14})$$

we get

$$I = \frac{2\pi r^2}{r^2} \cdot \frac{q}{\rho}, \quad (\text{I.15})$$

$$q = \frac{I\rho}{2\pi}, \quad (\text{I.16})$$

or:

$$\rho = \frac{2\pi q}{I}, \quad (\text{I.17})$$

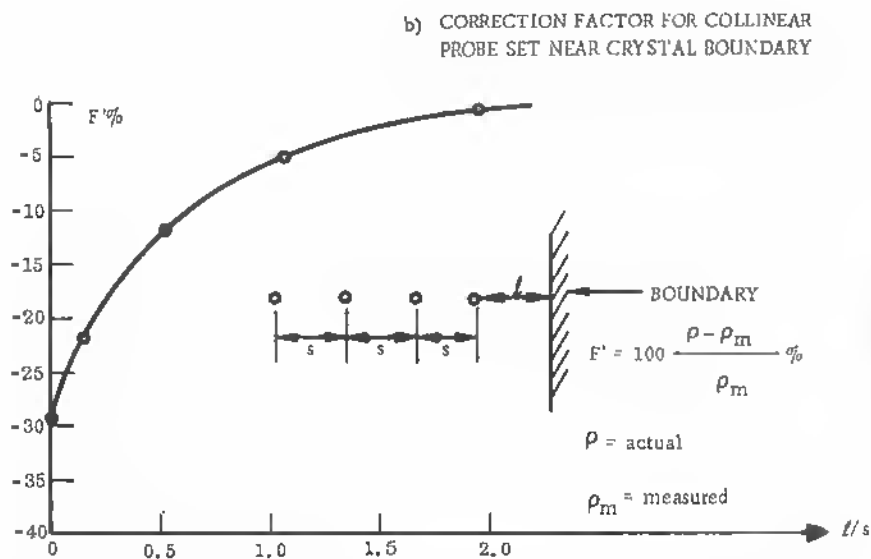
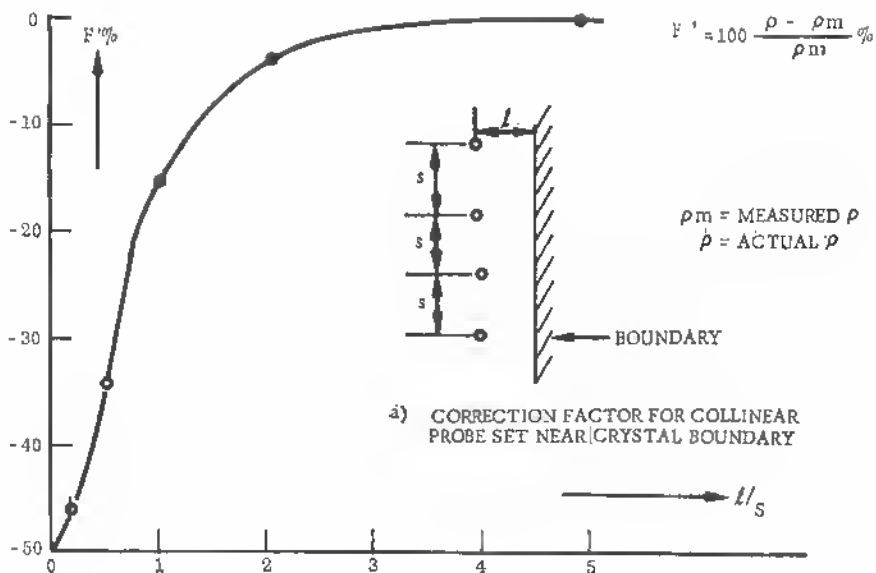


Fig. A1.6 (a) Correction factor  $F'$  (%) for line arrangement of probes parallel to a crystal boundary; (b) correction factor  $F'$  (%) for linear four-probe arrangement perpendicular to a crystal boundary.

and according to (I.12)

$$\rho = 2\pi \frac{\Delta V}{I} \cdot s. \quad (\text{I.18})$$

This is a resistivity expression in terms of  $\Delta V$  and  $s$  used generally for four probes. The current range can be chosen so that  $\Delta V$  is immediately read in terms of ohm centimeters by proper calibration:

$$I = 2\pi s.$$

This very idealized derivation of (I.18) shows the limitations. First, no infinite crystal surface being given, the limited crystal provides a conductivity boundary that reflects carriers and changes  $\rho$  into a value  $\rho$ -measured. In Figure AI.6a and b the error  $F'$  is plotted in percent against  $l/s$ , the ratio of boundary to probe distance. From  $\rho_m$  and  $F'$ , the actual  $\rho$  is found:

$$\rho = \rho_m(1 - |F'|). \quad (\text{I.19})$$

The actual resistivity, therefore, is smaller than the measured resistivity when a crystal boundary is present. Another correction is necessary if the probe diameter is close to the probe distance. If  $d/s \leq 0.05$ , an accuracy of better than 0.05 can be assumed.

### C. Measurement of Dice

Two types of dice are of importance for devices, those without a conducting layer (used, for example, in microcircuits) and those with a conducting layer (used, for example, in transistors of large size for power applications or in photoelectronic devices, etc.). The resistivity in the case where the wafer or dice thickness  $w$  determines the nearest boundary is given by

$$\rho = \frac{V}{I} \frac{\pi \cdot w}{\ln 2} F\left(\frac{w}{s}\right). \quad (\text{I.20})$$

This is the case of a nonconducting surface, and the correction factor  $F(w/s)$  drops considerably below 1 for small thickness  $w$  or small  $w/s$  values. This means that the actual resistivity measured appears too large compared the true resistivity. In the case of a conducting surface, the correction is just the reverse. The resistivity is given by

$$\rho = \frac{V}{I} \frac{2\pi}{1/s_1 + 1/s_3 - 1/(s_1 + s_2) - 1/(s_3 + s_2)} \cdot F'\left(\frac{w}{s}\right). \quad (\text{I.21})$$

For equal probe distances  $s_1 = s_2 = s_3 = s$ :

$$\rho = \frac{V}{I} \cdot 2\pi s \cdot F'\left(\frac{w}{s}\right). \quad (\text{I.22})$$

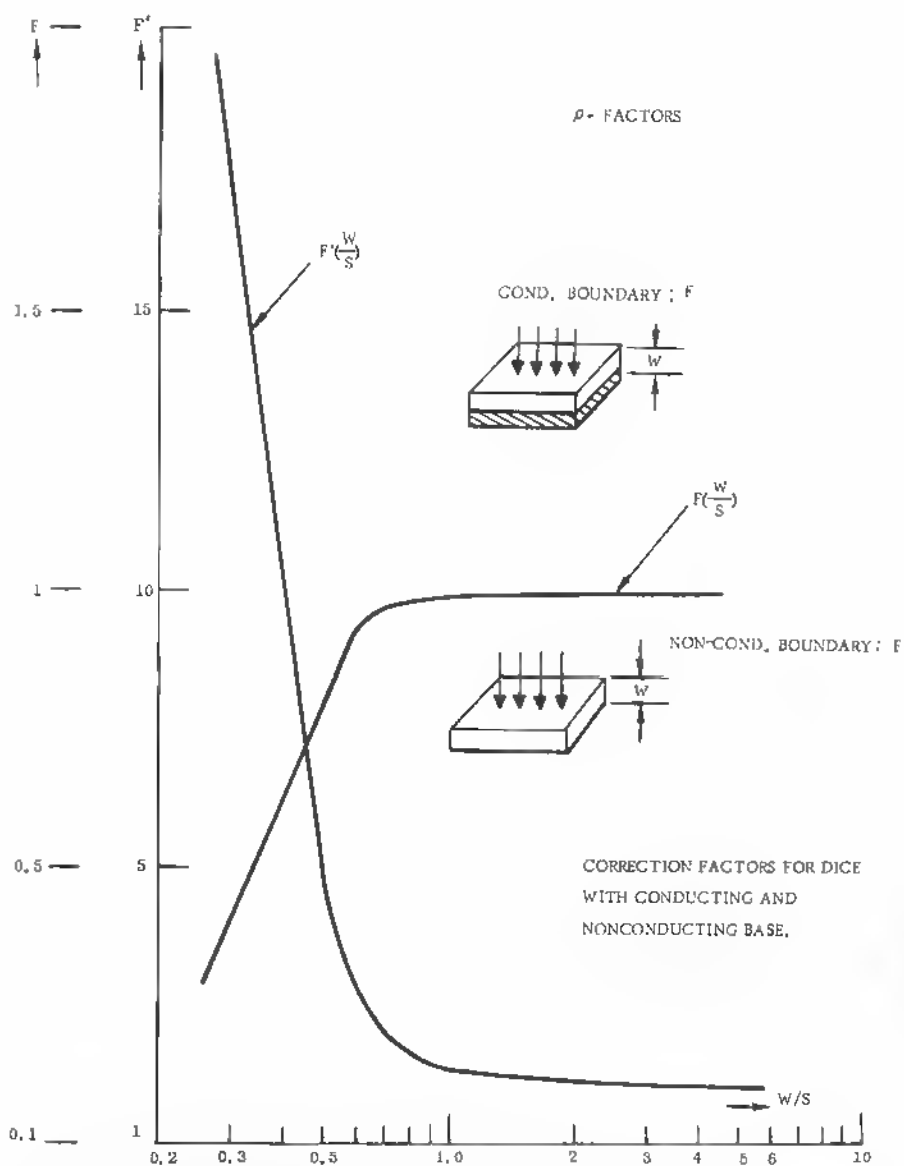


Fig. A1.7 Correction factor  $F(W/S)$  and  $F'(W/S)$  for nonconducting and conducting crystal-dice bases, respectively, in four-point probe measurements.

For the factors  $F$  and  $F'$  see Figure A1.7.  $F'(w/s)$  is high for small  $w/s$  values, because the apparent resistivity turns out to be too low when a conducting layer shunts the semiconductor on one side near to the contact probes. In any case, a value  $w/s$  near to 1 should be feasible (crystal thickness about equal to probe distance), and both correction factors  $F$  and  $F'$  are then near to 1. In much equipment for point probing, the four-contact electrodes are arranged in a square. S. Catalano<sup>1</sup> has treated this case in detail. As shown in Figure 1.8, a number of arrangements are possible, and the correction factors change, depending on whether the current-carrying probes are arranged either perpendicular to the boundary or parallel to it. Also, the distance between the current-carrying probes can generally be a multiple,  $n \cdot s$ , of the distance  $s$  in the other direction. For each case, there are two complementary solutions, depending on the nature of the boundary: conducting and nonconducting.

In the case of flat samples (films), it is often desirable to apply contacts to arbitrary places at the circumference of a flat sample (Figure A1.9). In this case the Van der Pauw relation

$$\exp\left(-\pi R_{AB,CD} \frac{d}{\rho}\right) + \exp\left(-\pi R_{BC,DA} \frac{d}{\rho}\right) = 1 \quad (1.23)$$

is valid and can be used to find the resistivity from

$$\rho = \frac{\pi \cdot d}{\ln 2} \frac{(R_{AB,CD} + R_{BC,DA})}{2} \cdot f\left(\frac{R_{AB,CD}}{R_{BC,DA}}\right), \quad (1.24)$$

where  $f$  is a correction function (Figure A1.10). The same method is applicable to Hall measurements.<sup>2</sup>

For probe arrangements in arbitrary form within rectangular samples, A. Mircea<sup>3</sup> has derived the geometric factor  $K$  (dimension of length) in the sheet resistivity

$$\rho_s = K \cdot \frac{V}{I}, \quad (1.25)$$

where  $V$  = potential difference between voltage probes,  
 $I$  = current through two current-carrying probes.

Of more general use is the derivation of arbitrary probe arrangements on arbitrary samples<sup>4</sup> by Mircea using the Green function method.

#### *Application to Thin Films*

In many instances the four-point probe surface measurements have been used to define impurity profiles within shallow layers and diffused barriers on bulk material by the lap-repeat method. This method has given quite reliable results in all cases where the impurity density in the measured layer (diffused

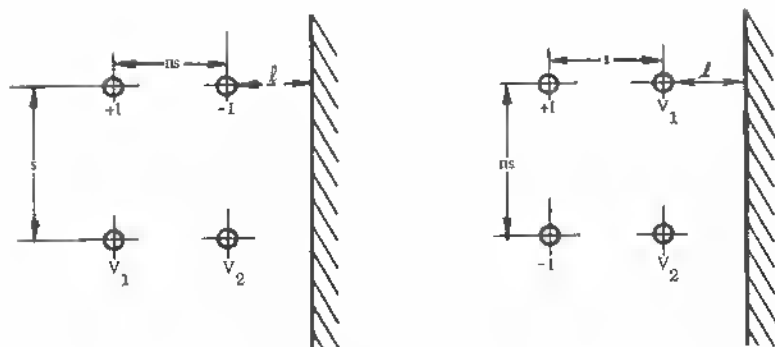
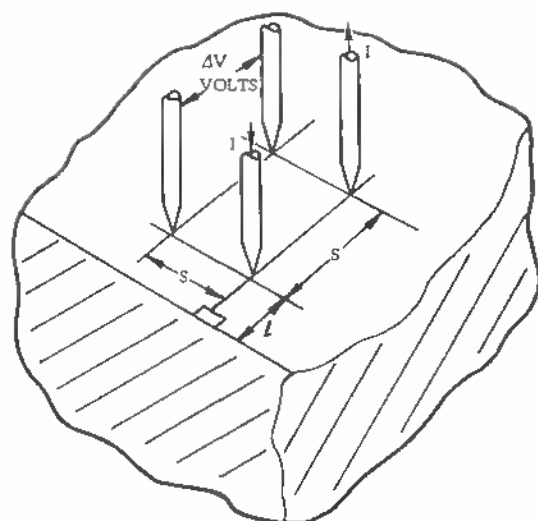
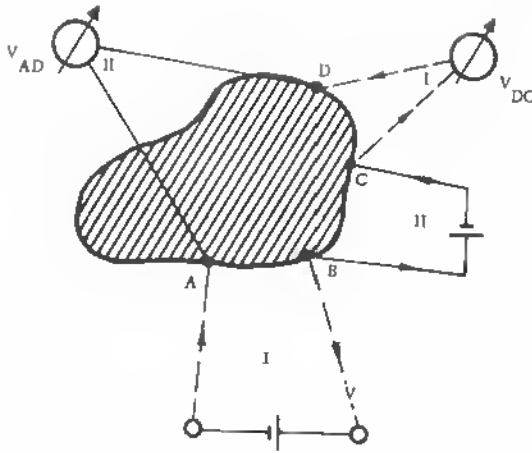


Fig. A1.8 Four-point probes in square arrangement near crystal boundaries.



$$R_{AB, CD} = \frac{V_D - V_C}{\text{UNIT } I_{AB}}$$

$$R_{BC, DA} = \frac{V_A - V_D}{\text{UNIT } I_{BC}}$$

Fig. A1.9 Van-du-Pauw probe arrangement on dice.

layer) is higher than in the underlying bulk crystal.<sup>5,6</sup> If one plots the slope of the  $G_s$  versus  $x$  curve

$$\frac{\partial G_s}{\partial x},$$

where  $G_s$  = sheet conductance, (ohms/square)<sup>-1</sup>,

$x$  = coordinate, measuring layer depth,

one gets a plot for all sheet conductivities  $\sigma_s$  parallel to the junction.<sup>6</sup>

The sheet conductance is given by

$$dG_s(x) = \frac{dI(x)}{V}. \quad (\text{I.26})$$

Here the sheet current  $I$  is also a function of  $x$ , or we have

$$dG_s(x) = \bar{N}(x)q \cdot \bar{\mu} dx, \quad (\text{I.27})$$

where  $\bar{N}(x)$  = average net impurity concentration in layer ( $x$ ),

$\bar{\mu}$  = average mobility,

$q$  = electron charge.



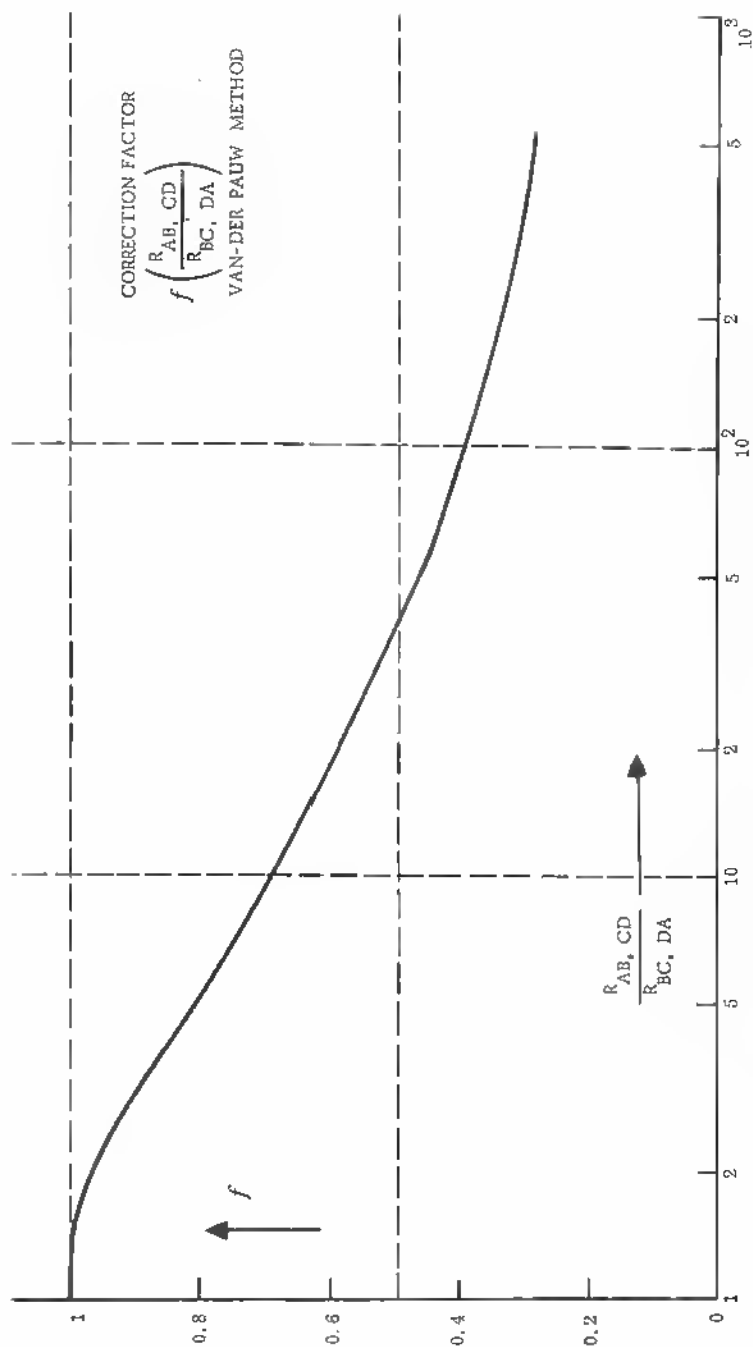


Fig. A1.10 Correction factor  $f(R_{AB, CD}/R_{BC, DA})$  in Van-du-Pauw method.

Within a diffused skin one may integrate this equation from  $x = 0$  to  $x = x_i$ , the result giving the sheet conductance of a diffused layer:

$$G_s(0) = q \int_0^{x_i} \bar{N}(x) \cdot \bar{\mu} dx, \quad (I.28)$$

If one uses a collinear array of four equally spaced ( $s$ ) probes for the resistivity measurements, one has, referring to (I.20),

$$\bar{\rho} = \frac{\pi}{\ln 2} \cdot x_i \cdot \frac{V}{I} \quad (I.29)$$

for the condition

$$x_i \ll \frac{1}{2}s,$$

or

$$\bar{\sigma} = \frac{\ln 2}{\pi} \cdot \frac{I}{V} \cdot \frac{1}{x_i}. \quad (I.30)$$

This change in conductance  $\Delta G_s(x)$  with penetration  $x_i$  can be written

$$\Delta G_s(x) = \bar{\sigma} \cdot x_i, \quad (I.31)$$

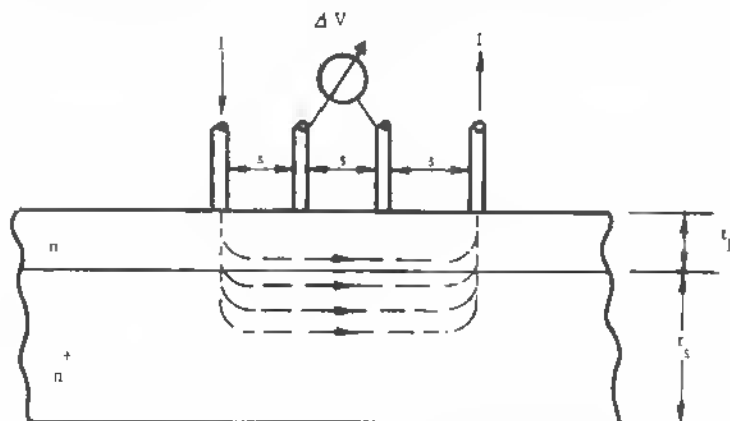
or

$$\Delta G_s(x) = \frac{\ln 2}{\pi} \left[ \frac{I(x)}{V(x)} - \frac{I(x + \Delta x)}{V(x + \Delta x)} \right]. \quad (I.32)$$

This change in conductance is sometimes difficult to obtain by four-probe measurements, and evaporated, ohmic contacts have to be applied to both sides of a sample. In this case  $\Delta G_s(x)$  is given by the expression above in brackets only, the factor  $(\ln 2)/\pi$  reducing to 1. From this the average net impurity concentration  $\bar{N}(x)$  follows:

$$\bar{N}(x) = \frac{1}{q\bar{\mu} \Delta x} \left[ \frac{I(x)}{V(x)} - \frac{I(x + \Delta x)}{V(x + \Delta x)} \right]. \quad (I.33)$$

These conditions are not met in cases where the substrate is of higher conductance than the layer to be measured. This situation, however, is the usual one for epitaxially deposited materials. In many instances the device substrate is a highly doped crystal for reasons of spreading or base resistance contact, and the shallow high-resistivity epitaxial film is used to form the planar device structures. In this case the usual four-point probe method measures the resistivity of the substrate rather than the one of the surface layer, since the main current flow goes through the high-conductivity substrate and the voltage probes measure the small voltage drop across  $s$ . In Figure AI.11 the dimensions are incorrect insofar as  $s$  is far in excess of the layer thickness  $t_f$ . If  $s$  can be lowered to a value essentially a factor of 10

Fig. AI.11 Four-point probes on epitaxial layer  $n$  on  $n^+$ 

higher than the film thickness, meaningful film resistivity values can be obtained if the resistivity ratio is  $\rho_n/\rho_n^+ \approx 10^3$ . For a ratio of  $\rho_n/\rho_n^+ \geq 10^3$ , the practical lower limit for  $t_f$  is  $4 \mu$ . In this case probe openings around  $25 \mu$  should be maintained, which is impracticable. If  $\rho_n/\rho_n^+ < 10^3$ , or for the values of substrate and film resistivity approaching each other, the film thickness has to increase to

$$t_f = 4 \frac{10^3}{\rho_n/\rho_n^+} \quad \text{in } \mu.$$

In cases where the substrate is of the opposite conduction type of the film, a junction forms and can be used to isolate the current flow through the epitaxial layer. This method works, of course, only up to a certain bias voltage or current value through the current probes. Beyond this value the voltage drop across the current probes (Figure I.12) adds markedly to the backbias-voltage  $V_b$ , and the barrier layer  $\delta$  starts to widen further into the film, diminishing the current flow and indicating an increase in resistance. This trend reaches a maximum value for  $V/I$  versus  $I$  and then a steeper fall-off to very low  $V/I$  values, according to the breakdown of the separating barrier.<sup>7</sup> Figure AI.13 shows the typical  $V/I$  versus  $I$ -graph for this situation. The weakness of the four-point probe method in cases of epitaxial films are, therefore:

1. Small probe spacing necessary (below 10 mils or  $254 \mu$  is possible, but technically difficult).
2. Mechanical damage likely to occur.
3. Very limited current-voltage ranges.

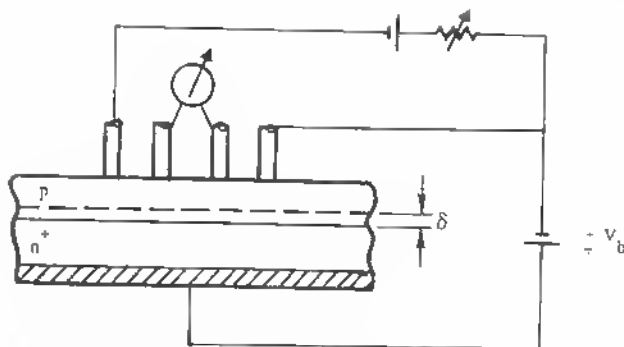


Fig. A1.12 Four-point probes on epitaxial layer  $p$  on  $n$  (or  $n^+$ ) with barrier formation.

A certain alleviation of spacing conditions is possible with the square probe arrangement in Figure A1.14. Since probes 1 and 3 are used for the current injection and 2 and 4 as voltage probes, the critical distance  $s$  is to be maintained only with two probes at either side. The solution of Laplace's equation for cylindrical symmetry yields<sup>8</sup> rather localized equipotential lines within the range of resistivities assumed:

$$\begin{aligned}\rho_e &\approx 1.0 \text{ ohms cm,} \\ \rho_s &\approx 10^{-2} \text{ ohms cm.}\end{aligned}$$

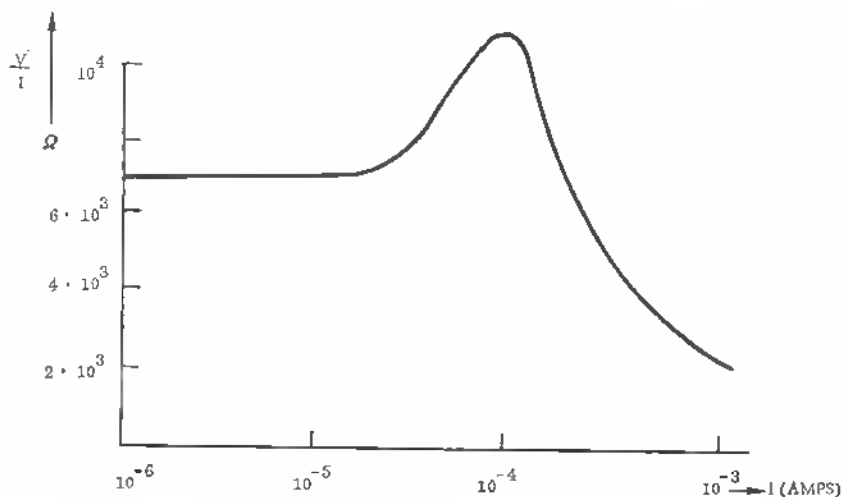


Fig. A1.13 Resistance as a function of current through the outer probes in a four-point test on a  $p$ -type epitaxial layer on  $n^+$ -type substrate.

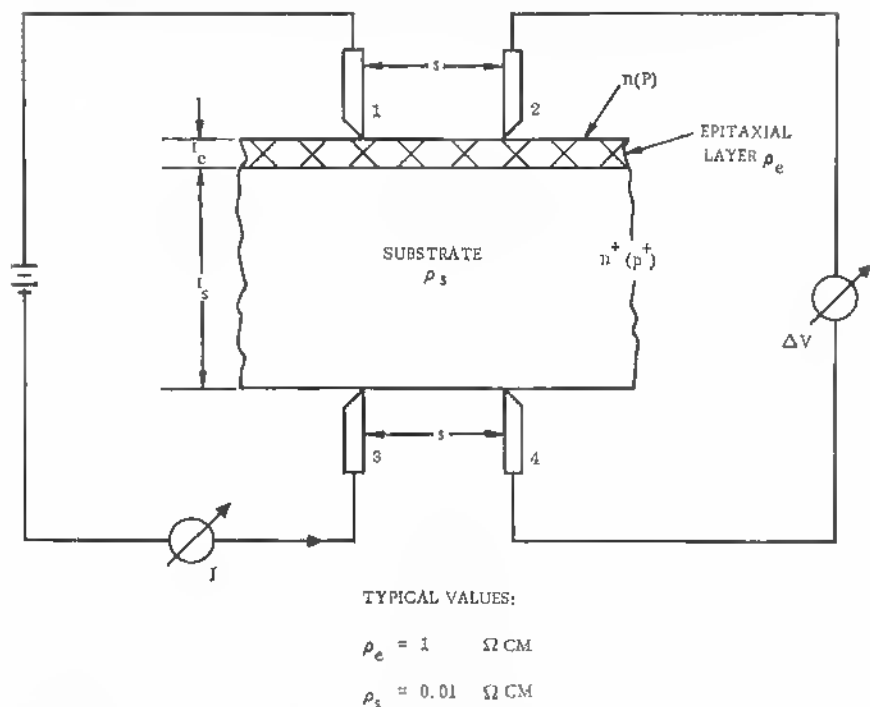


Fig. A1.14 Four-point probe arrangement for measurements of  $n$  on  $n^+$  or  $p$  on  $p^+$  epitaxial layers.

To achieve sensitivity to 0.1 ohm cm for  $\rho_e$ , the probe spacing  $s$  must be less than  $50 \mu$ . For higher resistivities correspondingly larger spacings are allowed.

#### D. Breakdown Technique

In this method the correlation between breakdown voltage and impurity concentration is exploited. Three probes are needed to carry through this type of test. Two probes form a current path so that a junction is formed on one probe (reverse biased probe), and the third probe is used as a potential sonde<sup>9</sup> (Figure A1.15). It must be understood that this is an empirical method for which a calibration curve has to be established. This is done by measuring the breakdown voltage of nonepitaxial monocrystalline material of known impurity content. If one plots the depletion layer width as a function of impurity concentration for different voltages and carries the breakdown voltage versus impurity concentration relation into this diagram, one obtains a chart showing the limitations (Figure A1.16).

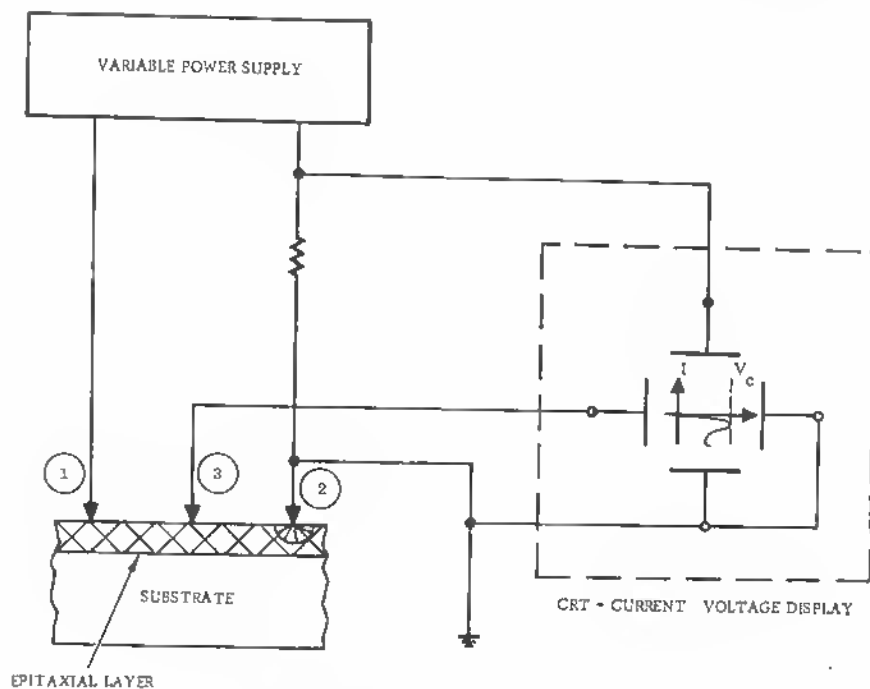


Fig. AI.15 Breakdown method for resistivity measurements.

It is important to know if the measured breakdown voltage value is depletion-layer-width limited or avalanche-limited. All points at the left of the breakdown voltage versus the impurity concentration-calibration curve are depletion-layer-width limited. In the double diagram one has to use, therefore, the depletion-layer-width-impurity-concentration relation for breakdown voltages below the points indicated by the bulk-calibration curve.

A similar procedure was applied by other authors<sup>10</sup> who used instrument reading and a contact to the bulk substrate or block, (in the case of slices), (Figure AI.17). A ramp generator allows scanning the point contact characteristics. Again, the avalanche breakdown plotted versus the impurity concentration is the upper limit into which all epitaxial-layer thickness versus  $N(x)$  curves have to merge. (Figure AI.18). For known layer thickness and breakdown voltage, the method yields a fairly precise reading of the resistivity  $\rho$ .

Because of the fact that in thin films the breakdown voltage is defined by the layer thickness rather than by the impurity concentration (area below the

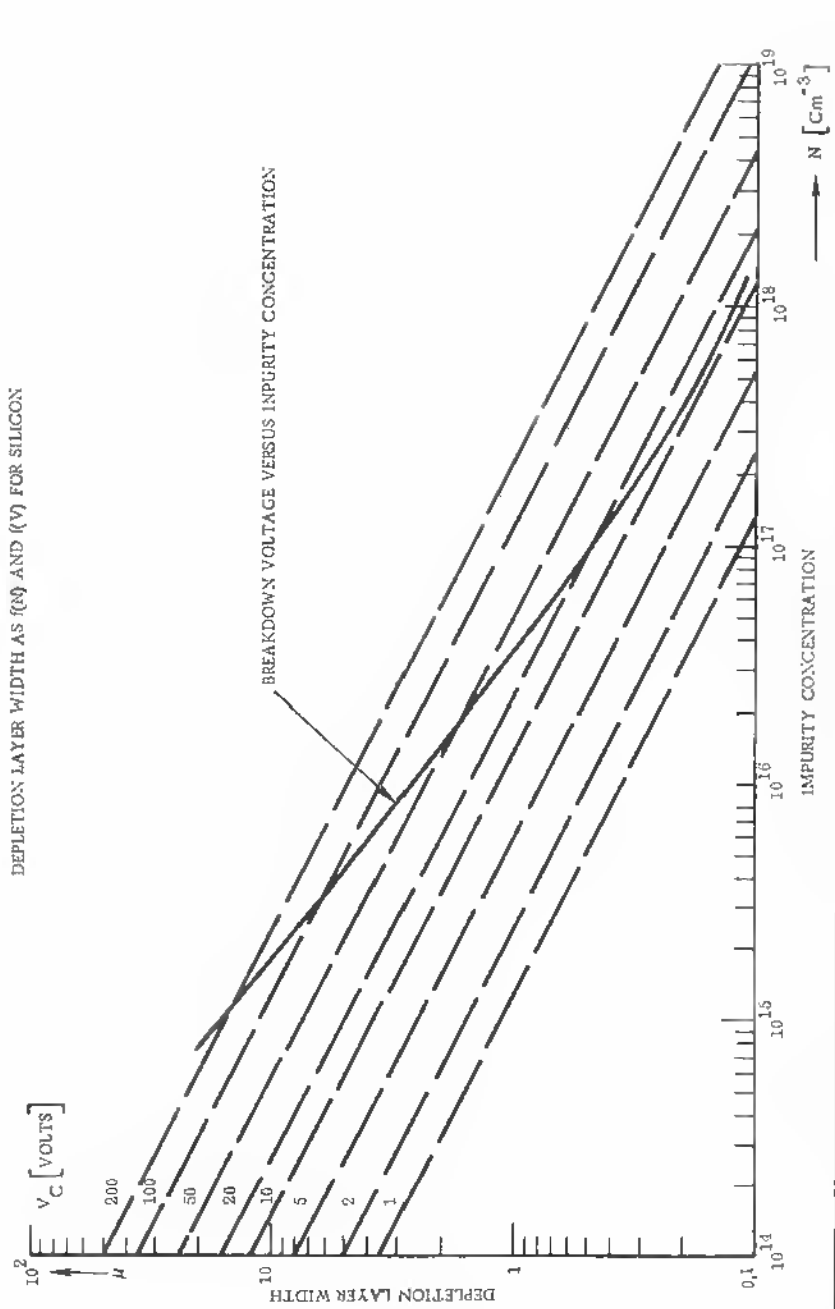


Fig. A1.16 Breakdown voltage versus impurity concentration for silicon and depletion layer width as a function of impurity concentration and breakdown voltage.

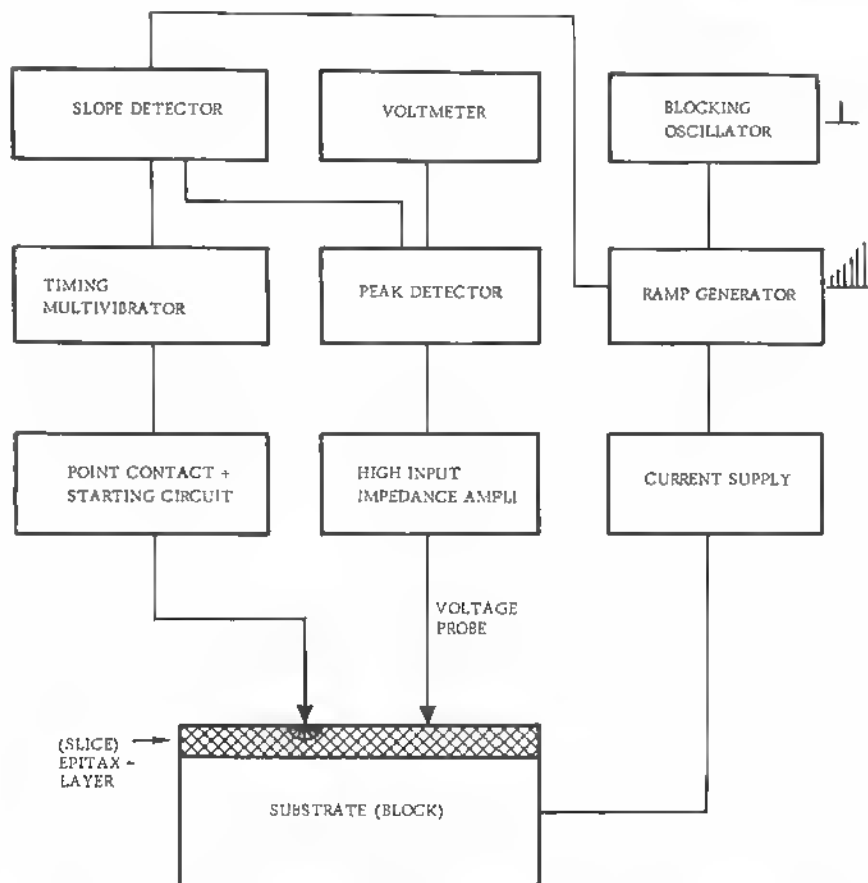


Fig. A1.17 Set-up for breakdown voltage measurements by instrument reading.

avalanche curve—Figure A1.18), this method is useful only in special cases of profiling within narrow limits. Especially profiling of high-resistivity films on low-resistivity substrates of the same type is difficult. In this case the differential capacitance technique is preferable.

### E Differential Capacitance Method

In order to carry through meaningful measurements of this type, a good mesodiode has to be made on the epitaxial layer. This is generally within the technical capability of a laboratory where such evaluation is of interest. The capacitance method has the advantage to be based on the usual MOS type of structure and to yield reproducible results without surface damage or probing.



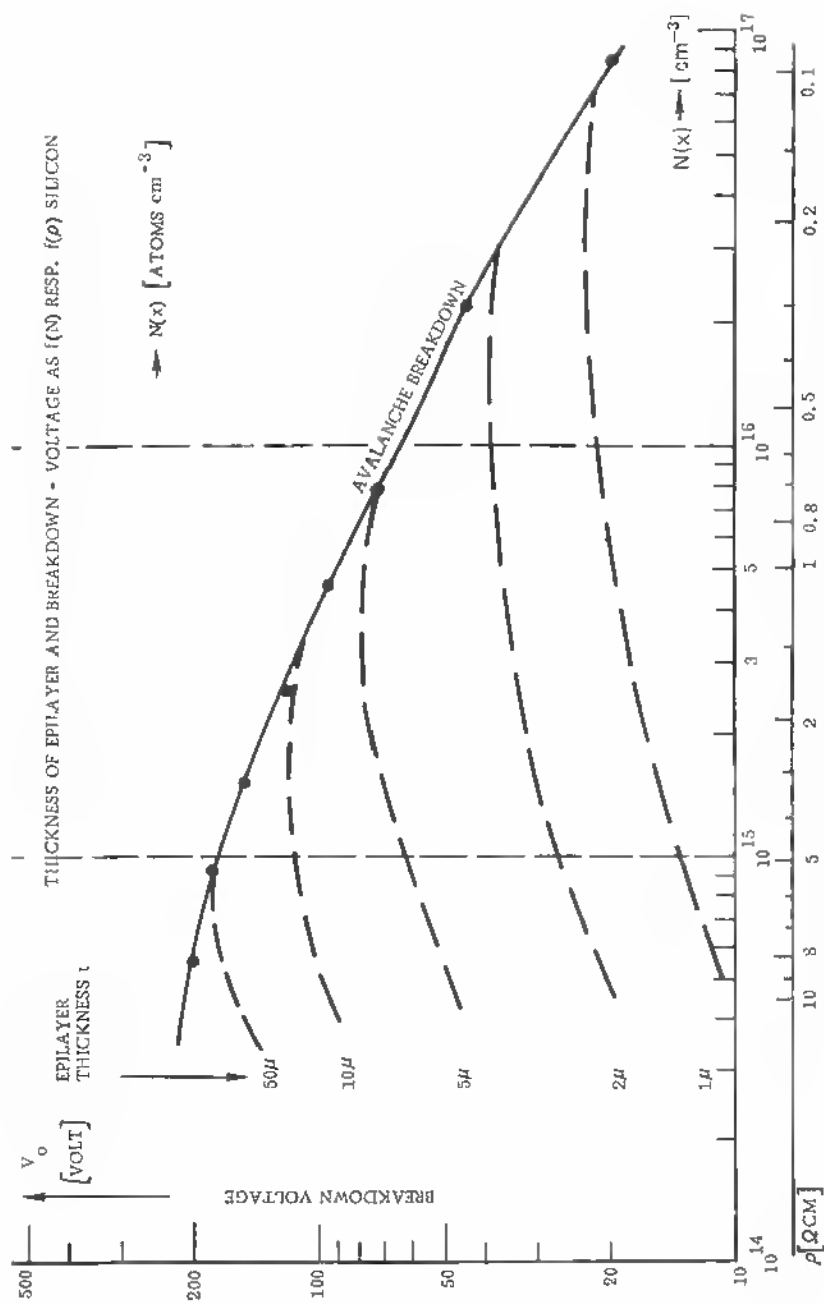


Fig. A1.18 Relations between breakdown voltage, resistivity  $\rho$ , and epitaxial layer thickness versus  $\rho$  (silicon).

On  $n$ -type silicon layers deposited on  $n^+$  or  $p$ -type on  $p^+$  substrates, a  $\text{SiO}_2$  or  $\text{SiO}$  layer of a few thousand angstroms is deposited, and small aluminum contact areas are applied to the surface of the oxide.

The capacitance of the total structure is the series capacitance of:

1. The oxide layer capacitance:  $C_0$
2. The barrier layer capacitance:  $C_s$ .

The barrier layer is formed by the surface charges at the semiconductor-oxide interface and the resultant space charge within the semiconductor. Thus

$$C = \frac{C_0 C_s}{C_0 + C_s}, \quad (\text{I.34})$$

$$C = \frac{C_0}{1 + (\epsilon_0/\epsilon_s)(x_d/x_0)}, \quad (\text{I.35})$$

$\epsilon_0, \epsilon_s$  = relative dielectric constants of oxide and semiconductor,  
 $x_d$  = depth of depletion region,  
 $x_0$  = oxide thickness.

With increasing bias a limiting capacity of the barrier layer is measured ( $\partial C/\partial V$ ) while  $C_0$  remains constant. We are interested only in

$$\frac{1}{C_{s\text{lim}}} = \frac{1}{C_{\text{lim}}} - \frac{1}{C_0}, \quad (\text{I.36})$$

or

$$C_{s\text{lim}} = \frac{C_0}{C_0/C_{\text{lim}} - 1}. \quad (\text{I.37})$$

In measuring  $C_{s\text{lim}}$ , one can derive impurity density values via a capacity per unit area versus  $N(x)$  plot, as shown for silicon in Figure A1.19.

In many cases it is possible to apply the capacitance directly to the epitaxial layer by a shallow, high surface concentration diffusion and metal contact, thereby forming a surface junction, whose dielectric is the depletion layer only. This is the same buildup, for example, as in a varactor diode. For an abrupt change from  $p$  to  $n$  at the junction, integration of Poisson's equation gives

$$\int_0^x \int \frac{\partial^2 V}{\partial x^2} dx^2 = \int_0^x \int \frac{4\pi q}{\epsilon} N(x) dx^2, \quad (\text{I.38})$$

where  $q$  = unit charge,

and for  $N(x)$  = constant =  $N$

$$V = \frac{4\pi q}{\epsilon} N \frac{x^2}{2}, \quad (\text{I.39})$$

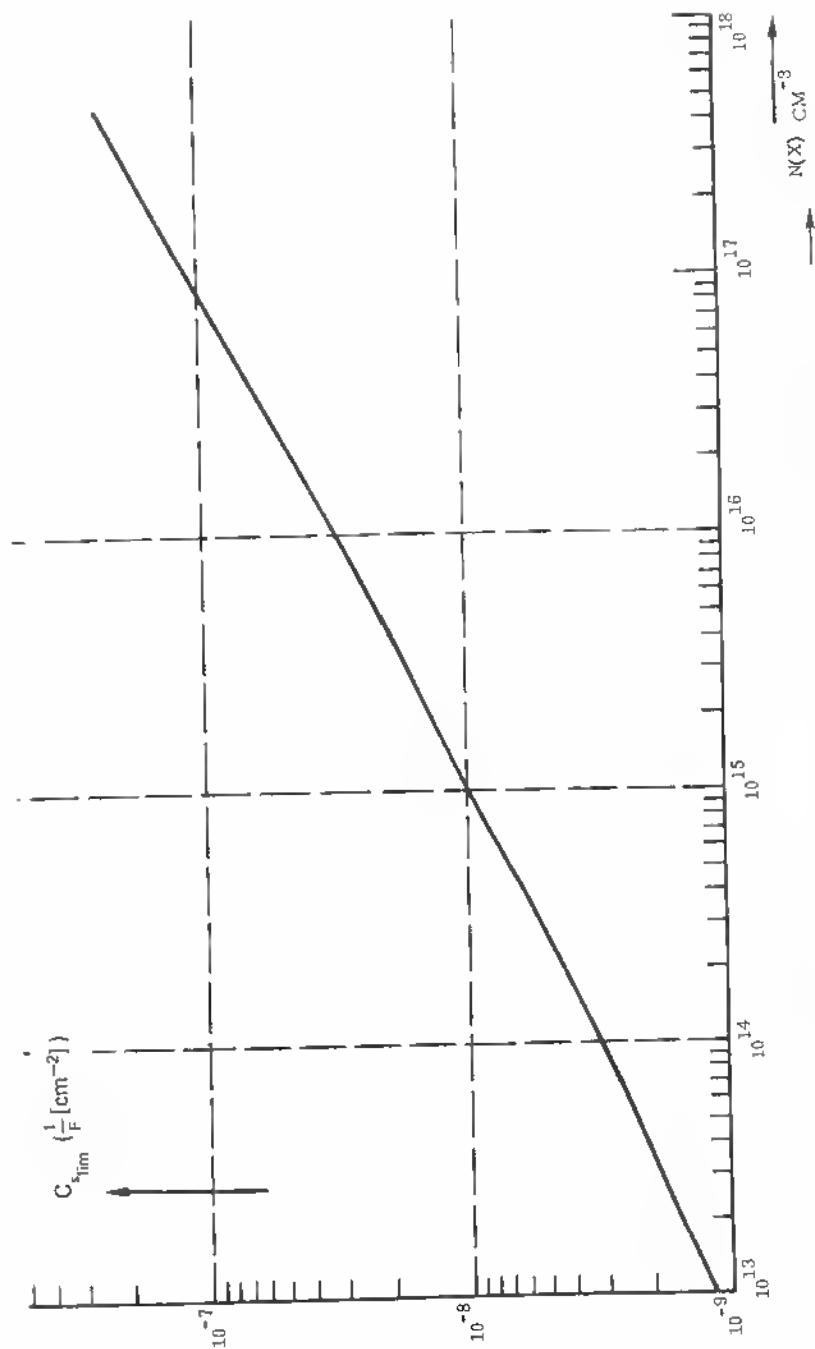


Fig. A1.19 Limit capacitance of depletion layer versus bulk concentration (silicon).

with  $C/F$  (capacity per unit area)  $= \frac{\epsilon}{4\pi x}$

$$\frac{C}{F} = \left( \frac{q\epsilon N}{8\pi} V^{-1} \right)^{1/2}. \quad (\text{I.40})$$

The capacity variation  $\frac{\partial(C/F)}{\partial V}$  is

$$\frac{\partial(C/F)}{\partial V} = -1/2 \left( \frac{q\epsilon N}{8\pi} \right)^{1/2} V^{-3/2}. \quad (\text{I.41})$$

Introducing  $V$  from (I.40) gives

$$\frac{\partial(C/F)}{\partial V} = -\frac{4\pi}{q\epsilon N} (C/F)^3 \quad (\text{I.42})$$

and

$$N = -\frac{4\pi(C/F)^3}{q\epsilon \frac{\partial(C/F)}{\partial V}}. \quad (\text{I.43})$$

$\epsilon$  is the dielectric constant defined in

$$C = \frac{\epsilon}{4\pi} \frac{F}{d} \quad \text{cm},$$

or if we use the permittivity  $\epsilon_R = \epsilon/\epsilon_0$ ,

$$C = \frac{\epsilon_0 \epsilon_R F}{d} \quad \text{farad},$$

with

$$\epsilon_0 = \frac{1}{4\pi \cdot 9} 10^{-11} \quad \text{farad/cm}.$$

In the case of a graded junction

$$N(x) = N(0) \cdot x \quad (\text{I.44})$$

the integration of the Poisson equation leads to

$$\int_0^x \int_0^x \frac{\partial^2 V}{\partial x^2} dx^2 = \int_0^x \int_0^x \frac{4\pi q}{\epsilon} N(0) dx^2, \quad (\text{I.45})$$

and

$$\frac{C}{F} = \left( \frac{q \cdot N(0)}{6} \cdot \frac{\epsilon^2}{4^2 \pi^2} V^{-1} \right)^{1/3}. \quad (\text{I.46})$$

Since here,

$$\frac{\partial(C/F)}{\partial V} = -1/3 \left( \frac{q \cdot N(0)}{6} \cdot \frac{\epsilon^2}{4^2 \cdot \pi^2} \right)^{1/3} V^{-4/3}, \quad (1.47)$$

we get

$$\frac{\partial(C/F)}{\partial V} = - \left( \frac{4\pi}{\epsilon} \right)^2 \cdot \frac{1}{qN(0)} \left( \frac{C}{F} \right)^4 \quad (1.48)$$

and

$$N(0) = - \frac{(4\pi)^2 \cdot (C/F)^4}{q\epsilon^2 \cdot \frac{\partial(C/F)}{\partial V}}. \quad (1.49)$$

The method of studying impurity densities by the surface capacitance variation is most useful for profiling high-resistivity films on low-resistivity substrates.<sup>18</sup>

#### F Spreading Resistance Technique

In the search for a method which may be applied to a wide variety of multilayered semiconductor structures and which at the same time does not require elaborate contacting procedures or device construction, one is led to the spreading resistance technique.

It has been applied with success to samples (films) of small physical dimensions and over a wide range of resistivities, from  $10^{-3} \Omega \text{ cm}$  to  $10^3 \Omega \text{ cm}$  on substrates of the same or opposite conductivity type.<sup>11,12</sup>

R. Holm<sup>13</sup> has shown that a semispherical metallic contact embedded in a homogeneous, semi-infinite solid of resistivity  $\rho$  generates a spreading resistance:

$$R_s = \int dR_s = \int_{r_0}^{\infty} \frac{\rho \, dr}{2\pi r^2}, \quad (1.50)$$

where  $r$  = radius of semisphere,

or

$$R_s = \frac{\rho}{2\pi r_0}. \quad (1.51)$$

If the metallic contact surface is flat instead of spherical, the spreading resistance is given by

$$R_s = \frac{\rho}{4\pi} \int_0^\mu \frac{d\mu}{(r^2 + \mu)\sqrt{\mu}} = \frac{\rho}{2\pi r} \arctan \frac{\sqrt{\mu}}{r}, \quad (1.52)$$

where  $\mu$  = parameter measuring equipotential-line extension into the semiconductor,

$r$  = contact radius.

For  $\mu = \infty$  (semi-infinite body of semiconductor) we have

$$R_s = \frac{\rho}{4r_0}, \quad (1.53)$$

where  $r_0$  = actual contact radius.

$R_s$  can be measured by a  $V/I$  relation, and the resistivity

$$\rho = 4r_0 \frac{V}{I} \quad (1.54)$$

can be derived. Therefore, such a measurement is basically a resistance plot for known contact radius. There are a number of constraints inherent in this method. As is well known, point contacts can have very many electrical features:

1. On  $n$ -type material it is difficult to establish ohmic contacts because of the strong formation of a surface barrier. The broken bonds at a surface have acceptor character, and the formation of a space charge is the consequence. On  $p$ -type semiconductors such surface barrier formation is less pronounced and can be induced only by high local fields.

2. At higher current levels in the forward direction, minority charge carriers are injected which reduce the apparent resistivity.

3. Even at moderate current densities the small contact area can cause joule heating, thereby changing the local carrier concentration, mobility, and band gap or causing a thermoelectric voltage.

4. Multicontacts may form under applied point electrodes and cause a spreading resistance

$$R_s = \frac{\rho}{4 \sum_v r_v}, \quad (1.55)$$

with local contact radii  $r_v$  much smaller than the contact wire area, thus inducing uneven current distribution and eventual heating.

Therefore, it was assumed for along time that this type of measurement is too ambiguous. However, a close check revealed that problems 1 to 4 can be minimized by:

1. The use of hard probes (pickup needles, osmium-tipped steel, tungsten-carbide points, etc.)
2. Voltage levels lower than a few  $kT/e$  volts. Since  $kT/e \approx 0.025$  volt, a voltage drop of  $< 1/10$  volt must be maintained. This is then below the diffusion voltage for most silicon and germanium surface barriers.

A remaining problem though is the all-present zero-bias-barrier resistance (Shive) in series with the spreading resistance itself. This and attendant effects should be accounted for by a calibration on monocrystalline material of well-known impurity density of high perfection and exacting surface treatment.

Figure A1.20 shows such calibration curves for  $n$ -type and  $p$ -type silicon. Obviously, the correction curve for  $n$ -type material gives a factor variation that is in excess of the one for  $p$ -type material. Direct measurements of the

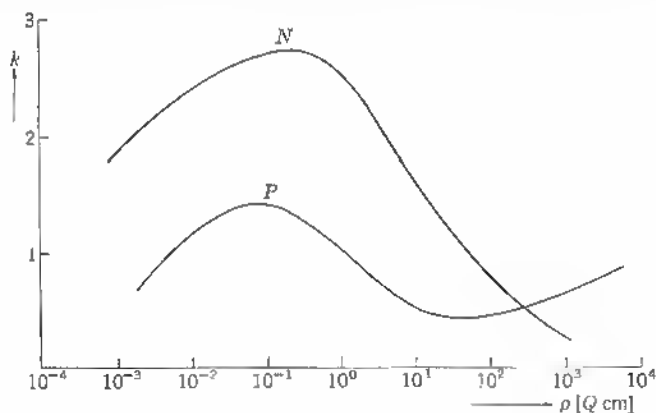


Fig. A1.20

spreading resistance by monitoring voltage and current (for example, measurement of  $R$  between probe and base contact with a Keithley 610 A instrument) at a point contact give high spatial resolution. This is important when local differences in diffusion profiles (microcircuits) have to be tested and when small samples of epitaxial layers on heavily doped substrates are being checked. If an isolating junction exists between films and substrate, all methods using breakdown voltage and differential capacitance measurements are difficult to apply. Spreading resistance measurements are applicable, however, and can be modified easily for such cases. At the sacrifice of some spatial resolution, a three-point probe can be used.

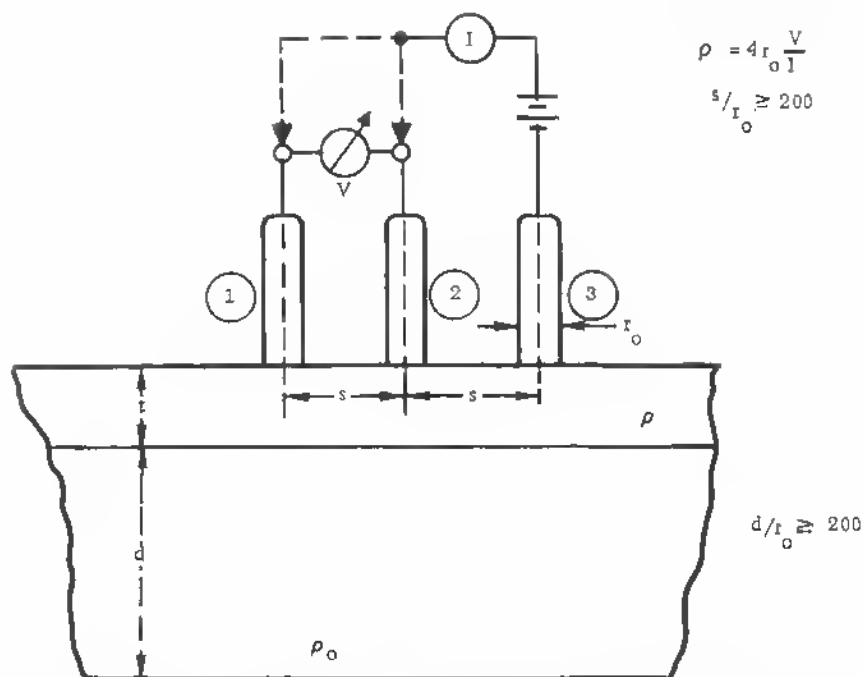


Fig. A1.21 Three-point probe spreading resistance set on epitaxial layer.

As shown in Figure A1.21, the small current injection can take place between two probes 1 and 3 or 2 and 3, and the voltage readings can be taken between probes 1 and 2 in either case. The spreading resistance is again given by  $R_s = \rho/4 \cdot r_0$  for a spacing  $s$  of a few times  $r_0$ . The critical dimension is the probe radius  $r_0$  in relation to the layer thickness  $t$ . For the semi-infinite case,

$$\frac{t}{r_0} \geq 10,$$

there is no correction, but below this value, we have to add a correction factor  $CF$ :

$$R_s = \frac{\rho}{4r_0} \cdot CF.$$

Two limiting cases are given as follows:

$\frac{\rho}{\rho_0} = 0$  for an insulating boundary between the upper layer and the substrate,

$\frac{\rho}{\rho_0} = \infty$  for a perfect conductor as substrate.



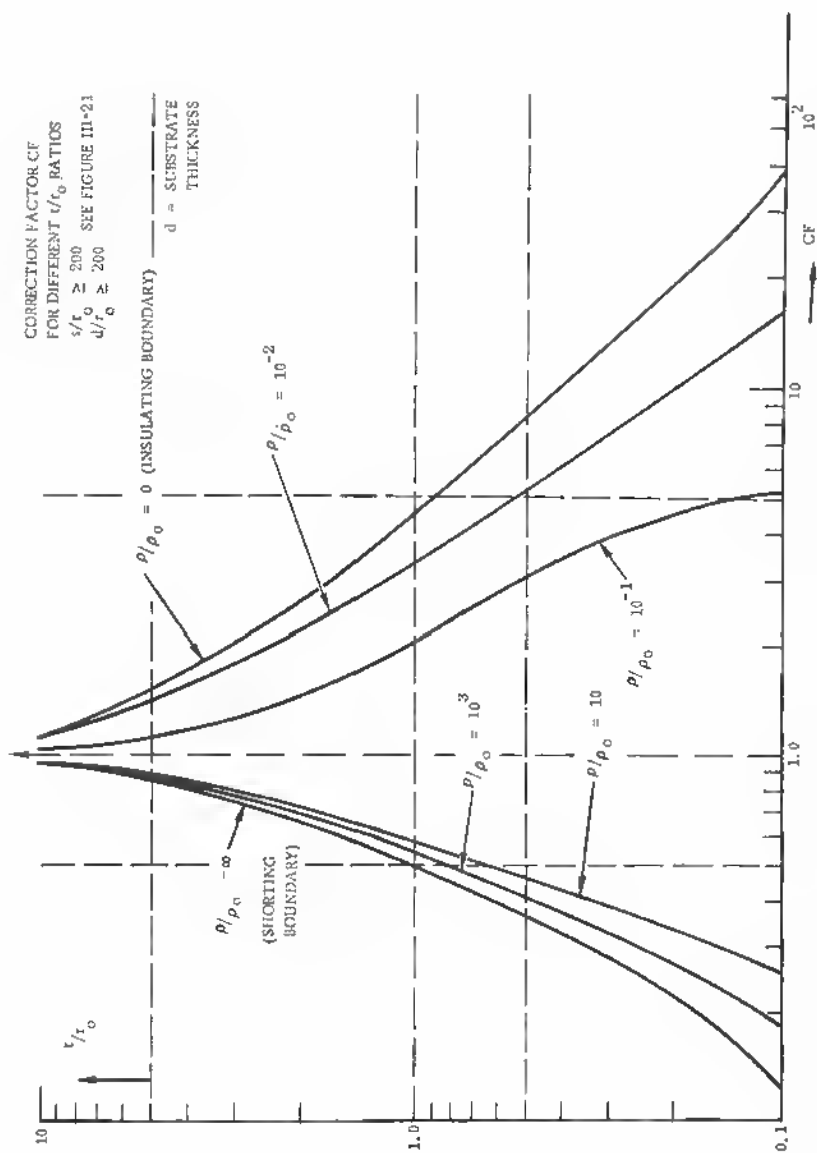


Fig. A1.22 Correction factor  $CF$  or different  $t/r_0$  (epilayer thickness probe radius). Ratios with  $s/r_0$  (probe distance radius).

Figure A1.22 shows the correction factor for the two limiting cases and intermediate values of  $\rho/\rho_0$ .

The total spreading resistance as measured contains again the zero-bias-barrier resistance. Therefore, the complete formula is

$$R_s = k \frac{\rho}{4r_0} \cdot CF,$$

where  $k$  is as given in Figure I.20 for silicon. Another way of writing the actually measured spreading resistance is

$$R_s = \frac{\rho}{4r_0} CF + R_{BR},$$

where  $R_{BR}$  is the additional resistance due to the zero-bias-barrier. In using this equation,  $R_{BR}$  has to be assessed separately.

The spreading resistance method applied with the necessary know-how offers a number of possibilities for routine layer measurements, since no special device formation is needed and since spatial resolution can be obtained that is within the requirement limits for microcircuit and thin-film testing. In conjunction with the differential capacity test, which determines carrier concentration  $N(x)$  directly, the carrier mobility

$$\mu = [q \cdot \rho \cdot N(x)]^{-1},$$

where  $q$  = electronic charge,

can be found directly (see under Mobility).

### G. Microwave Methods

Because of the time-consuming probe positioning and the eventual damage to the semiconductor surface, other methods have been devised. An elegant method of measuring the resistivity of large quantities of wafers is the microwave transmission or reflection method. In this method no contacts to the sample are established, and no correction is necessary because of probe positioning. Thin-film semiconductors that would be damaged by a point-probe method can be subjected to this type of measurement without applying evaporated contacts. The major correction in the case of microwave measurements stems from the penetration limitation. Three methods can be applied in this case:

1. Reflection coefficient
2. Transmission measurement
3. Measurement in a high  $Q$  cavity

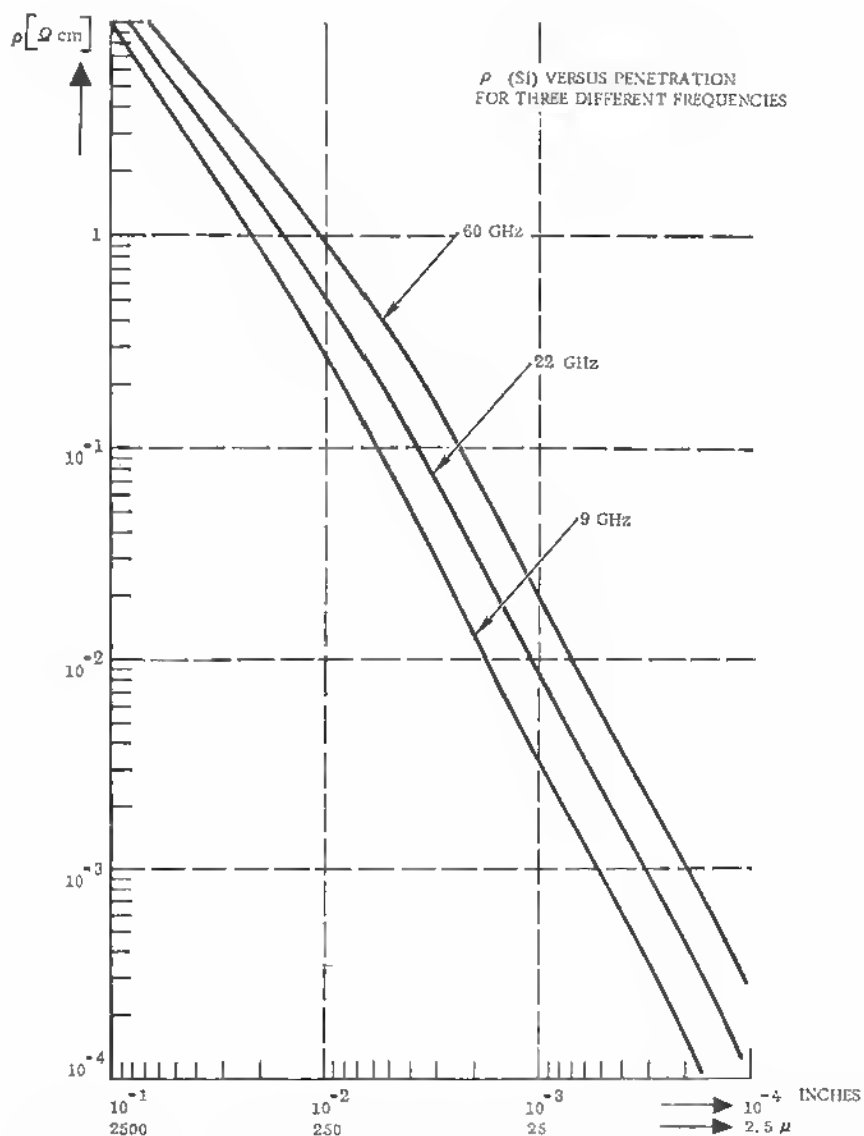


Fig. A1.23 Skin depth or three different microwave frequencies in silicon versus resistivity.

In case 1, the semiconductor crystal or slice or layer is used to terminate a transmission line, and the return loss is measured. This return loss is dependent only on resistivity if no transmission loss occurs. To assure a sufficient sample thickness, diagrams of the form given in Figure A1.23 should be used which show the correlation among, resistivity range, sample thickness, and frequency used. The skin depth is given by

$$\delta = \frac{1}{2\pi f \left[ \frac{\mu\epsilon}{2} \left( 1 + \frac{1}{(2\pi f)^2 \epsilon^2 \rho^2} \right)^{1/2} - 1 \right]^{1/2}},$$

where  $\delta$  in meters,

$f$  = frequency, c/s,

$\mu$  = permeability =  $4 \cdot 10^{-7}$  henries/meter,

$\epsilon$  = dielectric constant =  $8.85 \cdot 10^{-12}$  farads/meter (air),

$\epsilon$  =  $1.062 \cdot 10^{-10}$  farads/meter for silicon,

$\rho$  = resistivity, ohm meters.

The penetration in inches and also in microns is plotted in Figure A1.23 for three typical microwave frequencies. Change with resistivity (ordinate) is very strong. The frequency plotted as parameter has a minor influence. For small sample width, however, the frequency should be chosen that allows a reasonable resistivity range to be measured.

In another graph the skin depth versus resistivity for different frequencies up to 300 GHz is plotted for the lower values of  $\delta$  in microns. The increasing requirements with respect to frequency make measurements difficult in the range of thin films with normal impurity doping (Figure A1.24). For films of several microns thickness and within the resistivity range of  $10^{-3}$  to 10 ohm cm, a frequency of 9 GHz is necessary.

For the lower range of thicknesses, the necessary frequency gets already into the infrared range (1 to 30 microns). The reflection method works well for a limited range of resistivities (once a frequency is chosen). The dynamic range is limited to a few decibels difference, however, between a sample of low resistivity (return loss = 0 decibel, all power absorbed) and a sample of higher resistivity. (perfect impedance match, return loss is infinite.) A typical calibration curve is shown in Figure A1.25.

The second method—microwave transmission—is based on the measurement of power loss when the sample is inserted into a waveguide. In this case one must independently measure sample thickness and use a frequency-resistivity range for complete transmission through the sample. As Jacobs et. al.<sup>15</sup> have shown, a calibration of power transmission through semiconductor slabs (germanium) within a limited conductivity range can be represented by a linear relation.

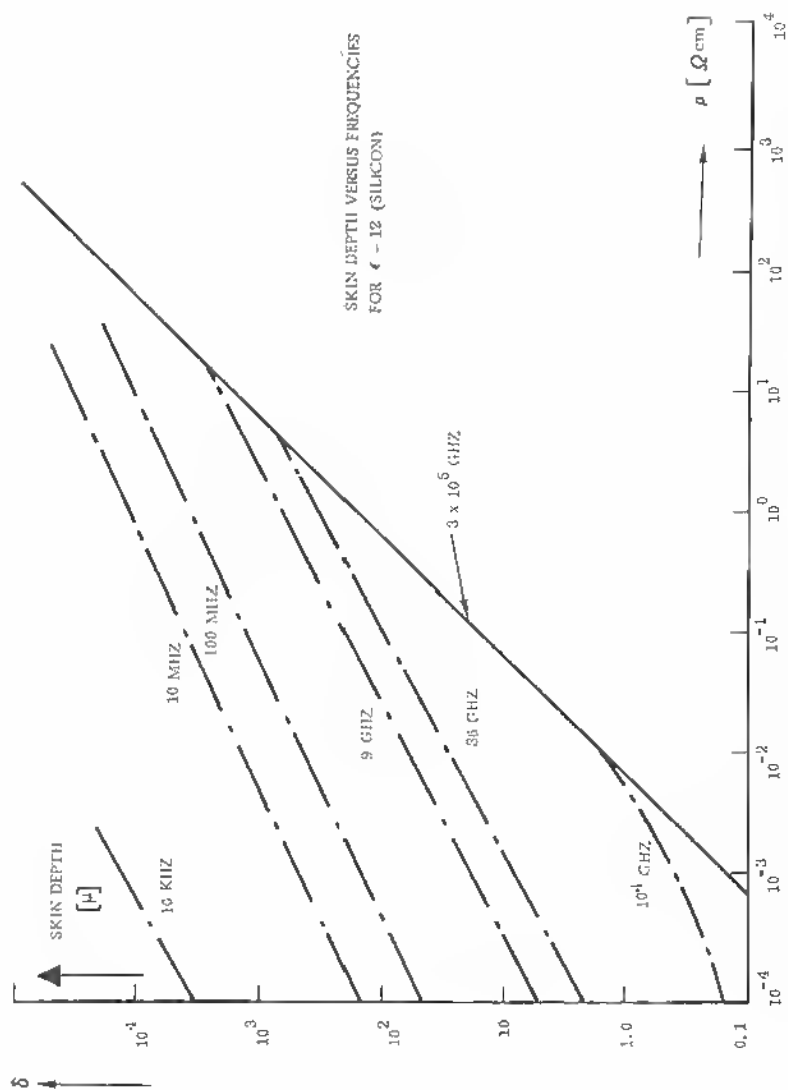


Fig. A1.24 Skin depth resistivity for silicon for a wider range of frequencies (10 kHz  $\rightarrow$  3.10<sup>5</sup> GHz).

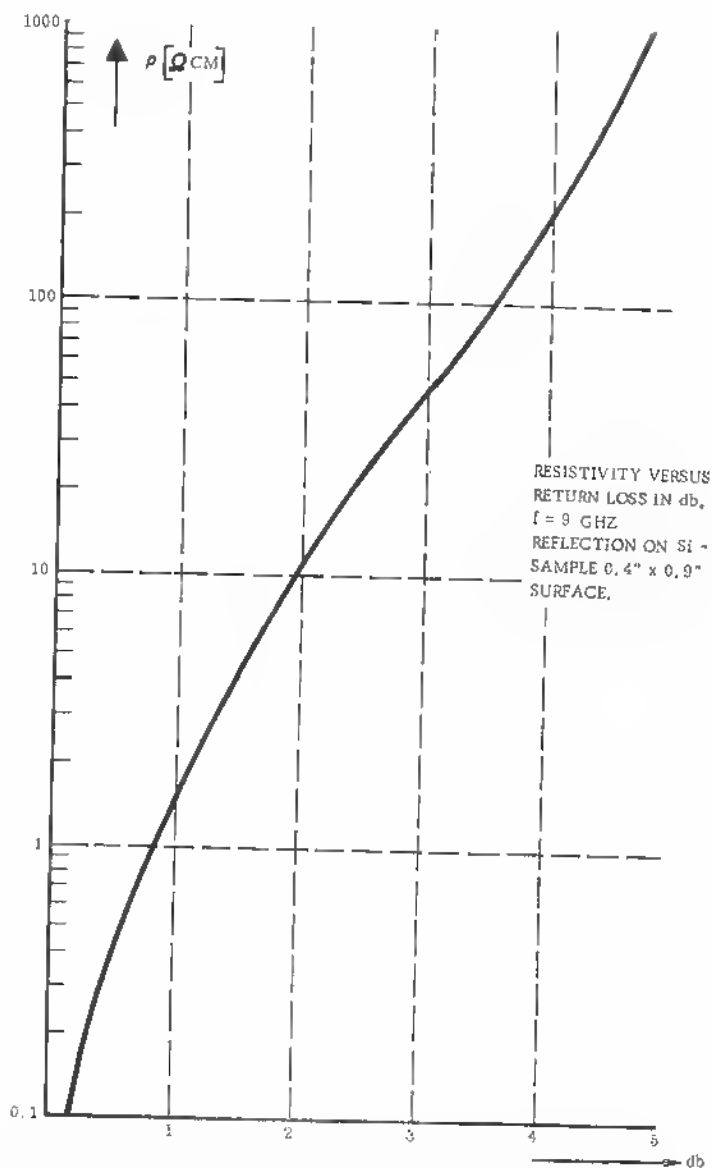


Fig. A1.25 Resistivity versus return loss in decibels of microwaves ( $f = 9$  GHz) on silicon crystal surface. Sample  $0.4 \times 0.9$  in. surface area.

The condition

$$\frac{\sigma}{\epsilon} \ll \omega,$$

where  $\sigma$  = conductivity, (ohm meter)<sup>-1</sup>,  
 $\epsilon$  = dielectric constant of semiconductor,  
 $\omega = 2\pi f$  = angular frequency,

for postinsertion into wave guides can be relaxed in the transmission method to include the range  $\sigma \geq \omega\epsilon$ . This method has special merit in lifetime studies (see under A 11).

It is advantageous that both methods—reflection and transmission—implement each other with respect to resistivity value and sample thickness. The third method is based on the  $Q$  change of a high  $Q$  cavity by making the test sample a section of the cavity wall (opening in the cavity is covered by the test sample.) The sensitivity amounts to 3 to 4 decibels per decade of resistivity change in a typical case and allows some interpolation for a frequency of, for example, 22 GHz.

These microwave methods have also been applied to Gallium Arsenide.<sup>16</sup> In all cases, empirical calibration is necessary, and in the case of thin samples, composite structures can only be measured by reflection methods, since transmission through an epitaxial layer + substrate would be difficult to interpret even for high resistivity substrates. But even in convenient ranges of resistivity (skin depth) and sample thickness, the reflectance method is limited because of the requirement of a certain minimum area for the sample surface under test. Generally, such areas lie shortly below 1/2 inch<sup>2</sup> and can be reduced by a partial cover with brass, which also reduces the sensitivity, or one may use a higher frequency, but there is no possibility of applying the microwave methods within areas of interest in microcircuits.

## REFERENCES

1. Catalano, S.: "Correction Factor Curves for Square Array and Rectangular Array Four-Point Probes Near Conducting and Nonconducting Boundaries." *IEEE Transactions, Electron Devices*, vol. ED-10, No. 3, pp. 185-188, May 1963.
2. Van der Pauw, L. J.: "A Method of Measuring Specific Resistivity and Hall Effect of Discs of Arbitrary Shape." *Phillips Research Reports*, vol. 13, No. 1, pp. 1-9, February 1958.
3. Mircea, A.: "Semiconductor Sheet Resistivity Measurements on Square Samples." *Jr. of Scientific Instruments*, vol. 41, pp. 679-681, 1964.
4. Mircea, A.: "The Geometric Factor in Semiconductor Four-Probe Resistivity Measurements." *Solid State Electronics*, 6, pp. 459-462, 1963.
5. Tannenbaum, E.: "Detailed Analysis of Thin Phosphorus-Diffused Layers in *p*-Type Silicon." *Solid State Electronics*, vol. 2, pp. 123-132, 1961.

6. Lamorte, M. F.: "Calculation of Concentration Profiles and Surface Concentration From Sheet Conductance Measurements of Diffused Layers." *Solid State Electronics* vol. 1, pp. 164-171, 1960.
7. Patrick, W. J.: "Measurement of Resistivity and Mobility in Silicon Epitaxial Layers on a Control Wafer." *Solid State Electronics*, vol. 9, pp. 203-211, 1966.
8. Schumann, Jr. P. A., and J. F. Hallenback, Jr.: "A Novel Four-Point Probe for Epitaxial and Bulk Semiconductor Resistivity Measurements." *Jr. of the Electrochemical Society*, vol. 110, pp. 538-542, 1963.
9. Gardner E. E. and P. A. Schumann, Jr.: "Measurement of Resistivity of Silicon Epitaxial Layers by the Three-Point Probe Technique." *Solid State Electronics*, vol. 8, pp. 165-174, 1965.
10. Allen, C. C., L. H. Clevenger, and D. C. Gupta: "A Point Contact Method of Evaluating Epitaxial Layer Resistivity." *Jr. of the Electrochemical Society*, May vol. 113, pp. 508-510, May 1966.
11. Mazur, R. G. and D. H. Dickey: "A Spreading Resistance Technique for Resistivity Measurements on Silicon." *Jr. of the Electrochemical Society*, vol. 113, pp. 255-259, 1966.
12. Gardner, E. E., P. A. Schumann, Jr., and E. F. Gorey: "Resistivity Profiles and Thickness Measurements on Multilayered Semiconductor Structures by the Spreading Resistance Technique." *Extended Abstracts, Jr. of the Electrochemical Society*, Edited by B. Schwartz and N. Schwartz, pp. 258-272, 1967.
13. Holm, R.: "Technical Physics of Electric Contacts," 3rd Edition, Springer, Berlin, 1958.
14. Allerton G. L. and J. R. Seifert: "Resistivity Measurements for Semiconductors," *The Western Electronic Engineer*, pp. 43-48, July 1961.
15. Jacobs, H. F., A. Brand, J. D. Meindl, S. Weitz, B. Benjamin, and D. A. Holmes: "New Microwave Techniques in Surface Recombination and Lifetime Studies." *Proceedings IEEE*, pp. 581-592, April 1963.
16. Quinn A. C. and J. C. Looney: "Microwave Methods for Measuring Resistivity of Gallium Arsenide." *Semiconductor Products ÷ Solid State Technology*, pp. 46-50, April 1967.
17. Keller, W.: "Messung des specif. Widerstandes von Halbleiter-kristallen mit Hochfrequenz." *Zschr.f.angewandte Physik* vol. II, 9, 1959 pp. 346-350.
18. Gupta, D. C.: "Diode-Voltage-Capacitance Method for Measuring Resistivity and Impurity Profile in a Silicon Epitaxial Layer," *Solid State Technology*, pp. 31-34, February 1968.

## II HOMOGENEITY

One of the most important characteristics of qualified monocrystals for devices is the homogeneity with respect to doping. It is well known that dopant clusters form around nucleation centers. Such centers may be formed by point defects, especially in the form of vacancies, but also by interstitials and partial dislocations. Dislocations and dislocation arrays (grain boundaries) present large area discontinuities and are considered unlikely in good



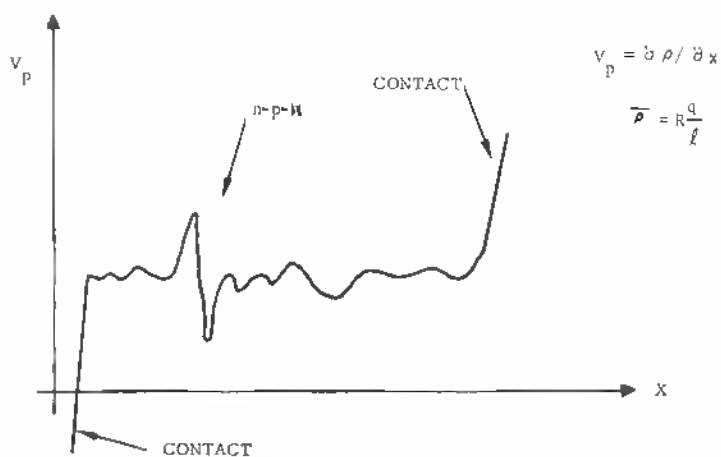
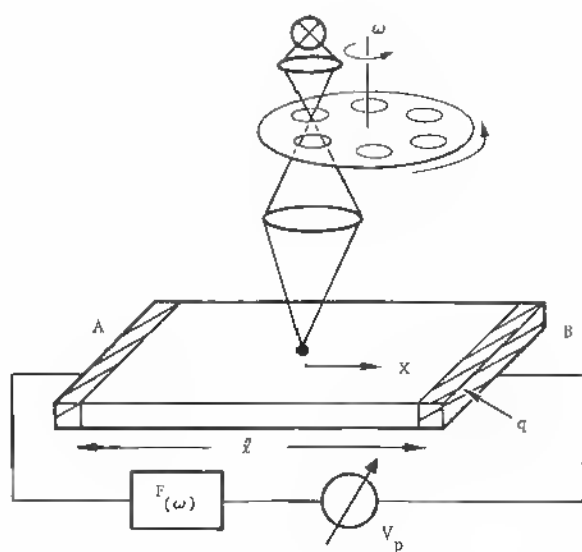


**Fig. AII.1** Crystal homogeneity test by the photo-injection method and photo-voltage versus distance  $x$ .

monocrystalline material of low dislocation count. But even so-called dislocation-free monocrystals show etch figures of different kinds (saucers, etc. which, in most cases, can be associated with impurity clusters or, in a more general way, with the uneven distribution of foreign atoms and active centers.)

In the search for a sensitive method of plotting resistivity profiles or doping topographs for crystals of high perfection, one is led to the use of the photo-injection method. This method consists of a light injector applied to the surface of the semiconductor crystal and two contacts applied to this crystal. These contacts are connected by leads to a tube voltmeter. The light source is modulated, for example, by a rotating disk. A bandpass filter only passes the frequency thus generated. The light source is a small point focussed onto the crystal surface by a bifocal lens (Figure AII.1). By the modulation with a low-frequency  $\omega$  and application of a filter, parasitic and noise injections can be eliminated.

The contacts *A* and *B* to the sample are not critical. They may even be formed by pressure contacts if soft tin-lead compounds are used, since a formation of depletion regions at the contacts does not change the plot of local injection differences with the crystal area scanned as long as the light point is more than a diffusion length away from the rectifying contact. The plot of the photovoltage  $V_p$  developed at the contacts due to light injection yields a conclusive view of the homogeneity of a crystal.  $V_p$  being proportional to  $\partial\rho/\partial x$  (resistivity gradient), all inhomogeneities resulting in a local resistivity gradient contribute to the photovoltage developed. Stoichiometric variations, however, are marked differently from, for example, variations in crystal orientation especially lineage and grain boundaries.

Because of the acceptor character of dislocations, the latter ones show up in a distinct manner as sharp zero passage (Figure AII.1), but doping gradients show only a slow decrease or increases in photovoltage. This is also the case for twin boundaries which generally separate zones of different doping because of the diagonal displacements without dangling bonds. By using the optical scanner in two directions, a two-dimensional plot (*xy*) of the resistivity profile is possible. Observation of the photovoltage on an oscilloscope in connection with *xy* scanner gives, at a glance, the location of an inhomogeneity of undesirable proportions.

The association of a light-intensity gradient with the *y* displacement of the scanner allows a separation of the  $V_p$  curves on the screen (Figure AII.2). Local inhomogeneities have been mapped recently by application of a laser beam as light source.<sup>2</sup>

Different light frequencies can be used to scan in depth or only at the surface. In general, the crystals to be tested are thin, and light frequencies with a

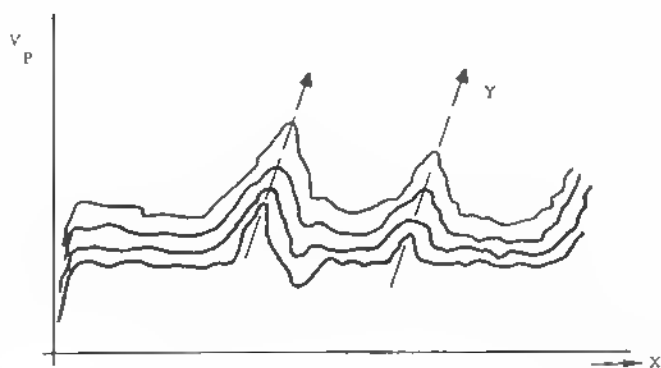
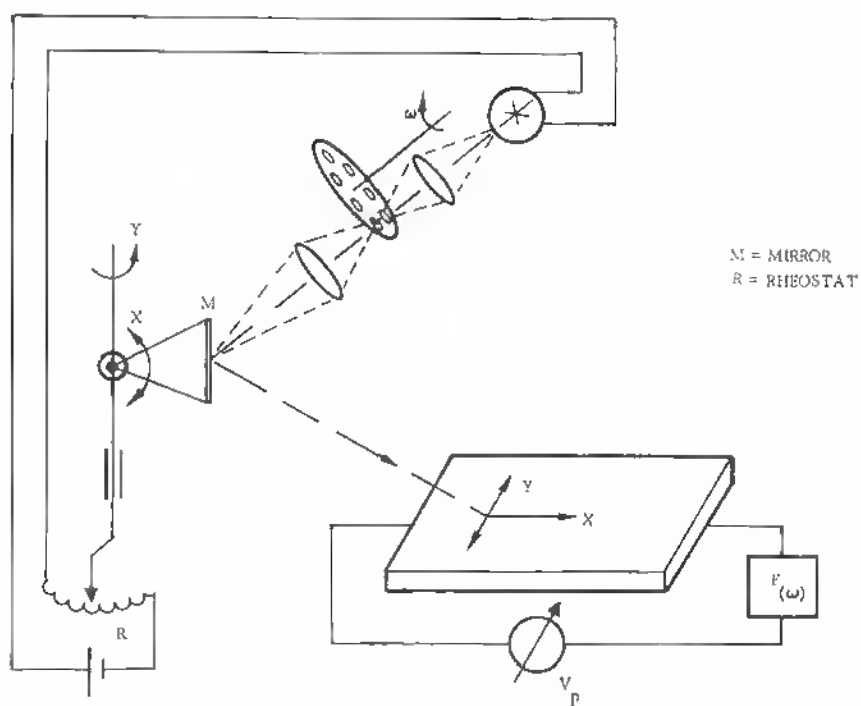


Fig. AII.2  $x$ - $y$  scanning of crystal for photovoltage-homogeneity test and photovoltage-profile.

near infrared component are always sufficiently penetrating to give a mean value across the wafer thickness.

The light-injection scanning method can be applied in principle also to a lifetime profile. In this case the light source has to allow for pulsed operation. As in the usual lifetime method (Section III), a light burst, for example, from an arc or high-pressure mercury lamp, is applied locally and the decay curve plotted on the oscilloscope. With a remanescant screen, several decay curves can be compared for different irradiated locations on the crystal. Again, a superposition on the cathode-ray screen is feasible if variable injection intensities are used. Local lifetime inhomogeneities are more difficult to measure than local resistivity variations. In general, the plot of the resistivity variations  $\partial\rho/\partial x$ ,  $\partial\rho/\partial y$  already shows sufficiently if the crystal is useful for devices within the dimensions tested.

Regions of large changes of  $\partial\rho/\partial x$  are generally connected to dislocations and trap levels and are, therefore, already recognized as the problem points in crystals also with respect to lifetime and mobility.

In highly dense arrangements of devices in microcircuits on wafers or thin films (epitaxial material) it is always desirable to eliminate the base material of doubtful perfection in order to cut down the costs of processing and eliminate reject from the start.

Therefore, the photoelectrical scanning method is extremely useful. The sensitivity is very high, since the actual gradient at the injection point defines the photovoltage developed.

Integration of the  $V_p$  versus  $x$  curve can easily be done<sup>1</sup>, but in this case the value of

$$\int_0^l \frac{\partial\rho}{\partial x} dx \quad (\text{II.1})$$

gives the mean value of the resistivity, and, therefore, nothing more than a four-point probe is able to produce.

## REFERENCES

1. Oroshnik J, and A. Many: "Photovoltaic Scanning," *Jr. of the Electrochemical Society*, 106, 4, 360, April, 1959.
2. Kikuchi, M: "Localized Nature of the Current Oscillation in Semiconductors Due to Deep Levels" *Jr. of Applied Physics*, 37, No. 11, pp. 4285-4286, October, 1966.
3. Avery D. G, and J. B. Gunn: "The Use of a Modulated Light Spot in Semiconductor Measurements," *Proceed. Phys. Soc. (London) Sec. B* pp. 918-921, 1955.

### III LIFETIME MEASUREMENTS

For bipolar transistors the lifetime is the most important crystal parameter that defines junction quality, injected carrier survival rate, and thus also the amplification. In order to study lifetime over the full range of crystal types (low-frequency power devices to high- and very high-frequency audio types), varied equipment is necessary, since we may have to cover values from  $10^{-3}$   $\mu\text{sec}$  or even below  $1 \text{ nsec}$  up to several thousand  $\mu\text{sec}$  ( $10^{-3}$  sec or range of milliseconds). A wealth of methods has been developed to effect these measurements. They can be classified in three main groups as described in the paragraphs that follow.

#### A Transient Methods

Measurement of the conductivity decay over time when a crystal between ohmic contacts is subjected to light pulses.

#### B Steady-State Methods

Measurement of the amplitude variation with displacement of a collector point under constant (modulated) illumination.

#### C PhotoMagnetoelectric Methods

Here the crystal is subjected to a steady-state light injection and to an electric field as well as to a magnetic field.

In addition to these methods, special processing has been developed to study the lifetime of minority carriers within a finished device like a junction diode. In this case the minority carriers are electrically injected by application of a pulse to the junction, and the current decay is followed on an oscilloscope.

More sophisticated methods are being used when the surface recombination velocity is high (silicon) and surface states have to be saturated before a bulk value can be determined. This is done either by additional dc light injection superimposed on the pulse light source or by the double-pulse method.<sup>9</sup>

Finally, we have to mention methods for resistivity measurements. They affect strongly the measurement of mobility values, since generally the conductivity is given by  $\sigma = \mu q N$ , where

$\mu$  = mobility,

$\frac{1}{\sigma}$  = resistivity,

$q$  = electron charge,

$N$  = carrier density.

*Method A, Transients*

The transient case is described in Figure AIII.1. Here the crystal sample (for example, silicon) is subjected to a light pulse (repetition rate long compared with lifetime), and the conductivity decay over time is observed on the oscilloscope (Figure AIII.2). If the conductivity decay at the half point is observed, we have, from the fundamental decay law,

$$\sigma \approx \exp\left(\frac{-t}{\tau}\right),$$

$$\ln 1/2 = \frac{-t}{\tau},$$

or

$$\tau_{1/2} = \frac{t}{\ln 2}.$$

Therefore, we only need to read the  $t$  value (abscissa) at the  $\sigma_{1/2}$  value and divide by  $\ln 2$  to obtain the actual lifetime. It is easier to plot the decay curve directly on semilogarithmic paper. In this case the  $\exp(-t/\tau)$ -curve is linearized (Figure AIII.3):

$$y = \ln \sigma = \frac{-t}{\tau}.$$

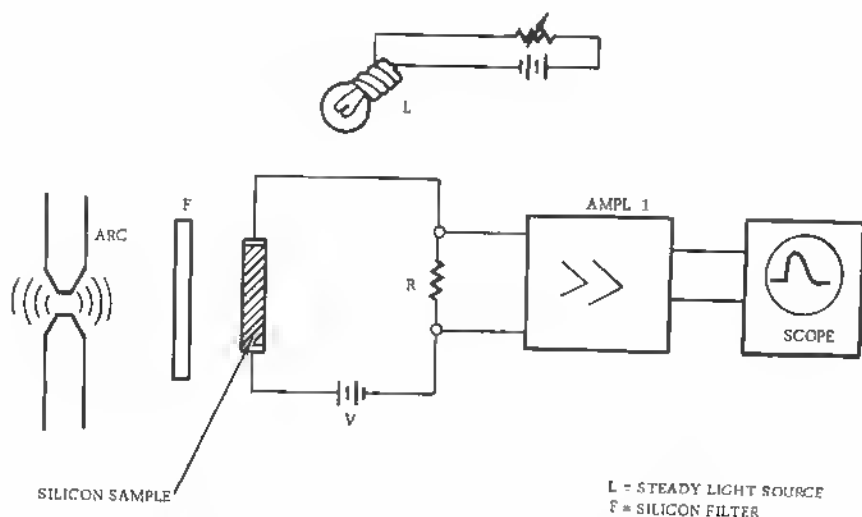


Fig. AIII.1 Lifetime check by light-pulse injection method.

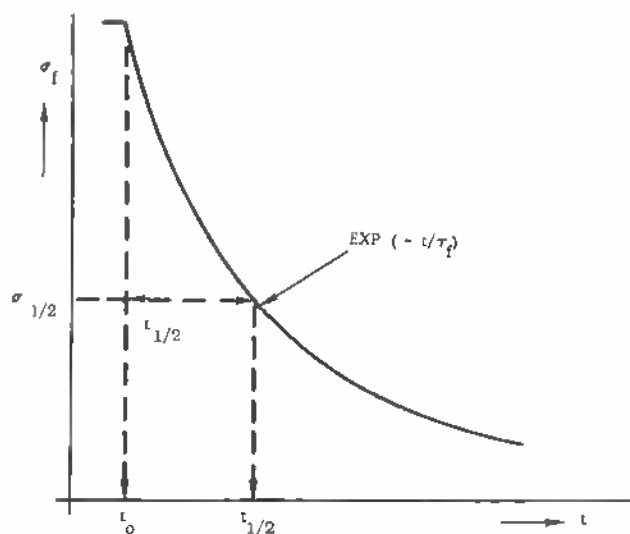


Fig. AIII.2 Exponential signal decay curve and lifetime  $\tau_f$ .

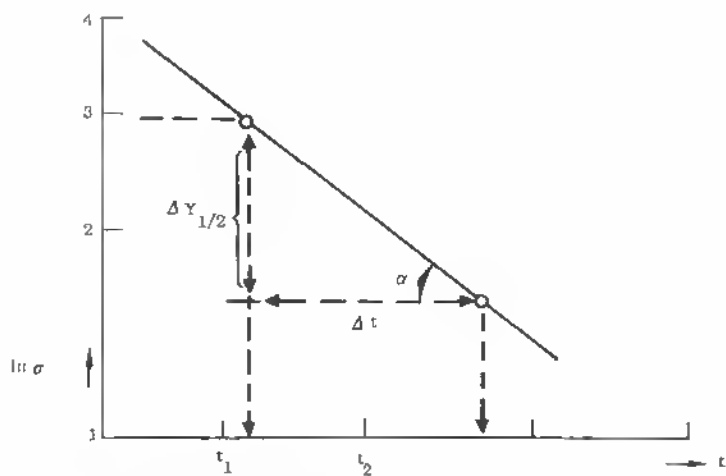


Fig. AIII.3 Semilogarithmic plot of  $\sigma$  versus  $t$  [ $\text{ctg } \alpha = T$ ].

We read

$$\tan \alpha = \frac{\Delta y_{1/2}}{\Delta t};$$

then

$$\tau = \frac{1}{\tan \alpha} = \operatorname{ctg} \alpha$$

(see Refs. 1 and 2).

Measurements of time-decay curves applied to diode structures are of a similar nature and belong to the same category. In this case, a current pulse is applied to the diode  $p$ - $n$  junction in the forward direction. The pulse generates a minority carrier cloud across the junction that decays in a time defined by the effective lifetime of the material (Figure AIII.4). A pulse generator delivers

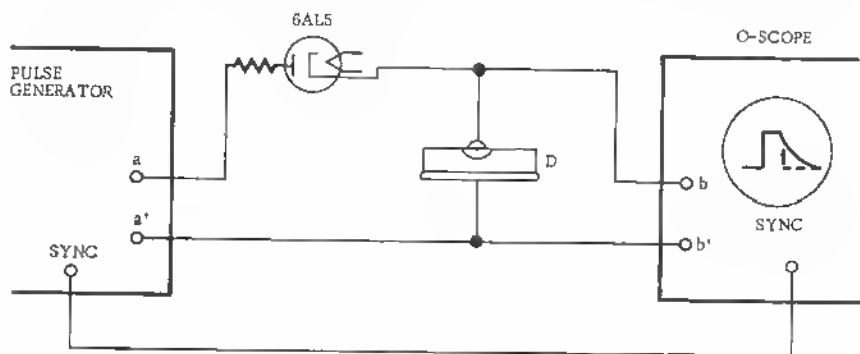


Fig. AIII.4 Lifetime test by electronic pulse injection into junction.

a rectangular pulse at  $a$ - $a'$  in a direction with the positive side on the  $p$ -type junction side, for example, indium on  $n$ -type germanium (rectifier tube 6AC5 in series). At  $b$ - $b'$  the pulse appears and is monitored by an oscilloscope. Here the pulse tail is plotted, and its slope serves to define the effective lifetime. Pulse rise and decay times have to be measured ( $\tau_r \approx 1/10 \tau_{eff}$ ). Pulse length and repetition frequency are usually in the  $10 \mu\text{sec}$  and  $3,000 \text{ p/sec}$  range, respectively.<sup>3</sup> The method is consistent with the known Haynes-Shockley method,<sup>4</sup> with the only difference that a defined, grown, or alloyed or diffused junction serves to inject the minority carrier pulse. In the latter case, we can use directly the junction equation to find the relation between excess hole density and voltage. The hole density at the  $p$ - $n$  junction being given by



$$p = p_n e^{\alpha V}, \quad (\text{III.1})$$

where  $\alpha = \frac{q}{kT}$ ,

$q$  = unit charge,

$kT$  = Boltzmann factor.

One may directly introduce the excess hole density  $\Delta p$  by writing

$$p = p_n + \Delta p \quad (\text{III.2})$$

in the  $n$ -type region. Equation (III.2) into (III.1) yields

$$V = \frac{kT}{q} \ln \frac{p_n + \Delta p}{p_n}. \quad (\text{III.3})$$

One may assume that the excess carrier concentration  $\Delta p$  decays exponentially with a single carrier effective lifetime. This means that

$$\Delta p \approx \Delta p_0 e^{-t/\tau}, \quad (\text{III.4})$$

where  $\Delta p_0$  = excess carrier concentration at the termination of the forward current pulse. Equation (III.4) with (III.3) yields

$$V = \frac{kT}{q} \ln \left( 1 + \frac{\Delta p_0}{p_n} e^{-t/\tau} \right). \quad (\text{III.5})$$

We may now define that a voltage  $V_0$  measured at  $\alpha\text{-}\alpha'$  (Figure III-4) is simply the stationary portion in (III.5):

$$V_0 = \frac{kT}{q} \ln \left( 1 + \frac{\Delta p_0}{p_n} \right). \quad (\text{III.6})$$

Therefore, we may express  $\Delta p_0/p_n$ , the relative excess hole density, by (III.6):

$$\frac{\Delta p_0}{p_n} = e^{qV_0/kT} - 1. \quad (\text{III.7})$$

Equation (III.7) into (III.5) yields

$$V = \frac{kT}{q} \ln [1 + (e^{qV_0/kT} - 1)e^{-t/\tau}]. \quad (\text{III.8})$$

For  $t/\tau$  small and  $V_0 \gg kT/q$  (voltages in excess of 1/40 volt are applied), one gets

$$V \approx V_0 - \frac{kT}{q} \frac{t}{\tau}, \quad (\text{III.9})$$

or

$$|\tau| = \frac{kT}{q} \left| \frac{\Delta t}{\Delta V} \right|. \quad (\text{III.10})$$

$\Delta t/\Delta V$  is the linear slope of the decay curve.

### Method B, Steady-state Methods

This case is described by the schematic in Figure AIII.5. Here a crystal is subjected to a light source, and injected carriers are collected by a collector point C. The light may be modulated for ease of amplification, and the collector point may be a small alloyed junction. While the modulated light, either

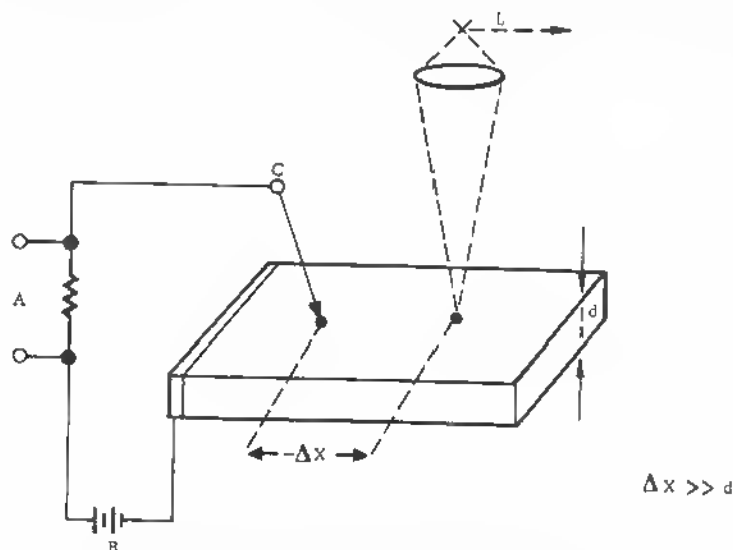


Fig. AIII.5  $\Delta x$  method for lifetime test.

as a light line or a light point source, is continuously injected, the distance of the light source from the collector point is varied. The linear portion of the decay curve in a semilogarithmic plot follows the law

$$R = C \cdot e^{-x/L_a}, \quad (\text{III.11})$$

where  $L_a$  = diffusion length.

$R$  can be a voltage or other response measured at position A (Figure III.5). Since the lifetime can be obtained from the diffusion length, we need only to correlate a response change at the half-point, where

$$e^{-\Delta x/L_a} = V_1 - V_2 = 2$$

(Fig. III.6), and thus

$$L_a = -\frac{\Delta x}{\ln 2}. \quad (\text{III.12})$$

Since for holes in germanium the diffusion constant is  $D_0 = 47 \text{ cm}^2/\text{sec}$ , one gets

$$\begin{aligned} L_a &= \sqrt{D_0 \tau} = -\frac{\Delta x}{\ln 2} \\ \tau &= \frac{\Delta x^2}{(\ln 2)^2 \cdot D_0} \approx \frac{\Delta x^2 \text{ cm}^2}{0.70 \cdot 47 \text{ cm}^2/\text{sec}} \\ \tau &\approx \frac{\Delta x^2}{\text{const}} \text{ sec} \end{aligned} \quad (\text{III.13})$$

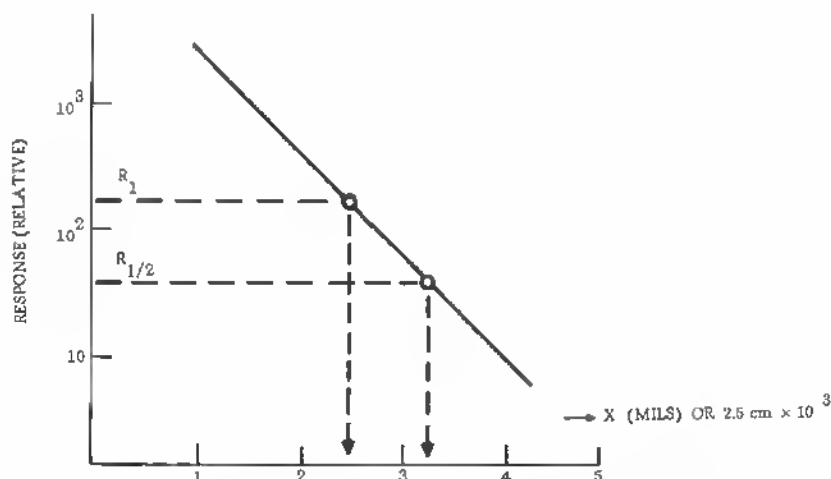


Fig. AIII.6 Solution of  $e^{-\Delta x/L_a} = 2$  by semilogarithmic graph.

Equation (III.11) is the solution of the diffusion equation for holes in  $n$ -type material:

$$\nabla^2 p - \frac{p}{L_p^2} = 0. \quad (\text{III.14})$$

It has to be solved for cylindrical coordinates in case of a light line to be used as an injector. In this case we get for radial flow the boundary conditions

$$\begin{aligned}
 p &= p_0 \cdot iH_0^{(1)}\left(i \frac{r_0}{L_p}\right) & \text{at } r = r_0, \\
 p &= 0 & \text{at } r = \infty,
 \end{aligned}
 \tag{III.15}$$

and the solution

$$p(r) = p_0 \cdot i \cdot H_0^{(1)}\left(i \frac{r}{L_p}\right), \tag{III.16}$$

where  $H_0^{(1)}$  = Hankel function of imaginary argument and order zero, rank (1),  
 $p$  = added hole density,  
 $L_p$  = diffusion length for holes.

The expression (III.16) approaches infinity as  $r \rightarrow 0$ , and at  $r/L_p$  very large, one may use the approximation

$$iH_0^{(1)}\left(i \frac{r}{L_p}\right) \simeq k e^{-r/L_p}, \tag{III.17}$$

where  $k$  is a normalizing constant, not important for the measurements. In very exact measurement procedures, the theoretical curve (III.16) has to be compared with the experimental one, and the corresponding displacement value  $x_0$  (abscissa) can be found:

$$\begin{aligned}
 \text{Experimental slope} &= \frac{d[\ln p(r)]}{dr} \\
 &= \frac{1}{L_p} \cdot \frac{H_1^{(1)}\left(i \frac{r}{L_p}\right)}{iH_0^{(1)}\left(i \frac{r}{L_p}\right)} \\
 &= -\frac{1}{L_p} F(x),
 \end{aligned}
 \tag{III.18}$$

where  $H_1^{(1)}$  = Hankel function of first order, rank (1).

$-\frac{r}{L_p} F(x)$  from (III.18) can be plotted against  $r/L_p = x$ . The experimental slope  $m(r_0)$  multiplied by the distance  $r_0$  is equal to

$$x_0 F(x_0),$$

so that  $x_0 = r_0/L_p$  can be found from the graph of curve (III.18). Other methods using point light sources have been described in Ref. 5. In this case, spherical coordinates have to be chosen, and the solution of the diffusion equation (III.14) is

$$p(r) = - \left( \frac{ir}{L_p} \right)^{-1/2} p_0 H_{1/2}^{(1)} \left( \frac{ir}{L_p} \right), \quad (\text{III.19})$$

where  $H_{1/2}^{(1)} \left( \frac{ir}{L_p} \right)$  = Hankel function of order 1/2 and first rank,  
 $p_0$  = source excess carrier density.

Equation (III.19) can be simplified to

$$p(r) = \sqrt{\frac{2}{\pi}} \frac{e^{-r/L_p}}{r/L_p} p_0, \quad (\text{III.20})$$

and, with the boundary condition,

$$p(r_0) = \sqrt{\frac{2}{\pi}} p_0 \frac{e^{-r_0/L_p}}{r_0/L_p}. \quad (\text{III.21})$$

The partial logarithm of (III.20) yields

$$\frac{\partial \ln p}{\partial r} = - \frac{1}{L_p} + \frac{1}{r} \quad (\text{III.22})$$

(Ref. 5).

#### *Method C, Photomagnetolectric Methods*

This is a Hall effect method associated with the diffusion of optically injected carriers (Ref. 2, pp. 320ff). The principle is a balancing of a light-induced hole-electron flow, the currents of which add up under an orthogonal magnetic field by an electric cross field applied to the crystal. In the case of the conductance measurements, the magnetic field is switched off. Integration is over the crystal thickness  $d$ . The open-circuit field  $F_p^{\text{oc}}$  is balanced by  $I$  (short circuit)/ $G$ , where  $G$  = conductance:

$$F_x^{\text{oc}} = - \frac{\int_0^d I_x^{\text{sc}} dy}{\int_0^d \sigma dy}, \quad (\text{III.23})$$

where oc = open circuit } index,  
       sc = short circuit }  
 $x$  = coordinate in length direction,  
 $y$  = coordinate in vertical direction of crystal.

Slabs of small width have to be used to avoid strong inhomogeneities in recombination velocity.

The photoelectromagnetic effect is known as the Kikoin effect, or the voltage so generated is called Kikoin-voltage<sup>6-8, 13</sup>. Incident photons  $h\nu$  liberate electron-hole pairs, which drift from the surface into the semiconductor and

represent elementary currents in different directions, deflected in opposite direction in an applied magnetic field parallel to the plane of injection. Therefore, holes drifting to one side and electrons to the other, a voltage is established across the sample which is called Kikoin voltage. Without the magnetic field, a voltage would also arise due to the different mobilities of holes and electrons (Dember voltage). In Figure AIII.7 the probe is subjected to a homogeneous and constant magnetic field which can be shut off however. The orientation is such that the positive and negative carriers produce the Kikoin

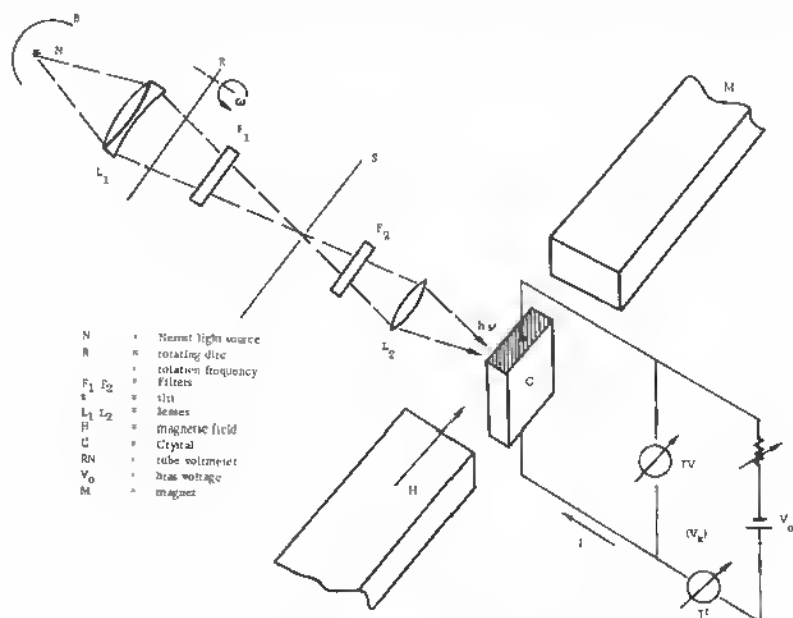


Fig. AIII.7 Setup for photoelectromagnetic lifetime check.

voltage  $V_k$  between the copper-plated ends of the specimen. This voltage is modulated with a low frequency ( $\omega$ ) of the light shutter  $R$  (Figure AIII.7). The light wavelength has to be chosen so that the dominant wavelength corresponds to the band-gap energy (for germanium a frequency range of  $1 \mu$  to  $1.7 \mu$ ). This allows the radiation to penetrate sufficiently to eliminate surface effects. When a direct current  $I$  is additionally set up in the crystal, another alternating voltage component results, since the light causes a variation  $\Delta r$  in the resistance of the specimen. As a result the modulated light produces an ac injection current. The polarity of the dc field can be arranged so that the two ac voltages oppose each other and eventually cancel out. Complete compensation can be obtained by varying the dc voltage  $V_0$ . The tube voltmeter

$TV$  is used as a null indicator. The dc current is checked by instrument  $I'$  (Figure AIII.7). The actual dc voltage is not measured, the tube-voltmeter only indicating the ac voltage.

The Kikoin voltage is given by the expression

$$V_k = \frac{h(H/c) \cdot D^2 \cdot \alpha \cdot \beta}{[1 + (\mu H/c)^2][\sigma + D(\alpha + \beta)]} \quad \text{cgs}, \quad (\text{III.24})$$

where  $H$  = magnetic field strength, gauss,

$h$  = height of light spot, cm,

$c$  = light velocity, cm/s,

$D$  = diffusion constant for minority carriers,

$D_p = 47$  (cm<sup>2</sup>/V sec) for holes ( $p$ )

$D_n = 92$  (cm<sup>2</sup>/V sec) for electrons ( $n$ ) } germanium,

$\mu = \bar{\mu}$  (average) =  $2\mu_n\mu_p/(\mu_n + \mu_p)$ ,

$\mu_n$  = electron mobility,

$\mu_p$  = hole mobility,

$\alpha$  = light absorption coefficient of sample,

$\beta = 1/L = 1/\text{diffusion length}$ ,

$\sigma$  = surface recombination velocity.

If the absolute value of  $H$  is limited ( $H \leq 5,000$  gauss) and light in the infrared region is used, one can set

$$\alpha \gg \beta,$$

$$\sigma \ll D \cdot \alpha.$$

In this equation (III.24) may be written

$$V_k \simeq \frac{1}{c} \cdot h \cdot H \cdot D \cdot \beta. \quad (\text{III.25})$$

Thus, only the size of the light spot, the magnetic field strength, the diffusion constant, and the reciprocal diffusion length are significant. Now an illumination intensity  $L'$  denotes the useful (signal) light intensity, and  $L$  is the constant illumination. The voltage at the sample is then

$$V_s = V_k \cdot \frac{L'}{L + L'}, \quad (\text{III.26})$$

because the ratio of the useful signal illumination to the overall illumination defines the voltage at the contacts. Since  $L' \ll L$ , one may write

$$V_s \simeq V_k \frac{L'}{L}. \quad (\text{III.27})$$

The relative resistance change by irradiation is

$$\frac{\Delta r}{r} = \frac{L'}{L} \quad (\text{III.28})$$

In the case of null compensation we have

$$V_s = I \cdot \Delta r = I \cdot r \cdot \frac{L'}{L}. \quad (\text{III.29})$$

Equalizing (III.27) and (III.29), we have

$$V_k \frac{L'}{L} = I \cdot r \cdot \frac{L'}{L}, \quad (\text{III.30})$$

or

$$V_k = I \cdot r, \quad (\text{III.31})$$

the diffusion length being defined as

$$L = \sqrt{D\tau}. \quad (\text{III.32})$$

Since  $L = 1/\beta$ , we have

$$\tau \cdot D \cdot \beta^2 = 1. \quad (\text{III.33})$$

Using the Einstein relation, the diffusion length may be written

$$L = \frac{1}{\beta} = \left( \mu \tau \frac{kT}{e} \right)^{1/2}. \quad (\text{III.34})$$

Expressing now  $\tau$  by introducing  $\beta$  from (III.25) and  $V_k$  from (III.29) we get, for the lifetime,

$$\tau = \frac{1}{D \cdot \beta^2} = \frac{h^2 H^2 D^2}{D(I \cdot r \cdot c)^2}, \quad (\text{III.35})$$

$$\tau = D \left( \frac{hH}{I \cdot r \cdot c} \right)^2. \quad (\text{III.36})$$

This formula allows the calculation of the lifetime from the diffusion constant, the light pattern height  $h$ , the magnetic field  $H$  and the compensating sample current  $I$ , the resistance and  $c$ , the light speed. Separating all constants,  $\tau$  is only a function of  $I$  and  $r$ :

$$\tau = D \left( \frac{hH}{cr} \right)^2 \cdot \left( \frac{1}{I} \right)^2, \quad (\text{III.37})$$

$$\tau = \frac{\text{const}}{I^2}.$$

Since  $r$  does not change because of the small signal injection, it is easy to find the constant by calibration.



*Experimental Procedure in Method C*

At the instrument  $I'$  (Figure AIII.7), the current  $I$  is checked at the zero reading of the tube voltmeter  $TV$ .  $\tau$  is obtained from (III.37). The semiconductor sample should be 1 to 2 cm in length and have several  $\text{mm}^2$  of illuminated area. The advantage of this method lies in the fact that the surface recombination can be kept unimportant, since the Kikoin voltage is based on volume effects. (The infrared light has a sufficient depth of penetration.) In the case of silicon crystals where surface trap density might be high, these traps can be filled by a supplementary, unmodulated light source.

*Description of the Apparatus and the Measurements (Method C)*

The infrared source  $N$  (projector  $B$ ) can be Nernst glower or glowbar. Lenses  $L_1$  and  $L_2$  affect the focusing through slit  $S$ . A rotating disk  $R$  with slits or teeth modulates the light with a frequency  $\omega$  in the 60 to 2,000 c/s range (Figure AIII.7).

Filters  $F_1$  and  $F_2$  cut off the short wavelength part, of the spectrum. One of these filters ( $F_1$ ) is preferably a water filter. While  $h\nu$ , the incident photon energy, generates electron-hole pairs, the current through the sample is carried by holes, since the space charge neutralization is only effective for these. The Nernst glower (for example, 95 volt, 0.5 amp, 20 mm diameter) is stabilized by a regulating transformer and an iron-hydrogen resistor. The light source has a long rectangular shape, and its effective length is cut off by a slit  $S$  (for example, 33 mm length). This slit is projected into the flat side of the sample crystal  $C$ . A red filter  $F_2$  cuts off all radiation below  $0.7 \mu$ . Mostly, the light is chopped (modulated) with a frequency  $\omega = 500$  c/s. The sample is fixed in a homogeneous magnetic field. The field coils can be iron-core electromagnets of only 1,000 gauss strength. The distance between the pole pieces should be 5 to 7 mm in this case. All parts of the equipment should be mounted on an optical bench for precise alignment.

The  $TV$  is a tube voltmeter, with preamplifier, having a range of 0 to 300 mv. The current meter  $I'$  (0 to 20  $\mu\text{amp}$ , 0 to 60  $\mu\text{amp}$ ) has a mid-zero scale. The measurement is based on the compensation of the Kikoin voltage (the voltage being due to hole injection in a magnetic field) with the ac voltage due to the resistance modulation when current  $I$  is flowing.

*Measurement Procedure (Method C)*

With the modulating light falling onto the crystal, but with current  $I$  and magnetic field off, the tube voltmeter  $TV$  should read zero. There might be a slight deviation due to differences in surface recombination and noise. This reading is taken as corrected zero position.

When the magnetic field is switched on, the current direction as affected by the bias voltage  $V_0$  has to be chosen opposed to the current due to the Kikoin

voltage. The current  $I$  is then regulated so that the tube voltmeter moves back to its zero position. In this condition both Kikoin voltage and circuit voltage (Hall voltage) are equal but opposite. The current  $I$  and the resistance value of sample  $C$  (over the irradiated length  $h$ ) is used for the calculation of  $\tau$ .

#### *Error Considerations (Method C)*

In (III.36),

$$\tau = D \left( \frac{hH}{cIr} \right)^2,$$

the following factors can be evaluated:

- $D$  = diffusion constant, 2 percent error from literature,
- $h$  = length of light spot, 10 to 0.1 mm, 1 percent error,
- $H$  = 1000 gauss  $\pm 1$  percent, calibration error,
- $I$  = 20 to 40  $\mu$ A, reading error  $\approx 1$  percent,
- $r$  = 5 percent error in resistance,
- $c = 3.10^{10}$  cm/sec, 0 percent within these limits as follows:

a) Errors in  $D$ ,  $h$ ,  $H$  are all systematic and the same with one setup for all measurements. If all these errors add up, the maximum deviation is 6 percent.

b) For each sample, the current  $I$  and resistance  $r$  are measured. The arithmetical average value of five successive measurements should be taken. The deviations of the individual measurements from this mean value give in a typical case a quadratic error of 5 percent for  $r$  and of 2.5 percent for  $I$ . In the error for  $I$  one has to include, above all, the deviations of  $TV$ , the tube voltmeter. So, the maximum error is 15 percent in this case.

c) A further error is due to the approximation of (III.24), by (III.25), and the use of monochromatic light. These errors are much smaller, however, than those under (a) and (b) if the above used conditions for (III.25) to (III.31) are fulfilled and lifetimes smaller than 200  $\mu$ sec are measured. If  $\tau > 200 \mu$ sec, the method cannot give reliable results, since the diffusion length gets into the range of the probe dimensions. If  $I$  approaches  $\sqrt{D\tau}$ , the resulting  $\tau$  values turn out to be too high. Reflected carriers at the contacts, running in opposite direction before recombining, can essentially diminish the Kikoin voltage and thus the compensating current  $I$  so that

$$\tau \approx \frac{1}{I^2}$$

is too high.

Typical values of  $\tau$  for a range of resistivities of  $n$ -type Ge are:

Ge type	$\rho$ , ohm cm	$\tau$ , sec
<i>n</i> -Type	1.5	13
<i>n</i> -Type	3.0	18
<i>n</i> -Type	8.0	50
<i>n</i> -Type	10.0	100
<i>n</i> -Type	17.0	175
Intrinsic	40.00	>1,000 (error)

Obviously  $\tau$  increases with  $\rho$ , since less impurity scattering is effective. With diminished temperature and deionization of impurities, the lifetime may increase. Here, the role of dislocations may be enhanced, however. Crystal perfection is the unknown in these measurements, and lifetime is also a direct weighting factor for perfection.

#### D Application to Thin Films

With the preponderance of unipolar structures in microcircuits of the MOS or FET variety and the quest for improved device isolation by the use of semiconductor layers on insulator substrates (SOS = silicon on sapphire), it appears less important to measure the lifetime. In most bipolar transistors in use today this parameter is measured on large silicon wafers before any diffusion step, and these devices are generally used as such in microcircuits (chipped-in) in combination with thin-film resistors and capacitors. But it may also be desirable to adapt the lifetime measurement methods to thin films, since  $\tau$  is a direct measurement parameter for crystal perfection.

Easiest to adapt for measurements on thin films and epitaxial layers on high-resistivity substrates seems the light pulse decay method described under III, 1.

The thinner the sample, however, the stronger the influence of the surface states on lifetime. Filling of traps by a dc supplemental light source may give a wrong value for the effective lifetime, since it is de facto strongly surface-dominated.

Microwave methods, as described,<sup>10</sup> can only be used if the semiconductor layer is supported by a substrate of insulator character (low transmission losses, which can be calibrated out by insertion of the substrate only), film thicknesses and resistivities within the ranges applicable, and sample sizes in line with the waveguide cross sections. In reflectivity measurements, as described under I (see Figure A1.25), the resistivity and thus the lifetime (with light injection) can be monitored by the return losses. It should be considered that the frequency must be necessarily high in order to keep the skin depth

below the sample thickness (see Figure AI.24). For 9 GHz, for example, the actual semiconductor material thickness would be in excess of anything used in devices (about 10  $\mu$ ). In the case of thin samples, infrared reflectivity measurements would be the only way to achieve meaningful results. This is, however, a strong impediment to lifetime checks, since additional light injection is needed to induce excess free carriers. Reflection losses would have to be monitored in this case with very low intensity light.

### E Mos Capacitance Method

This method, applied to carrier concentration measurements, has been described under Section I. Figure AI.19 gives the limit capacitance of the depletion region versus the bulk concentration of a MOS structure ( $\text{SiO}_2$ ). If a frequency variation or pulse method is used, the lifetime of minority carriers appears as a relaxation time in the capacitance voltage characteristics. In the physical model (Figure AIII.8) a positive charge at the semiconductor surface under the  $\text{SiO}_2$  accumulates during the negative cycle. In the  $n$ -type semiconductor this charge consists of minority carriers with smaller mobility. Plotted into a capacity versus voltage diagram, three different curves describe the frequency dependence of such a capacitance:

1. The depletion approximation or the dc behavior
2. The response for a high-frequency measurement
3. The low-frequency response curve

The frequency where 3 flattens out to 2 may be relatively high or in excess of 0.5 MHz.

The relaxation time from curve 1 to curve 2 can be used to find the minority carrier lifetime. This is done by exploring the device with a variable sweep time at high frequency<sup>11</sup>, for example, at 500 kHz, with 200 milli-seconds/div. with respect to 20 milli-sec/div. sweep time. Across the depletion layer we assume a constant space charge generation  $G$ :

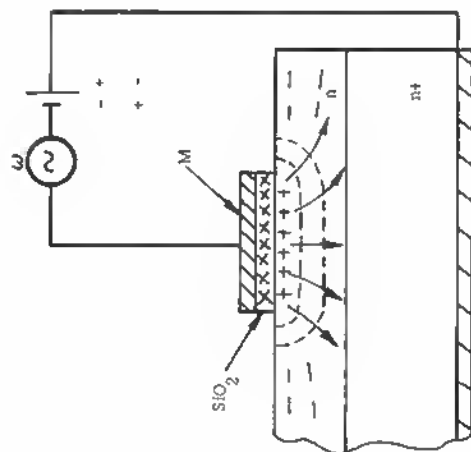
$$\frac{dQ_p}{dt} = G \cdot q \cdot x_d, \quad (\text{III.38})$$

where  $Q_p$  = charge density at capacitance,  
 $q$  = electronic charge,  
 $x_d$  = depletion layer width.

Since in neutrality the surface charge density  $Q_s$  has to be

$$Q_s = Q_p + qN_d x_d, \quad (\text{III.39})$$

where  $N_d$  = impurity density,



MOS - CAPACITANCE ON EPITAXIAL Si

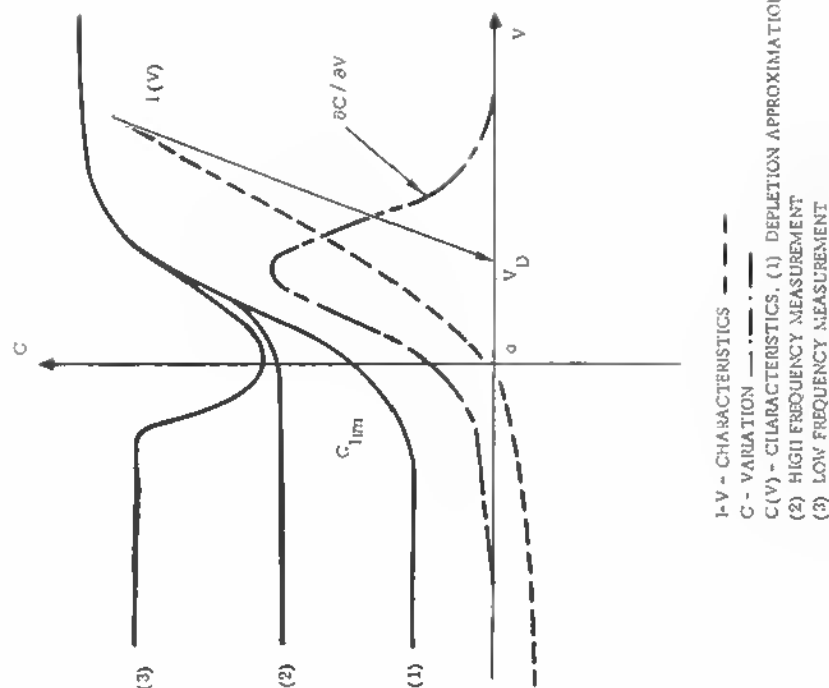


Fig. AIII.8 Lifetime study by means of capacitance variation with frequency.

and  $Q_s$  is approximately constant, we get another relation for  $dQ_p/dt$ :

$$\frac{dQ_p}{dt} = qN_d \frac{dx_d}{dt}. \quad (\text{III.40})$$

With (III.38) this gives the differential equation for  $x_d$ :

$$\frac{dx_d}{dt} + \frac{G}{N_d} x_d = 0, \quad (\text{III.41})$$

with the solution

$$x_d = \text{const} \exp\left(-\frac{G}{N_d} t\right). \quad (\text{III.42})$$

Hence the time constant for minority carrier accumulation is

$$\tau = \frac{N_d}{G}. \quad (\text{III.43})$$

For  $p$ - $n$  junctions in highly doped crystal material the excess hole density  $p-p_0$  ( $p_0$  = equilibrium density) is equal to  $\delta n$  if  $p_0$  and  $p$  are  $\ll n_0$ , the net rate of generation of minority carriers being

$$G = -\frac{(p_0 - p)}{\tau_0} = \frac{\delta n}{\tau_0}, \quad (\text{III.44})$$

where  $\tau_0$  = lifetime.<sup>12</sup>

Jund and Poirier<sup>11</sup> have argued that in highly doped semiconductors  $\delta n \approx n_i$  ( $n_i$  = the intrinsic density). This is concluded also from the temperature dependence of  $\tau$  as  $\exp(E_g/2kT)$ , as in the case for  $n_i$  ( $E_g$  = band gap energy). Thus  $\tau_0$  can be represented by

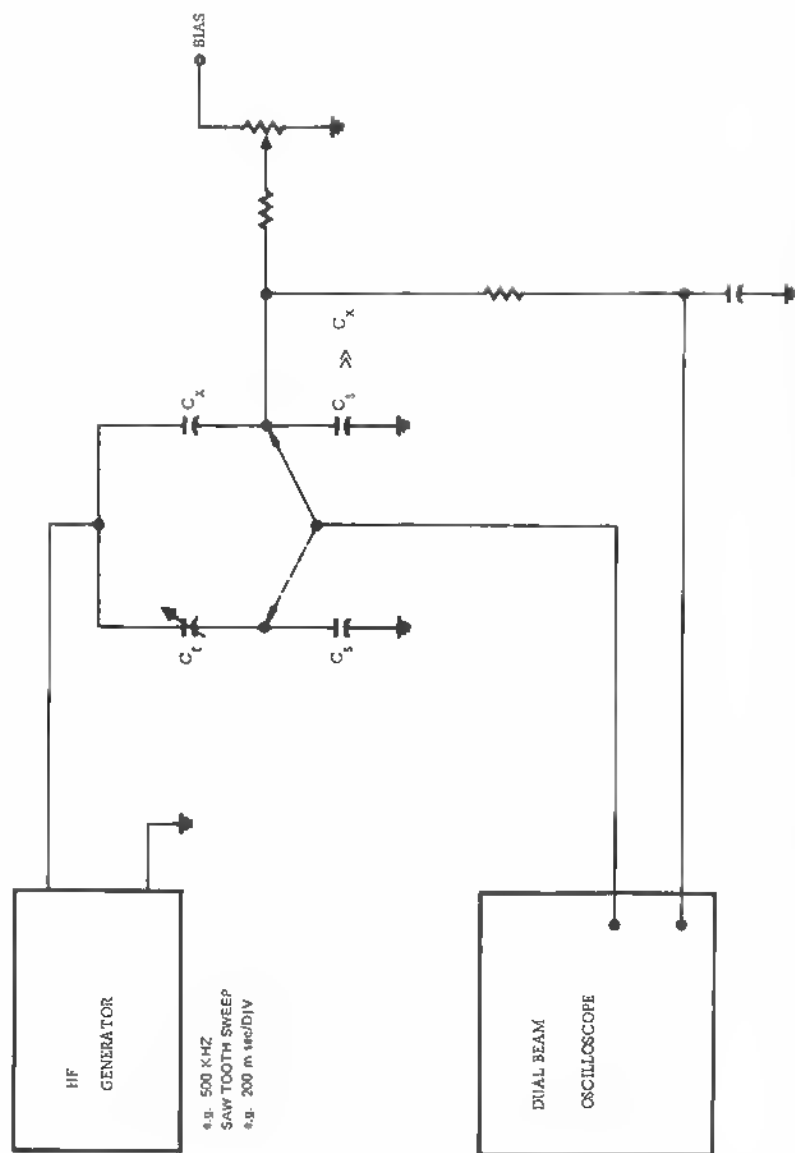
$$\tau_0 = \frac{n_i}{G}.$$

With the measured time constant  $\tau = N_d/G$  from (III.43) we have a lifetime:

$$\tau_0 = \frac{n_i}{N_d} \tau.$$

$N_d$  being known by the  $C_{s_{\text{lim}}}$  versus  $N(x)$  relation (Figure AI.19) and curve 2 in Figure AIII.8, the lifetime can be found by a measurement of  $C_{s_{\text{lim}}}$ \*. It is not yet established how precise the  $\tau_0$  values are that are derived by this technique. The values of resistivity so measured and compared with the four-point probe values seem to be in good agreement. The measurement circuit consists of a capacity bridge subjected to the generator pulse. A bias circuit allows a voltage shift on  $C_s$ .

\* Fig. AIII.9 shows the capacitance bridge used in these measurements.



\* Fig. AIII.9  $C_0$ ,  $C_{itot}$ -measuring circuit diagram for lifetime study.

\* Such capacity measurements can also be applied to epitaxial layer thickness tests. As the voltage (Figure AIII.8) is increased, the saturation value of  $C$  corresponds to the barrier layer extension to the  $n - /n -$  interface. In the total capacitance  $C = C_2/(1 + C_2/C_1)$ ,  $C_1$  corresponds to the metal -  $\text{SiO}_2$  - layer capacitance (which is large compared to  $C_2$  since  $d_2 \gg d_1$ ). Then

$$d_2 = \epsilon F / 4\pi C_2 \approx \epsilon F / 4\pi C$$

## REFERENCES

1. Bridgers A. E., J. H. Scaff, and J. N. Shive: *Transistor Technology, Vol. I*, Van Nostrand Co., pp. 264 ff, 1958.
2. Biondi F. J.: *Transistor Technology, Vol. III*, Van Nostrand Co., pp. 309 ff, 1958.
3. Lederhandler, S. R. and L. J. Giacoletto: "Measurement of Minority Carrier Lifetime and Surface Effects in Junction Devices." *Proceedings IRE*, pp. 477-483, April, 1955.
4. Haynes, J. R. and W. Shockley: "Mobility and Life of Injected Carriers in Germanium." *Phys. Rev.* 81, 835-843, March 1, 1951.
5. Mataré, H. F. and B. Reed: "Anomaly of Carrier Lifetime in Germanium Bicrystals." *Zschr. f. Naturforschung* 11a, 10, pp. 876-878, 1956.
6. Kikoin, K. and M. Noskow: *Phys. Journal USSR* 5, p. 586, 1934.
7. Aigrain, P. and H. Bulliard: *Comptes Rendues*, 236, 595 and 672, 1953.
8. Bulliard, H.: *Ann. Phys. (France)* 9, 52, 1954.
9. Lemke, H.: "Measurement of Lifetime by the Double-Pulse Method for Silicon." *Physica Status Solidi* 12, pp. 115-123, 1965.
10. Jacobs, H., F. A. Brand, J. D. Meindl, S. Weitz, B. Benjamin, and D. A. Holmes: "New Microwave Techniques in Surface Recombination and Lifetime Studies," *Proceedings IEEE*, pp. 581-592, April 1963.
11. Jund, R. and C. Poirier: "Carrier Concentration and Minority Carrier Lifetime Measurement in Semiconductor Epitaxial Layers by the MOS Capacitance Method." *Solid State Electronics*, 9, pp. 315-319, 1966.
12. Shockley, W. and W. T. Read: "Statistics of the Recombinations of Holes and Electrons." *Phys. Rev.* 87, pp. 835, 1952.
13. Kikoin, I. K. and S. D. Lazarev: "On the Anisotropy of Photomagnetic Effects in Germanium and Silicon," *Jr. Chem. Phys. Solids*, Vol. 28, pp. 1236-1255, 1967.
14. Keller, W.: "Messung der Traegerlebensdauer in Siliziumeinkristallen mit Hochfrequenz." *Zschr. f. angew. Physik* Vol. II, 9; pp. 351-352, 1959.
15. Lederhandler, S. R. and L. J. Giacoletto: "Measurement of Minority Carrier Lifetime and Surface Effects in Junction Devices." *Proceedings IRE*, pp. 477-483, April 1955.
16. Many, A.: "Measurement of Minority Carrier Lifetime and Contact Injection Ratio on Transistor Materials." *Proceedings Phys. Soc. (England)*, Section B, Vol. 67, pp. 9-16 1954.
17. Fritzsche, C.: "Oberflaechen und Geometriekorrekturen fuer die Messung der Lebensdauer von Minoritaetsstraegern in Halbleitern" *Zschr. f. angewandte Physik* Vol. 13; No. 2 pp. 576-580 1961.
18. Heiman, F. P.: "On the Determination of Minority Carrier Lifetime from the Transient Response of an MOS-Capacitor." *IEEE-Transactions on Electron Devices* Vol. ED14 No. 11, pp. 781-784, November 1967.
19. Hofstein, S. R.: "Minority Carrier Lifetime Determination from Inversion Layer Transient Response." *IEEE-Transactions on Electron Devices* Vol. ED14 No. 11, pp. 785-789, November 1967.
20. Brousseau, M. and R. Schuttler: "Use of Microwave Techniques for Measuring Carrier Lifetime and Mobility in Semiconductors." *Solid-State Electronics*, Vol. 12, No. 5, pp. 417-423, 1969.



## IV    MOBILITY

## A    Mobility (General)

As expressed by the fundamental equation for the current caused by a number  $n$  of electrons with charge  $e$  and drift velocity  $\bar{v}$ ,

$$i = -ne\bar{v}, \quad (\text{IV.1})$$

the conductivity is by definition  $\sigma = i/E$ , where  $E$  = local field strength in volts per centimeter. The magnitude  $\bar{v}/E$  or the acquired mean velocity within the field  $E$  is called the mobility  $\mu$  of the charge carrier under consideration.  $\mu$  can also be expressed in terms of the  $e/m$  ratio and the mean free time  $\tau$  of an electron by

$$\mu = \frac{\bar{v}}{E} = \frac{e}{m} \cdot \tau. \quad (\text{IV.2})$$

The conductivity is generally given as

$$\sigma = ne\mu_e + pe\mu_h \quad (\text{IV.3})$$

when two carrier types, electrons and holes, with their respective densities  $n$  and  $p$  and their mobilities  $\mu_e$  and  $\mu_h$  are present and contribute to the current flow under the same field strength.

In a measurement technique involving a magnetic field, the two types of carriers are not easily separated, since their respective transverse currents vectorially add up to produce the Hall voltage.<sup>1</sup>

In general, one or the other carrier type is predominant, and the mobility can be found directly by a measurement of the Hall voltage  $V_H$  across the sample, as shown in Figure IV.1. This cross field  $E_y$  depends, in its magnitude, on the magnetic field  $H_z$  and the current  $I_x$  with a proportionality constant  $R$ , which is the Hall constant. For small Hall angles  $\theta = \mu H/c$  the effective field  $E_y$  can be written

$$E_y = \pm \frac{\mu}{c_x} \cdot H_z \cdot I_x, \quad (\text{IV.4})$$

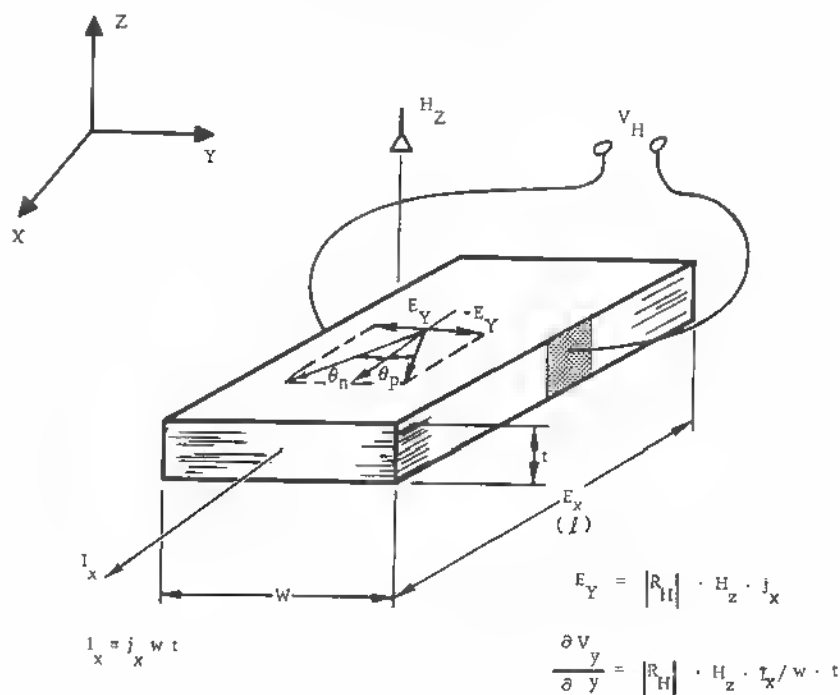
and

$$R = \pm \frac{\mu}{c\sigma_x} = \frac{\theta}{\sigma_x H_z}, \quad (\text{IV.5})$$

where  $c = 3 \cdot 10^{10}$  cm/sec.

Generally the current  $I_x$  is measured in terms of the current density  $j_x$  as  $j_x \cdot w \cdot t$  (see Figure IV.1), and the Hall coefficient is expressed in practical units ( $e$  in coulombs) so the one may write

$$|R_H| = \frac{E_H[\text{volt}] \cdot t[\text{cm}]}{I_x[\text{amp}] \cdot H_z[\text{gauss}]} \cdot 10^8 \text{ cm}^3/\text{A} \cdot \text{s} \quad (\text{IV.6})$$



$$\int_0^{V_H} \frac{\partial V}{\partial y} dy = \int_0^w |R_H| \cdot H_z \cdot j_x dy$$

$$V_H = |R_H| \cdot H_z \cdot j_x \cdot w$$

$$|R_H| = \frac{V_H \cdot t}{H_z \cdot j_x \cdot w} = \frac{V_H \cdot t}{H_z \cdot I_x}$$

Fig. AIV.1 Relations between Hall-angle  $\theta$ , Hall voltage  $V_H$  and current  $I_x$  in crystal slab.

It has to be kept in mind that the flux intensity can also be expressed in weber/cm<sup>2</sup> = 10<sup>8</sup> gauss or weber/m<sup>2</sup> = 10<sup>4</sup> gauss.

The expression of  $R_H$  (IV.6) in cm<sup>3</sup>/coulomb, with measured values for Hall voltage, sample thickness, current and magnetic field, can be used directly to assess the mobility, using the unit coulombs for the charge on the electron  $e = 1.60 \times 10^{-19}$  coulombs.

$|R_H|$  as above leads to

$$\sigma = ne\mu = \frac{\mu}{|R_H|} [\text{ohm cm}]^{-1}, \quad (IV.7)$$

$$\mu = \sigma |R_H| \text{ cm}^2/\text{V sec} \quad (IV.8)$$

For semiconductors with predominant thermal scattering (usual case of moderate doping at room temperature) a factor  $3\pi/8 = 1.18$  has to be added. Numerous sample geometries and contacting methods are described in the literature,<sup>2</sup> especially for cases where inhomogeneous carrier flow in the sample may cause a cross voltage that has to be bucked out (double contacts on one side and potentiometric voltage readings). Especially for small samples, epitaxial layers, or thin films, this method is useful, since only three contacts need to be applied to the sample (loss of half the Hall voltage, Figure IV.2a).

If the Hall effect is measured by a dc method, the Ettinghausen effect may easily cause a temperature gradient between the Hall probes. Since the probes are of a different material from the sample, this temperature gradient causes a Seebeck emf at the voltage probes. Furthermore, a thermal current may be present in the direction of the electric current because of a Peltier effect

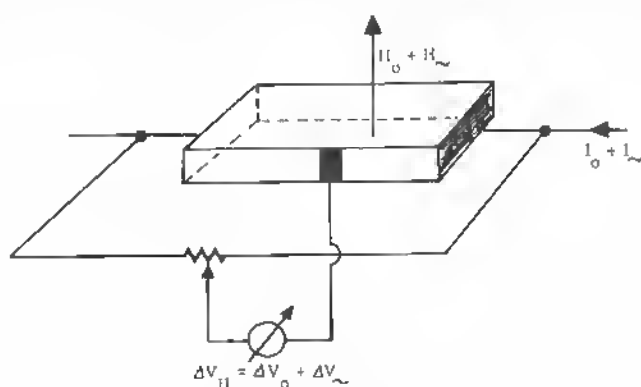


Fig. AIV.2 (a) Three-terminal mount for Hall measurements.

at the junctions between sample and current leads. This can cause an additional emf at the voltage probes because of the Ettinghausen-Nernst effect. This Peltier effect, combined with the Righi-Leduc effect, can cause an additional Seebeck emf to appear at the voltage probes. These errors can be eliminated to a large extent by remeasuring the Hall voltage immediately after reversal of (1) the current through the sample and (2) the magnetic field. This gives actually four  $V_H$  values, and the averaging should eliminate these effects if the thermal time constants are long compared with the time required for reversing current and field and taking the respective readings. In the case of a contact geometry, as in Figure IV.2a, this method also eliminates the shape effects.

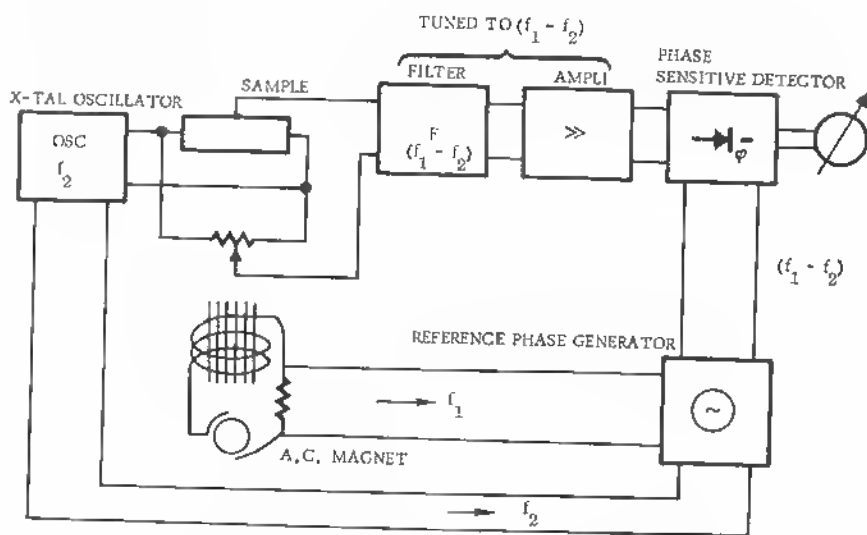
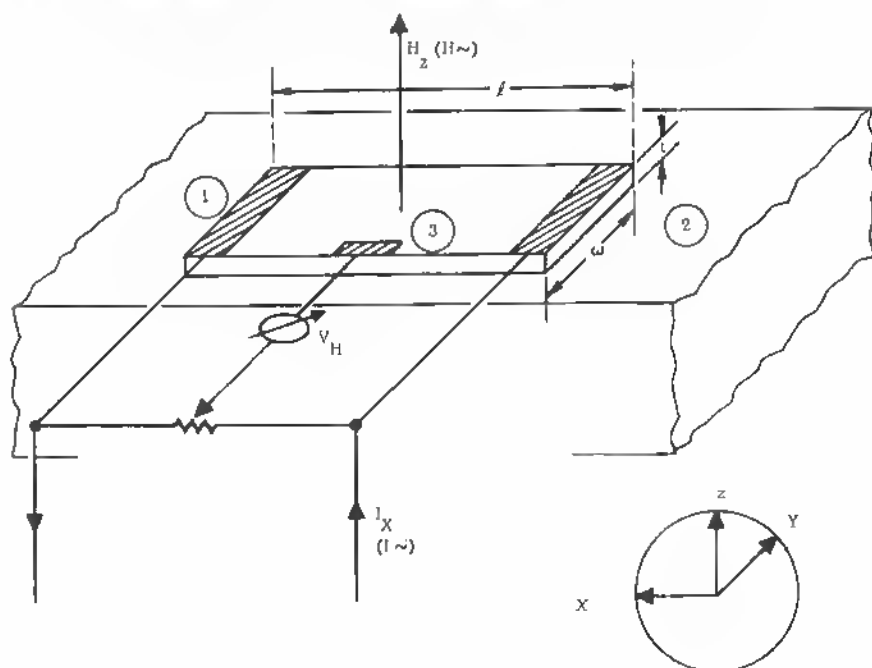


Fig. AIV.2 (b) Double ac system for Hall mobility measurements.

Thermal effects (joule heating) can largely be avoided by using small current values ( $I_x < 0.1$  mA). The consequently smaller Hall voltages may be difficult to measure, and, therefore, ac methods are most appropriate. Figure IV.2b gives a scheme used for such measurements that shows great independence of spurious signals because the sample is used as a difference frequency generator for the Hall field frequency  $f_1$  and the current frequency  $f_2$ . Especially in the case of thin films the sample current may be very small and the mobility also small so that it is important to find the necessary conditions (magnetic field, ac voltage amplification, dimensions) for a useful reading of the Hall voltage. In a general form of analysis for thin samples (Figure IV.3),



$$E_x = j_x \cdot \sigma$$

LONGITUDINAL FIELD

$$j_x = \frac{I_x}{w \cdot l}$$

LONGITUDINAL CURRENT DENSITY

$$V_x = E_x \cdot l$$

LONGITUDINAL VOLTAGE

$$R_x = \rho \frac{l}{w \cdot t}$$

LONGITUDINAL RESISTANCE

$$E_y = E_H = H_z \cdot \mu \cdot E_x$$

HALL-FIELD

$$= H_z \cdot |R_H| \cdot \sigma \cdot E_x$$

(R<sub>H</sub> = HALL CONSTANT)

$$= H_z \cdot |R_H| \cdot j_x$$

Fig. AIV.3 Contacts and equations for mobility test on thin films.

it should be considered that the measurement of  $\rho$  is carried out as a voltage-current measurement between electrodes 1 and 2. If the sample dimensions are as given, the current density  $j$  is  $I_x/tw$ , and the field strength  $E_x$  in the long direction of the sample is  $E_x = V_x/l$ . Therefore

$$\sigma = \frac{j_x}{E_x} = \frac{I_x}{tw} \frac{l}{V_x}, \quad (\text{IV.9})$$

For reasons of measurement precision, it is generally preferred to keep  $l > w > t$  (rectangular slab). With the need to measure the Hall field  $\Delta E_y$ , the sample width  $w$  should not be too small either. Since the Hall field is

$$\Delta E_y = R_H \cdot j_x \cdot H_z, \quad (\text{IV.10})$$

it can be increased by higher current density and magnetic field strength. This is a limited method, however, since magnetoresistance effects may become too strong, with  $H_z$  and  $j_x$  increasing. For higher Hall angles the electric field vector and the current vector do have to be considered to be divergent (see Figure IV.1), and  $\theta$  defined by:

$$\tan \theta = \frac{E_y}{E_x} \quad (\text{IV.11})$$

will be so large that new field components are generated. Therefore, small field and current measurements by the use of ac methods with attendant amplification of the Hall signal are necessary to increase the measurement sensitivity without the need to increase unduly field and current values.

The decrease in sample thickness  $t$  helps to increase the effective current density for normal current values  $I_x$ , since

$$j_x = \frac{I_x}{w \cdot t}. \quad (\text{IV.12})$$

In the expression for the Hall field

$$E_H = H_z |R_H| \cdot j_x, \quad (\text{IV.13})$$

however, we can express

$$|R_H| = \frac{1}{ne} = \mu \cdot \rho, \quad (\text{IV.14})$$

$$|R_H| = \mu R_x \frac{t \cdot w}{l}, \quad (\text{IV.15})$$

where  $R_x$  = sample resistance in  $x$  direction,  
and therefore

$$E_H = H_z \mu R_x \frac{t \cdot w}{l} \cdot j_x, \quad (\text{IV.16})$$

$$E_H = H_z \mu R_x \frac{I_x}{l},$$

and

$$V_H = H_z \mu R_x I_x \cdot \frac{w}{l}. \quad (\text{IV.17})$$

Therefore, the ratio  $w/l$  should be large if a low mobility has to be measured. Since  $R_x I_x / l = E_x$ , (IV.17) is equivalent to the definition equation  $V_H = H_z \mu E_x \cdot w$ . Of course, the measurement of the sample resistance  $R_x$  is less precise for short samples ( $l$  small), but as shown by (IV.15), it is more important to keep  $t \cdot w/l$  large for a precise measure of  $|R_H|$ , decisive for a measurement of  $\mu$ .

The resistance  $R_x$  (or resistivity  $\rho = R_x w \cdot t/l$ ) can be found by a simple voltage/current reading and, therefore, is less subject to measurement errors than  $V_H$ , the Hall voltage.

Introducing the expression (IV.15) for the Hall constant into (IV.17) gives

$$V_H = H_z |R_H| I_x \frac{1}{t} \quad (\text{IV.18})$$

and shows that it should be easier to measure  $V_H$  for thin samples for a given current  $I_x$ . Because thin samples have a current density limitation, we are, therefore, lead to ac methods.

Considering the measurable mobility values, we use the definition equation for the Hall constant (IV.14) and express  $|R_H| \cdot \sigma = \mu$  with the aid of (IV.18) and

$$\sigma = \frac{I_x}{V_x} \frac{l}{w \cdot t}, \quad (\text{IV.19})$$

$$\mu = |R_H| \cdot \sigma = \frac{V_H}{V_x} \cdot \frac{l}{t} \cdot \frac{1}{H_z}. \quad (\text{IV.20})$$

This equation is valid within the constraints of our model; that is, the Hall angle  $\theta$  is small, and  $H_z$  is sufficiently below the value of significant change of  $\sigma$  because of magnetoresistance effects.

Equation (IV.20) can also be written

$$\mu = \frac{V_H}{H_z \cdot E_x \cdot t}, \quad (\text{IV.21})$$

$$\mu = \frac{V_H [\text{volt}]}{H_z [\text{gauss}] E_x [\text{V/cm}] \cdot t [\text{cm}]} \cdot 10^8 \frac{(\text{cm/s})}{(\text{V/cm})}, \quad (\text{IV.22})$$

since

$$1 \text{ gauss} = 10^{-8} \frac{\text{Volt} \times \text{sec}}{\text{cm}^2} = 10^{-8} \frac{\text{weber}}{\text{cm}^2}.$$

Putting some values into (IV.22), we can find the mobility limit measurable in practical cases. Assume that a magnetic field of  $10^4$  gauss is still possible before magneto-resistance effects take place. Assume further that ac methods with amplification of  $(f_1 - f_2)$  allow one to monitor Hall voltages as small as a few  $\mu$  volts and that  $E_x$  is kept at or below 1 V/cm and that  $t = 0.1$  cm:

$$\mu = \frac{10^{-6}[\text{V}] \cdot 10^8}{10^4[\text{gauss}] \cdot 1[\text{V/cm}] \cdot 0.1 \text{ cm}}; \quad (\text{IV.23})$$

then

$$\mu = 10^{-1} \text{ cm}^2 \text{ V}^{-1} \text{ sec}^{-1}.$$

This is a low mobility but still measurable within the limits of the ac method. For smaller sample width down into the  $\mu$  range and below, we generally expect a much higher limit for

$$\mu = \left( \frac{10^{-2}}{t[\text{cm}]} \right)$$

within these measurement limits. For mobility values in the range of

$$1,000 \frac{\text{cm/s}}{\text{V/cm}}$$

we would expect Hall voltages of the same order of magnitude ( $10^{-6}$  V), but for values below this level Hall voltages could drop to  $10^{-7}$  [V] and lower, making it difficult to separate the signal from the noise generated within the sample especially if a granular structure (disordered structure) has to be measured.

The application of the above mobility measurements is relatively easy for samples on insulator substrates. In some cases, however, oxide layers on metallic or conducting substrates have to be evaluated. In these cases a flat geometry cannot be used, but a special arrangement of electrodes on a flat sample can lead to measurable results under certain conditions. Especially in the case of grown oxides as  $\text{SiO}_2$  on Si,  $\text{Al}_2\text{O}_3$  on Al, etc., an arrangement as shown in Figure IV.4, is conceivable. A thin substrate  $B$  is chosen ( $t$  very small) and the oxide grown onto it to a thickness  $l$  in this case. The lateral dimension is relatively unlimited here giving room for a relatively large value of  $\mu$ . This is important for a larger Hall voltage. The current passing through the oxide layer is divided into two equal portions  $I_1$  and  $I_2$  by means of a double potentiometer set  $P_1$  and  $P_2$ . The Hall probe is connected through the



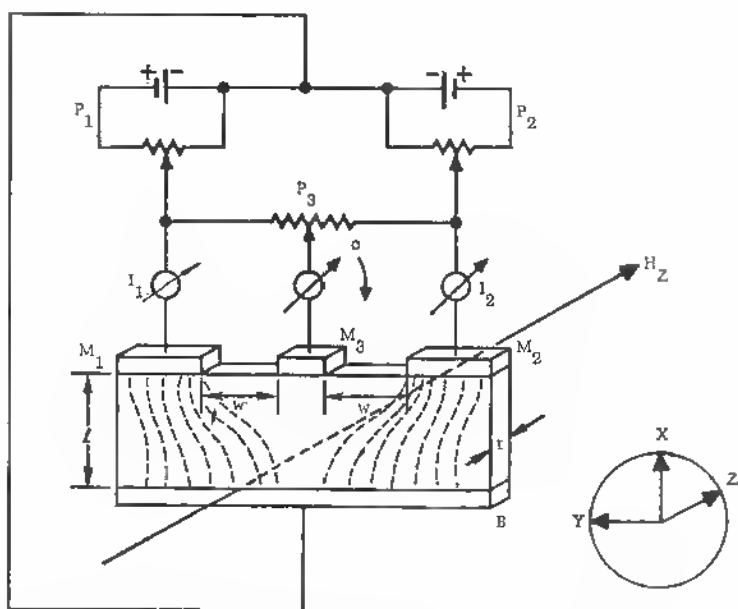
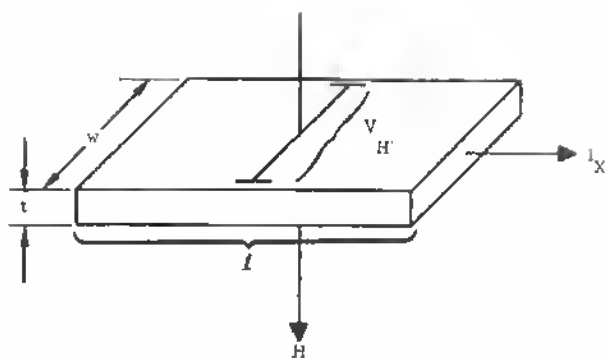


Fig. AIV.4 Special mount of contacts for mobility check on thin, high resistivity layers (e.g., oxides) on metallic substrates.

instrument for read-out (ac amplifier) to  $P_3$ . Without magnetic field  $H$ , the voltage at  $M_3$  is reduced to zero by adjusting the potentiometers. With a magnetic field, a Hall field

$$E_H = H_z \cdot \mu \cdot w \cdot E_x$$

originates, where  $w$  is the distance between the metal contacts  $M_1 - M_3$  with respect to  $M_2 - M_3$ . The resistivity of such layers being extremely high, the small value of  $l$  is less important while the thickness  $t$  can be adapted to the mobility value  $\mu$  (IV.21) to give reasonable values for  $V_H$ . As one sees from (IV.20), a certain ratio of  $l/t$ , sample length over thickness, defines a range of mobility values for different samples by essentially two voltage readings, ( $V_H/V_x$ ). Such measurements have been carried out successfully for a wide range of impurities<sup>3</sup> on epitaxial silicon on contrapolar substrates ( $n$  on  $p$ ).

### B Mobility Measurements Without the Use of Magnetic Fields

As we have seen, mobility measurements by way of Hall voltage measurements are relatively time consuming due to a number of necessary steps like sample preparations, holder design, magnetic field control, etc. In addition, the measurement results may be doubtful in the case of thin films and a number of considerations enter into the evaluation of final results. Therefore, it is desirable to find an alternate method for mobility evaluation. Such a method exists due to the fact that independent methods for the measurement of resistivity and impurity density are available. Since the mobility can be expressed by

$$\mu = \frac{1}{\rho \cdot N \cdot e},$$

where  $\rho$  = resistivity,  $\Omega$  cm,

$N$  = impurity density,  $\text{cm}^{-3}$ ,

$e$  = electron charge,

independent measurements of  $\rho$  and  $N(x)$  are sufficient to assess  $\mu$ . Such methods have been discussed in the foregoing. As most reliable and easy to apply also for thin films, we discuss a combination of

1. The spreading resistance method
2. The differential capacitance technique

As described in Section I, A (equation 1.43) the impurity density follows directly from the specific capacitance variation with voltage swing  $\partial(C/F)/\partial V$ :

$$|N| = \frac{4\pi \cdot (C/F)^3}{e \cdot \epsilon \cdot \frac{\partial(C/F)}{\partial V}},$$

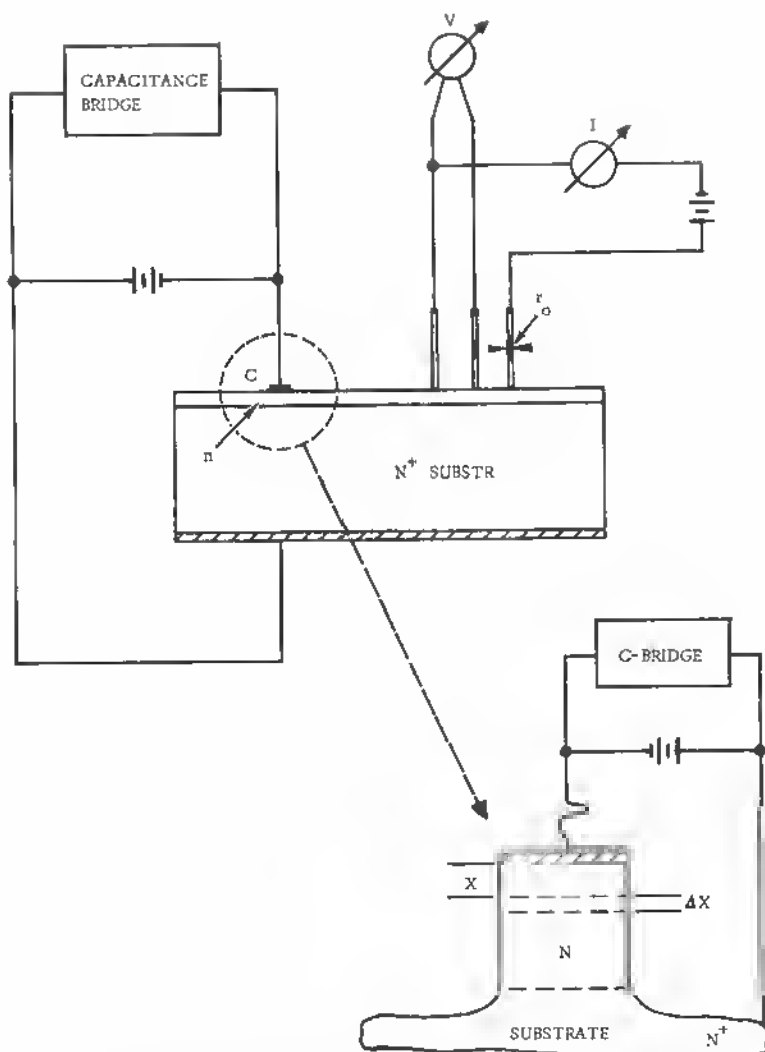


Fig. AIV.5 Mobility measurement by simultaneous measurements of differential capacitance and spreading resistance.

where  $C/F$  = capacity per unit area,  
 $e$  = electron charge,  
 $\epsilon$  = dielectric constant,

and  $\rho$  follows directly from the spreading resistance measurement:

$$\rho = 4r_0 R_s,$$

where  $r_0$  = contact radius,  
 $R_s$  = spreading resistance,  
 $R_s = \frac{V}{I}$ .

Therefore

$$\mu = \frac{\epsilon \frac{\partial(C/F)}{\partial V}}{16\pi r_0 R_s (C/F)^3}. \quad (\text{IV.24})$$

It is technically quite easy to apply both methods to a semiconductor wafer or layer. Measurements can be taken either simultaneously or in sequence. Both methods need a small area only for application. In fact, a spreading resistance reading can be taken at a point and a small capacitance can be applied subsequently for the  $N$  measurement, if necessary. Figure 1V.5 shows the principle. The capacitance is applied to the surface of the epitaxial layer by a shallow, high  $C_0$  (surface concentration) diffusion, which forms a junction with barrier layer  $x$  and a voltage-induced spread  $\Delta x$ . In special cases a metal surface layer could also be applied to avoid a second barrier at the point contact. For  $C_0$  in excess of  $10^{20} \text{ cm}^{-3}$ , this is not necessary. Both readings of  $\rho$  and  $N$  are very precise under the conditions outlined, and the result is a fairly good evaluation of the mobility of the material.

### C Measurements on Mos Devices

The special circumstances of the gate layer in MOS devices have made it difficult to judge the effective mobility in the source-drain channel from pure materials studies, as described above. In fact, the surface states in conjunction with the gate surface field applied have proved to create special effects escaping theoretical explanation. (See Chapter 14.1.)

Mobility values measured by conventional methods do not apply within the source-drain channel subjected to two fields, the source-drain longitudinal field  $E_{\parallel}$  and the vertical gate field  $E_{\perp}$ . Therefore, transconductance measurements do not give real mobility values, but those modified by the influence of the gate field on scattering processes.

There are cases of well-established device structures based on monocrystalline silicon crystals in which surface trapping is minimized and in which

no major defects are present within the source-drain channel. For conservative field values a rather good fit between transconductance and Hall mobility field dependences can be found.<sup>4</sup> However, more complications are expected if the frequency dependence of the surface states is considered. Recently the broad time-constant dispersion of states at the Si-SiO<sub>2</sub> interface has been explained by a tunneling model.<sup>5</sup>

The anisotropic conduction in solids near surfaces is in general a complex problem<sup>6</sup> especially when imperfections in the crystal layer are involved. Models to account for this have been developed<sup>7</sup> (Chapter 14.1) and further work remains to be carried out to fully understand the functioning of these devices. With increasing demands for reproducibility and reliability, it is imperative to solve the carrier transport problems in MOS and FET devices.

## REFERENCES

1. Shockley W.: "Electrons and Holes in Semiconductors," Van Nostrand, Princeton, N. J., p. 215 ff, 1958.
2. Putley, E. H.: "The Hall Effect and Related Phenomena." Butterworths, London, 1960.
3. Patrick, W. J.: "Measurement of Resistivity and Mobility in Silicon Epitaxial Layers on a Control Wafer." *Solid State Electronics*, 9, pp. 203-211, 1966.
4. Fowler, A. B., F. Fang, and F. Hochberg: "Hall Measurements on Silicon Field Effect Transistor Structures." *IBM Journal*, pp. 427-429, September, 1964.
5. Preier, H.: "Contributions of Surface States to MOS Impedance." *Applied Physics Letters*, vol. 10, No. 12, pp. 361-363, 15 June 1967.
6. Price, P. J.: "Anisotropic Conduction in Solids Near Surfaces." *IBM Journal*, pp. 152-157, April 1960.
7. Mataré, H. F. and J. J. Grossman: "Thin Film Semiconductors." *Proceedings of the Third International Vacuum Congress*, vol. 2, (Parts 1-3) pp. 317-327, 1966.
8. Haynes J. R. and W. Shockley: "Mobility and Life of Injected Holes and Electrons in Germanium," *Phy. Rev.* vol. 81, pp. 835-843, 1951.

## Symbol Index

$A$	amplitude (lattice waves)
$A$	activation energy (also space-charge constant, Chapter 13)
$A$	grain boundary scattering parameter (Chapter 11)
$A^*$	acceptor (neutral)
$A^-$	acceptor (negative)
$A_n$	Fourier coefficients in stress function
$a$	wave number ( $1/\lambda$ )
$\mathbf{a}$	wave number vector
$a$	cell length in reciprocal lattice
$a_1$	first Bohr radius
$\mathbf{a}_0, \mathbf{a}_k$	propagation vectors in reciprocal lattice
$a$	spacing of filled dislocation levels (Chapter 8)
$a_{ij}$	dislocation tensor
$B$	bulk reflection coefficient (Chapter 10)
$B$	grain boundary scattering parameter (Chapter 11)
$B$	matrix of translation vectors in reciprocal lattice
$B_n$	Fourier coefficients in stress function
$b_1, b_2, b_3$	translation vectors in reciprocal lattice
$b = \mu_n/\mu_b$	mobility ratio (electrons/holes)
$\mathbf{b}$	Burgers vector
$C_L, C_s$	heat capacity of liquid (solid) phase (Chapter 14)
$C$	conduction band
$C$	constant for $n$ -th eigenfunction
$C_n, C_p$	concentration of electrons-holes
$c$	$3 \cdot 10^{10}$ cm/sec
$c$	spacing between dangling bonds (Chapter 8)
$c_e$	capture probability for electron (Chapter 9)
$c_h$	capture probability for hole (Chapter 9)

$D$	matrix of translation vectors in direct lattice
$D^*$	donor (neutral)
$D^+$	donor (positive)
$D$	dislocation spacing (unambiguously, Chapter 4)
$D$	lattice density (unambiguously, Chapter 8)
$D_{\parallel}$	diffusion constant parallel to dislocation
$D_{\perp}$	diffusion constant vertical to dislocation
$D_n, D_p$	diffusion constants for electrons-holes
$D_d$	effective diffusion constant (for carriers in dislocation pipe, Ch. 9)
$d$	lattice constant (direct lattice)
$d_1, d_2, d_3$	translation vectors (direct lattice)
$E$	energy (mostly in eV for electrons/holes)
$E$	electric field vector
$E_F$	energy at Fermi level
$E_{\text{pot}}$	potential energy
$E_D$	electron energy at donor level
$E_A$	electron energy at acceptor level
$E_c$	electron energy at lower edge of conduction band
$E_v$	electron energy at upper edge of valence band
$E_p$	energy of a traveling wave
$E_2$	energy level of a dislocation (also $E_D$ )
$E_H$	ionization energy for hydrogen atom
$E_t$	energy level of trap center
$E_x$	energy of a Bloch wave at point $x$
$E_a$	activation energy
$E(k)$	energy in $k$ -space
$E_s$	energy of a screw dislocation
$E_e$	energy of an edge dislocation
$E_b$	atomic binding energy
$E_+$	activation energy for ionic motion
$E_f$	energy for formation of vacancy pair
$E_i$	electronic interaction energy
$E_{\text{eff}}$	effective band energy
$E_s(f)$	electrostatic energy per added electron (Fermi statistics)
$\langle E \rangle$	effective field value
$E_e$	energy of interaction per electron
$E_{+e}$	interaction energy of positive space charge on electron
$E_1, E_2$	fields at $n$ - $p$ - $n$ barrier sides
$E_{+e}$	interaction energy of electron on positive space charge
$E_0$	interaction energy of electrons in neighboring sites
$E_{\text{min}}$	minimum energy in atomic impact (Chapter 6)
$E_{rc}$	coefficient of band change by volume deformation
$e$	electron charge ( $1.6 \cdot 10^{-19}$ Coulomb) (also exponential function)
$F_e$	external force
$F(x)$	force expression for electrons in space

$f$	frequency
$f$	electronic filling factor (grain boundaries)
$f(E)$	Fermi distribution function
$f_t$	fraction of traps (occupied by electrons)
$f_p$	fraction of traps (occupied by holes)
$f^-, f^+$	Fermi energies in bulk on negative or positive boundary side
$G$	lattice cell number
$G$	modulus of rigidity (Chapter 8)
$G$	conductance per unit length of boundary (Chapter 9)
$G_0$	grain boundary conductance at zero bias
$g$	recombination cross section (Chapter 10 only)
$g$	generation rate (pair production)
$g(\epsilon)$	distortion factor
$H$	magnetic field
$H_T$	transversal magnetic field
$H_{pr}, H_{pl}$	parallel-transversal (parallel longitudinal) magnetic field in grain boundary layer (Chapter 11, Section 4)
$\mathbf{H}$	magnetic field vector
$H_0^{(1)}$	Hankel function (zero order, first rank)
$H_1^{(1)}$	Hankel function (first order, first rank)
$h$	dislocation distance (Chapter 10)
$h$	Planck's constant
$\hbar$	$h/2\pi$
$I_m$	imaginary portion of wave vector ( $I_m[k(x)]$ )
$\langle I \rangle$	effective current value
$\langle (\Delta I_m)^2 \rangle$	mean square noise current
$I_h$	hole current
$I_r$	electron saturation current
$I_s$	hole saturation current
$i$	current or $\sqrt{-1}$
$J_m$	Bessel function of order $m$ (first kind)
$j$	current density
$K$	ratio of carrier density (Chapter 10)
$K$	phonon wave vector
$k$	Boltzmann constant
$\mathbf{k}$	wave vector (also $k$ )



$L_{pb}$	diffusion length for holes in base	(Chapter 14)
$L_{ne}$	diffusion length for electrons in emitter	
$L$	lattice limit (length)	
$L$	dislocation length	
$L_c$	width of accumulation layer (Chapter 14)	
$L_p$	diffusion length for holes	
$L_n$	diffusion length for electrons	
$l$	coefficient (natural numbers)	
$l$	sample length and boundary length	
$l$	Miller index	
$M$	atomic mass	
$M^*$	reduced atomic mass	
$m$	electron mass (free)	
$m_{el}$	effective electron mass (also $m^*$ )	
$m_{en}^a, m_{pe}^a$	effective mass of electron (hole) in emitter	
$m_{nb}^a, m_{pb}^a$	effective mass of electron (hole) in base	
$N_D$	bulk donor density	
$N$	number of doping atoms	
$N_c$	effective state density	
$N$	number of carriers	
$N(x)$	local carrier density	
$n$	carrier density (Chapter 11)	
$n_a$	electron density	
$n_i$	intrinsic density	
$P$	pressure	
$\delta P$	increment of pressure	
$P_{mn}$	transition probabilities	
$P_x$	crystal momentum	
$p$	number of lattice planes	
$p$	index in displacement equation	
$p_{str}$	effective hole density in grain boundary	
$p$	hole density	
$p(x)$	hole density at point $x$	
$p_j$	dipole strength vector	
$Q$	total charge number	
$q_i$	point charges of dangling bonds (Chapter 9)	
$q_0$	equilibrium number of charges (Chapter 11)	
$q$	number of charges in boundary states (Chapters 9 and 11)	
$R$	gas constant (only Chapter 12, Section 4)	
$R$	dislocation space charge radius (also $r$ , in Chapter 9)	
$R$	resistance per unit length (only Chapter 9)	
$R_0(r), R_1(r)$ , etc.	Fourier coefficients in circular stress functions	

$\mathbf{r}$	displacement vector
$\mathbf{r}_{kd}$	dipole position vector
$r_c$	cyclotron radius
$S$	entropy (Chapter 3)
$S$	shear stress (unambiguously, Chapter 4, Section 5)
$S$	signal amplitude (Chapter 9)
$S_x, S_y, S_z$	structural coefficients
$s$	crystal surface
$T$	external force (components $T_x, T_y, T_z$ )
$T$	absolute temperature ( $^{\circ}\text{K}$ )
$T$	transmission coefficient of carriers through lineage structure (Chapter 10)
$t$	time
$t_d$	release time (carrier within dislocation pipe, Chapter 9)
$t_e$	average time of a hole within dislocation cylinder before release
$t_r$	average time of a hole within dislocation cylinder before recombination
$U$	recombination rate
$U_i$	binding energy of a foreign atom
$U(x)$	potential function
$u(x, k)$	periodic amplitude in Bloch wave expression
$V$	phase velocity (wave equation Chapter 2 only)
$V_g$	gate voltage
$V_s$	source-drain voltage
$V_B$	battery voltage
$V_0$	volume of gr-atom ( $\delta V =$ volume change)
$V_L$	local oscillator voltage
$V_e$	external voltage to a barrier
$V_1, V_2$	voltages at $n$ - $p$ - $n$ barrier sides
$v$	wave velocity
$v_e$	longitudinal wave velocity
$v_t$	transversal wave velocity
$v_d$	drift velocity of a carrier
$W$	probability
$W_D$	flux of solute atoms from grain boundary into bulk
$W(\theta)$	scattering probability
$W$	activation energy for vacancy formation
$w$	channel width
$X$	parameter of scattering factor $F(x)$
$X = l/l_0$	mean free path in bulk
	mean free path due to dislocations (Chapter 9)

$x$	dimension (length)
$Y$	functional sign
$y$	dimension (length)
$Z$	characteristic impedance (Chapter 9)
$Z_I$	excess core charge of atom
$z$	dimension (length)
$\alpha$	direction cosine for outgoing beam in Laue diffraction
$\alpha_o$	direction cosine for incoming beam in Laue diffraction
$\alpha(h\nu)$	absorption coefficient (radiation)
$\beta$	direction cosine (beam component in three dimensional
$\gamma$	direction cosine/ diffraction)
$\gamma$	capture rate (Chapter 11)
$\Delta$	atomic displacement
$\delta_{ik}$	Kronecker's Delta
$\delta$	distance between lattice rows
$\epsilon_{ij}$	strain tensor
$\epsilon$	fraction of volume occupied by space charge cylinders
$\bar{\epsilon}$	energy of radiation
$\zeta$	electrochemical potential ( $E_F - E_{pot}$ ) (also Fermi-level, Chapter 6)
$\eta$	fraction of hole drift time in space charge cylinder (Chapter 9) also: trapping level (Chapter 9)
$\eta_r$	non-radiative recombination efficiency (Chapter 9)
$\theta$	ratio of induced (free) charges to trapped charges (Chapter 14)
$\theta$	angle of misfit (grain boundaries, Chapter 4)
$\theta$	angle between lattice rows
$\theta$	phase shift (only Chapter 9)
$\theta_p$	Hall angle (holes)
$\theta_n$	Hall angle (electrons)
$\kappa$	susceptibility
$\kappa_{eff}$	effective dielectric constant
$\lambda$	wavelength in $\lambda\nu = v$ Also DeBroglie wavelength $h/p$ . (also unambiguously Lamé's constant, Chapter 5)
$\mu$	mobility (Chapter 2)
$\mu$	shear modulus (unambiguously, Chapter 4)
$\mu_n$	electron mobility
$\mu_p$	hole mobility
$\mu_o$	mobility of a vacancy
$\mu_{  }$	mobility of a charge carrier parallel to a dislocation
$\mu_{es}$	mobility due to lattice scattering restricted by a potential well
$\mu_{\perp}$	mobility of a charge carrier perpendicular to a dislocation
$\mu_v$	mobility of a vacancy
$\mu_L$	lattice mobility
$\mu_i$	mobility on account of ionized impurity scattering

$\mu_d$	mobility on account of scattering of carriers in the dislocation stress field
$\mu_{pd}$	hole mobility in dislocation pipe (Chapter 9)
$\nu$	frequency
$\nu$	Poisson's ratio (unambiguously, Chapter 4)
$\xi$	position variable $\left(2\pi \frac{x}{d}\right)$ (also $\arccos v_x/v$ )
$\pi$	circular constant
$\pi_{pq}$	piezo-resistance coefficients
$\rho$	resistivity
$\sigma$	conductivity
$\sigma_{xx}, \sigma_{xy},$ $\sigma_{yy}, \text{etc.}$	directional stress components
$\sigma_r$	radial stress function
$\sigma_n, \sigma_p$	$n$ -type ( $p$ -type) conductivity
$\Sigma$	sum sign
$t$	life-time
$\bar{t}$	mean free time
$\tau_r$	relaxation time
$\phi$	grain boundary orientation angle
$\phi$	barrier height in eV
$\phi$	angular direction of force lines (Chapter 7)
$\phi_{eo}$	potential of electron in electron plasma (Chapter 8)
$\phi$	dislocation scattering angle (Chapter 9)
$\varphi$	electrostatic potential
$\varphi$	phase angle
$\varphi$	angle of incidence in refraction
$\varphi$	scattering wave function (unambiguously, Chapter 8)
$\psi(x)$	wave function (in one dimensional Schrödinger equation)
$\psi(r)$	wave function (in three dimensional Schrödinger equation)
$\psi$	general wave function
$\psi_t$	potential function (Chapter 9)
$\omega$	$2\pi\nu$ ( $2\pi f$ ) = circular frequency
$\omega$	rotational vector (Chapter 4)
$\Omega$	sign for resistance (ohms)
$\omega_c$	cyclotron frequency



## Author Index

numbers = page number. (numbers) = literature citation at page of that number.

- Abeles, B., (326)  
 Adams, E. N., (326)  
 Aigrain, P., (599)  
 Alibozek, R. G., (508)  
 Allen, C. C., (575)  
 Allerton, G. L., (575)  
 Allred, W., (82)  
 Amelinckx, S., 71, (82), 103, (109),  
     138, (144), 445  
 Amith, A., 322, 323, 324, (326)  
 Ang, C. Y., 481  
 Aubuchon, K. G., (459)  
 Avery, D. G., (579)  
  
 Bakish, R., (68), (82)  
 Bardeen, J., 340  
 Bardsley, W., (82), 175, (249)  
 Barret, C. S., (382)  
 Bassett, G. A., 478, (506)  
 Bäuerlein, R., 115, (127)  
 Baynham, A. C., (171)  
 Beam, W. R., (68), (82)  
 Becker, R., 470, (506), 472, 477  
 Beaubien, M. W., (127), 355  
 Beli, R. L., 267, (281)  
 Benjamin, B., (575), (599)  
 Berghezan, A., (506)  
 Berglund, C. N., 523, (535)  
 Billig, E., (249)  
  
 Biondi, F. J., (599)  
 Birman, J., 363, (364)  
 Blackburn, D. A., (405)  
 Bloch, F., 17, 18, 19, 23, 28, 41,  
     57, 70, (81)  
 Boltaks, B. I., (507), (506)  
 Borkan, H., (459)  
 Born, M., 8  
 Bower, R. W., (459)  
 Bowen, E. J., (251)  
 Brack, K., (127), (459)  
 Bragg, W. L., 13, 16, 17  
 Brand, A., (575), (599)  
 Braunstein, M., 496, (508)  
 Breslin, J., (507)  
 Brice, D. K., (459)  
 Bridgers, A. E., (599)  
 Brillouin, L., 6, 22, 24, 28, 38,  
     39, (68)  
 Brinkman, J. A., 112, (126), (459)  
 Brooks, H., 473, (506)  
 Brousseau, M., (599)  
 Brown, A. F., (405)  
 Brown, N., (68), (82)  
 Brown, R. A., (171)  
 Brown, W. L., 538  
 Bruyere, J. C., (535)  
 Bube, R. H., (425)  
 Bulliard, H., (599)

- Bullough, R., (104)  
 Burgers, J. M., 84, 94  
 Burstein, E., (364)  
 Busse, J. J., 319, 324, 325,  
     (325), (326)  
 Cadoff, I. B., (507)  
 Cahn, J. H., (127)  
 Callaway, J., (127)  
 Casey, H. C., 210, (250)  
 Catalano, S., 549, (574)  
 Chadderton, L. T., (127)  
 Chakraverty, B. K., (535)  
 Chalmers, B., 103, (104)  
 Chase, B. D., (463)  
 Clark, A. H., (508)  
 Cho, K. S., (127), (364), (426)  
 Chu, T. L., (507), (508)  
 Chynoweth, A. G., 56, (68), (251),  
     (459), (462)  
 Clark, A. H., 497  
 Clevenger, L. H., (575)  
 Cohen, M. H., 530, (535)  
 Conwell, E. M., 62, 63, (312)  
 Copeland, J. A., 466, (469)  
 Corbett, J. W., (82)  
 Corey, H. E., 91  
 Cottrell, A. H., 3, (81), 227, 138,  
     (144), (506)  
 Couling, S. R. L., (382), 399, (405)  
 Cronmeyer, D. C., (127), 355  
 Cullen, G. W., (507)  
 Czaja, W., (250)  
 Das, B. N., (508)  
 Davies, J. A., (460)  
 DeAngelis, H. M., (459)  
 Debeye, P. P., 46  
 DeBroglie, L., 26, 70  
 Dekeyser, W., (109), 138, (144)  
 DeLuca, R. D., (507)  
 De Rudnay, A., 498  
 Dewald, J. F., (534)  
 DeWit, R., (109)  
 Dickey, D. H., (575)  
 Dill, G. H., (459)  
 Dirac, P. A. M., 40  
 Ditmars, D. A., (486)  
 Dorda, G., (489)  
 Döring, W., 470, 472, 477, (506)  
 Douglas, T. B., (486)  
 Dumin, D. J., (489), (508)  
 Edagawa, H., (508)  
 Einstein, A., 40  
 Eitel, W., (506)  
 Elinson, M. I., (326)  
 Elliott, R. J., (68)  
 Ericson, L., (460)  
 Fan, H. Y., 282, 291, 303, (306),  
     336, (535)  
 Fang, F., (612)  
 Fankuchen, I., 387, (393)  
 Farnsworth, H. E., 211, (250)  
 Fermi, E., 36  
 Figielski, T., (171), 227, 229, 230,  
     231, 232, 233, (250), (364)  
 Filby, J. D., (508)  
 Fisher, J. C., 471, 472, (506)  
 Flanagan, R., 395  
 Fletcher, R. C., 538  
 Floquet, G., 26, 27  
 Forbes, D. H., (171)  
 Foster, W. R., (486)  
 Fourdeux, A., (506)  
 Fowler, A. B., (612)  
 Fracombe, M. H., (508)  
 Frank, F. C., 96, 103, 106, (171)  
 Franz, W., 56  
 Friedel, J., (538)  
 Frisch, H. L., (306), (507)  
 Fritzsche, C., (599)  
 Fritzsche, H., 530, (535)  
 Fuchs, K., 321, (326)  
 Galacki, Z., (127), 357, (364)  
 Garblick, G. F. J., (251)  
 Gardner, E. E., (127), (459), (575)  
 Gatos, H. C., 169, (172), 379, (382),  
     474, 475  
 Gerasimov, A. B., (127)

- Giacoletto, L. J., (599)  
 Gippins, A. A., 283, (251), (463)  
 Givargizov, E. I., (507)  
 Glaenger, R. H., 305, 306,  
     (306), (459)  
 Golacki, Z., (127)  
 Goodier, J. N., (144)  
 Gorey, E. F., (575)  
 Gottlieb, O. E., (507)  
 Grant, J. T. P., (280)  
 Grossman, J. J., (459), (612), (508)  
 Grove, A. S., (508)  
 Gubanov, A., (513), (534)  
 Gudden, B., (534)  
 Gunn, J. B., (251), (462), 465, 466,  
     467, (579)  
 Haberland, D. R., 531, (535)  
 Hagon, P. J., (250)  
 Hallenback, J. F., (575)  
 Hamakawa, Y., (250), 278, (281)  
     307, 310, (312), 314, 316,  
     317, (325), 335, 337, (339),  
     525, (535)  
 Hamaker, R. W., (508)  
 Handler, P., 264, 265, 278, (281),  
     310, (325)  
 Haneman, D., (280)  
 Hang, A., (68)  
 Harris, J. S., (469)  
 Haynes, J. R., (599)  
 Heil, O., 340  
 Heiman, F. P., (507), (599)  
 Holloman, J. H., (81)  
 Hogarth, C. A., 162, (171), (281)  
 Holm, R., (575)  
 Holmes, D. K., (126), (575), (599)  
 Holmes, D. K., (226)  
 Holmes, P. J., (249)  
 Holstein, T. D., (326)  
 Holt, D. B., 379, (382), (463)  
 Hornstra, J., 167, (171), (172),  
     403, (405)  
 Hubner, K., (405), (459)  
 Huggins, R. A., (171)  
 Hughes, A. J., (127)  
 Hughes, K. A., (249)  
 Hunsperger, R. G. H., (507)  
 Itoh, T., (459), 492  
 Iuada, T., (459)  
 Ivanov, V. L., 237, (251)  
 Jacobs, H., 571, (575), (599)  
 Jacobson, R. L., (104), (250),  
     (172), (382)  
 James, H. M., 73, (82)  
 Jastrzebska, M., (364)  
 Jordan, A. G., 243, 247, (249), (251),  
     305, 306, (306), (459)  
 Joshi, M. L., (507)  
 Jund, R., 597, (599)  
 Johnson, G. W., (506)  
 Kaiser, W., (306)  
 Kanegawa, K., (459)  
 Keck, P. H., (507)  
 Kedesdy, H., (249), 376  
 Keller, W., (575), (599)  
 Kikoin, K., (599)  
 Kikuchi, M., (579)  
 Kittel, C., (68), 318, (325)  
 Kleinknecht, H. B., (508)  
 Klein, D. J., (171)  
 Kleinman, D. A., 185, 190,  
     214, (249)  
 Klontz, E. F., 111, (126)  
 Kohn, J. A., 98, 99, (104), (171),  
     484, 523  
 Kolomijets, B., 521, (534)  
 Kroemer, H., (68), 454, 455, (460),  
     463, 464, 465, 466, 467,  
     468, (469)  
 Kröner, E., 108, (109)  
 Kyaw, Htin, (249)  
 Laakso, C. W., (250), (312), (325)  
 Lagowski, J., (171), 210, (250)  
 Landwehr, G., 278, 280, (281), 310,  
     (312), 314, 315, 316, (325)  
 Lang, A. R., 445  
 Larin, F., (127)



- Lamorte, M. F., (575)  
 Lark-Horovitz, K., 73, (82),  
 111, (126)  
 Laue, von M., 18, 20  
 Lavine, M. C., (172), 382  
 Lawrence, J. H., (459)  
 Lax, B., (82)  
 Lax, M., 230, 231, 232, (250)  
 Lazarev, S. D., (599)  
 Lederhandler, S. R., (599)  
 Leistico, O., (508)  
 Leman, G., (538)  
 Lemke, H., (249), (599)  
 Lempicki, A., 363, (364)  
 Lindemann, W. W., (364)  
 Logan, R. A., 176, 185, 186, 190,  
 214, (249)  
 Longini, R. L., 243, 247 (249), (251),  
 252, 255, (260)  
 Looney, J. C., (575)  
 Love, G., 404, (405)  
 Lovell, L. C., (249)  
 Ludwig, G. W., (82)  
 Lutsikii, V. N., (326)
- Mackenzie, J. D., 518, 519, (534)  
 Maffit, R. N., (250), 277, (281)  
 Maiorov, A. V., (405)  
 Manasevit, H. M., (506), (507)  
 Many, A., (579), (599)  
 Maradudin, A. A., 2  
 Mastujian, J., 492, (508)  
 Mataré, H. F., (104), (127), (144),  
 (171), (249), (250), 265,  
 (281), (306), (312), (325),  
 (339), 343, 355, (364), 367,  
 (382), (393), 400, (405),  
 (414), (425), 426, (434),  
 (459), 498, 520, (507), (508),  
 (535), (599), (612)
- Marsh, O. J., (507)  
 Matukura, Y., 307, (312)  
 Maurer, R., (81)  
 Mavroides, J. G., (82)  
 Mayer, J. W., (460)  
 Mazur, R. G., (575)
- McDonald, A., (249)  
 McKay, K. G., 56, (68), (250)  
 McKelvey, J. P., 252, (260), 255,  
 256, 259  
 Mead, C. A., 515, (507)  
 Meiboom, S., (326)  
 Meindl, J. D., (525), (599)  
 Mercier, J., 484, (484)  
 Mikoshiba, N., 321, (326)  
 Miles, M. H., (364)  
 Miller, A., (507)  
 Miller, C. E., (534)  
 Millward, C., (249)  
 Milnes, G. A., (460)  
 Mil'vidskii, M. G., (251)  
 Mircea, A., 549, (574)  
 Mitchell, T. E., 144, (144), (405)  
 Moody, P. L., (172)  
 Morita, Y., (508)  
 Morin, F. J., (249), 519, (534)  
 Morritz, F. L., (507)  
 Morrison, S. R., 222, 224, 226, 247,  
 (250), (251)  
 Morizana, K., (506)  
 Mössbauer, R. L., 2  
 Mott, N. F., (103), 395, 411, 512,  
 519, 521, 524, 525, 530,  
 (534), (535)  
 Mueller, R. K., 93, (104), (250),  
 (281), (339)  
 Muss, D. R., (364)  
 Myoczkowski, R. S., (506)
- Nabarro, F. R. N., (171)  
 Nasledov, D. N., (460)  
 Naunichi, Y., (469)  
 Nealey, C. C., (250)  
 Neumark, G. F., 453, (459), (507)  
 Newman, R. C., (127), (249)  
 Newnham, R. E., (486)  
 Nielson, S., (508)  
 Nikitina, S., (81)  
 Nishino, T., (281), (312)  
 Nolder, R. L., (171), (507)  
 Northover, W. R., (534)  
 Noskow, M., (599)

- Novikov, S. R., (127)  
 Nunn, D. E., 119,  
 120, (127)  
 Oberly, J. J., (507), (508)  
 Odell, N. H., (306), 337, (535)  
 Ogurtani, T. O., (171)  
 Oldham, W. G., (460)  
 Oroshnik, J., (579)  
 Osmun, J. W., 530, (535)  
 Ovenskii, V. B., (251), (463)  
 Ovshinsky, S. R., 516, 517, 522,  
 (534), (535)  
 Panish, M. B., (82)  
 Pantelev, V. A., (405)  
 Patel, J. R., (250), 366  
 Patric, W. J., (575), (612)  
 Paul, W., 361, (506)  
 Pauling, L., 489  
 Pavlov, P. V., 404, 405, (405)  
 Pease, R. F. W., 195, (249)  
 Pearson, A. D., 515, 522, (534)  
 Pearson, G. L., 176, 185, 190, 230,  
 (249), (250), 340, 468, (469)  
 Peck, W. F., (534)  
 Peterson, A., (249)  
 Pfann, W. G., 91, 493, (508)  
 Pick, H., (70), (81)  
 Picus, G., (364)  
 Planck, M., 40  
 Poirier, C., 597, (599)  
 Pomerantz, D. I., 533  
 Portnoy, W. M., 264, (281)  
 Postnikov, V. V., (507)  
 Preier, H., (612)  
 Price, P. J., (612)  
 Proshko, G. P., (251)  
 Putley, E. H., (612)  
 Queisser, H. J., (171), 282, 283,  
 (306), 395, 401, 402, 403,  
 (405), (459)  
 Quinn, A. C., (575)  
 Read, W. T., (68), 71, (82), 35, 85,  
 (104), 175, 183, 185, 189,  
 Read (*Continued*)  
 190, 204, 214, 227, 232, 244,  
 (249), (250), (109), 164, 165,  
 (171), 265, 394, 443, (599)  
 Reed, B., (127), (249), (281), (339),  
 (364), (414), (434), (599)  
 Reiss, H., (306), 477, 478,  
 (506), (507)  
 Rhodes, R. G., (249), (459)  
 Ridley, B. K., 465, (469), 466  
 Roots, W. D., (280)  
 Roth, W. C., 167, (171)  
 Royal, H. F., (486)  
 Rozhanskii, V. N., (507)  
 Sah, C. T., (508)  
 Sautter, D., 243, (251)  
 Scaff, J. H., (599)  
 Schell, H. A., (364)  
 Schlier, R. E., 211, (250)  
 Schlötterer, H., 490, 491, (508)  
 Schmid, A. P., 528, 530, (535)  
 Schottky, W., 30, (68), 514, (534)  
 Schottmiller, J. S., (534)  
 Schrödinger, E., 26, 40, 48  
 Schumann, P. A., Jr., (575)  
 Schuttler, R., (599)  
 Schwuttke, G. H., (127), 444, (459)  
 Sclar, N., (364)  
 Seeger, A., (81), (109)  
 Seidensticker, R. G., (508)  
 Seifert, J. R., (575)  
 Seitz, F., 69, 70, (81)  
 Seybold, A. V., (405)  
 Shewmon, P. G., (405)  
 Shive, J. N., (599)  
 Shockley, W., 30, 35, (68), 93, (104),  
 173, 247, 265, 282, (325)  
 (339), 340, 342, 394, (405),  
 (425), (459), (599), (612)  
 Sideris, G., (534)  
 Simpson, W. J., (507)  
 Smith, C. S., (441)  
 Smoluchowski, R., 367, (382), 394,  
 395, 398, 399, 404, (405)  
 Sondheimer, E. H., 320, 322, (325)

- Southgate, P. D., 241, (251)  
 Spenke, E., (68), (81)  
 Spitzer, W. G., (82)  
 Stern, E. A., 280  
 Stocker, H. J., 522, 525  
 Stratton, R., 305, (306)  
 Sugita, Y., (506)  
 Sugawara, K., (506)
- Tallman, R. L., (507), (508)  
 Tamura, M., (506)  
 Tanaka, S., (312)  
 Tannenbaum, E., (574)  
 Tauc, J., 512, (534)  
 Taulbee, C. D., 119, 120, (127)  
 Taylor, W. E., (306), 337, 525, (535)  
 Theuerer, H. C., 487  
 Thomas, R. N., (508)  
 Thomas, E. E., 91  
 Thomson, G. P., (506)  
 Thompson, S. A., (459)  
 Thornton, P. R., (249)  
 Timoshenko, S., 87, (104), (144)  
 Turnbull, D., 398, 399, (405), 471,  
 472, (506)  
 Tweet, A. G., 265, (281), 306, (312),  
 367, (382)
- Valdes, L. B., 327, (339)  
 Van Bueren, H. G., 70, (81)  
 Van der Merwe, J. H., (104), 473  
 Van der Pauw, L. J., 549, (574)  
 Van Vliet, K. M., 245, 247, (251)  
 Van der Ziel, A., 433, (434)  
 Vavilov, V. S., 238, (127),  
 (251), (463)  
 Vogel, F. L., 91, 175, (249),  
 365, (535)  
 Vogel, R., 527, 528  
 Volmer, M., 471, 472, 477, (506)  
 Vonnegat, B., (506)
- Wagner, R. S., 103, (104)  
 Wakefield, J., (249)  
 Walker, (82)  
 Wallis, G., 533  
 Walton, D., 477, (506)  
 Wang, C. C., (507)  
 Watkins, G. D., (82), (538)  
 Waxman, A., (459)  
 Wegener, H. A. R., (144), (250),  
 (281), 367, (382), (393)  
 Weimer, P. K., (459), (508)  
 Weinreich, O. A., (127), 271, (281),  
 (364), (414), (434)  
 Weiss, H., (326)  
 Weisskopf, V., 62, 70, (81)  
 Weitz, S., (575), (599)  
 Welker, H., (127)  
 Wertheim, G. K., 230, (249), (250)  
 Westbrook, J. H., (405)  
 Whelan, M. V., 446, (459)  
 White, T. G., 167, (171)  
 White, W. B., (508)  
 Williams, V. F., (463), (507)  
 Willis, J. B., (249)  
 Wilson, W. B., 519, (534)  
 Witt, A. F., (506)  
 Wolff, G. A., (508)  
 Woo, T. C., (506)  
 Wrigley, C., (507)
- Yamaguchi, J., 278, (281), 307, (312),  
 314, (325), 335, (339), (535)  
 Yeh, T. H., (507)  
 Yu, K. K., 243, 247, (249), (251)
- Zaininger, K. H., (507)  
 Zastrow, R. L., (414)  
 Zener, C., 53  
 Zhirnov, A. A., (326)  
 Ziman, J. M., 148, (171)

## Subject Index

- $\alpha$ -dislocation, 168, 169, 277, 379, 461
- absorbate diffusion length, 500
- absorption processes, 239
- absorption tail (slope), 242
- acceptor dislocation, 174
- acoustical branch, 9
- activation energy, 46
- additional local modes, 12
- adhesive forces, 496
- allowed energy value, 54
- alternating dilation-compression zones, 393
- amorphous conduction, 521
- amorphous semiconductors, 509, 511
- amphoteric impurity, 113
- Andrate-creep, 483
- anisotropic effects, 175, 190
- anisotropy of conduction, 454
- annealing steps, 482, 505
- annealing process, 485
- anomalies in the spectral response, 355
- anomalous lattice wave coupling, 37
- anomalous magneto-resistance, 314
- apparent activation energy, 398
- apparent lifetime, 330
- area state density, 218
- asymmetric dislocation tensor, 108
- atomic impact, 111
- atomic misfit, 85
- augmented plane-wave method (APW), 153
- autodoping, 492
- avalanche breakdown, 287
- avalanche multiplication, 56
- average impurity spacing, 146
- average transition probability, 61
- $\beta$ -dislocation, 168, 169, 277, 379, 461
- band gap narrowing, 158
- band gap widening, 158
- band tail states, 241
- barrier height, 246, 350, 351
- barrier potential, 283
- barrier tunneling, 233
- base current modulation, 433
- Becker-Döring frequency, 470
- Beryllium oxide, 487
- bias dependence of the optical frequency response, 415
- bicrystal, 155
- bicrystal characteristics, 118
- bicrystal field effect, 344, 346, 345, 347
- bicrystal growth, 386
- bicrystal photocell, 409
- bicrystal seed, 370
- bicrystal sheet in stress-strain transducers, 439
- bicrystal transistor, 431
- binding energy, 403
- Bloch-Grüneisen formula, 279
- Bloch wave function, 18, 146, 510

- Bloch wave function superposition, 220  
 Bohr radius, 231  
 Boltzmann approximation, 216  
 Boltzmann statistics, 215  
 Born's model, 8  
 Bragg condition, 13  
 Bravais lattice, 13  
 breakdown technique (of resistivity measurements), 557  
 Brillouin scattering, 39  
 Brillouin zone, 12, 13, 14, 22, 23, 24, 159  
 Brooks-Herring formula (scattering), 146  
 broadened optical reflectivity, 511  
 bulk modulus (reciprocal compressibility), 42  
 Burgers' vector (cycle), 84, 105, 106, 94, 128, 130, 131, 161, 168, 285, 365, 438, 301  
  
 cadmium sulfide films, 451  
 cantilever deflection, 481  
 capacitance (of grain boundary), 336  
 capture cross section, 225, 230  
 capture probability (of minority carriers), 414  
 capture radius, 230  
 capture rate, 224, 230, 302, 465  
 carrier density, 540  
 carrier mobility, 45  
 carrier multiplication, 326  
 carrier removal rate, 118  
 carrier transport phenomena, 173, 193  
 cascade process, 230, 232, 235  
 catalytic case of nucleation, 471  
 catastrophic failures, 454  
 channel conduction, 509, 521  
 characteristic impedance, 176  
 charge cloud extension, 231  
 charged centers, 64, 70, 71, 146  
 charge imbalance, 79  
 charge redistribution, 146  
 chemical changes (epitaxy), 476  
 chemical potential, 58  
 circular space charge, 199  
 cis-acceptor, 33, 160  
 Clausius-Mosotti formula, 503  
 climb of dislocations, 74  
 closely spaced surface bonds, 264  
 closure failure, 84, 94, 105  
 clusters, 70  
 clustering of atoms, 480  
 clustering of vacancies, 93  
 coalescing zones, 24  
 coevaporation, 489  
 coherency energy, 252  
 coherency of growth, 92  
 cohesive forces, 480, 496  
 collapsed Brillouin zones, 24  
 collimated beam, 500  
 collinear array of probes, 552  
 color-centers, 70  
 compatibility equation, 87  
 compensating current, 593  
 compensation, 489  
 complete degeneracy, 278  
 complete shells, 79  
 composite vectorial  
     displacements, 128  
 compound formation in situ, 504  
 compression/dilation, 65, 119, 134, 142  
 concentration perfection, 78  
 conductivity by hopping, 514  
 contact potential, 166, 167, 278  
 contaminated surface layer, 470  
 continuity equation, 256  
 controlled growth (of  
     dislocations), 365  
 Conwell-Weisskopf scattering  
     formula, 62, 70, 146  
 coordination (primary, tertiary,  
     etc.), 98  
 cophase-contraphase movement, 9  
 copper accumulation, 401  
 coring (crystal growth), 443  
 Cottrell atmosphere, 3, 174, 227  
 covalent bonding, 72  
 crack (surface), 394  
 crysoberyl, 486, 487

- critical cyclotron field, 317
- critical filament thickness, 526
- critical voltage, 515, 524
- crystal field forces, 48
- crystal momentum, 18, 41, 511
- crystal pulling fixture, 387
- crystal quality control, 442
- curved-up valence band, 264
- cyclic path (trochoidal), 317
- cyclic twins, 150
- cyclotron radius, 316, 319
- cyclotron resonance, 71, 318, 539
- cyclotron frequency, 316
- cyclotron frequency-relaxation time product, 317
- Czochralski equipment, 282
- Czochralski for GaAs, 238
- Czochralski growth method, 98, 169, 444
- d-p*-electrons, 519
- dangling bond, 3, 22, 33, 57, 70, 160
- dangling bond acceptor, 514
- dangling bond array, 4
- dangling bond density, 93
- dangling bond line, 176
- dangling bond spacing, 278
- dangling bond states, 351
- DeBroglie equation, 26
- DeBroglie wavelength, 47, 70
- Debye temperature, 530
- decay curve, 269
- deep levels, 489
- defect clusters, 148
- defect energy levels, 121, 122
- deformable ion, 43
- deformation by torsion, 366
- deformation potentials, 42, 148, 158
- degeneracy, 58
- degeneracy factor, 310
- degenerate channel conduction, 3
- degenerate core, 209
- degradation (laser), 237
- DeHaas-Van Alphen oscillations, 317
- Dember voltage, 589
- densely packed dislocations, 214
- density gap model, 524
- density of strain energy, 85
- depletion-layer-width-impurity-concentration relation, 557
- depletion mode (Gunn oscillator), 466
- deposition temperature cycling, 505
- destructive irradiation level, 119
- detailed balance, 241
- device performance, 442
- device reproducibility, 442
- device yield, 442
- Dexter-Seitz formula, 310
- diamond, 486
- difference in expansion coefficient, 477
- differential capacitance method, 559
- diffuse scattering, 323
- diffusion, block-, 399
  - coefficient-, 403
  - peaks-, 399
  - in pipes-, 399
  - preferential-, 399
- dilation region, 119, 143
- dilation transitions, 37, 236
- dilation zone, 37
- dipole layer, 81
- directional growth, 492
- direct transition, 37, 236
- dislocation agglomerations (lineage), 448
- dislocation array (plane), 64, 175, 176
- dislocation (bent), 181
- dislocation capture, 228
- dislocation climb, 365
- dislocation core radius, 109
- dislocation density, 473, 475, 476
- dislocation field effect transistor, 426
- dislocation free crystals, 444
- dislocation misfit area, 286
- dislocation occupation factor, 215
- dislocation plane, 143
- dislocation scattering, 65, 186, 190
- dislocation space charge cylinder, 71
- dislocation space charge pipe, 64, 173, 185
- dislocation spacing, 301, 474

- dislocation tangles, 367
- disordered lattice structures, 394
- dispersion center, 39
- dispersion relation, 11
- displacement characteristics, 354
- displacement energy, 117, 128
- disregistry (epitaxy), 473
- disrupted bond, 110, 43
- distance of dislocations, 161
- distorted surface bond, 211
- distortion factor, 187
- disturbed region, 132
- disturbed screw dislocation, 181
- divacancy, 125, 537
- doping fluctuations, 466
- double seed technique, 367, 368
- drop model, 471
  
- edge dislocation, 129, 157
- effective charge carrier concentration
  - in grain boundaries, 310
- effective diffusion constant, 178
- effective hole mass, 46
- effective mass, 47, 510
- effective mobility, 179, 180
- effective momentum, 220
- effective state density, 58, 510
- eigenfunction, 231
- Einstein relation, 591
- elastance coefficients, 131
- elastance tensor, 131
- elastic displacements, 84
- elastic-plastic-solid range, 480, 482
- elastic scattering, 39
- electrical properties (of
  - dislocations), 145
- electroluminescence, 240
- electron beam recrystallization, 492
- electron beam scanning, 194
- electron capture, 227
- electron depletion, 184
- electron distribution, 186
- electronic sublattice, 81
- electronic width (of a grain
  - boundary), 276
- electron-probe microanalysis, 461
  
- electron wave package, 12
- electrostatic focussing, 498
- electrostatic interaction, 215
- emission coefficient, 228
- empty site, 160
- energy contours, 51
- energy cusps, 100
- energy shell, 60
- energy surface, 50
- equivalent noise source, 425
- etch pit micrograph, 56
- Ettinghausen effect, 602
- Ettinghausen-Nernst effect, 603
- Euler's constant, 166
- enthalpy (Be), 486
- evanescent parts to the wave
  - function, 264
- excess charge of holes (trapped
  - at dislocations), 229
- exchange forces, 79
- excited capture, 230
- excited states of dislocations, 231
- excited states, 230, 240
- exciton, 69
- exhaustion creep, 483
- expansion coefficient, 477, 480
- extension of photoresponse, 355
- extension of spectral response, 355
- extra-half plane, 128
  
- Fabry-Perot cavity, 514
- Fankuchen's equiinclination
  - method, 387
- Fan's model, 303
- fast photoconductors, 409
- Fermi distribution, 161, 164
- Fermi level, 113
- Fermi statistics, 215, 312
- FET (devices), 182, 450, 488
- field acceleration (in dislocation
  - pipes), 240
- field assisted localized tunneling, 55
- field effect transistor, 340, 441
- field effect transistors (MOS,
  - FET), 450
- field induced recombination, 260

- field induced dipole ordering, 532
- field ionization, 56
- field ordering, 521
- filament of degenerate material, 189, 523
- filling factor, 160, 218, 300
- filling of the *p*-orbitals, 379
- first-order perturbation theory, 146
- Fisher-Whipple diffusion theory, 395
- Fisher-Whipple formation, 401
- floating zone (crystal growth), 444
- Floquet's theorem, 26
- flow control electrode, 120
- flow pattern (impurity at grain boundaries), 143
- forces between dislocations, 70
- forest-dislocations, 367
- four point probe method, 542, 553
- fractional occupancy, 246
- fractional recrystallization, 401
- Frank's formula, 106, 107, 108
- Franz-Keldysh-shift, 420
- Fraunhofer diffraction pattern, 477
- free-energy difference (epitaxy), 472
- free energy of a dislocation, 70
- free energy of formation (epitaxy), 472
- Frenkel defect, 73, 110, 112, 113
- Frenkel pair, 112
- frequency hole, 24
- frequency modulated signal, 425
- frequency of nuclei formation, 470
- frequency response (bicrystal photocells), 409
- frozen-in energy, 96
- full site, 160
- Gallium arsenide, 167, 457
- galvanomagnetomorphic effects, 317, 319
- gate voltage, 120
- Geiger counter, 387
- generation rate of carriers, 229
- generation recombination noise, 242
- germanium bicrystals, 282, 287
- germanium grain boundary barriers, 282
- giant trap, 230
- glassy interface, 485
- glassy layer, 103
- glide planes, 365
- gliding twin axis, 148
- goniometer, 387
- grain boundary, 119
- grain boundary amplifier, 428
- grain boundary barriers, 282
- grain boundary barrier height, 293
- grain boundary conductance, 265
- grain boundary diffusion, 267, 393
- grain boundary energy, 134
- grain boundary field effect (transistor), 120
- grain boundary orientation (tangent relations), 376
- grain boundary photocell, 409
- grain boundary plane resistance, 428
- grain boundary pole, 375
- grain boundary scattering parameters, 323
- grain boundary space charge layer, 314
- grain boundary surface states, 291
- Green function method, 549
- group velocity, 57
- grown-in dislocations, 450
- growth plane, 374
- Hall drift-mobility ratio, 186
- Hall measurements, 44, 313, 539
- Hall mobility, 451
- Hall voltage, 120, 314
- Hankel functions, 333
- hardened structures, 119
- harmonic oscillator, 215
- Haynes-Shockley method (lifetime), 327, 583
- healing of defects, 366
- heat generated channel, 522
- heat of fusion, 494
- heavy holes, 51
- heterodyning of an optical signal, 422
- heteroepitaxial process, 442



- heteroepitaxy, 367, 454, 469
- high conducting state, 515
- high conductivity path, 523
- higher order twinning, 149
- high field domain breakup, 464
- high frequency extension of the photoresponse, 415
- high frequency performance, 426
- high preferential diffusion, 394
- hole accumulation, 261
- hole sink, 64
- homoepitaxial process, 442, 469
- homogeneity measurements, 540, 575, 577
- homopolar lattice, 78
- Hooke's law, 84, 107, 108
- hook effect, 326
- hopping charge transfer, 519
- hopping theory, 521
- hydride dopant sources, 492
- hybridized bond, 72, 204
- hydrogenic approximation, 519
- hydrostatic pressure, 481
  
- identity translations, 128
- imparted energy, 115
- impenetrable space charge cylinder, 64, 183
- imperfect dislocation, 128
- impurity atmosphere, 174, 404
- impurity band conduction, 521
- impurity cluster, 70
- impurity clustering, 448
- impurity environment, 174
- impurity penetration, 140
- impurity scattering, 62
- impurity vacancy configurations, 124
- inclusions, 70
- incomplete orbitals, 73
- indirect transition, 236
- indium-antimonide bicrystals, 3, 277, 379
- indium-antimonide grain boundaries, 379
- individual shear stress, 140
- in-grown defects, 449
  
- inhomogeneity (electron distribution), 186
- injection efficiency, 455
- inner surface structures, 262
- in situ measurements, 542
- in situ observations, 478
- insulated breakdown, 519
- integrated flux rate, 116, 118
- integrated neutron dose, 118
- interatomic bond deformation, 99
- interatomic bond distortion, 97
- interaction energy, 102, 232
- interaction between defect and impurity, 112, 113
- interband levels, 56, 461
- interband states, 409
- interband transitions, 56
- interband tunneling, 56
- interface dislocations, 457
- interface irregularities, 464
- interfacial energy, 470
- intervalley electron transfer, 463
- ion-beam deposition, 498
- ion-gun, 500
- ionic crystals, 167
- ionic radii, 448
- ion implantation, 125, 454
- ion sputtering process, 498
- ionized centers, 56
- irradiation of semiconductors, 112
- irreversible changes, 515
- island density (epitaxy), 480
- isolated dislocation lines, 162
- isomorphous case (epitaxy), 469, 470
- isomorphous growth, 505
  
- James-Lark-Horovitz model, 73
- jumping frequency (nuclei in epitaxy), 478
- junction delineation, 462
  
- Kikoin method (lifetime), 588
- Kikoin voltage, 588, 590, 592, 593
- Kronecker's  $\delta$ , 14, 108

- Lame's constant, 108
- lap-repeat method, 549
- large angle boundaries, 394
- large area growth, 495
- laser recrystallization, 505
- lasing inhomogeneities, 460
- lateral bias, 207
- lateral film growth, 498
- lateral overlap (of dislocations), 162, 174
- lateral transistor, 182
- lateral twin, 149
- laterally moving liquid-solid interface, 495
- lattice compression, 64
- lattice deformation, 83
- lattice dilation, 64
- lattice mismatch (epitaxy), 252, 462, 474
- lattice mobility, 308
- lattice modulated amplitude, 28, 513
- lattice slip, 154
- lattice strain, 79
- lattice translation vector, 128
- lattice vibrational modes, 7
- Laue backreflection technique, 375
- Laue diffraction, 18
- left-right discrimination, 353
- lifetime (change), 174
- lifetime measurements, 540, 580
- light emitting structures, 457
- light injection scanning, 579
- light-pulse decay method, 594
- light spot probing, 194
- limiting capacity of the barrier layer, 561
- lineage, 91, 136
- lineage boundary, 252, 256, 368
- lineage plane, 254
- linearly repetitive steps, 160
- linear photovoltage-bias dependence, 417
- line charge, 189
- line imperfection, 70
- liquid-solid interface, 493
- liquid-solid vapor growth, 469
- localized barrier, 195
- localized defect, 110
- localized deposition, 498
- localized liquid-solid growth mechanism, 495
- localized microplasma breakdown, 461
- localized remelting, 492
- localized spin ordering, 321
- localized state, 1, 512, 514
- localized transition process, 514
- localizing sensitivity, 406
- local lifetime inhomogeneities, 579
- locked-in Wurtzite, 363
- longitudinal stress, 436
- longitudinal stress gage factor, 435
- long range order, 509
- low angle grain boundary, 92, 261
- low energy boundary, 400
- low energy cusps (in grain boundary energy versus  $\theta$ ), 151
- low energy rotation (lattice), 392
- low threshold spots, 457
- LSI (large scale integration), 444
- macroscopic resistivity gradients, 463
- magnetoresistance, 4, 190, 313
  - negative, 321
  - oscillatory, 321
- magnetoresistance effects, 605
- magnetostatics, 108
- MASER-receiver, 431
- mated surfaces, 262
- Mathieu's equation, 26
- maximum binding energy (foreign atom), 401
- Maxwellian statistics, 216, 312
- mechanical properties of dislocation, 128
- mean collision time, 65
- mean free scattering time, 65
- mean free time, 60
- mean impulse (Bloch wave), 57
- mean square noise current, 243
- medium angle grain boundary, 92, 143, 261, 283, 394
- metastable equilibrium, 76

- microalloy dots, 307
- microcracking, 4, 93, 103, 142, 162
  - 368, 394, 403
- micrometrical applications (of grain boundaries), 406
- microminiaturization, 510
- microplasma, 56, 181
- microscopic doping changes, 468
- microscopic order, 514, 519
- microscopic spatial fluctuations, 464
- microscopic transport
  - phenomena, 519
- microwave generation, 468
- microwave reflectance method, 574
- microwave reflection, 569
- microwave transmission, 569
- microzone melting, 492
- microtwinning region, 199
- midband levels, 409
- midband recombination centers, 79
  - 234, 239, 462
- minimum energy (statistics), 215
- minimum radiative detectable
  - power, 355
- minority carrier pulse method, 583
- misfit angle, 151
- mismatch of thermal expansion
  - coefficients, 367
- mixer diodes, 488
- mobile dislocation, 139
- mobility (temperature dependence of), 307
- mobility (due to ionized impurities), 308
- mobility (due to scattering in dislocation stress field), 308
- mobility gap, 530
- mobility measurements, 540, 600, 609
- mobility poison, 78
- mobility ratio, 465
- mobility reduction, 489
- mobility versus temperature, 311
- modified Brillouin zone scheme, 28
- modified Bridgman method, 496
- molten channel, 523
- monatomic linear chain, 6
- monocrystallizing step, 492
- monomolecular interface, 495
- mosaic structure (of films), 541
- MOS capacitance method, 595
- MOS devices, 611
- MOS technology, 515
- MOS transistors, 450, 454, 515
- Mott-Nabarro-creep, 483
- movable slotted mask deposition, 496
- moving charge deflection, 146
- moving mask deposition, 487
- multioriented crystal sheet, 437
- multiple Bragg reflections, 264
- multiple dislocations, 96
- multiple reflections, 254
- multiple twins, 150
- multiplicity of SiO-bonds, 484
- multiplicity of (Si<sub>x</sub>O<sub>y</sub>) chains, 484
- multicontacts, 565
- multi-seed crystals, 370
- multistage annealing, 482
- nearest neighbor violations, 96
- near zero activation energy, 526
- negative core charge, 204, 261
- negative differential conductivity, 465
- negative differential mobility, 463
- negative effective mass, 46, 52
- negative magnetoresistance, 314
- negative mobility, 466
- neutral plane (axis), 365
- neutral scattering, 145, 485, 489
- neutron irradiation, 115
- noise fluctuations, 463
- noise (mean square noise current), 243
- noise (recombination-generation), 242
- nonoxidic glass, 519, 521
- non-isomorphous case (epitaxy), 469
- normal Gunn mode, 467
- nuclei alignment, 495
- nuclei merger, 480
- nuclei misalignment (epitaxy), 477, 252
- nuclear bombardment, 112
- nucleation of dislocations, 483
- nucleation phase, 480
- Nye's equation, 107, 108

- one phonon transition, 230
- optical branch, 9
- optical frequency response, 406
- orientational misfit, 140
- orientation of bicrystals, 371
- oriented overgrowth, 471
- orthogonal fields, 515
- orthogonalized-plane-wave
  - method (OPW), 153
- orthogonal pipe field, 180
- orthogonal stress, 131
- oscillatory effects in thin films, 320
- oscillatory magnetoresistance, 314, 317, 322
- outdiffusion, 468
- overlapping dilation and
  - compression regions, 252
- overlapping dislocation pipes, 162
- overlapping wave functions, 273, 525
- overlap integral, 519
- oxide chains, 519
- oxidic glasses, 518
- paired (non-closed) configurations
  - of stacking faults, 485
- pairing (of dangling bonds), 270
- parallel-transversal - parallel-longitudinal magnetoresistance, 314
- paramagnetic resonance (spin resonance), 71
- partial dislocations, 76, 96, 148, 153
- particle clustering, 504
- Pauling-radius, 489
- Peltier effect, 602, 603
- Peltier heating, 493, 495
- perfect dislocation, 128
- perfect grain boundary, 89
- perfection of a grain boundary, 382
- periodic fault, 77
- periodicity deviations, 510
- periodicity function, 54
- periodicity perturbations, 19
- periodic substructure, 24
- perturbing potential, 270
- phase boundary, 70
- phase shift, 176
- phase velocity, 6
- phonon assisted hopping, 530
- phonon assisted process, 236
- phonon energy, 37
- phonon spectrum, 37
- photoconductive mode, 357
- photoconductivity, 120, 267
- photoconductors, 463
- photoelectric applications, 406
- photoelectric effects, 349
- photoelectric frequency
  - converters, 414
- photoelectric sensitivity, 353, 406
- photoluminescence, 241
- photo-magneto-electric
  - method, 580, 588
- photo-micrograph, 252
- photon energy, 66
- photoresponse, 357
- photoresponse measurements, 307, 352
- photosensitivity extension, 122
- photovoltage, 329
- photovoltage reversal, 283
- photovoltaic junction detector, 417
- piezo-resistance coefficients, 435, 436
- piled-up dislocations, 366
- pipe diffusion, 399
- pipe orientation, 185
- planar transistor, 182
- plane deformation theory, 130
- plane wave scattering, 148
- plastically deformed crystal, 173, 366
- plastic deformation, 365
- plastic flow, 70, 483
- plasticity range, 483
- point defects, 64, 69, 110
- point imperfections, 146
- Poisson's constant, 108, 109, 131, 154
- Poisson's equation, 223, 298
- polar lattice, 78
- polar scattering, 146
- polarized optical absorption, 71
- polaron formation, 521
- polaron theory, 529
- polygonization, 365, 366
- polymorphism, 484

- potential plot, 286
- potential well, 523
- precipitates, 461
- precision production of bicrystals, 367
- preferential diffusion, 399
- preferred pipe conduction, 312
- preferred recombination, 57
- prenucleation phase, 480
- probability of band penetration, 54
- process induced dislocations, 442, 449
- prolonged heat treatment, 485
- propagation velocity, 6
- pseudogap, 524
- pseudomomentum vector, 39
- p-type channel, 267
- pulled bicrystal, 370
- pulsed deposition, 480
- punched emitter-collector junctions, 488
- quantum efficiency, 352
- quantum-mechanical selection rule, 37
- quantum noise, 425
- Quasi-Fermi level, 36
- quasi-free carrier, 44
- quasi-long range order, 523, 524
- quasi-periodic Bloch waves, 513
- radial (and longitudinal) resistivity gradient, 442
- radial charge density, 224
- radiation damage, 110, 114, 115, 537
- radiation hardening, 115
- radiation induced defect, 113
- radiative recombination, 78, 234, 241, 362
- radiative rate constant, 241
- radius (of space charge cylinders), 218
- randomized charge centers, 146
- randomized doping, 465
- Rayleigh-scattering, 145
- reactive gas loading, 500
- Read-Shockley energy expressions, 90, 286, 395
- reciprocal lattice, 13
- recombination, 236
- recombination flux, 457
- recombination light, 237
- recombination radiation efficiency, 461
- recombination velocity, 120, 256
- recovery processes, 537
- reduced resistivity, 271
- reflection coefficient (of carriers on dislocations), 254
- Reiss' formula, 494
- relative change in density, 145
- relative change of the modulus of rigidity, 145
- relative resistance change, 436
- relaxation time, 61, 64
- relaxation time relations, 240
- repaired bonds, 374
- repaired lattice, 99, 283
- repaired lattice joints, 283
- resistivity anisotropy, 305
- resistivity measurements, 539
- resistivity profiles, 577
- response edge (photoelectric), 424
- Righi-Leduc effect, 603
- rod structure (model) (diffusion theory), 398
- rotational diffusion (epitaxy), 478
- rotational misfit, 477
- Sah-Noyce-Shockley formula, 446
- sapphire, 486, 487
- sapphire orientation, 487
- scanning electron replica, 313
- scanning oscillator technique (SOT), 445
- scattering angle, 187
- scattering cross section, 146, 148
- scattering factor, 187
- scattering influence, 64, 194
- scattering model, 147, 190
- scattering parameter, 61
- scattering sources, 57
- Schottky barrier layer, 209, 487, 514, 524
- Schottky defect, 110

- Schottky double barrier, 296  
 Schottky process, 73  
 scratch, 199  
 Schrödinger equation, 53, 264,  
     510, 512  
 screening, 162, 241  
 screw dislocation, 129, 146, 156  
 SEB-scanning electron beam, 194  
 Seebeck emf, 602  
 selenides, 518  
 self consistent field potential, 146  
 self energy, 102  
 self stabilizing energy, 91  
 semiconductor plasma devices, 463  
 semiconductor laser degradation, 460  
 semiconductor layers on  
     insulator substrates, 594  
 semioordered structure, 523  
 sensitivity (photoelectric)  
     extensions, 358, 359  
 shared bonding, 72  
 shear stress (at dislocation), 128, 130  
 sheet conductance, 273, 275  
 sheet conduction, 426  
 sheet characteristics, 342  
 Shockley-form of saturation  
     current, 418, 419  
 Shockley-Read theory, 222, 225, 226,  
     243, 247  
 short range order, 509  
 signal attenuation, 177  
 silica, 487  
 silicon bicrystals, 282  
 silicon (as substrate), 486  
 silicon on sapphire, 150, 252  
 SiO, SiO<sub>2</sub>-complexes, 282  
 SiO-stretching bond vibrations, 484  
 slightly overlapping wave  
     functions, 524  
 slip boundary, 77  
 slip vector, 129  
 smeared-out conduction (valence)  
     band edge, 511  
 smoothing of dislocation pipes, 311  
 sodium chloride crystals, 168  
 soft breakdown, 56  
 source-drain channel, 426  
 space charge cylinder, 163  
 space charge cylinder model, 305  
 space charge extension, 209  
 space charge fluctuations, 466  
 space charge pipe radius, 300  
 space charge pipe (tube), 71, 176, 199,  
     157, 163, 461  
 space charge potential, 165  
 spacing (between added electrons), 208  
 s-p-orbitals, 169  
 spectral density (current  
     fluctuations), 246  
 spectral distribution of  
     photocurrent, 420  
 spectral response, 352  
 spectral response change, 420  
 specular reflection, 323  
 spike behavior (diffusion), 394  
 spike velocity, 395, 403, 404  
 spiking phenomenon, 454  
 spin resonance, 120  
 spinel, 486, 487  
 spiral ramp, 96, 154  
 spreading resistance technique, 564  
 sputtering, 497  
 stacking faults, 70, 77, 96, 152,  
     153, 485  
 stationary high field domain, 466  
 steady state (lifetime) measurement  
     method, 580, 585  
 steep impurity gradient, 444  
 stereographic projection, 374  
 stoichiometric combinations, 518  
 stoichiometric variations, 577  
 stoichiometric triangle, 521  
 strain-induced dislocations, 482  
 strain of nuclei, 471  
 strain-propelled cluster centers, 446  
 striations (crystal), 461  
 striations in epitaxial growth, 468  
 strength of materials, 70  
 stress-component overlap, 437  
 stress jumping, 445  
 stress-strain transducers, 434, 463  
 stress distribution, 87

- structural perfection, 539
- subsurface condition, 194, 195
- surface effects, 264
- surface energy, 477
- surface imperfections, 70
- surface potential, 194, 210
- surface state band, 264
- surface states, 340
- superlattice, 149
- supersaturation, 400
- switching device, 515
- switching path, 528
- symmetric cubic structure, 434
- symmetric grain boundary, 106, 204, 283
- Tamm level, 264
- tellurides, 518
- temperature activated hopping, 511
- temperature independent conductivity, 426
- tensor (dislocation density), 541, 594, 442
- tetrahedral coordination, 484
- tetrahedral radii, 448
- tetrahedral formation, 485
- thermal effects (in Hall measurements), 603
- thermal expansion coefficient, 475, 480
- thermally induced phase transitions, 523
- thermal scattering, 190
- thermal vibrations, 62
- thin film conductivity, 320
- thin film deposition, 498, 499
- thin film magnetoresistance, 322
- thin film resistivity, 549
- thin films, 541, 594, 442
- Thomas-Fermi method, 278
- threshold energy (irradiation), 113
- threshold value (resistivity), 111
- tight binding method, 363
- tilted bands, 56
- tilt process, 103
- tracking, 406
- transacceptor, 33
- transconductance, 348, 429
- transient lifetime methods, 580
- transient radiation effects, 123
- transistor injection layer, 282
- transition coefficients, 246
- transition metal oxides, 528
- transition process, 246
- translational activation energy, 478
- translational misfit, 477
- transmission-electron-microscopy, 461
- transmission line model, 176
- transversal barrier measurements, 282
- transversal magnetoresistance, 314, 315, 322
- transversal stress, 436
- trap density, 592
- trapping level, 228
- trapping time, 179
- traveling liquid-solid interface, 498
- traveling solvent growth, 495
- traveling solvent recrystallization, 492
- triangular mask growth, 496
- tunnel contacts, 530
- tunnel diodes, 488
- tunnel effects, 514
- tunnel emitters, 515
- tunnel transistor, 515
- twin axis, 98
- twin boundary, 70, 77, 283
- twin configurations, 100, 148
- twin (cyclic), 98
- twist error, 98
- twist process, 103
- two point probe, 256
- two dimensional deposition, 492
- two dimensional hetero-deposition, 492
- two particle Coulomb interaction interaction, 241
- two source deposition, 504
- ultra-high vacuum deposition, 492
- ultra-violet absorption, 120
- unipolar transistor, 340
- untrapped excess carriers, 540

- vacancy-impurity cluster, 126
- vacancy interstitial pairs, 124
- vacancy pairs, 70
- vacuum deposition, 491
- Van der Pauw method, 549
- Van Vliet's admittance functions, 245
- valence band peak, 231
- vapor deposition, 470, 492
- vapor-liquid-solid moving mask  
    growth, 496
- variable grain boundary state  
    density, 300
- velocity of interface motion, 494
- velocity of space charge waves, 465
- velocity vector, 61
- vibrational dislocation level, 232
- vibrational energy, 66
- vibrational fine structure, 12
- vibrational modes, 7, 9, 37, 110
- viscous yield, 481, 482
- voids, 70, 173
- Volterra derivation, 85, 102
- volume deformation, 362
- volume densities, 161
- volume imperfections, 70
- Wagner-Schottky type I-V  
    characteristics, 417
- wall of dislocations, 138
- Wannier-functions, 220
- wave function overlap, 81, 210, 216,  
    278, 448, 519
- wave number, 5
- wave vector adjustment, 39
- WBK-solutions, 220
- web-dendrite crystals, 445
- x-ray diffraction topograph, 445
- Zener's solution, 54
- zero-bias barrier resistance, 566
- zinc blende structure, 168
- zone coalescence, 28
- zone leveling equipment, 496
- zone refining, 493





*Books of Related Interest  
from Wiley-Interscience—*

## PHYSICS OF SEMICONDUCTOR DEVICES

By S. M. SZE

"This book on electronic devices should prove very appealing to solid-state physicists. In every case the theory that underlies the mechanism under discussion is elaborated with sufficient detail and references so that an interested reader may work out the complete picture for himself. In addition, there are many features that one does not usually find in a physics book, making this book a joy to read... there are untold numbers of diagrams illustrating problems; ample tabular data is available, and technical glossaries. These become particularly necessary in view of an avalanche of new devices having exotic names...."

—*Physics Today*

"... the book should be a highly useful reference to research scientists and engineers in the solid state field and a valuable source book for students."

—*Science*

1969 812 pages

## INTRODUCTORY QUANTUM MECHANICS FOR THE SOLID STATE

By RICHARD L. LONGINI

*Introductory Quantum Mechanics for the Solid State* describes the basic fundamentals of quantum mechanics for atomic binding and for solids. The use of higher mathematics has been avoided as much as possible, though needed mathematical concepts are introduced. Linear aspects are emphasized and the Fermi-Dirac distribution is derived on the basis of dynamics in order to convey the idea that equilibrium phenomena are the result of dynamic balances.

1971 157 pages

## THEORY AND APPLICATIONS OF FIELD-EFFECT TRANSISTORS

By RICHARD S. C. COBBOLD

"Deals comprehensively with the theory, fabrication, properties, and application of field effect transistors. Device physics gets strong attention; throughout, the book relates theory to experimental measurements, the performance of real devices, and the restrictions that are usually imposed by fabrication technology."

—*Electronics*

"As a consolidation of published data and reports on the subject of FET's and their applications, this book should provide a helpful adjunct to the libraries of all those who use, specify, or fabricate FET's and the equipment in which they are used."

—*Electronics World*

1970 534 pages

## WILEY-INTERSCIENCE

a division of JOHN WILEY & SONS, Inc.  
605 Third Avenue, New York, N.Y. 10016  
New York • London • Sydney • Toronto

DEFECT  
ELECTRONICS IN  
SEMICONDUCTORS

548.  
642

MAT



Wiley-  
Interscience

ISBN 0 471 57618-2